Understanding Deep Learning

Simon J.D. Prince

February 25, 2023

The most recent version of this document can be found at http://udlbook.com.

I would really appreciate help improving this document. No detail too small! Please mail suggestions, factual inaccuracies, ambiguities, questions, and errata to udlbookmail@gmail.com.

This book is dedicated to Blair, Calvert, Coppola, Ellison, Faulkner, Kerpatenko, Morris, Robinson, Sträussler, Wallace, Waymon, Wojnarowicz, and all the others whose work is perhaps even more important and interesting than deep learning.

Contents

Preface

The history of deep learning is unusual in science. The perseverance of a small cabal of scientists, working over twenty-five years in a seemingly unpromising area, has revolutionized a field and dramatically impacted society. Usually, when researchers investigate an esoteric and apparently impractical corner of science or engineering, it remains just that — esoteric and impractical. However, this was a notable exception. Despite widespread skepticism, the systematic efforts of Yoshua Bengio, Geoff Hinton, Yann LeCun, and others eventually paid off.

The title of this book is "Understanding Deep Learning" to distinguish it from volumes that cover coding and other practical aspects. This text is primarily about the *ideas* that underlie deep learning. The first part of the book introduces deep learning models and discusses how to train them, measure their performance, and improve this performance. The next part considers architectures that are specialized to images, text, and graph data. These chapters require only introductory linear algebra, calculus, and probability and should be accessible to any second-year undergraduate in a quantitative discipline. Subsequent parts of the book tackle generative models and reinforcement learning. These chapters require more knowledge of probability and calculus and target more advanced students.

The title is also partly a joke — *no-one* really understands deep learning at the time of writing. Modern deep networks learn piecewise linear functions with more regions than there are atoms in the universe and can be trained with fewer data examples than model parameters. It is neither obvious that we should be able to fit these functions reliably nor that they should generalize well to new data. The final chapter addresses these and other aspects that are not yet fully understood.

Your time is precious, and I have striven to curate and present the material so you can understand it as efficiently as possible. The main body of each chapter comprises a succinct description of only the most essential ideas, together with accompanying illustrations. The appendices review all mathematical prerequisites, and there should be no need to refer to external material. For readers who wish to delve deeper, each chapter has associated problems, Python notebooks, and notes that summarize the area's history and the latest research.

Writing a book is a lonely, grinding, multiple-year process and is only worthwhile if the volume is widely adopted. If you enjoy reading this or have suggestions for improving it, please contact me via the accompanying website. I would love to hear your thoughts, which will inform and motivate subsequent editions.

Acknowledgements

Writing this book would not have been possible without the generous help and advice of these individuals: Kathryn Hume, Kevin Murphy, Christopher Bishop, Peng Xu, Yann Dubois, Justin Domke, Chris Fletcher, Yanshuai Cao, Wendy Tay, Corey Toler-Franklin, Dmytro Mishkin, Guy McCusker, Daniel Worrall, Paul McIlroy, Roy Amoyal, Austin Anderson, Romero Barata de Morais, Gabriel Harrison, Peter Ball, Alf Muir, David Bryson, Vedika Parulkar, Patryk Lietzau, Jessica Nicholson, Alexa Huxley, Oisin Mac Aodha, Giuseppe Castiglione, Josh Akylbekov, Alex Gougoulaki, Joshua Omilabu, Alister Guenther, Joe Goodier, Logan Wade, Joshua Guenther, Kylan Tobin, Benedict Ellett, Jad Araj, Andrew Glennerster, Giorgos Sfikas, Diya Vibhakar, Sam Mansat-Bhattacharyya, Ben Ross, Ivor Simpson, Amedeo Buonanno, Gaurang Aggarwal, Shakeel Sheikh, Jacob Horton, Felix Rammell, Sasha Luccioni, Akshil Patel, Mark Hudson, Alessandro Gentilini, Kevin Mercier, Krzysztof Lichocki, Chuck Krapf, Tyler Mills, Brian Ha, Chris Kang, Leonardo Viotti, Kai Li, Himan Abdollahpouri, Ari Pakman, Giuseppe Antonio Di Luna, Dan Oneață, Conrad Whiteley, Joseph Santarcangelo, Brad Shook, Gabriel Brostow, Lei He, Ali Satvaty, and Romain Sabathé, Qiang Zhou, Prasanna Vigneswaran, Siqi Zheng, Stephan Grein, Jonas Klesen, and Giovanni Stilo.

I'm particularly grateful to Andrew Fitzgibbon, Daniyar Turmukhambetov, and Konstantinos Derpanis, all of whom provided detailed comments on multiple chapters of the book and whose enthusiasm helped me complete this project. I'd also like to thank Neill Campbell and Özgür Şimşek who hosted me at the University of Bath where I taught a course based on this material for the first time.

Chapter 12 (transformers) and chapter 17 (variational auto-encoders) were first published as blogs for Borealis AI and adapted versions are reproduced here with permission. I am grateful for their support in this endeavor. Chapter 16 (normalizing flows) is loosely based on the review article by Kobyzev et al. (2020) on which I was a co-author.

Chapter 1

Introduction

Artificial intelligence or *AI* is concerned with building systems that simulate intelligent behavior. It encompasses a wide range of approaches, including those based on logic, search, and probabilistic reasoning. *Machine learning* is a subset of AI that learns to make decisions by fitting mathematical models to observed data. This area has seen explosive growth and is now (incorrectly) almost synonymous with the term AI.

A *deep neural network* is a type of machine learning model, and when a deep network is fitted to data, this is referred to as *deep learning*. At the time of writing, deep networks are the most powerful and practical machine learning models and are often encountered in day-to-day life. It is commonplace to translate text from another language using a *natural language processing* algorithm, to search the internet for images of a particular object using a *computer vision* system, or to converse with a digital assistant via a *speech recognition* interface. All of these applications are powered by deep learning.

As the title suggests, this book aims to help a reader new to this field understand the principles behind deep learning. The book is neither terribly theoretical (there are no proofs) nor extremely practical (there is almost no code). The goal is to explain the underlying *ideas*; after consuming this volume, the reader will be able to apply deep learning to novel situations where there is no existing recipe for success.

Machine learning methods can coarsely be divided into three areas: supervised, unsupervised, and reinforcement learning. At the time of writing, the cutting-edge methods in all three areas rely on deep learning (figure 1.1). This introductory chapter describes these three areas at a high level, and this taxonomy is also loosely reflected in the book's organization.

1.1 Supervised learning

Supervised learning models define a mapping from input data to an output prediction. In the following sections, we discuss the inputs, the outputs, the model itself, and what is meant by "learning" a model.

Figure 1.1 Machine learning is an area of artificial intelligence that fits mathematical models to observed data. It can coarsely be divided into supervised learning, unsupervised learning, and reinforcement learning. Deep neural networks contribute to each of these areas.

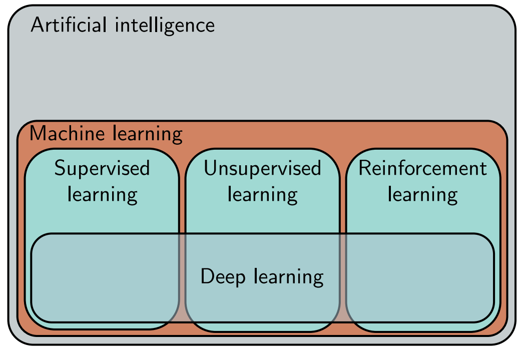

1.1.1 Regression and classification problems

Figure 1.2 depicts several regression and classification problems. In each case, there is a meaningful real-world input (a sentence, a sound file, an image, etc.), and this is encoded as a vector of numbers. This vector forms the model input. The model maps the input to an output vector which is then “translated” back to a meaningful real-world prediction. For now, we focus on the inputs and outputs and treat the model as a black box that ingests a vector of numbers and returns another vector of numbers.

The model in figure 1.2a predicts the price of a house based on input characteristics such as the square footage and the number of bedrooms. This is a *regression* problem because the model returns a continuous number (rather than a category assignment). In contrast, the model in 1.2b takes the chemical structure of a molecule as an input and predicts both the melting and boiling points. This is a *multivariate regression* problem since it predicts more than one number.

The model in figure 1.2c receives a text string containing a restaurant review as input and predicts whether the review is positive or negative. This is a *binary classification* problem because the model attempts to assign the input to one of two categories. The output vector contains the probabilities that the input belongs to each category. Figures 1.2d and 1.2e depict multiclass classification problems. Here, the model assigns the input to one of $N > 2$ categories. In the first case, the input is an audio file, and the model predicts which genre of music it contains. In the second case, the input is an image, and the model predicts which object it contains. In each case, the model returns a vector of size N that contains the probabilities of the N categories.

1.1.2 Inputs

The input data in figure 1.2 varies widely. In the house pricing example, the input is a fixed-length vector containing values that characterize the property. This is an example of *tabular data* because it has no internal structure; if we change the order of the inputs and build a new model, then we expect the model prediction to remain the same.

Conversely, the input in the restaurant review example is a body of text. This may be of variable length depending on the number of words in the review, and here input

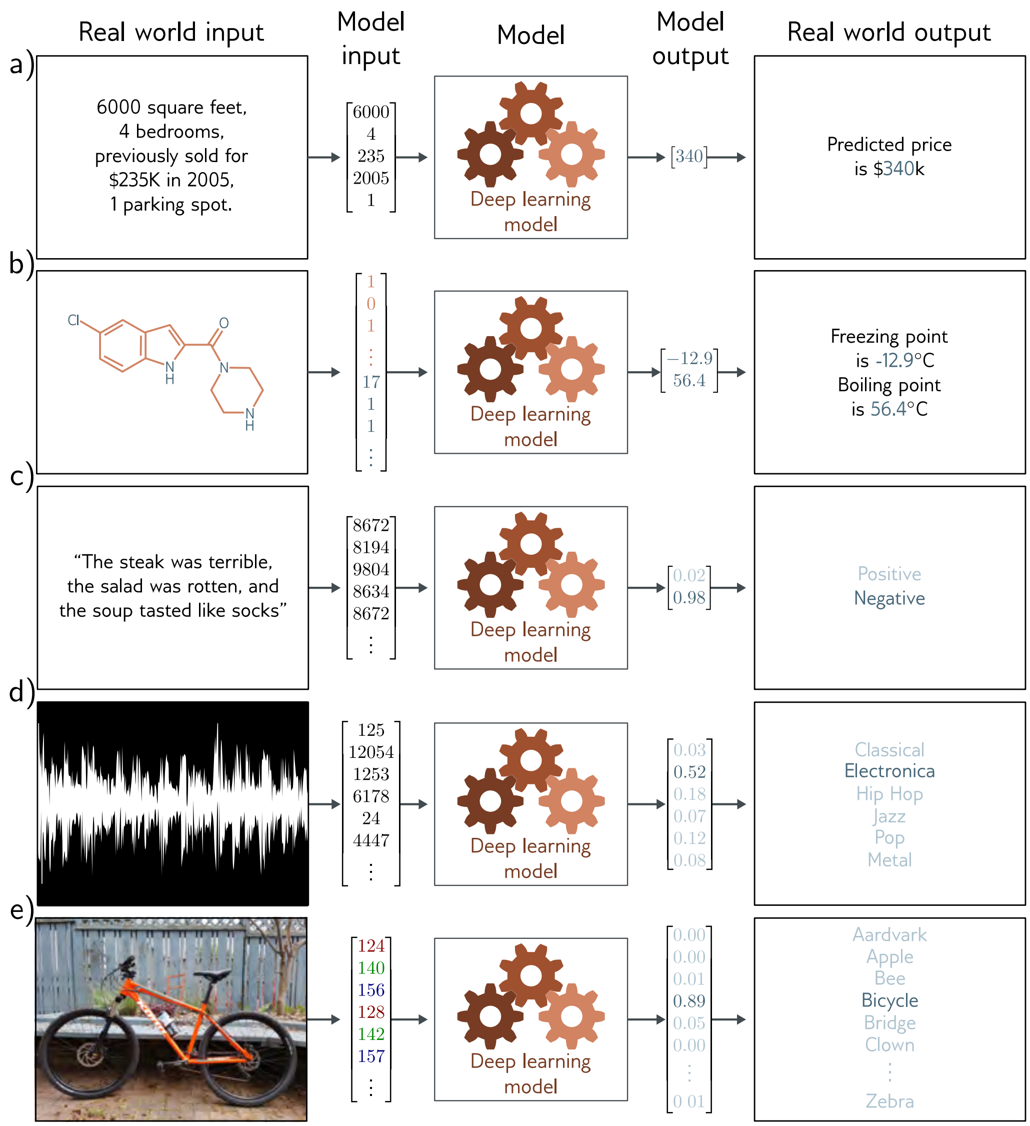

Figure 1.2 Regression and classification problems. a) This *regression* model takes a vector of numbers that characterize a property and predicts its price. b) This *multivariate regression* model takes the structure of a chemical molecule and predicts its melting and boiling points. c) This *binary classification* model takes a restaurant review and classifies it as either positive or negative. d) This *multiclass classification* problem assigns a snippet of audio to one of N genres. e) A second multiclass classification problem in which the model classifies an image according to which of N possible objects that it might contain.

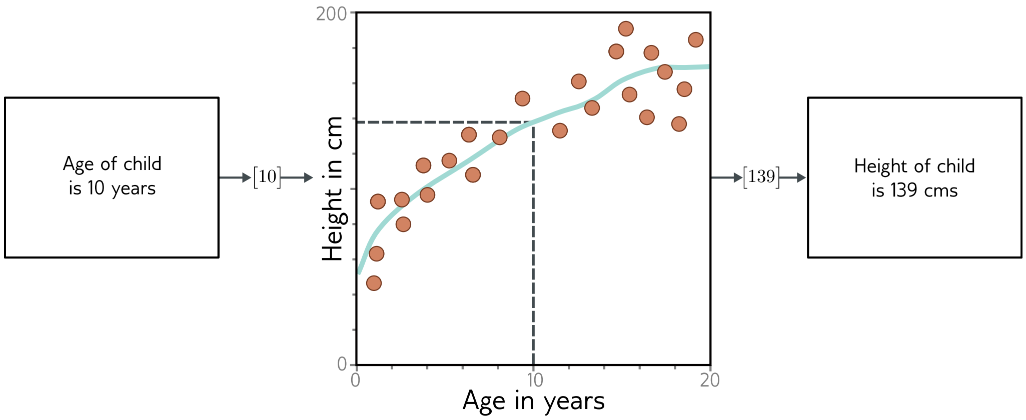

Figure 1.3 Machine learning model. The model represents a family of relationships that relate the input (age of child) to the output (height of child). The particular relationship is chosen using training data, which consists of input/output pairs (orange points). When we train the model, we search through the possible relationships for one that describes the data well. Here, the trained model is the cyan curve and can be used to compute the height for any age.

order is important; *my wife ate the chicken* is not the same as *the chicken ate my wife*. The text must be encoded into numerical form before passing it to the model. Here, we use a fixed vocabulary of size 10,000 and simply concatenate the word indices.

For the music classification example, the input vector might be of fixed size (perhaps a 10-second clip) but is very high-dimensional. Digital audio is usually sampled at 44.1 kHz and represented by 16-bit integers, so a ten-second clip consists of $441,000$ integers. Clearly, supervised learning models will have to be able to process sizeable inputs. The input in the image classification example (which consists of the concatenated RGB values at every pixel) is also enormous. Moreover, its structure is naturally two-dimensional; two pixels above and below one another are closely related, even if they are not adjacent in the input vector.

Finally, consider the input for the model that predicts the melting and boiling points of the molecule. A molecule may contain varying numbers of atoms that can be connected in different ways. In this case, we must pass both the geometric structure of the molecule and the constituent atoms to the model.

1.1.3 Machine learning models

Until now, we have treated the machine learning model as a black box that takes an input vector and returns an output vector. But what exactly is in this black box? Consider a model to predict the height of a child from their age (figure 1.3). The machine learning model is a mathematical equation that describes how the average height varies as a function of age (cyan curve in figure 1.3). When we run the age through this equation, it returns the height. For example, if the age is 10 years, then we predict that the height will be 139 cm.

More precisely, the model represents a family of equations mapping the input to the output (i.e., a family of different cyan curves). The particular equation (curve) is chosen using *training data* (examples of input/output pairs). In figure 1.3, these pairs are represented by the orange points, and we can see that the model (cyan line) describes these data reasonably. When we talk about *training* or *fitting* a model, we mean that we search through the family of possible equations (possible cyan curves) relating input to output to find the one that describes the training data most accurately.

It follows that the models in figure 1.2 require labeled input/output pairs for training. For example, the music classification model would require a large number of audio clips where a human expert had identified the genre of each. These input/output pairs take the role of a teacher or supervisor for the training process, and this gives rise to the term *supervised learning*.

1.1.4 Deep neural networks

This book concerns deep neural networks, which are a particularly useful type of machine learning model. They are equations that can represent an extremely broad family of relationships between input and output, and where it is particularly easy to search through this family to find the relationship that describes the training data.

Deep neural networks can process inputs that are very large, of variable length, and contain various kinds of internal structure. They can output single real numbers (regression), multiple numbers (multivariate regression), or probabilities over two or more classes (binary and multiclass classification, respectively). As we shall see in the next section, their outputs may also be very large, of variable length, and contain internal structure. It is probably hard to imagine equations with these properties, and the reader should endeavor to suspend disbelief for now.

1.1.5 Structured outputs

Figure 1.4a depicts a multivariate binary classification model for semantic segmentation. Here, every pixel of an input image is assigned a binary label that indicates whether it belongs to a cow or the background. Figure 1.4b shows a multivariate regression model where the input is an image of a street scene and the output is the depth at each pixel. In both cases, the output is high-dimensional and structured. However, this structure is closely tied to the input, and this can be exploited; if a pixel is labeled as “cow”, then a neighbor with a similar RGB value probably has the same label.

Figures 1.4c–e depict three models where the output has a complex structure that is not so closely tied to the input. Figure 1.4c shows a model where the input is an audio file and the output is the transcribed words from that file. Figure 1.4d is a translation

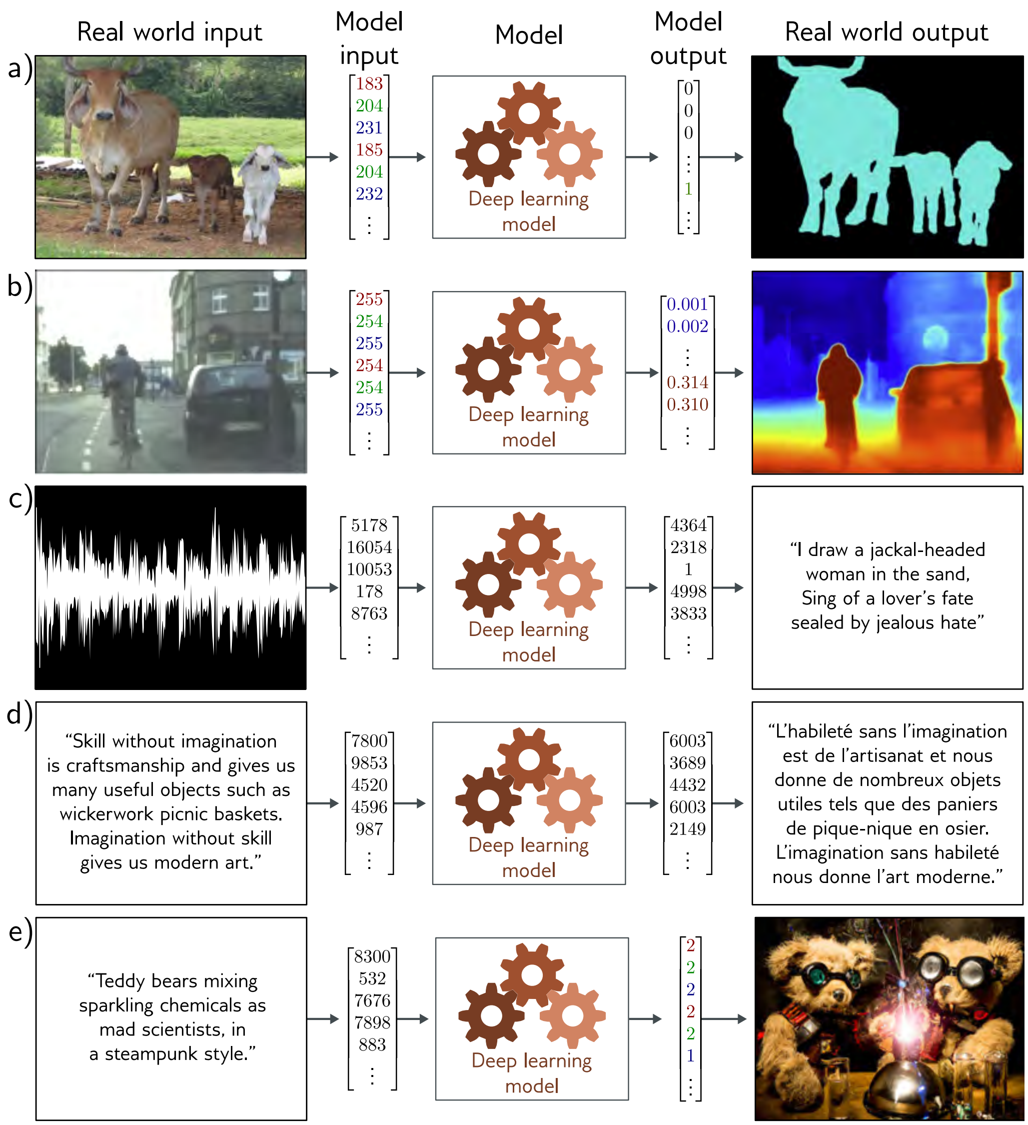

Figure 1.4 Supervised learning tasks with structured outputs. a) This semantic segmentation model maps an RGB image to a binary image indicating whether each pixel belongs to the background or a cow (adapted from Noh et al., 2015). b) This monocular depth estimation model maps an RGB image to an output image where each pixel represents the depth (adapted from Cordts et al., 2016). c) This audio transcription model maps an audio sample to a transcription of the spoken words in the audio. d) This translation model maps an English text string to its French translation. e) This image synthesis model maps a caption to an image (example from https://openai.com/dall-e-2/). In each case, the output has a complex internal structure or grammar. In some cases, many outputs are compatible with the input.

model in which the input is a body of text in English and the output contains the French translation. Figure 1.4e depicts a very challenging task in which the input is descriptive text and the model must produce an image that matches this description.

In principle, the latter three tasks can be tackled in the standard supervised learning framework, but they are more difficult for two reasons. First, the output may genuinely be ambiguous; there are multiple valid translations from an English sentence to a French one and multiple images that are compatible with any caption. Second, the output contains considerable structure; not all strings of words make valid English and French sentences, and not all collections of RGB values make plausible images. In addition to learning the mapping, we also have to respect the "grammar" of the output.

Fortunately, this "grammar" can be learned without the need for output labels. For example, we can learn how to form valid English sentences by learning the statistics of a large corpus of text data. This provides a connection with the next section of the book, which considers *unsupervised learning models*. These do not have access to labels.

1.2 Unsupervised learning

Constructing a model from input data without corresponding output labels is termed *unsupervised learning*; the absence of output labels means there can be no "supervision". Rather than learning a mapping from input to output, the goal is to describe or understand the structure of the data. As for supervised learning, the data may have very different characteristics; it may be discrete or continuous, low-dimensional or high-dimensional, and of constant or variable length.

1.2.1 Generative models

This book focuses on *generative unsupervised models*, which learn to synthesize new data examples that are statistically indistinguishable from the training data. Some generative models explicitly describe the probability distribution over the input domain, and here new examples are generated by sampling from this distribution. Others merely learn a mechanism that generates new examples.

State-of-the-art generative models can synthesize examples that are extremely plausible but distinct from the training examples. They have been particularly successful at generating images (figure 1.5) and text (figure 1.6). They can also synthesize data under the constraint that some outputs are predetermined (termed *conditional synthesis*). Examples include image inpainting (figure 1.7) and text completion (figure 1.8). Indeed, modern generative models for text are so powerful that they can appear intelligent. Given a body of text followed by a question, the model can often "fill in" the missing answer by generating the most likely completion of the document. However, in reality, the model only knows about the statistics of language and does not understand the significance of its answers.

Figure 1.5 Generative models for images. Left: two images were generated from a model trained on pictures of cats. These are not real cats, but samples from a probability model. Right: two images generated from a model trained on images of buildings. Adapted from Karras et al. (2020b).

The moon had risen by the time I reached the edge of the forest, and the light that filtered through the trees was silver and cold. I shivered, though I was not cold, and quickened my pace. I had never been so far from the village before, and I was not sure what to expect. I had been walking for hours, and I was tired and hungry. I had left in such a hurry that I had not thought to pack any food, and I had not thought to bring a weapon. I was unarmed and alone in a strange place, and I did not know what I was doing.

I had been walking for so long that I had lost all sense of time, and I had no idea how far I had come. I only knew that I had to keep going. I had to find her. I was getting close. I could feel it. She was nearby, and she was in trouble. I had to find her and help her, before it was too late.

Figure 1.6 Short story synthesized from a generative model of text data. The model describes a probability distribution that assigns a probability to every output string. Sampling from the model creates strings that follow the statistics of the training data (here, short stories) but have never been seen before.

Figure 1.7 Inpainting. In the original image (left), the boy is obscured by metal cables. These undesirable regions (center) are removed and the generative model synthesizes a new image (right) under the constraint that the remaining pixels must stay the same. Adapted from Saharia et al. (2022a).

I was a little nervous before my first lecture at the University of Bath. It seemed like there were hundreds of students and they looked intimidating. I stepped up to the lectern and was about to speak when something bizarre happened.

Suddenly, the room was filled with a deafening noise, like a giant roar. It was so loud that I couldn't hear anything else and I had to cover my ears. I could see the students looking around, confused and frightened. Then, as quickly as it had started, the noise stopped and the room was silent again.

I stood there for a few moments, trying to make sense of what had just happened. Then I realized that the students were all staring at me, waiting for me to say something. I tried to think of something witty or clever to say, but my mind was blank. So I just said, "Well, that was strange,' and then I started my lecture.

Figure 1.8 Conditional text synthesis. Given an initial body of text (in black), generative models of text can continue the string plausibly by synthesizing the "missing" remaining part of the string. Generated by GPT3 (Brown et al., 2020).

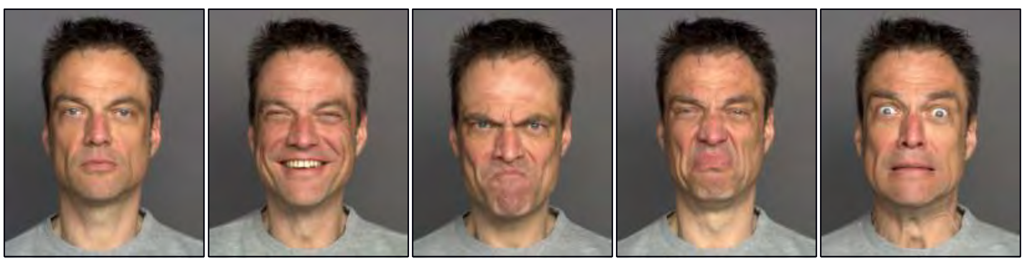

Figure 1.9 Variation of the human face. The human face contains roughly 42 muscles, so it's possible to describe most of the variation in images of the same person in the same lighting with just 42 numbers. In general, datasets of images, music, and text can be described by a relatively small number of underlying variables although it is typically more difficult to tie these to particular physical mechanisms. Images from Dynamic FACES database (Holland et al., 2019).

1.2.2 Latent variables

Some (but not all) generative models exploit the observation that data can be lower dimensional than the raw number of observed variables suggests. For example, the number of valid and meaningful English sentences is considerably smaller than the number of strings created by drawing words at random. Similarly, real-world images are a tiny subset of the images that can be created by drawing random RGB values for every pixel. This is because images are generated by physical processes (see figure 1.9).

This leads to the idea that we can describe each data example using a smaller number of underlying *latent variables*. Here, the role of deep learning is to describe the mapping between these latent variables and the data. The latent variables typically have a simple

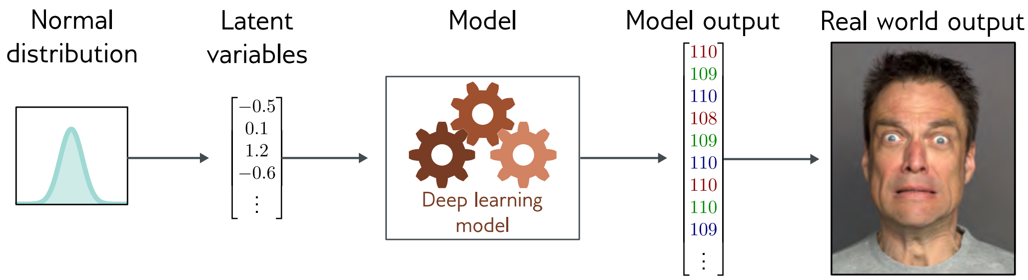

Figure 1.10 Latent variables. Many generative models use a deep learning model to describe the relationship between a low-dimensional "latent" variable and the observed high-dimensional data. The latent variables have a simple probability distribution by design. Hence, new examples can be generated by sampling from the simple distribution over the latent variables and then using the deep learning model to map the sample to the observed data space.

Figure 1.11 Image interpolation. In each row the left and right images are real and the three images in between represent a sequence of interpolations created by a generative model. The generative models that underpin these interpolations have learned that all images can be created by a set of underlying latent variables. By finding these variables for the two real images, interpolating their values, and then using these intermediate variables to create new images, we can generate intermediate results that are both visually plausible and mix the characteristics of the two original images. Top row adapted from Sauer et al. (2022). Bottom row adapted from Ramesh et al. (2022).

Figure 1.12 Multiple images generated from the caption "A teddy bear on a skateboard in Times Square." Generated by DALL·E-2 (Ramesh et al., 2022).

probability distribution by design. By sampling from this distribution and passing the result through the deep learning model, we can create new samples (figure 1.10).

These models lead to new methods for manipulating real data. For example, consider finding the latent variables that underpin two real examples. We can interpolate between these examples by interpolating between their latent representations and mapping the intermediate positions back into the data space (figure 1.11).

1.2.3 Connecting supervised and unsupervised learning

Generative models with latent variables can also benefit supervised learning models where the outputs have structure (figure 1.4). For example, consider learning to predict the images corresponding to a caption. Rather than directly map the text input to an image, we can learn a relation between latent variables that explain the text and the latent variables that explain the image.

This has three advantages. First, we may need fewer text/image pairs to learn this mapping now that the inputs and outputs are lower dimensional. Second, we are more likely to generate a plausible-looking image; any sensible values of the latent variables should produce something that looks like a plausible example. Third, if we introduce randomness to either the mapping between the two sets of latent variables or the mapping from the latent variables to the image, then we can generate multiple images that are all described well by the caption (figure 1.12).

1.3 Reinforcement learning

The final area of machine learning is reinforcement learning. This paradigm introduces the idea of an agent which lives in a world and can perform certain actions at each time step. The actions change the state of the system but not necessarily in a deterministic way. Taking an action can also produce rewards, and the goal of reinforcement learning is for the agent to learn to choose actions that lead to high rewards on average.

One complication is that the reward may occur some time after the action is taken, so associating a reward with an action is not straightforward. This is known as the *temporal credit assignment problem*. As the agent learns, it must trade-off *exploration* and *exploitation* of what it already knows; perhaps the agent has already learned how to receive modest rewards; should it follow this strategy (exploit what it knows), or should it try different actions to see if it can improve (explore other opportunities)?

1.3.1 Two examples

Consider teaching a humanoid robot to locomote; the robot can perform a limited number of actions at a given time (moving various joints), and these change the state of the world (its pose). We might reward the robot for reaching checkpoints in an obstacle course. To reach each checkpoint, it must perform many actions, and it's unclear which ones contributed to the reward when it is received, and which were irrelevant. This is an example of the temporal credit assignment problem.

A second example is learning to play chess. Again, the agent has a set of valid actions (chess moves) at any given time. However, these actions change the state of the system in a non-deterministic way; for any choice of action, the opposing player might respond with many different moves. Here, we might set up a reward structure based on capturing pieces, or just have a single reward at the end of the game for winning. In the latter case, the temporal credit assignment problem is extreme; the system must learn which of the many moves it made were instrumental to success or failure.

The exploration-exploitation trade-off is also apparent in these two examples. The robot may have discovered that it can make progress by lying on its side and pushing with one leg. This strategy will move the robot and yields rewards, but much more slowly than the optimal solution: to balance on its legs and walk. So, it faces a choice between exploiting what it already knows (how to slide along the floor awkwardly) and exploring the space of actions (which might result in much faster locomotion). Similarly, in the chess example, the agent may learn a reasonable sequence of opening moves. Should it exploit this knowledge or explore different opening sequences?

It is perhaps not obvious how deep learning fits into the reinforcement learning framework. There are several possible approaches, but one technique is to use deep networks to build a mapping from the observed world state to an action. This is known as a *policy network*. In the robot example, the policy network would learn a mapping from its sensor measurements to joint movements. In the chess example, the network would learn a mapping from the current state of the board to the choice of move (figure 1.13).

1.4 Structure of book

The structure of the book follows the structure of this introduction. Chapters 2–9 walk through the supervised learning pipeline. We describe shallow and deep neural networks

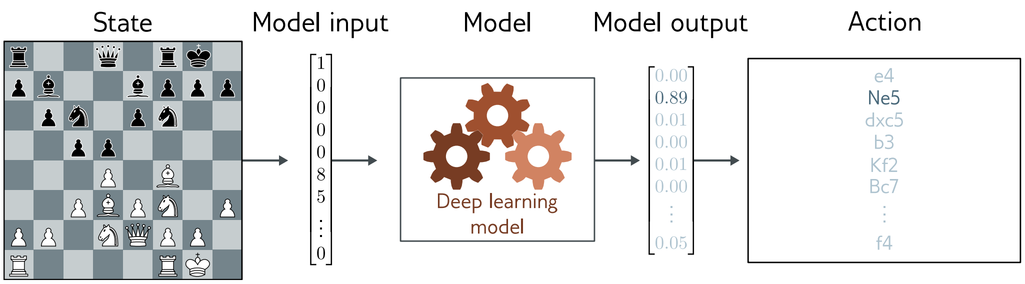

Figure 1.13 Policy networks for reinforcement learning. One way to incorporate deep neural networks into reinforcement learning is to use them to define a mapping from the state (here position on chessboard) to the actions (possible moves). This mapping is known as a *policy*. Adapted from Pablok (2017).

and discuss how to train them, and measure and improve their performance. Chapters 10–13 describe common architectural variations of deep neural networks, including convolutional networks, residual connections, and transformers. These architectures are used across supervised, unsupervised, and reinforcement learning.

Chapters 14–18 tackle unsupervised learning using deep neural networks. We devote a chapter each to four modern deep generative models: generative adversarial networks, variational autoencoders, normalizing flows, and diffusion models. Chapter 19 is a brief introduction to deep reinforcement learning. This is a topic that easily justifies its own book, so the treatment is necessarily superficial, but this is intended to be a good starting point for readers unfamiliar with this area.

Despite the title of this book, some aspects of deep learning remain poorly understood. Chapter 20 poses some fundamental questions. Why are deep networks so easy to train? Why do they generalize so well? Why do they need so many parameters? Do they need to be deep? Along the way, we explore unexpected phenomena such as the structure of the loss function, double descent, grokking, and lottery tickets.

1.5 Ethics

It would be irresponsible to write this book without discussing the ethical implications of artificial intelligence. This potent technology will change the world to at least the same extent as electricity, the internal combustion engine, the transistor, or the internet. The potential benefits in healthcare, design, entertainment, transport, education, and almost every area of commerce are enormous. However, scientists and engineers are often unrealistically optimistic about the outcomes of their work, and the potential for harm is just as great. The following paragraphs highlight five concerns.

Bias and fairness: If we train a system to predict salary levels for individuals based on historical data, then this system will reproduce historical biases; for example, it will probably predict that women should be paid less than men. Several such cases have already become international news stories: an AI system for super-resolving face images made non-white people look more white; a system for generating images produced only pictures of men when asked to synthesize pictures of lawyers. Careless application of algorithmic decision-making using AI has the potential to entrench or aggravate existing biases. See Binns (2018) for further discussion.

Explainability: Deep learning systems make decisions, but we do not usually know exactly how or based on what information. They may contain billions of parameters, and there is no way we can understand how they work based on examination. This has led to the sub-field of explainable AI. One moderately successful area is producing local explanations; we cannot explain the entire system, but we can produce an interpretable description of why a particular decision was made. However, it remains unknown whether it is possible to build complex decision-making systems that are fully transparent to their users or even their creators. See Grennan et al. (2022) for further information.

Weaponizing AI: All significant technologies have been applied directly or indirectly toward war. Sadly, violent conflict seems to be an inevitable feature of human behavior. AI is arguably the most powerful technology ever built and will doubtless be deployed extensively in a military context. Indeed, this is already happening (Heikkilä, 2022).

Concentrating power: It is not from a benevolent interest in improving the lot of the human race that the world's most powerful companies are investing heavily in AI. They know that these technologies will allow them to reap enormous profits. Like any advanced technology, AI is likely to concentrate power in the hands of the few organizations that control it. Automating jobs that are currently done by humans will change the economic environment and disproportionately affect the livelihoods of lower-paid workers with fewer skills. Optimists argue similar disruptions happened during the industrial revolution resulted in shorter working hours. The truth is that we simply do not know what effects the large-scale adoption of AI will have on society (see David, 2015).

Existential risk: The major risks to the human race all result from technology. Climate change has been driven by industrialization. Nuclear weapons derive from the study of physics. Pandemics are more probable and spread faster because innovations in transport, agriculture, and construction have allowed a larger, denser, and more interconnected population. AI brings new existential risks. We should be very cautious about building systems that are more capable and extensible than human beings. In the most optimistic case, it will put vast power in the hands of the owners. In the most pessimistic case, we will be unable to control it or even understand its motives (see Tegmark, 2018).

This list is far from exhaustive. AI could also enable surveillance, disinformation, violations of privacy, fraud, and manipulation of financial markets, and the energy required to train AI systems contributes to climate change. Moreover, these concerns are not speculative; there are already many examples of ethically dubious applications of AI (consult Dao, 2021, for a partial list). In addition, the recent history of the internet has shown how new technology can cause harm in unexpected ways. The online community of the eighties and early nineties could hardly have predicted the proliferation of fake news, spam, online harassment, fraud, cyber-bullying, incel culture, political manipulation, doxxing, online radicalization, and revenge porn.

Everyone studying or researching (or writing books about) AI should contemplate to what degree scientists are accountable for the uses of their technology. We should consider that capitalism primarily drives the development of AI and that legal advances and deployment for social good are likely to lag significantly behind. We should reflect on whether it's possible as scientists and engineers to control progress in this field and to reduce the potential for harm. We should consider what kind of organizations we are prepared to work for. How serious are they in their commitment to reducing the potential harms of AI? Are they simply "ethics-washing" to reduce reputational risk, or do they actually implement mechanisms to halt ethically-suspect projects?

All readers are encouraged to investigate these issues further. The online course at https://ethics-of-ai.mooc.fi/ is an excellent place to start. Appendix D points to further reading about AI ethics. If you are a professor teaching from this book, you are encouraged to raise these issues with your students. If you are a student taking a course where this is not done, then lobby your professor to make this happen. If you are deploying or researching AI in a corporate environment, you are encouraged to scrutinize your employer's values and to help change them (or leave) if they are wanting.

1.6 Other books

This book is self-contained but is limited to coverage of deep learning. It is intended to be the spiritual successor to *Deep Learning* (Goodfellow et al., 2016) which is a fantastic resource but does not cover recent advances. For a broader look at machine learning, the most up-to-date and encyclopedic resource is *Probabilistic Machine Learning* (Murphy, 2022, 2023). However, *Pattern Recognition and Machine Learning* (Bishop, 2006) is still an excellent and relevant book.

If you enjoy this book, then my previous volume, *Computer Vision: Models, Learning, and Inference* (Prince, 2012) is still worth reading. Some parts have dated badly, but it contains a thorough introduction to probability, including Bayesian methods, and good introductory coverage of latent variable models, geometry for computer vision, Gaussian processes, and graphical models. It uses identical notation to this book and can be found online. A detailed treatment of graphical models can be found in *Probabilistic Graphical Models: Principles and Techniques* (Koller & Friedman, 2009) and Gaussian processes are covered by *Gaussian Processes for Machine Learning* (Williams & Rasmussen, 2006).

For background mathematics, consult *Mathematics for Machine Learning* (Deisenroth et al., 2020). For a more coding-oriented approach, consult *Dive into Deep Learning* (Zhang et al., 2023). The standard reference for computer vision is Szeliski (2022) and there is also the impending book *Computer Vision: A Deep Learning Approach* (Torralba et al., forthcoming). A good starting point to learn about graph neural networks is *Graph Representation Learning* (Hamilton, 2020). The definitive work on reinforcement learning is *Reinforcement Learning: An Introduction* (Sutton & Barto, 2018).

1.7 How to read this book

The remaining chapters in this book each have a main body of text, a notes section, and a set of problems. The main body of the text is intended to be self-contained and can be read without recourse to the other parts of the chapter. As much as possible, background mathematics is incorporated into the main body of the text. However, for larger topics that would be a distraction to the main thread of the argument, the background material is appendicised and a reference is provided in the margin. Most notation in this book is standard. However, some conventions are less widely used, and the reader is encouraged to consult appendix A before proceeding.

Appendix A Notation

The main body of text includes many novel illustrations and visualizations of deep learning models and results. I've worked hard to provide new explanations of existing ideas rather than merely curate the work of others. Deep learning is a new field, and sometimes phenomena are poorly understood. I try to make it clear where this is the case and when my explanations should be treated with caution.

References are included in the main body of the chapter only where results are depicted. Instead, they can be found in the notes section at the end of the chapter. I do not generally respect historical precedent in the main text; if an ancestor of a current technique is no longer useful, then I will not mention it. However, the historical development of the field is described in the notes section and hopefully credit is fairly assigned. The notes are organized into paragraphs and provide pointers for further reading. They should help the reader orient themselves within the sub-area and understand how it relates to other parts of machine learning. The notes are less self-contained than the main text. Depending on your level of background knowledge and interest, you may find these sections more or less useful.

Each chapter has a number of associated problems. They are referenced in the margin of the main text at the point that they should be attempted. As George Pólya noted, "Mathematics, you see, is not a spectator sport." He was correct, and I highly recommend that you attempt the problems as you go. In some cases, they provide insights that will help you understand the main text. Problems for which the answers are provided on the associated website are indicated with an asterisk. Additionally, Python notebooks that will help you understand the ideas in this book are also available via the website, and these are also referenced in the margins of the text. Indeed, if you are feeling rusty, it might be worth working through the notebook on background mathematics right now.

Notebook 1.1 Background mathematics

Unfortunately, the pace of research in AI makes it inevitable that this book will be a constant work in progress. If there are parts you find hard to understand, notable omissions, or sections that seem extraneous, please get in touch via the associated website. Together, we can make the next edition better.

Chapter 2

Supervised learning

A *supervised learning model* defines a mapping from one or more inputs to one or more outputs. For example, the input might be the age and mileage of a secondhand Toyota Prius and the output might be the estimated value of the car in dollars.

The model is just a mathematical equation; when the inputs are passed through this equation, it computes the output, and this is termed *inference*. The model equation also contains *parameters*. Different parameter values change the outcome of the computation; the model equation describes a family of possible relationships between inputs and outputs, and the parameters specify the particular relationship.

When we *train* or *learn* a model, we find parameters that describe the true relationship between inputs and outputs. A learning algorithm takes a training set of input/output pairs and manipulates the parameters until the inputs predict their corresponding outputs as closely as possible. If the model works well for these training pairs, then we hope it will make good predictions for new inputs where the true output is unknown.

The goal of this chapter is to expand on these ideas. First, we describe this framework more formally and introduce some notation. Then we work through a simple example in which we use a straight line to describe the relationship between input and output. This linear model is both familiar and easy to visualize, but nevertheless illustrates all the main ideas of supervised learning.

2.1 Supervised learning overview

In supervised learning, we aim to build a model that takes an input $\mathbf{x}$ and outputs a prediction $\mathbf{y}$. For simplicity, we assume that both the input $\mathbf{x}$ and output $\mathbf{y}$ are vectors of a predetermined and fixed size, and that the elements of each vector are always ordered in the same way; in the Prius example above, the input $\mathbf{x}$ would always contain the age of the car and then the mileage, in that order. This is termed *structured* or *tabular* data.

To make the prediction, we need a model $\mathbf{f}[\bullet]$ that takes input $\mathbf{x}$ and returns $\mathbf{y}$, so:

$$\mathbf{y} = \mathbf{f}[\mathbf{x}]. \tag{2.1}$$

When we compute the prediction $\mathbf{y}$ from the input $\mathbf{x}$, we call this *inference*.

The model is just a mathematical equation with a fixed form. It represents a family of different relations between the input and the output. The model also contains *parameters* $\boldsymbol{\phi}$. The choice of parameters determines the particular relation between input and output, so we should really write:

$$\mathbf{y} = \mathbf{f}[\mathbf{x}, \boldsymbol{\phi}]. \tag{2.2}$$

When we talk about *learning* or *training* a model, we mean that we attempt to find parameters $\boldsymbol{\phi}$ that make sensible output predictions from the input. We learn these parameters using a *training dataset* of I pairs of input and output examples $\{\mathbf{x}_i, \mathbf{y}_i\}$. We aim to select parameters that map each training input to its associated output as closely as possible. We quantify the degree of mismatch in this mapping with the *loss* L. This is a scalar value that summarizes how poorly the model predicts the training outputs from their corresponding inputs for parameters $\boldsymbol{\phi}$.

We can treat the loss as a function $\mathrm{L}[\boldsymbol{\phi}]$ of these parameters. When we train the model, we are seeking parameters $\hat{\boldsymbol{\phi}}$ that minimize this *loss function*:[1]

$$\hat{\boldsymbol{\phi}} = \underset{\boldsymbol{\phi}}{\mathrm{argmin}}\Big[\mathrm{L}\left[\boldsymbol{\phi}\right]\Big]. \tag{2.3}$$

If the loss is small after this minimization, we have found model parameters that accurately predict the training outputs $\mathbf{y}_i$ from the training inputs $\mathbf{x}_i$.

After training a model, we must now assess its performance; we run the model on separate *test data* to see how well it *generalizes* to examples that it didn't observe during training. If the performance is adequate, then we are ready to deploy the model.

2.2 Linear regression example

Let's now make these ideas concrete with a simple example. We consider a model $y = \mathrm{f}[x, \boldsymbol{\phi}]$ that predicts a single output y from a single input x. Then we develop a loss function, and finally, we discuss model training.

2.2.1 1D linear regression model

A *1D linear regression model* describes the relationship between input x and output y as a straight line:

$$\begin{aligned} y &= \mathrm{f}[x, \boldsymbol{\phi}] \\ &= \phi_0 + \phi_1 x. \end{aligned} \tag{2.4}$$

[1]More properly, the loss function also depends on the training data $\{\mathbf{x}_i, \mathbf{y}_i\}$, so we should write $\mathrm{L}\left[\{\mathbf{x}_i, \mathbf{y}_i\}, \boldsymbol{\phi}\right]$, but this is rather cumbersome.

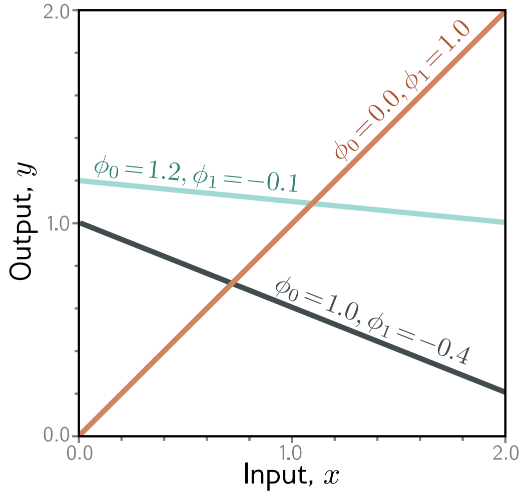

Figure 2.1 Linear regression model. For a given choice of parameters $\boldsymbol{\phi} = [\phi_0, \phi_1]^T$, the model makes a prediction for the output (y-axis) based on the input (x-axis). Different choices for the y-intercept ϕ_0 and the slope ϕ_1 change these predictions (cyan, orange, and gray lines). The linear regression model (equation 2.4) defines a family of input/output relations (lines) and the parameters determine the member of the family (the particular line).

This model has two parameters $\boldsymbol{\phi} = [\phi_0, \phi_1]^T$, where ϕ_0 is the y-intercept of the line and the ϕ_1 is the slope. Different choices for the y-intercept and slope result in different relations between input and output (figure 2.1). Hence, equation 2.4 defines a family of possible input-output relations (all possible lines), and the choice of parameters determines the member of this family (the particular line).

2.2.2 Loss

For this model, the training dataset (figure 2.2a) consists of I input/output pairs $\{x_i, y_i\}$. Figures 2.2b–d show three lines defined by three sets of parameters. The green line in figure 2.2d describes the data more accurately than the other two since it is much closer to the data points. However, we need a principled approach for deciding which parameters $\boldsymbol{\phi}$ are better than others. To this end, we assign a numerical value to each choice of parameters that quantifies the degree of mismatch between the model and the data. We term this value the *loss*; a lower loss means a better fit.

The mismatch is captured by the deviation between the model predictions $\text{f}[x_i, \boldsymbol{\phi}]$ (height of the line at x_i) and the ground truth outputs y_i. These deviations are depicted as orange dashed lines in figures 2.2b–d. We quantify the total mismatch, *training error*, or *loss* as the sum of the squares of these deviations for all I training pairs:

$$\begin{aligned} \text{L}[\phi] &= \sum_{i=1}^{I} \left(\text{f}[x_i, \boldsymbol{\phi}] - y_i\right)^2 \\ &= \sum_{i=1}^{I} \left(\phi_0 + \phi_1 x_i - y_i\right)^2. \end{aligned} \tag{2.5}$$

Since the best parameters minimize this expression, we call this a *least-squares* loss. The squaring operation means that the direction of the deviation (i.e., whether the line is

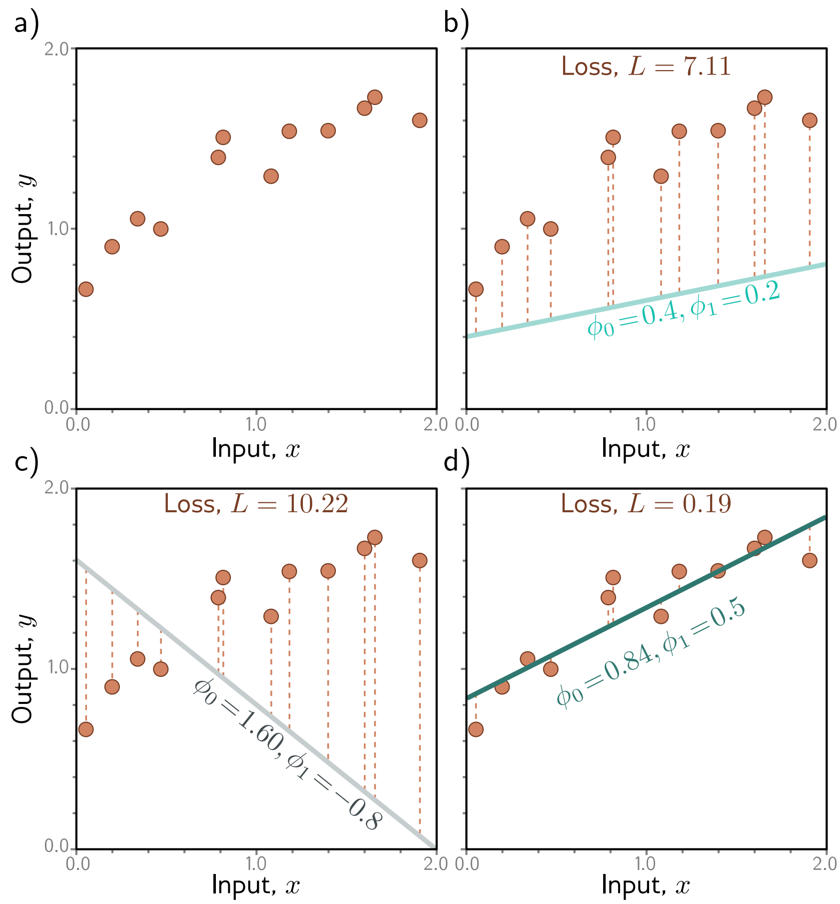

Figure 2.2 Linear regression training data, model, and loss. a) The training data (orange points) consist of $I = 12$ input/output pairs $\{x_i, y_i\}$. b–d) Each panel shows the linear regression model with different parameters. Depending on the choice of y-intercept and slope parameters $\boldsymbol{\phi} = [\phi_0, \phi_1]^T$, the model errors (orange dashed lines) may be larger or smaller. The loss L is the sum of the squares of these errors. The parameters that define the lines in panels (b) and (c) have large losses $L = 7.11$ and $L = 10.22$, respectively because the models fit badly. The loss $L = 0.19$ in panel (d) is smaller because the model fits well; in fact, this has the smallest loss of all possible lines and so these are the optimal parameters.

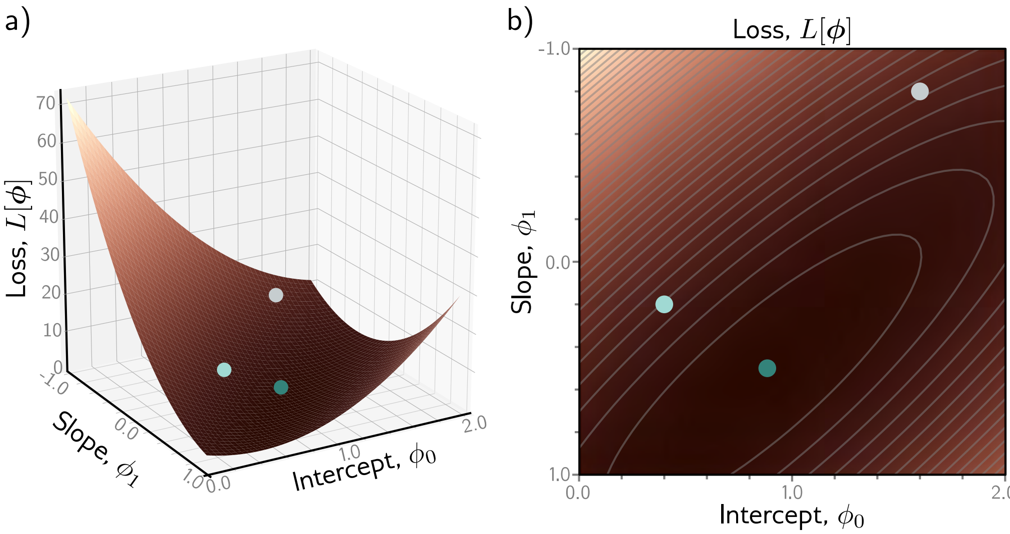

Figure 2.3 Loss function for linear regression model with the dataset in figure 2.2a. a) Each combination of parameters $\boldsymbol{\phi} = [\phi_0, \phi_1]$ has an associated loss. The resulting loss function $\mathrm{L}[\boldsymbol{\phi}]$ can be visualized as a surface. The three circles represent the three lines from figure 2.2b–d. b) The loss can also be visualized as a heatmap, where brighter regions represent larger losses; here we are looking straight down at the surface in (a) from above and gray ellipses represent isocontours. The best fitting line (figure 2.2d) has the parameters with the smallest loss (green circle).

above or below the data) is unimportant. There are also theoretical reasons for this choice which we return to in chapter 5.

The loss L is a function of the parameters $\boldsymbol{\phi}$; it will be larger when the model fit is poor (figure 2.2b,c) and smaller when it is good (figure 2.2d). Considered in this light, we term $\mathrm{L}[\boldsymbol{\phi}]$ the *loss function* or *cost function*. The goal is to find the parameters $\hat{\boldsymbol{\phi}}$ that minimize this quantity:

Notebook 2.1 Supervised learning

$$
\begin{aligned}
\hat{\boldsymbol{\phi}} &= \underset{\boldsymbol{\phi}}{\operatorname{argmin}}\Big[\mathrm{L}[\boldsymbol{\phi}]\Big] \\
&= \underset{\boldsymbol{\phi}}{\operatorname{argmin}}\left[\sum_{i=1}^{I}\left(\mathrm{f}[x_i, \boldsymbol{\phi}] - y_i\right)^2\right] \\
&= \underset{\boldsymbol{\phi}}{\operatorname{argmin}}\left[\sum_{i=1}^{I}\left(\phi_0 + \phi_1 x_i - y_i\right)^2\right]. \qquad (2.6)
\end{aligned}
$$

There are only two parameters (the y-intercept ϕ_0 and slope ϕ_1) and so we can calculate the loss for every combination of values and visualize the loss function as a surface (figure 2.3). The "best" parameters are at the minimum of this surface.

Problems 2.1–2.2

2.2.3 Training

The process of finding parameters that minimize the loss is termed *model fitting*, *training*, or *learning*. The basic method is to choose the initial parameters randomly and then improve them by "walking down" the loss function until we reach the bottom (figure 2.4). One way to do this is to measure the gradient of the surface at the current position and take a step in the direction that is most steeply downhill. Then we repeat this process until the gradient is flat and we can improve no further.[2]

2.2.4 Testing

Having trained the model, we want to know how it will perform in the real world. We do this by computing the loss on a separate set of *test data*. The degree to which the prediction accuracy *generalizes* to the test data depends in part on how representative and complete the training data was. However, it also depends on the how expressive the model is. A simple model like a line might not be able to capture the true relationship between input and output. This is known as *underfitting*. Conversely, a very expressive model may describe statistical peculiarities of the training data that are atypical and lead to unusual predictions. This is known as *overfitting*.

2.3 Summary

A supervised learning model is a function $\mathbf{y} = \mathbf{f}[\mathbf{x}, \boldsymbol{\phi}]$ that relates inputs $\mathbf{x}$ to outputs $\mathbf{y}$. The particular relationship is determined by parameters $\boldsymbol{\phi}$. To train the model, we define a loss function $\mathrm{L}[\boldsymbol{\phi}]$ over a training dataset $\{\mathbf{x}_i, \mathbf{y}_i\}$. This quantifies the mismatch between the model predictions $\mathbf{f}[\mathbf{x}_i, \boldsymbol{\phi}]$ and observed outputs $\mathbf{y}_i$ as a function of the parameters $\boldsymbol{\phi}$. Then we search for the parameters that minimize the loss. We evaluate the model on a different set of test data to see how well it generalizes to new inputs.

Chapters 3–9 expand on these ideas. First, we tackle the model itself; linear regression has the obvious drawback that it can only describe the relation between the input and output as a straight line. Shallow neural networks (chapter 3) are only slightly more complex than linear regression but describe a much larger family of input/output relationships. Deep neural networks (chapter 4) are just as expressive but can describe complex functions with fewer parameters and work better in practice.

Chapter 5 investigates loss functions for different tasks and reveals the theoretical underpinnings of the least-squares loss. Chapters 6 and 7 discuss the training process. Chapter 8 discusses how to measure model performance. Chapter 9 considers *regularization* techniques, which aim to improve that performance.

[2]This iterative approach is not actually necessary for the linear regression model. Here, it's possible to find closed-form expressions for the parameters. However, this *gradient descent* approach works for more complex models, where there is no closed-form solution, and where there are too many parameters to evaluate the loss for every combination of values.

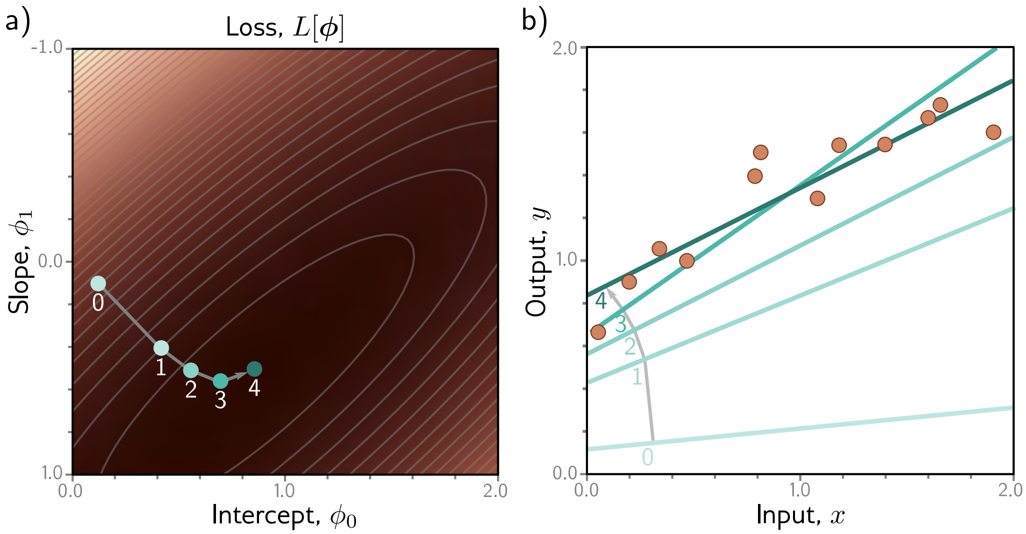

Figure 2.4 Linear regression training. The goal is to find the y-intercept and slope parameters that correspond to the smallest loss. a) Iterative training algorithms initialize the parameters randomly and then improve them by "walking downhill" until no further improvement can be made. Here, we start at position 0 and move a certain distance downhill (perpendicular to the contours) to position 1. Then we re-calculate the downhill direction and move to position 2. Eventually, we reach the minimum of the function (position 4). b) Each position 0–4 from panel (a) corresponds to a different y-intercept and slope and so represents a different line. As the loss decreases, the lines fit the data more closely.

Notes

Loss functions vs. cost functions: In much of machine learning and in this book, the terms loss function and cost function are used interchangeably. However, more properly a loss function is the individual term associated with a data point (i.e., each of the squared terms on the right-hand side of equation 2.5) and the cost function is the overall quantity that is minimized (i.e., the entire right-hand side of equation 2.5). A cost function can contain additional terms that are not associated with individual data points (e.g., see section 9.1). More generally, an *objective function* is any function that is to be maximized or minimized.

Generative vs. discriminative models: The models $\mathbf{y} = \mathbf{f}[\mathbf{x}, \boldsymbol{\phi}]$ in this chapter are *discriminative models*. These make an output prediction $\mathbf{y}$ from real-world measurements $\mathbf{x}$. Another approach is to build a *generative model* $\mathbf{x} = \mathbf{g}[\mathbf{y}, \boldsymbol{\phi}]$, in which the real-world measurements $\mathbf{x}$ are computed as a function of the output $\mathbf{y}$. Problem 2.3

The generative approach has the disadvantage that it doesn't directly predict $\mathbf{y}$. To perform inference, we must invert the generative equation as $\mathbf{y} = \mathbf{g}^{-1}[\mathbf{x}, \boldsymbol{\phi}]$ and this may be difficult. However, generative models have the advantage that we can build in prior knowledge about how the data were generated. For example, if we wanted to predict the 3D position and orientation $\mathbf{y}$

of a car in an image $\mathbf{x}$, then we could build knowledge about car shape, 3D geometry, and light transport into the function $\mathbf{x} = \mathbf{g}[\mathbf{y}, \boldsymbol{\phi}]$.

This seems like a good idea, but in fact, discriminative models dominate modern machine learning; the advantage gained from exploiting prior knowledge in generative models is usually trumped by learning very flexible discriminative models with large amounts of training data.

Problems

Problem 2.1 To walk "downhill" on the loss function (equation 2.5), we measure its gradient with respect to the parameters ϕ_0 and ϕ_1. Calculate expressions for the slopes $\partial L/\partial \phi_0$ and $\partial L/\partial \phi_1$.

Problem 2.2 Show that we can find the minimum of the loss function in closed-form by setting the expression for the derivatives from problem 2.1 to zero and solving for ϕ_0 and ϕ_1. Note that this works for linear regression but not for more complex models; this is why we use iterative model fitting methods like gradient descent (figure 2.4).

Problem 2.3* Consider reformulating linear regression as a generative model so we have $x = \mathrm{g}[y, \boldsymbol{\phi}] = \phi_0 + \phi_1 y$. What is the new loss function? Find an expression for the inverse function $y = \mathrm{g}^{-1}[x, \boldsymbol{\phi}]$ that we would use to perform inference. Will this model make the same predictions as the discriminative version for a given training dataset $\{x_i, y_i\}$? One way to establish this is to write code that fits a line to three data points using both methods and see if the result is the same.

Chapter 3

Shallow neural networks

Chapter 2 introduced supervised learning using 1D linear regression. However, this model can only describe the input/output relationship as a line. This chapter introduces shallow neural networks. These describe piecewise linear functions and are flexible enough to approximate arbitrarily complex relationships between multi-dimensional inputs and outputs.

3.1 Neural network example

Shallow neural networks are functions $\mathbf{y} = \mathbf{f}[\mathbf{x}, \boldsymbol{\phi}]$ with parameters $\boldsymbol{\phi}$ that map multivariate inputs $\mathbf{x}$ to multivariate outputs $\mathbf{y}$. We defer a full definition until section 3.4 and introduce the main ideas using an example network $\mathrm{f}[x, \boldsymbol{\phi}]$ that maps a scalar input x to a scalar output y and has ten parameters $\boldsymbol{\phi} = \{\phi_0, \phi_1, \phi_2, \phi_3, \theta_{10}, \theta_{11}, \theta_{20}, \theta_{21}, \theta_{30}, \theta_{31}\}$:

$$\begin{aligned} y &= \mathrm{f}[x, \boldsymbol{\phi}] \\ &= \phi_0 + \phi_1 \mathrm{a}[\theta_{10} + \theta_{11}x] + \phi_2 \mathrm{a}[\theta_{20} + \theta_{21}x] + \phi_3 \mathrm{a}[\theta_{30} + \theta_{31}x]. \end{aligned} \tag{3.1}$$

We can break down this calculation into three parts: first, we compute three linear functions of the input data ($\theta_{10} + \theta_{11}x$, $\theta_{20} + \theta_{21}x$, and $\theta_{30} + \theta_{31}x$). Second, we pass the three results through an *activation function* $\mathrm{a}[\bullet]$. Finally, we weight the three resulting activations with ϕ_1, ϕ_2, and ϕ_3, sum them, and add an offset ϕ_0.

To complete the description, we must define the activation function $\mathrm{a}[\bullet]$. There are many possibilities but the most common choice is the *rectified linear unit* or *ReLU*:

$$\mathrm{a}[z] = \mathrm{ReLU}[z] = \begin{cases} 0 & z < 0 \\ z & z \geq 0 \end{cases}. \tag{3.2}$$

This returns the input when it is positive and zero otherwise (figure 3.1).

It is probably not obvious which family of input/output relations is represented by equation 3.1. Nonetheless, the ideas from the previous chapter are all applicable. Equation 3.1 represents a family of functions where the particular member of the family

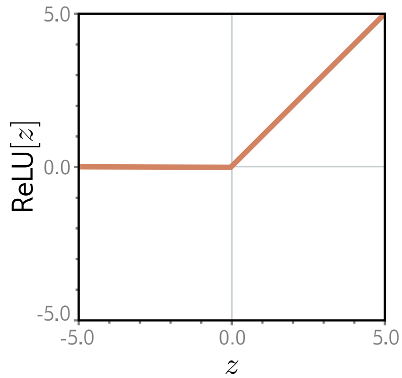

Figure 3.1 Rectified linear unit (ReLU). This activation function returns zero if the input is less than zero and returns the input unchanged otherwise. In other words, it clips negative values to zero. Note that there are many other possible choices for the activation function (see figure 3.13), but the ReLU is the most commonly used and the easiest to understand.

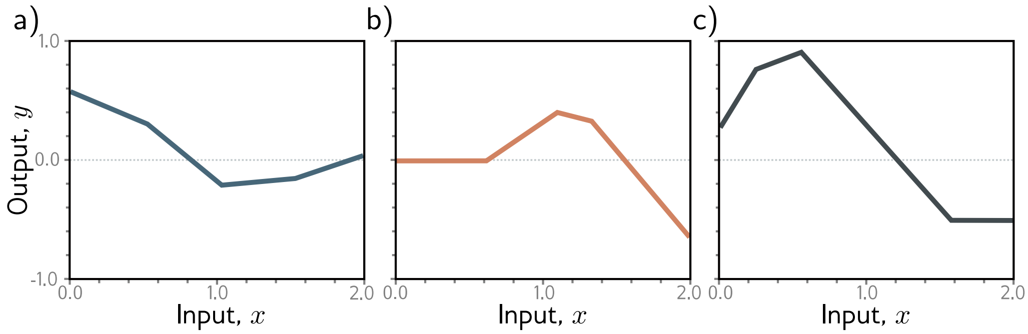

Figure 3.2 Family of functions defined by equation 3.1. a–c) Functions for three different choices of the ten parameters $\boldsymbol{\phi}$. In each case, the input/output relation is piecewise linear. However, the positions of the joints, the slopes of the linear regions between them, and the overall height vary.

depends on the ten parameters in $\boldsymbol{\phi}$. If we know these parameters, we can perform inference (predict y) by evaluating the equation for a given input x. Given a training dataset $\{x_i, y_i\}_{i=1}^{I}$, we can define a least squares loss function $\mathrm{L}[\boldsymbol{\phi}]$, and use this to measure how effectively the model describes this dataset for any given parameter values $\boldsymbol{\phi}$. To train the model, we search for the values $\hat{\boldsymbol{\phi}}$ that minimize this loss.

3.1.1 Neural network intuition

In fact, equation 3.1 represents a family of continuous piecewise linear functions (figure 3.2) with up to four linear regions. We now break down equation 3.1 and show *why* it describes this family. To make this easier to understand, we split the function into two parts. First, we introduce the intermediate quantities:

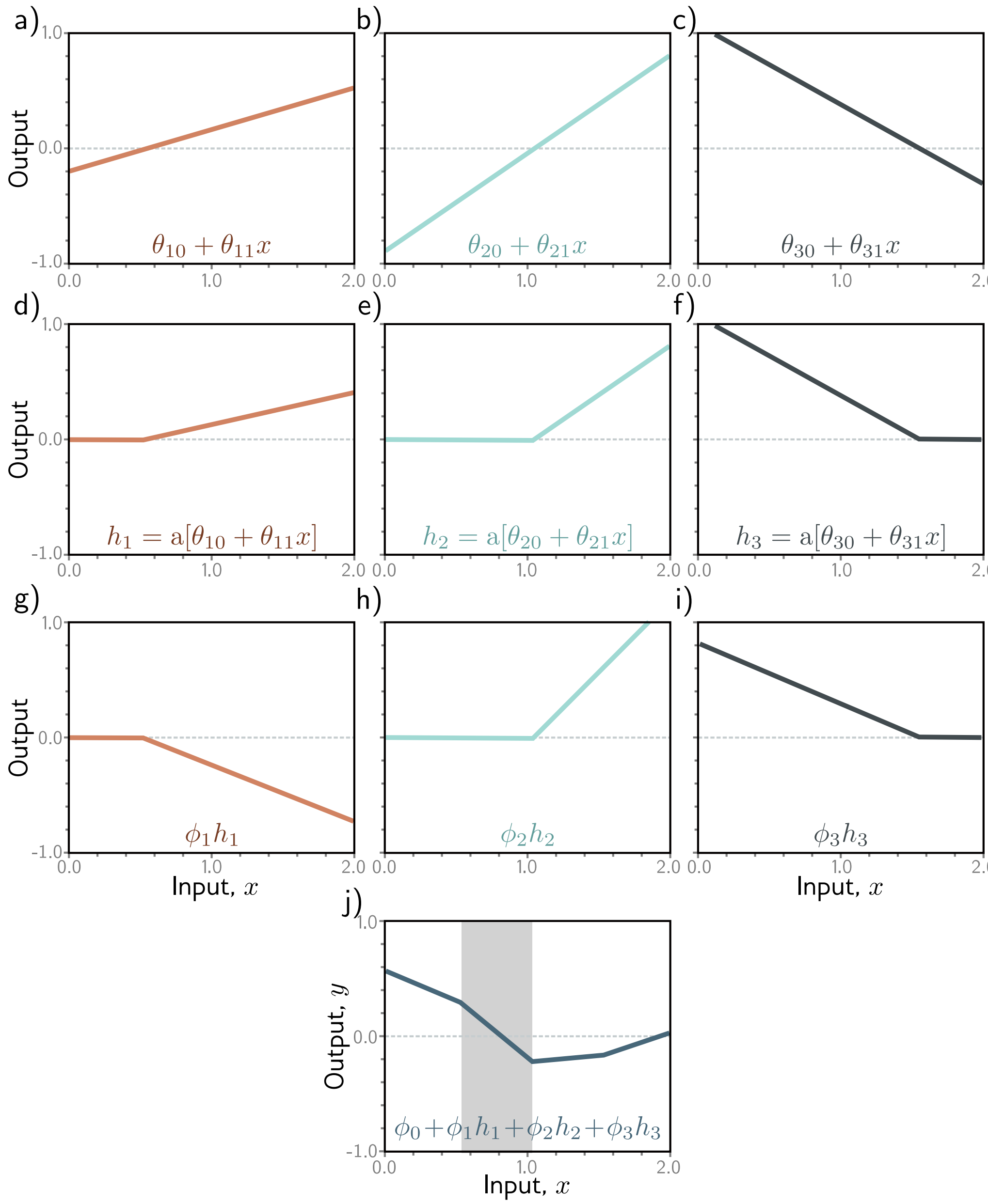

Figure 3.3 Computation for function in figure 3.2a. a–c) The input x is passed through three linear functions, each with a different y-intercept $\theta_{\bullet 0}$ and slope $\theta_{\bullet 1}$. d–f) Each line is passed through the ReLU activation function, which clips negative values to zero. g–i) The three clipped lines are then weighted (scaled) by ϕ_1, ϕ_2, and ϕ_3, respectively. j) Finally, the clipped and weighted functions are summed, and an offset ϕ_0 that controls the height is added. Each of the four linear regions corresponds to a different activation pattern in the hidden units. In the shaded region, h_2 is inactive (clipped), but h_1 and h_3 are both active.

$$
\begin{aligned}
h_1 &= a[\theta_{10} + \theta_{11}x] \\
h_2 &= a[\theta_{20} + \theta_{21}x] \\
h_3 &= a[\theta_{30} + \theta_{31}x],
\end{aligned} \tag{3.3}
$$

where we refer to h_1, h_2, and h_3 as *hidden units*. Second, we compute the output by combining these hidden units with a linear function:[1]

$$
y = \phi_0 + \phi_1 h_1 + \phi_2 h_2 + \phi_3 h_3. \tag{3.4}
$$

Figure 3.3 shows the flow of computation that creates the function in figure 3.2a. Each hidden unit contains a linear function $\theta_{\bullet 0} + \theta_{\bullet 1}x$ of the input, and that line is clipped by the ReLU function $a[\bullet]$ below zero. The positions where the three lines cross zero become the three "joints" in the final output. The three clipped lines are then weighted by ϕ_1, ϕ_2, and ϕ_3, respectively. Finally, the offset ϕ_0 is added, which controls the overall height of the final function.

Problems 3.2–3.8

Each linear region in figure 3.3j corresponds to a different *activation pattern* in the hidden units. When a unit is clipped, we refer to it as *inactive*, and when it is not clipped, we refer to it as *active*. For example, the shaded region receives contributions from h_1 and h_3 (which are active) but not from h_2 (which is inactive). The slope of each linear region is determined by (i) the original slopes $\theta_{\bullet 1}$ of the active inputs for this region and (ii) the weights $\phi_\bullet$ that were subsequently applied. For example, the slope in the shaded region (see problem 3.3) is $\theta_{11}\phi_1 + \theta_{31}\phi_3$, where the first term is the slope in panel (g) and the second term is the slope in panel (i).

Notebook 3.1
Shallow networks I

Problem 3.9

Each hidden unit contributes one "joint" to the function, so with three hidden units, there can be four linear regions. However, only three of the slopes of these regions are independent; the fourth is either zero (if all the hidden units are inactive in this region) or is a sum of slopes from the other regions.

3.1.2 Depicting neural networks

We have been discussing a neural network with one input, one output, and three hidden units. We visualize this network in figure 3.4a. The input is on the left, the hidden units are in the middle, and the output is on the right. Each connection represents one of the ten parameters. To simplify this representation, we do not typically draw the intercept parameters, so this network is usually depicted as in figure 3.4b.

[1] For the purposes of this book, a linear function has the form $z' = \phi_0 + \sum_i \phi_i z_i$. Any other type of function is nonlinear. For instance, the ReLU function (equation 3.2) and the example neural network that contains it (equation 3.1) are both nonlinear. See notes at end of chapter for further clarification.

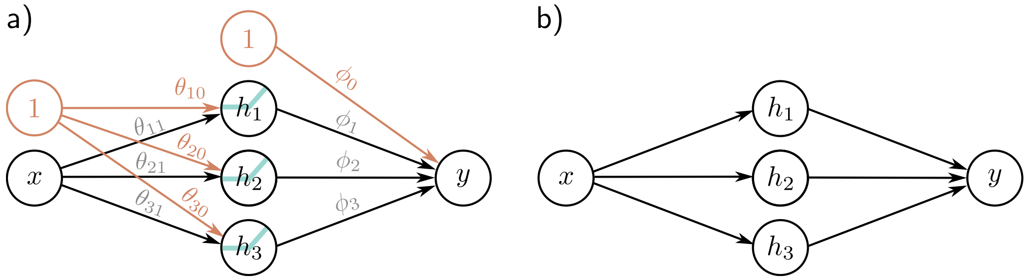

Figure 3.4 Depicting neural networks. a) The input x is on the left, the hidden units h_1, h_2, and h_3 in the center, and the output y on the right. Computation flows from left to right. The input is used to compute the hidden units, which are combined to create the output. Each of the ten arrows represents a parameter (intercepts in orange and slopes in black). Each parameter multiplies its source and adds the result to its target. For example, we multiply the parameter ϕ_1 by source h_1 and add it to y. We introduce additional nodes containing ones (orange circles) to incorporate the offsets into this scheme, so we multiply ϕ_0 by one (with no effect) and add it to y. ReLU functions are applied at the hidden units. b) More typically, the intercepts, ReLU functions, and parameter names are omitted; this simpler depiction represents the same network.

3.2 Universal approximation theorem

In the previous section, we introduced an example neural network with one input, one output, ReLU activation functions, and three hidden units. Let's now generalize this slightly and consider the case with D hidden units where the d^{th} hidden unit is:

$$h_d = \mathrm{a}[\theta_{d0} + \theta_{d1}x], \tag{3.5}$$

and these are combined linearly to create the output:

$$y = \phi_0 + \sum_{d=1}^{D} \phi_d h_d. \tag{3.6}$$

The number of hidden units in a shallow network is a measure of the *network capacity*. With ReLU activation functions, the output of a network with D hidden units has at most D joints and so is a piecewise linear function with at most $D+1$ linear regions. As we add more hidden units, the model can approximate more complex functions. Problem 3.10

Indeed, with enough capacity (hidden units), a shallow network can describe any continuous 1D function defined on a compact subset of the real line to arbitrary precision. To see this, consider that every time we add a hidden unit, we add another linear region to the function. As these linear regions become more numerous, they represent smaller and smaller sections of the function, which are increasingly well approximated by a line (figure 3.5). The ability of a neural network to approximate any continuous function can be formally proven, and this is known as the *universal approximation theorem*.

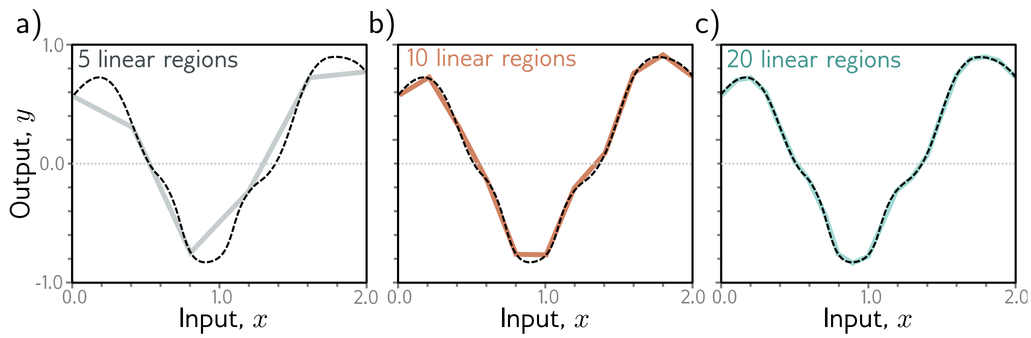

Figure 3.5 Approximation of a 1D function (dashed line) by a piecewise linear model. a–c) As the number of regions increases, the model becomes closer and closer to the continuous function. A neural network with a scalar input creates one extra linear region per hidden unit. The universal approximation theorem proves that, with enough hidden units, a shallow neural network can describe any continuous function defined on a compact subset of $\mathbb{R}^D$ to arbitrary precision.

3.3 Multivariate inputs and outputs

In the above example, the network has a single scalar input x and a single scalar output y. However, the universal approximation theorem also holds for the more general case where the network maps multivariate inputs $\mathbf{x} = [x_1, x_2, \ldots, x_{D_i}]^T$ to multivariate output predictions $\mathbf{y} = [y_1, y_2, \ldots, y_{D_o}]^T$. This section explores how to extend the model to predict multivariate outputs. Then we consider multivariate inputs. Finally, in section 3.4, we present a general definition of a shallow neural network.

3.3.1 Visualizing multivariate outputs

To extend the network to multivariate outputs $\mathbf{y}$, we simply use a different linear function of the hidden units for each output. So, a network with a scalar input x, four hidden units h_1, h_2, h_3, and h_4, and a 2D multivariate output $\mathbf{y} = [y_1, y_2]^T$ would be defined as:

$$
\begin{aligned}
h_1 &= \mathrm{a}[\theta_{10} + \theta_{11}x] \\
h_2 &= \mathrm{a}[\theta_{20} + \theta_{21}x] \\
h_3 &= \mathrm{a}[\theta_{30} + \theta_{31}x] \\
h_4 &= \mathrm{a}[\theta_{40} + \theta_{41}x],
\end{aligned}
\tag{3.7}
$$

and

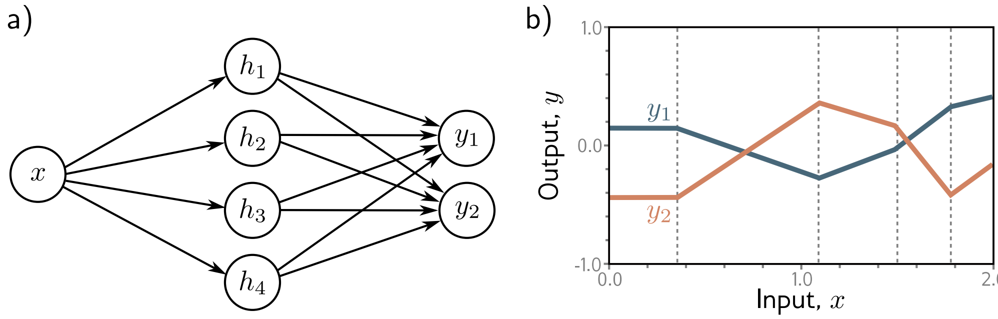

Figure 3.6 Network with one input, four hidden units, and two outputs. a) Visualization of network structure. b) This network produces two piecewise linear functions, $y_1[x]$ and $y_2[x]$. The four "joints" of these functions (at vertical dotted lines) are constrained to be in the same places since they share the same hidden units, but the slopes and overall height may differ.

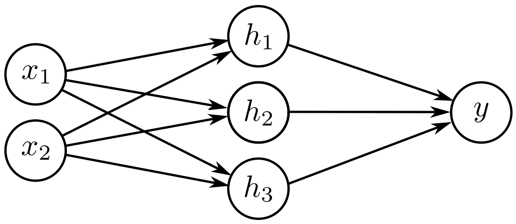

Figure 3.7 Visualization of neural network with 2D multivariate input $\mathbf{x} = [x_1, x_2]^T$ and scalar output y.

$$
\begin{aligned}
y_1 &= \phi_{10} + \phi_{11}h_1 + \phi_{12}h_2 + \phi_{13}h_3 + \phi_{14}h_4 \\
y_2 &= \phi_{20} + \phi_{21}h_1 + \phi_{22}h_2 + \phi_{23}h_3 + \phi_{24}h_4.
\end{aligned}
\tag{3.8}
$$

The two outputs are two different linear functions of the hidden units.

As we saw in figure 3.3, the "joints" in the piecewise functions depend on where the initial linear functions $\theta_{\bullet 0} + \theta_{\bullet 1}x$ are clipped by the ReLU functions $\mathrm{a}[\bullet]$ at the hidden units. Since both outputs y_1 and y_2 are different linear functions of the same four hidden units, the four "joints" in each must be in the same places. However, the slopes of the linear regions and the overall vertical offset can differ (figure 3.6). Problem 3.11

3.3.2 Visualizing multivariate inputs

To cope with multivariate inputs $\mathbf{x}$, we extend the linear relations between the input and the hidden units. So a network with two inputs $\mathbf{x} = [x_1, x_2]^T$ and a scalar output y (figure 3.7) might have three hidden units defined by:

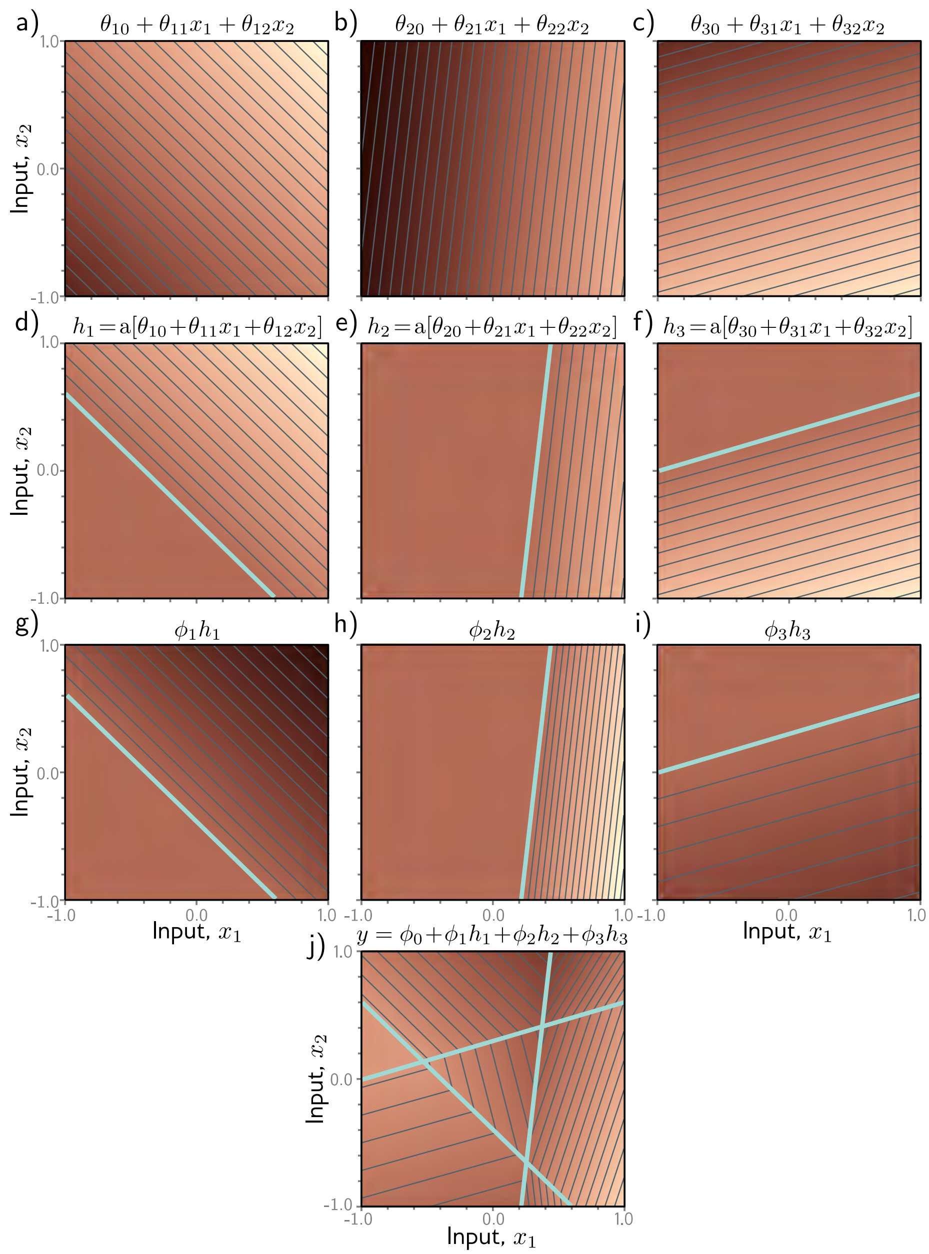

Figure 3.8 Processing in network with two inputs $\mathbf{x} = [x_1, x_2]^T$, three hidden units h_1, h_2, h_3, and one output y. a–c) The input to each hidden unit is a linear function of the two inputs, which corresponds to an oriented plane. Brightness indicates function output. For example, in panel (a), the brightness represents $\theta_{10} + \theta_{11}x_1 + \theta_{12}x_2$. Thin lines are contours. d–f) Each plane is clipped by the ReLU activation function (cyan lines are equivalent to "joints" in figures 3.3d–f). g-i) The clipped planes are then weighted, and j) summed together with an offset that determines the overall height of the surface. The result is a continuous surface made up of convex piecewise linear polygonal regions.

$$
\begin{aligned}
h_1 &= \mathrm{a}[\theta_{10} + \theta_{11}x_1 + \theta_{12}x_2] \\
h_2 &= \mathrm{a}[\theta_{20} + \theta_{21}x_1 + \theta_{22}x_2] \\
h_3 &= \mathrm{a}[\theta_{30} + \theta_{31}x_1 + \theta_{32}x_2],
\end{aligned}
\tag{3.9}
$$

where there is now one slope parameter for each input. The hidden units are combined to form the output in the usual way:

$$
y = \phi_0 + \phi_1 h_1 + \phi_2 h_2 + \phi_3 h_3. \tag{3.10}
$$

Figure 3.8 illustrates the processing of this network. Each hidden unit receives a linear combination of the two inputs, which forms an oriented plane in the 3D input/output space. The activation function clips the negative values of these planes to zero. The clipped planes are then recombined in a second linear function (equation 3.10) to create a continuous piecewise linear surface consisting of convex polygonal regions (figure 3.8j). Each region corresponds to a different activation pattern. For example, in the central triangular region, the first and third hidden units are active, and the second is inactive.

Problems 3.12–3.13

Notebook 3.2 Shallow networks II

Appendix C.3 Convex region

When there are more than two inputs to the model, it becomes difficult to visualize. However, the interpretation is similar. The output will be a continuous piecewise linear function of the input, where the linear regions are now convex polytopes in the multi-dimensional input space.

Note that as the input dimensions grow, the number of linear regions increases rapidly (figure 3.9). To get a feeling for how rapidly, consider that each hidden unit defines a hyperplane that delineates the part of space where this unit is from the part where it is not (cyan lines in 3.8d–f). If we had the same number of hidden units as input dimensions D_i, we could align each hyperplane with one of the coordinate axes (figure 3.10). For two input dimensions, this would divide the space into four quadrants. For three dimensions this would create eight octants, and for D_i dimensions, this would create 2^{D_i} orthants. Shallow neural networks usually have more hidden units than input dimensions, so they typically create more than 2^{D_i} linear regions.

Notebook 3.3 Shallow network regions

3.4 Shallow neural networks: general case

We have described several example shallow networks to help develop intuition about how they work. We now define a general equation for a shallow neural network $\mathbf{y} = \mathbf{f}[\mathbf{x}, \boldsymbol{\phi}]$ that maps a multi-dimensional input $\mathbf{x} \in \mathbb{R}^{D_i}$ to a multi-dimensional output $\mathbf{y} \in \mathbb{R}^{D_o}$ using $\mathbf{h} \in \mathbb{R}^{D}$ hidden units. Each hidden unit is computed as:

$$
h_d = \mathrm{a}\left[\theta_{d0} + \sum_{i=1}^{D_i} \theta_{di} x_i\right], \tag{3.11}
$$

and these are combined linearly to create the output:

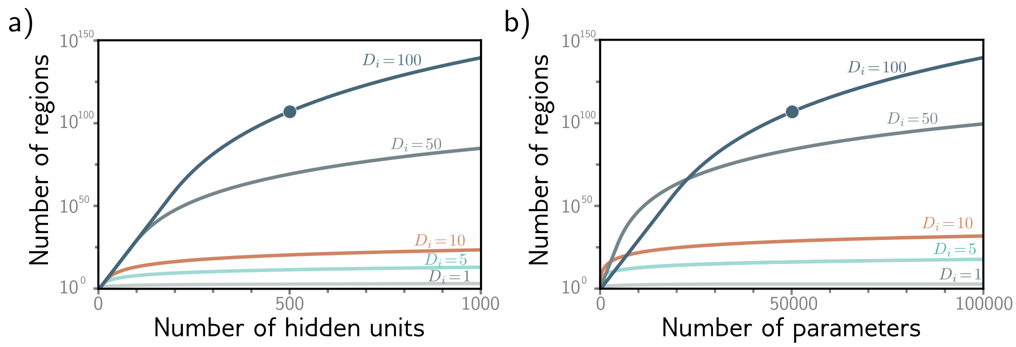

Figure 3.9 Linear regions vs. hidden units. a) Maximum possible regions as a function of the number of hidden units for five different input dimensions $D_i = \{1, 5, 10, 50, 100\}$. The number of regions increases rapidly in high dimensions; with $D = 500$ units and input size $D_i = 100$, there can be greater than 10^{107} regions (solid circle). b) The same data is plotted as a function of the number of parameters. The solid circle represents the same model as in panel (a) with $D = 500$ hidden units. This network has $51,001$ parameters and would be considered very small by modern standards.

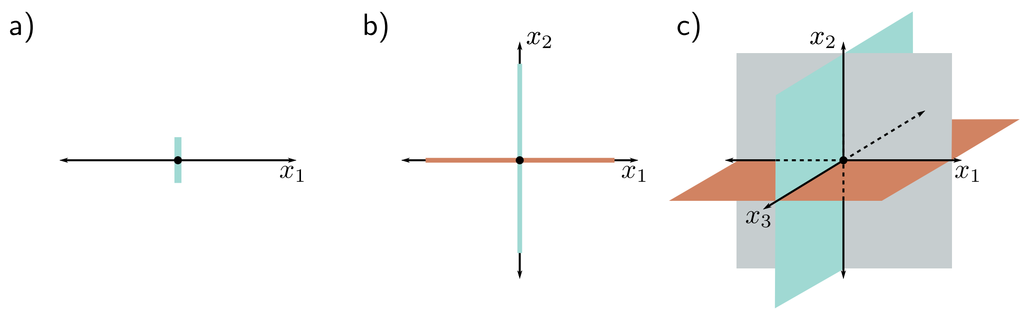

Figure 3.10 Number of linear regions vs. input dimensions. a) With a single input dimension, a model with one hidden unit creates one joint, which divides the axis into two linear regions. b) With two input dimensions, a model with two hidden units can divide the input space using two lines (here aligned with axes) to create four regions. c) With three input dimensions, a model with three hidden units can divide the input space using three planes (again aligned with axes) to create eight regions. Continuing this argument, it follows that a model with D_i input dimensions and D_i hidden units can divide the input space with D_i hyperplanes to create 2^{D_i} linear regions.

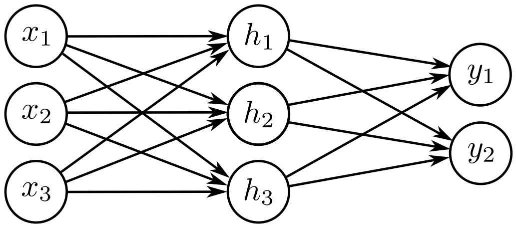

Figure 3.11 Visualization of neural network with three inputs and two outputs. This network has twenty parameters. There are fifteen slopes (indicated by arrows) and five offsets (not shown).

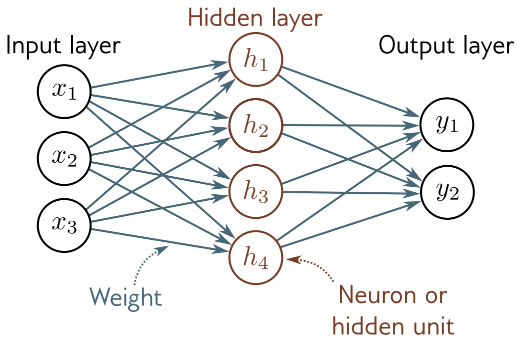

Figure 3.12 Terminology. A shallow network consists of an input layer, a hidden layer, and an output layer. Each layer is connected to the next by forward connections (arrows). For this reason, these models are referred to as feed-forward networks. When every variable in one layer connects to every variable in the next, we call this a fully connected network. Each connection represents a slope parameter in the underlying equation, and these parameters are termed weights. The variables in the hidden layer are termed neurons or hidden units. The values feeding into the hidden units are termed pre-activations, and the values at the hidden units (i.e., after the ReLU function is applied) are termed activations.

$$y_j = \phi_{j0} + \sum_{d=1}^{D} \phi_{jd} h_d, \tag{3.12}$$

where $a[\bullet]$ is a nonlinear activation function. The model has parameters $\boldsymbol{\phi} = \{\theta_{\bullet\bullet}, \phi_{\bullet\bullet}\}$. Figure 3.11 shows an example with three inputs, three hidden units, and two outputs.

Problems 3.14–3.17

The activation function permits the model to describe nonlinear relations between input and the output, and as such, it must be nonlinear itself; with no activation function, or a linear activation function, the overall mapping from input to output would be restricted to be linear. Many different activation functions have been tried (figure 3.13), but the most common choice is the ReLU (figure 3.1), which has the merit of being easily interpretable. With ReLU activations, the network divides the input space into convex polytopes defined by the intersections of hyperplanes computed by the "joints" in the ReLU functions. Each convex polytope contains a different linear function. The polytopes are the same for each output, but the linear functions they contain can differ.

Notebook 3.4
Activation functions

3.5 Terminology

We conclude this chapter by introducing some terminology. Regrettably, neural networks have a lot of associated jargon. They are often referred to in terms of *layers*. The left of figure 3.12 is the *input layer*, the center is the *hidden layer*, and to the right is the *output layer*. We would say that the network in figure 3.12 has one hidden layer containing four hidden units. The hidden units themselves are sometimes referred to as *neurons*. When we pass data through the network, the values of the inputs to the hidden layer (i.e., before the ReLU functions are applied) are termed *pre-activations*. The values at the hidden layer (i.e., after the ReLU functions) are termed *activations*.

For historical reasons, any neural network with at least one hidden layer is also called a *multi-layer perceptron*, or *MLP* for short. Networks with one hidden layer (as described in this chapter) are sometimes referred to as *shallow neural networks*. Networks with multiple hidden layers (as described in the next chapter) are referred to as *deep neural networks*. Neural networks in which the connections form an acyclic graph (i.e., a graph with no loops, as in all the examples in this chapter) are referred to as *feed-forward networks*. If every element in one layer connects to every element in the next (as in all the examples in this chapter), the network is *fully connected.* These connections represent slope parameters in the underlying equations and are referred to as *network weights*. The offset parameters (not shown in figure 3.12) are called *biases*.

3.6 Summary

Shallow neural networks have one hidden layer. They (i) compute several linear functions of the input, (ii) pass each result through an activation function, and then (iii) take a linear combination of these activations to form the outputs. Shallow neural networks make predictions $\mathbf{y}$ based on inputs $\mathbf{x}$ by dividing the input space into a continuous surface of piecewise linear regions. With enough hidden units (neurons), shallow neural networks can approximate any continuous function to arbitrary precision.

Chapter 4 discusses deep neural networks, which extend the models from this chapter by adding more hidden layers. Chapters 5–7 describe how to train these models.

Notes

"Neural" networks: If the models in this chapter are just functions, why are they called "neural networks"? The connection is unfortunately tenuous. Visualizations like figure 3.12 consist of nodes (inputs, hidden units, and outputs) that are densely connected to one another. This bears a superficial similarity to neurons in the mammalian brain, which also have dense connections. However, there is scant evidence that brain computation works in the same way as neural networks, and it is unhelpful to think about biology going forward.

History of neural networks: McCulloch & Pitts (1943) first came up with the notion of an artificial neuron that combined inputs to produce an output, but this model did not have a prac-

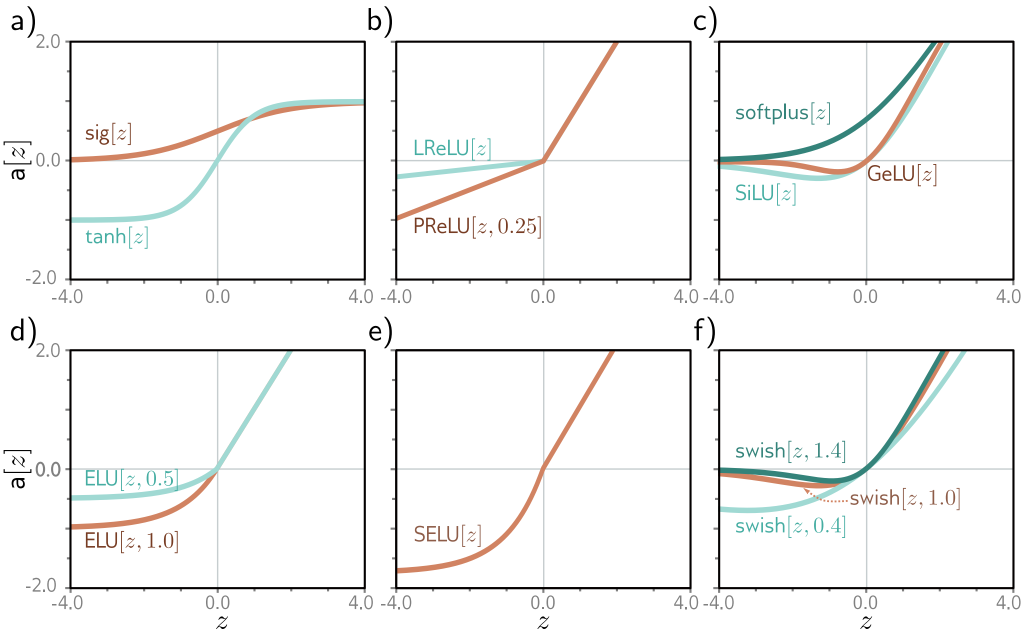

Figure 3.13 Activation functions. a) Logistic sigmoid and tanh functions. b) Leaky ReLU and parametric ReLU with parameter 0.25. c) SoftPlus, Gaussian error linear unit, and sigmoid linear unit. d) Exponential linear unit with parameters 0.5 and 1.0, e) Scaled exponential linear unit. f) Swish with parameters 0.4, 1.0, and 1.4.

tical learning algorithm. Rosenblatt (1958) developed the *perceptron*, which linearly combined inputs and then thresholded them to make a yes/no decision. He also provided an algorithm to learn the weights from data. Minsky & Papert (1969) argued that the linear function was inadequate for general classification problems but that adding hidden layers with nonlinear activation functions (hence the term multi-layer perceptron) could allow the learning of more general input/output relations. However, they concluded that Rosenblatt's algorithm could not learn the parameters of such models. It was not until the 1980s that a practical algorithm (backpropagation, see chapter 7) was developed, and significant work on neural networks resumed. The history of neural networks is chronicled by Kurenkov (2020), Sejnowski (2018), and Schmidhuber (2022).

Activation functions: The ReLU function has been used as far back as Fukushima (1969). However, in the early days of neural networks, it was more common to use the logistic sigmoid or tanh activation functions (figure 3.13a). The ReLU was re-popularized by Jarrett et al. (2009), Nair & Hinton (2010), and Glorot et al. (2011) and is an important part of the success story of modern neural networks. It has the nice property that the derivative of the output with respect to the input is always one for inputs greater than zero. This contributes to the stability and efficiency of training (see chapter 7) and contrasts with the derivatives of sigmoid activation functions, which saturate (become close to zero) for large positive and large negative inputs.

However, the ReLU function has the disadvantage that its derivative is zero for negative inputs.

If all the training examples produce negative inputs to a given ReLU function, then we cannot improve the parameters feeding into this ReLU during training. The gradient with respect to the incoming weights is locally flat, so we cannot "walk downhill". This is known as the *dying ReLU* problem. Many variations on the ReLU have been proposed to resolve this problem (figure 3.13b), including (i) the leaky ReLU (Maas et al., 2013), which also has a linear output for negative values with a smaller slope of 0.1, (ii) the parametric ReLU (He et al., 2015), which treats the slope of the negative portion as an unknown parameter, and (iii) the concatenated ReLU (Shang et al., 2016), which produces two outputs, one of which clips below zero (i.e., like a typical ReLU) and one of which clips above zero.

A variety of smooth functions have also been investigated (figure 3.13c–d), including the softplus function (Glorot et al., 2011), Gaussian error linear unit (Hendrycks & Gimpel, 2016), sigmoid linear unit (Hendrycks & Gimpel, 2016), and exponential linear unit (Clevert et al., 2015). Most of these are attempts to avoid the dying neuron problem while limiting the gradient for negative values. Klambauer et al. (2017) introduced the scaled exponential linear unit (figure 3.13e), which is particularly interesting as it helps stabilize the variance of the activations when the input variance has a limited range (see section 7.5). Ramachandran et al. (2017) adopted an empirical approach to choosing an activation function. They searched the space of possible functions to find the one that performed best over a variety of supervised learning tasks. The optimal function was found to be $a[x] = x/(1 + \exp[-\beta x])$, where β is a learned parameter (figure 3.13f). They termed this function *Swish*. Interestingly, this was a rediscovery of activation functions previously proposed by Hendrycks & Gimpel (2016) and Elfwing et al. (2018). Howard et al. (2019) approximated Swish by the HardSwish function, which has a very similar shape but is faster to compute:

$$\text{HardSwish}[z] = \begin{cases} 0 & z < -3 \\ z(z+3)/6 & -3 \leq z \leq 3 \\ z & z > 3 \end{cases}. \tag{3.13}$$

There is no definitive answer as to which of these activations functions is empirically superior However, the leaky ReLU, parameterized ReLU, and many of the continuous functions can be shown to provide minor performance gains over the ReLU in particular situations. We restrict attention to neural networks with the basic ReLU function for the rest of this book because it's easy to characterize the functions they create in terms of the number of linear regions.

Universal approximation theorem: The *width version* of this theorem states that a network with one hidden layer containing a finite number of hidden units and an activation function can approximate any continuous function on a compact subset of $\mathbb{R}^n$ to arbitrary accuracy. This was proved by Cybenko (1989) for sigmoid activations and was later shown to be true for a larger class of nonlinear activation functions (Hornik, 1991).

Number of linear regions: Consider a shallow network with $D_i \geq 2$-dimensional inputs and D hidden units. The number of linear regions is determined by the intersections of the D hyperplanes created by the "joints" in the ReLU functions (e.g., figure 3.8d–f). Each region is created by a different combination of the ReLU functions clipping or not clipping the input. The number of regions created by D hyperplanes in the $D_i \leq D$-dimensional input space was shown by Zaslavsky (1975) to be at most $\sum_{j=0}^{D_i} \binom{D}{j}$ (i.e., a sum of binomial coefficients). As a rule of thumb, shallow neural networks almost always have a larger number D of hidden units than input dimensions D_i and create between 2^{D_i} and 2^D linear regions.

Appendix C.8 Binomial coefficient

Problem 3.18

Linear, affine, and nonlinear functions: Technically, a linear transformation $\text{f}[\bullet]$ is any function that obeys the principle of superposition, so $\text{f}[a+b] = \text{f}[a]+\text{f}[b]$. This definition implies that $\text{f}[2a] = 2\text{f}[a]$.The weighted sum $\text{f}[h_1, h_2, h_3] = \phi_1 h_1 + \phi_2 h_2 + \phi_3 h_3$ is linear, but once the offset (bias) is added so $f[h_1, h_2, h_3] = \phi_0 + \phi_1 h_1 + \phi_2 h_2 + \phi_3 h_3$, this is no longer true. To see this, consider that the output is doubled when we double the arguments of the former function. This is not the case for the latter function, which is more properly termed an *affine* function. However, it is common in machine learning to conflate these terms. We follow this convention in this book and refer to both as linear. All other functions we will encounter are nonlinear.

Problems

Problem 3.1 What kind of mapping from input to output would be created if the activation function in equation 3.1 was linear so that $a[z] = \psi_0 + \psi_1 z$? What kind of mapping would be created if the activation function was removed, so $a[z] = z$?

Problem 3.2 For each of the four linear regions in figure 3.3j, indicate which hidden units are inactive and which are active (i.e., which do and do not clip their inputs).

Problem 3.3* Derive expressions for the positions of the "joints" in function in figure 3.3j in terms of the ten parameters $\boldsymbol{\phi}$ and the input x. Derive expressions for the slopes of the four linear regions.

Problem 3.4 Draw a version of figure 3.3 where the y-intercept and slope of the third hidden unit have changed as in figure 3.14c. Assume that the remaining parameters remain the same.

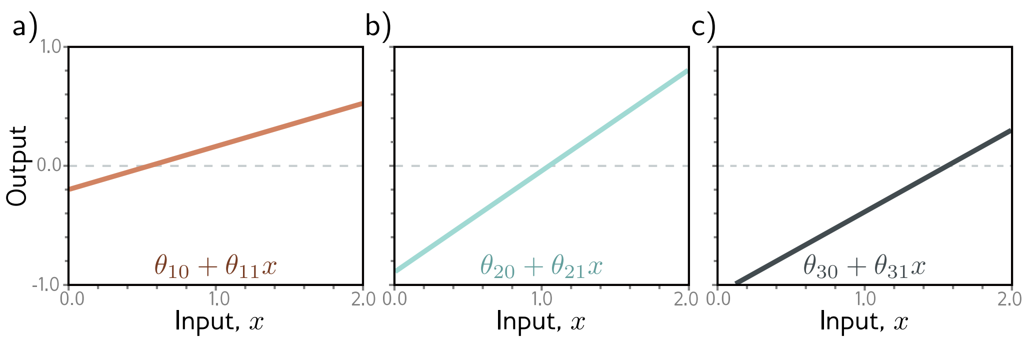

Figure 3.14 Processing in network with one input, three hidden units, and one output for problem 3.4. a–c) The input to each hidden unit is a linear function of the inputs. The first two are the same as in figure 3.3, but the last one differs.

Problem 3.5 Prove that the following property holds for $\alpha \in \mathbb{R}^+$:

$$\text{ReLU}[\alpha \cdot z] = \alpha \cdot \text{ReLU}[z]. \tag{3.14}$$

This is known as the *non-negative homogeneity* property of the ReLU function.

Problem 3.6 Following on from problem 3.5, what happens to the shallow network defined in equations 3.3 and 3.4 when we multiply the parameters θ_{10} and θ_{11} by a positive constant α and divide the slope ϕ_1 by the same parameter α? What happens if α is negative?

Problem 3.7 Consider fitting the model in equation 3.1 using a least squares loss function. Does this loss function have a unique minimum? i.e., is there is a single "best" set of parameters?

Problem 3.8 Consider replacing the ReLU activation function with (i) the Heaviside step function heaviside[z], (ii) the hyperbolic tangent function tanh[z], (iii) the rectangular function rect[z], and (iv) the sinusoidal function sin[z], where:

$$\text{heaviside}[z] = \begin{cases} 0 & z < 0 \\ 1 & z \geq 0 \end{cases}, \tag{3.15}$$

$$\text{rect}[z] = \begin{cases} 0 & z < 0 \\ 1 & 0 \leq z \leq 1 \\ 0 & z > 1 \end{cases}. \tag{3.16}$$

Redraw a version of figure 3.3 for each of these functions. The original parameters were: $\boldsymbol{\phi} = \{\phi_0, \phi_1, \phi_2, \phi_3, \theta_{10}, \theta_{11}, \theta_{20}, \theta_{21}, \theta_{30}, \theta_{31}\} = \{-0.23, -1.3, 1.3, 0.66, -0.2, 0.4, -0.9, 0.9, 1.1, -0.7\}$. Provide an informal description of the family of functions that can be created by neural networks with one input, three hidden units, and one output for each activation function.

Problem 3.9* Show that the third linear region in figure 3.3 has a slope that is the sum of the slopes of the first and fourth linear regions.

Problem 3.10 Consider a neural network with one input, one output, and three hidden units. The construction in figure 3.3 shows how this creates four linear regions. Under what circumstances could this network produce a function with fewer than four linear regions?

Problem 3.11* How many parameters does the model in figure 3.6 have?

Problem 3.12 How many parameters does the model in figure 3.7 have?

Problem 3.13 What is the activation pattern for each of the seven regions in figure 3.8? In other words, which hidden units are active (pass the input) and which are inactive (clip the input) for each region?

Problem 3.14 Write out the equations that define the network in figure 3.11. There should be three equations to compute the three hidden units from the inputs and two equations to compute the outputs from the hidden units.

Problem 3.15* What is the maximum possible number of 3D linear regions that can be created by the network in figure 3.11?

Problem 3.16 Write out the equations for a network with two inputs, four hidden units, and three outputs. Draw this model in the style of figure 3.11.

Problem 3.17* Equations 3.11 and 3.12 define a general neural network with D_i inputs, one hidden layer containing D hidden units, and D_o outputs. Find an expression for the number of parameters in the model in terms of D_i, D, and D_o.

Problem 3.18* Show that the maximum number of regions created by a shallow network with $D_i = 2$-dimensional input, $D_o = 1$-dimensional output, and $D = 3$ hidden units is seven as in figure 3.8j. Use the result of Zaslavsky (1975) that the maximum number of regions created by partitioning a D_i-dimensional space with D hyperplanes is $\sum_{j=0}^{D_i} \binom{D}{j}$. What is the maximum number of regions if we add two more hidden units to this model so $D = 5$?

Chapter 4

Deep neural networks

The last chapter described shallow neural networks, which have a single hidden layer. This chapter introduces deep neural networks, which have more than one hidden layer. With ReLU activation functions, both shallow and deep networks describe piecewise linear mappings from input to output.

As the number of hidden units increases, shallow neural networks improve their descriptive power. Indeed, with enough hidden units, shallow networks can describe arbitrarily complex functions in high dimensions. However, it turns out that for some functions, the required number of hidden units is impractically large. Deep networks can produce many more linear regions than shallow networks for a given number of parameters. Hence, from a practical standpoint, they can be used to describe a broader family of functions.

4.1 Composing neural networks

To gain insight into the behavior of deep neural networks, we first consider composing two shallow networks so the output of the first becomes the input to the second. Consider two shallow networks with three hidden units each (figure 4.1a). The first network takes an input x and returns output y and is defined by:

$$\begin{aligned} h_1 &= \mathrm{a}[\theta_{10} + \theta_{11}x] \\ h_2 &= \mathrm{a}[\theta_{20} + \theta_{21}x] \\ h_3 &= \mathrm{a}[\theta_{30} + \theta_{31}x], \end{aligned} \tag{4.1}$$

and

$$y = \phi_0 + \phi_1 h_1 + \phi_2 h_2 + \phi_3 h_3. \tag{4.2}$$

The second network takes y as input and returns y' and is defined by:

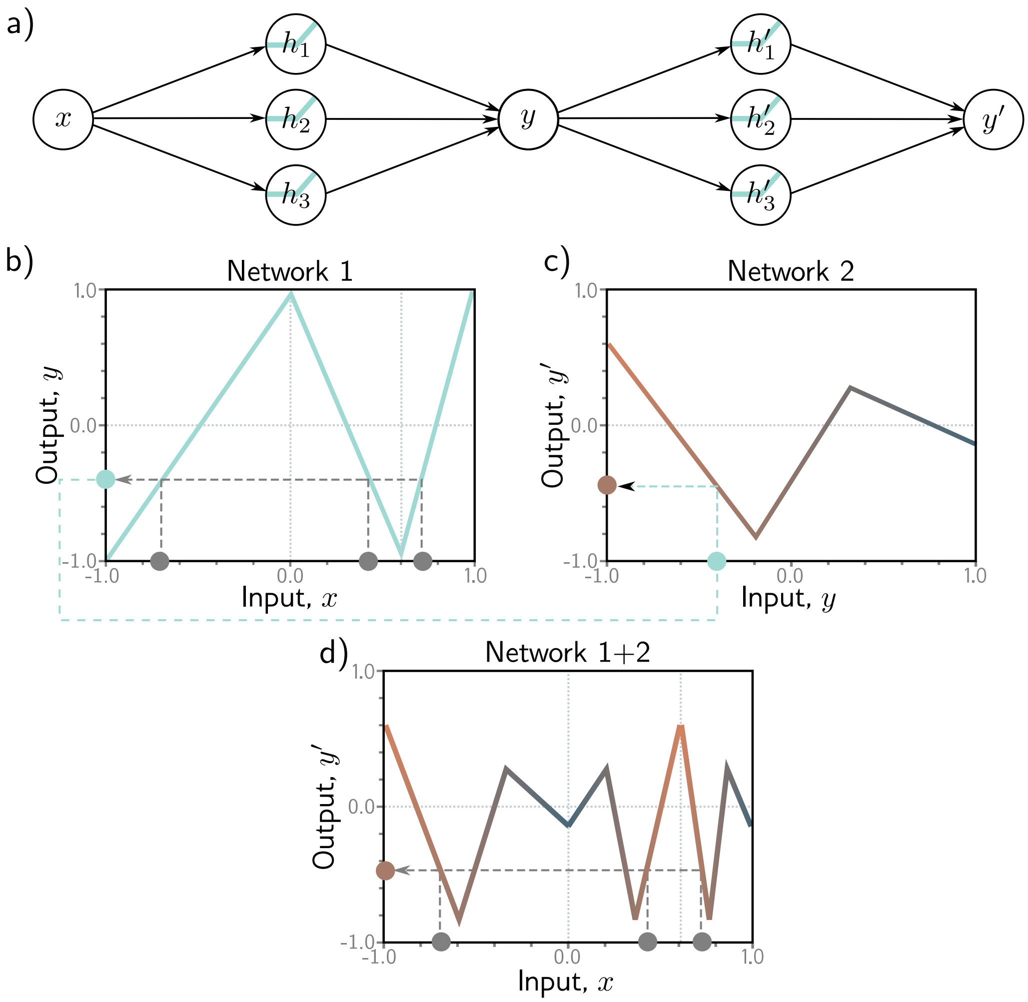

Figure 4.1 Composing two single-layer networks with three hidden units each. a) The output y of the first network constitutes the input to the second network. b) The first network maps inputs $x \in [-1, 1]$ to outputs $y \in [-1, 1]$ using a function comprised of three linear regions that are chosen so that they alternate the sign of their slope. Multiple inputs x (gray circles) now map to the same output y (cyan circle). c) The second network defines a function comprising three linear regions that takes y and returns y' (i.e., the cyan circle is mapped to the brown circle). d) The combined effect of these two functions when composed is that (i) three different inputs x are mapped to any given value of y by the first network and (ii) are processed in the same way by the second network; the result is that the function defined by the second network in panel (c) is duplicated three times, variously flipped and re-scaled according to the slope of the regions of panel (b).

$$\begin{aligned} h'_1 &= \mathrm{a}[\theta'_{10} + \theta'_{11}y] \\ h'_2 &= \mathrm{a}[\theta'_{20} + \theta'_{21}y] \\ h'_3 &= \mathrm{a}[\theta'_{30} + \theta'_{31}y], \end{aligned} \tag{4.3}$$

and

$$y' = \phi'_0 + \phi'_1 h'_1 + \phi'_2 h'_2 + \phi'_3 h'_3. \tag{4.4}$$

With ReLU activations, this model also describes a family of piecewise linear functions. However, the number of linear regions is potentially greater than for a shallow network with six hidden units. To see this, consider choosing the first network to produce three alternating regions of positive and negative slope (figure 4.1b). This means that three different ranges of x are mapped to the same output range $y \in [-1, 1]$, and the subsequent mapping from this range of y to y' is applied three times. The overall effect is that the function defined by the second network is duplicated three times to create nine linear regions. The same principle applies in higher dimensions (figure 4.2).

Problem 4.1

Notebook 4.1 Composing networks

A different way to think about composing networks is that the first network "folds" the input space x back onto itself so that multiple inputs generate the same output. Then the second network applies a function, which is replicated at all points that were folded on top of one another (figure 4.3).

4.2 From composing networks to deep networks

The previous section showed that we could create complex functions by passing the output of one shallow neural network into a second network. We now show that this is a special case of a deep network with two hidden layers.

The output of the first network ($y = \phi_0 + \phi_1 h_1 + \phi_2 h_2 + \phi_3 h_3$) is linear and so are the first operations of the second network (equation 4.3 in which we calculate $\theta'_{10} + \theta'_{11}y$, $\theta'_{20} + \theta'_{21}y$, and $\theta'_{30} + \theta'_{31}y$). Applying one linear function to another yields another linear function. When we substitute the expression for y into equation 4.3 the result is:

$$\begin{aligned} h'_1 &= \mathrm{a}[\theta'_{10} + \theta'_{11}y] &= \mathrm{a}[\theta'_{10} + \theta'_{11}\phi_0 + \theta'_{11}\phi_1 h_1 + \theta'_{11}\phi_2 h_2 + \theta'_{11}\phi_3 h_3] \\ h'_2 &= \mathrm{a}[\theta'_{20} + \theta'_{21}y] &= \mathrm{a}[\theta'_{20} + \theta'_{21}\phi_0 + \theta'_{21}\phi_1 h_1 + \theta'_{21}\phi_2 h_2 + \theta'_{21}\phi_3 h_3] \\ h'_3 &= \mathrm{a}[\theta'_{30} + \theta'_{31}y] &= \mathrm{a}[\theta'_{30} + \theta'_{31}\phi_0 + \theta'_{31}\phi_1 h_1 + \theta'_{31}\phi_2 h_2 + \theta'_{31}\phi_3 h_3], \end{aligned} \tag{4.5}$$

which we can rewrite as:

$$\begin{aligned} h'_1 &= \mathrm{a}[\psi_{10} + \psi_{11}h_1 + \psi_{12}h_2 + \psi_{13}h_3] \\ h'_2 &= \mathrm{a}[\psi_{20} + \psi_{21}h_1 + \psi_{22}h_2 + \psi_{23}h_3] \\ h'_3 &= \mathrm{a}[\psi_{30} + \psi_{31}h_1 + \psi_{32}h_2 + \psi_{33}h_3], \end{aligned} \tag{4.6}$$

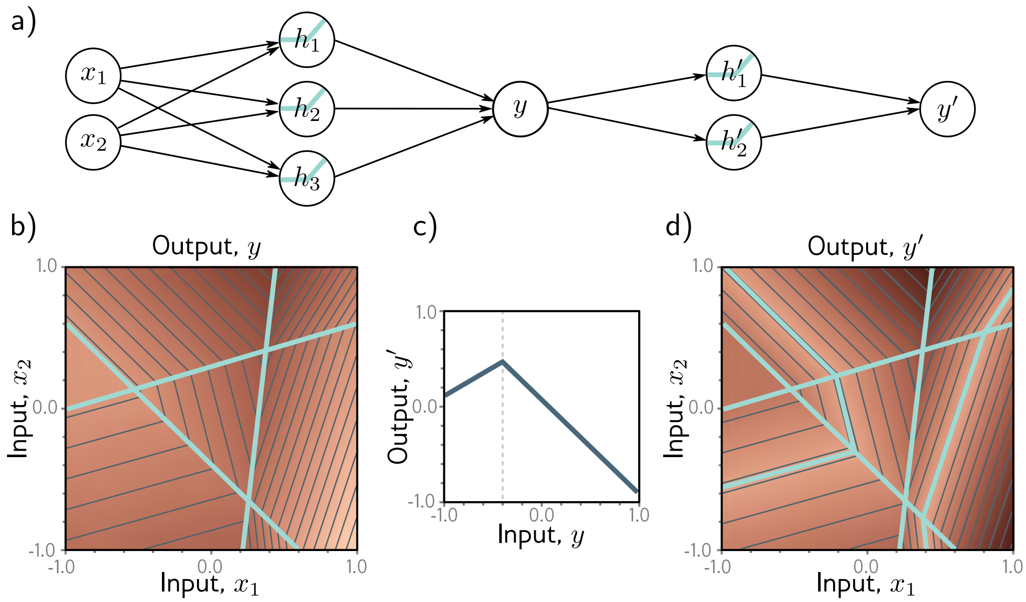

Figure 4.2 Composing neural networks with a 2D input. a) The first network (from figure 3.8) has three hidden units and takes two inputs x_1 and x_2 and returns a scalar output y. This is passed into a second network with two hidden units to produce y'. b) The first network produces a function consisting of seven linear regions, one of which is flat. c) The second network defines a function comprising two linear regions in $y \in [-1, 1]$. d) When these networks are composed, each of the six non-flat regions from the first network is divided into two new regions by the second network to create a total of 13 linear regions.

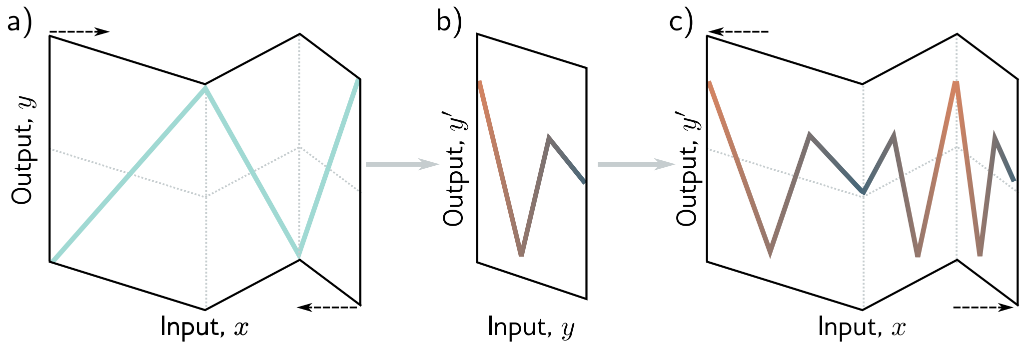

Figure 4.3 Deep networks as folding input space. a) One way to think about the first network from figure 4.1 is that it "folds" the input space back on top of itself. b) The second network applies its function to the folded space. c) The final output is revealed by "unfolding" again.

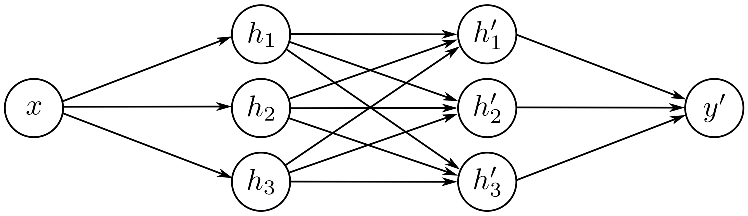

Figure 4.4 Neural network with one input, one output, and two hidden layers, each containing three hidden units.

where $\psi_{10} = \theta'_{10} + \theta'_{11}\phi_0, \psi_{11} = \theta'_{11}\phi_1, \psi_{12} = \theta'_{11}\phi_2$ and so on. The result is a network with two hidden layers (figure 4.4).

It follows that a network with two layers can represent the family of functions created by passing the output of one single-layer network into another. In fact, it represents a broader family because in equation 4.6, the nine slope parameters $\psi_{11}, \psi_{21}, \ldots, \psi_{33}$ can take arbitrary values, whereas, in equation 4.5, these parameters are constrained to be the outer product $[\theta'_{11}, \theta'_{21}, \theta'_{31}]^T[\phi_1, \phi_2, \phi_3]$.

4.3 Deep neural networks

In the previous section, we showed that composing two shallow networks yields a special case of a deep network with two hidden layers. Now we consider the general case of a deep network with two hidden layers, each containing three hidden units (figure 4.4). The first layer is defined by:

$$
\begin{aligned}
h_1 &= \mathrm{a}[\theta_{10} + \theta_{11}x] \\
h_2 &= \mathrm{a}[\theta_{20} + \theta_{21}x] \\
h_3 &= \mathrm{a}[\theta_{30} + \theta_{31}x],
\end{aligned}
\tag{4.7}
$$

the second layer by:

$$
\begin{aligned}
h'_1 &= \mathrm{a}[\psi_{10} + \psi_{11}h_1 + \psi_{12}h_2 + \psi_{13}h_3] \\
h'_2 &= \mathrm{a}[\psi_{20} + \psi_{21}h_1 + \psi_{22}h_2 + \psi_{23}h_3] \\
h'_3 &= \mathrm{a}[\psi_{30} + \psi_{31}h_1 + \psi_{32}h_2 + \psi_{33}h_3],
\end{aligned}
\tag{4.8}
$$

and the output by:

$$
y' = \phi'_0 + \phi'_1 h'_1 + \phi'_2 h'_2 + \phi'_3 h'_3. \tag{4.9}
$$

Notebook 4.2 Clipping functions

Considering these equations leads to a different way to think about how the network constructs an increasingly complicated function (figure 4.5):

1. The three hidden units h_1, h_2, and h_3 in the first layer are computed as usual by forming linear functions of the input and passing these through ReLU activation functions (equation 4.7).
2. The pre-activations at the second layer are computed by taking three new linear functions of these hidden units (arguments of the activation functions in equation 4.8). At this point, we effectively have a shallow network with three outputs; we have computed three piecewise linear functions with the "joints" between linear regions in the same places (see figure 3.6).
3. At the second hidden layer, another ReLU function $\mathrm{a}[\bullet]$ is applied to each function (equation 4.8), which clips them and adds new "joints" to each.
4. The final output is a linear combination of these hidden units (equation 4.9).

In conclusion, we can either think of each layer as "folding" the input space or as creating new functions, which are clipped (creating new regions) and then recombined. The former view emphasizes the dependencies in the output function but not how clipping creates new joints, and the latter has the opposite emphasis. Ultimately, both descriptions provide only partial insight into how deep neural networks operate. Regardless, it's important not to lose sight of the fact that this is still merely an equation relating input x to output y'. Indeed, we can combine equations 4.7–4.9 to get one expression:

$$\begin{aligned} y' \;\; = \;\; & \phi'_0 + \phi'_1 \mathrm{a}\left[\psi_{10} + \psi_{11}\mathrm{a}[\theta_{10} + \theta_{11}x] + \psi_{12}\mathrm{a}[\theta_{20} + \theta_{21}x] + \psi_{13}\mathrm{a}[\theta_{30} + \theta_{31}x]\right] \\ & \quad + \phi'_2 \mathrm{a}[\psi_{20} + \psi_{21}\mathrm{a}[\theta_{10} + \theta_{11}x] + \psi_{22}\mathrm{a}[\theta_{20} + \theta_{21}x] + \psi_{23}\mathrm{a}[\theta_{30} + \theta_{31}x]] \\ & \quad + \phi'_3 \mathrm{a}[\psi_{30} + \psi_{31}\mathrm{a}[\theta_{10} + \theta_{11}x] + \psi_{32}\mathrm{a}[\theta_{20} + \theta_{21}x] + \psi_{33}\mathrm{a}[\theta_{30} + \theta_{31}x]], \end{aligned} \tag{4.10}$$

although this is admittedly rather difficult to understand.

4.3.1 Hyperparameters

We can extend the deep network construction to more than two hidden layers; modern networks might have more than a hundred layers with thousands of hidden units at each layer. The number of hidden units in each layer is referred to as the *width* of the network, and the number of hidden layers as the *depth*. The total number of hidden units is a measure of the network's *capacity*.

Problem 4.2

We denote the number of layers as K and the number of hidden units in each layer as $D_1, D_2, \ldots, D_K$. These are examples of *hyperparameters*. They are quantities chosen before we learn the model parameters (i.e., the slope and intercept terms). For fixed hyperparameters (e.g., $K = 2$ layers with $D_k = 3$ hidden units in each), the model describes a family of functions, and the parameters determine the particular function. Hence, when we also consider the hyperparameters, we can think of neural networks as representing a family of families of functions relating input to output.

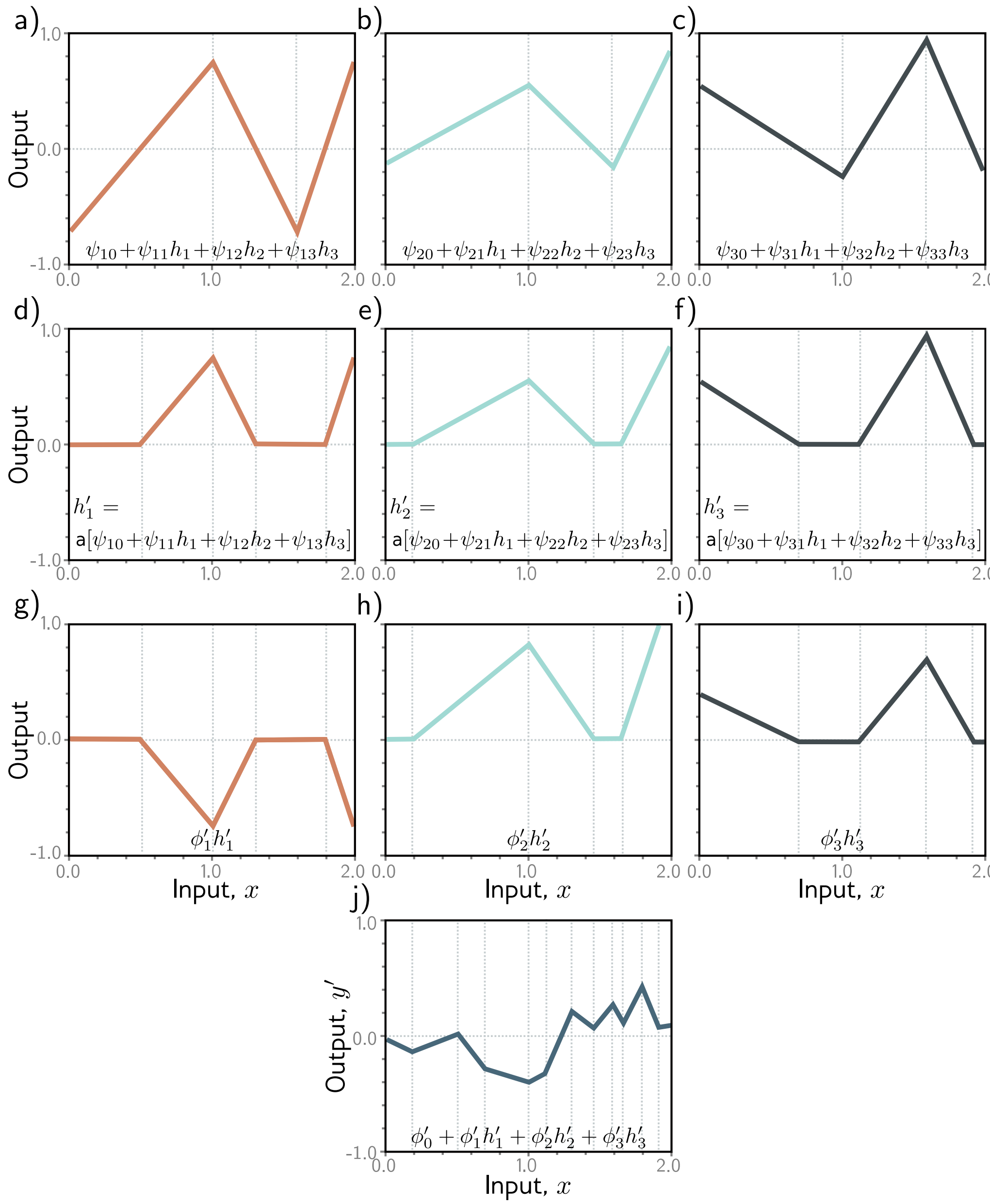

Figure 4.5 Computation for the deep network in figure 4.4. a–c) The inputs to the second hidden layer (i.e., the pre-activations) are three piecewise linear functions where the "joints" between the linear regions are at the same places (see figure 3.6). d–f) Each piecewise linear function is clipped to zero by the ReLU activation function. g–i) These clipped functions are then weighted with parameters ϕ'_1, ϕ'_2, and ϕ'_3, respectively. j) Finally, the clipped and weighted functions are summed and an offset ϕ'_0 that controls the overall height is added.

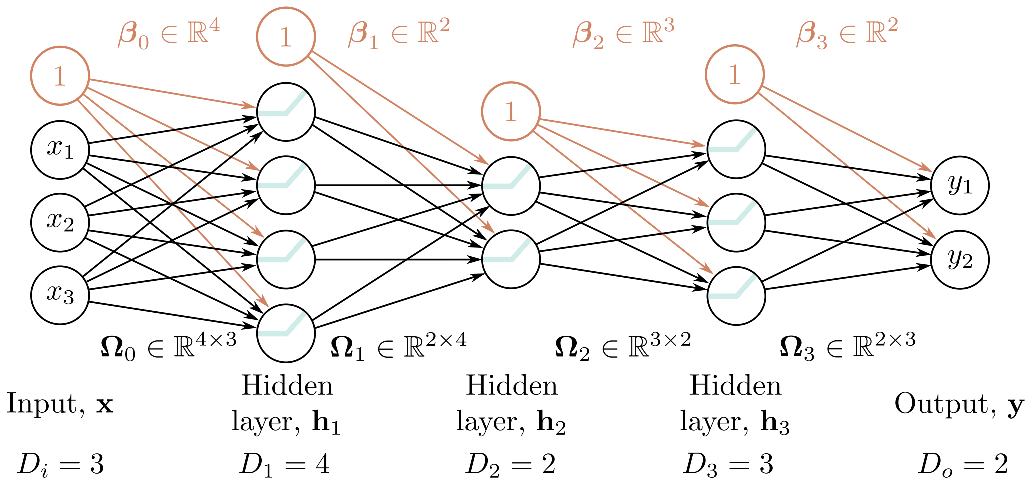

Figure 4.6 Matrix notation for network with $D_i = 3$-dimensional input $\mathbf{x}$, $D_o = 2$-dimensional output $\mathbf{y}$, and $K = 3$ hidden layers $\mathbf{h}_1, \mathbf{h}_2$, and $\mathbf{h}_3$ of dimensions $D_1 = 4$, $D_2 = 2$, and $D_3 = 3$ respectively. The weights are stored in matrices $\boldsymbol{\Omega}_k$ that pre-multiply the activations from the preceding layer to create the pre-activations at the subsequent layer. For example, the weight matrix $\boldsymbol{\Omega}_1$ that computes the pre-activations at $\mathbf{h}_2$ from the activations at $\mathbf{h}_1$ has dimension 2×4. It is applied to the four hidden units in layer one and creates the inputs to the two hidden units at layer two. The biases are stored in vectors $\boldsymbol{\beta}_k$ and have the dimension of the layer into which they feed. For example, the bias vector $\boldsymbol{\beta}_2$ is length three because layer $\mathbf{h}_3$ contains three hidden units.

4.4 Matrix notation

Appendix C.4.1 Matrices

We have seen that a deep neural network consists of linear transformations alternating with activation functions. We could equivalently describe equations 4.7–4.9 in matrix notation as:

$$\begin{bmatrix} h_1 \\ h_2 \\ h_3 \end{bmatrix} = \mathbf{a}\left[\begin{bmatrix} \theta_{10} \\ \theta_{20} \\ \theta_{30} \end{bmatrix} + \begin{bmatrix} \theta_{11} \\ \theta_{21} \\ \theta_{31} \end{bmatrix} x\right], \tag{4.11}$$

$$\begin{bmatrix} h'_1 \\ h'_2 \\ h'_3 \end{bmatrix} = \mathbf{a}\left[\begin{bmatrix} \psi_{10} \\ \psi_{20} \\ \psi_{30} \end{bmatrix} + \begin{bmatrix} \psi_{11} & \psi_{12} & \psi_{13} \\ \psi_{21} & \psi_{22} & \psi_{23} \\ \psi_{31} & \psi_{32} & \psi_{33} \end{bmatrix} \begin{bmatrix} h_1 \\ h_2 \\ h_3 \end{bmatrix}\right], \tag{4.12}$$

and

$$y' = \phi'_0 + \begin{bmatrix} \phi'_1 & \phi'_2 & \phi'_3 \end{bmatrix} \begin{bmatrix} h'_1 \\ h'_2 \\ h'_3 \end{bmatrix}, \tag{4.13}$$

or even more compactly in matrix notation as:

$$
\begin{aligned}
\mathbf{h} &= \mathbf{a}\left[\boldsymbol{\theta}_0 + \boldsymbol{\theta}x\right] \\
\mathbf{h}' &= \mathbf{a}\left[\boldsymbol{\psi}_0 + \boldsymbol{\Psi}\mathbf{h}\right] \\
y &= \phi'_0 + \boldsymbol{\phi}'\mathbf{h}',
\end{aligned} \tag{4.14}
$$

where, in each case, the function $\mathbf{a}[\bullet]$ applies the activation function separately to every element of its vector input.

4.4.1 General formulation

This notation becomes cumbersome for networks with many layers. Hence, from now on, we will describe the vector of hidden units at layer k as $\mathbf{h}_k$, the vector of biases (intercepts) that contribute to hidden layer $k+1$ as $\boldsymbol{\beta}_k$, and the weights (slopes) that are applied to the k^{th} layer and contribute to the $(k+1)^{th}$ layer as $\boldsymbol{\Omega}_k$. A general deep network $\mathbf{y} = \mathrm{f}[\mathbf{x}, \boldsymbol{\phi}]$ with K layers can now be written as:

$$
\begin{aligned}
\mathbf{h}_1 &= \mathbf{a}[\boldsymbol{\beta}_0 + \boldsymbol{\Omega}_0\mathbf{x}] \\
\mathbf{h}_2 &= \mathbf{a}[\boldsymbol{\beta}_1 + \boldsymbol{\Omega}_1\mathbf{h}_1] \\
\mathbf{h}_3 &= \mathbf{a}[\boldsymbol{\beta}_2 + \boldsymbol{\Omega}_2\mathbf{h}_2] \\
&\vdots \\
\mathbf{h}_K &= \mathbf{a}[\boldsymbol{\beta}_{K-1} + \boldsymbol{\Omega}_{K-1}\mathbf{h}_{K-1}] \\
\mathbf{y} &= \boldsymbol{\beta}_K + \boldsymbol{\Omega}_K\mathbf{h}_K.
\end{aligned} \tag{4.15}
$$

The parameters $\boldsymbol{\phi}$ of this model comprise all of these weight matrices and bias vectors $\boldsymbol{\phi} = \{\boldsymbol{\beta}_k, \boldsymbol{\Omega}_k\}_{k=0}^{K}$.

If the k^{th} layer has D_k hidden units, then the bias vector $\boldsymbol{\beta}_{k-1}$ will be of size D_k. The last bias vector $\boldsymbol{\beta}_K$ has the size D_o of the output. The first weight matrix $\boldsymbol{\Omega}_0$ has size $D_1 \times D_i$ where D_i is the size of the input. The last weight matrix $\boldsymbol{\Omega}_K$ is $D_o \times D_K$, and the remaining matrices $\boldsymbol{\Omega}_k$ are $D_k \times D_{k-1}$ (figure 4.6).

Notebook 4.3
Deep networks

We can equivalently write the network as a single function:

Problems 4.3–4.6

$$
\mathbf{y} = \boldsymbol{\beta}_K + \boldsymbol{\Omega}_K\mathbf{a}\left[\boldsymbol{\beta}_{K-1} + \boldsymbol{\Omega}_{K-1}\mathbf{a}\left[\ldots\boldsymbol{\beta}_2 + \boldsymbol{\Omega}_2\mathbf{a}\left[\boldsymbol{\beta}_1 + \boldsymbol{\Omega}_1\mathbf{a}\left[\boldsymbol{\beta}_0 + \boldsymbol{\Omega}_0\mathbf{x}\right]\right]\ldots\right]\right]. \tag{4.16}
$$

4.5 Shallow vs. deep neural networks

Chapter 3 discussed shallow networks (with a single hidden layer), and here we have described deep networks (with multiple hidden layers). We now compare these models.

4.5.1 Ability to approximate different functions

In section 3.2, we argued that shallow neural networks with enough capacity (hidden units) could model any continuous function arbitrarily closely. In this chapter, we saw that a deep network with two hidden layers could represent the composition of two shallow networks. If the second of these networks computes the identity function, then this deep network replicates a single shallow network. Hence, it can also approximate any continuous function arbitrarily closely given sufficient capacity.

Problem 4.7

4.5.2 Number of linear regions per parameter

Problems 4.8–4.11

A shallow network with one input, one output, and $D > 2$ hidden units can create up to $D+1$ linear regions and is defined by $3D+1$ parameters. A deep network with one input, one output, and K layers of $D > 2$ hidden units can create a function with up to $(D+1)^K$ linear regions using $3D+1+(K-1)D(D+1)$ parameters.

Figure 4.7a shows how the maximum number of linear regions increases as a function of the number of parameters for networks mapping scalar input x to scalar output y. Deep neural networks create much more complex functions for a fixed parameter budget. This effect is magnified as the number of input dimensions D_i increases (figure 4.7b), although computing the maximum number of regions is less straightforward.

This seems attractive, but the flexibility of the functions is still limited by the number of parameters. Deep networks can create extremely large numbers of linear regions, but these contain complex dependencies and symmetries. We saw some of these when we considered deep networks as "folding" the input space (figure 4.3). So, it's not clear that the greater number of regions is an advantage unless (i) there are similar symmetries in the real-world functions that we wish to approximate or (ii) we have reason to believe that the mapping from input to output really does involve a composition of simpler functions.

4.5.3 Depth efficiency

Both deep and shallow networks can model arbitrary functions, but some functions can be approximated much more efficiently with deep networks. Functions have been identified that require a shallow network with exponentially more hidden units to achieve an equivalent approximation to that of a deep network. This phenomenon is referred to as the *depth efficiency* of neural networks. This property is also attractive, but it's not clear that the real-world functions that we want to approximate fall into this category.

4.5.4 Large, structured inputs

We have discussed fully connected networks where every element of each layer contributes to every element of the subsequent one. However, these are not practical for large,

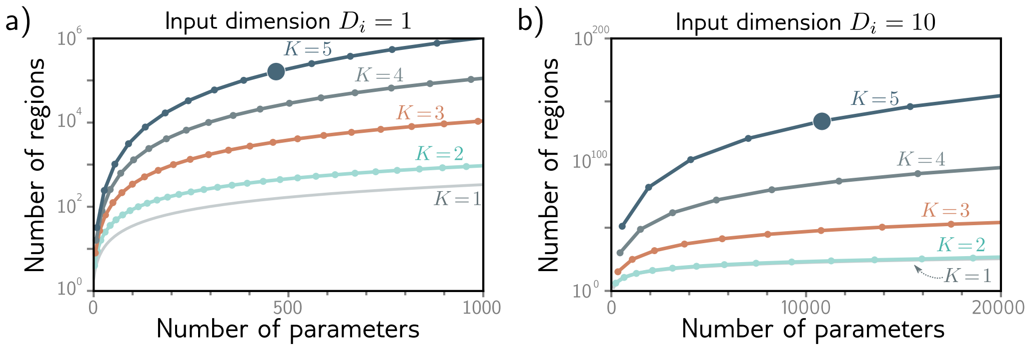

Figure 4.7 The maximum number of linear regions for neural networks increases rapidly with the network depth. a) Network with $D_i = 1$ input. Each curve represents a fixed number of hidden layers K, as we vary the number of hidden units D per layer. For a fixed parameter budget (horizontal position), deeper networks produce more linear regions than shallower ones. A network with $K = 5$ layers and $D = 10$ hidden units per layer has 471 parameters (highlighted point) and can produce 161,051 regions. b) Network with $D_i = 10$ inputs. Each subsequent point along a curve represents ten hidden units. Here, a model with $K = 5$ layers and $D = 50$ hidden units per layer has 10,801 parameters (highlighted point) and can create more than 10^{134} linear regions.

structured inputs like images, where the input might comprise $\sim 10^6$ pixels. The number of parameters would be prohibitive, and moreover, we want different parts of the image to be processed similarly; there is no point in independently learning to recognize the same object at every possible position in the image.

The solution is to process local image regions in parallel and then gradually integrate information from increasingly large regions. This kind of local-to-global processing is difficult to specify without using multiple layers (see chapter 10).

4.5.5 Training and generalization

A further possible advantage of deep networks is ease of fitting; it is easier to train moderately deep networks than shallow ones. It may be that over-parameterized deep models have a large family of roughly equivalent solutions that are easy to find. However, with more depth, training becomes more difficult again, although there are many methods to mitigate this problem (see chapter 11). Deep networks also seem to generalize to new data better than shallow ones. These phenomena are not well understood, and we return to them in chapter 20. In practice, the best results for most tasks have been achieved using networks with tens or hundreds of layers. This is discussed further in chapter 20.

4.6 Summary

In this chapter, we first considered what happens when we compose two shallow networks. We argued that the first network "folds" the input space and the second network then applies a piecewise linear function. The effects of the second network are duplicated where the input space is folded onto itself.

We then showed that this composition of shallow networks is a special case of a deep network with two layers. We interpreted the ReLU functions in each layer as clipping the input functions in multiple places and creating more "joints" in the output function. We introduced the idea of hyperparameters, which for the networks we've seen so far comprise the number of hidden layers and the number of hidden units in each.

Finally, we compared shallow and deep networks. We saw that (i) both networks can approximate any function given enough capacity, (ii) deep networks produce many more linear regions per parameter, (iii) some functions can be approximated much more efficiently by deep networks, (iv) large, structured inputs like images are best processed in multiple stages, and (v) in practice, the best results for most tasks are achieved using deep networks with many layers.

Now that we understand deep and shallow network models, we turn our attention to training them. In the next chapter, we discuss loss functions. For any given parameter values $\boldsymbol{\phi}$, the loss function returns a single number that indicates the mismatch between the model outputs and the ground truth predictions for a training dataset. In chapters 6 and 7, we deal with the training process itself, in which we seek the parameter values that minimize this loss.

Notes

Deep learning: It has long been understood that it is possible to build more complex functions by composing shallow neural networks or developing networks with more than one hidden layer. Indeed, the term "deep learning" was first used by Dechter (1986). However, interest was limited due to practical concerns; it was not possible to train such networks well. The modern era of deep learning was kick-started by startling improvements in image classification reported by Krizhevsky et al. (2012). This sudden progress was arguably due to the confluence of four factors: larger training datasets, improved processing power for training, the use of the ReLU activation function, and the use of stochastic gradient descent (see chapter 6). LeCun et al. (2015) present an overview of early advances in the modern era of deep learning.

Number of linear regions: For deep networks using a total of D hidden units with ReLU activations, the upper bound on the number of regions is 2^D (Montufar et al., 2014). The same authors show that a deep ReLU network with D_i-dimensional input and K layers, each containing $D \geq D_i$ hidden units has $\mathcal{O}\left((D/D_i)^{(K-1)D_i} D^{D_i}\right)$ linear regions. Montúfar (2017), Arora et al. (2016) and Serra et al. (2018) all provide tighter upper bounds that consider the possibility that each layer has different numbers of hidden units. Serra et al. (2018) provide an algorithm that counts the number of linear regions in a neural network, although it is only practical for very small networks.

If the number of hidden units D in each of the K layers is the same, and D is an integer multiple of the input dimensionality D_i, then the maximum number of linear regions N_r can be computed exactly and is:

$$N_r = \prod_{k=1}^{K-1} \left(\frac{D}{D_i} + 1 \right)^{D_i} \sum_{j=0}^{D_i} \binom{D}{j}. \tag{4.17}$$

The first term in this expression corresponds to the first $K-1$ layers of the network, which can be thought of as repeatedly folding the input space. However, we now need to devote D/D_i hidden units to each input dimension to create these folds. The last term in this equation (a sum of binomial coefficients) is the number of regions that a shallow network can create and is attributable to the last layer. For further information, consult Montufar et al. (2014), Pascanu et al. (2013), and Montúfar (2017).

Appendix C.8 Binomial coefficient

Universal approximation theorem: We argued in section 4.5.1 that if the layers of a deep network have enough hidden units, then the width version of the universal approximation theorem applies: the network can approximate any continuous function on a compact subset of $\mathbb{R}^{D_i}$ to arbitrary accuracy. Lu et al. (2017) proved that a network with ReLU activation functions and at least D_i+4 hidden units in each layer can approximate any D_i-dimensional Lebesgue integrable function to arbitrary accuracy given enough layers. This is known as the *depth version* of the universal approximation theorem.

Depth efficiency: Several results show that there are functions that can be realized by deep networks but not by any shallow network whose capacity is bounded above exponentially. In other words, it would take an exponentially larger number of units in a shallow network to describe these functions accurately. This is known as the *depth efficiency* of neural networks.

Telgarsky (2016) shows that for any integer k, it is possible to construct networks with one input, one output, and $\mathcal{O}[k^3]$ layers of constant width, which cannot be realized with $\mathcal{O}[k]$ layers and less than 2^k width. Perhaps surprisingly, Eldan & Shamir (2016) showed that when there are multivariate inputs, there is a three-layer network that cannot be realized by any two-layer network if the capacity is sub-exponential in the input dimension. Cohen et al. (2016), Safran & Shamir (2017), and Poggio et al. (2017) also demonstrate functions that deep networks can approximate efficiently, but shallow ones cannot. Liang & Srikant (2016) show that for a broad class of functions including univariate functions, shallow networks require exponentially more hidden units than deep networks for a given upper bound on the approximation error.

Width efficiency: Lu et al. (2017) investigate whether there are wide shallow networks (i.e., shallow networks with lots of hidden units) that cannot be realized by narrow networks whose depth is not substantially larger. They show that there exist classes of wide, shallow networks that can only be expressed by narrow networks with polynomial depth. This is known as the *width efficiency* of neural networks. This polynomial lower bound on width is less restrictive than the exponential lower bound on depth, suggesting that depth is more important. Vardi et al. (2022) subsequently showed that the price for making the width small is only a linear increase in the network depth for networks with ReLU activations.

Problems

Problem 4.1* Consider composing the two neural networks in figure 4.8. Draw a plot of the relationship between the input x and output y' for $x \in [-1, 1]$.

Problem 4.2 Identify the hyperparameters in figure 4.6. (Hint: there are four!)

Problem 4.3 Using the non-negative homogeneity property of the ReLU function (see problem 3.5), show that:

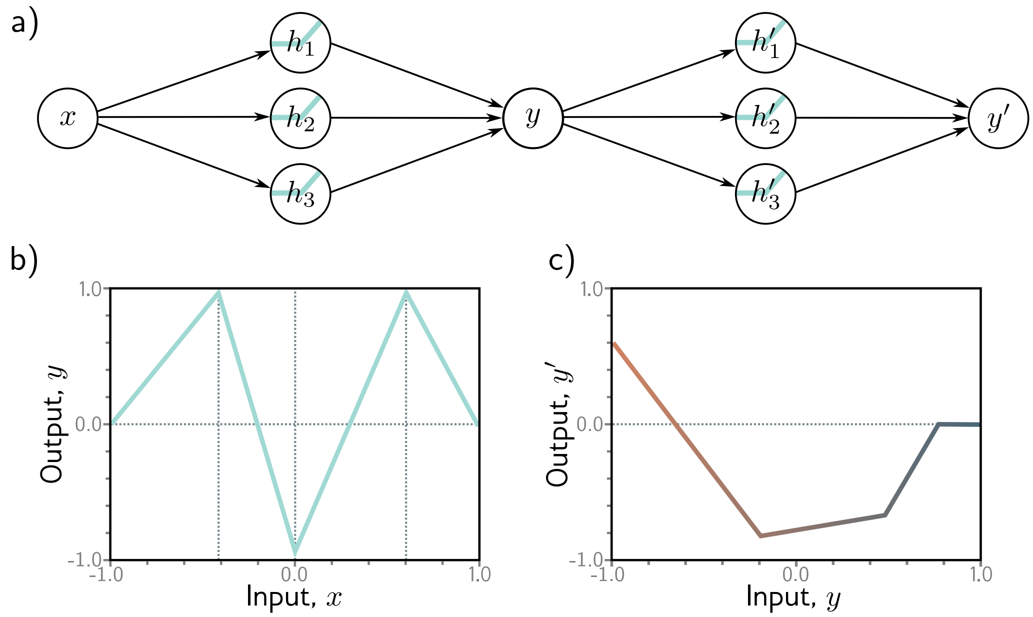

Figure 4.8 Composition of two networks for problem 4.1. a) The output y of the first network becomes the input to the second. b) The first network computes this function with output values $y \in [-1, 1]$. c) The second network computes this function on the input range $y \in [-1, 1]$.

$$\mathrm{ReLU}\left[\boldsymbol{\beta}_1+\lambda_1\cdot\boldsymbol{\Omega}_1\mathrm{ReLU}\left[\boldsymbol{\beta}_0+\lambda_0\cdot\boldsymbol{\Omega}_0\mathbf{x}\right]\right]=\lambda_0\lambda_1\cdot\mathrm{ReLU}\left[\frac{1}{\lambda_0\lambda_1}\boldsymbol{\beta}_1+\boldsymbol{\Omega}_1\mathrm{ReLU}\left[\frac{1}{\lambda_0}\boldsymbol{\beta}_0+\boldsymbol{\Omega}_0\mathbf{x}\right]\right], \tag{4.18}$$

where λ_0 and λ_1 are non-negative scalars. From this, we see that the weight matrices can be re-scaled by any magnitude as long as the biases are also adjusted, and the scale factors can be re-applied at the end of the network.

Problem 4.4 Write out the equations for a deep neural network that takes $D_i = 5$ inputs, $D_o = 4$ outputs and has three hidden layers of sizes $D_1 = 20$, $D_2 = 10$, and $D_3 = 7$, respectively in both the forms of equations 4.15 and 4.16. What are the sizes of each weight matrix $\boldsymbol{\Omega}_\bullet$ and bias vector $\boldsymbol{\beta}_\bullet$?

Problem 4.5 Consider a deep neural network with $D_i = 5$ inputs, $D_o = 1$ output, and $K = 20$ hidden layers containing $D = 30$ hidden units each. What is the depth of this network? What is the width?

Problem 4.6 Consider a network with $D_i = 1$ input, $D_o = 1$ output, $K = 10$ layers, with $D = 10$ hidden units in each. Would the number of weights increase more if we increased the depth by one or the width by one? Provide your reasoning.

Problem 4.7 Choose values for the parameters $\boldsymbol{\phi} = \{\phi_0, \phi_1, \phi_2, \phi_3, \theta_{10}, \theta_{11}, \theta_{20}, \theta_{21}, \theta_{30}, \theta_{31}\}$ for the shallow neural network in equation 3.1 that will define an identity function over a finite range $x \in [a, b]$.

Problem 4.8* Figure 4.9 shows the activations in the three hidden units of a shallow network (as in figure 3.3). The slopes in the hidden units are 1.0, 1.0, and -1.0, respectively, and the "joints" in the hidden units are at positions 1/6, 2/6, and 4/6. Find values of ϕ_0, ϕ_1, ϕ_2, and ϕ_3 that will combine the hidden unit activations as $\phi_0 + \phi_1 h_1 + \phi_2 h_2 + \phi_3 h_3$ to create a function with four linear regions that oscillate between output values of zero and one. The slope of the leftmost region should be positive, the next one negative, and so on. How many linear regions will we create if we compose this network with itself? How many will we create if we compose it with itself K times?

Problem 4.9* Following problem 4.8, is it possible to create a function with three linear regions that oscillates back and forth between output values of zero and one using a shallow network with two hidden units? Is it possible to create a function with five linear regions that oscillates in the same way using a shallow network with four hidden units?

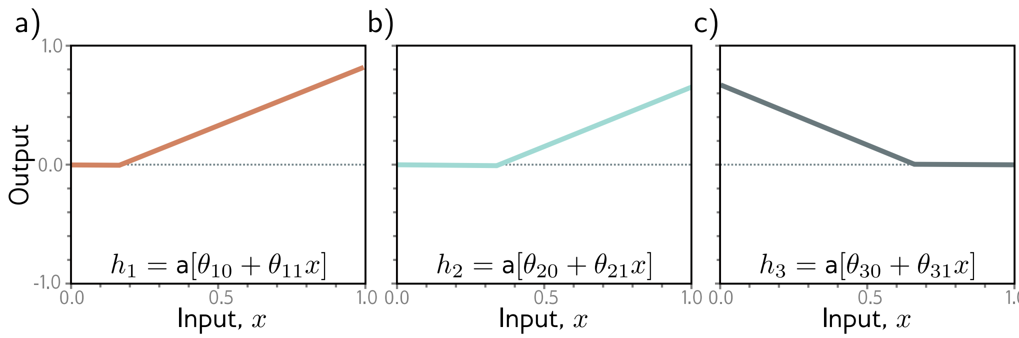

Figure 4.9 Hidden unit activations for problem 4.8. a) First hidden unit has a joint at position $x = 1/6$ and a slope of one in the active region. b) Second hidden unit has a joint at position $x = 2/6$ and a slope of one in the active region. c) Third hidden unit has a joint at position $x = 4/6$ and a slope of minus one in the active region.

Problem 4.10 Consider a deep neural network with a single input, a single output, and K hidden layers, each of which contains D hidden units. Show that this network will have a total of $3D + 1 + (K - 1)D(D + 1)$ parameters.

Problem 4.11* Consider two neural networks that map a scalar input x to a scalar output y. The first network is shallow and has $D = 95$ hidden units. The second is deep and has $K = 10$ layers, each containing $D = 5$ hidden units. How many parameters does each network have? How many linear regions can each network make? Which would run faster?

Chapter 5

Loss functions

The last three chapters described linear regression, shallow neural networks, and deep neural networks. Each represents a family of functions that map input to output, where the particular member of the family is determined by the model parameters $\boldsymbol{\phi}$. When we train these models, we seek the parameters that produce the best possible mapping from input to output for the task we are considering. This chapter defines what is meant by the "best possible" mapping.

That definition requires a training dataset $\{\mathbf{x}_i, \mathbf{y}_i\}$ of input/output pairs. A *loss function* or *cost function* $L[\boldsymbol{\phi}]$ returns a single number that describes the mismatch between the model predictions $\mathbf{f}[\mathbf{x}_i, \boldsymbol{\phi}]$ and their corresponding ground-truth outputs $\mathbf{y}_i$. During training, we seek parameter values $\boldsymbol{\phi}$ that minimize the loss and hence map the training inputs to the outputs as closely as possible. We saw one example of a loss function in chapter 2; the least squares loss function is suitable for univariate regression problems for which the target is a real number $y \in \mathbb{R}$. It computes the sum of the squares of the deviations between the model predictions $\mathrm{f}[\mathbf{x}_i, \boldsymbol{\phi}]$ and the true values y_i.

Appendix A
Number sets

This chapter provides a framework that both justifies the choice of the least squares criterion for real-valued outputs and allows us to build loss functions for other prediction types. We consider *binary classification*, where the prediction $y \in [0, 1]$ is one of two categories, *multiclass classification*, where the prediction $y \in [1, 2, \ldots, K]$ is one of K categories, and more complex cases. In the following two chapters, we address model training, where the goal is to find the parameter values that minimize these loss functions.

5.1 Maximum likelihood

In this section, we develop a recipe for constructing loss functions. Consider a model $\mathbf{f}[\mathbf{x}, \boldsymbol{\phi}]$ with parameters $\boldsymbol{\phi}$ that computes an output from input $\mathbf{x}$. Until now, we have implied that the model directly computes a prediction $\mathbf{y}$. We now shift perspective and consider the model as computing a conditional probability distribution $Pr(\mathbf{y}|\mathbf{x})$ over possible outputs $\mathbf{y}$ given input $\mathbf{x}$. The loss encourages each training output $\mathbf{y}_i$ to have a high probability under the distribution $Pr(\mathbf{y}_i|\mathbf{x}_i)$ computed from the corresponding input $\mathbf{x}_i$ (figure 5.1).

Appendix B.1.3
Conditional
probability

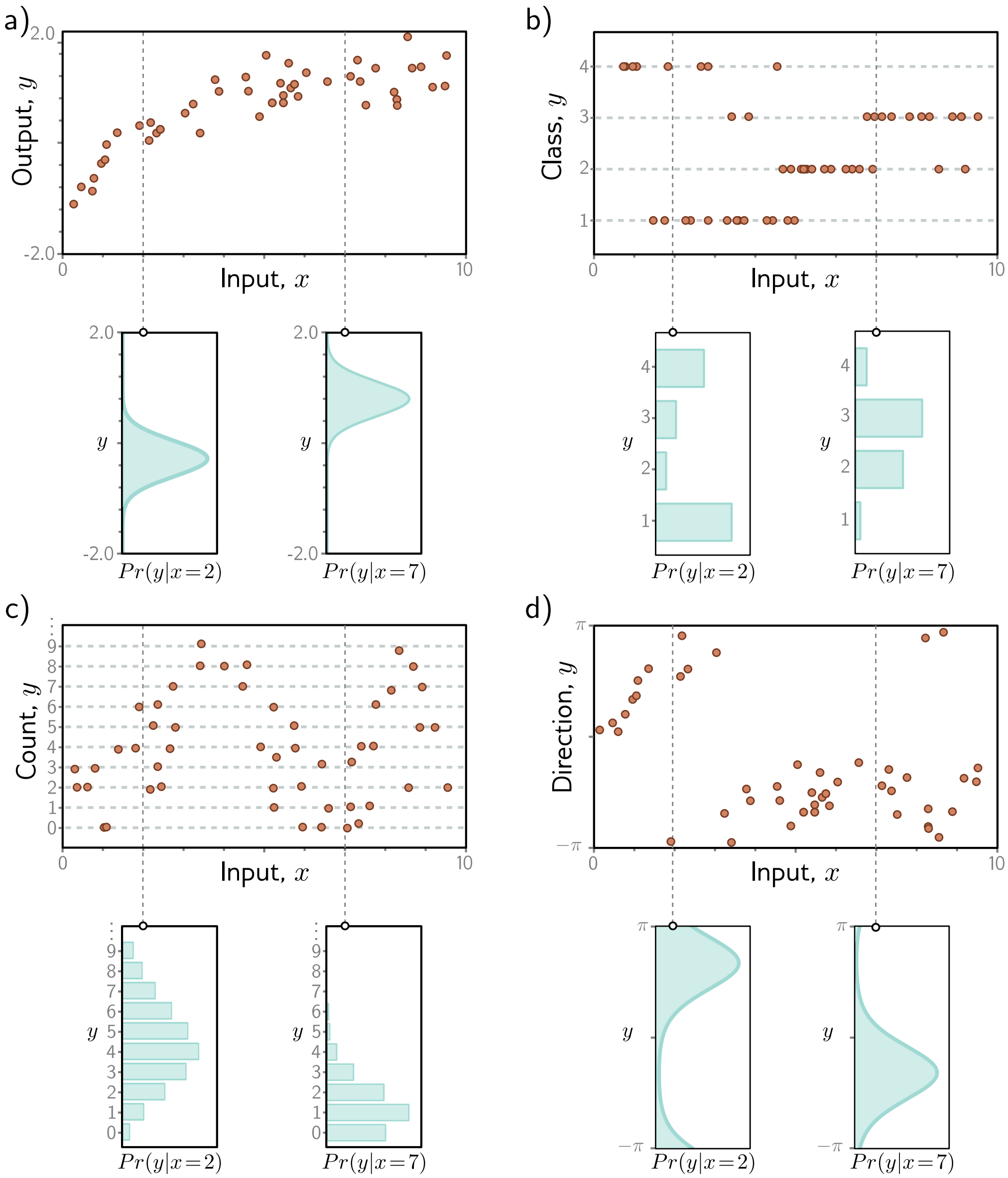

Figure 5.1 Predicting distributions over outputs. a) Regression task, where the goal is to predict a real-valued output y from the input x based on training data $\{x_i, y_i\}$ (orange points). For each input value x, the machine learning model predicts a distribution $Pr(y|x)$ over the output $y \in \mathcal{R}$ (cyan curves show distributions for $x = 2.0$ and $x = 7.0$). The loss function aims to maximize the probability of the observed training outputs y_i under the distribution predicted from the corresponding inputs x_i. b) To predict discrete classes $y \in \{1, 2, 3, 4\}$ in a classification task, we use a discrete probability distribution. c) To predict counts $y \in \{0, 1, 2, \ldots\}$ and d) direction $y \in (-\pi, \pi]$, we use distributions defined over these domains.

5.1.1 Computing a distribution over outputs

This raises the question of exactly how a model $\mathbf{f}[\mathbf{x}, \boldsymbol{\phi}]$ can be adapted to compute a probability distribution. The solution is simple. First, we choose a parametric distribution $Pr(\mathbf{y}|\boldsymbol{\theta})$ defined on the output domain $\mathbf{y}$. Then we use the network to compute one or more of the parameters $\boldsymbol{\theta}$ of this distribution.

For example, suppose the prediction domain is $y \in \mathbb{R}$. Here, we might choose the univariate normal distribution, which is defined on $y \in \mathbb{R}$. This distribution is defined by the mean μ and variance σ^2, so $\boldsymbol{\theta} = \{\mu, \sigma^2\}$. The machine learning model $\mathbf{f}[\mathbf{x}, \boldsymbol{\phi}]$ might predict the mean μ, and the variance σ^2 could be treated as an unknown constant.

5.1.2 Maximum likelihood criterion

The model now computes different distribution parameters $\boldsymbol{\theta}_i = \mathbf{f}[\mathbf{x}_i, \boldsymbol{\phi}]$ for each training input $\mathbf{x}_i$. Each observed training output $\mathbf{y}_i$ should have high probability under its corresponding distribution $Pr(\mathbf{y}_i|\boldsymbol{\theta}_i)$. Hence, we choose the model parameters $\boldsymbol{\phi}$ so that they maximize the combined probability across all I training examples:

$$
\begin{aligned}
\hat{\boldsymbol{\phi}} &= \underset{\boldsymbol{\phi}}{\operatorname{argmax}} \left[\prod_{i=1}^{I} Pr(\mathbf{y}_i|\mathbf{x}_i) \right] \\
&= \underset{\boldsymbol{\phi}}{\operatorname{argmax}} \left[\prod_{i=1}^{I} Pr(\mathbf{y}_i|\boldsymbol{\theta}_i) \right] \\
&= \underset{\boldsymbol{\phi}}{\operatorname{argmax}} \left[\prod_{i=1}^{I} Pr(\mathbf{y}_i|\mathbf{f}[\mathbf{x}_i, \boldsymbol{\phi}]) \right]. \qquad (5.1)
\end{aligned}
$$

The combined probability term is the *likelihood* of the parameters, and hence equation 5.1 is known as the *maximum likelihood* criterion.[1]

Here we are implicitly making two assumptions. First, we assume that the data are identically distributed (the form of the probability distribution over the outputs $\mathbf{y}_i$ is the same for each data point). Second, we assume that the conditional distributions $Pr(\mathbf{y}_i|\mathbf{x}_i)$ of the output given the input are independent, so the total likelihood of the training data decomposes as:

Appendix B.1.5 Independence

$$
Pr(\mathbf{y}_1, \mathbf{y}_2, \ldots, \mathbf{y}_I|\mathbf{x}_1, \mathbf{x}_2, \ldots, \mathbf{x}_I) = \prod_{i=1}^{I} Pr(\mathbf{y}_i|\mathbf{x}_i). \qquad (5.2)
$$

In other words, we assume the data are *independent and identically distributed* (*i.i.d.*).

[1] A conditional probability $Pr(z|\psi)$ can be considered in two ways. As a function of z, it is a probability distribution that sums to one. As a function of ϕ, it is known as a *likelihood* and does not generally sum to one.

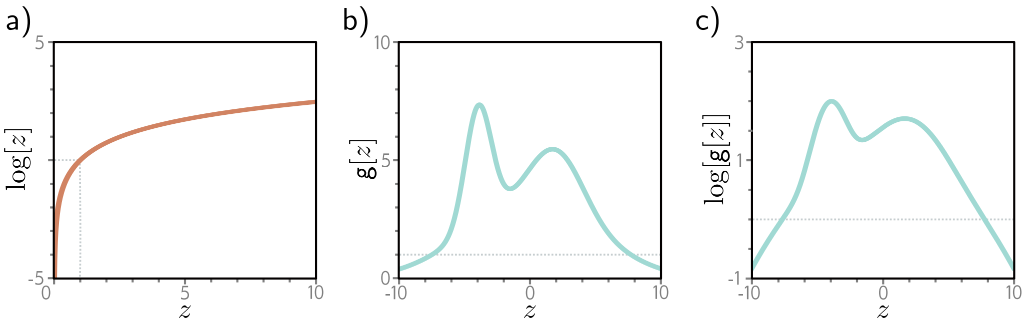

Figure 5.2 The log transform. a) The log function is monotonically increasing. If $z > z'$, then $\log[z] > \log[z']$. It follows that the maximum of any function $\text{g}[z]$ will be at the same position as the maximum of $\log[\text{g}[z]]$. b) A function $\text{g}[z]$. c) The logarithm of this function $\log[\text{g}[z]]$. All positions on $\text{g}[z]$ with a positive slope retain a positive slope after the log transform, and those with a negative slope retain a negative slope. The position of the maximum remains the same.

5.1.3 Maximizing log-likelihood

The maximum likelihood criterion (equation 5.1) is not very practical. Each term $Pr(\mathbf{y}_i|\mathbf{f}[\mathbf{x}_i, \boldsymbol{\phi}])$ can be small, so the product of many of these terms can be tiny. It may be difficult to represent this quantity with finite precision math. Fortunately, we can equivalently maximize the logarithm of the likelihood:

$$
\begin{aligned}
\hat{\boldsymbol{\phi}} &= \underset{\boldsymbol{\phi}}{\operatorname{argmax}}\left[\prod_{i=1}^{I} Pr(\mathbf{y}_i|\mathbf{f}[\mathbf{x}_i, \boldsymbol{\phi}])\right] \\
&= \underset{\boldsymbol{\phi}}{\operatorname{argmax}}\left[\log\left[\prod_{i=1}^{I} Pr(\mathbf{y}_i|\mathbf{f}[\mathbf{x}_i, \boldsymbol{\phi}])\right]\right] \\
&= \underset{\boldsymbol{\phi}}{\operatorname{argmax}}\left[\sum_{i=1}^{I} \log\Big[Pr(\mathbf{y}_i|\mathbf{f}[\mathbf{x}_i, \boldsymbol{\phi}])\Big]\right].
\end{aligned}
\tag{5.3}
$$

This *log-likelihood* criterion is equivalent because the logarithm is a monotonically increasing function: if $z > z'$, then $\log[z] > \log[z']$ and vice versa (figure 5.2). It follows that when we change the model parameters $\boldsymbol{\phi}$ to improve the log-likelihood criterion, we also improve the original maximum likelihood criterion. It also follows that the overall maxima of the two criteria must be in the same place, so the best model parameters $\hat{\boldsymbol{\phi}}$ are the same in both cases. However, the log-likelihood criterion has the practical advantage of using a sum of terms, not a product, so representing it with finite precision isn't problematic.

5.1.4 Minimizing negative log-likelihood

Finally, we note that, by convention, model fitting problems are framed in terms of minimizing a loss. To convert the maximum log-likelihood criterion to a minimization problem, we multiply by minus one, which gives us the *negative log-likelihood criterion*:

$$
\begin{aligned}
\hat{\boldsymbol{\phi}} &= \underset{\boldsymbol{\phi}}{\operatorname{argmin}}\left[-\sum_{i=1}^{I}\log\Bigl[Pr(\mathbf{y}_i|\mathbf{f}[\mathbf{x}_i,\boldsymbol{\phi}])\Bigr]\right] \\
&= \underset{\boldsymbol{\phi}}{\operatorname{argmin}}\Bigl[\mathrm{L}[\boldsymbol{\phi}]\Bigr], \qquad (5.4)
\end{aligned}
$$

which is what forms the final loss function $\mathrm{L}[\boldsymbol{\phi}]$.

5.1.5 Inference

The network no longer directly predicts the outputs $\mathbf{y}$ but instead determines a probability distribution over $\mathbf{y}$. When we perform inference, we often want a point estimate rather than a distribution, and so we return the maximum of the distribution:

$$
\hat{\mathbf{y}} = \underset{\mathbf{y}}{\operatorname{argmax}}\Bigl[Pr(\mathbf{y}|\mathbf{f}[\mathbf{x},\boldsymbol{\phi}])\Bigr]. \qquad (5.5)
$$

It is usually possible to find an expression for this in terms of the distribution parameters $\boldsymbol{\theta}$ predicted by the model. For example, in the univariate normal distribution, the maximum occurs at the mean μ.

5.2 Recipe for constructing loss functions

Let's summarize the recipe for constructing loss functions for training data $\{\mathbf{x}_i, \mathbf{y}_i\}$ using the maximum likelihood approach:

1. Choose a suitable probability distribution $Pr(\mathbf{y}|\boldsymbol{\theta})$ defined over the domain of the predictions $\mathbf{y}$ with distribution parameters $\boldsymbol{\theta}$.
2. Set the machine learning model $\mathbf{f}[\mathbf{x},\boldsymbol{\phi}]$ to predict one or more of these parameters, so $\boldsymbol{\theta} = \mathbf{f}[\mathbf{x},\boldsymbol{\phi}]$ and $Pr(\mathbf{y}|\boldsymbol{\theta}) = Pr(\mathbf{y}|\mathbf{f}[\mathbf{x},\boldsymbol{\phi}])$.
3. To train the model, find the network parameters $\hat{\boldsymbol{\phi}}$ that minimize the negative log-likelihood loss function over the training dataset pairs $\{\mathbf{x}_i, \mathbf{y}_i\}$:

$$
\hat{\boldsymbol{\phi}} = \underset{\boldsymbol{\phi}}{\operatorname{argmin}}\Bigl[L[\boldsymbol{\phi}]\Bigr] = \underset{\boldsymbol{\phi}}{\operatorname{argmin}}\left[-\sum_{i=1}^{I}\log\Bigl[Pr(\mathbf{y}_i|\mathbf{f}[\mathbf{x}_i,\boldsymbol{\phi}])\Bigr]\right]. \qquad (5.6)
$$

4. To perform inference for a new test example $\mathbf{x}$, return either the full distribution $Pr(\mathbf{y}|\mathbf{f}[\mathbf{x},\hat{\boldsymbol{\phi}}])$ or the maximum of this distribution.

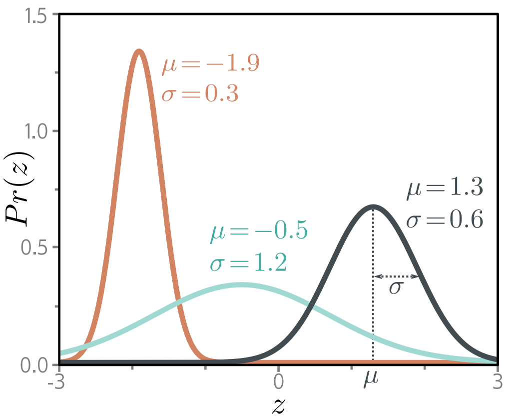

Figure 5.3 The univariate normal distribution (also known as the Gaussian distribution) is defined on the real line $z \in \mathbb{R}$ and has parameters μ and σ^2. The mean μ determines the position of the peak. The positive root of the variance σ^2 (the standard deviation) determines the width of the distribution. Since the total probability density sums to one, the peak becomes higher as the variance decreases and the distribution becomes narrower.

We devote most of the rest of this chapter to constructing loss functions for common prediction types using this recipe.

5.3 Example 1: univariate regression

We start by considering univariate regression models. Here the goal is to predict a single scalar output $y \in \mathbb{R}$ from input $\mathbf{x}$ using a model $\mathrm{f}[\mathbf{x}, \boldsymbol{\phi}]$ with parameters $\boldsymbol{\phi}$. Following the recipe, we choose a probability distribution over the output domain y. We select the univariate normal (figure 5.3), which is defined over $y \in \mathbb{R}$. This distribution has two parameters (mean μ and variance σ^2) and has a probability density function:

$$Pr(y|\mu, \sigma^2) = \frac{1}{\sqrt{2\pi\sigma^2}} \exp\left[-\frac{(y-\mu)^2}{2\sigma^2}\right]. \tag{5.7}$$

Second, we set the machine learning model $\mathrm{f}[\mathbf{x}, \boldsymbol{\phi}]$ to compute one or more of the parameters of this distribution. Here, we just compute the mean so $\mu = \mathrm{f}[\mathbf{x}, \boldsymbol{\phi}]$:

$$Pr(y|\mathrm{f}[\mathbf{x}, \boldsymbol{\phi}], \sigma^2) = \frac{1}{\sqrt{2\pi\sigma^2}} \exp\left[-\frac{(y-\mathrm{f}[\mathbf{x}, \boldsymbol{\phi}])^2}{2\sigma^2}\right]. \tag{5.8}$$

We aim to find the parameters $\boldsymbol{\phi}$ that make the training data $\{\mathbf{x}_i, y_i\}$ most probable under this distribution (figure 5.4). To accomplish this, we choose a loss function $L[\boldsymbol{\phi}]$ based on the negative log-likelihood:

$$\begin{aligned} L[\boldsymbol{\phi}] &= -\sum_{i=1}^{I} \log\left[Pr(y_i|\mathrm{f}[\mathbf{x}_i, \boldsymbol{\phi}], \sigma^2)\right] \\ &= -\sum_{i=1}^{I} \log\left[\frac{1}{\sqrt{2\pi\sigma^2}} \exp\left[-\frac{(y_i-\mathrm{f}[\mathbf{x}_i, \boldsymbol{\phi}])^2}{2\sigma^2}\right]\right]. \end{aligned} \tag{5.9}$$

When we train the model, we seek parameters $\hat{\boldsymbol{\phi}}$ that minimize this loss.

5.3.1 Least squares loss function

Now let's perform some algebraic manipulations on the loss function. We seek:

$$\begin{aligned}
\hat{\boldsymbol{\phi}} &= \underset{\boldsymbol{\phi}}{\operatorname{argmin}}\left[-\sum_{i=1}^{I}\log\left[\frac{1}{\sqrt{2\pi\sigma^2}}\exp\left[-\frac{(y_i-\mathrm{f}[\mathbf{x}_i,\boldsymbol{\phi}])^2}{2\sigma^2}\right]\right]\right]\\
&= \underset{\boldsymbol{\phi}}{\operatorname{argmin}}\left[-\sum_{i=1}^{I}\log\left[\frac{1}{\sqrt{2\pi\sigma^2}}\right]-\frac{(y_i-\mathrm{f}[\mathbf{x}_i,\boldsymbol{\phi}])^2}{2\sigma^2}\right]\\
&= \underset{\boldsymbol{\phi}}{\operatorname{argmin}}\left[-\sum_{i=1}^{I}-\frac{(y_i-\mathrm{f}[\mathbf{x}_i,\boldsymbol{\phi}])^2}{2\sigma^2}\right]\\
&= \underset{\boldsymbol{\phi}}{\operatorname{argmin}}\left[\sum_{i=1}^{I}(y_i-\mathrm{f}[\mathbf{x}_i,\boldsymbol{\phi}])^2\right],
\end{aligned} \tag{5.10}$$

where we have removed the first term between the second and third lines because it does not depend on $\boldsymbol{\phi}$. We have removed the denominator between the third and fourth lines, as this is just a constant scaling factor that does not affect the position of the minimum.

The result of these manipulations is the least squares loss function that we originally introduced when we discussed linear regression in chapter 2:

$$L[\boldsymbol{\phi}] = \sum_{i=1}^{I}(y_i-\mathrm{f}[\mathbf{x}_i,\boldsymbol{\phi}])^2. \tag{5.11}$$

Notebook 5.1 Least squares loss

We see that the least squares loss function follows naturally from the assumptions that the prediction errors are (i) independent and (ii) drawn from a normal distribution with mean $\mu = \mathrm{f}[\mathbf{x}_i, \boldsymbol{\phi}]$ (figure 5.4).

5.3.2 Inference

The network no longer directly predicts y but instead predicts the mean $\mu = \mathrm{f}[\mathbf{x}, \boldsymbol{\phi}]$ of the normal distribution over y. When we perform inference, we usually want a single "best" point estimate $\hat{y}$, and so we take the maximum of the predicted distribution:

$$\hat{y} = \underset{y}{\operatorname{argmax}}\left[Pr(y|\mathbf{f}[\mathbf{x},\hat{\boldsymbol{\phi}}])\right]. \tag{5.12}$$

For the univariate normal, the maximum position is determined by the mean parameter μ (figure 5.3). This is precisely what the model computed, so $\hat{y} = \mathrm{f}[\mathbf{x}, \hat{\boldsymbol{\phi}}]$.

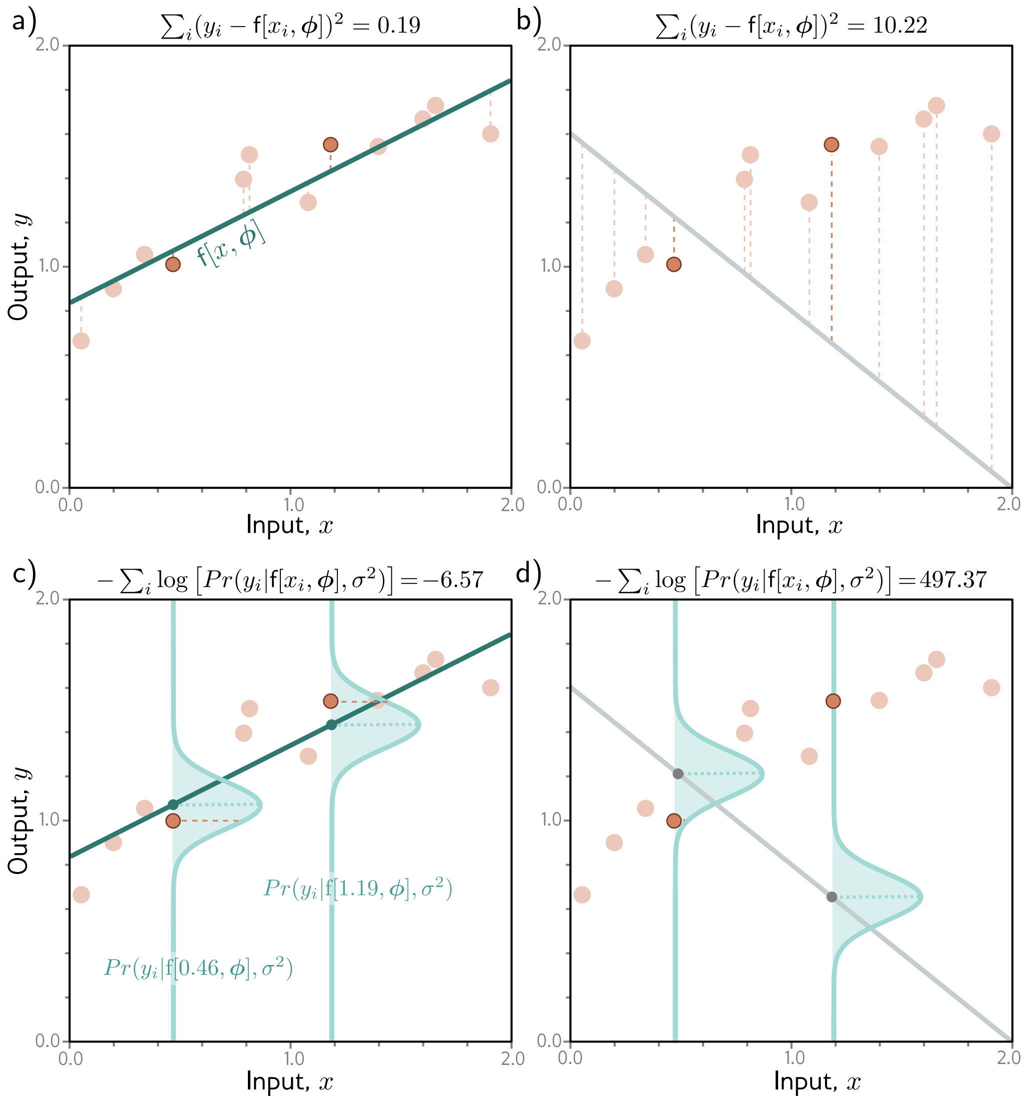

Figure 5.4 Equivalence of least squares and maximum likelihood loss for the normal distribution. a) Consider the linear model from figure 2.2. The least squares criterion minimizes the sum of the squares of the deviations (dashed lines) between the model prediction $\mathrm{f}[x_i, \boldsymbol{\phi}]$ (green line) and the true output values y_i (orange points). Here the fit is good, so these deviations are small (e.g., for the two highlighted points). b) For these parameters, the fit is bad, and the squared deviations are large. c) The least squares criterion follows from the assumption that the model predicts the mean of a normal distribution over the outputs and that we maximize the probability. For the first case, the model fits well, so the probability $Pr(y_i|x_i)$ of the data (horizontal orange dashed lines) is large (and the negative log probability is small). d) For the second case, the model fits badly, so the probability is small and the negative log probability is large.

5.3.3 Estimating variance

To formulate the least squares loss function, we assumed that the network predicted the mean of a normal distribution. The final expression in equation 5.11 (perhaps surprisingly) does not depend on the variance σ^2. However, there is nothing to stop us from treating σ^2 as a parameter of the model and minimizing equation 5.9 with respect to both the model parameters $\boldsymbol{\phi}$ and the distribution variance σ^2:

$$\hat{\boldsymbol{\phi}}, \hat{\sigma}^2 = \underset{\boldsymbol{\phi},\sigma^2}{\operatorname{argmin}} \left[-\sum_{i=1}^{I} \log\left[\frac{1}{\sqrt{2\pi\sigma^2}} \exp\left[-\frac{(y_i - \mathrm{f}[\mathbf{x}_i, \boldsymbol{\phi}])^2}{2\sigma^2} \right] \right] \right]. \tag{5.13}$$

In inference, the model predicts the mean $\mu = \mathrm{f}[\mathbf{x}, \hat{\boldsymbol{\phi}}]$ from the input, and we learned the variance σ^2 during the training process. The former is the best prediction. The latter tells us about the uncertainty of the prediction.

5.3.4 Heteroscedastic regression

The model above assumes that the variance of the data is constant everywhere. However, this might be unrealistic. When the uncertainty of the model varies as a function of the input data, we refer to this as *heteroscedastic* (as opposed to *homoscedastic*, where the uncertainty is constant).

A simple way to model this is to train a neural network $\mathbf{f}[\mathbf{x}, \boldsymbol{\phi}]$ that computes both the mean and the variance. For example, consider a shallow network with two outputs. We denote the first output as $\mathrm{f}_1[\mathbf{x}, \boldsymbol{\phi}]$ and use this to predict the mean, and we denote the second output as $\mathrm{f}_2[\mathbf{x}, \boldsymbol{\phi}]$ and use it to predict the variance.

There is one complication; the variance must be positive, but we can't guarantee that the network will always produce a positive output. To ensure that the computed variance is positive, we pass the second network output through a function that maps an arbitrary value to a positive one. A suitable choice is the squaring function, giving:

$$\begin{aligned} \mu &= \mathrm{f}_1[\mathbf{x}, \boldsymbol{\phi}] \\ \sigma^2 &= \mathrm{f}_2[\mathbf{x}, \boldsymbol{\phi}]^2, \end{aligned} \tag{5.14}$$

which results in the loss function:

$$\hat{\boldsymbol{\phi}} = \underset{\boldsymbol{\phi}}{\operatorname{argmin}} \left[-\sum_{i=1}^{I} \log\left[\frac{1}{\sqrt{2\pi \mathrm{f}_2[\mathbf{x}_i, \boldsymbol{\phi}]^2}} \right] - \frac{(y_i - \mathrm{f}_1[\mathbf{x}_i, \boldsymbol{\phi}])^2}{2\mathrm{f}_2[\mathbf{x}_i, \boldsymbol{\phi}]^2} \right]. \tag{5.15}$$

Homoscedastic and heteroscedastic models are compared in figure 5.5.

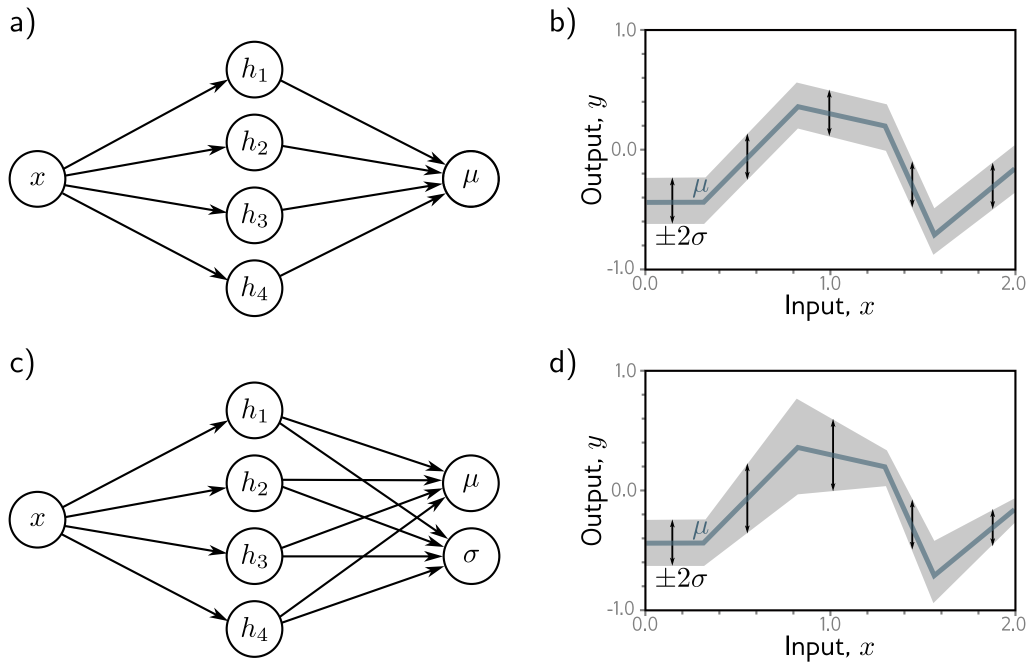

Figure 5.5 Homoscedastic vs. heteroscedastic regression. a) A shallow neural network for homoscedastic regression predicts just the mean μ of the output distribution from the input x. b) The result is that while the mean (blue line) is a piecewise linear function of the input x, the variance is constant everywhere (arrows and gray region show ± 2 standard deviations). c) A shallow neural network for heteroscedastic regression also predicts the variance σ^2 (or, more precisely, computes its square root, which we then square). d) The standard deviation now also becomes a piecewise linear function of the input x.

5.4 Example 2: binary classification

In *binary classification*, the goal is to assign the data $\mathbf{x}$ to one of two discrete classes $y \in \{0, 1\}$. In this context, we refer to y as a *label*. Examples of binary classification include (i) predicting whether a restaurant review is positive ($y = 1$) or negative ($y = 0$) from text data $\mathbf{x}$ and (ii) predicting whether a tumor is present ($y = 1$) or absent ($y = 0$) from an MRI scan $\mathbf{x}$.

Once again, we follow the recipe from section 5.2 to construct the loss function. First, we choose a probability distribution over the output space $y \in \{0, 1\}$. A suitable choice is the Bernoulli distribution, which is defined on the domain $\{0, 1\}$. This has a single parameter $\lambda \in [0, 1]$ that represents the probability that y takes the value one (figure 5.6):

$$Pr(y|\lambda) = \begin{cases} 1 - \lambda & y = 0 \\ \lambda & y = 1 \end{cases}, \tag{5.16}$$

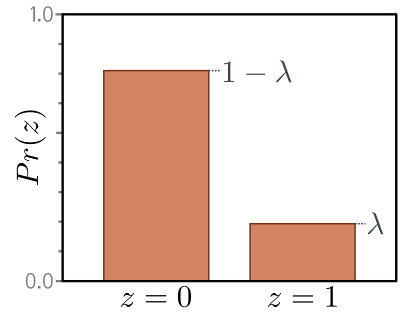

Figure 5.6 Bernoulli distribution. The Bernoulli distribution is defined on the domain $z \in \{0,1\}$ and has a single parameter λ that denotes the probability of observing $z=1$. It follows that the probability of observing $z=0$ is $1-\lambda$.

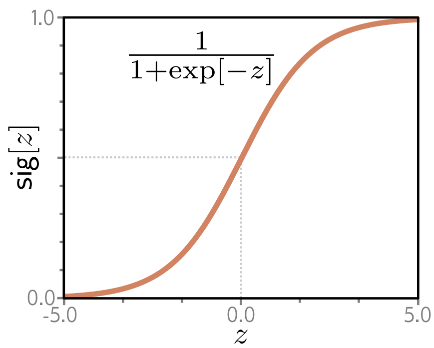

Figure 5.7 Logistic sigmoid function. This function maps the real line $z \in \mathbb{R}$ to numbers between zero and one, and so $\text{sig}[z] \in [0,1]$. An input of 0 is mapped to 0.5. Negative inputs are mapped to numbers below 0.5, and positive inputs to numbers above 0.5.

which can equivalently be written as:

$$Pr(y|\lambda) = (1-\lambda)^{1-y} \cdot \lambda^{y}. \tag{5.17}$$

Second, we set the machine learning model $\text{f}[\mathbf{x}, \boldsymbol{\phi}]$ to predict the single distribution parameter λ. However, λ can only take values in the range $[0,1]$, and we cannot guarantee that the network output will lie in this range. Consequently, we pass the network output through a function that maps the real numbers $\mathbb{R}$ to $[0,1]$. A suitable function is the *logistic sigmoid* (figure 5.7):

Problem 5.1

$$\text{sig}[z] = \frac{1}{1+\exp[-z]}. \tag{5.18}$$

Hence, we predict the distribution parameter as $\lambda = \text{sig}[\text{f}[\mathbf{x}, \boldsymbol{\phi}]]$. The likelihood is now:

$$Pr(y|\mathbf{x}) = (1-\text{sig}[\text{f}[\mathbf{x}, \boldsymbol{\phi}]])^{1-y} \cdot \text{sig}[\text{f}[\mathbf{x}, \boldsymbol{\phi}]]^{y}. \tag{5.19}$$

This is depicted in figure 5.8 for a shallow neural network model. The loss function is the negative log-likelihood of the training set:

$$L[\boldsymbol{\phi}] = \sum_{i=1}^{I} -(1-y_i)\log\Bigl[1-\text{sig}[\text{f}[\mathbf{x}_i, \boldsymbol{\phi}]]\Bigr] - y_i \log\Bigl[\text{sig}[\text{f}[\mathbf{x}_i, \boldsymbol{\phi}]]\Bigr]. \tag{5.20}$$

For reasons to be explained in section 5.7, this is known as the *binary cross-entropy loss*.

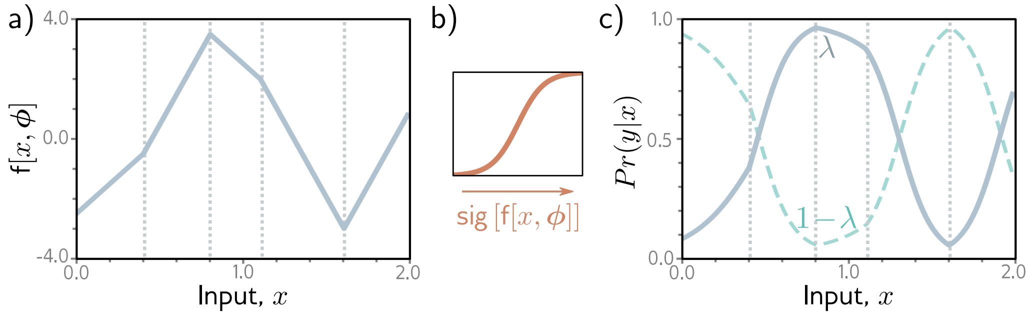

Figure 5.8 Binary classification model. a) The network output is a piecewise linear function that can take arbitrary real values. b) This is transformed by the logistic sigmoid function, which compresses these values to the range $[0, 1]$. c) The transformed output predicts the probability λ that $y = 1$ (solid line). The probability that $y = 0$ is hence $1 - \lambda$ (dashed line). For any fixed x (vertical slice), we retrieve the two values of a Bernoulli distribution similar to that in figure 5.6. The loss function favors model parameters that produce large values of λ at positions x_i that are associated with positive examples $y_i = 1$ and small values of λ at positions associated with negative examples $y_i = 0$.

The transformed model output $\text{sig}[\text{f}[\mathbf{x}, \boldsymbol{\phi}]]$ predicts the parameter λ of the Bernoulli distribution. This represents the probability that $y = 1$, and it follows that $1 - \lambda$ represents the probability that $y = 0$. When we perform inference, we may want a point estimate of y, so we set $y = 1$ if $\lambda > 0.5$ and $y = 0$ otherwise.

Notebook 5.2
Binary cross-entropy loss

Problem 5.2

5.5 Example 3: multiclass classification

The goal of *multiclass classification* is to assign an input data example $\mathbf{x}$ to one of $K > 2$ classes, so $y \in \{1, 2, \ldots, K\}$. Real-world examples include (i) predicting which of $K = 10$ digits y is present in an image $\mathbf{x}$ of a handwritten number and (ii) predicting which of K possible words y follows an incomplete sentence $\mathbf{x}$.

We once more follow the recipe from section 5.2. We first choose a distribution over the prediction space y. In this case, we have $y \in \{1, 2, \ldots, K\}$, so we choose the categorical distribution (figure 5.9), which is defined on this domain. This has K parameters $\lambda_1, \lambda_2, \ldots, \lambda_K$, which determine the probability of each category:

$$Pr(y = k) = \lambda_k. \tag{5.21}$$

The parameters are constrained to take values between zero and one, and they must collectively sum to one to ensure a valid probability distribution.

Then we use a network $\mathbf{f}[\mathbf{x}, \boldsymbol{\phi}]$ with K outputs to compute these K parameters from the input $\mathbf{x}$. Unfortunately, the network outputs will not necessarily obey the afore-

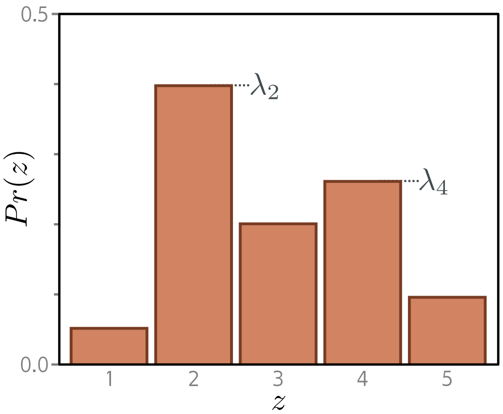

Figure 5.9 Categorical distribution. The categorical distribution assigns probabilities to $K>2$ categories, with probabilities $\lambda_1, \lambda_2, \ldots, \lambda_K$. There are five categories in this example, so $K=5$. To ensure that this is a valid probability distribution, each parameter λ_k must lie in the range $[0,1]$, and all K parameters must sum to one.

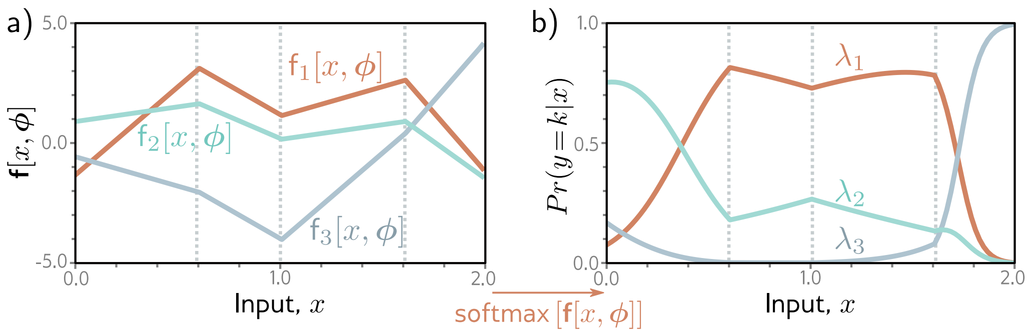

Figure 5.10 Multiclass classification for $K=3$ classes. a) The network has three piecewise linear outputs, which can take arbitrary values. b) After the softmax function, these outputs are constrained to be non-negative and to sum to one. Hence, for a given input $\mathbf{x}$, we calculate a valid set of parameters of the categorical distribution. Any vertical slice of this plot produces three values sum to one and would form the heights of the bars in a categorical distribution similar to figure 5.9.

mentioned constraints. Consequently, we pass the K outputs of the network through a function that ensures these constraints are respected. A suitable choice is the *softmax* function (figure 5.10). This takes an arbitrary vector of length K and returns a vector of the same length but where the elements are now in the range $[0,1]$ and sum to one. The k^{th} output of the softmax function is:

$$\mathrm{softmax}_k[\mathbf{z}] = \frac{\exp[z_k]}{\sum_{k'=1}^{K}\exp[z_{k'}]}, \tag{5.22}$$

where the exponential functions ensure positivity, and the sum in the denominator ensures that the K numbers sum to one.

The likelihood that input $\mathbf{x}$ has label y (figure 5.10) is hence:

$$Pr(y = k|\mathbf{x}) = \text{softmax}_k\Big[\mathbf{f}[\mathbf{x}, \boldsymbol{\phi}]\Big]. \tag{5.23}$$

The loss function is the negative log-likelihood of the training data:

$$\begin{aligned} L[\boldsymbol{\phi}] &= -\sum_{i=1}^{I} \log\Big[\text{softmax}_{y_i}\Big[\mathbf{f}[\mathbf{x}_i, \boldsymbol{\phi}]\Big]\Big] \\ &= -\sum_{i=1}^{I} \text{f}_{y_i}[\mathbf{x}_i, \boldsymbol{\phi}] - \log\left[\sum_{k'=1}^{K} \exp\left[\, \text{f}_{k'}[\mathbf{x}_i, \boldsymbol{\phi}]\right]\right], \end{aligned} \tag{5.24}$$

where $\text{f}_k[\mathbf{x}, \boldsymbol{\phi}]$ denotes the k^{th} output of the neural network. For reasons that will be explained in section 5.7, this is known as the *multiclass cross-entropy loss*.

The transformed model output represents a categorical distribution over possible classes $y \in \{1, 2, \ldots, K\}$. For a point estimate, we take the most probable category $\hat{y} = \text{argmax}_k[Pr(y = k|\mathbf{f}[\mathbf{x}, \hat{\boldsymbol{\phi}}])]$. This corresponds to whichever curve is highest for that value of $\mathbf{x}$ in figure 5.10.

Notebook 5.3 Multiclass cross-entropy loss

5.5.1 Predicting other data types

In this chapter, we have focused on regression and classification because these problems are widespread. However, to make different types of predictions, we simply choose an appropriate distribution over that domain and apply the recipe in section 5.2. Figure 5.11 enumerates a series of probability distributions and their prediction domains. Some of these are explored in the problems at the end of the chapter.

Problems 5.3–5.6

5.6 Multiple outputs

Often, we wish to make more than one prediction with the same model, so the target output $\mathbf{y}$ is a vector. For example, we might want to predict a molecules melting and boiling point (a multivariate classification problem, figure 1.2b) or the object class at every point in an image (a multivariate classification problem, figure 1.4a). While it is possible to define multivariate probability distributions and use a neural network to model their parameters as a function of the input, it is more usual to treat each prediction as *independent*.

Independence implies that we treat the probability $Pr(\mathbf{y}|\mathbf{f}[\mathbf{x}_i, \boldsymbol{\phi}])$ as a product of univariate terms for each element $y_d \in \mathbf{y}$:

Appendix B.1.5 Independence

$$Pr(\mathbf{y}|\mathbf{f}[\mathbf{x}_i, \boldsymbol{\phi}]) = \prod_d Pr(y_d|\mathbf{f}_d[\mathbf{x}_i, \boldsymbol{\phi}]), \tag{5.25}$$

where $\mathbf{f}_d[\mathbf{x}_i, \boldsymbol{\phi}]$ is the d^{th} set of network outputs, which describe the parameters of the distribution over y_d. For example, to predict multiple continuous variables $y_d \in \mathbb{R}$, we

Data Type	Domain	Distribution	Use
univariate, continuous, unbounded	$y \in \mathbb{R}$	univariate normal	regression
univariate, continuous, unbounded	$y \in \mathbb{R}$	Laplace or t-distribution	robust regression
univariate, continuous, unbounded	$y \in \mathbb{R}$	mixture of Gaussians	multimodal regression
univariate, continuous, bounded below	$y \in \mathbb{R}^+$	exponential or gamma	predicting magnitude
univariate, continuous, bounded	$y \in [0,1]$	beta	predicting proportions
multivariate, continuous, unbounded	$\mathbf{y} \in \mathbb{R}^K$	multivariate normal	multivariate regression
univariate, continuous, circular	$y \in (-\pi, \pi]$	von Mises	predicting direction
univariate, discrete, binary	$y \in \{0,1\}$	Bernoulli	binary classification
univariate, discrete, bounded	$y \in \{1,2,\ldots,K\}$	categorical	multiclass classification
univariate, discrete, bounded below	$y \in [0,1,2,3,\ldots]$	Poisson	predicting event counts
multivariate, discrete, permutation	$\mathbf{y} \in \text{Perm}[1,2,\ldots,K]$	Plackett-Luce	ranking

Figure 5.11 Distributions for loss functions for different prediction types.

use normal distributions for each y_d, and the network outputs $\mathrm{f}_d[\mathbf{x}_i, \boldsymbol{\phi}]$ predict the means of these distributions. To predict multiple discrete variables $y_d \in [1, 2, \ldots, K]$, we use categorical distributions, and each set of network outputs $\mathbf{f}_d[\mathbf{x}_i, \boldsymbol{\phi}])$ predicts K values.

When we minimize the negative log probability, this product becomes a sum of terms:

$$L[\boldsymbol{\phi}] = -\sum_{i=1}^{I} \log\Big[Pr(\mathbf{y}|\mathbf{f}[\mathbf{x}_i, \boldsymbol{\phi}])\Big] = -\sum_{i=1}^{I}\sum_{d} \log\Big[Pr(y_{id}|\mathbf{f}_d[\mathbf{x}_i, \boldsymbol{\phi}])\Big]. \tag{5.26}$$

where y_{id} is the d^{th} output from the i^{th} training example.

Problems 5.7–5.10

To make two or more prediction types simultaneously, we similarly assume the errors in each are independent. For example, to predict wind direction and strength, we might choose the von Mises distribution (defined on circular domains) for the direction and the exponential distribution (defined on positive real numbers) for the strength. The independence assumption implies that the joint likelihood of the two predictions is the product of individual likelihoods. These terms will become additive when we compute the negative log-likelihood.

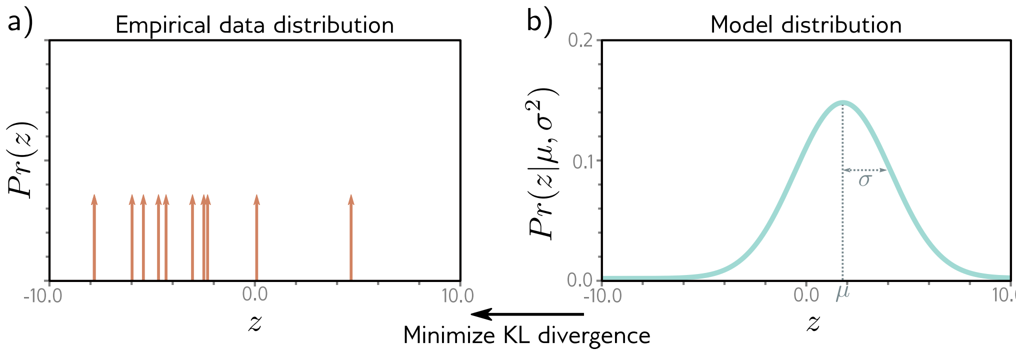

Figure 5.12 Cross-entropy method. a) Empirical distribution of training samples (arrows denote Dirac delta functions). b) Model distribution (a normal distribution with parameters $\boldsymbol{\theta} = \mu, \sigma^2$). In the cross-entropy approach, we minimize the distance (KL divergence) between these two distributions as a function of the model parameters $\boldsymbol{\theta}$.

5.7 Cross-entropy loss

In this chapter, we developed loss functions that minimize negative log-likelihood. However, the term *cross-entropy* loss is also commonplace. In this section, we describe the cross-entropy loss and show that it is equivalent to using negative log-likelihood.

The cross-entropy loss is based on the idea of finding parameters $\boldsymbol{\theta}$ that minimize the distance between the empirical distribution $q(y)$ of the observed data y and a model distribution $Pr(y|\boldsymbol{\theta})$ (figure 5.12). The distance between two probability distributions $q(z)$ and $p(z)$ can be evaluated using the Kullback-Leibler (KL) divergence:

Appendix B.5.1
KL Divergence

$$\mathrm{KL}[q||p] = \int_{-\infty}^{\infty} q(z)\log[q(z)]dz - \int_{-\infty}^{\infty} q(z)\log[p(z)]dz. \tag{5.27}$$

Now consider that we observe an empirical data distribution at points $\{y_i\}_{i=1}^{I}$. We can describe this as a weighted sum of point masses:

$$q(y) = \frac{1}{I}\sum_{i=1}^{I}\delta[y - y_i], \tag{5.28}$$

where $\delta[\bullet]$ is the Dirac delta function. We want to minimize the KL divergence between the model distribution $Pr(y|\boldsymbol{\theta})$ and this empirical distribution:

Appendix C.3.1
Dirac delta

$$\begin{aligned}
\hat{\boldsymbol{\theta}} &= \underset{\boldsymbol{\theta}}{\mathrm{argmin}}\left[\int_{-\infty}^{\infty} q(y)\log[q(y)]dy - \int_{-\infty}^{\infty} q(y)\log\left[Pr(y|\boldsymbol{\theta})\right]dy\right] \\
&= \underset{\boldsymbol{\theta}}{\mathrm{argmin}}\left[-\int_{-\infty}^{\infty} q(y)\log\left[Pr(y|\boldsymbol{\theta})\right]dy\right],
\end{aligned} \tag{5.29}$$

where the first term disappears, as it has no dependence on $\boldsymbol{\theta}$. The remaining second term is known as the *cross-entropy*. It can be interpreted as the amount of uncertainty that remains in one distribution after taking into account what we already know from the other. Now, we substitute in the definition of $q(y)$ from equation 5.28:

$$\begin{aligned}
\hat{\boldsymbol{\theta}} &= \underset{\theta}{\operatorname{argmin}}\left[-\int_{-\infty}^{\infty}\left(\frac{1}{I}\sum_{i=1}^{I}\delta[y-y_i]\right)\log\left[Pr(y|\boldsymbol{\theta})\right]dy\right] \\
&= \underset{\boldsymbol{\theta}}{\operatorname{argmin}}\left[-\frac{1}{I}\sum_{i=1}^{I}\log\left[Pr(y_i|\boldsymbol{\theta})\right]\right] \\
&= \underset{\boldsymbol{\theta}}{\operatorname{argmin}}\left[-\sum_{i=1}^{I}\log\left[Pr(y_i|\boldsymbol{\theta})\right]\right].
\end{aligned} \tag{5.30}$$

The product of the two terms in the first line corresponds to pointwise multiplying the point masses in figure 5.12a with the logarithm of the distribution in figure 5.12b. We are left with a finite set of weighted probability masses centered on the data points. In the last line, we have eliminated the constant scaling factor $1/I$, as this does not affect the position of the minimum.

In machine learning, the distribution parameters $\boldsymbol{\theta}$ are computed by the model $\mathbf{f}[\mathbf{x}_i, \boldsymbol{\phi}]$, and so we have:

$$\hat{\boldsymbol{\phi}} = \underset{\boldsymbol{\phi}}{\operatorname{argmin}}\left[-\sum_{i=1}^{I}\log\left[Pr(y_i|\mathbf{f}[\mathbf{x}_i,\boldsymbol{\phi}])\right]\right]. \tag{5.31}$$

This is precisely the negative log-likelihood criterion from the recipe in section 5.2.

It follows that the negative log-likelihood criterion (from maximizing the data likelihood) and the cross-entropy criterion (from minimizing the distance between the model and empirical data distributions) are equivalent.

5.8 Summary

We previously considered neural networks as directly predicting outputs $\mathbf{y}$ from data $\mathbf{x}$. In this chapter, we shifted perspective to think about neural networks as computing the parameters $\boldsymbol{\theta}$ of probability distributions $Pr(\mathbf{y}|\boldsymbol{\theta})$ over the output space. This led to a principled approach to building loss functions. We selected model parameters $\boldsymbol{\phi}$ that maximized the likelihood of the observed data under these distributions. We saw that this is equivalent to minimizing the negative log-likelihood.

The least squares criterion for regression is a natural consequence of this approach; it follows from the assumption that y is normally distributed and that we are predicting the mean. We also saw how the regression model can be (i) extended to estimate the uncertainty over the prediction and (ii) extended to make that uncertainty dependent on the input (the heteroscedastic model). We applied the same approach to both binary and multiclass classification and derived loss functions for each. We discussed how to tackle more complex data types and how to deal with multiple outputs. Finally, we argued that cross-entropy is an equivalent way to think about fitting models.

In previous chapters, we developed neural network models. In this chapter, we developed loss functions for deciding how well a model describes the training data for a given set of parameters. The next chapter considers model training, in which we aim to find the model parameters that minimize this loss.

Notes

Losses based on the normal distribution: Nix & Weigend (1994) and Williams (1996) investigated heteroscedastic nonlinear regression in which both the mean and the variance of the output are functions of the input. In the context of unsupervised learning, Burda et al. (2016) use a loss function based on a multivariate normal distribution with diagonal covariance, and Dorta et al. (2018) use a loss function based on a normal distribution with full covariance.

Robust regression: Qi et al. (2020) investigate the properties of regression models that minimize mean absolute error rather than mean squared error. This loss function follows from assuming a Laplace distribution over the outputs and estimates the median output for a given input rather than the mean. Barron (2019) presents a loss function that parameterizes the degree of robustness. When interpreted in a probabilistic context, it yields a family of univariate probability distributions that includes the normal and Cauchy distributions as special cases.

Estimating quantiles: Sometimes, we may not want to estimate the mean or median in a regression task but may instead want to predict a quantile. For example, this is useful for risk models, where we want to know that the true value will be less than the predicted value 90% of the time. This is known as *quantile regression* (Koenker & Hallock, 2001). This could be done by fitting a heteroscedastic regression model and then estimating the quantile based on the predicted normal distribution. Alternatively, the quantiles can be estimated directly using *quantile loss* (also known as *pinball loss*). In practice, this minimizes the absolute deviations of the data from the model but weights the deviations in one direction more than the other. Recent work has investigated simultaneously predicting multiple quantiles to get an idea of the overall distribution shape (Rodrigues & Pereira, 2020).

Class imbalance and focal loss: Lin et al. (2017c) address data imbalance in classification problems. If the number of examples for some classes is much greater than for others, then the standard maximum likelihood loss does not work well; the model may concentrate on becoming more confident about well-classified examples from the dominant classes and classify less well-represented classes poorly. Lin et al. (2017c) introduce *focal loss*, which adds a single extra parameter that down-weights the effect of well-classified examples to improve performance.

Learning to rank: Cao et al. (2007), Xia et al. (2008), and Chen et al. (2009) all used the Plackett-Luce model in loss functions for learning to rank data. This is the *listwise* approach to learning to rank as the model ingests an entire list of objects to be ranked at once. Alternative approaches are the *pointwise* approach, in which the model ingests a single object, and the *pairwise* approach, where the model ingests pairs of objects. Chen et al. (2009) summarize different approaches for learning to rank.

Other data types: Fan et al. (2020) use a loss based on the beta distribution for predicting values between zero and one. Jacobs et al. (1991) and Bishop (1994) investigated *mixture density networks* for multimodal data. These model the output as a mixture of Gaussians

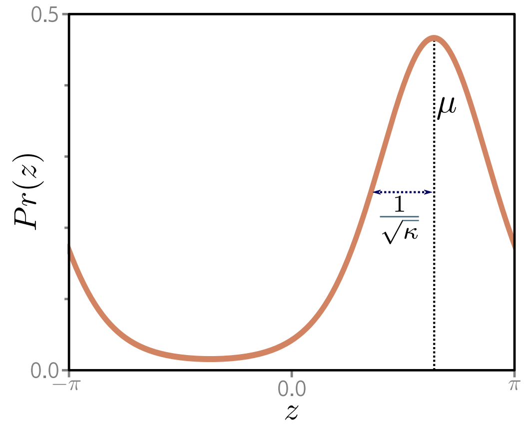

Figure 5.13 The von Mises distribution is defined over the circular domain $(-\pi, \pi]$. It has two parameters. The mean μ determines the position of the peak. The concentration $\kappa > 0$ acts like the inverse of the variance. Hence $1/\sqrt{\kappa}$ is roughly equivalent to the standard deviation in a normal distribution.

(see figure 5.14) that is conditional on the input. Prokudin et al. (2018) used the von Mises distribution to predict direction (see figure 5.13). Fallah et al. (2009) constructed loss functions for prediction counts using the Poisson distribution (see figure 5.15). Ng et al. (2017) used loss functions based on the gamma distribution to predict duration.

Non-probabilistic approaches: It is not strictly necessary to adopt the probabilistic approach discussed in this chapter, but this has become the default in recent years; any loss function that aims to reduce the distance between the model output and the training outputs will suffice, and distance can be defined in any way that seems sensible. There are several well-known non-probabilistic machine learning models for classification, including support vector machines (Vapnik, 1995; Cristianini & Shawe-Taylor, 2000), which use *hinge loss*, and AdaBoost (Freund & Schapire, 1997), which uses *exponential loss*.

Problems

Problem 5.1 Show that the logistic sigmoid function $\text{sig}[z]$ maps $z = -\infty$ to 0, $z = 0$ to 0.5 and $z = \infty$ to 1 where:

$$\text{sig}[z] = \frac{1}{1 + \exp[-z]}. \tag{5.32}$$

Problem 5.2 The loss L for binary classification for a single training pair $\{\mathbf{x}, y\}$ is:

$$L = -(1-y)\log\Big[1 - \text{sig}[\text{f}[\mathbf{x}, \boldsymbol{\phi}]]\Big] - y\log\Big[\text{sig}[\text{f}[\mathbf{x}, \boldsymbol{\phi}]]\Big], \tag{5.33}$$

where $\text{sig}[\bullet]$ is defined in equation 5.32. Plot this loss as a function of the transformed network output $\text{sig}[\text{f}[\mathbf{x}, \boldsymbol{\phi}]] \in [0, 1]$ (i) when the training label $y = 0$ and (ii) when $y = 1$.

Problem 5.3* Suppose we want to build a model that predicts the direction y in radians of the prevailing wind based on local measurements of barometric pressure $\mathbf{x}$. A suitable distribution over circular domains is the von Mises distribution (figure 5.13):

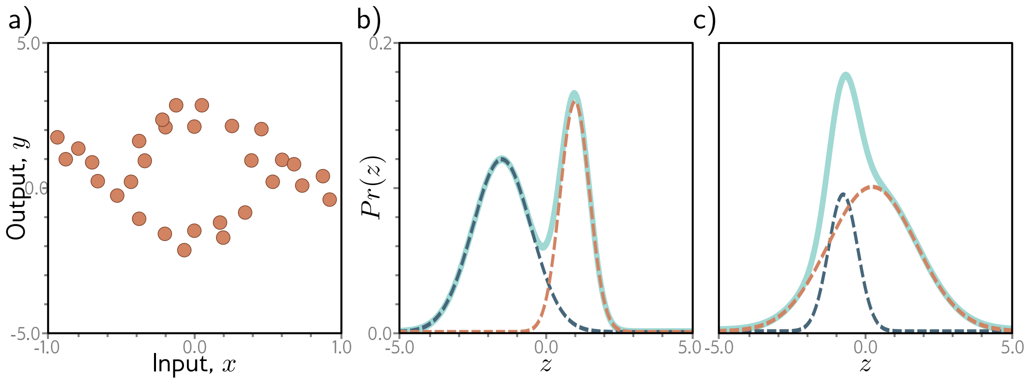

Figure 5.14 Multimodal data and mixture of Gaussians density. a) Example training data where, for intermediate values of the input x, the corresponding output y follows one of two paths. For example, at $x = 0$, the output y might be roughly -2 or $+3$ but is unlikely to be between these values. b) The mixture of Gaussians is a probability model suited to this kind of data. As the name suggests, the model is a weighted sum (solid cyan curve) of two or more normal distributions with different means and variances (here, two weighted distributions, dashed blue and orange curves). When the means are far apart, this forms a multimodal distribution. c) When the means are close, the mixture can model unimodal but non-normal densities.

$$Pr(y|\mu,\kappa) = \frac{\exp[\kappa\cos[y-\mu]]}{2\pi\cdot\text{Bessel}_0[\kappa]}, \tag{5.34}$$

where μ is a measure of the mean direction and κ is a measure of the concentration (i.e., the inverse of the variance). The term $\text{Bessel}_0[\kappa]$ is a modified Bessel function of order 0.

Use the recipe from section 5.2 to develop a loss function for learning the parameter μ of a model $\text{f}[\mathbf{x},\boldsymbol{\phi}]$ to predict the most likely wind direction. Your solution should treat the concentration κ as constant. How would you perform inference?

Problem 5.4* Sometimes, the outputs y for input $\mathbf{x}$ are multimodal as (figure 5.14a); there is more than one valid prediction for a given input. Here, we might use a weighted sum of normal components as the distribution over the output. This is known as a *mixture of Gaussians* model. For example, a mixture of two Gaussians has parameters $\boldsymbol{\theta} = \{\lambda,\mu_1,\sigma_1^2,\mu_2,\sigma_2^2\}$:

$$Pr(y|\lambda,\mu_1,\mu_2,\sigma_1^2,\sigma_2^2) = \frac{\lambda}{\sqrt{2\pi\sigma_1^2}}\exp\left[\frac{-(y-\mu_1)^2}{2\sigma_1^2}\right] + \frac{1-\lambda}{\sqrt{2\pi\sigma_2^2}}\exp\left[\frac{-(y-\mu_2)^2}{2\sigma_2^2}\right], \tag{5.35}$$

where $\lambda\in[0,1]$ controls the relative weight of the two components, which have means μ_1,μ_2 and variances σ_1^2, σ_2^2, respectively. This model can represent a distribution with two peaks (figure 5.14b) or a distribution with one peak but a more complex shape (figure 5.14c).

Use the recipe from section 5.2 to construct a loss function for training a model $\mathbf{f}[x,\boldsymbol{\phi}]$ that takes input x, has parameters $\boldsymbol{\phi}$, and predicts a mixture of two Gaussians. The loss should be based on I training data pairs $\{x_i,y_i\}$. What problems do you foresee when performing inference?

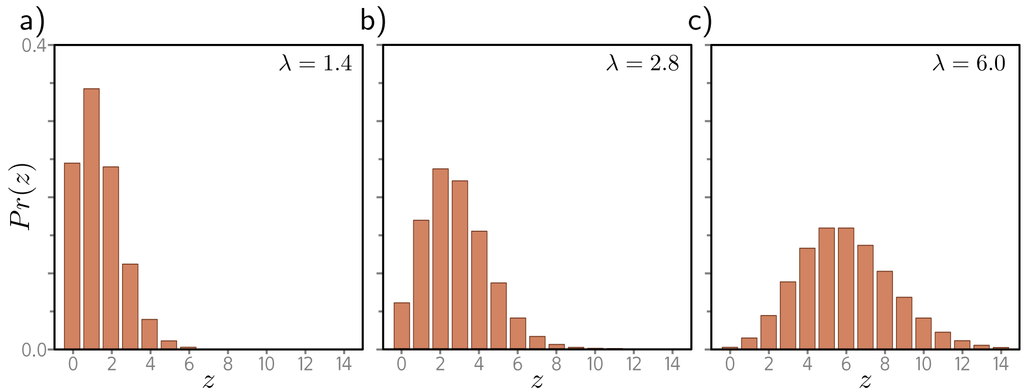

Figure 5.15 Poisson distribution. This discrete distribution is defined over non-negative integers $z \in \{0, 1, 2, \ldots\}$. It has a single parameter $\lambda \in \mathbb{R}^+$, which is known as the rate and is the mean of the distribution. a–c) Poisson distributions with rates of 1.4, 2.8, and 6.0, respectively.

Problem 5.5 Consider extending the model from problem 5.3 to predict the wind direction using a mixture of two von Mises distributions. Write an expression for the likelihood $Pr(y|\boldsymbol{\theta})$ for this model. How many outputs will the network need to produce?

Problem 5.6 Consider building a model to predict the number of pedestrians $y \in \{0, 1, 2, \ldots\}$ that will pass a given point in the city in the next minute, based on data $\mathbf{x}$ that contains information about the time of day, the longitude and latitude, and the type of neighborhood. A suitable distribution for modeling counts is the Poisson distribution (figure 5.15). This has a single parameter $\lambda > 0$ called the *rate* that represents the mean of the distribution. The distribution has probability density function:

$$Pr(y = k) = \frac{\lambda^k e^{-\lambda}}{k!}. \tag{5.36}$$

Design a loss function for this model assuming we have access to I training pairs $\{\mathbf{x}_i, y_i\}$.

Problem 5.7 Consider a multivariate regression problem where we predict ten outputs, so $\mathbf{y} \in \mathbb{R}^{10}$, and model each with an independent normal distribution where the means μ_d are predicted by the network, and variances σ^2 are constant. Write an expression for the likelihood $Pr(\mathbf{y}|\mathbf{f}[\mathbf{x}, \boldsymbol{\phi}])$. Show that minimizing the negative log-likelihood of this model is still equivalent to minimizing a sum of squared terms if we don't estimate the variance σ^2.

Problem 5.8* Construct a loss function for multivariate $\mathbf{y}$ based on independent normal distributions with different variances σ_d^2 for each dimension. Assume a heteroscedastic model so that both the means μ_d and variances σ_d^2 vary as a function of the data.

Problem 5.9* Consider a multivariate regression problem in which we predict the height of a person in meters and their weight in kilos from data $\mathbf{x}$. Here, the units take quite different ranges. What problems do you see this causing? Propose two solutions to these problems.

Problem 5.10 Extend the model from problem 5.3 to predict both the wind direction and the wind speed and define the associated loss function.

Chapter 6

Fitting models

Chapters 3 and 4 described shallow and deep neural networks. These represent families of piecewise linear functions, where the parameters determine the particular function. Chapter 5 introduced the loss — a single number representing the mismatch between the network predictions and the ground truth for a training set.

The loss depends on the parameters of the network, and we now consider how to find parameter values that minimize this loss. This is known as *learning* the network's parameters or simply as *training* or *fitting* the model. The process is to choose initial parameter values and then iterate the following two steps: (i) compute the derivatives (gradients) of the loss with respect to the parameters, and (ii) adjust the parameters based on the gradients to decrease the loss. After many steps, we hope to reach the overall minimum of the loss function.

This chapter tackles the second of these steps; we consider algorithms that adjust the parameters to decrease the loss. Chapter 7 discusses how to initialize the parameters and compute the gradients for neural networks.

6.1 Gradient descent

To fit a model, we need a training set $\{\mathbf{x}_i, \mathbf{y}_i\}$ of input/output pairs. We seek parameters $\boldsymbol{\phi}$ for the model $\mathbf{f}[\mathbf{x}_i, \boldsymbol{\phi}]$ that map the inputs $\mathbf{x}_i$ to the outputs $\mathbf{y}_i$ as well as possible. To this end, we define a loss function $\mathrm{L}[\boldsymbol{\phi}]$ that returns a single number that quantifies the mismatch in this mapping. The goal of an *optimization algorithm* is to find parameters $\hat{\boldsymbol{\phi}}$ that minimize the loss:

$$\hat{\boldsymbol{\phi}} = \underset{\boldsymbol{\phi}}{\mathrm{argmin}}\Big[\mathrm{L}[\boldsymbol{\phi}]\Big]. \tag{6.1}$$

There are many families of optimization algorithms, but the standard methods for training neural networks are iterative. These algorithms initialize the parameters heuristically and then adjust them repeatedly in such a way that the loss decreases.

The simplest method in this class is *gradient descent*. This starts with initial parameters $\boldsymbol{\phi} = [\phi_0, \phi_1, \ldots, \phi_N]^T$ and iterates two steps:

Step 1. Compute the derivatives of the loss with respect to the parameters:

$$\frac{\partial L}{\partial \boldsymbol{\phi}} = \begin{bmatrix} \frac{\partial L}{\partial \phi_0} \\ \frac{\partial L}{\partial \phi_1} \\ \vdots \\ \frac{\partial L}{\partial \phi_N} \end{bmatrix}. \tag{6.2}$$

Step 2. Update the parameters according to the rule:

$$\boldsymbol{\phi} \longleftarrow \boldsymbol{\phi} - \alpha \cdot \frac{\partial L}{\partial \boldsymbol{\phi}}, \tag{6.3}$$

where the positive scalar α determines the magnitude of the change.

The first step computes the gradient of the loss function at the current position. This determines the *uphill* direction of the loss function. The second step moves a small distance α *downhill* (hence the negative sign). The parameter α may be fixed (in which case, we call it a *learning rate*), or we may perform a *line search* where we try several values of α to find the one that most decreases the loss.

Notebook 6.1
Line search

At the minimum of the loss function, the surface must be flat (or we could improve further by going downhill). Hence, the gradient will be zero, and the parameters will stop changing. In practice, we monitor the gradient magnitude and terminate the algorithm when it becomes too small.

6.1.1 Linear regression example

Consider applying gradient descent to the 1D linear regression model from chapter 2. The model $\mathrm{f}[x, \boldsymbol{\phi}]$ maps a scalar input x to a scalar output y and has parameters $\boldsymbol{\phi} = [\phi_0, \phi_1]^T$, which represent the y-intercept and the slope:

$$\begin{aligned} y &= \mathrm{f}[x, \boldsymbol{\phi}] \\ &= \phi_0 + \phi_1 x. \end{aligned} \tag{6.4}$$

Given a dataset $\{x_i, y_i\}$ containing I input/output pairs, we choose the least squares loss function:

$$\begin{aligned} \mathrm{L}[\boldsymbol{\phi}] = \sum_{i=1}^{I} \ell_i &= \sum_{i=1}^{I} \left(\mathrm{f}[x_i, \boldsymbol{\phi}] - y_i\right)^2 \\ &= \sum_{i=1}^{I} \left(\phi_0 + \phi_1 x_i - y_i\right)^2, \end{aligned} \tag{6.5}$$

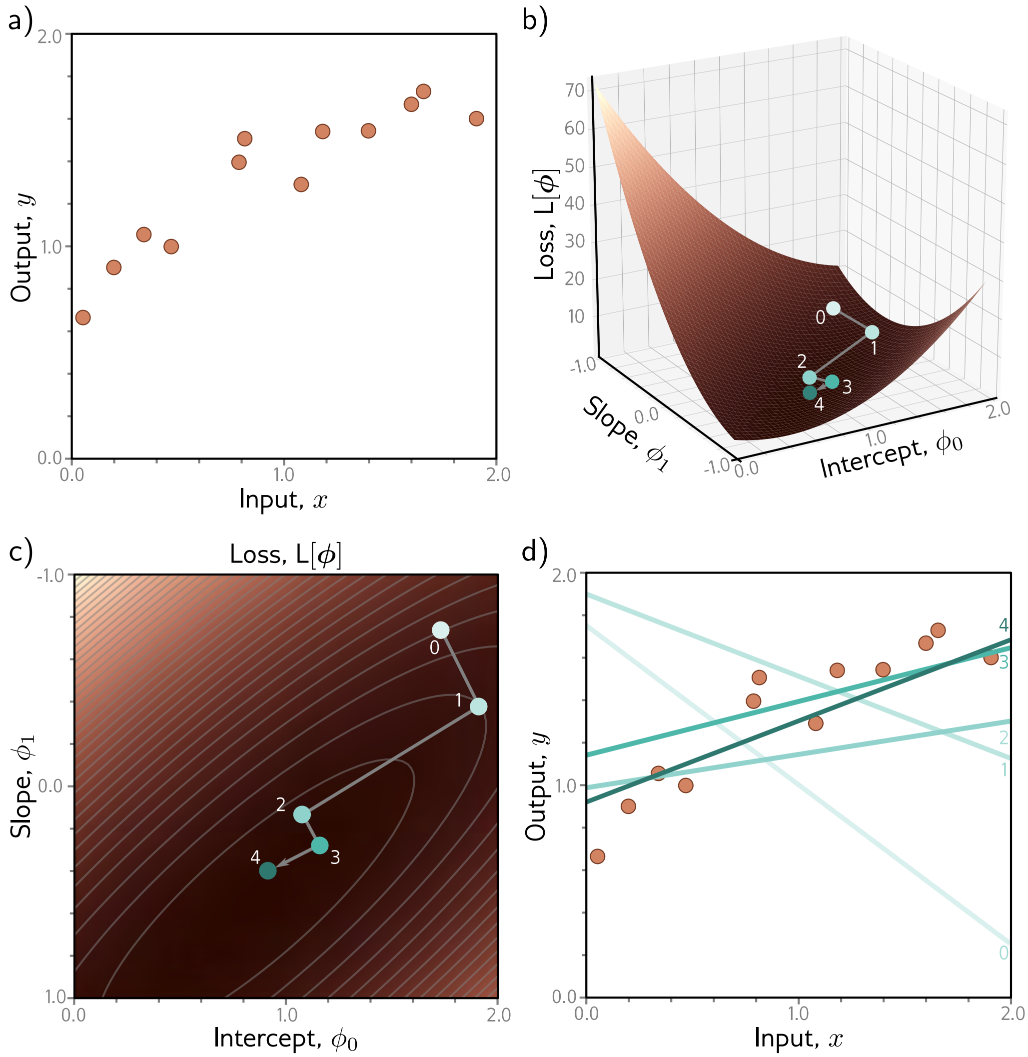

Figure 6.1 Gradient descent for the linear regression model. a) Training set of $I = 12$ input/output pairs $\{x_i, y_i\}$. b) Loss function showing iterations of gradient descent. We start at point 0 and move in the steepest downhill direction until we can improve no further to arrive at point 1. We then repeat this procedure. We measure the gradient at point 1 and move downhill to point 2 and so on. c) This can be visualized better as a heatmap, where the brightness represents the loss. After only four iterations, we are already close to the minimum. d) The model with the parameters at point 0 (lightest line) describes the data very badly, but each successive iteration improves the fit. The model with the parameters at point 4 (darkest line) is already a reasonable description of the training data.

where the term $\ell_i = (\phi_0 + \phi_1 x_i - y_i)^2$ is the individual contribution to the loss from the i^{th} training example.

The derivative of the loss function with respect to the parameters can be decomposed into the sum of the derivatives of the individual contributions:

$$\frac{\partial L}{\partial \boldsymbol{\phi}} = \frac{\partial}{\partial \boldsymbol{\phi}} \sum_{i=1}^{I} \ell_i = \sum_{i=1}^{I} \frac{\partial \ell_i}{\partial \boldsymbol{\phi}}, \tag{6.6}$$

Problem 6.1

where these are given by:

$$\frac{\partial \ell_i}{\partial \boldsymbol{\phi}} = \begin{bmatrix} \frac{\partial \ell_i}{\partial \phi_0} \\ \frac{\partial \ell_i}{\partial \phi_1} \end{bmatrix} = \begin{bmatrix} 2(\phi_0 + \phi_1 x_i - y_i) \\ 2x_i(\phi_0 + \phi_1 x_i - y_i) \end{bmatrix}. \tag{6.7}$$

Notebook 6.2 Gradient descent

Figure 6.1 shows the progression of this algorithm as we iteratively compute the derivatives according to equations 6.6 and 6.7 and then update the parameters using the rule in equation 6.3. In this case, we have used a line search procedure to find the value of α that decreases the loss the most at each iteration.

6.1.2 Gabor model example

Problem 6.2

Loss functions for linear regression problems (figure 6.1c) always have a single well-defined global minimum. More formally, they are *convex*, which means that no chord (line segment between two points on the surface) intersects the function. Convexity implies that wherever we initialize the parameters, we are bound to reach the minimum if we keep walking downhill; the training procedure can't fail.

Unfortunately, loss functions for most nonlinear models, including both shallow and deep networks, are *non-convex*. Visualizing neural network loss functions is challenging due to the number of parameters. Hence, we first explore a simpler nonlinear model with two parameters to gain insight into the properties of non-convex loss functions:

$$\mathrm{f}[x, \boldsymbol{\phi}] = \sin[\phi_0 + 0.06 \cdot \phi_1 x] \cdot \exp\left(-\frac{(\phi_0 + 0.06 \cdot \phi_1 x)^2}{32.0}\right). \tag{6.8}$$

Problems 6.3–6.6

This *Gabor model* maps scalar input x to scalar output y and consists of a sinusoidal component (creating an oscillatory function) multiplied by a negative exponential component (causing the amplitude to decrease as we move from the center). It has two parameters $\boldsymbol{\phi} = [\phi_0, \phi_1]^T$, where $\phi_0 \in \mathbb{R}$ determines the mean position of the function and $\phi_1 \in \mathbb{R}^+$ stretches or squeezes it along the x-axis (figure 6.2).

Consider a training set of I examples $\{x_i, y_i\}$ (figure 6.3). The least squares loss function for I training examples is defined as:

$$\mathrm{L}[\boldsymbol{\phi}] = \sum_{i=1}^{I} (\mathrm{f}[x_i, \boldsymbol{\phi}] - y_i)^2. \tag{6.9}$$

Once more, the goal is to find the parameters $\hat{\boldsymbol{\phi}}$ that minimize this loss.

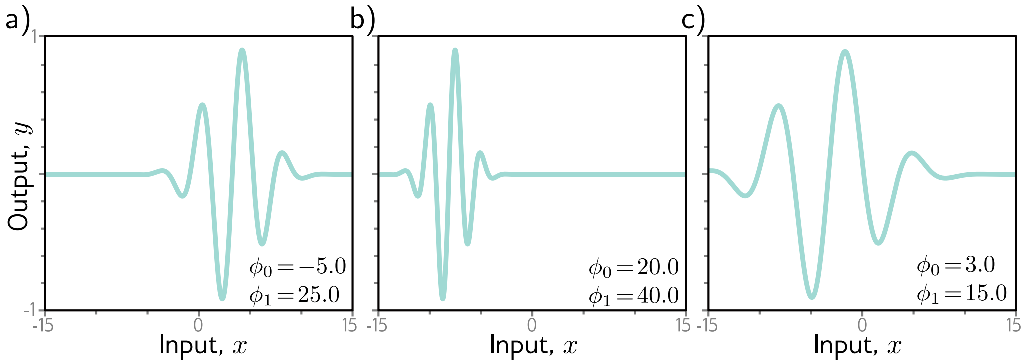

Figure 6.2 Gabor model. This nonlinear model maps scalar input x to scalar output y and has parameters $\boldsymbol{\phi} = [\phi_0, \phi_1]^T$. It describes a sinusoidal function that decreases in amplitude with distance from its center. Parameter $\phi_0 \in \mathbb{R}$ determines the position of the center. As ϕ_0 increases, the function moves left. Parameter $\phi_1 \in \mathbb{R}^+$ squeezes the function along the x-axis relative to the center. As ϕ_1 increases, the function narrows. a–c) Model with different parameters.

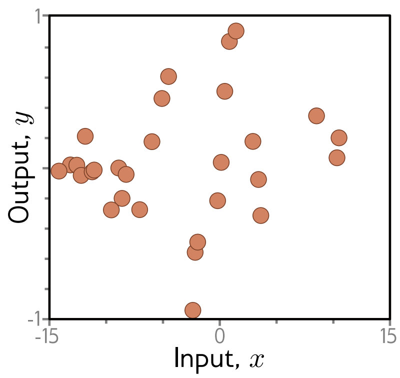

Figure 6.3 Training data for fitting the Gabor model. The training dataset contains 28 input/output examples $\{x_i, y_i\}$. These were created by uniformly sampling $x_i \in [-15, 15]$, passing the samples through a Gabor model with parameters $\boldsymbol{\phi} = [0.0, 16.6]^T$, and adding normally distributed noise.

6.1.3 Local minima and saddle points

Figure 6.4 depicts the loss function associated with the Gabor model for this dataset. There are numerous *local minima* (cyan circles). Here the gradient is zero, and the loss increases if we move in any direction, but we are *not* at the overall minimum of the function. The point with the lowest loss is known as the *global minimum* and is depicted by the gray circle.

Problem 6.4

If we start in a random position and use gradient descent to go downhill, there is no guarantee that we will wind up at the global minimum and find the best parameters (figure 6.5a). It's equally or even more likely that the algorithm will terminate in one of the local minima. Furthermore, there is no way of knowing whether there is a better solution elsewhere.

Problems 6.7–6.8

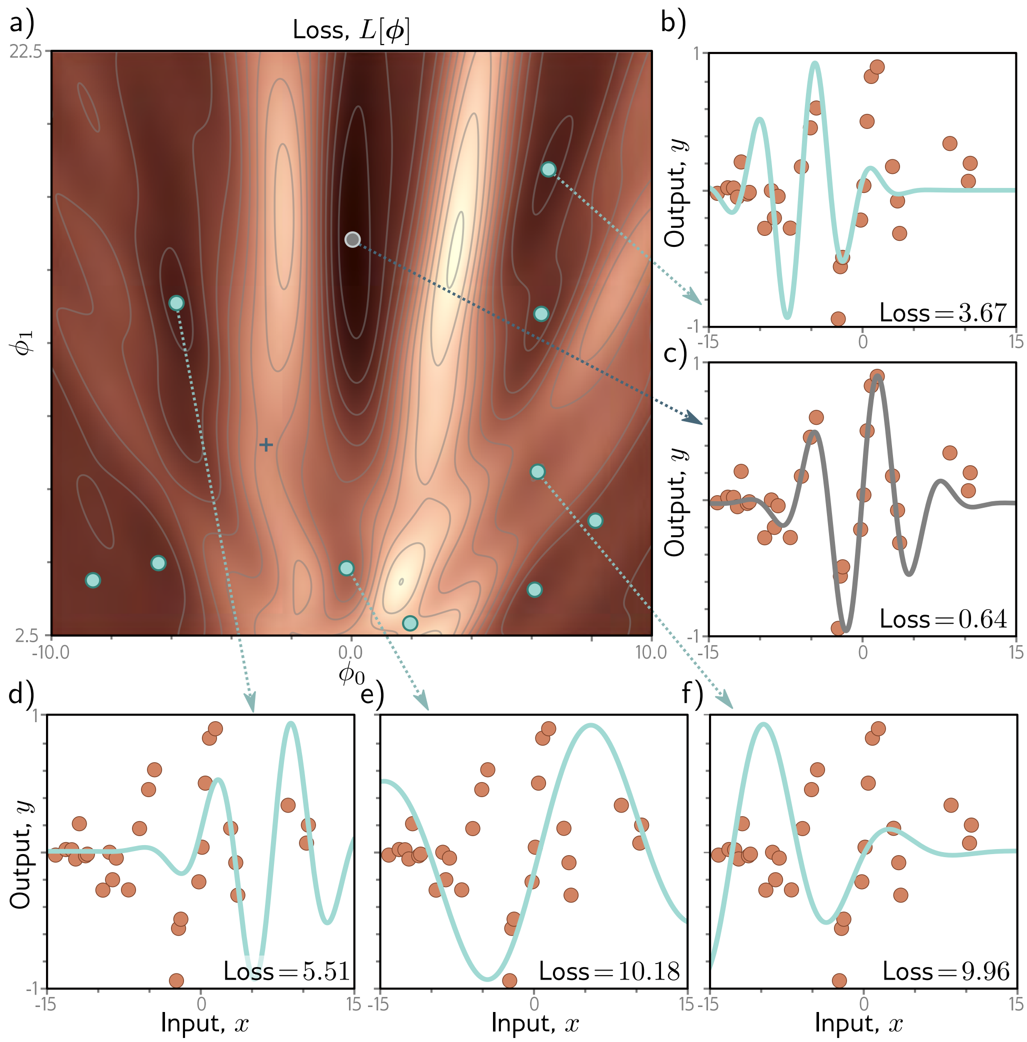

Figure 6.4 Loss function for the Gabor model. a) The loss function is non-convex, with multiple local minima (cyan circles) in addition to the global minimum (gray circle). It also contains saddle points where the gradient is locally zero, but the function increases in one direction and decreases in the other. The blue cross is an example of a saddle point; the function decreases as we move horizontally in either direction but increases as we move vertically. b–f) Models associated with the different minima. In each case, there is no small change that decreases the loss. Panel (c) shows the global minimum, which has a loss of 0.64.

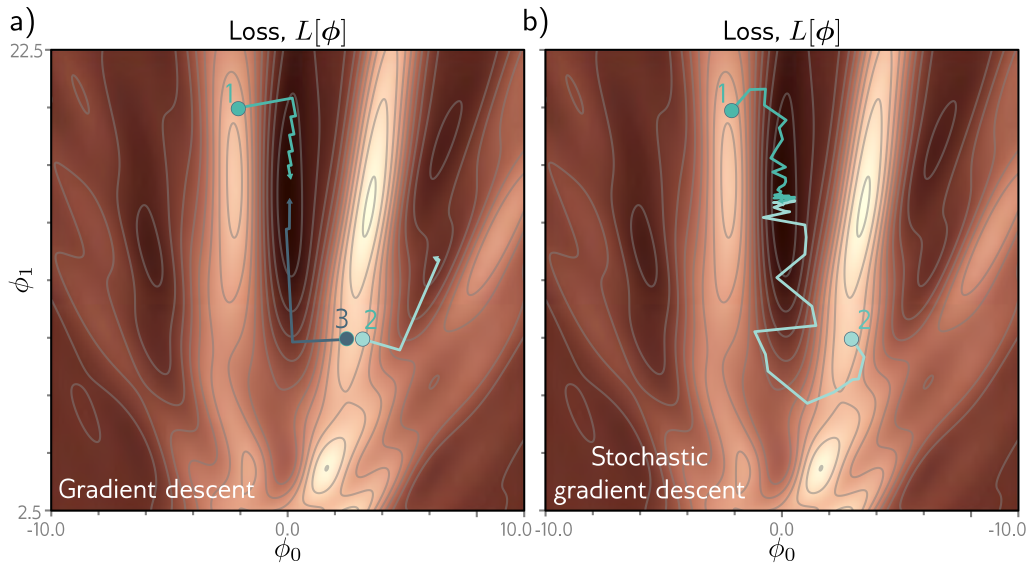

Figure 6.5 Gradient descent vs. stochastic gradient descent. a) Gradient descent with line search. As long as the gradient descent algorithm is initialized in the right "valley" of the loss function (e.g., points 1 and 3), the parameter estimate will move steadily toward the global minimum. However, if it is initialized outside this valley (e.g., point 2), it will descend toward one of the local minima. b) Stochastic gradient descent adds noise to the optimization process, so it is possible to escape from the wrong valley (e.g., point 2) and still reach the global minimum.

In addition, the loss function contains *saddle points* (e.g., the blue cross in figure 6.4). Here, the gradient is zero, but the function increases in some directions and decreases in others. If the current parameters are not exactly at the saddle point, then gradient descent can escape by moving downhill. However, the surface near the saddle point is flat, so it's hard to be sure that training hasn't converged; if we terminate our algorithm when the gradient is small, we may erroneously stop near a saddle point.

6.2 Stochastic gradient descent

The Gabor model has two parameters, so we could find the global minimum by either (i) exhaustively searching the parameter space or (ii) repeatedly starting gradient descent from different positions and choosing the result with the lowest loss. However, neural network models can have millions of parameters, so neither approach is practical. In short, using gradient descent to find the global optimum of a high-dimensional loss function is challenging. We can find *a* minimum, but there is no way to tell whether this

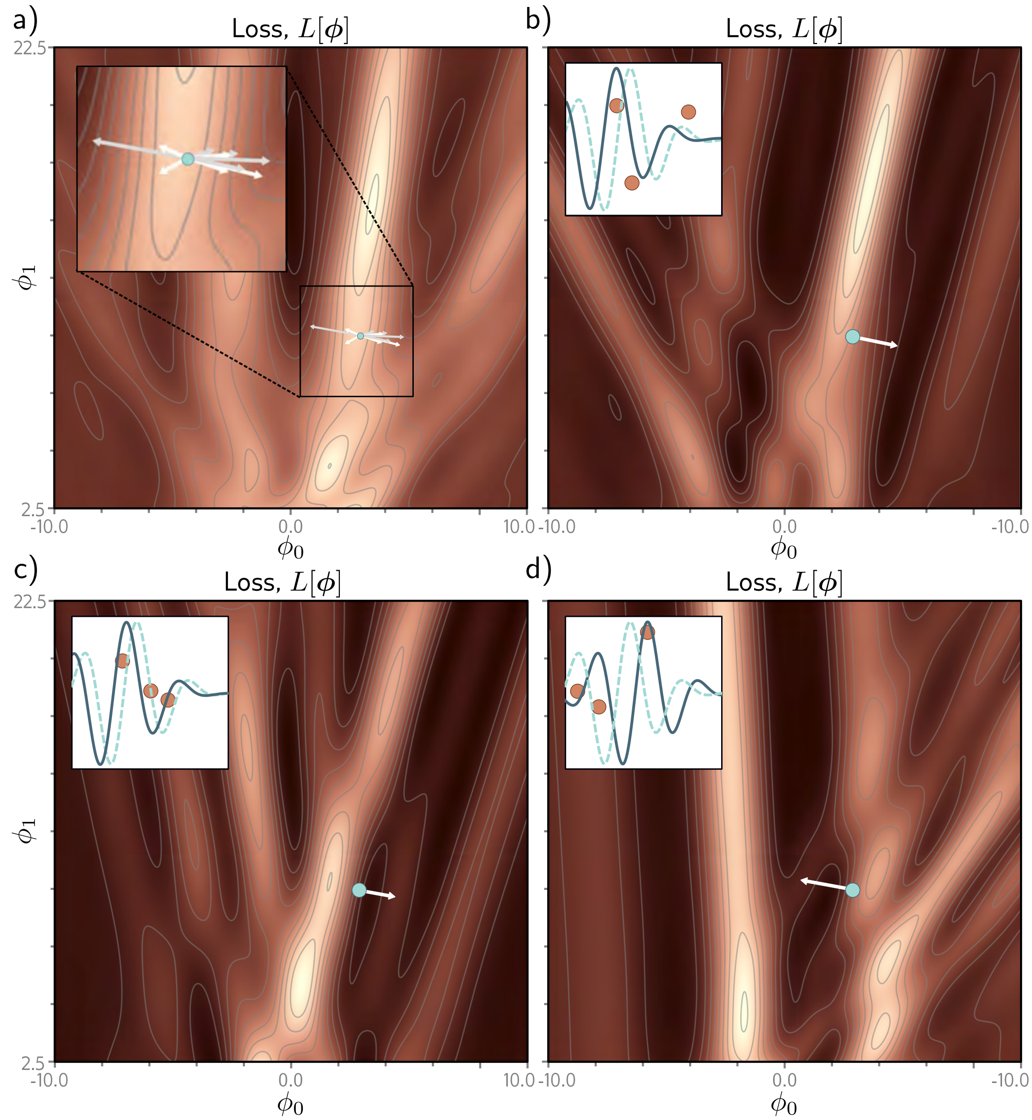

Figure 6.6 Alternative view of SGD for the Gabor model with a batch size of three. a) Loss function for the entire training dataset. At each iteration, there is a probability distribution of possible parameter changes (inset shows samples). These correspond to different choices of the three batch elements. b) Loss function for one possible batch. The SGD algorithm moves in the downhill direction on this function for a distance that is determined by the learning rate and the local gradient magnitude. The current model (dashed function in inset) changes to better fit the batch data (solid function). c) A different batch creates a different loss function and results in a different update. d) For this batch, the algorithm moves *downhill* with respect to the batch loss function but *uphill* with respect to the global loss function in panel (a). This is how SGD can escape local minima.

is the global minimum or even a good one.

One of the main problems is that the final destination of a gradient descent algorithm is entirely determined by the starting point. *Stochastic gradient descent (SGD)* attempts to remedy this problem by adding some noise to the gradient at each step. The solution still moves downhill on average, but at any given iteration, the direction chosen is not necessarily in the steepest downhill direction. Indeed, it might not be downhill at all. The SGD algorithm has the possibility of moving temporarily uphill and hence jump from one "valley" of the loss function to another (figure 6.5b).

Notebook 6.3 Stochastic gradient descent

6.2.1 Batches and epochs

The mechanism for introducing randomness is simple. At each iteration, the algorithm chooses a random subset of the training data and computes the gradient from these examples alone. This subset is known as a *minibatch* or *batch* for short. The update rule for the model parameters $\boldsymbol{\phi}_t$ at iteration t is hence:

$$\boldsymbol{\phi}_{t+1} \longleftarrow \boldsymbol{\phi}_t - \alpha \cdot \sum_{i\in\mathcal{B}_t} \frac{\partial \ell_i[\boldsymbol{\phi}_t]}{\partial \boldsymbol{\phi}}, \tag{6.10}$$

where $\mathcal{B}_t$ is a set containing the indices of the input/output pairs in the current batch and, as before, ℓ_i is the loss due to the i^{th} pair. The term α is the learning rate, and together with the gradient magnitude, determines the distance moved at each iteration. The learning rate is chosen at the start of the procedure and does not depend on the local properties of the function.

The batches are usually drawn from the dataset without replacement. The algorithm works through the training examples until it has used all the data, at which point it starts sampling from the full training dataset again. A single pass through the entire training dataset is referred to as an *epoch*. A batch may be as small as a single example or as large as the whole dataset. The latter case is called *full-batch gradient descent* and is identical to regular (non-stochastic) gradient descent.

Problem 6.9

An alternative interpretation of SGD is that it computes the gradient of a different loss function at each iteration; the loss function depends on both the model and the training data and hence will differ for each randomly selected batch. In this view, SGD performs deterministic gradient descent on a constantly changing loss function (figure 6.6). However, despite this variability, the expected loss and expected gradients at any point remain the same as for gradient descent.

6.2.2 Properties of stochastic gradient descent

SGD has several attractive features. First, although it adds noise to the trajectory, it still improves the fit to a subset of the data at each iteration. Hence, the updates tend to be sensible even if they are not optimal. Second, because it draws training examples without replacement and iterates through the dataset, the training examples all still contribute equally. Third, it is less computationally expensive to compute the gradient from just a subset of the training data. Fourth, it can (in principle) escape local minima. Fifth, it reduces the chances of getting stuck near saddle points; it is likely that at least some of the possible batches will have a significant gradient at any point on the loss function. Finally, there is some evidence that SGD finds parameters for neural networks that cause them to generalize well to new data in practice (see section 9.2).

SGD does not necessarily "converge" in the traditional sense. However, the hope is that when we are close to the global minimum, all the data points will be well described by the model. Consequently, the gradient will be small, whichever batch is chosen, and the parameters will cease to change much. In practice, SGD is often applied with a *learning rate schedule*. The learning rate α starts at a high value and is decreased by a constant factor every N epochs. The logic is that in the early stages of training, we want the algorithm to explore the parameter space, jumping from valley to valley to find a sensible region. In later stages, we are roughly in the right place and are more concerned with fine-tuning the parameters, so we decrease α to make smaller changes.

6.3 Momentum

A common modification to stochastic gradient descent is to add a *momentum* term. We update the parameters with a weighted combination of the gradient computed from the current batch and the direction moved in the previous step:

$$\begin{aligned}\mathbf{m}_{t+1} &\leftarrow \beta \cdot \mathbf{m}_t + (1-\beta)\sum_{i\in\mathcal{B}_t}\frac{\partial \ell_i[\boldsymbol{\phi}_t]}{\partial \boldsymbol{\phi}} \\ \boldsymbol{\phi}_{t+1} &\leftarrow \boldsymbol{\phi}_t - \alpha\cdot\mathbf{m}_{t+1},\end{aligned} \tag{6.11}$$

where $\mathbf{m}_t$ is the momentum (which drives the update at iteration t), $\beta \in [0,1)$ controls the degree to which the gradient is smoothed over time, and α is the learning rate.

Problem 6.10

The recursive formulation of the momentum calculation means that the gradient step is an infinite weighted sum of all the previous gradients, where the weights get smaller as we move back in time. The effective learning rate increases if all these gradients are aligned over multiple iterations but decreases if the gradient direction repeatedly changes as the terms in the sum cancel out. The overall effect is a smoother trajectory and reduced oscillatory behavior in valleys (figure 6.7).

6.3.1 Nesterov accelerated momentum

Notebook 6.4 Momentum

The momentum term can be considered a coarse prediction of where the SGD algorithm will move next. Nesterov accelerated momentum (figure 6.8) computes the gradients at this predicted point rather than at the current point:

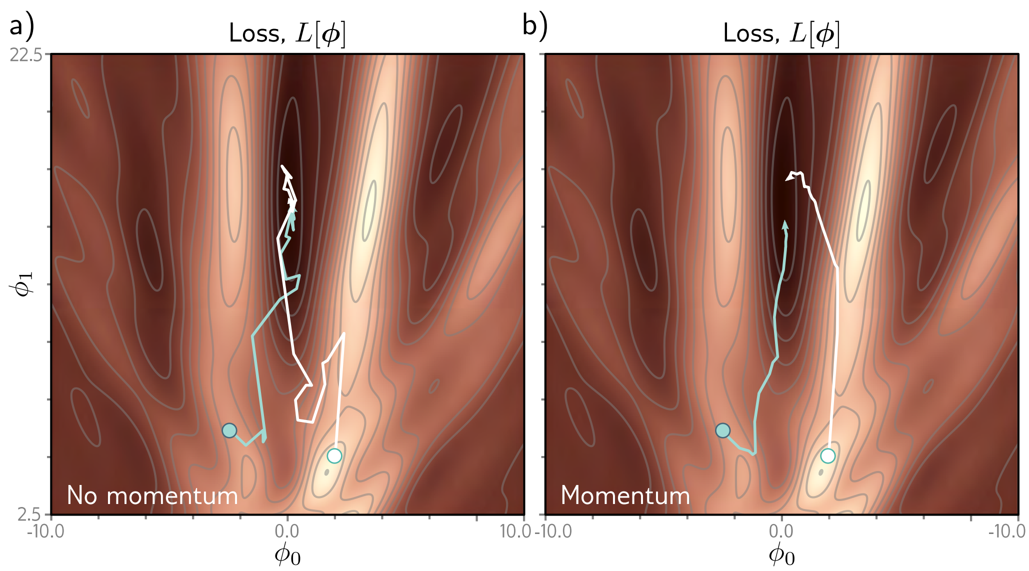

Figure 6.7 Stochastic gradient descent with momentum. a) Regular stochastic descent takes a very indirect path toward the minimum. b) With a momentum term, the change at the current step is a weighted combination of the previous change and the gradient computed from the batch. This smooths out the trajectory and increases the speed of convergence.

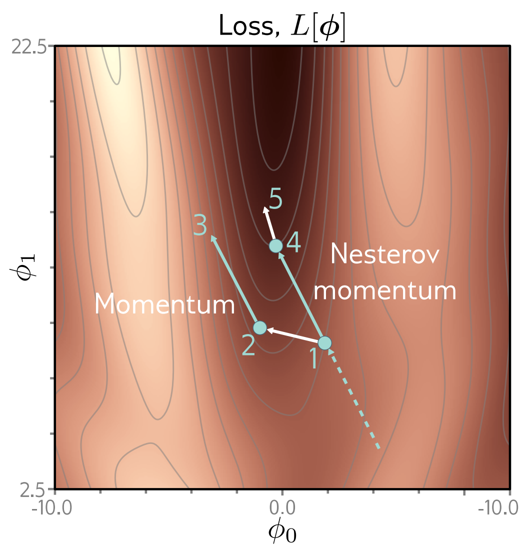

Figure 6.8 Nesterov accelerated momentum. The solution has traveled along the dashed line to arrive at point 1. A traditional momentum update measures the gradient at point 1, moves some distance in this direction to point 2, and then adds the momentum term from the previous iteration (i.e., in the same direction as the dashed line), arriving at point 3. The Nesterov momentum update first applies the momentum term (moving from point 1 to point 4) and then measures the gradient and applies an update to arrive at point 5.

$$\begin{aligned}\mathbf{m}_{t+1} &\leftarrow \beta \cdot \mathbf{m}_t + (1-\beta)\sum_{i\in\mathcal{B}_t}\frac{\partial \ell_i[\boldsymbol{\phi}_t - \alpha\cdot\mathbf{m}_t]}{\partial \boldsymbol{\phi}} \\ \boldsymbol{\phi}_{t+1} &\leftarrow \boldsymbol{\phi}_t - \alpha\cdot\mathbf{m}_{t+1},\end{aligned} \tag{6.12}$$

where now the gradients are evaluated at $\boldsymbol{\phi}_t - \alpha\cdot\mathbf{m}_t$. One way to think about this is that the gradient term now corrects the path provided by momentum alone.

6.4 Adam

Gradient descent with a fixed step size has the following undesirable property: it makes large adjustments to parameters associated with large gradients (where perhaps we should be more cautious) and small adjustments to parameters associated with small gradients (where perhaps we should explore further). When the gradient of the loss surface is much steeper in one direction than another, it is difficult to choose a learning rate that (i) makes good progress in both directions and (ii) is stable (figures 6.9a–b).

A straightforward approach is to normalize the gradients so that we move a fixed distance (governed by the learning rate) in each direction. To do this, we first measure the gradient $\mathbf{m}_{t+1}$ and the pointwise squared gradient $\mathbf{v}_{t+1}$:

$$\begin{aligned}\mathbf{m}_{t+1} &\leftarrow \frac{\partial L[\boldsymbol{\phi}_t]}{\partial \boldsymbol{\phi}} \\ \mathbf{v}_{t+1} &\leftarrow \frac{\partial L[\boldsymbol{\phi}_t]}{\partial \boldsymbol{\phi}}^2.\end{aligned} \tag{6.13}$$

Then we apply the update rule:

$$\boldsymbol{\phi}_{t+1} \leftarrow \boldsymbol{\phi}_t - \alpha\cdot\frac{\mathbf{m}_{t+1}}{\sqrt{\mathbf{v}_{t+1}}+\epsilon}, \tag{6.14}$$

where the square root and division are both pointwise, α is the learning rate, and ϵ is a small constant that prevents division by zero when the gradient magnitude is zero. The term $\mathbf{v}_{t+1}$ is the squared gradient, and the positive root of this is used to normalize the gradient itself, so all that remains is the sign in each coordinate direction. The result is that the algorithm moves a fixed distance α along each coordinate, where the direction is determined by whichever way is downhill (figure 6.9c). This simple algorithm makes good progress in both directions but will not converge unless it happens to land exactly at the minimum. Instead, it will bounce back and forth around the minimum.

Adaptive moment estimation, or *Adam*, takes this idea and adds momentum to both the estimate of the gradient and the squared gradient:

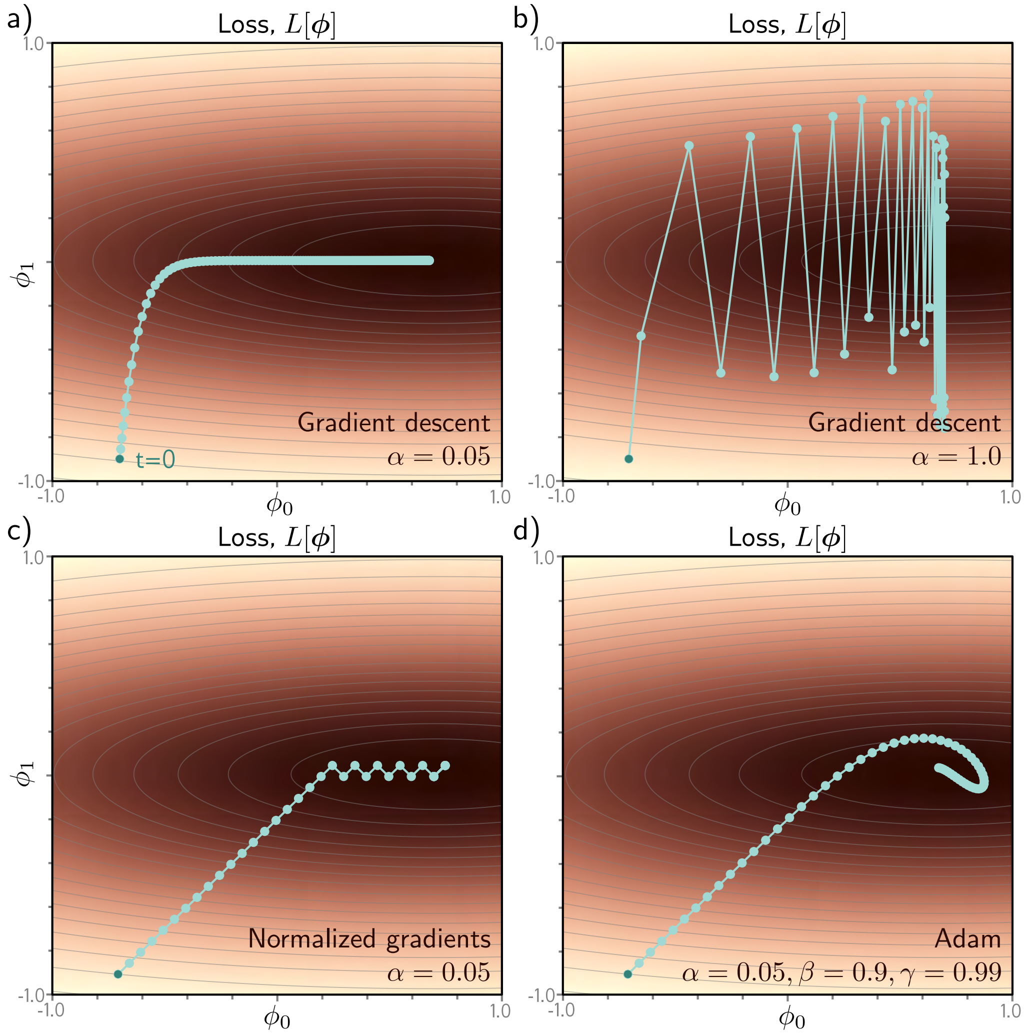

Figure 6.9 Adaptive moment estimation (Adam). a) This loss function changes quickly in the vertical direction but slowly in the horizontal direction. If we run full-batch gradient descent with a learning rate that makes good progress in the vertical direction, then the algorithm takes a long time to reach the final horizontal position. b) If the learning rate is chosen so that the algorithm makes good progress in the horizontal direction, it overshoots in the vertical direction and becomes unstable. c) A straightforward approach is to move a fixed distance along each axis at each step so that we move downhill in both directions. This is accomplished by normalizing the gradient magnitude and retaining only the sign. However, this does not usually converge to the exact minimum but instead oscillates back and forth around it (here between the last two points). d) The Adam algorithm uses momentum in both the estimated gradient and the normalization term, which creates a smoother path.

$$\begin{aligned}\mathbf{m}_{t+1} &\leftarrow \beta\cdot\mathbf{m}_t + (1-\beta)\frac{\partial L[\boldsymbol{\phi}_t]}{\partial\boldsymbol{\phi}}\\ \mathbf{v}_{t+1} &\leftarrow \gamma\cdot\mathbf{v}_t + (1-\gamma)\left(\frac{\partial L[\boldsymbol{\phi}_t]}{\partial\boldsymbol{\phi}}\right)^2,\end{aligned} \tag{6.15}$$

where β and γ are the momentum coefficients for the two statistics.

Using momentum is equivalent to taking a weighted average over the history of each of these statistics. At the start of the procedure, all the previous measurements are effectively zero, resulting in unrealistically small estimates. Consequently, we modify these statistics using the rule:

$$\begin{aligned}\tilde{\mathbf{m}}_{t+1} &\leftarrow \frac{\mathbf{m}_{t+1}}{1-\beta^{t+1}}\\ \tilde{\mathbf{v}}_{t+1} &\leftarrow \frac{\mathbf{v}_{t+1}}{1-\gamma^{t+1}}.\end{aligned} \tag{6.16}$$

Since β and γ are in the range $[0,1)$, the terms with exponents $t+1$ become smaller with each time step, the denominators become closer to one, and this modification has a diminishing effect.

Finally, we update the parameters as before, but with the modified terms:

$$\boldsymbol{\phi}_{t+1} \leftarrow \boldsymbol{\phi}_t - \alpha\cdot\frac{\tilde{\mathbf{m}}_{t+1}}{\sqrt{\tilde{\mathbf{v}}_{t+1}}+\epsilon}. \tag{6.17}$$

Notebook 6.5
Adam

The result is an algorithm that can converge to the overall minimum and makes good progress in every direction in the parameter space. Note that Adam is usually used in a stochastic setting where the gradients and their squares are computed from mini-batches:

$$\begin{aligned}\mathbf{m}_{t+1} &\leftarrow \beta\cdot\mathbf{m}_t + (1-\beta)\sum_{i\in\mathcal{B}_t}\frac{\partial \ell_i[\boldsymbol{\phi}_t]}{\partial\boldsymbol{\phi}}\\ \mathbf{v}_{t+1} &\leftarrow \gamma\cdot\mathbf{v}_t + (1-\gamma)\sum_{i\in\mathcal{B}_t}\left(\frac{\partial \ell_i[\boldsymbol{\phi}_t]}{\partial\boldsymbol{\phi}}\right)^2,\end{aligned} \tag{6.18}$$

and so the trajectory is noisy in practice.

As we shall see in chapter 7, the gradient magnitudes of neural network parameters can depend on their depth in the network. Adam helps compensate for this tendency and balances out changes across the different layers. In practice, Adam also has the advantage of being less sensitive to the initial learning rate because it avoids situations like those in figures 6.9a–b, so it doesn't need complex learning rate schedules.

6.5 Training algorithm hyperparameters

The choices of learning algorithm, batch size, learning rate schedule, and momentum coefficients are all considered *hyperparameters* of the training algorithm; these directly affect the final model performance but are distinct from the model parameters. Choosing these can be more art than science, and it's common to train many models with different hyperparameters and choose the best one. This is known as *hyperparameter tuning*. We return to this issue in chapter 8.

6.6 Summary

This chapter discussed model training. This problem was framed as finding parameters $\boldsymbol{\phi}$ that corresponded to the minimum of a loss function $L[\boldsymbol{\phi}]$. The gradient descent method measures the gradient of the loss function for the current parameters (i.e., how the loss changes when we make a small change to the parameters). Then it moves the parameters in the direction that decreases the loss fastest. This is repeated until convergence.

For nonlinear functions, the loss function may have both local minima (where gradient descent gets trapped) and saddle points (where gradient descent may appear to have converged but has not). Stochastic gradient descent helps mitigate these problems.[1] At each iteration, we use a different random subset of the data (a batch) to compute the gradient. This adds noise to the process and helps prevent the algorithm from getting trapped in a sub-optimal region of parameter space. Each iteration is also computationally cheaper since it only uses a subset of the data. We saw that adding a momentum term makes convergence more efficient. Finally, we introduced the Adam algorithm.

The ideas in this chapter apply to optimizing *any* model. The next chapter tackles two aspects of training specific to neural networks. First, we address how to compute the gradients of the loss with respect to the parameters of a neural network. This is accomplished using the famous backpropagation algorithm. Second, we discuss how to initialize the network parameters before optimization begins. Without careful initialization, the gradients used by the optimization can become extremely large or extremely small, which can hinder the training process.

Notes

Optimization algorithms: Optimization algorithms are used extensively throughout engineering, and it is generally more typical to use the term *objective function* rather than loss function or cost function. Gradient descent was invented by Cauchy (1847), and stochastic gradient descent dates back to at least Robbins & Monro (1951). A modern compromise between the two is stochastic variance-reduced descent (Johnson & Zhang, 2013), in which the full gradient is computed periodically, with stochastic updates interspersed. Reviews of optimization algorithms for neural networks can be found in Ruder (2016), Bottou et al. (2018), and Sun (2020). Bottou (2012) discusses best practice for SGD, including shuffling without replacement.

[1] Chapter 20 discusses the extent to which saddle points and local minima really *are* problems for typical deep learning problems. In practice, deep networks are surprisingly easy to train.

Convexity, minima, and saddle points: A function is convex if no chord (line segment between two points on the surface) intersects the function. This can be tested algebraically by considering the *Hessian matrix* (the matrix of second derivatives):

$$\mathbf{H}[\boldsymbol{\phi}] = \begin{bmatrix} \frac{\partial^2 L}{\partial \phi_0^2} & \frac{\partial^2 L}{\partial \phi_0 \partial \phi_1} & \cdots & \frac{\partial^2 L}{\partial \phi_0 \partial \phi_N} \\ \frac{\partial^2 L}{\partial \phi_1 \partial \phi_0} & \frac{\partial^2 L}{\partial \phi_1^2} & \cdots & \frac{\partial^2 L}{\partial \phi_1 \partial \phi_N} \\ \vdots & \vdots & \ddots & \vdots \\ \frac{\partial^2 L}{\partial \phi_N \partial \phi_0} & \frac{\partial^2 L}{\partial \phi_N \partial \phi_1} & \cdots & \frac{\partial^2 L}{\partial \phi_N^2} \end{bmatrix}. \tag{6.19}$$

Appendix C.5.4 Eigenvalues

If the Hessian matrix is positive definite (has positive eigenvalues) for all possible parameter values, then the function is convex; the loss function will look like a smooth bowl (as in figure 6.1c), so training will be relatively easy. There will be a single global minimum and no local minima or saddle points.

For any loss function, the eigenvalues of the Hessian matrix at places where the gradient is zero allow us to classify this position as (i) a minimum (the eigenvalues are all positive), (ii) a maximum (the eigenvalues are all negative), or (iii) a saddle point (positive eigenvalues are associated with directions in which we are at a minimum and negative ones with directions where we are at a maximum).

Line search: Gradient descent with a fixed step size is inefficient because the distance moved depends entirely on the magnitude of the gradient. It moves a long distance when the function is changing fast (where perhaps it should be more cautious) but a short distance when the function is changing slowly (where perhaps it should explore further). For this reason, gradient descent methods are usually combined with a line search procedure in which we sample the function along the desired direction to try to find the optimal step size. One such approach is bracketing (figure 6.10). Another problem with gradient descent is that it tends to lead to inefficient oscillatory behavior when descending valleys (e.g., path 1 in figure 6.5a).

Beyond gradient descent: Numerous algorithms have been developed that remedy the problems of gradient descent. Most notable is the Newton method, which takes the curvature of the surface into account using the inverse of the Hessian matrix; if the gradient of the function is changing quickly, then it applies a more cautious update. This method eliminates the need for line search and does not suffer from oscillatory behavior. However, it has its own problems; in its simplest form, it moves toward the nearest extremum, but this may be a maximum if we are closer to the top of a hill than we are to the bottom of a valley. Moreover, computing the inverse Hessian is intractable when the number of parameters is large, as in neural networks.

Problem 6.11

Properties of SGD: The limit of SGD as the learning rate tends to zero is a stochastic differential equation. Jastrzębski et al. (2018) showed that this equation relies on the learning-rate to batch size ratio and that there there is a relation between the learning rate to batch size ratio and the width of the minimum found. Wider minima are considered more desirable; if the loss function for test data is similar, then small errors in the parameter estimates will have little effect on test performance. He et al. (2019) prove a generalization bound for SGD that has a positive correlation with the ratio of batch size to learning rate. They train a large number of models on different architectures and datasets and find empirical evidence that test accuracy improves when the ratio of batch size to learning rate is low.

Momentum: The idea of using momentum to speed up optimization dates to Polyak (1964). Goh (2017) presents an in-depth discussion of the properties of momentum. The Nesterov accelerated gradient method was introduced by Nesterov (1983). Nesterov momentum was first applied in the context of stochastic gradient descent by Sutskever et al. (2013).

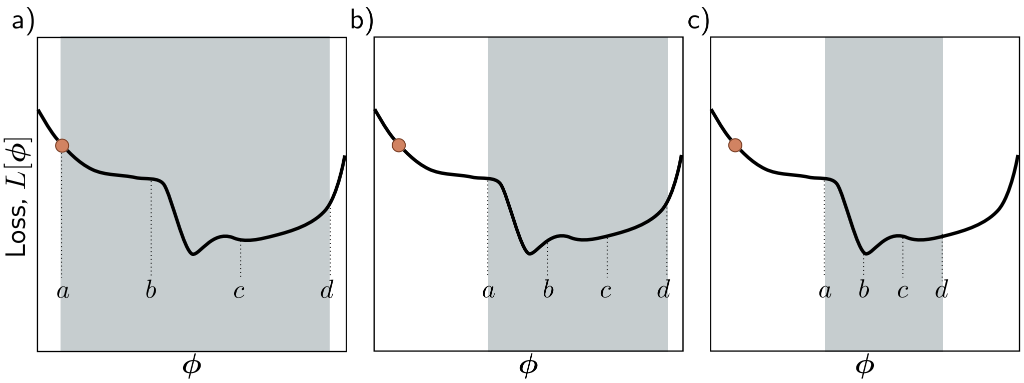

Figure 6.10 Line search using the bracketing approach. a) The current solution is at position a (orange point), and we wish to search the region $[a, d]$ (gray shaded area). We define two points b, c interior to the search region and evaluate the loss function at these points. Here $L[b] > L[c]$, and so we eliminate the range $[a, b]$. b) We now repeat this procedure in the refined search region and find that $L[b] < L[c]$, and so we eliminate the range $[c, d]$. c) We repeat this process until this minimum is closely bracketed.

Adaptive training algorithms: AdaGrad (Duchi et al., 2011) is an optimization algorithm that addresses the possibility that some parameters may have to move further than others by assigning a different learning rate to each parameter. AdaGrad uses the cumulative squared gradient for each parameter to attenuate its learning rate. This has the disadvantage that the learning rates decrease over time, and learning can halt before the minimum is found. RMSProp (Hinton et al., 2012a) and AdaDelta (Zeiler, 2012) modified this algorithm to help prevent these problems by recursively updating the squared gradient term.

By far the most widely used adaptive training algorithm is adaptive moment optimization or Adam (Kingma & Ba, 2015). This combines the ideas of momentum (in which the gradient vector is averaged over time) and AdaGrad, AdaDelta, and RMSProp (in which a smoothed squared gradient term is used to modify the learning rate for each parameter). The original paper on the Adam algorithm provided a convergence proof for convex loss functions, but a counterexample was identified by Reddi et al. (2018), who developed a modification of Adam called AMSGrad, which does converge. Of course, in deep learning, the loss functions are non-convex, and Zaheer et al. (2018) subsequently developed an adaptive algorithm called YOGI and proved that it converges in this scenario. Regardless of these theoretical objections, the original Adam algorithm works well in practice and is widely used, not least because it works well over a broad range of hyperparameters and makes rapid initial progress.

One potential problem with adaptive training algorithms is that the learning rates are based on accumulated statistics of the observed gradients. At the start of training, when there are few samples, these statistics may be very noisy. This can be remedied by *learning rate warm-up* (Goyal et al., 2018), in which the learning rates are gradually increased over the first few thousand iterations. An alternative solution is rectified Adam (Liu et al., 2021a), which gradually changes the momentum term over time in a way that helps avoid high variance. Dozat (2016) incorporated Nesterov momentum into the Adam algorithm.

SGD vs. Adam: There has been a lively discussion about the relative merits of SGD and Adam. Wilson et al. (2017) provided evidence that SGD with momentum can find lower minima than Adam, which generalize better over a variety of deep learning tasks. However, this is strange since SGD is a special case of Adam (when $\epsilon = \gamma = 0$) once the modification term (equation 6.16) becomes one, which happens quickly. It is hence more likely that SGD outperforms Adam *when we use Adam's default hyperparameters*. Loshchilov & Hutter (2019) proposed AdamW, which substantially improves the performance of Adam in the presence of L2 regularization (see section 9.1). Choi et al. (2019) provide evidence that if we search for the best Adam hyperparameters, it performs just as well as SGD and converges faster. Keskar & Socher (2017) proposed a method called SWATS that starts using Adam (to make rapid initial progress) and then switches to SGD (to get better final generalization performance).

Exhaustive search: All the algorithms discussed in this chapter are iterative. A completely different approach is to quantize the network parameters and exhaustively search the resulting discretized parameter space using SAT solvers (Mézard & Mora, 2009). This approach has the potential to find the global minimum and provide a guarantee that there is no lower loss elsewhere but is only practical for very small models.

Problems

Problem 6.1 Show that the derivatives of the least squares loss function in equation 6.5 are given by the expressions in equation 6.7.

Problem 6.2 A surface is convex if the eigenvalues of the Hessian $\mathbf{H}[\boldsymbol{\phi}]$ are positive everywhere. In this case, the surface has a unique minimum, and optimization is easy. Find an algebraic expression for the Hessian matrix,

$$\mathbf{H}[\boldsymbol{\phi}] = \begin{bmatrix} \frac{\partial^2 L}{\partial \phi_0^2} & \frac{\partial^2 L}{\partial \phi_0 \partial \phi_1} \\ \frac{\partial^2 L}{\partial \phi_1 \partial \phi_0} & \frac{\partial^2 L}{\partial \phi_1^2} \end{bmatrix}, \tag{6.20}$$

Appendix C.5.4 Eigenvalues
Appendix C.5.5 Trace
Appendix C.5.5 Determinant

for the linear regression model (equation 6.5). Prove that this function is convex by showing that the eigenvalues are always positive. This can be done by showing that both the trace and the determinant of the matrix are positive.

Problem 6.3 Compute the derivatives of the least squares loss $L[\boldsymbol{\phi}]$ with respect to the parameters, ϕ_0 and ϕ_1 for the Gabor model (equation 6.8).

Problem 6.4 Which of the functions in figure 6.11 is convex? Justify your answer. Characterize each of the points 1–7 as (i) a local minimum, (ii) the global minimum, or (iii) neither.

Problem 6.5* The logistic regression model uses a linear function to assign an input $\mathbf{x}$ to one of two classes $y \in \{0, 1\}$. For a 1D input and a 1D output, it has two parameters, ϕ_0 and ϕ_1, and is defined by:

$$Pr(y = 1|x) = \text{sig}[\phi_0 + \phi_1 x], \tag{6.21}$$

where sig[•] is the logistic sigmoid function:

$$\text{sig}[z] = \frac{1}{1 + \exp[-z]}. \tag{6.22}$$

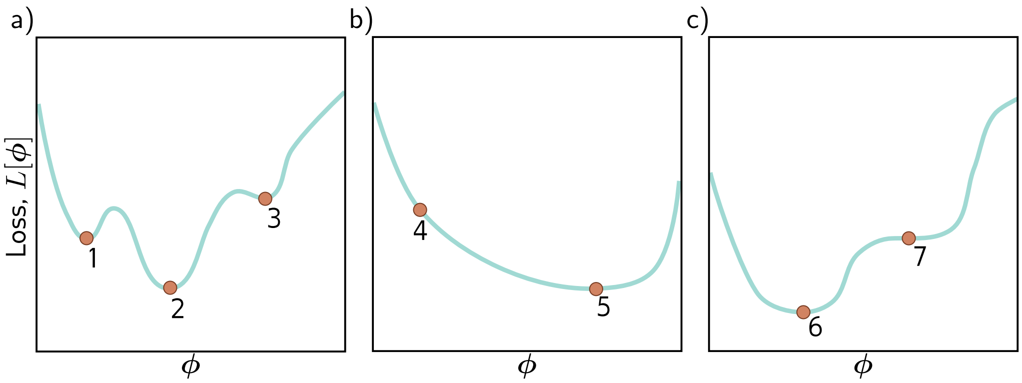

Figure 6.11 Three 1D loss functions for problem 6.4.

(i) Plot y against x for this model for different values of ϕ_0 and ϕ_1 and explain the qualitative meaning of each parameter. (ii) What is a suitable loss function for this model? (iii) Compute the derivatives of this loss function with respect to the parameters. (iv) Generate ten data points from a normal distribution with mean -1 and standard deviation 1 and assign them the label $y = 0$. Generate another ten data points from a normal distribution with mean 1 and standard deviation 1 and assign these the label $y = 1$. Plot the loss as a heatmap in terms of the two parameters ϕ_0 and ϕ_1. (v) Is this loss function convex? How could you prove this?

Problem 6.6* Compute the derivatives of the least squares loss with respect to the ten parameters of the simple neural network model introduced in equation 3.1:

$$\mathrm{f}[x, \boldsymbol{\phi}] = \phi_0 + \phi_1 \mathrm{a}[\theta_{10} + \theta_{11} x] + \phi_2 \mathrm{a}[\theta_{20} + \theta_{21} x] + \phi_3 \mathrm{a}[\theta_{30} + \theta_{31} x]. \tag{6.23}$$

Think carefully about what the derivative of the ReLU function $a[\bullet]$ will be.

Problem 6.7* The gradient descent trajectory for path 1 in figure 6.5a oscillates back and forth inefficiently as it moves down the valley toward the minimum. It's also notable that it turns at right angles to the previous direction at each step. Provide a qualitative explanation for these phenomena. Propose a solution that might help prevent this behavior.

Problem 6.8* Can (non-stochastic) gradient descent with a *fixed* learning rate escape local minima?

Problem 6.9 We run the stochastic gradient descent algorithm for 1,000 iterations on a dataset of size 100 with a batch size of 20. For how many epochs did we train the model?

Problem 6.10 Show that the momentum term $\mathbf{m}_t$ (equation 6.11) is an infinite weighted sum of the gradients at the previous iterations and derive an expression for the coefficients (weights) of that sum.

Problem 6.11 What dimensions will the Hessian have if the model has one million parameters?

Chapter 7

Gradients and initialization

Chapter 6 introduced iterative optimization algorithms. These are general-purpose methods for finding the minimum of a function. In the context of neural networks, they find parameters that minimize the loss so that the model accurately predicts the training outputs from the inputs. The basic approach is to choose initial parameters randomly and then make a series of small changes that decrease the loss on average. Each change is based on the gradient of the loss with respect to the parameters at the current position.

This chapter discusses two issues that are specific to neural networks. First, we consider how to calculate the gradients efficiently. This is a serious challenge since the largest models at the time of writing have $\sim 10^{12}$ parameters, and the gradient needs to be computed for every parameter at every iteration of the training algorithm. Second, we consider how to initialize the parameters. If this is not done carefully, the initial losses and their gradients can be extremely large or small. In either case, this impedes the training process.

7.1 Problem definitions

Consider a network $\mathbf{f}[\mathbf{x}, \boldsymbol{\phi}]$ with multivariate input $\mathbf{x}$, parameters $\boldsymbol{\phi}$, and three hidden layers $\mathbf{h}_1, \mathbf{h}_2$, and $\mathbf{h}_3$:

$$
\begin{aligned}
\mathbf{h}_1 &= \mathbf{a}[\boldsymbol{\beta}_0 + \boldsymbol{\Omega}_0 \mathbf{x}] \\
\mathbf{h}_2 &= \mathbf{a}[\boldsymbol{\beta}_1 + \boldsymbol{\Omega}_1 \mathbf{h}_1] \\
\mathbf{h}_3 &= \mathbf{a}[\boldsymbol{\beta}_2 + \boldsymbol{\Omega}_2 \mathbf{h}_2] \\
\mathbf{f}[\mathbf{x}, \boldsymbol{\phi}] &= \boldsymbol{\beta}_3 + \boldsymbol{\Omega}_3 \mathbf{h}_3,
\end{aligned}
\tag{7.1}
$$

where the function $\mathbf{a}[\bullet]$ applies the activation function separately to every element of the input. The model parameters $\boldsymbol{\phi} = \{\boldsymbol{\beta}_0, \boldsymbol{\Omega}_0, \boldsymbol{\beta}_1, \boldsymbol{\Omega}_1, \boldsymbol{\beta}_2, \boldsymbol{\Omega}_2, \boldsymbol{\beta}_3, \boldsymbol{\Omega}_3\}$ consist of the bias vectors $\boldsymbol{\beta}_k$ and weight matrices $\boldsymbol{\Omega}_k$ for each of the K layers (figure 7.1).

We also have individual loss terms ℓ_i, which return the negative log-likelihood of the ground truth label y_i given the model prediction $\mathbf{f}[\mathbf{x}_i, \boldsymbol{\phi}]$ for training input $\mathbf{x}_i$. For example, this might be the least squares loss $\ell_i = (\mathrm{f}[\mathbf{x}_i, \boldsymbol{\phi}] - y_i)^2$. The total loss is the sum of these terms over the training data:

$$L[\boldsymbol{\phi}] = \sum_{i=1}^{I} \ell_i. \tag{7.2}$$

The most commonly used optimization algorithm for training neural networks is stochastic gradient descent (SGD), which updates the parameters as:

$$\boldsymbol{\phi}_{t+1} \longleftarrow \boldsymbol{\phi}_t - \alpha \sum_{i \in \mathcal{B}_t} \frac{\partial \ell_i[\boldsymbol{\phi}_t]}{\partial \boldsymbol{\phi}}, \tag{7.3}$$

where α is the learning rate and $\mathcal{B}_t$ contains the batch indices at iteration t. To compute this update, we need to calculate the derivatives:

$$\frac{\partial \ell_i}{\partial \boldsymbol{\beta}_k} \qquad \text{and} \qquad \frac{\partial \ell_i}{\partial \boldsymbol{\Omega}_k}, \tag{7.4}$$

for the parameters $\{\boldsymbol{\beta}_k, \boldsymbol{\Omega}_k\}$ at every layer $k \in \{0, 1, \ldots, K\}$ and for each index i in the batch. The first part of this chapter describes the *backpropagation algorithm*, which computes these derivatives efficiently. Problem 7.2

In the second part of the chapter, we consider how to initialize the network parameters before we commence training. We describe methods to choose the initial weights $\boldsymbol{\Omega}_k$ and biases $\boldsymbol{\beta}_k$ so that training is stable.

7.2 Computing derivatives

The derivatives of the loss tell us how the loss changes when we make a small change to the parameters. Optimization algorithms exploit this information to manipulate the parameters so that the loss becomes smaller. The *backpropagation algorithm* computes these derivatives. The mathematical details are somewhat involved, so we first make two observations that provide some intuition.

Observation 1: Each weight (element of $\boldsymbol{\Omega}_k$) multiplies the activation at a source hidden unit and adds the result to a destination hidden unit in the next layer. It follows that the effect of any small change to the weight is amplified or attenuated by the activation at the source hidden unit. Hence, we run the network for each data example in the batch and store the activations of all the hidden units. This is known as the *forward pass* (figure 7.1). The stored activations will subsequently be used to compute the gradients.

Observation 2: A small change in a bias or weight causes a ripple effect of changes through the subsequent network. The change modifies the value of its destination hidden

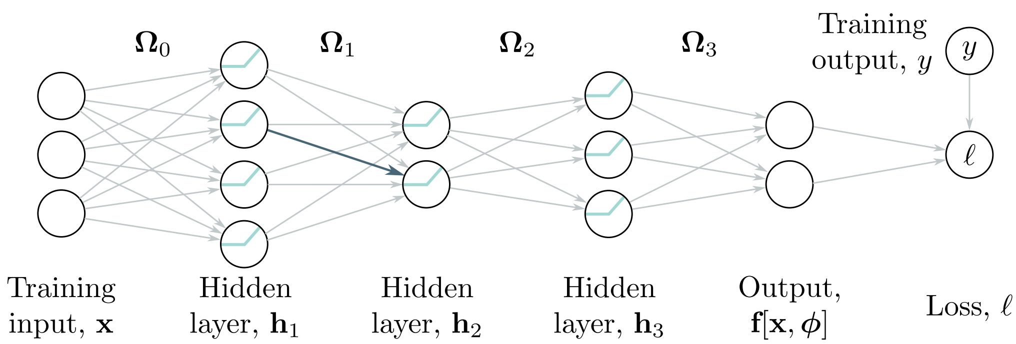

Figure 7.1 Backpropagation forward pass. The goal is to compute the derivatives of the loss ℓ with respect to each of the weights (arrows) and biases (not shown). In other words, we want to know how a small change to each parameter will affect the loss. Each weight multiplies the hidden unit at its source and contributes the result to the hidden unit at its destination. Consequently, the effects of any small change to the weight will be scaled by the activation of the source hidden unit. For example, the blue weight is applied to the second hidden unit at layer 1; if the activation of this unit doubles, then the effect of a small change to the blue weight will double too. Hence, to compute the derivatives of the weights, we need to calculate and store the activations at the hidden layers. This is known as the *forward pass* since it involves running the network equations sequentially.

unit. This, in turn, changes the values of the hidden units in the subsequent layer, which will change the hidden units in the layer after that, and so on, until a change is made to the model output and, finally, the loss.

Hence, to know how changing a parameter modifies the loss, we also need to know how changes to every subsequent hidden layer will, in turn, modify their successor. These same quantities are required when considering other parameters in the same or earlier layers. It follows that we can calculate them once and reuse them. For example, consider computing the effect of a small change in weights that feed into hidden layers $\mathbf{h}_3$, $\mathbf{h}_2$, and $\mathbf{h}_1$, respectively:

- To calculate how a small change in a weight or bias feeding into hidden layer $\mathbf{h}_3$ modifies the loss, we need to know (i) how a change in layer $\mathbf{h}_3$ changes the model output $\mathbf{f}$, and (ii) how a change in this output changes the loss ℓ (figure 7.2a).

- To calculate how a small change in a weight or bias feeding into hidden layer $\mathbf{h}_2$ modifies the loss, we need to know (i) how a change in layer $\mathbf{h}_2$ affects $\mathbf{h}_3$, (ii) how $\mathbf{h}_3$ changes the model output, and (iii) how this output changes the loss (figure 7.2b).

- To calculate how a small change in a weight or bias feeding into hidden layer $\mathbf{h}_1$ modifies the loss, we need to know (i) how a change in layer $\mathbf{h}_1$ affects layer $\mathbf{h}_2$, (ii) how a change in layer $\mathbf{h}_2$ affects layer $\mathbf{h}_3$, (iii) how layer $\mathbf{h}_3$ changes the model output, and (iv) how the model output changes the loss (figure 7.2c).

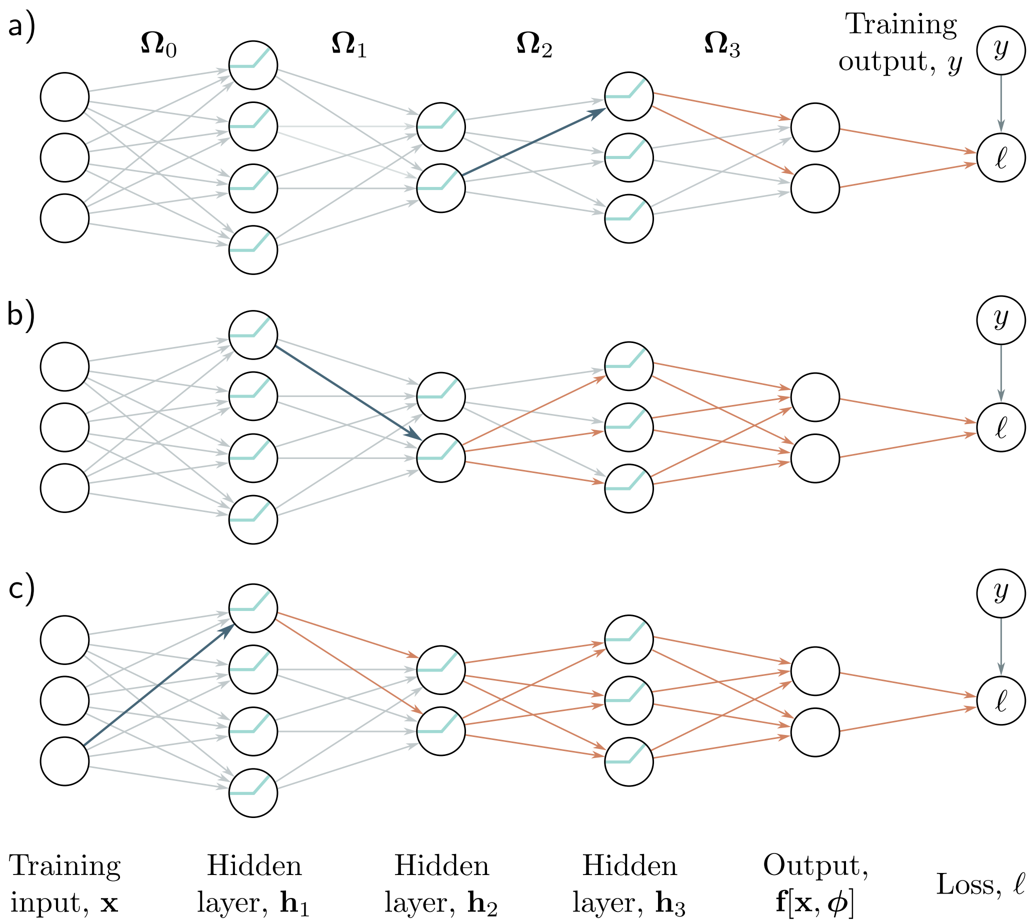

Figure 7.2 Backpropagation backward pass. a) To compute how a change to a weight feeding into layer $\mathbf{h}_3$ (blue arrow) changes the loss, we need to know how the hidden unit in $\mathbf{h}_3$ changes the model output $\mathbf{f}$ and how $\mathbf{f}$ changes the loss (orange arrows). b) To compute how a small change to a weight feeding into $\mathbf{h}_2$ (blue arrow) changes the loss, we need to know (i) how the hidden unit in $\mathbf{h}_2$ changes $\mathbf{h}_3$, (ii) how $\mathbf{h}_3$ changes $\mathbf{f}$, and (iii) how $\mathbf{f}$ changes the loss (orange arrows). c) Similarly, to compute how a small change to a weight feeding into $\mathbf{h}_1$ (blue arrow) changes the loss, we need to know how $\mathbf{h}_1$ changes $\mathbf{h}_2$ and how these changes propagate through to the loss (orange arrows). The backward pass first computes derivatives at the end of the network and then works backward to exploit the inherent redundancy of these computations.

As we move backward through the network, we see that most of the terms we need were already calculated in the previous step, so we do not need to re-compute them. Proceeding backward through the network in this way to compute the derivatives is known as the *backward pass*.

The ideas behind backpropagation are relatively easy to understand. However, the derivation requires matrix calculus because the bias and weight terms are vectors and matrices, respectively. To help grasp the underlying mechanics, the following section derives backpropagation for a simpler toy model with scalar parameters. We then apply the same approach to a deep neural network in section 7.4.

7.3 Toy example

Consider a model $\mathrm{f}[x,\boldsymbol{\phi}]$ eight scalar parameters $\boldsymbol{\phi}=\{\beta_0,\omega_0,\beta_1,\omega_1,\beta_2,\omega_2,\beta_3,\omega_3\}$ that consists of a composition of the functions $\sin[\bullet], \exp[\bullet]$, and $\cos[\bullet]$:

$$\mathrm{f}[x,\boldsymbol{\phi}]=\beta_3+\omega_3\cdot\cos\Bigl[\beta_2+\omega_2\cdot\exp\bigl[\beta_1+\omega_1\cdot\sin[\beta_0+\omega_0 x]\bigr]\Bigr], \tag{7.5}$$

and a least squares loss function $\mathrm{L}[\boldsymbol{\phi}]=\sum_i \ell_i$ with individual terms:

$$\ell_i=(\mathrm{f}[x_i,\boldsymbol{\phi}]-y_i)^2, \tag{7.6}$$

where, as usual, x_i is the i^{th} training input and y_i is the i^{th} training output. You can think of this as a simple neural network with one input, one output, one hidden unit at each layer, and different activation functions $\sin[\bullet], \exp[\bullet]$, and $\cos[\bullet]$ between each layer.

We aim to compute the derivatives:

$$\frac{\partial \ell_i}{\partial \beta_0},\quad \frac{\partial \ell_i}{\partial \omega_0},\quad \frac{\partial \ell_i}{\partial \beta_1},\quad \frac{\partial \ell_i}{\partial \omega_1},\quad \frac{\partial \ell_i}{\partial \beta_2},\quad \frac{\partial \ell_i}{\partial \omega_2},\quad \frac{\partial \ell_i}{\partial \beta_3},\quad \text{and}\quad \frac{\partial y}{\partial \omega_3}.$$

Of course, We could find expressions for these derivatives by hand and compute them directly. However, some of these expressions are quite complex. For example:

$$\begin{aligned}\frac{\partial \ell_i}{\partial \omega_0} \;=\;& -2\Bigl(\beta_3+\omega_3\cdot\cos\Bigl[\beta_2+\omega_2\cdot\exp\bigl[\beta_1+\omega_1\cdot\sin[\beta_0+\omega_0 x]\bigr]\Bigr]-y_i\Bigr)\\ &\cdot\omega_1\omega_2\omega_3\cdot x_i\cdot\cos[\beta_0+\omega_0\cdot x]\cdot\exp\Bigl[\beta_1+\omega_1\cdot\sin[\beta_0+\omega_0\cdot x_i]\Bigr]\\ &\cdot\sin\Bigl[\beta_2+\omega_2\cdot\exp\Bigl[\beta_1+\omega_1\cdot\sin[\beta_0+\omega_0\cdot x_i]\Bigr]\Bigr].\end{aligned} \tag{7.7}$$

Such expressions are awkward to derive and code without mistakes and do not exploit the inherent redundancy; notice that the three exponential terms are the same.

The backpropagation algorithm is an efficient method for computing all of these derivatives at once. It consists of (i) a forward pass, in which we compute and store a series of intermediate values and the network output, and (ii) a backward pass, in which

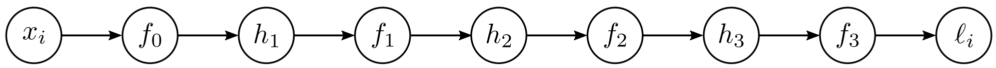

Figure 7.3 Backpropagation forward pass. We compute and store each of the intermediate variables in turn until we finally calculate the loss.

we calculate the derivatives of each parameter, starting at the end of the network, and re-using previous calculations as we move toward the start.

Forward pass: We treat the computation of the loss as a series of calculations:

$$
\begin{aligned}
f_0 &= \beta_0 + \omega_0 \cdot x_i \\
h_1 &= \sin[f_0] \\
f_1 &= \beta_1 + \omega_1 \cdot h_1 \\
h_2 &= \exp[f_1] \\
f_2 &= \beta_2 + \omega_2 \cdot h_2 \\
h_3 &= \cos[f_2] \\
f_3 &= \beta_3 + \omega_3 \cdot h_3 \\
\ell_i &= (f_3 - y_i)^2.
\end{aligned}
\tag{7.8}
$$

We compute and store the values of the intermediate variables f_k and h_k (figure 7.3).

Backward pass #1: We now compute the derivatives of ℓ_i with respect to these intermediate variables, but in reverse order:

$$
\frac{\partial \ell_i}{\partial f_3}, \quad \frac{\partial \ell_i}{\partial h_3}, \quad \frac{\partial \ell_i}{\partial f_2}, \quad \frac{\partial \ell_i}{\partial h_2}, \quad \frac{\partial \ell_i}{\partial f_1}, \quad \frac{\partial \ell_i}{\partial h_1}, \quad \text{and} \quad \frac{\partial \ell_i}{\partial f_0}. \tag{7.9}
$$

The first of these derivatives is straightforward:

$$
\frac{\partial \ell_i}{\partial f_3} = 2(f_3 - y_i). \tag{7.10}
$$

The next derivative can be calculated using the chain rule:

$$
\frac{\partial \ell_i}{\partial h_3} = \frac{\partial \ell_i}{\partial f_3}\frac{\partial f_3}{\partial h_3}. \tag{7.11}
$$

The left-hand side asks how ℓ_i changes when h_3 changes. The right-hand side says we can decompose this into (i) how ℓ_i changes when f_3 changes and how f_3 changes when h_3 changes. In the original equations, h_3 changes f_3, which changes ℓ_i, and the derivatives

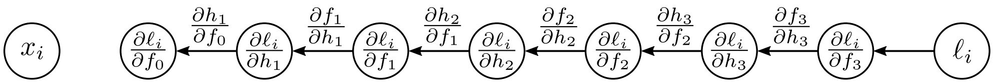

Figure 7.4 Backpropagation backward pass #1. We work backwards from the end of the function computing the derivatives $\partial \ell_i/\partial f_\bullet$ and $\partial \ell_i/\partial h_\bullet$ of the loss with respect to the intermediate quantities. Each derivative is computed from the previous one by multiplying by terms of the form $\partial f_k/\partial h_k$ or $\partial h_k/\partial f_{k-1}$.

represent the effects of this chain. Notice that we already computed the first of these derivatives, and the other is the derivative of $\beta_3 + \omega_3 \cdot h_3$ with respect to h_3, which is ω_3.

We continue in this way, computing the derivatives of the output with respect to these intermediate quantities (figure 7.4):

$$
\begin{aligned}
\frac{\partial \ell_i}{\partial f_2} &= \left(\frac{\partial \ell_i}{\partial f_3}\frac{\partial f_3}{\partial h_3}\right)\frac{\partial h_3}{\partial f_2} \\
\frac{\partial \ell_i}{\partial h_2} &= \left(\frac{\partial \ell_i}{\partial f_3}\frac{\partial f_3}{\partial h_3}\frac{\partial h_3}{\partial f_2}\right)\frac{\partial f_2}{\partial h_2} \\
\frac{\partial \ell_i}{\partial f_1} &= \left(\frac{\partial \ell_i}{\partial f_3}\frac{\partial f_3}{\partial h_3}\frac{\partial h_3}{\partial f_2}\frac{\partial f_2}{\partial h_2}\right)\frac{\partial h_2}{\partial f_1} \\
\frac{\partial \ell_i}{\partial h_1} &= \left(\frac{\partial \ell_i}{\partial f_3}\frac{\partial f_3}{\partial h_3}\frac{\partial h_3}{\partial f_2}\frac{\partial f_2}{\partial h_2}\frac{\partial h_2}{\partial f_1}\right)\frac{\partial f_1}{\partial h_1} \\
\frac{\partial \ell_i}{\partial f_0} &= \left(\frac{\partial \ell_i}{\partial f_3}\frac{\partial f_3}{\partial h_3}\frac{\partial h_3}{\partial f_2}\frac{\partial f_2}{\partial h_2}\frac{\partial h_2}{\partial f_1}\frac{\partial f_1}{\partial h_1}\right)\frac{\partial h_1}{\partial f_0}.
\end{aligned} \tag{7.12}
$$

Problem 7.1

In each case, we have already computed the quantities in the brackets in the previous step, and the last term has a simple expression. These equations embody Observation 2 from the previous section (figure 7.2); we can reuse the previously computed derivatives if we calculate them in reverse order.

Backward pass #2: Finally, we consider how the loss ℓ_i changes when we change the parameters $\beta_\bullet$ and $\omega_\bullet$. Once more, we apply the chain rule (figure 7.5):

$$
\begin{aligned}
\frac{\partial \ell_i}{\partial \beta_k} &= \frac{\partial \ell_i}{\partial f_k}\frac{\partial f_k}{\partial \beta_k} \\
\frac{\partial \ell_i}{\partial \omega_k} &= \frac{\partial \ell_i}{\partial f_k}\frac{\partial f_k}{\partial \omega_k}.
\end{aligned} \tag{7.13}
$$

In each case, the first term on the right-hand side was computed in equation 7.12. When $k > 0$, we have $f_k = \beta_k + \omega_k \cdot h_k$, so:

$$
\frac{\partial f_k}{\partial \beta_k} = 1 \qquad \text{and} \qquad \frac{\partial f_k}{\partial \omega_k} = h_k. \tag{7.14}
$$

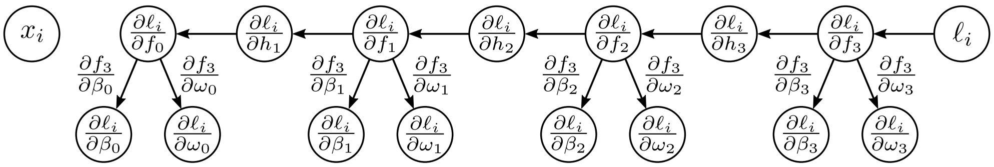

Figure 7.5 Backpropagation backward pass #2. Finally, we compute the derivatives $\partial \ell_i / \partial \beta_\bullet$ and $\partial \ell_i / \partial \omega_\bullet$. Each derivative is computed by multiplying the term $\partial \ell_i / \partial f_k$ by $\partial f_k / \partial \beta_k$ or $\partial f_k / \partial \omega_k$ as appropriate.

This is consistent with Observation 1 from the previous section; the effect of a change in the weight ω_k is proportional to the value of the source variable h_k (which was stored in the forward pass). The final derivatives from the term $f_0 = \beta_0 + \omega \cdot x_i$ are:

Notebook 7.1 Backpropagation in toy model

$$\frac{\partial f_0}{\partial \beta_0} = 1 \qquad \text{and} \qquad \frac{\partial f_0}{\partial \omega_0} \quad = \quad x_i. \tag{7.15}$$

Backpropagation is both simpler and more efficient than computing the derivatives individually, as in equation 7.7.

7.4 Backpropagation algorithm

Now we repeat this process for a three-layer network (figure 7.1). The intuition and much of the algebra are identical. The main differences are that intermediate variables $\mathbf{f}_k, \mathbf{h}_k$ are vectors, the biases β_k are vectors, the weights $\boldsymbol{\Omega}_k$ are matrices, and we are using ReLU functions rather than simple algebraic functions like $\cos[\bullet]$.

Forward pass: We write the network as a series of sequential calculations:

$$\begin{aligned}
\mathbf{f}_0 &= \boldsymbol{\beta}_0 + \boldsymbol{\Omega}_0 \mathbf{x}_i \\
\mathbf{h}_1 &= \mathbf{a}[\mathbf{f}_0] \\
\mathbf{f}_1 &= \boldsymbol{\beta}_1 + \boldsymbol{\Omega}_1 \mathbf{h}_1 \\
\mathbf{h}_2 &= \mathbf{a}[\mathbf{f}_1] \\
\mathbf{f}_2 &= \boldsymbol{\beta}_2 + \boldsymbol{\Omega}_2 \mathbf{h}_2 \\
\mathbf{h}_3 &= \mathbf{a}[\mathbf{f}_2] \\
\mathbf{f}_3 &= \boldsymbol{\beta}_3 + \boldsymbol{\Omega}_3 \mathbf{h}_3 \\
\ell_i &= \mathrm{l}[\mathbf{f}_3, y_i],
\end{aligned} \tag{7.16}$$

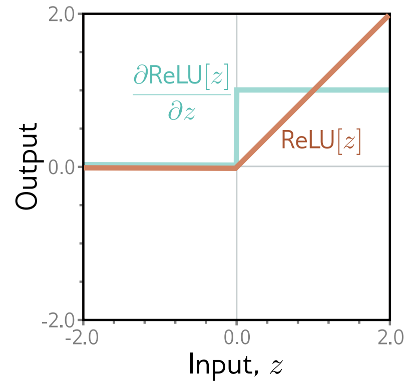

Figure 7.6 Derivative of rectified linear unit. The rectified linear unit (orange curve) returns zero when the input is less than zero and returns the input otherwise. Its derivative (cyan curve) returns zero when the input is less than zero (since the slope here is zero) and one when the input is greater than zero (since the slope here is one).

where $\mathbf{f}_{k-1}$ represents the pre-activations at the k^{th} hidden layer (i.e., the values before the ReLU function $\mathbf{a}[\bullet]$) and $\mathbf{h}_k$ contains the activations at the k^{th} hidden layer (i.e., after the ReLU function). The term $\mathrm{l}[\mathbf{f}_3, y_i]$ represents the loss function (e.g., least squares or binary cross-entropy loss). In the forward pass, we work through these calculations and store all the intermediate quantities.

Appendix C.6 Matrix calculus

Backward pass #1: Now let's consider how the loss changes when we modify the pre-activations $\mathbf{f}_0, \mathbf{f}_1, \mathbf{f}_2$. Applying the chain rule, the expression for the derivative of the loss ℓ_i with respect to $\mathbf{f}_2$ is:

$$\frac{\partial \ell_i}{\partial \mathbf{f}_2} = \frac{\partial \mathbf{h}_3}{\partial \mathbf{f}_2}\frac{\partial \mathbf{f}_3}{\partial \mathbf{h}_3}\frac{\partial \ell_i}{\partial \mathbf{f}_3}. \tag{7.17}$$

The three terms on the right-hand side have sizes $D_3 \times D_3, D_3 \times D_f$, and $D_f \times 1$, respectively, where D_3 is the number of hidden units in the third layer and D_f is the dimensionality of the model output $\mathbf{f}_3$.

Similarly, we can compute how the loss changes when we change $\mathbf{f}_1$ and $\mathbf{f}_0$:

$$\begin{aligned}\frac{\partial \ell_i}{\partial \mathbf{f}_1} &= \frac{\partial \mathbf{h}_2}{\partial \mathbf{f}_1}\frac{\partial \mathbf{f}_2}{\partial \mathbf{h}_2}\left(\frac{\partial \mathbf{h}_3}{\partial \mathbf{f}_2}\frac{\partial \mathbf{f}_3}{\partial \mathbf{h}_3}\frac{\partial \ell_i}{\partial \mathbf{f}_3}\right)\\ \frac{\partial \ell_i}{\partial \mathbf{f}_0} &= \frac{\partial \mathbf{h}_1}{\partial \mathbf{f}_0}\frac{\partial \mathbf{f}_1}{\partial \mathbf{h}_1}\left(\frac{\partial \mathbf{h}_2}{\partial \mathbf{f}_1}\frac{\partial \mathbf{f}_2}{\partial \mathbf{h}_2}\frac{\partial \mathbf{h}_3}{\partial \mathbf{f}_2}\frac{\partial \mathbf{f}_3}{\partial \mathbf{h}_3}\frac{\partial \ell_i}{\partial \mathbf{f}_3}\right).\end{aligned} \tag{7.18}$$

Problem 7.3

Note that in each case, the term in brackets was computed in the previous step. By working backward through the network, we can reuse the previous computations.

Problems 7.4–7.5

Moreover, the terms themselves are simple. Working backward through the right-hand side of equation 7.17, we have:

- The derivative $\partial \ell_i / \partial \mathbf{f}_3$ of the loss ℓ_i with respect to the network output $\mathbf{f}_3$ will depend on the loss function but usually has a simple form.

Problem 7.6

- The derivative $\partial \mathbf{f}_3 / \partial \mathbf{h}_3$ of the network output with respect to hidden layer $\mathbf{h}_3$ is:

$$\frac{\partial \mathbf{f}_3}{\partial \mathbf{h}_3} = \frac{\partial}{\partial \mathbf{h}_3}\left(\boldsymbol{\beta}_3 + \boldsymbol{\Omega}_3\mathbf{h}_3\right) = \boldsymbol{\Omega}_3^T. \tag{7.19}$$

If you are unfamiliar with matrix calculus, this result is not obvious. It is explored in problem 7.6.

- The derivative $\partial\mathbf{h}_3/\partial\mathbf{f}_2$ of the output $\mathbf{h}_3$ of the activation function with respect to its input $\mathbf{f}_2$ will depend on the activation function. It will be a diagonal matrix since each activation only depends on the corresponding pre-activation. For ReLU functions, the diagonal terms are zero everywhere $\mathbf{f}_2$ is less than zero and one otherwise (figure 7.6). Rather than multiply by this matrix, we extract the diagonal terms as a vector $\mathbb{I}[\mathbf{f}_2 > 0]$ and pointwise multiply, which is more efficient.

Problems 7.7–7.8

The terms on the right-hand side of equations 7.18 and 7.18 have similar forms. As we progress back through the network, we alternately (i) multiply by the transpose of the weight matrices $\boldsymbol{\Omega}_k^T$ and (ii) threshold based on the inputs $\mathbf{f}_{k-1}$ to the hidden layer. These inputs were stored during the forward pass.

Backward pass #2: Now that we know how to compute $\partial\ell_i/\partial\mathbf{f}_k$, we can focus on calculating the derivatives of the loss with respect to the weights and biases. To calculate the derivatives of the loss with respect to the biases $\boldsymbol{\beta}_k$, we again use the chain rule:

$$\begin{aligned}\frac{\partial \ell_i}{\partial \boldsymbol{\beta}_k} &= \frac{\partial \mathbf{f}_k}{\partial \boldsymbol{\beta}_k}\frac{\partial \ell_i}{\partial \mathbf{f}_k}\\ &= \frac{\partial}{\partial \boldsymbol{\beta}_k}\left(\boldsymbol{\beta}_k + \boldsymbol{\Omega}_k\mathbf{h}_k\right)\frac{\partial \ell_i}{\partial \mathbf{f}_k}\\ &= \frac{\partial \ell_i}{\partial \mathbf{f}_k},\end{aligned} \tag{7.20}$$

which we already calculated in equations 7.17 and 7.18.

Similarly, the derivative for the weights vector $\boldsymbol{\Omega}_k$, is given by:

$$\begin{aligned}\frac{\partial \ell_i}{\partial \boldsymbol{\Omega}_k} &= \frac{\partial \mathbf{f}_k}{\partial \boldsymbol{\Omega}_k}\frac{\partial \ell_i}{\partial \mathbf{f}_k}\\ &= \frac{\partial}{\partial \boldsymbol{\Omega}_k}\left(\boldsymbol{\beta}_k + \boldsymbol{\Omega}_k\mathbf{h}_k\right)\frac{\partial \ell_i}{\partial \mathbf{f}_k}\\ &= \frac{\partial \ell_i}{\partial \mathbf{f}_k}\mathbf{h}_k^T.\end{aligned} \tag{7.21}$$

Again, the progression from line two to line three is not obvious and is explored in problem 7.9. However, the result makes sense. The final line is a matrix of the same size as $\boldsymbol{\Omega}_k$. It depends linearly on $\mathbf{h}_k$, which was multiplied by $\boldsymbol{\Omega}_k$ in the original expression. This is also consistent with the initial intuition that the derivative of the weights in $\boldsymbol{\Omega}_k$ will be proportional to the values of the hidden units $\mathbf{h}_k$ that they multiply. Recall that we already computed these during the forward pass.

Problem 7.9

7.4.1 Backpropagation algorithm summary

We now briefly summarize the final backpropagation algorithm. Consider a deep neural network $\mathbf{f}[\mathbf{x}_i, \boldsymbol{\phi}]$ that takes input $\mathbf{x}_i$, has K hidden layers with ReLU activations, and individual loss term $\ell_i = \mathrm{l}[\mathbf{f}[\mathbf{x}_i, \boldsymbol{\phi}], \mathbf{y}_i]$. The goal of backpropagation is to compute the derivatives $\partial \ell_i / \partial \boldsymbol{\beta}_k$ and $\partial \ell_i / \partial \boldsymbol{\Omega}_k$ with respect to the biases $\boldsymbol{\beta}_k$ and weights $\boldsymbol{\Omega}_k$.

Forward pass: We compute and store the following quantities:

$$
\begin{aligned}
\mathbf{f}_0 &= \boldsymbol{\beta}_0 + \boldsymbol{\Omega}_0 \mathbf{x}_i \\
\mathbf{h}_k &= \mathbf{a}[\mathbf{f}_{k-1}] && k \in \{1, 2, \ldots, K\} \\
\mathbf{f}_k &= \boldsymbol{\beta}_k + \boldsymbol{\Omega}_k \mathbf{h}_k. && k \in \{1, 2, \ldots, K\}
\end{aligned}
\tag{7.22}
$$

Backward pass: We start with the derivative $\partial \ell_i / \partial \mathbf{f}_K$ of the loss function ℓ_i with respect to the network output $\mathbf{f}_K$ and work backward through the network:

$$
\begin{aligned}
\frac{\partial \ell_i}{\partial \boldsymbol{\beta}_k} &= \frac{\partial \ell_i}{\partial \mathbf{f}_k} && k \in \{K, K-1, \ldots, 1\} \\
\frac{\partial \ell_i}{\partial \boldsymbol{\Omega}_k} &= \frac{\partial \ell_i}{\partial \mathbf{f}_k} \mathbf{h}_k^T && k \in \{K, K-1, \ldots, 1\} \\
\frac{\partial \ell_i}{\partial \mathbf{f}_{k-1}} &= \mathbb{I}[\mathbf{f}_{k-1} > 0] \odot \left(\boldsymbol{\Omega}_k^T \frac{\partial \ell_i}{\partial \mathbf{f}_k} \right), && k \in \{K, K-1, \ldots, 1\}
\end{aligned}
\tag{7.23}
$$

where $\odot$ denotes pointwise multiplication, and $\mathbb{I}[\mathbf{f}_{k-1} > 0]$ is a vector containing ones where $\mathbf{f}_{k-1}$ is greater than zero and zeros elsewhere. Finally, we compute the derivatives with respect to the first set of biases and weights:

$$
\begin{aligned}
\frac{\partial \ell_i}{\partial \boldsymbol{\beta}_0} &= \frac{\partial \ell_i}{\partial \mathbf{f}_0} \\
\frac{\partial \ell_i}{\partial \boldsymbol{\Omega}_0} &= \frac{\partial \ell_i}{\partial \mathbf{f}_0} \mathbf{x}_i^T.
\end{aligned}
\tag{7.24}
$$

Problem 7.10

We calculate these derivatives for every training example in the batch and sum them together to retrieve the gradient for the SGD update.

Notebook 7.2 Backpropagation

Note that the backpropagation algorithm is extremely efficient; the most demanding computational step in both the forward and backward pass is matrix multiplication (by $\boldsymbol{\Omega}$ and $\boldsymbol{\Omega}^T$, respectively) which only requires additions and multiplications. However, it is not memory efficient; the intermediate values in the forward pass must all be stored, and this can limit the size of the model we can train.

7.4.2 Algorithmic differentiation

Although it's important to understand the backpropagation algorithm, it's unlikely that you will need to code it in practice. Modern deep learning frameworks such as PyTorch and TensorFlow calculate the derivatives automatically, given the model specification. This is known as *algorithmic differentiation*.

Each functional component (linear transform, ReLU activation, loss function) in the framework knows how to compute its own derivative. For example, the PyTorch ReLU function $\mathbf{z}_{out} = \mathbf{relu}[\mathbf{z}_{in}]$ knows how to compute the derivative of its output $\mathbf{z}_{out}$ with respect to its input $\mathbf{z}_{in}$. Similarly, a linear function $\mathbf{z}_{out} = \boldsymbol{\beta} + \boldsymbol{\Omega}\mathbf{z}_{in}$ knows how to compute the derivatives of the output $\mathbf{z}_{out}$ with respect to the input $\mathbf{z}_{in}$ and with respect to the parameters $\boldsymbol{\beta}$ and $\boldsymbol{\Omega}$. The algorithmic differentiation framework also knows the sequence of operations in the network and thus has all the information required to perform the forward and backward passes.

These frameworks exploit the massive parallelism of modern graphics processing units (GPUs). Computations such as matrix multiplication (which features in both the forward and backward pass) are naturally amenable to parallelization. Moreover, it's possible to perform the forward and backward passes for the entire batch in parallel if the model and intermediate results in the forward pass do not exceed the available memory.

Problem 7.11

Since the training algorithm now processes the entire batch in parallel, the input becomes a multi-dimensional *tensor*. In this context, a tensor can be considered the generalization of a matrix to arbitrary dimensions. Hence, a vector is a 1D tensor, a matrix is a 2D tensor, and a 3D tensor is a 3D grid of numbers. Until now, the training data have been 1D, so the input for backpropagation would be a 2D tensor where the first dimension indexes the batch element and the second indexes the data dimension. In subsequent chapters, we will encounter more complex structured input data. For example, in models where the input is an RGB image, the original data examples are 3D (height $\times$ width $\times$ channel). Here, the input to the learning framework would be a 4D tensor, where the extra dimension indexes the batch element.

7.4.3 Extension to arbitrary computational graphs

We have described backpropagation in a deep neural network that is naturally sequential; we calculate the intermediate quantities $\mathbf{f}_0, \mathbf{h}_1, \mathbf{f}_1, \mathbf{h}_2 \ldots, \mathbf{f}_k$ in turn. However, models need not be restricted to sequential computation. Later in this book, we will meet models with branching structures. For example, we might take the values in a hidden layer and process them through two different sub-networks before recombining.

Problems 7.12–7.13

Fortunately, the ideas of backpropagation still hold if the computational graph is acyclic. Modern algorithmic differentiation frameworks such as PyTorch and TensorFlow can handle arbitrary acyclic computational graphs.

7.5 Parameter initialization

The backpropagation algorithm computes the derivatives that are used by training algorithms like stochastic gradient descent. We now address how to initialize the parameters before we start training. To see why this is crucial, consider that during the forward pass, each set of pre-activations $\mathbf{f}_k$ is computed as:

$$\begin{aligned}\mathbf{f}_k &= \boldsymbol{\beta}_k + \boldsymbol{\Omega}_k \mathbf{h}_k \\ &= \boldsymbol{\beta}_k + \boldsymbol{\Omega}_k \mathrm{a}[\mathbf{f}_{k-1}],\end{aligned} \tag{7.25}$$

where $\mathbf{a}[\bullet]$ applies the ReLU functions and $\boldsymbol{\Omega}_k$ and $\boldsymbol{\beta}_k$ are the weights and biases, respectively. Imagine that we initialize all the biases to zero and the elements of $\boldsymbol{\Omega}_k$ according to a normal distribution with mean zero and variance σ^2. Consider two scenarios:

- If the variance σ^2 is very small (e.g., 10^{-5}), then each element of $\boldsymbol{\beta}_k + \boldsymbol{\Omega}_k \mathbf{h}_k$ will be a weighted sum of $\mathbf{h}_k$ where the weights are very small; the result will likely have a smaller magnitude than the input. In addition, the ReLU function clips values less than zero, so the range of $\mathbf{h}_k$ will be half that of $\mathbf{f}_{k-1}$. Consequently, the magnitudes of the pre-activations at the hidden layers will get smaller and smaller as we progress through the network.
- If the variance σ^2 is very large (e.g., 10^5), then each element of $\boldsymbol{\beta}_k + \boldsymbol{\Omega}_k \mathbf{h}_k$ will be a weighted sum of $\mathbf{h}_k$ where the weights are very large; the result is likely to have a much larger magnitude than the input. The ReLU function halves the range of the inputs, but if σ^2 is large enough, the magnitudes of the pre-activations will still get larger as we progress through the network.

In these two situations, the values at the pre-activations can become so small or so large that they cannot be represented with finite precision floating point math.

Even if the forward pass is tractable, the same logic applies to the backward pass. Each gradient update (equation 7.23) consists of multiplying by $\boldsymbol{\Omega}^T$. If the values of $\boldsymbol{\Omega}$ are not initialized sensibly, then the gradient magnitudes may decrease or increase uncontrollably during the backward pass. These cases are known as the *vanishing gradient problem* and the *exploding gradient problem*, respectively. In the former case, updates to the model become vanishingly small. In the latter case, they become unstable.

7.5.1 Initialization for forward pass

We now present a mathematical version of the same argument. Consider the computation between adjacent pre-activations $\mathbf{f}$ and $\mathbf{f}'$ with dimensions D_h and $D_{h'}$, respectively:

$$\begin{aligned}\mathbf{h} &= \mathbf{a}[\mathbf{f}], \\ \mathbf{f}' &= \boldsymbol{\beta} + \boldsymbol{\Omega}\mathbf{h}\end{aligned} \tag{7.26}$$

where $\mathbf{f}$ represents the pre-activations, $\boldsymbol{\Omega}$, and $\boldsymbol{\beta}$ represent the weights and biases, and $\mathbf{a}[\bullet]$ is the activation function.

Assume the preactivations f_j in the input layer $\mathbf{f}$ have variance σ_f^2. Consider initializing the biases β_i to zero and the weights Ω_{ij} as normally distributed with mean zero and variance σ_Ω^2. Now we derive expressions for the mean and variance of the pre-activations $\mathbf{f}'$ in the subsequent layer.

The expectation (mean) $\mathbb{E}[f_i]$ of the intermediate values f_i is:

Appendix B.2 Expectation

$$\begin{aligned}
\mathbb{E}[f_i'] &= \mathbb{E}\left[\beta_i + \sum_{j=1}^{D_h} \Omega_{ij} h_j\right] \\
&= \mathbb{E}\left[\beta_i\right] + \sum_{j=1}^{D_h} \mathbb{E}\left[\Omega_{ij} h_j\right] \\
&= \mathbb{E}\left[\beta_i\right] + \sum_{j=1}^{D_h} \mathbb{E}\left[\Omega_{ij}\right] \mathbb{E}\left[h_j\right] \\
&= 0 + \sum_{j=1}^{D_h} 0 \cdot \mathbb{E}\left[h_j\right] = 0,
\end{aligned} \tag{7.27}$$

where D_h is the dimensionality of the input layer $\mathbf{h}$. We have used the rules for manipulating expectations and we have assumed that the distributions over the hidden units h_j and the network weights Ω_{ij} are independent between the second and third lines.

Appendix B.2.1 Expectation rules

Using this result, we see that the variance $\sigma^2_{f'}$ of the pre-activations f_i' is:

$$\begin{aligned}
\sigma^2_{f'} &= \mathbb{E}[f_i'^2] - \mathbb{E}[f_i']^2 \\
&= \mathbb{E}\left[\left(\beta_i + \sum_{j=1}^{D_h} \Omega_{ij} h_j\right)^2\right] - 0 \\
&= \mathbb{E}\left[\left(\sum_{j=1}^{D_h} \Omega_{ij} h_j\right)^2\right] \\
&= \sum_{j=1}^{D_h} \mathbb{E}\left[\Omega_{ij}^2\right] \mathbb{E}\left[h_j^2\right] \\
&= \sum_{j=1}^{D_h} \sigma^2_\Omega \mathbb{E}\left[h_j^2\right] = \sigma^2_\Omega \sum_{j=1}^{D_h} \mathbb{E}\left[h_j^2\right],
\end{aligned} \tag{7.28}$$

where we have used the variance identity $\sigma^2 = \mathbb{E}[(z - \mathbb{E}[z])^2] = \mathbb{E}[z^2] - \mathbb{E}[z]^2$. We have assumed once more that the distributions of the weights Ω_{ij} and the hidden units h_j are independent between lines three and four.

Appendix B.2.3 Variance identity

Assuming that the input distribution of pre-activations f_j is symmetric about zero, half of these preactivations will be clipped by the ReLU function, and the second moment $\mathbb{E}[h_j]^2$ will be half the variance σ^2_f of f_j (see problem 7.14):

Problem 7.14

$$\sigma^2_{f'} = \sigma^2_\Omega \sum_{j=1}^{D_h} \frac{\sigma^2_f}{2} = \frac{1}{2} D_h \sigma^2_\Omega \sigma^2_f. \tag{7.29}$$

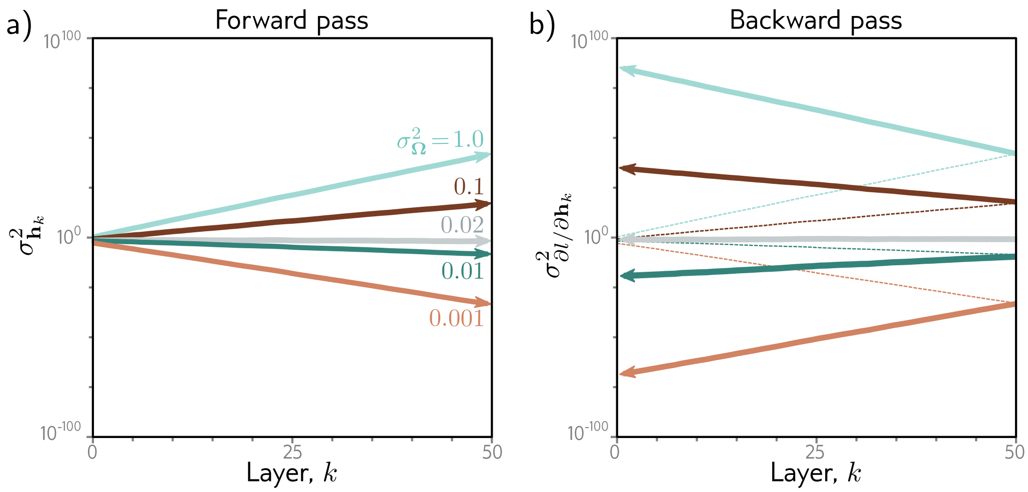

Figure 7.7 Weight initialization. Consider a deep network with 50 hidden layers and $D_h = 100$ hidden units per layer. The network has a 100-dimensional input $\mathbf{x}$ initialized with values from a standard normal distribution, a single output fixed at $y = 0$, and a least squares loss function. The bias vectors $\boldsymbol{\beta}_k$ are initialized to zero, and the weight matrices $\mathbf{\Omega}_k$ are initialized with a normal distribution with mean zero and five different variances $\sigma^2_{\mathbf{\Omega}} \in \{0.001, 0.01, 0.02, 0.1, 1.0\}$. a) Variance of hidden unit activations computed in forward pass as a function of the network layer. For He initialization ($\sigma^2_{\mathbf{\Omega}} = 2/D_h = 0.02$), the variance is stable. However, for larger values, it increases rapidly, and for smaller values, it decreases rapidly. b) The variance of the gradients in the backward pass (solid lines) continues this trend; if we initialize with a value larger than 0.02, the magnitude of the gradients increases rapidly as we pass back through the network. If we initialize with a value smaller, then the magnitude decreases. These are known as the *exploding gradient* and *vanishing gradient* problems, respectively.

This, in turn, implies that if we want the variance $\sigma^2_{f'}$ of the subsequent pre-aactivations $\mathbf{f}'$ to be the same as the variance σ^2_f of the original pre-activations $\mathbf{f}$ during the forward pass, we should set:

$$\sigma^2_{\Omega} = \frac{2}{D_h}, \tag{7.30}$$

where D_h is the dimension of the original layer to which the weights were applied. This is known as *He initialization*.

7.5.2 Initialization for backward pass

A similar argument establishes how the variance of the gradients $\partial l/\partial f_k$ changes during the backward pass. During the backward pass, we multiply by the transpose $\mathbf{\Omega}^T$ of the weight matrix (equation 7.23), so the equivalent expression becomes:

$$\sigma_\Omega^2 = \frac{2}{D_{h'}}, \tag{7.31}$$

where $D_{h'}$ is the dimension of the layer that the weights feed into.

7.5.3 Initialization for both forward and backward pass

If the weight matrix $\boldsymbol{\Omega}$ is not square (i.e., there are different numbers of hidden units in the two adjacent layers, so D_h and $D_{h'}$ differ), then it is not possible to choose the variance to satisfy both equations 7.30 and 7.31 simultaneously. One possible compromise is to use the mean $(D_h + D_{h'})/2$ as a proxy for the number of terms which gives:

$$\sigma_\Omega^2 = \frac{1}{D_h + D_{h'}}. \tag{7.32}$$

Figure 7.7 shows empirically that both the variance of the hidden units in the forward pass and the variance of the gradients in the backward pass remain stable when the parameters are initialized appropriately.

Notebook 7.3
Initialization

7.6 Example training code

The primary focus of this book is scientific; this is not a guide for implementing deep learning models. Nonetheless, in figure 7.8, we present PyTorch code that implements the ideas explored in this book so far. The code defines a neural network and initializes the weights. It creates random input and output datasets and defines a least squares loss function. The model is trained from the data using SGD with momentum in batches of size 10 over 100 epochs. The learning rate starts at 0.01 and halves every 10 epochs.

Problems 7.15–7.16

The takeaway is that although the underlying ideas in deep learning are quite complex, implementation is relatively simple. For example, all of the details of the backpropagation are hidden in the single line of code: `loss.backward()`.

7.7 Summary

The previous chapter introduced stochastic gradient descent (SGD), an iterative optimization algorithm that aims to find the minimum of a function. In the context of neural networks, this algorithm finds the parameters that minimize the loss function. SGD relies on the gradient of the loss function with respect to the parameters, which must be initialized before optimization. This chapter has addressed these two problems for deep neural networks.

The gradients must be evaluated for a very large number of parameters, for each member of the batch, and at each SGD iteration. It is hence imperative that the gradient

```
import torch, torch.nn as nn
from torch.utils.data import TensorDataset, DataLoader
from torch.optim.lr_scheduler import StepLR

# define input size, hidden layer size, output size
D_i, D_k, D_o = 10, 40, 5
# create model with two hidden layers
model = nn.Sequential(
    nn.Linear(D_i, D_k),
    nn.ReLU(),
    nn.Linear(D_k, D_k),
    nn.ReLU(),
    nn.Linear(D_k, D_o))

# He initialization of weights
def weights_init(layer_in):
    if isinstance(layer_in, nn.Linear):
        nn.init.kaiming_uniform(layer_in.weight)
        layer_in.bias.data.fill_(0.0)
model.apply(weights_init)

# choose least squares loss function
criterion = nn.MSELoss()
# construct SGD optimizer and initialize learning rate and momentum
optimizer = torch.optim.SGD(model.parameters(), lr = 0.1, momentum=0.9)
# object that decreases learning rate by half every 10 epochs
scheduler = StepLR(optimizer, step_size=10, gamma=0.5)

# create 100 dummy data points and store in data loader class
x = torch.randn(100, D_i)
y = torch.randn(100, D_o)
data_loader = DataLoader(TensorDataset(x,y), batch_size=10, shuffle=True)

# loop over the dataset 100 times
for epoch in range(100):
    epoch_loss = 0.0
    # loop over batches
    for i, data in enumerate(data_loader):
        # retrieve inputs and labels for this batch
        x_batch, y_batch = data
        # zero the parameter gradients
        optimizer.zero_grad()
        # forward pass
        pred = model(x_batch)
        loss = criterion(pred, y_batch)
        # backward pass
        loss.backward()
        # SGD update
        optimizer.step()
        # update statistics
        epoch_loss += loss.item()
    # print error
    print(f'Epoch {epoch:5d}, loss {epoch_loss:.3f}')
    # tell scheduler to consider updating learning rate
    scheduler.step()
```

Figure 7.8 Sample code for training two-layer network on random data.

computation is efficient, and to this end, the backpropagation algorithm was introduced. Careful parameter initialization is also critical. The magnitudes of the hidden unit activations can either decrease or increase exponentially in the forward pass. The same is true of the gradient magnitudes in the backward pass, where these behaviors are known as the vanishing gradient and exploding gradient problems. Both impede training but can be avoided with appropriate initialization.

We've now defined the model and the loss function, and we can train a model for a given task. The next chapter discusses how to measure the model performance.

Notes

Backpropagation: Efficient reuse of partial computations while calculating gradients in computational graphs has been repeatedly discovered, including by Werbos (1974), Bryson et al. (1979), LeCun (1985), and Parker (1985). However, the most celebrated description of this idea was by Rumelhart et al. (1985) and Rumelhart et al. (1986), who also coined the term "backpropagation." This latter work kick-started a new phase of neural network research in the eighties and nineties; for the first time, it was practical to train networks with hidden layers. However, progress stalled due (in retrospect) to a lack of training data, limited computational power, and the use of sigmoid activations. Areas such as natural language processing and computer vision did not rely on neural network models until the remarkable image classification results of Krizhevsky et al. (2012) ushered in the modern era of deep learning.

The implementation of backpropagation in modern deep learning frameworks such as PyTorch and TensorFlow is an example of reverse-mode algorithmic differentiation. This is distinguished from forward-mode algorithmic differentiation in which the derivatives from the chain rule are accumulated while moving forward through the computational graph (see problem 7.13). Further information about algorithmic differentiation can be found in Griewank & Walther (2008) and Baydin et al. (2018).

Initialization: He initialization was first introduced by He et al. (2015). It follows closely from *Glorot* or *Xavier* initialization (Glorot & Bengio, 2010), which is very similar but does not consider the effect of the ReLU layer and so differs by a factor of two. Essentially the same method was proposed much earlier by LeCun et al. (2012) but with a slightly different motivation; in this case, sigmoidal activation functions were used, which naturally normalize the range of outputs at each layer, and hence help prevent an exponential increase in the magnitudes of the hidden units. However, if the pre-activations are too large, they fall into the flat regions of the sigmoid function and result in very small gradients. Hence, it is still important to initialize the weights sensibly. Klambauer et al. (2017) introduce the scaled exponential linear unit (SeLU) and show that, within a certain range of inputs, this activation function tends to make the activations in network layers automatically converge to mean zero and unit variance.

A completely different approach is to pass data through the network and then normalize by the empirically observed variance. *Layer-sequential unit variance initialization* (Mishkin & Matas, 2016) is an example of this kind of method, in which the weight matrices are initialized as orthonormal. GradInit (Zhu et al., 2021) randomizes the initial weights and temporarily fixes them while it learns non-negative scaling factors for each weight matrix. These factors are selected to maximize the decrease in the loss for a fixed learning rate subject to a constraint on the maximum gradient norm. *Activation normalization* or *ActNorm* adds a learnable scaling and offset parameter after each network layer at each hidden unit. They run an initial batch through the network and then choose the offset and scale so that the mean of the activations is zero and the variance one. After this, these extra parameters are learned as part of the model.

Closely related to these methods are schemes such as *BatchNorm* (Ioffe & Szegedy, 2015), in which the network normalizes the variance of each batch as part of its processing at every step. BatchNorm and its variants are discussed in chapter 11. Other initialization schemes have been proposed for specific architectures, including the *ConvolutionOrthogonal* initializer (Xiao et al., 2018a) for convolutional networks, *Fixup* (Zhang et al., 2019a) for residual networks, and *TFixup* (Huang et al., 2020a) and *DTFixup* (Xu et al., 2021b) for transformers.

Reducing memory requirements: Training neural networks is memory intensive. We must store both the model parameters and the pre-activations at the hidden units for every member of the batch during the forward pass. Two methods that decrease memory requirements are *gradient checkpointing* (Chen et al., 2016a) and *micro-batching* (Huang et al., 2019). In gradient checkpointing, the activations are only stored every N layers during the forward pass. During the backward pass, the intermediate missing activations are recalculated from the nearest checkpoint. In this manner, we can drastically reduce the memory requirements at the computational cost of performing the forward pass twice (problem 7.11). In micro-batching, the batch is subdivided into smaller parts, and the gradient updates are aggregated from each sub-batch before being applied to the network. A completely different approach is to build a reversible network (e.g., Gomez et al., 2017), in which the activations at the previous layer can be computed from the activations at the current one, so there is no need to cache anything during the forward pass (see chapter 16). Sohoni et al. (2019) review approaches to reducing memory requirements.

Distributed training: For sufficiently large models, the memory requirements or total required time may be too much for a single processor. In this case, we must use *distributed training*, in which training takes place in parallel across multiple processors. There are several approaches to parallelism. In *data parallelism*, each processor or *node* contains a full copy of the model but runs a subset of the batch (see Xing et al., 2015; Li et al., 2020b). The gradients from each node are aggregated centrally and then redistributed back to each node to ensure that the models remain consistent. This is known as *synchronous training.* The synchronization required to aggregate and redistribute the gradients can be a performance bottleneck, and this leads to the idea of asynchronous training. For example, in the *Hogwild!* algorithm (Recht et al., 2011), the gradient from a node is used to update a central model whenever it is ready. The updated model is then redistributed to the node. This means that each node may have a slightly different version of the model at any given time, so the gradient updates may be stale; however, it works well in practice. Other decentralized schemes have also been developed. For example, in Zhang et al. (2016a), the individual nodes update one another in a ring structure.

Data parallelism methods still assume that the entire model can be held in the memory of a single node. *Pipeline model parallelism* stores different layers of the network on different nodes and hence does not have this requirement. In a naïve implementation, the first node runs the forward pass for the batch on the first few layers and passes the result to the next node, which runs the forward pass on the next few layers and so on. In the backward pass, the gradients are updated in the opposite order. The obvious disadvantage of this approach is that each machine lies idle for most of the cycle. Various schemes revolving around each node processing micro-batches sequentially have been proposed to reduce this inefficiency (e.g., Huang et al., 2019; Narayanan et al., 2021a). Finally, in *tensor model parallelism*, computation at a single network layer is distributed across nodes (e.g., Shoeybi et al., 2019). A good overview of distributed training methods can be found in Narayanan et al. (2021b), who combine tensor, pipeline, and data parallelism to train a language model with one trillion parameters on 3072 GPUs.

Problems

Problem 7.1 Find an expression for the final term in each of the five chains of derivatives in equation 7.12.

Problem 7.2 A two-layer network with two hidden units in each layer can be defined as:

$$\begin{aligned} y &= \phi_0 + \phi_1 \mathrm{a}\left[\psi_{01} + \psi_{11}\mathrm{a}[\theta_{01} + \theta_{11}x] + \psi_{21}\mathrm{a}[\theta_{02} + \theta_{12}x]\right] \\ &\qquad + \phi_2 \mathrm{a}[\psi_{02} + \psi_{12}\mathrm{a}[\theta_{01} + \theta_{11}x] + \psi_{22}\mathrm{a}[\theta_{02} + \theta_{12}x]], \end{aligned} \tag{7.33}$$

where the functions $a[\bullet]$ are ReLU functions. Compute the derivatives of the output y with respect to each of the 13 parameters $\boldsymbol{\phi}_{\bullet}, \theta_{\bullet\bullet}$, and $\psi_{\bullet\bullet}$ directly (i.e., not using the backpropagation algorithm). The derivative of the ReLU function with respect to its input $\partial a[z]/\partial z$ is the indicator function $\mathbb{I}[z > 0]$, which returns one if the argument is greater than zero and zero otherwise (figure 7.6).

Problem 7.3 What size are each of the terms in equation 7.18?

Problem 7.4 Calculate the derivative $\partial \ell_i / \partial f[\mathbf{x}_i, \boldsymbol{\phi}]$ for the least squares loss function:

$$\ell_i = (y_i - \mathrm{f}[\mathbf{x}_i, \boldsymbol{\phi}])^2. \tag{7.34}$$

Problem 7.5 Calculate the derivative $\partial \ell_i / \partial \mathrm{f}[\mathbf{x}_i, \boldsymbol{\phi}]$ for the binary classification loss function:

$$\ell_i = -(1 - y_i)\log\left[1 - \mathrm{sig}[\mathrm{f}[\mathbf{x}_i, \boldsymbol{\phi}]]\right] - y_i \log\left[\mathrm{sig}[\mathrm{f}[\mathbf{x}_i, \boldsymbol{\phi}]]\right], \tag{7.35}$$

where the function $\mathrm{sig}[\bullet]$ is the logistic sigmoid and is defined as:

$$\mathrm{sig}[z] = \frac{1}{1 + \exp[-z]}. \tag{7.36}$$

Problem 7.6* Show that for $\mathbf{z} = \boldsymbol{\beta} + \boldsymbol{\Omega}\mathbf{h}$:

$$\frac{\partial \mathbf{z}}{\partial \mathbf{h}} = \boldsymbol{\Omega}^T, \tag{7.37}$$

where $\partial \mathbf{z}/\partial \mathbf{h}$ is a matrix containing the term $\partial z_j / \partial h_i$ in it's j^{th} row and i^{th} column. To do this, first find an expression for the constituent elements $\partial z_j / \partial h_i$, and then consider the form that the matrix $\partial \mathbf{z}/\partial \mathbf{h}$ must take.

Problem 7.7 Consider the case where we use the logistic sigmoid (see equation 7.36) as an activation function, so $h = \mathrm{sig}[f]$. Compute the derivative $\partial h / \partial f$ for this activation function. What happens to the derivative when the input takes (i) a large positive value and (ii) a large negative value?

Problem 7.8 Consider using (i) the Heaviside function and (ii) the rectangular function as activation functions:

$$\mathrm{Heaviside}[z] = \begin{cases} 0 & z < 0 \\ 1 & z \geq 0 \end{cases}, \tag{7.38}$$

and

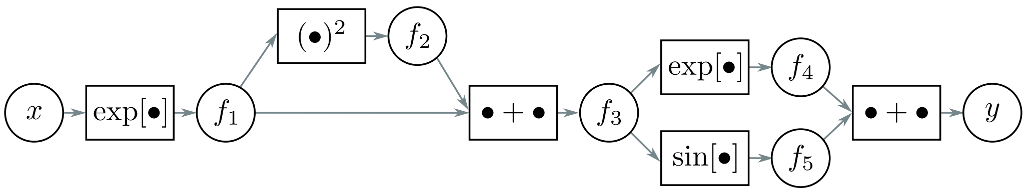

Figure 7.9 Computational graph for problem 7.12 and problem 7.13. Adapted from Domke (2010).

$$\mathrm{rect}[z] = \begin{cases} 0 & z < 0 \\ 1 & 0 \leq z \leq 1 \\ 0 & z > 1 \end{cases}. \tag{7.39}$$

Discuss why these functions are problematic for neural network training with gradient-based optimization methods.

Problem 7.9* Consider a loss function $\ell[\mathbf{f}]$, where $\mathbf{f} = \boldsymbol{\beta} + \boldsymbol{\Omega}\mathbf{h}$. We want to find how the loss ℓ changes when we change $\boldsymbol{\Omega}$, which we'll express with a matrix that contains the derivative $\partial\ell/\partial\Omega_{ij}$ at the i^{th} row and j^{th} column. Find an expression for $\partial f_i/\partial\Omega_{ij}$ and using the chain rule, show that:

$$\frac{\partial \ell}{\partial \boldsymbol{\Omega}} = \frac{\partial \ell}{\partial \mathbf{f}}\mathbf{h}^T. \tag{7.40}$$

Problem 7.10* Derive the equations for the backward pass of the backpropagation algorithm for a network that uses leaky ReLU activations, which are defined as:

$$\mathrm{a}[z] = \mathrm{ReLU}[z] = \begin{cases} \alpha z & z < 0 \\ z & z \geq 0 \end{cases}, \tag{7.41}$$

where α is a small positive constant (typically 0.1).

Problem 7.11 Consider the training a network with fifty layers, where we only have enough memory to store the values at every tenth hidden layer during the forward pass. Explain how to compute the derivatives in this situation using gradient checkpointing.

Problem 7.12* This problem explores computing derivatives on general acyclic computational graphs. Consider the function:

$$y = \exp\left[\exp[x] + \exp[x]^2\right] + \sin[\exp[x] + \exp[x]^2]. \tag{7.42}$$

We can break this down into a series of intermediate computations so that:

$$
\begin{aligned}
f_1 &= \exp[x] \\
f_2 &= f_1^2 \\
f_3 &= f_1 + f_2 \\
f_4 &= \exp[f_3] \\
f_5 &= \sin[f_3] \\
y &= f_4 + f_5.
\end{aligned} \tag{7.43}
$$

The associated computational graph is depicted in figure 7.9. Compute the derivative $\partial y/\partial x$ by *reverse-mode differentiation*. In other words, compute in order:

$$
\frac{\partial y}{\partial f_5}, \frac{\partial y}{\partial f_4}, \frac{\partial y}{\partial f_3}, \frac{\partial y}{\partial f_2}, \frac{\partial y}{\partial f_1} \text{ and } \frac{\partial y}{\partial x}, \tag{7.44}
$$

using the chain rule in each case to make use of the derivatives already computed.

Problem 7.13[*] For the same function in problem 7.42, compute the derivative $\partial y/\partial x$ by *forward-mode differentiation*. In other words, compute in order:

$$
\frac{\partial f_1}{\partial x}, \frac{\partial f_2}{\partial x}, \frac{\partial f_3}{\partial x}, \frac{\partial f_4}{\partial x}, \frac{\partial f_5}{\partial x}, \text{ and } \frac{\partial y}{\partial x}, \tag{7.45}
$$

using the chain rule in each case to make use of the derivatives already computed. Why do we not use forward-mode differentiation when we calculate the parameter gradients for deep networks?

Problem 7.14 Consider a random variable a with mean $\mathbb{E}[a] = 0$ and variance $\text{Var}[a] = \sigma^2$. Prove that if we pass this variable through the ReLU function:

$$
b = \text{ReLU}[a] = \begin{cases} 0 & a < 0 \\ a & a \geq 0 \end{cases}, \tag{7.46}
$$

then the second moment of the transformed variable is $\mathbb{E}[b^2] = \sigma^2/2$.

Problem 7.15 Implement the code in figure 7.8 in PyTorch and plot the training loss as a function of the number of epochs.

Problem 7.16 Change the code in figure 7.8 to tackle a binary classification problem. You will need to (i) change the targets y so they are binary, (ii) change the network to predict numbers between zero and one (iii) change the loss function appropriately.

Chapter 8

Measuring performance

Previous chapters described neural network models, loss functions, and training algorithms. This chapter considers how to measure the performance of the trained models. With sufficient capacity (i.e., number of hidden units), a neural network model will often perform perfectly on the training data. However, this does not necessarily mean it will generalize well to new test data.

We will see that the test errors have three distinct causes and that their relative contributions depend on (i) the inherent uncertainty in the task, (ii) the amount of training data, and (iii) the choice of model. The latter dependency raises the issue of hyperparameter search. We discuss how to select both the model hyperparameters (e.g., the number of hidden layers and the number of hidden units in each) and the learning algorithm hyperparameters (e.g., the learning rate and batch size).

8.1 Training a simple model

We explore model performance using the MNIST-1D dataset (figure 8.1). This consists of ten classes $y \in \{0, 1, \ldots, 9\}$, representing the digits 0–9. The data are derived from 1D templates for each of the digits. Each data example $\mathbf{x}$ is created by randomly transforming one of these templates and adding noise. The full training dataset $\{\mathbf{x}_i, y_i\}$ consists of $I = 4000$ training examples, each consisting of $D_i = 40$ dimensions representing the horizontal offset at 40 positions. The ten classes are drawn uniformly during data generation, so there are ~ 400 examples of each class.

We use a network with $D_i = 40$ inputs and $D_o = 10$ outputs which are passed through a softmax function to produce class probabilities (see section 5.5). The network has two hidden layers with $D = 100$ hidden units each. It is trained using stochastic gradient descent with batch size 100 and learning rate 0.1 for 6000 steps (150 epochs) with a multi-class cross-entropy loss (equation 5.24). Figure 8.2 shows that the training error decreases as training proceeds. The training data are classified perfectly after about 4000 steps. The training loss also decreases, eventually approaching zero.

Problem 8.1

However, this doesn't imply that the classifier is perfect; the model might have mem-

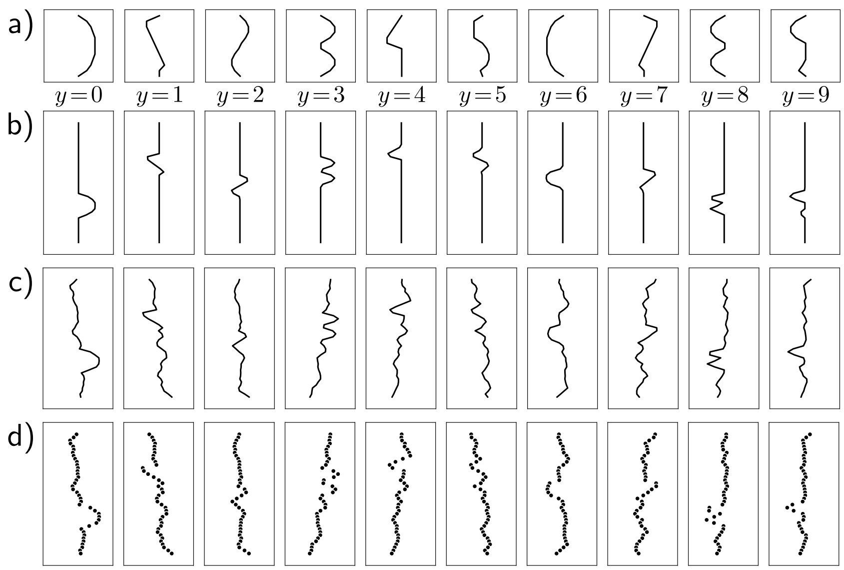

Figure 8.1 MNIST-1D. a) Templates for 10 classes $y \in \{0, \ldots, 9\}$, based on digits 0–9. b) Training examples $\mathbf{x}$ are created by randomly transforming a template and c) adding noise. d) The horizontal position of the transformed template is then sampled at 40 positions. Adapted from (Greydanus, 2020)

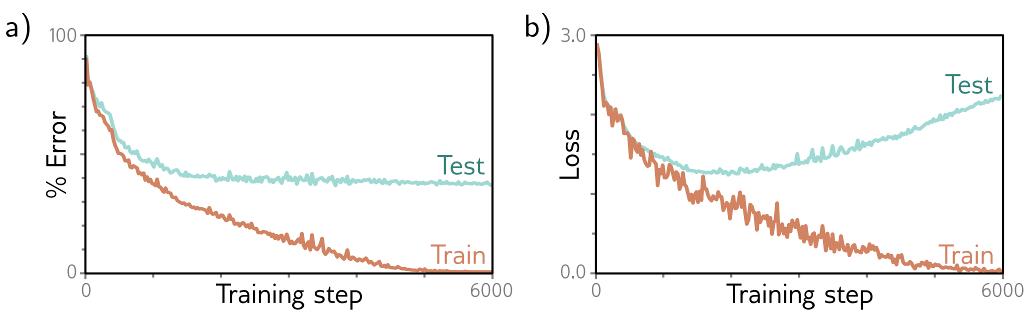

Figure 8.2 MNIST-1D results. a) Percent classification error as a function of the training step. The training set errors decrease to zero, but the test errors do not drop below $\sim 40\%$. This model doesn't generalize well to new test data. b) Loss as a function of the training step. The training loss decreases steadily towards zero. The test loss decreases at first but subsequently increases as the model becomes increasingly confident about its (wrong) predictions.

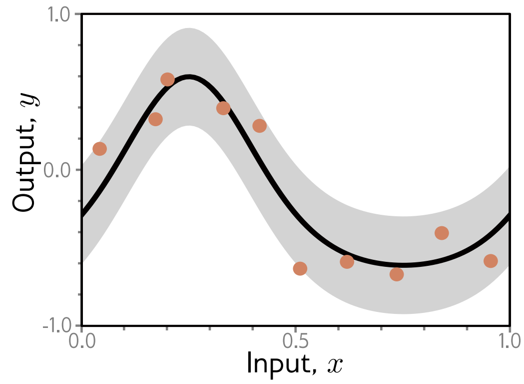

Figure 8.3 Regression function. Solid black line shows the ground truth function. To generate I training examples $\{x_i, y_i\}$, the input space $x \in [0, 1]$ is divided into I equal segments and one sample x_i is drawn from a uniform distribution within each segment. The corresponding value y_i is created by evaluating the function at x_i, and adding Gaussian noise (gray region shows ± 2 standard deviations). The test data are generated in the same way.

orized the training set but be unable to predict new examples. To estimate the true performance, we need a separate *test set* of input/output pairs $\{\mathbf{x}_i, y_i\}$. To this end, we generate 1000 more examples using the same process. Figure 8.2a also shows the errors for this test data as a function of the training step. These decrease as training proceeds, but only to around 40%. This is better than the chance error rate of 90% error rate but far worse than for the training set; the model has not *generalized* well to the test data.

Notebook 8.1 MNIST-1D performance

The test loss (figure 8.2b) decreases for the first 1500 training steps but then increases again. At this point, the test error rate is fairly constant; the model makes the same mistakes but with increasing confidence. This decreases the probability of the correct answers and thus increases the negative log-likelihood. This increasing confidence is a side-effect of the softmax function; the pre-softmax activations are driven to increasingly extreme values to make the probability of the training approach data one (see figure 5.10).

8.2 Sources of error

We now consider the sources of the errors that occur when a model fails to generalize. To make this easier to visualize, we revert to a 1D linear least squares regression problem where we know exactly how the ground truth data were generated. Figure 8.3 shows a quasi-sinusoidal function; both training and test data are generated by sampling input values in the range $[0, 1]$, passing them through this function, and adding Gaussian noise with a fixed standard deviation.

We fit a simplified shallow neural net to this data (figure 8.4). The weights and biases that connect the input layer to the hidden layer are chosen so that the "joints" of the function are evenly spaced across the interval. If there are D hidden units, then these joints will be at $0, 1/D, 2/D, \ldots, (D-1)/D$. This model can represent any piecewise linear function with D equally-sized regions in the range $[0, 1]$. As well as being easy to understand, this model also has the advantage that it can be fit in closed form without the need for stochastic optimization algorithms (see problem 8.3). Consequently, we can guarantee to find the global minimum of the loss function during training.

Problems 8.2–8.3

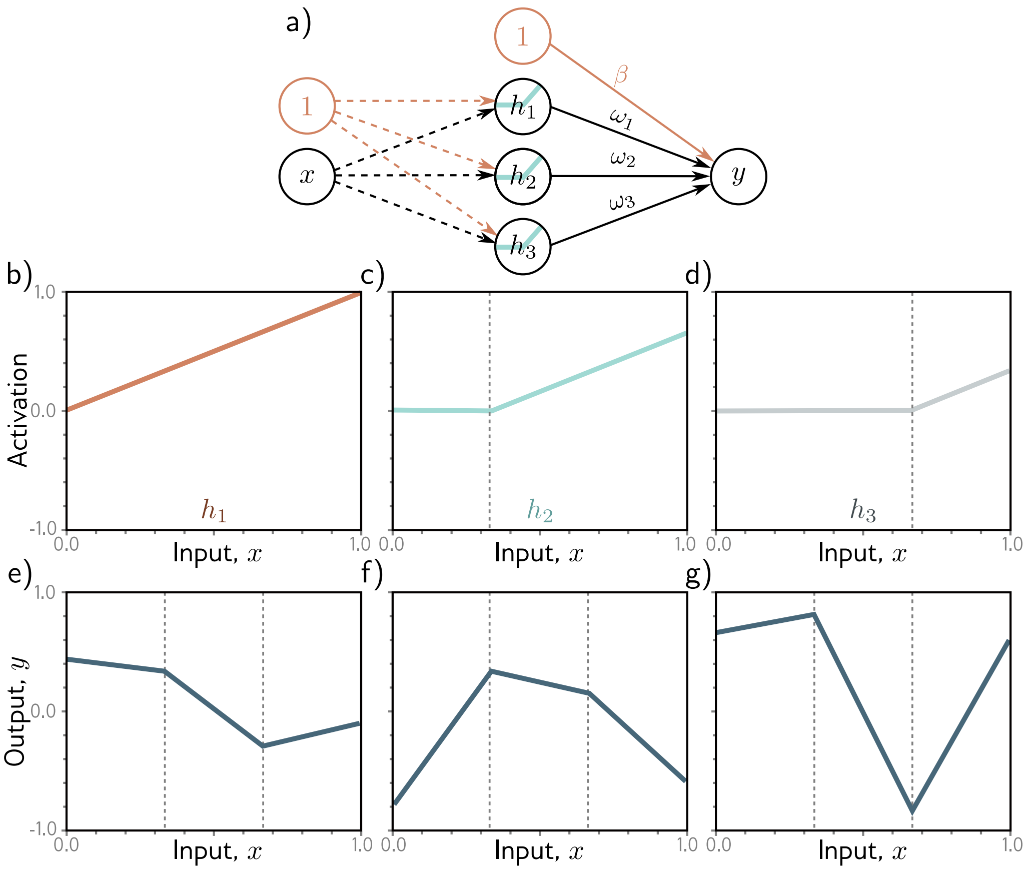

Figure 8.4 Simplified neural network with three hidden units. a) The weights and biases between the input and hidden layer are fixed (dashed arrows). b–d) They are chosen so that the hidden unit activations have slope one, and their joints are equally spaced across the interval, with joints at $x = 0$, $x = 1/3$, and $x = 2/3$, respectively. Modifying the remaining parameters $\boldsymbol{\phi} = \{\beta, \omega_1, \omega_2, \omega_3\}$ can create any piecewise linear function over $x \in [0, 1]$ with joints at $1/3$ and $2/3$. e–g) Three example functions with different values of the parameters $\boldsymbol{\phi}$.

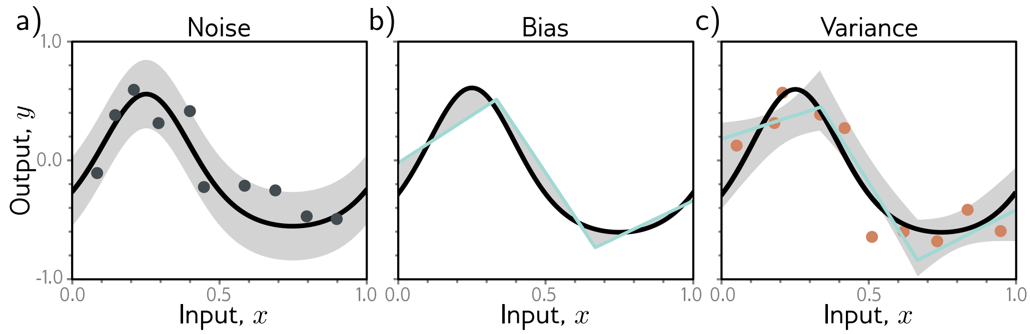

Figure 8.5 Sources of test error. a) Noise. Data generation is noisy, so even if the model exactly replicates the true underlying function (black line), the noise in the test data (gray points) means that some error will remain (gray region represents two standard deviations). b) Bias. Even with the best possible parameters, the three-region model (cyan line) cannot exactly fit the true function (black line). This bias is another source of error (gray regions represent signed error). c) Variance. In practice, we have limited noisy training data (orange points). When we fit the model, we don't recover the best possible function from panel (b) but a slightly different function (cyan line) that reflects idiosyncrasies of the training data. This provides an additional source of error (gray region represents two standard deviations). Figure 8.6 shows how this region was calculated.

8.2.1 Noise, bias, and variance

There are three possible sources of error, which are known as *noise*, *bias*, and *variance* respectively (figure 8.5):

Noise The data generation process includes the addition of noise, so there are multiple possible valid outputs y for each input x (figure 8.5a). This source of error is insurmountable for the test data. Note that it does not necessarily limit the training performance; we will likely never see the same input x twice during training, so it is still possible to fit the training data perfectly.

Noise may arise because there is a genuine stochastic element to the data generation process, because some of the data are mislabeled, or because there are further explanatory variables that were not observed. In rare cases, noise may be absent; for example, a network might approximate a function that is deterministic but requires significant computation to evaluate. However, noise is usually a fundamental limitation on the possible test performance.

Bias A second potential source of error may occur because the model is not flexible enough to fit the true function perfectly. For example, the three-region neural network model cannot exactly describe the quasi-sinusoidal function, even when the parameters are chosen optimally (figure 8.5b). This is known as *bias*.

Variance We have limited training examples, and there is no way to distinguish systematic changes in the underlying function from noise in the underlying data. When we fit a model, we do not get the closest possible approximation to the true underlying function. Indeed, for different training datasets, the result will be slightly different each time. This additional source of variability in the fitted function is termed *variance* (figure 8.5c). In practice, there might also be additional variance due to the stochastic learning algorithm, which does not necessarily converge to the same solution each time.

8.2.2 Mathematical formulation of test error

We now make the notions of noise, bias, and variance mathematically precise. Consider a 1D regression problem where the data generation process has additive noise with variance σ^2 (e.g., figure 8.3); we can observe different outputs y for the same input x and so for each x there is a distribution $Pr(y|x)$ with expected value (mean) $\mu[x]$:

Appendix B.2 Expectation

$$\mu[x] = \mathbb{E}_y[y[x]] = \int y[x]Pr(y|x)dy, \tag{8.1}$$

and fixed noise $\sigma^2 = \mathbb{E}_y\left[(\mu[x]-y[x])^2\right]$. Here we have used the notation $y[x]$ to specify that we are considering the output y at a given input position x.

Now consider a least squares loss between the model prediction $\mathrm{f}[x,\boldsymbol{\phi}]$ at position x and the observed value $y[x]$ at that position:

$$\begin{aligned} L[x] &= \bigl(\mathrm{f}[x,\boldsymbol{\phi}] - y[x]\bigr)^2 \\ &= \Bigl(\bigl(\mathrm{f}[x,\boldsymbol{\phi}] - \mu[x]\bigr) + \bigl(\mu[x] - y[x]\bigr)\Bigr)^2 \\ &= \bigl(\mathrm{f}[x,\boldsymbol{\phi}] - \mu[x]\bigr)^2 + 2\bigl(\mathrm{f}[x,\boldsymbol{\phi}]) - \mu[x]\bigr)\bigl(\mu[x] - y[x]\bigr) + \bigl(\mu[x] - y[x]\bigr)^2, \end{aligned} \tag{8.2}$$

where we have both added and subtracted the mean $\mu[x]$ of the underlying function in the second line and have expanded out the squared term in the third line.

The underlying function is stochastic, and so this loss depends on the particular $y[x]$ we observe. The expected loss is:

$$\begin{aligned} \mathbb{E}_y\bigl[L[x]\bigr] &= \mathbb{E}_y\Bigl[\bigl(\mathrm{f}[x,\boldsymbol{\phi}]-\mu[x]\bigr)^2 + 2\bigl(\mathrm{f}[x,\boldsymbol{\phi}]-\mu[x]\bigr)\bigl(\mu[x]-y[x]\bigr) + \bigl(\mu[x]-y[x]\bigr)^2\Bigr] \\ &= \bigl(\mathrm{f}[x,\boldsymbol{\phi}]-\mu[x]\bigr)^2 + 2\bigl(\mathrm{f}[x,\boldsymbol{\phi}] - \mu[x]\bigr)\bigl(\mu[x]-\mathbb{E}_y\left[y[x]\right]\bigr) + \mathbb{E}_y\left[(\mu[x]-y[x])^2\right] \\ &= \bigl(\mathrm{f}[x,\boldsymbol{\phi}]-\mu[x]\bigr)^2 + 2\bigl(\mathrm{f}[x,\boldsymbol{\phi}]-\mu[x]\bigr)\cdot 0 + \mathbb{E}_y\left[\bigl(\mu[x]-y[x]\bigr)^2\right] \\ &= \bigl(\mathrm{f}[x,\boldsymbol{\phi}] - \mu[x]\bigr)^2 + \sigma^2, \end{aligned} \tag{8.3}$$

where we have made use of the rules for manipulating expectations. In the second line, we have distributed the expectation operator and removed it from terms with no dependence on $y[x]$, and in the third line, we note that the second term is zero since $\mathbb{E}_y[y[x]] = \mu[x]$ by definition. Finally, in the fourth line, we have substituted in the definition of the

Appendix B.2.1 Expectation rules

noise σ^2. We can see that the expected loss has been broken down into two terms; the first term is the squared deviation between the model and the true function mean, and the second term is the noise.

The first term can be further partitioned into bias and variance. The parameters $\boldsymbol{\phi}$ of the model $\mathrm{f}[x, \boldsymbol{\phi}]$ depend on the training dataset $\mathcal{D} = \{x_i, y_i\}$, so really, we should write $\mathrm{f}[x, \boldsymbol{\phi}[\mathcal{D}]]$. The training dataset is a random sample from the data generation process; with a different sample of training data, we would learn different parameter values. The expected model output $f_\mu[x]$ with respect to all possible datasets $\mathcal{D}$ is hence:

$$f_\mu[x] = \mathbb{E}_\mathcal{D}\big[\mathrm{f}[x, \boldsymbol{\phi}[\mathcal{D}]]\big]. \tag{8.4}$$

Returning to the first term of equation 8.3, we add and subtract $\mathrm{f}_\mu[x]$ and expand:

$$\begin{aligned}
&\big(\mathrm{f}[x, \boldsymbol{\phi}[\mathcal{D}]] - \mu[x]\big)^2 \\
&\qquad = \Big(\big(\mathrm{f}[x, \boldsymbol{\phi}[\mathcal{D}]] - f_\mu[x]\big) + \big(f_\mu[x] - \mu[x]\big)\Big)^2 \\
&\qquad = \big(\mathrm{f}[x, \boldsymbol{\phi}[\mathcal{D}]] - f_\mu[x]\big)^2 + 2\big(\mathrm{f}[x, \boldsymbol{\phi}[\mathcal{D}]] - f_\mu[x]\big)\big(f_\mu[x] - \mu[x]\big) + \big(f_\mu[x] - \mu[x]\big)^2.
\end{aligned} \tag{8.5}$$

We then take the expectation with respect to the training data set $\mathcal{D}$:

$$\mathbb{E}_\mathcal{D}\Big[\big(\mathrm{f}[x, \boldsymbol{\phi}[\mathcal{D}]] - \mu[x]\big)^2\Big] = \mathbb{E}_\mathcal{D}\Big[\big(\mathrm{f}[x, \boldsymbol{\phi}[\mathcal{D}]] - f_\mu[x]\big)^2\Big] + \big(f_\mu[x] - \mu[x]\big)^2, \tag{8.6}$$

where we have simplified using similar steps as for equation 8.3. Finally, we substitute this result into equation 8.3:

$$\mathbb{E}_\mathcal{D}\Big[\mathbb{E}_y[L[x]]\Big] = \underbrace{\mathbb{E}_\mathcal{D}\Big[\big(\mathrm{f}[x, \boldsymbol{\phi}[\mathcal{D}]] - f_\mu[x]\big)^2\Big]}_{\text{variance}} + \underbrace{\big(f_\mu[x] - \mu[x]\big)^2}_{\text{bias}} + \underbrace{\sigma^2}_{\text{noise}} \tag{8.7}$$

This equation says that the expected loss after considering the uncertainty in the training data $\mathcal{D}$ and the test data y consists of three additive components. The variance is uncertainty in the fitted model due to the particular training dataset we sample. The bias is the systematic deviation of the model from the mean of the function we are modeling. The noise is the inherent uncertainty in the true mapping from input to output. These three sources of error will be present for any task. They combine additively for linear regression with a least squares loss. However, their interaction can be more complex for other types of problems.

8.3 Reducing error

In the previous section, we saw that test error results from three sources: noise, bias, and variance. The noise component is insurmountable; there is nothing we can do to circumvent this, and it represents a fundamental limit on model performance. However, it is possible to reduce the other two terms.

8.3.1 Reducing variance

Recall that the variance results from limited noisy training data. Fitting the model to two different training sets results in slightly different parameters. It follows we can reduce the variance by increasing the quantity of training data. This averages out the inherent noise and ensures that the input space is well sampled.

Figure 8.6 shows the effect of training with 6, 10, and 100 samples. For each dataset size, we show the best-fitting model for three training datasets. With only six samples, the fitted function is quite different each time; the variance is significant. As we increase the number of samples, the fitted models become very similar, and the variance reduces. In general, adding training data almost always improves test performance.

8.3.2 Reducing bias

The bias term results from the inability of the model to describe the true underlying function. This suggests that we can reduce this error by making the model more flexible. This is usually done by increasing the model *capacity*. For neural networks, this means adding more hidden units and/or hidden layers.

In the simplified model, adding capacity corresponds to adding more hidden units so that the interval $[0, 1]$ is divided into more linear regions. Figures 8.7a–c show that (unsurprisingly) this does indeed reduce the bias; as we increase the number of linear regions to ten, the model becomes flexible enough to fit the true function closely.

8.3.3 Bias-variance trade-off

However, figures 8.7d–f show an unexpected side-effect of increasing the model capacity. For a fixed-size training dataset, the variance term increases as the model capacity increases. Consequently, increasing the model capacity does not necessarily reduce the test error. This is known as the *bias-variance trade-off*.

Figure 8.8 explores this phenomenon. In panels a–c), we fit the simplified three-region model to three different datasets of fifteen points. Although the datasets differ, the final model is much the same; the noise in the dataset roughly averages out in each linear region. In panels d–f), we fit a model with ten regions to the same three datasets. This model has more flexibility, but this is disadvantageous; the model certainly fits the data better, and the training error will be lower, but much of the extra descriptive power is devoted to modeling the noise. This phenomenon is known as *overfitting*.

We've seen that as we add capacity to the model, the bias will decrease, but the variance will increase for a fixed-size training dataset. This suggests that there is an optimal capacity where the bias is not too large and the variance is still relatively small. Figure 8.9 shows how these terms vary numerically for the toy model as we increase the capacity, using the data from figure 8.8. For regression models, the total expected error is the sum of the bias and the variance and this sum is minimized when the model capacity is four (i.e., with four hidden units and four linear regions).

Notebook 8.2 Bias-variance trade-off

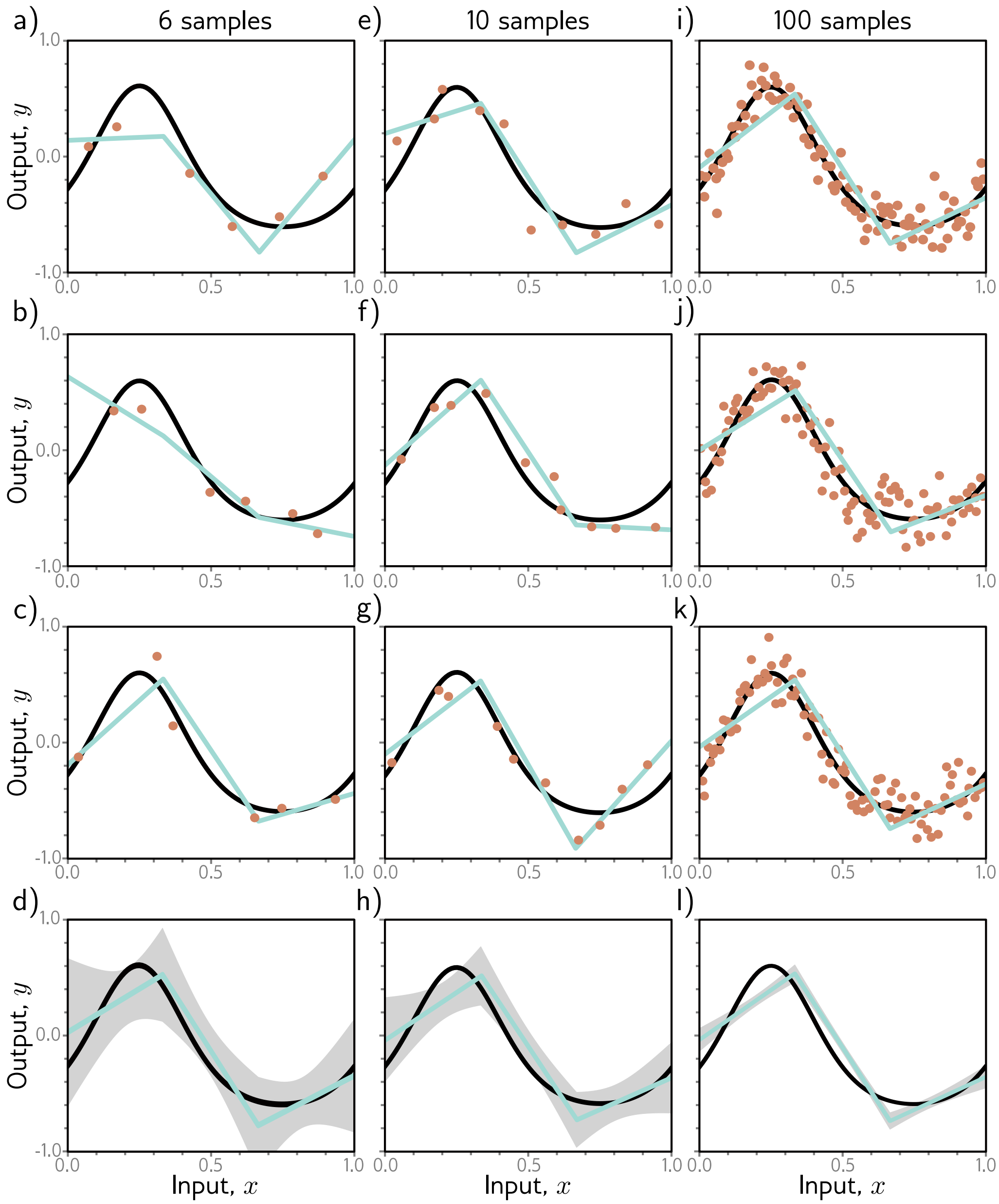

Figure 8.6 Reducing variance by increasing training data. a–c) The three-region model fitted to three different randomly sampled datasets of six points. The fitted model is quite different each time. d) We repeat this experiment many times and plot the mean model predictions (cyan line) and the variance of the model predictions (gray area shows two standard deviations). e–h) We do the same experiment, but this time with datasets of size ten. The variance of the predictions is reduced. i–l) We repeat this experiment with datasets of size 100. Now the fitted model is always similar, and the variance is small.

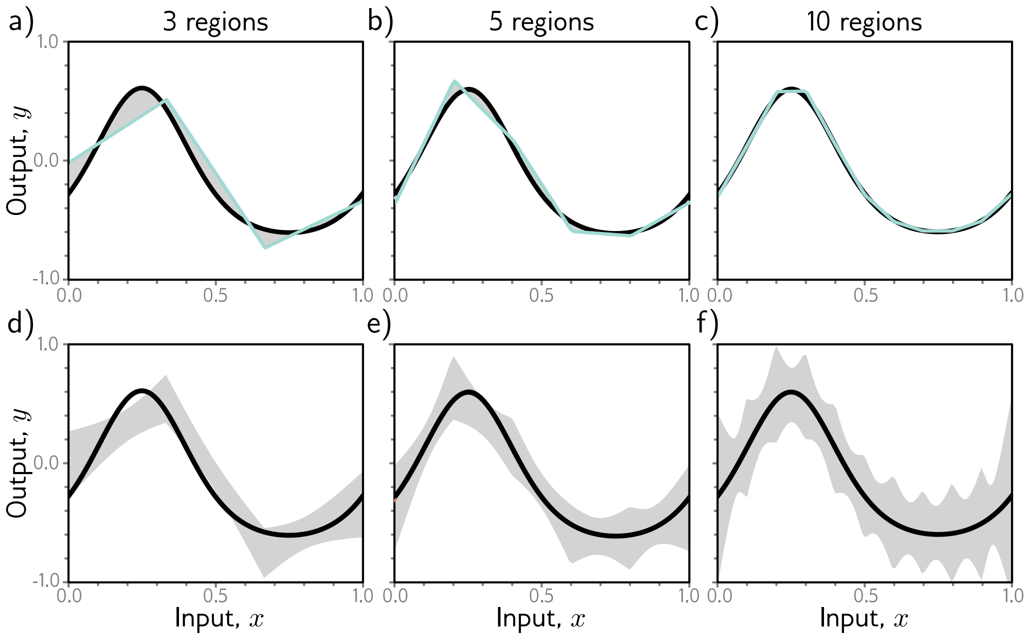

Figure 8.7 Bias and variance as a function of model capacity. a–c) As we increase the number of hidden units of the toy model, the number of linear regions increases, and the model becomes able to fit the true function closely; the bias (gray region) decreases. d–f) Unfortunately, increasing the model capacity has the side-effect of increasing the variance term (gray region). This is known as the bias-variance trade-off.

8.4 Double descent

In the previous section, we examined the bias-variance trade-off as we increased the capacity of a model. Let's now return to the MNIST-1D dataset and see whether this happens in practice. We use 10,000 training examples, test with another 5,000 examples and examine the training and test performance as we increase the capacity (number of parameters) in the model. We train the model with Adam and a step size of 0.005 using a full batch of 10,000 examples for 4000 steps.

Figure 8.10a shows the training and test error for a neural network with two hidden layers as the number of hidden units increases. The training error decreases as the capacity grows and quickly becomes close to zero. The vertical dashed line represents the capacity where the model has the same number of parameters as there are training examples, but the model memorizes the dataset before this point. The test error decreases as we add model capacity but does not increase as predicted by the bias-variance trade-off curve; it keeps decreasing.

In figure 8.10b, we repeat this experiment, but this time, we randomize 15% of the

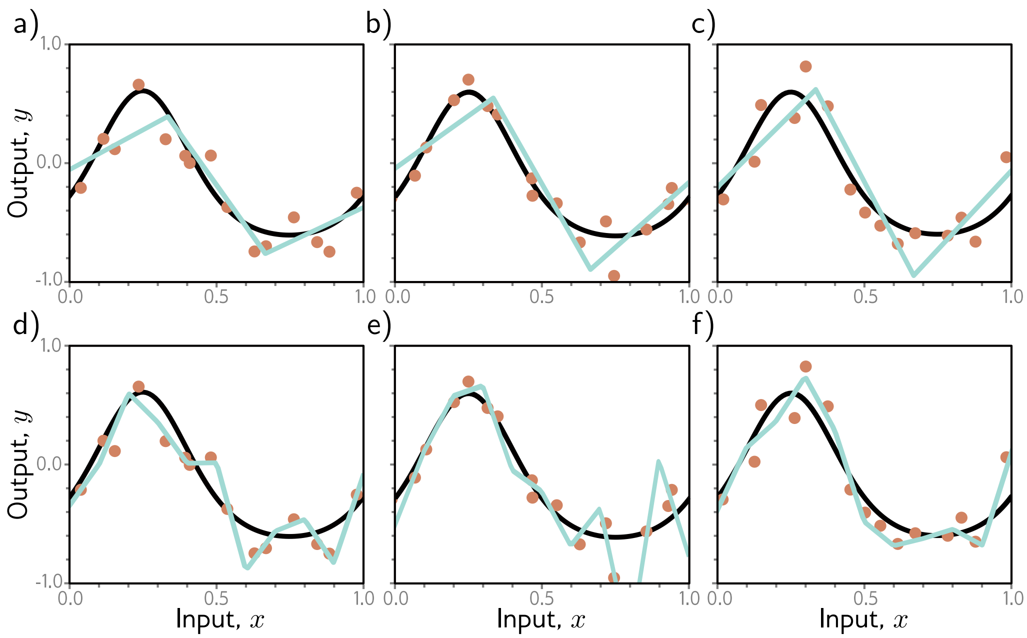

Figure 8.8 Overfitting. a–c) A model with three regions is fit to three different datasets of fifteen points each. The result is similar in all three cases (i.e., the variance is low). d–f) A model with ten regions is fit to the same datasets. The additional flexibility does not necessarily produce better predictions. While these three models each describe the training data better, they are not necessarily closer to the true underlying function (black curve). Instead, they overfit the data and describe the noise, and the variance (difference between fitted curves) is larger.

Figure 8.9 Bias-variance trade-off. The bias and variance terms from equation 8.7 are plotted as a function of the model capacity (number of hidden units / linear regions) in the simplified model using training data from figure 8.8. As the capacity increases, the bias (solid orange line) decreases, but the variance (solid cyan line) increases. The sum of these two terms (dashed gray line) is minimized when the capacity is four.

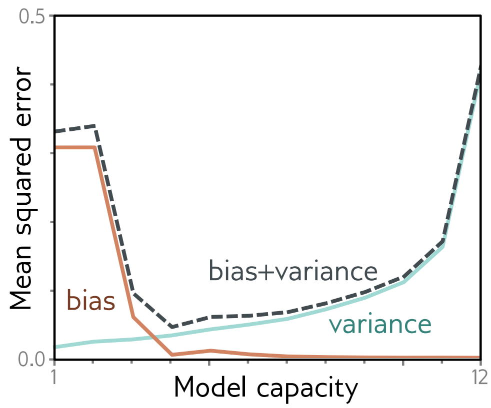

training labels. Once more, the training error decreases to zero. This time, there is more randomness, and the model requires almost as many parameters as there are data points to memorize the data. The test error does show the typical bias-variance trade-off as we increase the capacity to the point where the model fits the training data exactly. However, then it does something unexpected; it starts to decrease again. Indeed, if we add enough capacity, the test loss reduces to below the minimal level that we achieved in the first part of the curve.

This phenomenon is known as *double descent*. For some datasets like MNIST, it is present with the original data (figure 8.10c). For others, like MNIST-1D and CIFAR (figure 8.10d), it emerges or becomes more prominent when we add noise to the labels. The first part of the curve is referred to as the *classical* or *under-parameterized regime*, and the second part as the *modern* or *over-parameterized regime*. The central part where the error increases is termed the *critical regime*.

Notebook 8.3 Double descent

8.4.1 Explanation

The discovery of double descent is recent, unexpected, and somewhat puzzling. It results from an interaction of two phenomena. First, the test performance becomes temporarily worse when the model has just enough capacity to memorize the data. Second, the test performance continues to improve with capacity even after the training performance is perfect. The first phenomenon is exactly as predicted by the bias-variance trade-off. The second phenomenon is more confusing; it's unclear why performance should be better in the over-parameterized regime, given that there are now not even enough training data points to constrain the model parameters uniquely.

To understand why performance continues to improve as we add more parameters, note that once the model has enough capacity to drive the training loss to near zero, the model fits the training data almost perfectly. This implies that further capacity cannot help the model fit the training data any better; any change must occur *between* the training points. The tendency of a model to prioritize one solution over another as it extrapolates between data points is known as its *inductive bias*.

Problems 8.4–8.5

The model's behaviour between data points is critical because, in high-dimensional space, the training data are extremely sparse. The MNIST-1D dataset has 40 dimensions, and we trained with 10,000 examples. If this seems like plenty of data, consider what would happen if we quantized each input dimension into 10 bins. There would be 10^{40} bins in total, constrained by only 10^5 examples. Even with this coarse quantization, there will only be one data point in every 10^{35} bins! The tendency of the volume of high-dimensional space to overwhelm the number of training points is termed the *curse of dimensionality*.

The implication is that problems in high dimensions might look more like figure 8.11a; there are small regions of the input space where we observe data with significant gaps between them. The putative explanation for double descent is that as we add capacity to the model, it interpolates between the nearest data points increasingly smoothly. In the absence of information about what happens between the training points, assuming smoothness is sensible and will probably generalize reasonably to new data.

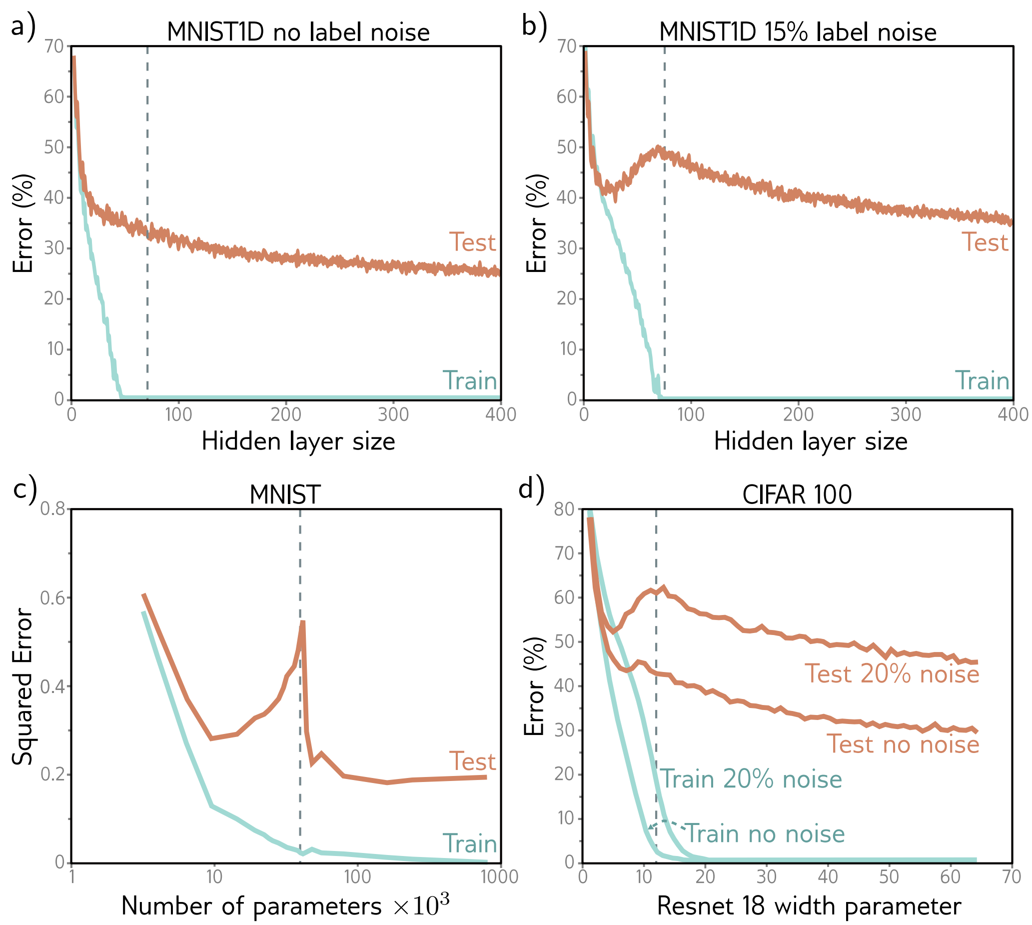

Figure 8.10 Double descent. a) Training and test loss on MNIST-1D for a two-hidden layer network as we increase the number of hidden units (and hence parameters) in each layer. The training loss decreases to zero as the number of parameters approaches the number of training examples (vertical dashed line). The test error does not show the expected bias-variance trade-off but continues to decrease even after the model has memorized the dataset. b) The same experiment is repeated with noisier training data. Again, the training error reduces to zero, although it now takes almost as many parameters as training points to memorize the dataset. The test error shows the predicted bias/variance trade-off; it decreases as the capacity increases but then increases again as we near the point where the training data is exactly memorized. However, it subsequently decreases again and ultimately reaches a better performance level. This is known as double descent. Depending on the loss, the model, and the amount of noise in the data, the double descent pattern can be seen to a greater or lesser degree across many datasets. c) Results on MNIST (without label noise) with shallow neural network from Belkin et al. (2019). d) Results on CIFAR 100 with ResNet18 network (see chapter 11) from Nakkiran et al. (2021). See original papers for details.

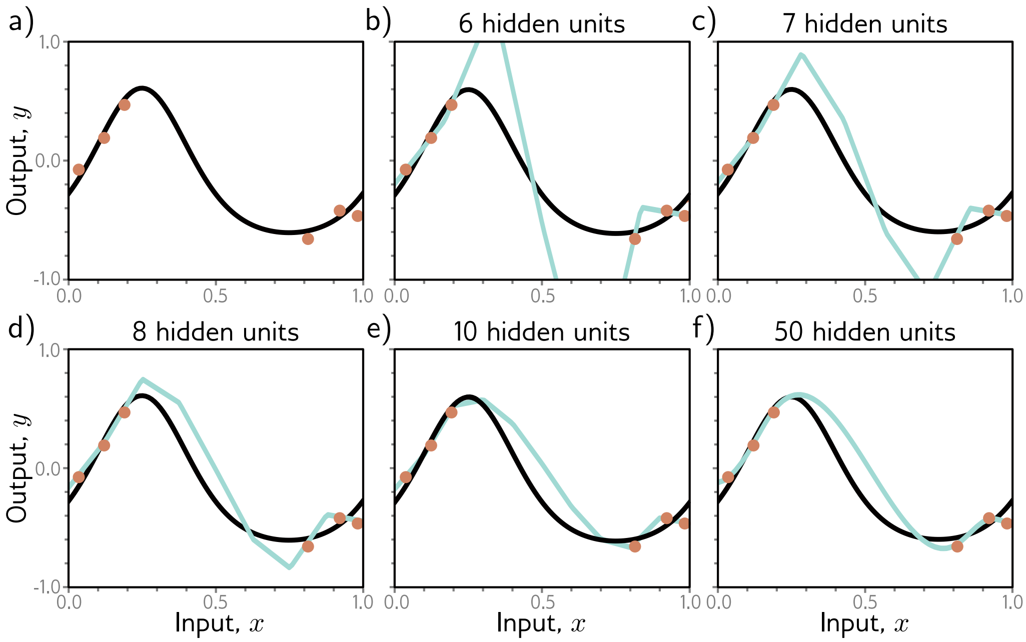

Figure 8.11 Increasing capacity (hidden units) allows smoother interpolation between sparse data points. a) Consider this situation where the training data (orange circles) are sparse; there is a large region in the center with no data examples to constrain the model to mimic the true function (black curve). b) If we fit a model with just enough capacity to fit the training data (cyan curve), then it has to contort itself to pass through the training data, and the output predictions will not be smooth. c–f) However, as we add more hidden units, the model has the *ability* to interpolate between the points more smoothly (smoothest possible curve plotted in each case). However, unlike in this figure, it is not obliged to.

This argument is plausible. It's certainly true that as we add more capacity to the model, it will have the capability to create smoother functions. Figures 8.11b–f show the smoothest possible functions that still pass through the data points as we increase the number of hidden units. When the number of parameters is very close to the number of training data examples (figure 8.11), the model is forced to contort itself to fit exactly, resulting in erratic predictions. This explains why the peak in the double descent curve is so pronounced. As we add more hidden units, the model has the ability to construct smoother functions that are likely to generalize better to new data.

However, this does not explain *why* over-parameterized models should produce smooth functions. Figure 8.12 shows three functions that can be created by the simplified model with 50 hidden units. In each case, the model fits the data exactly, so the loss is zero. If the modern regime of double descent is explained by increasing smoothness, then what exactly is encouraging this smoothness?

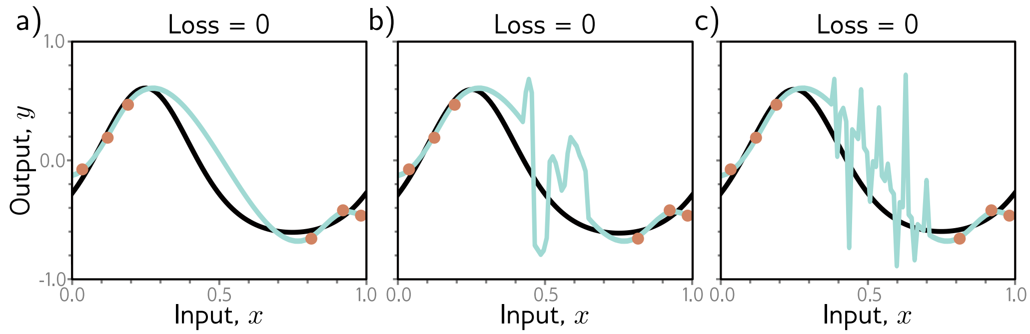

Figure 8.12 Regularization. a–c) Each of the three fitted curves passes through the data points exactly, so the training loss for each is zero. However, we might expect the smooth curve in panel (a) to generalize much better to new data than the erratic curves in panels (b) and (c). Any factor that biases a model towards a subset of the solutions with a similar training loss is known as a regularizer. It is thought that the initialization and/or fitting of neural networks have an implicit regularizing effect. Consequently, in the over-parameterized regime, more reasonable solutions, such as that in panel (a), are encouraged.

The answers to this question is uncertain, but there are two likely possibilities. First, the network initialization may encourage smoothness and the model never departs from the sub-domain of smooth function during the training processs. Second, the training algorithm may somehow "prefer" to converge to smooth functions. Any factor that biases a solution towards a subset of equivalent solutions is known as a *regularizer*, so one possibility is that the training algorithm acts as an implicit regularizer (see section 9.2).

8.5 Choosing hyperparameters

In the previous section, we discussed how test performance changes with model capacity. Unfortunately, in the classical regime, we don't have access to either the bias (which requires knowledge of the true underlying function) or the variance (which requires multiple independently sampled datasets to estimate). In the modern regime, there is no way to tell how much capacity should be added before the test error stops improving. This raises the question of exactly how we should choose model capacity in practice.

For a deep network, the model capacity depends on the numbers of hidden layers and hidden units per layer as well as other aspects of architecture that we have yet to introduce. Furthermore, the choice of learning algorithm and any associated parameters (learning rate, etc.) also affects the test performance. These elements are collectively termed *hyperparameters*. The process of finding the best hyperparameters is known as *hyperparameter search*.

Hyperparameters are typically chosen empirically; we train many models with different hyperparameters on the same training set, measure their performance, and retain the best model. However, we do not measure their performance on the test set; this would admit the possibility that these hyperparameters just happen to work well for the test set but don't generalize to further data. Instead, we introduce a third dataset known as a *validation set*. For every choice of hyperparameters, we train the associated model using the training set and evaluate performance on the validation set. Finally, we select the model that worked best on the validation set and measure its performance on the test set. In principle, this should give a reasonable estimate of the true performance.

The hyperparameter space is generally smaller than the parameter space but still too large to try every combination exhaustively. Unfortunately, many hyperparameters are discrete (e.g., the number of hidden layers), and others may be conditional on one another (e.g., we only need to specify the number of hidden units in the tenth hidden layer if there are ten or more layers). Hence, we cannot rely on gradient descent methods as we did for learning the model parameters. Hyperparameter optimization algorithms intelligently sample the space of hyperparameters, contingent on previous results. This procedure is computationally expensive since we must train an entire model and measure the validation performance for each combination of hyperparameters.

8.6 Summary

To measure performance, we use a separate test set. The degree to which performance is maintained on this test set is known as generalization. Test errors can be explained by three factors: noise, bias, and variance. These combine additively in regression problems with least squares losses. Adding training data decreases the variance. When the model capacity is less than the number of training examples, increasing the capacity decreases bias but increases variance. This is known as the bias-variance trade-off, and there is a capacity where the trade-off is optimal.

However, this is balanced against a tendency for performance to improve with capacity, even when the parameters exceed the training examples. Together, these two phenomena create the double descent curve. It is thought that the model interpolates more smoothly between the training data points in the over-parameterized "modern regime," although it is unclear what drives this. To choose the capacity and other model and training algorithm hyperparameters, we fit multiple models and evaluate their performance using a separate validation set.

Notes

Bias-variance trade-off: We showed that the test error for regression problems with least squares loss decomposes into the sum of noise, bias, and variance terms. These factors are all present for models with other losses, but their interaction is typically more complicated (Friedman, 1997; Domingos, 2000). For classification problems, there are some counter-intuitive predictions; for example, if the model is biased toward selecting the wrong class in a region of the input space, then increasing the variance can improve the classification rate as this pushes some of the predictions over the threshold to be classified correctly.

Cross-validation: We saw that it is typical to divide the data into three parts: training data (which is used to learn the model parameters), validation data (which is used to choose the hyperparameters), and test data (which is used to estimate the final performance). This approach is known as *cross-validation*. However, this division may cause problems where the total number of data examples is limited; if the number of training examples is comparable to the model capacity, then the variance will be large.

One way to reduce this problem is to use *k-fold cross-validation*. The training and validation data are partitioned into K disjoint subsets. For example, we might divide these data into five parts. We train with four and validate with the fifth for each of the five permutations and choose the hyperparameters based on the average validation performance. The final test performance is assessed using the average of the predictions from the five models with the best hyperparameters on an entirely different test set. There are many variations of this idea, but all share the general goal of using a larger proportion of the data to train the model, thereby reducing variance.

Capacity: We have used the term *capacity* informally to mean the number of parameters or hidden units in the model (and hence indirectly, the ability of the model to fit functions of increasing complexity). The *representational capacity* of a model describes the space of possible functions it can construct when we consider all possible parameter values. When we take into account the fact that an optimization algorithm may not be able to reach all of these solutions, what is left is the *effective capacity*.

The Vapnik-Chervonenkis (VC) dimension (Vapnik & Chervonenkis, 1971) is a more formal measure of capacity. It is the largest number of training examples that a binary classifier can label arbitrarily. Bartlett et al. (2019) derive upper and lower bounds for the VC dimension in terms of the number of layers and weights. An alternative measure of capacity is the Rademacher complexity, which is the expected empirical performance of a classification model (with optimal parameters) for data with random labels. Neyshabur et al. (2017) derive a lower bound on the generalization error in terms of the Rademacher complexity.

Double descent: The term "double descent" was coined by Belkin et al. (2019), who demonstrated that the test error decreases again in the over-parameterized regime for two-layer neural networks and random features. They also claimed that this occurs in decision trees, although Buschjäger & Morik (2021) subsequently provided evidence to the contrary. Nakkiran et al. (2021) show that double descent occurs for various modern datasets (CIFAR-10, CIFAR-100, IWSLT'14 de-en), architectures (CNNs, ResNets, transformers), and optimizers (SGD, Adam). The phenomenon is more pronounced when noise is added to the target labels (Nakkiran et al., 2021) and when some regularization techniques are used (Ishida et al., 2020).

Nakkiran et al. (2021) also provide empirical evidence that test performance depends on *effective model capacity* (the largest number of samples for which a given model and training method can achieve zero training error). At this point, the model starts to devote its efforts to interpolating smoothly. As such, the test performance depends not just on the model but also on the training algorithm and length of training. They observe the same pattern when they study a model with fixed capacity and increase the number of training iterations. They term this *epoch-wise double descent*. This phenomenon has been modeled by Pezeshki et al. (2022) in terms of different features in the model being learned at different speeds.

Double descent makes the rather strange prediction that adding training data can sometimes worsen test performance. Consider an over-parameterized model in the second descending part of the curve. If we increase the training data to match the model capacity, we will now be in the critical region of the new test error curve, and the test loss may increase.

Bubeck & Sellke (2021) prove that overparameterization is necessary to interpolate data smoothly in high dimensions. They demonstrate a trade-off between the number of parameters and the Lipschitz constant of a model (the fastest the output can change for a small input change). A review of the theory of over-parameterized machine learning can be found in Dar et al. (2021).

Appendix C.2 Lipschitz constant

Curse of dimensionality: As dimensionality increases, the volume of space grows so fast that the amount of data needed to densely sample it increases exponentially. This phenomenon is known as the curse of dimensionality. High-dimensional space has many unexpected properties, and caution should be used when trying to reason about it based on low-dimensional examples. This book visualizes many aspects of deep learning in one or two dimensions, but these visualizations should be treated with healthy skepticism.

Surprising properties of high-dimensional spaces include: (i) Two randomly sampled data points from a standard normal distribution are very close to orthogonal to one another (relative to the origin) with high likelihood. (ii) The distance from the origin of samples from a standard normal distribution is roughly constant. (iii) Most of a volume of a high-dimensional sphere (hypersphere) is adjacent to its surface (a common metaphor is that most of the volume of a high-dimensional orange is in the peel, not in the pulp). (iv) If we place a unit-diameter hypersphere inside a hypercube with unit-length sides, then the hypersphere takes up a decreasing proportion of the volume of the cube as the dimension increases. Since the volume of the cube is fixed at size one, this implies that the volume of a high-dimensional hypersphere becomes close to zero. (v) For random points drawn from a uniform distribution in a high-dimensional hypercube, the ratio of the Euclidean distance between the nearest and furthest points becomes close to one. For further information, consult Beyer et al. (1999) and Aggarwal et al. (2001).

Problems 8.6–8.9

Notebook 8.4 High-dimensional spaces

Real-world performance: In this chapter, we argued that model performance could be evaluated using a held-out test set. However, the result won't be indicative of real-world performance if the statistics of the test set don't match those of real-world data. Moreover, the statistics of real-world data may change over time, causing the model to become increasingly stale and performance to decrease. This is known as *data drift* and means that deployed models must be carefully monitored.

There are three main reasons why real-world performance may be worse than the test performance implies. First, the statistics of the input data $\mathbf{x}$ may change; we may now be observing parts of the function that were sparsely sampled or not sampled at all during training. This is known as *covariate shift*. Second, the statistics of the output data $\mathbf{y}$ may change; if some output values are infrequent during training, then the model may learn not to predict these in ambiguous situations and will make mistakes if they are more common in the real world. This is known as *prior shift*. Third, the relationship between input and output may change. This is known as *concept shift*. These issues are discussed in Moreno-Torres et al. (2012).

Hyperparameter search: Finding the best hyperparameters is a challenging optimization task. Testing a single configuration of hyperparameters is expensive; we must train an entire model and measure its performance. We have no easy way to access the derivatives (i.e., how performance changes when we make a small change to a hyperparameter). Moreover, many of the hyperparameters are discrete, so we cannot use gradient descent methods. There are multiple local minima and no way to tell if we are close to the global minimum. The noise level is high since each training/validation cycle uses a stochastic training algorithm; we expect different results if we train a model twice with the same hyperparameters. Finally, some variables are conditional and only exist if others are set. For example, the number of hidden units in the third hidden layer is only relevant if we have at least three hidden layers.

A simple approach is to sample the space randomly (Bergstra & Bengio, 2012). However, for continuous variables, it is better to build a model of performance as a function of the hyperparameters and the uncertainty in this function. This can be exploited to test where the uncertainty is great (explore the space) or home in on regions where performance looks promising (exploit previous knowledge). Bayesian optimization is a framework based on Gaussian processes that does just this, and its application to hyperparameter search is described in Snoek et al. (2012). The Beta-Bernoulli bandit (see Lattimore & Szepesvári, 2020) is a roughly equivalent model for describing uncertainty in results due to discrete variables.

The sequential model-based configuration (SMAC) algorithm (Hutter et al., 2011) can cope with continuous, discrete, and conditional parameters. The basic approach is to use a random forest to model the objective function where the mean of the tree predictions is the best guess about the objective function, and their variance represents the uncertainty. A completely different approach that can also cope with combinations of continuous, discrete, and conditional parameters is Tree-Parzen Estimators (Bergstra et al., 2011). The previous methods modeled the probability of the model performance given the hyperparameters. In contrast, the Tree-Parzen estimator models the probability of the hyperparameters given the model performance.

Hyperband (Li et al., 2017b) is a multi-armed bandit strategy for hyperparameter optimization. It assumes that there are computationally cheap but approximate ways to measure performance (e.g., by not training to completion) and that these can be associated with a budget (e.g., by training for a fixed number of iterations). A number of random configurations are sampled and run until the budget is used up. Then the best fraction η of runs is kept, and the budget is multiplied by $1/\eta$. This is repeated until the maximum budget is reached. This approach has the advantage of efficiency; for bad configurations, it does not need to run the experiment to the end. However, each sample is just chosen randomly, which is inefficient. The BOHB algorithm (Falkner et al., 2018) combines the efficiency of Hyperband with the more sensible choice of parameters from Tree Parzen estimators to construct an even better method.

Problems

Problem 8.1 Will the multi-class cross-entropy training loss in figure 8.2 ever reach zero? Explain your reasoning.

Problem 8.2 What values should we choose for the three weights and biases in the first layer of the model in figure 8.4a so that the responses at the hidden units are as depicted in figures 8.4b–d?

Problem 8.3* Given a training dataset consisting of I input/output pairs $\{x_i, y_i\}$, show how the parameters $\{\beta, \omega_1, \omega_2, \omega_3\}$ for the model in figure 8.4a using the least squares loss function can be found in closed form.

Problem 8.4 Consider the curve in figure 8.10b at the point where we train a model with a hidden layer of size 200, which would have 50,410 parameters. What do you predict will happen to the training and test performance if we increase the number of training examples from 10,000 to 50,410?

Problem 8.5 Consider the case where the model capacity exceeds the number of training data points, and the model is flexible enough to reduce the training loss to zero. What are the implications of this for fitting a heteroscedastic model? Propose a method to resolve any problems that you identify.

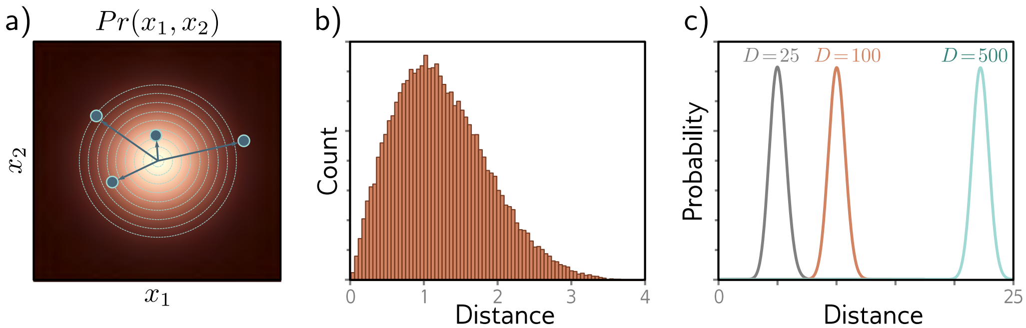

Figure 8.13 Typical sets. a) Standard normal distribution in two dimensions. Circles are four samples from this distribution. As the distance from the center increases, the probability decreases, but the volume of space at that radius (i.e., the area between adjacent evenly spaced circles) increases. b) These factors trade off so that the histogram of distances of samples from the center has a pronounced peak. c) In higher dimensions, this effect becomes more extreme, and the probability of observing a sample close to the mean becomes vanishingly small. Although the most likely point is at the mean of the distribution, the *typical samples* are found in a relatively narrow shell.

Problem 8.6 Show that the angle between two random samples from a 1000-dimensional standard Gaussian distribution is are orthogonal with high probability.

Problem 8.7 The volume of a hypersphere with radius r in D dimensions is:

$$\text{Vol}[r] = \frac{r^D \pi^{D/2}}{\Gamma[D/2+1]}, \tag{8.8}$$

where $\Gamma[\bullet]$ is the Gamma function. Show using Stirling's formula that the volume of a hypersphere of diameter one (radius $r=0.5$) becomes zero as the dimension increases.

Appendix C.3.1 Gamma function

Appendix C.3.2 Stirling's formula

Problem 8.8* Consider a hypersphere of radius $r = 1$. Find an expression for the proportion of the total volume that in lies in the outermost 1% of the distance from the center (i.e., in the outermost shell of thickness 0.01). Show that this becomes one as the dimension increases.

Problem 8.9 Figure 8.13c shows the distribution of distances of samples of a standard normal distribution as the dimension increases. Empirically verify this finding by sampling from the standard normal distributions in 25, 100, and 500 dimensions and plotting a histogram of the distances from the center. What closed-form probability distribution describes these distances?

Chapter 9

Regularization

Chapter 8 described how to measure model performance and identified that there could be a significant performance gap between the training and test data. Possible reasons for this discrepancy include: (i) the model describes statistical peculiarities of the training data that are not representative of the true mapping from input to output (overfitting), and (ii) the model is unconstrained in areas with no training examples, leading to sub-optimal predictions.

This chapter discusses *regularization* techniques. These are a family of methods that reduce the generalization gap between training and test performance. Strictly speaking, regularization involves adding explicit terms to the loss function that favor certain parameter choices. However, in machine learning, this term is commonly used to refer to any strategy that improves generalization.

We start by considering regularization in its strictest sense. Then we consider how the stochastic gradient descent algorithm itself favors certain solutions. This is known as implicit regularization. Following this, we consider a set of heuristic methods that improve test performance. These include early stopping, ensembling, dropout, label smoothing, and transfer learning.

9.1 Explicit regularization

Consider fitting a model $\mathrm{f}[\mathbf{x},\boldsymbol{\phi}]$ with parameters $\boldsymbol{\phi}$ using a training set $\{\mathbf{x}_i,\mathbf{y}_i\}$ of input/output pairs. We seek the minimum of the loss function $L[\boldsymbol{\phi}]$:

$$\begin{aligned}\hat{\boldsymbol{\phi}} &= \underset{\boldsymbol{\phi}}{\operatorname{argmin}}\Bigl[\mathrm{L}[\boldsymbol{\phi}]\Bigr] \\ &= \underset{\boldsymbol{\phi}}{\operatorname{argmin}}\left[\sum_{i=1}^{I}\ell_i[\mathbf{x}_i,\mathbf{y}_i]\right], \end{aligned} \tag{9.1}$$

where the individual terms $\ell_i[\mathbf{x}_i,\mathbf{y}_i]$ measure the mismatch between the network predictions $\mathrm{f}[\mathbf{x}_i,\boldsymbol{\phi}]$ and output targets $\mathbf{y}_i$ for each training pair. To bias this minimization

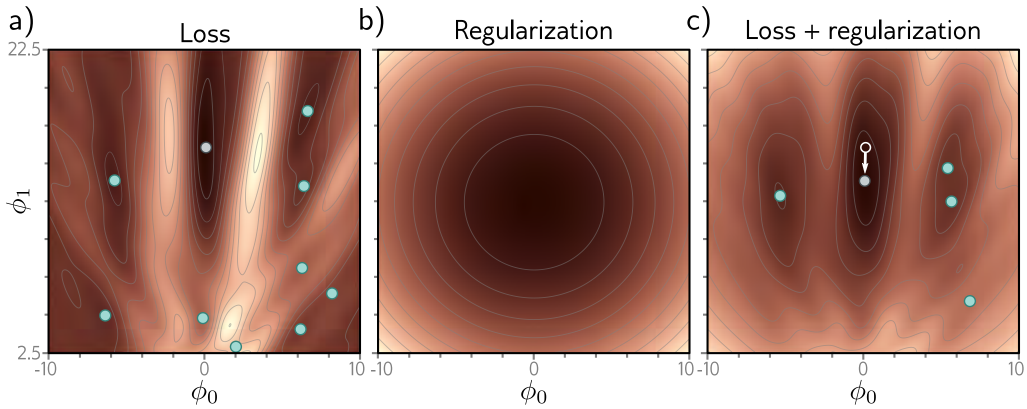

Figure 9.1 Explicit regularization. a) Loss function for Gabor model (see section 6.1.2). Cyan circles represent local minima. Gray circle represents the global minimum. b) The regularization term favors parameters close to the center of the plot by adding an increasing penalty as we move away from this point. c) The final loss function is the sum of the original loss function plus the regularization term. This surface has fewer local minima, and the global minimum has moved to a different position (arrow shows change).

toward certain solutions, we include an additional term:

$$\hat{\boldsymbol{\phi}} = \underset{\boldsymbol{\phi}}{\operatorname{argmin}} \left[\sum_{i=1}^{I} \ell_i[\mathbf{x}_i, \mathbf{y}_i] + \lambda \cdot \mathrm{g}[\boldsymbol{\phi}] \right], \tag{9.2}$$

where $\mathrm{g}[\boldsymbol{\phi}]$ is a function that returns a scalar that takes a larger value when the parameters are less preferred. The term λ is a positive scalar that controls the relative contribution of the original loss function and the regularization term. The minima of the regularized loss function usually differ from those in the original, so the training procedure converges to different parameter values (figure 9.1).

9.1.1 Probabilistic interpretation

Regularization can be viewed from a probabilistic perspective. Section 5.1 shows how loss functions are constructed from the maximum likelihood criterion:

$$\hat{\boldsymbol{\phi}} = \underset{\boldsymbol{\phi}}{\operatorname{argmax}} \left[\prod_{i=1}^{I} Pr(\mathbf{y}_i | \mathbf{x}_i, \boldsymbol{\phi}) \right]. \tag{9.3}$$

The regularization term can be considered as a prior $Pr(\boldsymbol{\phi})$ that represents knowledge about the parameters before we observe the data:

$$\hat{\boldsymbol{\phi}} = \underset{\boldsymbol{\phi}}{\operatorname{argmax}} \left[\prod_{i=1}^{I} Pr(\mathbf{y}_i|\mathbf{x}_i, \boldsymbol{\phi}) Pr(\boldsymbol{\phi}) \right]. \tag{9.4}$$

Moving back to the negative log-likelihood loss function by taking the log and multiplying by minus one, we see that $\lambda \cdot \mathrm{g}[\boldsymbol{\phi}] = -\log[Pr(\boldsymbol{\phi})]$.

9.1.2 L2 regularization

This discussion has sidestepped the question of *which* solutions the regularization term should penalize (or equivalently that the prior should favor). Since neural networks are used in an extremely broad range of applications, these can only be very generic preferences. The most commonly used regularization term is the *L2 norm*, which penalizes the sum of the squares of the parameter values:

$$\hat{\boldsymbol{\phi}} = \underset{\boldsymbol{\phi}}{\operatorname{argmin}} \left[\mathrm{L}[\boldsymbol{\phi}, \{\mathbf{x}_i, \mathbf{y}_i\}] + \lambda \sum_j \phi_j^2 \right], \tag{9.5}$$

Problems 9.1–9.2

where j indexes the parameters. This is also referred to as *Tikhonov regularization* or *ridge regression*, or (when applied to matrices) *Frobenius norm regularization*.

Notebook 9.1 L2 regularization

For neural networks, L2 regularization is usually applied to the weights but not the biases and is hence referred to as a *weight decay* term. The effect is to encourage smaller weights, so the output function is smoother. To see this, consider that the output prediction is a weighted sum of the activations at the last hidden layer. If the weights have a smaller magnitude, the output will vary less. The same logic applies to the computation of the pre-activations at the last hidden layer and so on, progressing backward through the network. In the limit, if we forced all the weights to be zero, the network would produce a constant output determined by the final bias parameter.

Figure 9.2 shows the effect of fitting the simplified network from figure 8.4 with weight decay and different values of the regularization coefficient λ. When λ is small, it has little effect. However, as λ increases, the fit to the data becomes less accurate, and the function becomes smoother. This might improve the test performance for two reasons:

- If the network is overfitting, then adding the regularization term means that the network must trade off slavish adherence to the data against the desire to be smooth. One way to think about this is that the error due to variance reduces (the model no longer needs to pass through every data point) at the cost of increased bias (the model can only describe smooth functions).
- When the network is over-parameterized, some of the extra model capacity describes areas with no training data. Here, the regularization term will favor functions that smoothly interpolate between the nearby points. This is reasonable behavior in the absence of knowledge about the true function.

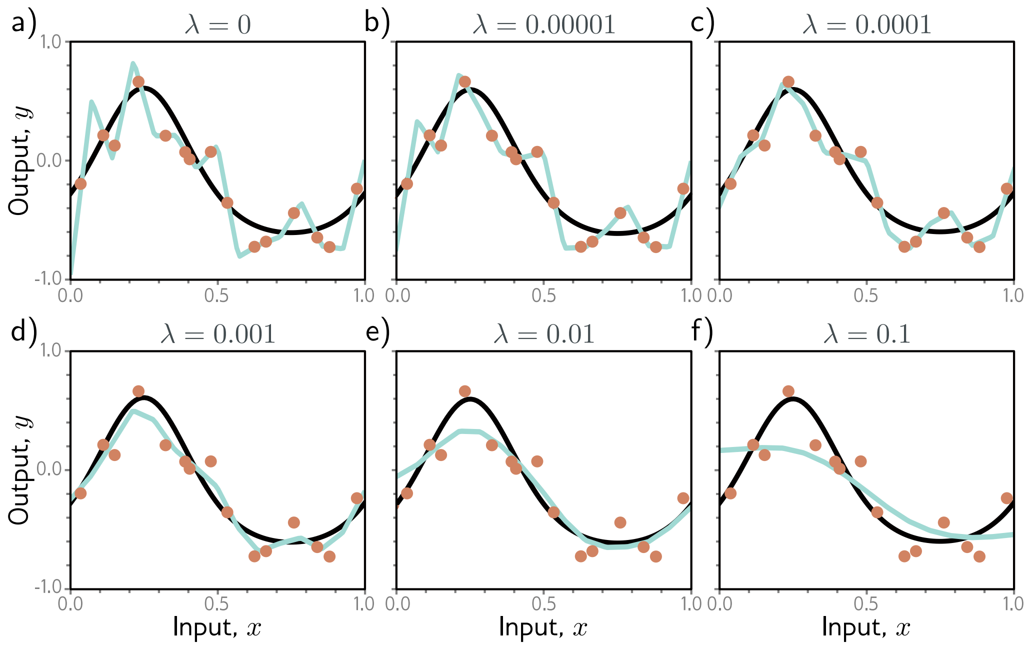

Figure 9.2 L2 regularization in simplified network (see figure 8.4). a–f) Fitted functions as we increase the regularization coefficient λ. The black curve is the true function, the orange circles are the noisy training data, and the cyan curve is the fitted model. For small λ (panels a–b), the fitted function passes exactly through the data points. For intermediate λ (panels c–d), the function is smoother and more similar to the ground truth. For large λ (panels e–f), the fitted function is smoother than the ground truth, so the fit is worse.

9.2 Implicit regularization

An intriguing recent finding is that neither gradient descent nor stochastic gradient descent moves neutrally to the minimum of the loss function; each exhibits a preference for some solutions over others. This is known as *implicit regularization*.

9.2.1 Implicit regularization in gradient descent

Consider a continuous version of gradient descent where the step size is infinitesimal. The change in parameters $\boldsymbol{\phi}$ will be governed by the differential equation:

$$\frac{\partial \boldsymbol{\phi}}{\partial t} = -\frac{\partial L}{\partial \boldsymbol{\phi}}. \tag{9.6}$$

Gradient descent approximates this process with a series of discrete steps of size α:

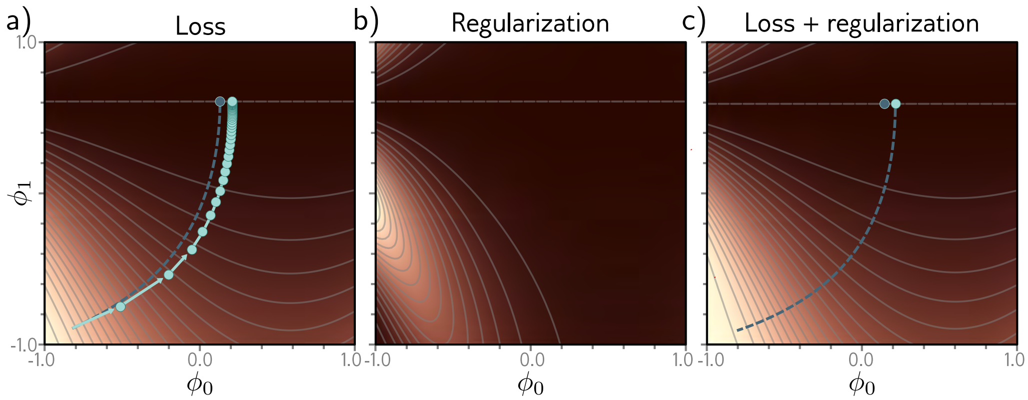

Figure 9.3 Implicit regularization in gradient descent. a) Loss function with family of global minima on horizontal line $\phi_1 = 0.61$. Dashed blue line shows continuous gradient descent path starting in bottom-left. Cyan trajectory shows discrete gradient descent with step size 0.1 (first few steps shown explicitly as arrows). The finite step size causes the paths to diverge and reach a different final position. b) This disparity can be approximated by adding a regularization term to the continuous gradient descent loss function that penalizes the squared gradient magnitude. c) After adding this term, the continuous gradient descent path converges to the same place that the discrete one did on the original function.

$$\boldsymbol{\phi}_{t+1} = \boldsymbol{\phi}_t - \alpha \frac{\partial L[\boldsymbol{\phi}_t]}{\partial \boldsymbol{\phi}}, \tag{9.7}$$

The discretization causes a deviation from the continuous path (figure 9.3).

This deviation can be understood by deriving a modified loss term $\tilde{L}$ for the continuous case that arrives at the same place as the discretized version on the original loss L. It can be shown (see end of chapter) that this modified loss is:

$$\tilde{\mathrm{L}}_{GD}[\boldsymbol{\phi}] = \mathrm{L}[\boldsymbol{\phi}] + \frac{\alpha}{4} \left\| \frac{\partial L}{\partial \boldsymbol{\phi}} \right\|^2. \tag{9.8}$$

In other words, the discrete trajectory is repelled from places where the gradient norm is large (the surface is steep). This doesn't change the position of the minima (where the gradients are zero) but changes the effective loss function elsewhere and modifies the optimization trajectory, which potentially converges to a different minimum. Implicit regularization due to gradient descent may be responsible for the observation that full batch gradient descent generalizes better with larger step sizes (figure 9.5a).

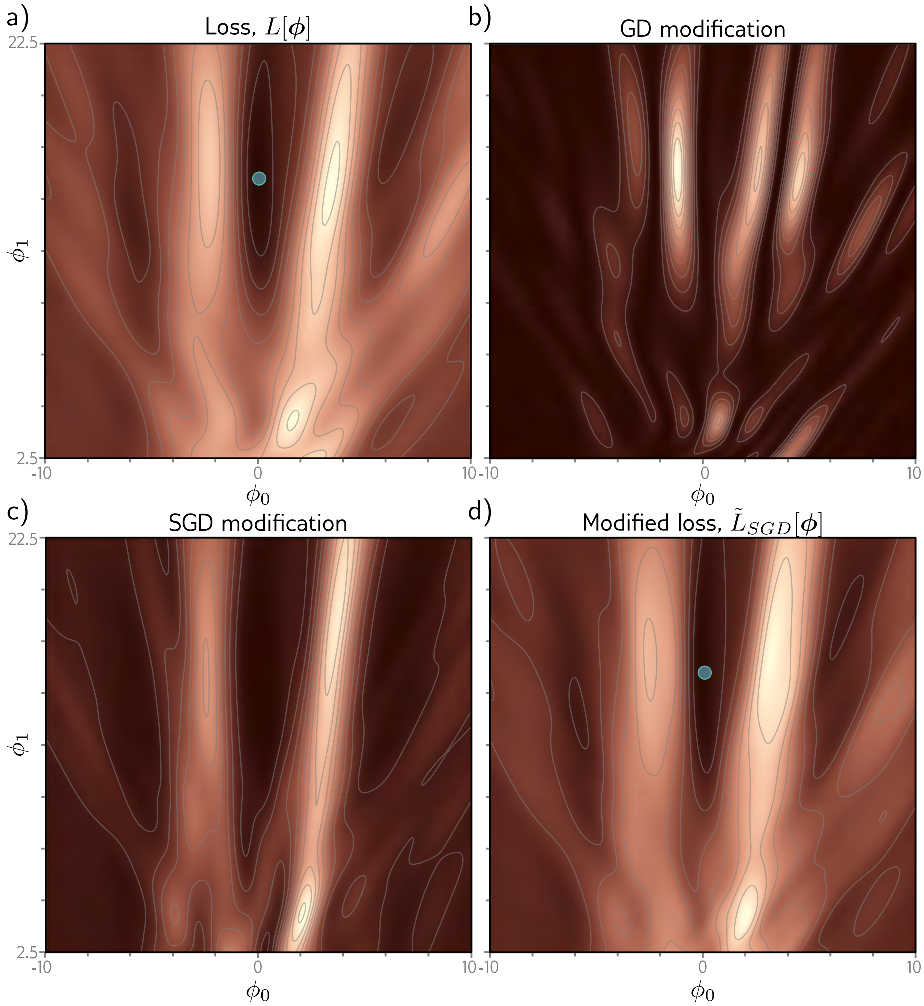

Figure 9.4 Implicit regularization for stochastic gradient descent. a) Original loss function for Gabor model (section 6.1.2). b) Implicit regularization term from gradient descent penalizes the squared gradient magnitude. c) Additional implicit regularization from stochastic gradient descent penalizes the variance of the batch gradients. d) Modified loss function (sum of original loss plus two implicit regularization components).

9.2.2 Implicit regularization in stochastic gradient descent

A similar analysis can be applied to stochastic gradient descent. Now we seek a modified loss function such that the continuous version reaches the same place as the average of the possible random SGD updates. This can be shown to be:

$$\begin{aligned}\tilde{\mathrm{L}}_{SGD}[\boldsymbol{\phi}] &= \tilde{\mathrm{L}}_{GD}[\boldsymbol{\phi}] + \frac{\alpha}{4B}\sum_{b=1}^{B}\left\|\frac{\partial L_b}{\partial \boldsymbol{\phi}} - \frac{\partial L}{\partial \boldsymbol{\phi}}\right\|^2 \\ &= \mathrm{L}[\boldsymbol{\phi}] + \frac{\alpha}{4}\left\|\frac{\partial L}{\partial \boldsymbol{\phi}}\right\|^2 + \frac{\alpha}{4B}\sum_{b=1}^{B}\left\|\frac{\partial L_b}{\partial \boldsymbol{\phi}} - \frac{\partial L}{\partial \boldsymbol{\phi}}\right\|^2. \end{aligned} \tag{9.9}$$

Here, L_b is the loss for the b^{th} of the B batches in an epoch, and both L and L_b now represent the means of the I individual losses in the full dataset and the $|\mathcal{B}|$ individual losses in the batch, respectively:

$$L = \frac{1}{I}\sum_{i=1}^{I}\ell_i[\mathbf{x}_i, y_i] \qquad \text{and} \qquad L_b = \frac{1}{|\mathcal{B}|}\sum_{i\in\mathcal{B}_b}\ell_i[\mathbf{x}_i, y_i]. \tag{9.10}$$

Equation 9.9 reveals an extra regularization term, which corresponds to the variance of the gradients of the batch losses L_b. In other words, SGD implicitly favors places where the gradients are stable (where all the batches agree on the slope). Once more, this modifies the trajectory of the optimization process (figure 9.4) but does not necessarily change the position of the global minimum; if the model is over-parameterized, then it may fit all the training data exactly, so *all* of these gradient terms will all be zero at the global minimum.

Notebook 9.2 Implicit regularization

SGD generalizes better than gradient descent, and smaller batch sizes usually perform better than larger ones (figure 9.5b). One possible explanation is that the inherent randomness allows the algorithm to reach different parts of the loss function. However, it's also possible that some or all of this performance increase is due to implicit regularization; this encourages solutions where all the data fits well (so the batch variance is small) rather than solutions where some of the data fit extremely well and other data less well (perhaps with the same overall loss, but with larger batch variance). The former solutions are likely to generalize better.

9.3 Heuristics to improve performance

We've seen that adding explicit regularization terms encourages the training algorithm to find a good solution by adding extra terms to the loss function. This also occurs implicitly as an unintended (but seemingly helpful) byproduct of stochastic gradient descent. This section describes other heuristic methods used to improve generalization.

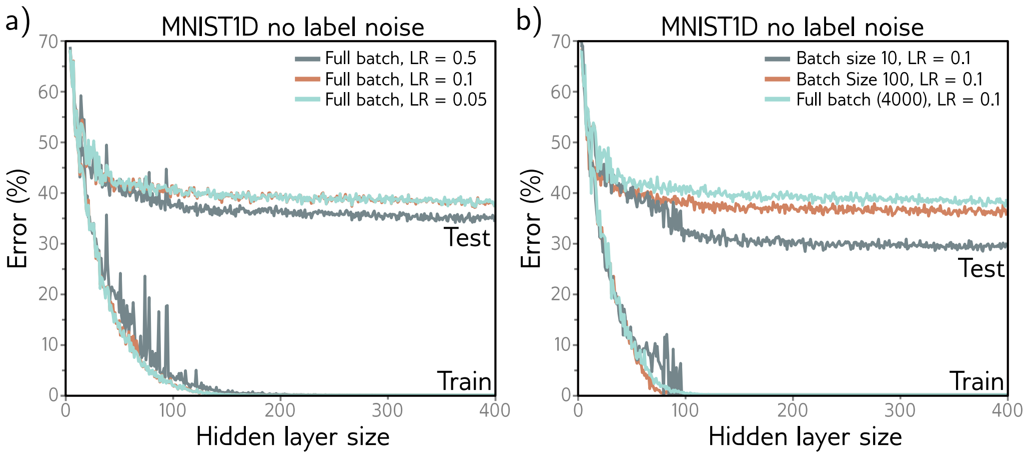

Figure 9.5 Effect of learning rate and batch size for 4000 training and 4000 test examples from MNIST-1D (see figure 8.1) for a neural network with two hidden layers. a) Performance is better for large learning rates than for intermediate or small ones. In each case, the number of iterations is 6000× the learning rate, so each solution has the opportunity to move the same distance. b) Performance is superior for smaller batch sizes. In each case, the number of iterations was chosen so that the training data were memorized at roughly the same model capacity.

9.3.1 Early stopping

Early stopping refers to stopping the training procedure before it has fully converged. This can reduce overfitting if the model has already captured the coarse shape of the underlying function but has not yet had time to overfit to the noise (figure 9.6). One way of thinking about this is that since the weights are initialized to small values (see section 7.5), they simply don't have time to become large, so early stopping has a similar effect to explicit L2 regularization. A different view is that early stopping reduces the effective model complexity. Hence, we move back down the bias/variance trade-off curve from the critical region, and performance improves (see figures 8.9 and 8.10).

Early stopping has a single hyperparameter, the number of steps after which learning is terminated. As usual, this is chosen empirically using a validation set (section 8.5). However, for early stopping, the hyperparameter can be selected without the need to train multiple models. The model is trained once, the performance on the validation set is monitored every T iterations, and the associated models are stored. The stored model where the validation performance was best is selected.

9.3.2 Ensembling

Another approach to reducing the generalization gap between training and test data is to build several models and average their predictions. A group of such models is known

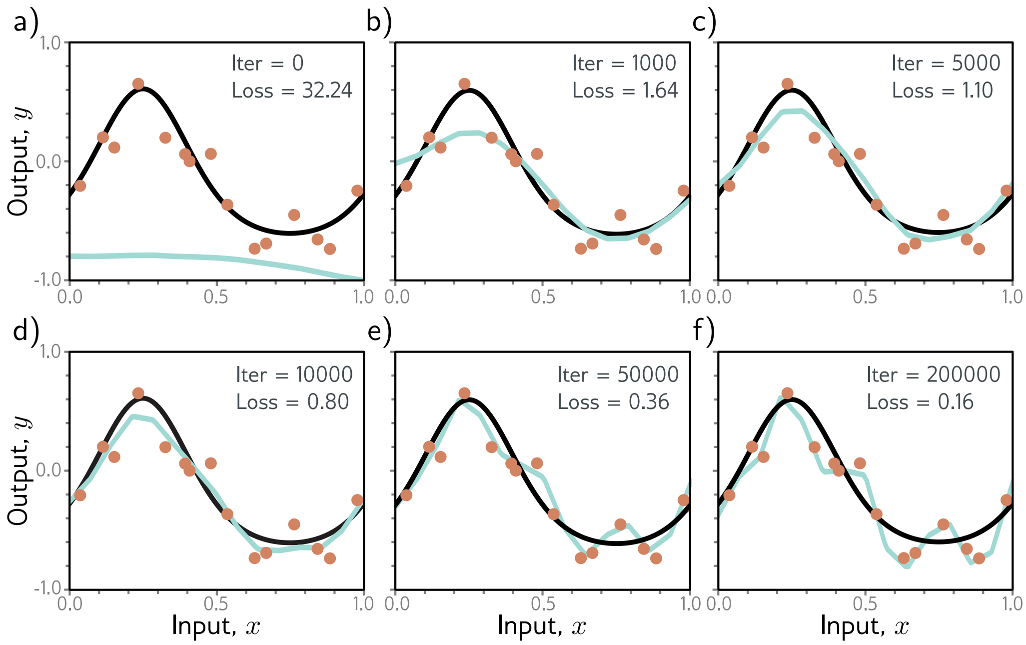

Figure 9.6 Early stopping. a) Simplified shallow network model with 14 linear regions (figure 8.4) is initialized randomly (cyan curve) and trained with SGD using a batch size of five and a learning rate of 0.05. b–d) As training proceeds, the function first captures the coarse structure of the true function (black curve) before e–f) overfitting to the noisy training data (orange points). Although the training loss continues to decrease throughout this process, the learned models in panels (c) and (d) are closest to the true underlying function. They will generalize better on average to test data than those in panels (e) or (f).

as an *ensemble*. This technique reliably improves test performance at the cost of training and storing multiple models and performing inference multiple times.

The models can be combined by taking the mean of the outputs (for regression problems) or the mean of the pre-softmax activations (for classification problems). The assumption is that model errors are independent and will cancel out. Alternatively, we can take the median of the outputs (for regression problems) or the most frequent predicted class (for classification problems) to make the predictions more robust.

Notebook 9.3 Ensembling

One way to train different models is just to use different random initializations. This may help in regions of input space far from the training data. Here, the fitted function is relatively unconstrained, and different models may produce different predictions, so the average of several models may generalize better than any single model.

A second approach is to generate several different datasets by re-sampling the training data with replacement and training a different model from each. This is known as *bootstrap aggregating* or *bagging* for short (figure 9.7). It has the effect of smoothing out the data; if a data point is not present in one training set, the model will interpo-

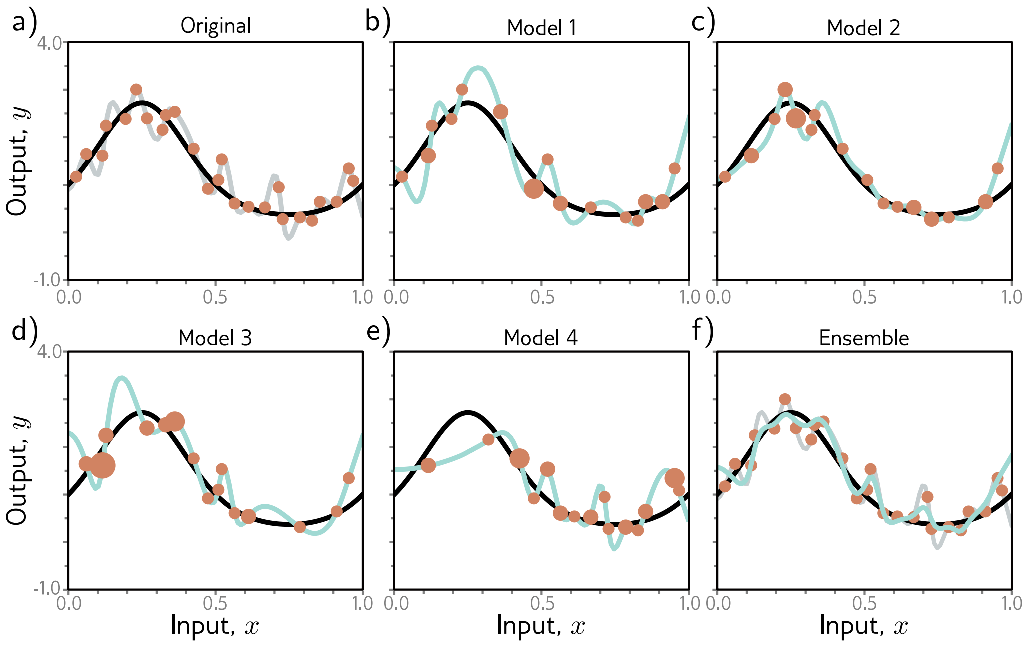

Figure 9.7 Ensemble methods. a) Fitting a single model (gray curve) to the entire dataset (orange points). b–e) Four models created by re-sampling the data with replacement (bagging) four times (size of orange point indicates number of times the data point was re-sampled). f) When we average the predictions of this ensemble, the result (cyan curve) is smoother than the result from panel (a) for the full dataset (gray curve) and will probably generalize better.

late from nearby points; hence, if that point was an outlier, the fitted function will be more moderate in this region. Other approaches include training models with different hyperparameters or training completely different families of models.

9.3.3 Dropout

Dropout randomly clamps a subset (typically 50%) of hidden units to zero at each iteration of SGD (figure 9.8). This makes the network less dependent on any given hidden unit and encourages the weights to have smaller magnitudes so that the change in the function due to the presence or absence of the hidden unit is reduced.

This technique has the positive benefit that it can eliminate undesirable "kinks" in the function that are far from the training data and don't affect the loss. For example, consider three hidden units that become active sequentially as we move along the curve (figure 9.9a). The first hidden unit causes a large increase in the slope. A second hidden

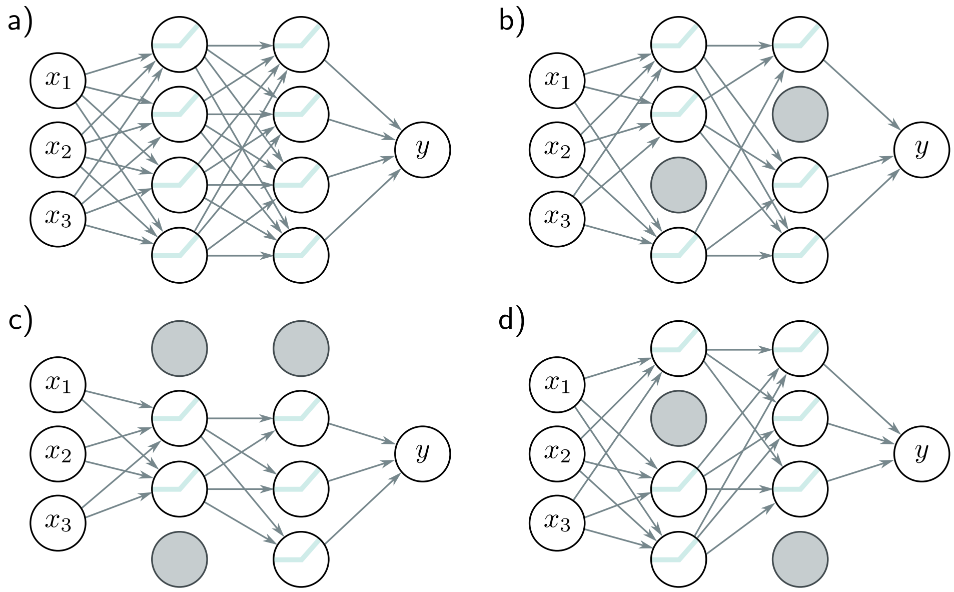

Figure 9.8 Dropout. a) Original network. b–d) At each training iteration, a random subset of hidden units is clamped to zero (gray nodes). The result is that the incoming and outgoing weights from these units have no effect, so we are training with a slightly different network each time.

unit decreases the slope, so the function goes back down. Finally, the third unit cancels out this decrease and returns the curve to its original trajectory. These three units conspire to make an undesirable local change in the function. This will not change the training loss but is unlikely to generalize well.

When several units conspire in this way, eliminating one (as would happen in dropout) causes a considerable change to the output function that is propagated to the half-space where that unit was active (figure 9.9b). A subsequent gradient descent step will attempt to compensate for the change that this induces, and such dependencies will be eliminated over time. The overall effect is that large unnecessary changes between training data points are gradually removed even though they contribute nothing to the loss (figure 9.9).

At test time, we can run the network as usual with all the hidden units active; however, the network now has more hidden units than it was trained with at any given iteration, so we multiply the weights by one minus the dropout probability to compensate. This is known as the *weight scaling inference rule*. A different approach to inference is to use *Monte Carlo dropout*, in which we run the network multiple times with different random subsets of units clamped to zero (as in training) and combine the results. This is closely related to ensembling in that every random version of the network is a different model; however, we do not have to train or store multiple networks here.

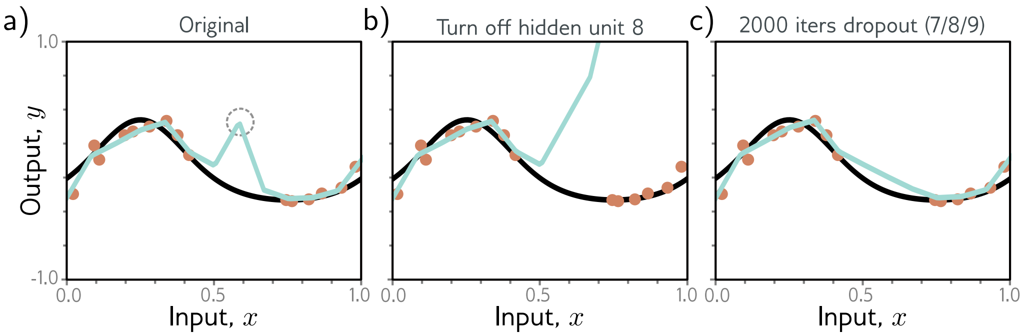

Figure 9.9 Dropout mechanism. a) An undesirable kink in the curve is caused by a sequential increase in the slope, decrease in the slope (at circled joint), and then another increase to return the curve to its original trajectory. Here we are using full-batch gradient descent, and the model already fits the data as well as possible, so further training won't remove the kink. b) Consider what happens if we remove the hidden unit that produced the circled joint in panel (a), as might happen using dropout. Without the decrease in the slope, the right-hand side of the function takes an upwards trajectory, and a subsequent gradient descent step will aim to compensate for this change. c) Curve after 2000 iterations of (i) randomly removing one of the three hidden units that cause the kink and (ii) performing a gradient descent step. The kink does not affect the loss but is nonetheless removed by this approximation of the dropout mechanism.

9.3.4 Applying noise

Dropout can be interpreted as applying multiplicative Bernoulli noise to the network activations. This leads to the idea of applying noise to other parts of the network during training to make the final model more robust.

One option is to add noise to the input data; this smooths out the learned function (figure 9.10). For regression problems, it can be shown to be equivalent to adding a regularizing term that penalizes the derivatives of the network's output with respect to its input. An extreme variant is *adversarial training*, in which the optimization algorithm actively searches for small perturbations of the input that cause large changes to the output. These can be thought of as worst-case additive noise vectors. Problem 9.3

A second possibility is to add noise to the weights. This encourages the network to make sensible predictions even for small perturbations of the weights. The result is that the training converges to local minima in the middle of wide, flat regions, where changing the individual weights does not matter much.

Finally, we can perturb the labels. The maximum-likelihood criterion for multi-class classification aims to predict the correct class with absolute certainty (equation 5.24). To this end, the final network activations (i.e., before the softmax function) are pushed to very large values for the correct class and very small values for the wrong classes.

We could discourage this overconfident behavior by assuming that a proportion ρ of

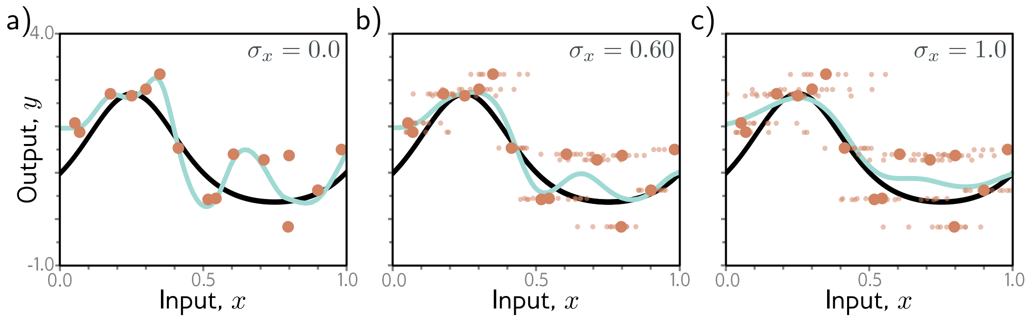

Figure 9.10 Adding noise to inputs. At each step of SGD, random noise with variance σ_x^2 is added to the batch data. a–c) Fitted model with different noise levels (small dots represent ten samples). Adding more noise smooths out the fitted function (cyan line).

the training labels are incorrect and belong with equal probability to the other classes. This could be done by randomly changing the labels at each training iteration. However, the same end can be achieved by changing the loss function to minimize the cross-entropy between the predicted distribution and a distribution where the true label has probability $1-\rho$, and the other classes have equal probability. This is known as *label smoothing* and improves generalization in diverse scenarios.

Problem 9.4

9.3.5 Bayesian inference

The maximum likelihood approach is generally overconfident; in the training phase, it selects the most likely parameters and bases its predictions on the model defined by these. However, many parameter values may be broadly compatible with the data and only slightly less likely. The Bayesian approach treats the parameters as unknown variables and computes a distribution $Pr(\boldsymbol{\phi}|\{\mathbf{x}_i, \mathbf{y}_i\})$ over these parameters $\boldsymbol{\phi}$ conditioned on the training data $\{\mathbf{x}_i, \mathbf{y}_i\}$ using Bayes' rule:

Appendix B.1.4 Bayes' rule

$$Pr(\boldsymbol{\phi}|\{\mathbf{x}_i, \mathbf{y}_i\}) = \frac{\prod_{i=1}^{I} Pr(\mathbf{y}_i|\mathbf{x}_i, \boldsymbol{\phi})Pr(\boldsymbol{\phi})}{\int \prod_{i=1}^{I} Pr(\mathbf{y}_i|\mathbf{x}_i, \boldsymbol{\phi})Pr(\boldsymbol{\phi})d\boldsymbol{\phi}}, \tag{9.11}$$

where $Pr(\boldsymbol{\phi})$ is the prior probability of the parameters, and the denominator is a normalizing term. Hence, every parameter choice is assigned a probability (figure 9.11).

The prediction $\mathbf{y}$ for new input $\mathbf{x}$ is an infinite weighted sum (i.e., an integral) of the predictions for each parameter set, where the weights are the associated probabilities:

$$Pr(\mathbf{y}|\mathbf{x}, \{\mathbf{x}_i, \mathbf{y}_i\}) = \int Pr(\mathbf{y}|\mathbf{x}, \boldsymbol{\phi})Pr(\boldsymbol{\phi}|\{\mathbf{x}_i, \mathbf{y}_i\})d\boldsymbol{\phi}. \tag{9.12}$$

This is effectively an infinite weighted ensemble, where the weight depends on (i) the prior probability of the parameters and (ii) their agreement with the data.

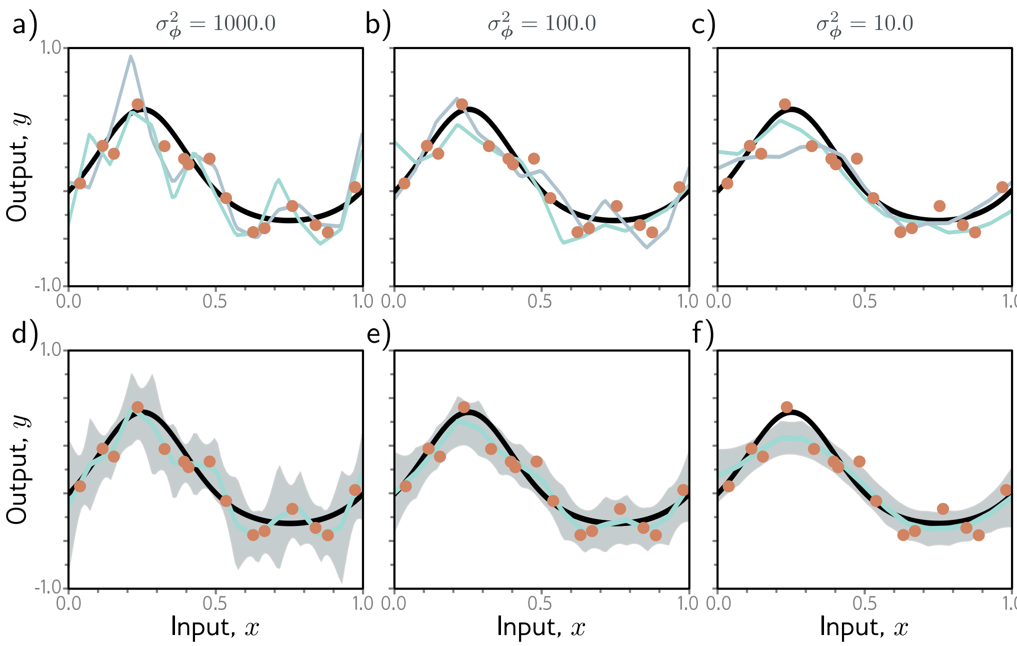

Figure 9.11 Bayesian approach for simplified network model (see figure 8.4). The parameters are treated as uncertain. The posterior probability $Pr(\boldsymbol{\phi}|\{\mathbf{x}_i, \mathbf{y}_i\})$ for a set of parameters is determined by their compatibility with the data $\{\mathbf{x}_i, \mathbf{y}_i\}$ and a prior distribution $Pr(\boldsymbol{\phi})$. a–c) Two sets of parameters (cyan curves) sampled from the posterior using normally distributed priors with mean zero and three variances. When the prior variance is small, the parameters also tend to be small, and the functions smoother. d–f) Inference proceeds by taking a weighted sum over all possible parameter values where the weights are the posterior probabilities. This produces both a prediction of the mean (cyan curves) and the associated uncertainty (gray region is two standard deviations).

The Bayesian approach is elegant and can provide more robust predictions than those that derive from maximum likelihood. Unfortunately, for complex models like neural networks, there is no practical way to represent the full probability distribution over the parameters or to integrate over it during the inference phase. Consequently, all current methods of this type make approximations of some kind, and typically these add considerable complexity to learning and inference.

Notebook 9.4 Bayesian approach

9.3.6 Transfer learning and multi-task learning

When training data is limited, other datasets can be exploited to improve performance. In *transfer learning* (figure 9.12a), the network is trained to perform a related secondary task for which data are more plentiful. The resulting model is subsequently adapted to the original task. This is typically done by removing the last layer and adding one or more layers that produce a suitable output. The main model may be fixed and the new layers trained for the original task, or we may *fine-tune* the entire model.

The principle is that the network will build a good internal representation of the data from the secondary task, which can subsequently be exploited for the original task. Equivalently, transfer learning can be viewed as initializing most of the parameters of the final network in a sensible part of the space that is likely to produce a good solution.

Multi-task learning (figure 9.12b) is a related technique in which the network is trained to solve several problems concurrently. For example, the network might take an image and simultaneously learn to segment the scene, estimate the pixel-wise depth, and predict a caption describing the image. All of these tasks require some understanding of the image and when learned simultaneously, the model performance for each may improve.

9.3.7 Self-supervised learning

The above discussion assumes that we have plentiful data for a secondary task or data for multiple tasks to be learned concurrently. If not, we can create large amounts of "free" labeled data using *self-supervised* learning and use this for transfer learning. There are two families of methods for self-supervised learning: *generative* and *contrastive*.

In generative self-supervised learning, part of each data example is masked, and the secondary task is to predict the missing part (figure 9.12c). For example, we might use a corpus of unlabeled images and a secondary task that aims to *inpaint* (fill in) missing parts of the image (figure 9.12c). Similarly, we might use a large corpus of text and mask some words. We train the network to predict the missing words and then fine-tune it for the actual language task we are interested in (see chapter 12).

In contrastive self-supervised learning, two versions of each unlabeled example are presented, where one has been distorted in some way. The system is trained to predict which is the original. For example, we might use a corpus of unlabeled images where the secondary task is to identify which version of the image is upside-down. Similarly, we might use a large corpus of text, where the secondary task is to determine whether two sentences followed one another or not in the original text.

9.3.8 Augmentation

Transfer learning improves performance by exploiting a different dataset. Multi-task learning improves performance using additional labels. A third option is to expand the dataset. We can often transform each input data example in such a way that the label stays the same. For example, we might aim to determine if there is a bird in an image (figure 9.13). Here, we could rotate, flip, blur, or manipulate the color balance of the image, and the label "bird" remains valid. Similarly, for tasks where the input is text, we can substitute synonyms or translate to another language and back again. For tasks where the input is audio, we can amplify or attenuate different frequency bands.

Notebook 9.5
Augmentation

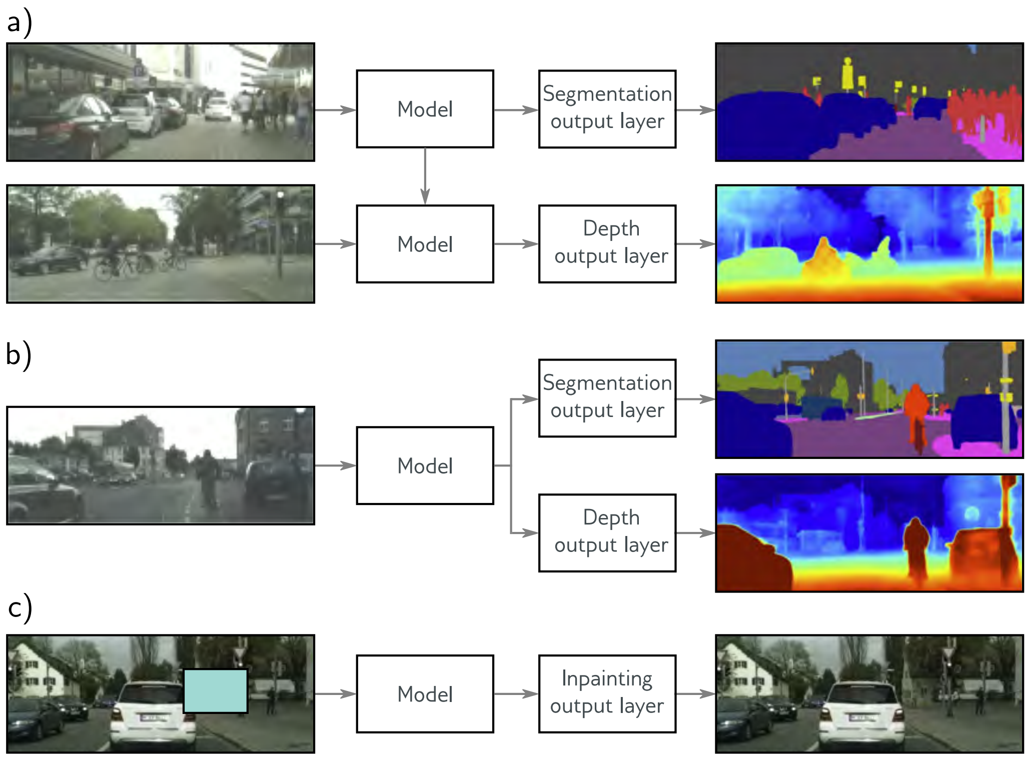

Figure 9.12 Transfer, multi-task, and self-supervised learning. a) Transfer learning is used when we have limited labeled data for the primary task (here depth estimation) but plentiful data for a secondary task (here segmentation). We train a model for the secondary task, remove the final layers, and replace them with new layers appropriate to the primary task. We then train only the new layers or fine-tune the entire network for the primary task. The network learns a good internal representation from the secondary task that is then exploited for the primary task. b) In multi-task learning, we train a model to perform multiple tasks simultaneously, hoping that performance on each will improve. c) In generative self-supervised learning, we remove part of the data and train the network to complete the missing information. Here, the task is to fill in (inpaint) a masked portion of the image. This permits transfer learning when no labels are available. Images from Cordts et al. (2016).

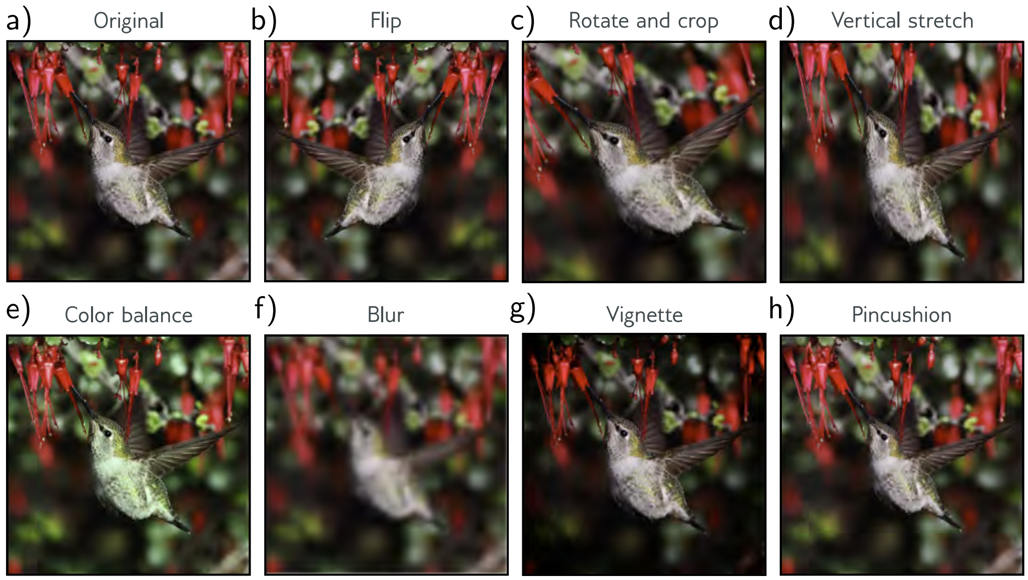

Figure 9.13 Data augmentation. For some problems, each data example can be transformed to augment the dataset. a) Original image. b–h) Various geometric and photometric transformations of this image. For image classification, all these images still have the same label, "bird." Adapted from Wu et al. (2015a).

Generating extra training data in this way is known as *data augmentation*. The aim is to teach the model to be indifferent to these irrelevant data transformations.

9.4 Summary

Explicit regularization involves adding an extra term to the loss function that changes the position of the minimum. The term can be interpreted as a prior probability over the parameters. Stochastic gradient descent with a finite step size does not neutrally descend to the minimum of the loss function. This bias can be interpreted as adding additional terms to the loss function, and this is known as implicit regularization.

There are also many heuristics for improving generalization, including early stopping, dropout, ensembling, the Bayesian approach, adding noise, transfer learning, multi-task learning, and data augmentation. There are four main principles behind these methods (figure 9.14). We can (i) encourage the function to be smoother (e.g., L2 regularization), (ii) increase the amount of data (e.g., data augmentation), (iii) combine models (e.g., ensembling), or (iv) search for wider minima (e.g., applying noise to network weights).

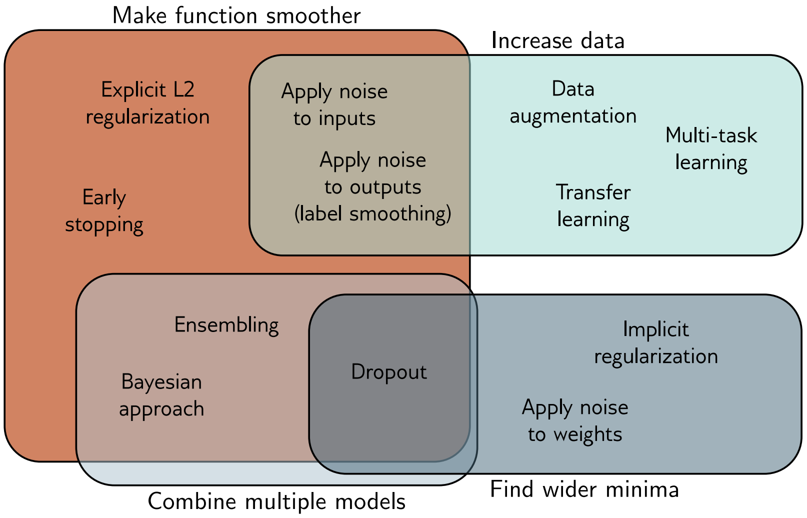

Figure 9.14 Regularization methods. The regularization methods discussed in this chapter aim to improve generalization by one of four mechanisms. Some methods aim to make the modeled function smoother. Other methods increase the effective amount of data. The third group of methods combine multiple models and hence mitigate against uncertainty in the fitting process. Finally, the fourth group of methods encourages the training process to converge to a wide minimum where small errors in the estimated parameters are less important (see also figure 20.11).

Another way to improve generalization is to choose the model architecture to suit the task. For example, in image segmentation, we can share parameters within the model, so we don't need to independently learn what a tree looks like at every image location. Chapters 10–13 consider architectural variations designed for different tasks.

Notes

An overview and taxonomy of regularization techniques in deep learning can be found in Kukačka et al. (2017). Notably missing from the discussion in this chapter is BatchNorm (Szegedy et al., 2016) at its variants, which are described in chapter 11.

Regularization: L2 regularization penalizes the sum of squares of the network weights. This encourages the output function to change slowly (i.e., become smoother) and is the most used regularization term. It is sometimes referred to as Frobenius norm regularization as it penalizes the Frobenius norms of the weight matrices. It is often also mistakenly referred to as "weight decay" although this is a separate technique devised by Hanson & Pratt (1988) in which the parameters $\boldsymbol{\phi}$ are updated as:

$$\boldsymbol{\phi} \longleftarrow (1-\lambda')\boldsymbol{\phi} - \alpha\frac{\partial L}{\partial \boldsymbol{\phi}}, \tag{9.13}$$

where, as usual, α is the learning rate, and L is the loss. This is identical to gradient descent, except that the weights are reduced by a factor of $1-\lambda'$ before the gradient update. For standard SGD, weight decay is equivalent to L2 regularization (equation 9.5) with coefficient $\lambda = \lambda'/2\alpha$. However, for Adam the learning rate α is different for each parameter, so L2 regularization and weight decay differ. Loshchilov & Hutter (2019) present AdamW, which modifies Adam to implement weight decay correctly and show that this improves performance.

Problem 9.5

Other choices of vector norm encourage sparsity in the weights. The L0 regularization term applies a fixed penalty for every non-zero weight. The effect is to "prune" the network. L0 regularization can also be used to encourage group sparsity; this might apply a fixed penalty if any of the weights contributing to a given hidden unit are non-zero. If they are all zero, we can remove the unit, decreasing the model size, and making inference faster.

Appendix C.5.6 Vector norms

Unfortunately, L0 regularization is challenging to implement since the derivative of the regularization term is not smooth, and more sophisticated fitting methods are required (see Louizos et al., 2018). Somewhere between L2 and L0 regularization is L1 regularization or *LASSO* (least absolute shrinkage and selection operator), which imposes a penalty on the absolute values of the weights. L2 regularization somewhat discourages sparsity in that the derivative of the squared penalty decreases as the weight becomes smaller, lowering the pressure to make it smaller still. L1 regularization does not have this disadvantage as the derivative of the penalty is constant. This can produce sparser solutions than L2 regularization but is much easier to optimize than L0 regularization. Sometimes both L1 and L2 regularization terms are used, which is termed an *elastic net* penalty (Zou & Hastie, 2005).

Problem 9.6

A different approach to regularization is to modify the gradients of the learning algorithm without ever explicitly formulating a new loss function (e.g., equation 9.13). This approach has been used to promote sparsity during backpropagation (Schwarz et al., 2021).

The evidence on the effectiveness of explicit regularization is mixed. Zhang et al. (2017a) showed that L2 regularization contributes little to generalization. It has been proven that the Lipschitz constant of the network (how fast the function can change as we modify the input) bounds the generalization error (Bartlett et al., 2017; Neyshabur et al., 2018). However, the Lipschitz constant depends on the product of the spectral norms of the weight matrices $\mathbf{\Omega}_k$, which are only indirectly dependent on the magnitudes of the individual weights. Bartlett et al. (2017), Neyshabur et al. (2018), and Yoshida & Miyato (2017) all add terms that indirectly encourage the spectral norms to be smaller. Gouk et al. (2021) take a different approach and develop an algorithm that constrains the Lipschitz constant of the network to be below a particular value.

Appendix C.2 Lipschitz constant

Appendix C.5.6 Spectral norm

Implicit regularization in gradient descent: The gradient descent step is:

$$\boldsymbol{\phi}_1 = \boldsymbol{\phi}_0 + \alpha \cdot \mathbf{g}[\boldsymbol{\phi}_0], \tag{9.14}$$

where $\mathbf{g}[\boldsymbol{\phi}_0]$ is the negative of the gradient of the loss function and α is the step size. As $\alpha \to 0$, the gradient descent process can be described by a differential equation:

$$\frac{\partial \boldsymbol{\phi}}{\partial t} = \mathbf{g}[\boldsymbol{\phi}]. \tag{9.15}$$

For typical step sizes α, the discrete and continuous versions converge to different solutions. We can use *backward error analysis* to find a correction $\mathbf{g}_1[\boldsymbol{\phi}]$ to the continuous version:

$$\frac{\partial \boldsymbol{\phi}}{\partial t} \approx \mathbf{g}[\boldsymbol{\phi}] + \alpha \mathbf{g}_1[\boldsymbol{\phi}] + \ldots, \tag{9.16}$$

so that it gives the same result as the discrete version.

Consider the first two terms of a Taylor expansion of the modified continuous solution $\boldsymbol{\phi}$ around initial position $\boldsymbol{\phi}_0$:

$$\begin{aligned}
\boldsymbol{\phi}[\alpha] &\approx \boldsymbol{\phi} + \alpha\frac{\partial \boldsymbol{\phi}}{\partial t} + \frac{\alpha^2}{2}\frac{\partial^2 \boldsymbol{\phi}}{\partial t^2}\bigg|_{\boldsymbol{\phi}=\boldsymbol{\phi}_0} \\
&\approx \boldsymbol{\phi} + \alpha\left(\mathbf{g}[\boldsymbol{\phi}] + \alpha\mathbf{g}_1[\boldsymbol{\phi}]\right) + \frac{\alpha^2}{2}\left(\frac{\partial \mathbf{g}[\boldsymbol{\phi}]}{\partial \boldsymbol{\phi}}\frac{\partial \boldsymbol{\phi}}{\partial t} + \alpha\frac{\partial \mathbf{g}_1[\boldsymbol{\phi}]}{\partial \boldsymbol{\phi}}\frac{\partial \boldsymbol{\phi}}{\partial t}\right)\bigg|_{\boldsymbol{\phi}=\boldsymbol{\phi}_0} \\
&= \boldsymbol{\phi} + \alpha\left(\mathbf{g}[\boldsymbol{\phi}] + \alpha\mathbf{g}_1[\boldsymbol{\phi}]\right) + \frac{\alpha^2}{2}\left(\frac{\partial \mathbf{g}[\boldsymbol{\phi}]}{\partial \boldsymbol{\phi}}\mathbf{g}[\boldsymbol{\phi}] + \alpha\frac{\partial \mathbf{g}_1[\boldsymbol{\phi}]}{\partial \boldsymbol{\phi}}\mathbf{g}[\boldsymbol{\phi}]\right)\bigg|_{\boldsymbol{\phi}=\boldsymbol{\phi}_0} \\
&\approx \boldsymbol{\phi} + \alpha\mathbf{g}[\boldsymbol{\phi}] + \alpha^2\left(\mathbf{g}_1[\boldsymbol{\phi}] + \frac{1}{2}\frac{\partial \mathbf{g}[\boldsymbol{\phi}]}{\partial \boldsymbol{\phi}}\mathbf{g}[\boldsymbol{\phi}]\right)\bigg|_{\boldsymbol{\phi}=\boldsymbol{\phi}_0}, \qquad (9.17)
\end{aligned}$$

where in the second line, we have introduced the correction term (equation 9.16), and in the final line, we have removed terms of greater order than α^2.

Note that the first two terms on the right-hand side $\boldsymbol{\phi}_0 + \alpha\mathbf{g}[\boldsymbol{\phi}_0]$ are the same as the discrete update (equation 9.14). Hence, to make the continuous and discrete versions arrive at the same place, the second term on the right-hand side must equal zero, allowing us to solve for $\mathbf{g}_1[\boldsymbol{\phi}]$:

$$\mathbf{g}_1[\boldsymbol{\phi}] = -\frac{1}{2}\frac{\partial \mathbf{g}[\boldsymbol{\phi}]}{\partial \boldsymbol{\phi}}\mathbf{g}[\boldsymbol{\phi}]. \qquad (9.18)$$

During training, the evolution function $\mathbf{g}[\boldsymbol{\phi}]$ is the negative of the gradient of the loss:

$$\begin{aligned}
\frac{\partial \boldsymbol{\phi}}{\partial t} &\approx \mathbf{g}[\boldsymbol{\phi}] + \alpha\mathbf{g}_1[\boldsymbol{\phi}] \\
&= -\frac{\partial L}{\partial \boldsymbol{\phi}} - \frac{\alpha}{2}\left(\frac{\partial^2 L}{\partial \boldsymbol{\phi}^2}\right)\frac{\partial L}{\partial \boldsymbol{\phi}}. \qquad (9.19)
\end{aligned}$$

This is equivalent to performing continuous gradient descent on the loss function:

$$\mathrm{L}_{GD}[\boldsymbol{\phi}] = \mathrm{L}[\boldsymbol{\phi}] + \frac{\alpha}{4}\left\|\frac{\partial L}{\partial \boldsymbol{\phi}}\right\|^2, \qquad (9.20)$$

because the right-hand side of equation 9.19 is the derivative of that in equation 9.20.

This formulation of implicit regularization was developed by Barrett & Dherin (2021) and extended to stochastic gradient descent by Smith et al. (2021). Smith et al. (2020) and others have shown that stochastic gradient descent with small or moderate batch sizes outperforms full batch gradient descent on the test set, and this may in part be due to implicit regularization.

Early stopping: Bishop (1995) and Sjöberg & Ljung (1995) argued that early stopping limits the effective solution space that the training procedure can explore; given that the weights are initialized to small values, this leads to the idea that early stopping helps prevent the weights from getting too large. Goodfellow et al. (2016) show that under a quadratic approximation of the loss function with parameters initialized to zero, early stopping is equivalent to L2 regularization in gradient descent. The effective regularization weight λ is approximately $1/(\tau\alpha)$ where α is the learning rate, and τ is the early stopping time.

Ensembling: Ensembles can be trained using different random seeds (Lakshminarayanan et al., 2017), hyperparameters (Wenzel et al., 2020b), or even entirely different families of model. The models can be combined by averaging their predictions, weighting the predictions, or *stacking* (Wolpert, 1992), in which the results are combined using another machine learning model. Lakshminarayanan et al. (2017) showed that averaging the output of independently trained networks can improve accuracy, calibration, and robustness. Conversely, Frankle et al. (2020) showed that if we average together the weights to make one model, then the network fails. Fort et al. (2019) compared ensembling solutions that resulted from different initializations with ensembling solutions that were generated from the same original model. For example, in the latter case, they consider exploring around the solution in a limited subspace to find other good nearby points. They found that both techniques provide complementary benefits but that genuine ensembling from different random starting points provides a bigger improvement.

Appendix C.5.3 Subspaces

An efficient way of ensembling is to combine models from intermediate stages of training. To this end, Izmailov et al. (2018) introduce *stochastic weight averaging*, in which the model weights are sampled at different time steps and averaged together. As the name suggests, *snapshot ensembles* (Huang et al., 2017a) also store the models from different time steps and average their predictions. The diversity of these models can be improved by cyclically increasing and decreasing the learning rate. Garipov et al. (2018) observed that different minima of the loss function are often connected by a low-energy path (i.e., a path with a low loss everywhere along it). Motivated by this observation, they developed a method that explores low-energy regions around an initial solution to provide diverse models without retraining. This is known as *fast geometric ensembling*. A review of ensembling methods can be found in Ganaie et al. (2022).

Dropout: Dropout was first introduced by Hinton et al. (2012b) and Srivastava et al. (2014). Dropout is applied at the level of hidden units. Dropping a hidden unit has the same effect as temporarily setting all the incoming and outgoing weights and the bias to zero. Wan et al. (2013) generalized dropout by randomly setting individual weights to zero. Gal & Ghahramani (2016) and Kendall & Gal (2017) proposed Monte-Carlo dropout, in which inference is computed with several dropout patterns, and the results are averaged together. Gal & Ghahramani (2016) argued that this could be interpreted as approximating Bayesian inference.

Dropout is equivalent to applying multiplicative Bernoulli noise to the hidden units. Similar benefits derive from using other noise distributions, including the normal distribution (Srivastava et al., 2014; Shen et al., 2017), uniform distribution (Shen et al., 2017), and beta distribution (Liu et al., 2019b).

Adding noise: Bishop (1995) and An (1996) added Gaussian noise to the network inputs to improve performance. Bishop (1995) showed that this is equivalent to weight decay. An (1996) also investigated adding noise to the weights. DeVries & Taylor (2017a) added Gaussian noise to the hidden units. Xu et al. (2015) apply noise in a different way with the *randomized ReLU* by making the activation functions stochastic.

Finding wider minima: It is thought that wider minima generalize better (see figure 20.11). Here, the exact values of the weights are less important, so performance should be robust to errors in their estimates. One of the reasons that applying noise to parts of the network during training is effective is that it encourages the network to be indifferent to their exact values.

Chaudhari et al. (2019) developed a variant of SGD that biases the optimization toward flat minima, which they call *entropy SGD*. The idea is to incorporate local entropy as a term in the loss function. In practice, this takes the form of one SGD-like update within another. Keskar et al. (2017) showed that SGD finds wider minima as the batch size is reduced. This may be because of the batch variance term that results from implicit regularization by SGD.

Ishida et al. (2020) use a technique named *flooding*, in which they intentionally prevent the training loss from becoming zero. This encourages the solution to perform a random walk over the loss landscape and drift into a flatter area with better generalization.

Label smoothing: Label smoothing was introduced by Szegedy et al. (2016) for image classification but has since been shown to be helpful in speech recognition (Chorowski & Jaitly, 2017), machine translation (Vaswani et al., 2017), and language modeling (Pereyra et al., 2017). The precise mechanism by which label smoothing improves test performance isn't well understood, although Müller et al. (2019a) show that it improves the calibration of the predicted output probabilities. A closely related technique is *DisturbLabel* (Xie et al., 2016), in which a certain percentage of the labels in each batch are randomly switched at each training iteration.

Bayesian approaches: For some models, including the simplified neural network model in figure 9.11, the Bayesian predictive distribution can be computed in closed form (see Bishop, 2006; Prince, 2012). For neural networks, the posterior distribution over the parameters cannot be represented in closed form and must be approximated. The two main approaches are variational Bayes (Hinton & van Camp, 1993; MacKay, 1995; Barber & Bishop, 1997; Blundell et al., 2015), in which the posterior is approximated by a simpler tractable distribution, and Markov Chain Monte Carlo (MCMC) methods, which approximate the distribution by drawing a set of samples (Neal, 1995; Welling & Teh, 2011; Chen et al., 2014; Ma et al., 2015; Li et al., 2016a). The generation of samples can be integrated into SGD, and this is known as stochastic gradient MCMC (see Ma et al., 2015). It has recently been discovered that "cooling" the posterior distribution over the parameters (making it sharper) improves predictions from these models (Wenzel et al., 2020a), but this is not currently fully understood (see Noci et al., 2021).

Transfer learning: Transfer learning for visual tasks works extremely well (Sharif Razavian et al., 2014) and has supported rapid progress in computer vision, including the original AlexNet results (Krizhevsky et al., 2012). Transfer learning has also impacted natural language processing (NLP), where many models are based on pre-trained features from the BERT model (Devlin et al., 2019). More information can be found in Zhuang et al. (2020) and Yang et al. (2020b).

Self-supervised learning: Self-supervised learning techniques for images have included inpainting masked image regions (Pathak et al., 2016), predicting the relative position of patches in an image (Doersch et al., 2015), re-arranging permuted image tiles back into their original configuration (Noroozi & Favaro, 2016), colorizing grayscale images (Zhang et al., 2016b), and transforming rotated images back to their original orientation (Gidaris et al., 2018). In SimCLR (Chen et al., 2020c), a network is learned that maps versions of the same image that have been photometrically and geometrically transformed to the same representation while repelling versions of different images, with the goal of becoming indifferent to irrelevant image transformations. Jing & Tian (2020) present a survey of self-supervised learning in images.

Self-supervised learning in NLP can be based on predicting masked words(Devlin et al., 2019), or predicting the next word in a sentence (Radford et al., 2019; Brown et al., 2020), or predicting whether two sentences follow one another (Devlin et al., 2019). In automatic speech recognition, the Wav2Vec model (Schneider et al., 2019) aims to distinguish an original audio sample from one where 10ms of audio has been swapped out from elsewhere in the clip. Self-supervision has also been applied to graph neural networks (chapter 13). Tasks include recovering masked features (You et al., 2020) and recovering the adjacency structure of the graph (Kipf & Welling, 2016). Liu et al. (2023a) review self-supervised learning for graph models.

Data augmentation: Data augmentation for images dates back to at least LeCun et al. (1998) and contributed to the success of AlexNet (Krizhevsky et al., 2012), in which the dataset was increased by a factor of 2048. Image augmentation approaches include geometric transformations, changing or manipulating the color space, noise injection, and applying spatial filters. More elaborate techniques include randomly mixing images (Inoue, 2018; Summers & Dinneen, 2019), randomly erasing parts of the image (Zhong et al., 2020), style transfer (Jackson et al., 2019), and randomly swapping image patches (Kang et al., 2017). In addition, many studies have used generative adversarial networks or GANs (see chapter 15) to produce novel but plausible data examples (e.g., Calimeri et al., 2017). In other cases, the data have been augmented with adversarial examples (Goodfellow et al., 2015a), which are minor perturbations of the training data that cause the example to be misclassified. A review of data augmentation for images can be found in Shorten & Khoshgoftaar (2019).

Augmentation methods for acoustic data include pitch shifting, time stretching, dynamic range compression, and adding random noise (e.g., Abeßer et al., 2017; Salamon & Bello, 2017; Xu et al., 2015; Lasseck, 2018), as well as mixing data pairs (Zhang et al., 2017c; Yun et al., 2019), masking features (Park et al., 2019), and using GANs to generate new data (Mun et al., 2017). Augmentation for speech data includes vocal tract length perturbation (Jaitly & Hinton, 2013; Kanda et al., 2013), style transfer (Gales, 1998; Ye & Young, 2004), adding noise (Hannun et al., 2014), and synthesizing speech (Gales et al., 2009).

Augmentation methods for text include adding noise at a character level by switching, deleting, and inserting letters (Belinkov & Bisk, 2018; Feng et al., 2020), or by generating adversarial examples (Ebrahimi et al., 2018), using common spelling mistakes (Coulombe, 2018), randomly swapping or deleting words (Wei & Zou, 2019), using synonyms (Kolomiyets et al., 2011), altering adjectives (Li et al., 2017c), passivization (Min et al., 2020), using generative models to create new data (Qiu et al., 2020), and round-trip translation to another language and back(Aiken & Park, 2010). Augmentation methods for text are reviewed by Bayer et al. (2022).

Problems

Problem 9.1 Consider a model where the prior distribution over the parameters is a normal distribution with mean zero and variance $\sigma^2_{\boldsymbol{\phi}}$ so that

$$Pr(\boldsymbol{\phi}) = \prod_{j=1}^{J} \text{Norm}_{\phi_j}[0, \sigma^2_{\boldsymbol{\phi}}]. \tag{9.21}$$

where j indexes the model parameters. We now maximize $\prod_{i=1}^{I} Pr(\mathbf{y}_i|\mathbf{x}_i, \boldsymbol{\phi})Pr(\boldsymbol{\phi})$. Show that the associated loss function of this model is equivalent to L2 regularization.

Problem 9.2 How do the gradients of the loss function change when L2 regularization (equation 9.5) is added?

Problem 9.3* Consider a linear regression model $y = \phi_0 + \phi_1 x$ where x is the input, y is the output, and ϕ_0 and ϕ_1 are the intercept and slope parameters, respectively. Assume we have I training examples $\{x_i, y_i\}$ and use a least squares loss. Consider adding Gaussian noise with mean zero and variance σ^2_x to the inputs x_i at each training iteration. What is the expected gradient update?

Problem 9.4* Derive the loss function for multi-class classification when we use label smoothing so that the target probability distribution has 0.9 at the correct class and the remaining probability mass of 0.1 is divided between the remaining $D_o - 1$ classes.

Problem 9.5 Show that the weight decay parameter update with decay rate λ:

$$\boldsymbol{\phi} \longleftarrow (1-\lambda)\boldsymbol{\phi} - \alpha\frac{\partial L}{\partial \boldsymbol{\phi}}, \tag{9.22}$$

on the original loss function $\text{L}[\boldsymbol{\phi}]$ is equivalent to a standard gradient update using L2 regularization so that the modified loss function $\tilde{\text{L}}[\boldsymbol{\phi}]$ is:

$$\tilde{\text{L}}[\boldsymbol{\phi}] = \text{L}[\boldsymbol{\phi}] + \frac{\lambda}{2\alpha}\sum_k \phi_k^2, \tag{9.23}$$

where $\boldsymbol{\phi}$ are the parameters, and α is the learning rate.

Problem 9.6 Consider a model with parameters $\boldsymbol{\phi} = [\boldsymbol{\phi}_0, \boldsymbol{\phi}_1]^T$. Draw the L0, $\text{L}\frac{1}{2}$, and L1 regularization terms in a similar form to figure 9.1b. The LP regularization term is $\sum_{d=1}^{D} |\phi_d|^P$.

Chapter 10

Convolutional networks

Chapters 2–9 introduced the supervised learning pipeline for deep neural networks. However, these chapters only considered fully connected networks with a single path from input to output. Chapters 10–13 introduce more specialized network components with sparser connections, shared weights, and parallel processing paths. This chapter describes *convolutional layers*, which are mainly used for processing image data.

Images have three properties that suggest the need for a specialized architecture. First, they are high-dimensional. A typical image for a classification task contains 224×224 RGB values (i.e., 150,528 input dimensions). Hidden layers in fully connected networks are generally larger than the input size, so even for a shallow network, the number of weights would exceed $150,528^2$, or 22 billion. This poses obvious practical problems in terms of the required training data, memory, and computation.

Second, nearby image pixels are statistically related. However, fully connected networks have no notion of "nearby" and treat the relationship between every input equally. If the pixels of the training and test images were randomly permuted in the same way, the network could still be trained with no practical difference. Third, the interpretation of an image is stable under geometric transformations. An image of a tree is still an image of a tree if we shift it leftwards by a few pixels. However, this shift changes every input to the network. Hence, a fully connected model must learn the patterns of pixels that signify a tree separately at every position, which is clearly inefficient.

Convolutional layers process each local image region independently, using parameters shared across the whole image. They use fewer parameters than fully connected layers, exploit the spatial relationships between nearby pixels, and don't have to re-learn the interpretation of the pixels at every position. A network predominantly consisting of convolutional layers is known as a *convolutional neural network* or *CNN*.

10.1 Invariance and equivariance

We argued above that some properties of images (e.g., tree texture) are stable under transformations. In this section, we make this idea more mathematically precise. A

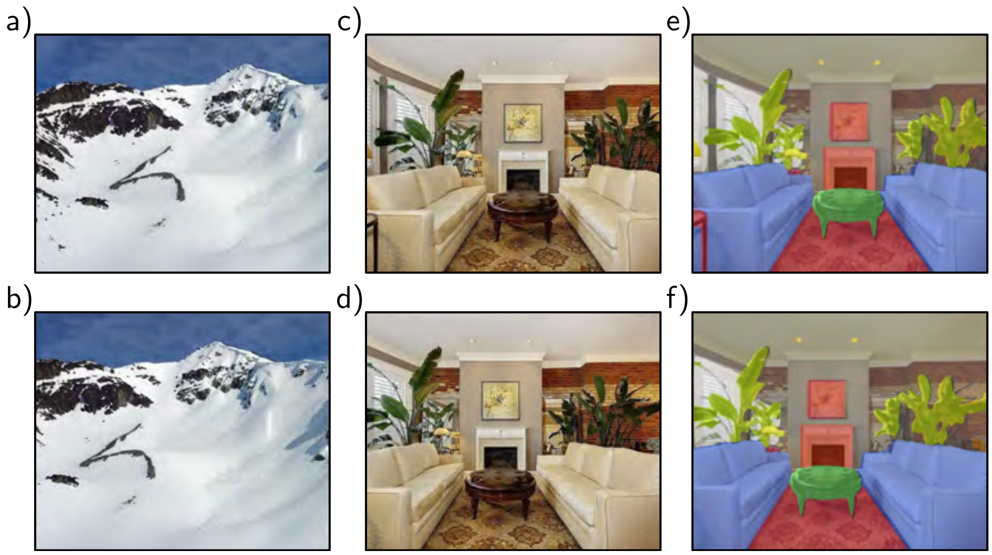

Figure 10.1 Invariance and equivariance for translation. a–b) In image classification, the goal is to categorize both images as "mountain" regardless of the horizontal shift that has occurred. In other words, we require the network prediction to be invariant to translation. c–d) The goal of semantic segmentation is to associate a label with each pixel. e–f) When the input image is translated, we want the output (colored overlay) to translate in the same way. In other words, we require the output to be equivariant with respect to translation. Panels c–f) adapted from Bousselham et al. (2021).

function $\mathrm{f}[\mathbf{x}]$ of an image $\mathbf{x}$ is *invariant* to a transformation $\mathbf{t}[\mathbf{x}]$ if:

$$\mathbf{f}\left[\mathbf{t}[\mathbf{x}]\right] = \mathbf{f}[\mathbf{x}]. \tag{10.1}$$

In other words, the output of the function $\mathrm{f}[\mathbf{x}]$ is the same regardless of the transformation $\mathbf{t}[\mathbf{x}]$. Networks for image classification should be invariant to geometric transformations of the image (figure 10.1a–b). The network $\mathbf{f}[\mathbf{x}]$ should identify an image as containing the same object, even if it has been translated, rotated, flipped, or warped.

A function $\mathrm{f}[\mathbf{x}]$ of an image $\mathbf{x}$ is *equivariant* or *covariant* to a transformation $\mathbf{t}[\mathbf{x}]$ if:

$$\mathbf{f}\left[\mathbf{t}[\mathbf{x}]\right] = \mathbf{t}\left[\mathbf{f}[\mathbf{x}]\right]. \tag{10.2}$$

In other words, $\mathbf{f}[\mathbf{x}]$ is equivariant to the transformation $\mathbf{t}[\mathbf{x}]$ if its output changes in the same way under the transformation as the input. Networks for per-pixel image segmentation should be equivariant to transformations (figure 10.1c–f); if the image is translated, rotated, or flipped, the network $\mathbf{f}[\mathbf{x}]$ should return a segmentation that has been transformed in the same way.

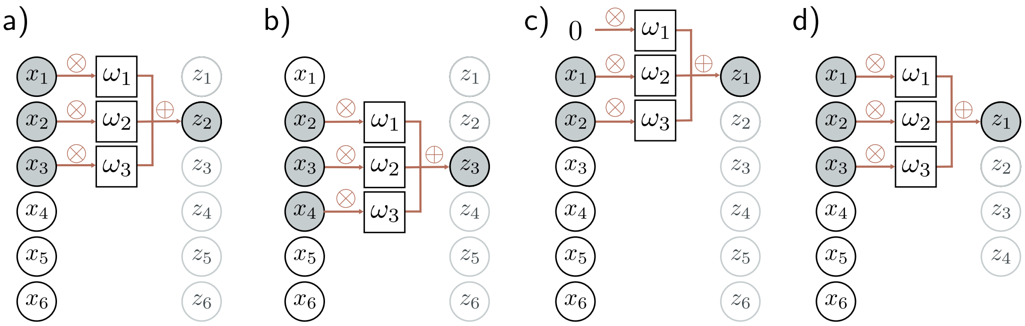

Figure 10.2 1D convolution with kernel size three. Each output z_i is a weighted sum of the nearest three inputs x_{i-1}, x_i, and x_{i+1}, where the weights are $\boldsymbol{\omega} = [\omega_1, \omega_2, \omega_3]$. a) Output z_2 is computed as $z_2 = \omega_1 x_1 + \omega_2 x_2 + \omega_3 x_3$. b) Output z_3 is computed as $z_3 = \omega_1 x_2 + \omega_2 x_3 + \omega_3 x_4$. c) At position z_1, the kernel extends beyond the first input x_1. This can be handled by zero padding, in which we assume values outside the input are zero. The final output is treated similarly. d) Alternatively, we could only compute outputs where the kernel fits within the input range ("valid" convolution); now, the output will be smaller than the input.

10.2 Convolutional networks for 1D inputs

Convolutional networks consist of a series of convolutional layers, each of which is equivariant to translation. They also typically include pooling mechanisms that induce partial invariance to translation. For clarity of exposition, we first consider convolutional networks for 1D data, which are easier to visualize. In section 10.3, we progress to 2D convolution, which can be applied to image data.

10.2.1 1D convolution operation

Convolutional layers are network layers based on the *convolution* operation. In 1D, a convolution transforms an input vector $\mathbf{x}$ into an output vector $\mathbf{z}$ so that each output z_i is a weighted sum of nearby inputs. The same weights are used at every position and are collectively called the *convolution kernel* or *filter*. The region over which inputs are weighted and summed is termed the *kernel size*. For a kernel size of three, we have:

$$z_i = \omega_1 x_{i-1} + \omega_2 x_i + \omega_3 x_{i+1}, \tag{10.3}$$

where $\boldsymbol{\omega} = [\omega_1, \omega_2, \omega_3]^T$ is the kernel (figure 10.2). Notice that the convolution operation is equivariant with respect to translation.[1] If we translate the input x, then the corresponding output z is translated in the same way. Problem 10.1

[1]Strictly speaking, this is a cross-correlation and not a convolution, in which the weights would be flipped relative to the input (so we would switch x_{i-1} with x_{i+1}). Regardless, this (incorrect) definition is the usual convention in machine learning.

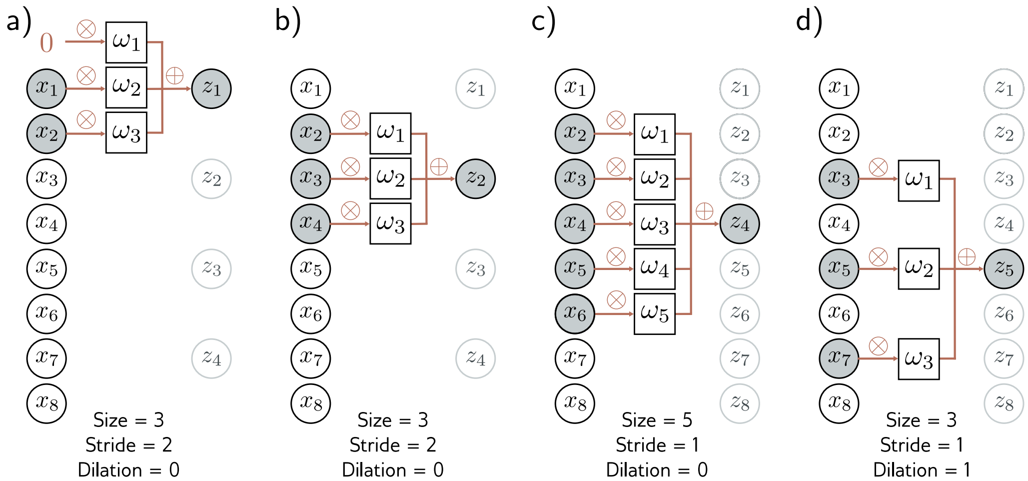

Figure 10.3 Stride, kernel size, and dilation. a) With a stride of two, we evaluate the kernel at every other position, so the first output z_1 is computed from a weighted sum centered at x_1, and b) the second output z_2 is computed from a weighted sum centered at x_3 and so on. c) The kernel size can also be changed. With a kernel size of five, we take a weighted sum of the nearest five inputs. d) In dilated or atrous convolution, we intersperse zeros in the weight vector to allow us to combine information over a large area using fewer weights.

10.2.2 Padding

Equation 10.3 shows that each output is computed by taking a weighted sum of the previous, current, and subsequent positions in the input. This begs the question of how to deal with the first output (where there is no previous input) and the final output (where there is no subsequent input).

There are two common approaches. The first is to pad the edges of the inputs with new values and proceed as usual. *Zero padding* assumes the input is zero outside its valid range (figure 10.2c). Other possibilities include treating the input as circular or reflecting it at the boundaries. The second approach is to discard the output positions where the kernel exceeds the range of input positions. These *valid convolutions* have the advantage of introducing no extra information at the edges of the input. However, they have the disadvantage that the representation decreases in size.

10.2.3 Stride, kernel size, and dilation

In the example above, each output was a sum of the nearest three inputs. However, this is just one of a larger family of convolution operations, the members of which are distinguished by their *stride*, *kernel size*, and *dilation rate*. When we evaluate the output at every position, we term this a *stride* of one. However, it is also possible to shift the kernel by a stride greater than one. If we have a stride of two, we create roughly half the number of outputs (figure 10.3a–b).

The *kernel size* can be increased to integrate over a larger area (figure 10.3c). However, it typically remains an odd number so that it can be centered around the current position. Increasing the kernel size has the disadvantage of requiring more weights. This leads to the idea of *dilated* or *atrous* convolutions, in which the kernel values are interspersed with zeros. For example, we can turn a kernel of size five into a dilated kernel of size three by setting the second and fourth elements to zero. We still integrate information from a larger input region but only require three weights to do this (figure 10.3d). The number of zeros we intersperse between the weights is termed the *dilation rate*.

Problems 10.2–10.4

10.2.4 Convolutional layers

A convolutional layer computes its output by convolving the input, adding a bias β, and passing each result through an activation function $\mathrm{a}[\bullet]$. With kernel size three, stride one, and dilation rate zero, the i^{th} hidden unit h_i would be computed as:

$$\begin{aligned} h_i &= \mathrm{a}\left[\beta + \omega_1 x_{i-1} + \omega_2 x_i + \omega_3 x_{i+1}\right] \\ &= \mathrm{a}\left[\beta + \sum_{j=1}^{3} \omega_j x_{i+j-2}\right], \end{aligned} \tag{10.4}$$

where the bias β and kernel weights $\omega_1, \omega_2, \omega_3$ are trainable parameters, and (with zero padding) we treat the input x as zero when it is out of the valid range. This is a special case of a fully connected layer that computes the i^{th} hidden unit as:

$$h_i = \mathrm{a}\left[\beta_i + \sum_{j=1}^{D} \omega_{ij} x_j\right]. \tag{10.5}$$

If there are D inputs $x_\bullet$ and D hidden units $h_\bullet$, this fully connected layer would have D^2 weights $\omega_{\bullet\bullet}$ and D biases $\beta_\bullet$. The convolutional layer only uses three weights and one bias. A fully connected layer can exactly reproduce this if most weights are set to zero and others are constrained to be identical (figure 10.4).

Problem 10.5

10.2.5 Channels

If we only apply a single convolution, then information will inevitably be lost; we are averaging nearby inputs, and the ReLU activation function clips results that are less than zero. Hence, it is usual to compute several convolutions in parallel. Each convolution produces a new set of hidden variables, termed a *feature map* or *channel*.

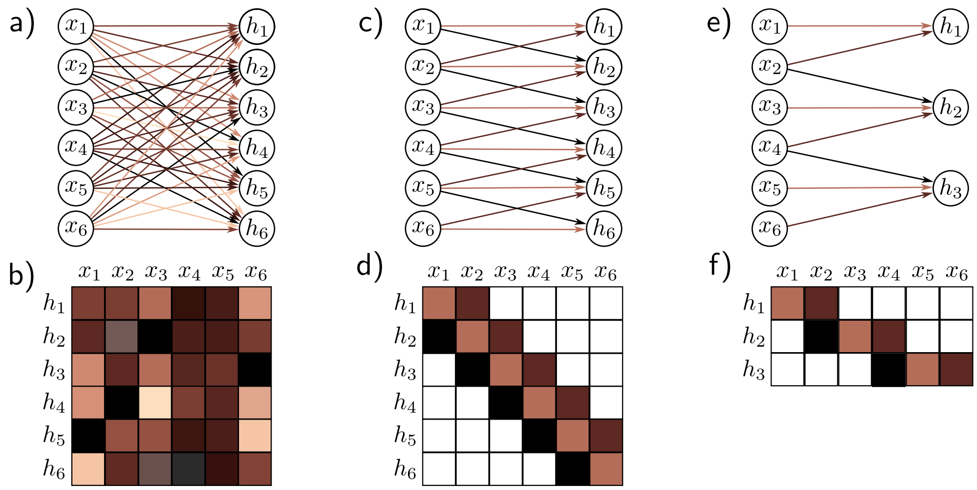

Figure 10.4 Fully connected vs. convolutional layers. a) A fully connected layer has a weight connecting each input x to each hidden unit h (colored arrows) and a bias for each hidden unit (not shown). b) Hence, the associated weight matrix $\mathbf{\Omega}$ contains 36 weights relating the six inputs to the six hidden units. c) A convolutional layer with kernel size three computes each hidden unit as the same weighted sum of the three neighboring inputs (arrows) plus a bias (not shown). d) The weight matrix is a special case of the fully connected matrix where many weights are zero and others are repeated (same colors indicate same value, white indicates zero weight). e) A convolutional layer with kernel size three and stride two computes a weighted sum at every other position. f) This is also a special case of a fully connected network with a different sparse weight structure.

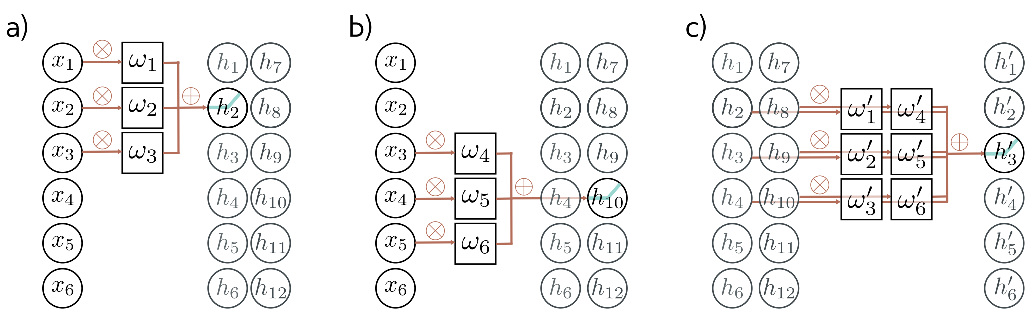

Figure 10.5 Channels. Typically multiple convolutions are applied to the input $\mathbf{x}$ and stored in channels. a) A convolution is applied to create hidden units h_1 to h_6, which form the first channel. b) A second convolution operation is applied to create hidden units h_7 to h_{12}, which form the second channel. The channels are stored in a 2D array $\mathbf{H}_1$ that contains all the hidden units in the first hidden layer. c) If we add a further convolutional layer, there are now two channels at each input position. Here, the 1D convolution defines a weighted sum over both input channels at the three closest positions to create each new output channel.

Figure 10.5a–b illustrates this with two convolution kernels of size three and with zero padding. The first kernel computes a weighted sum of the nearest three pixels, adds a bias, and passes the results through the activation function to produce hidden units h_1 to h_6. These comprise the first channel. The second kernel computes a different weighted sum of the nearest three pixels, adds a different bias, and passes the results through the activation function to create hidden units h_7 to h_{12}. These comprise the second channel.

In general, the input and the hidden layers all have multiple channels (figure 10.5c). If the incoming layer has C_i channels and kernel size K, thes hidden units in each output channel are computed as a weighted sum over all C_i channels and K kernel position using the weight matrix $\boldsymbol{\Omega} \in \mathbb{R}^{C_i \times K}$ and one bias. Hence, if there are C_o channels in the next layer, then we need $\boldsymbol{\Omega} \in \mathbb{R}^{C_i \times C_o \times K}$ weights and $\boldsymbol{\beta} \in \mathbb{R}^{C_o}$ biases.

Problems 10.6–10.8

Notebook 10.1
1D convolution

10.2.6 Convolutional networks and receptive fields

Chapter 4 described deep networks, which consisted of a series of fully connected layers. Similarly, convolutional network typically include a sequence of convolutional layers. The *receptive field* of a hidden unit in the network is the region of the original input that feeds into it. Consider a convolutional network where each convolutional layer has kernel size three. The hidden units in the first layer take a weighted sum of the three closest input positions, so they have receptive fields of size three. The hidden units in the second layer take a weighted sum of the three closest positions in the first layer. However, these are themselves weighted sums of three inputs. Hence, the hidden units in the second layer have a receptive field of size five. In this way, the receptive field of hidden units in successive layers increases, and information from across the input is gradually integrated (figure 10.6).

Problems 10.9–10.11

10.2.7 Example: MNIST-1D

We now apply a convolutional network to the MNIST-1D data (see figure 8.1). The input $\mathbf{x}$ is a 40D vector, and the output $\mathbf{f}$ is a 10D vector that is passed through a softmax layer to produce class probabilities. We use a network with three hidden layers (figure 10.7). The fifteen channels of the first hidden layer $\mathbf{H}_1$ are each computed using a kernel size of three and a stride of two with "valid" padding, giving nineteen spatial positions. The second hidden layer $\mathbf{H}_2$ is also computed using a kernel size of three, a stride of two, and "valid" padding. The third hidden layer is computed similarly. At this stage, the representation has four spatial positions and fifteen channels. These values are reshaped into a vector of size sixty, which is mapped by a fully connected layer to the ten output activations.

This network was trained for 100,000 steps using SGD without momentum, a learning rate of 0.01, and a batch size of 100 on a dataset of 4,000 examples. We compare this to a fully connected network with the same number of layers and hidden units (i.e., three hidden layers with 285, 135, and 60 hidden units, respectively). The convolutional network has 2,050 parameters, and the fully-connected network has 150,185 parameters. By

Problem 10.12

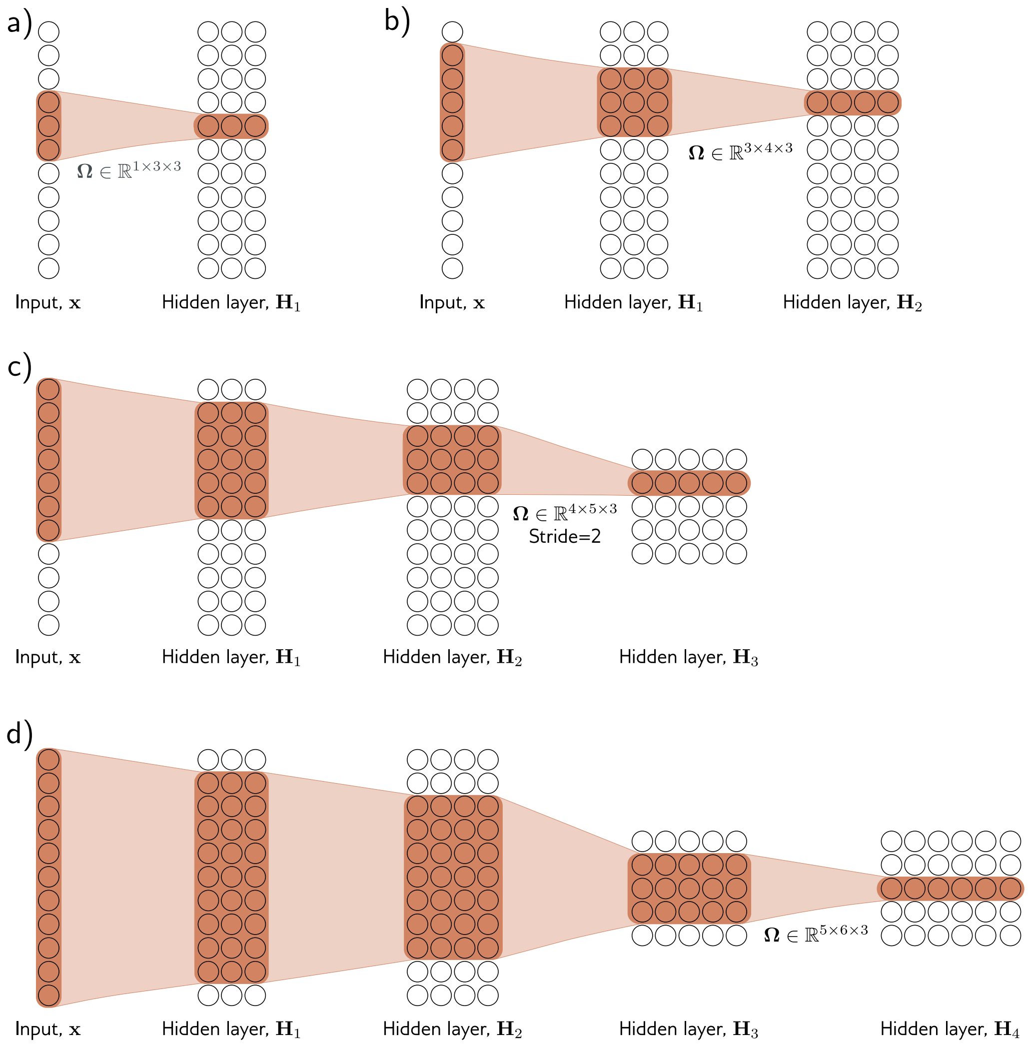

Figure 10.6 Receptive fields for network with kernel width of three. a) An input with eleven dimensions feeds into a hidden layer with three channels and convolution kernel of size three. The pre-activations of the three highlighted hidden units in the first hidden layer $\mathbf{H}_1$ are different weighted sums of the nearest three inputs, so the receptive field in $\mathbf{H}_1$ has size three. b) The pre-activations of the four highlighted hidden units in layer $\mathbf{H}_2$ each take a weighted sum of the three channels in layer $\mathbf{H}_1$ at each of the three nearest positions. Each hidden unit in layer $\mathbf{H}_1$ weights the nearest three input positions. Hence, hidden units in $\mathbf{H}_2$ have a receptive field size of five. c) The hidden units in the third layer (kernel size three, stride two) increases the receptive field size to seven. d) By the time we add a fourth layer, the receptive field of the hidden units at position three have a receptive field that covers the entire input.

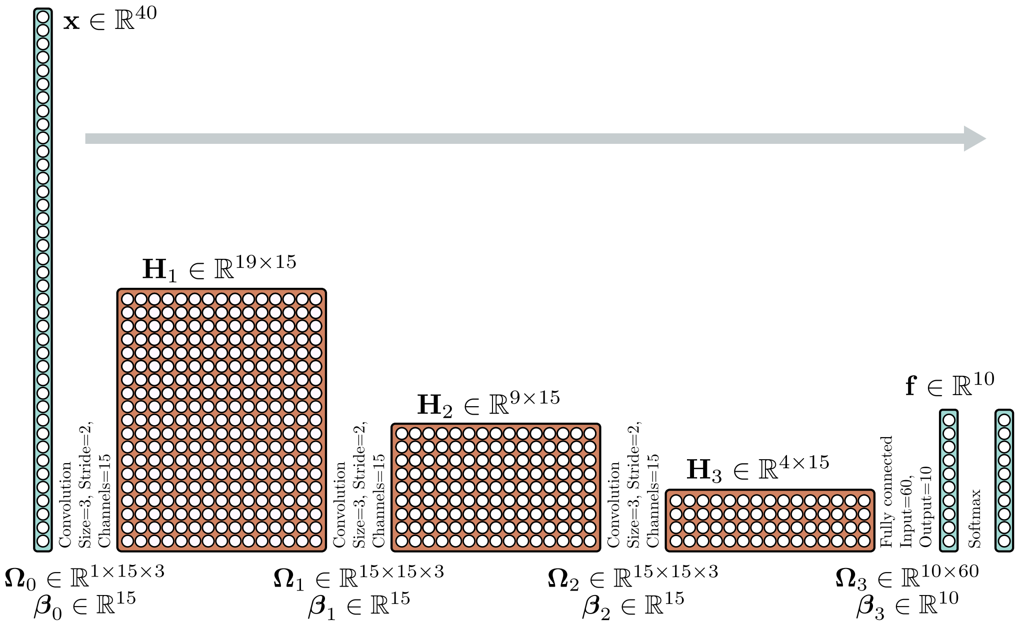

Figure 10.7 Convolutional network for classifying MNIST-1D data (see figure 8.1). The MNIST-1D input has dimension $D_i = 40$. The first convolutional layer has fifteen channels, kernel size three, stride two, and only retains "valid" positions to make a representation with nineteen positions and fifteen channels. The following two convolutional layers have the same settings, gradually reducing the representation size. Finally, a fully connected layer takes all sixty hidden units from the third hidden layer. It outputs ten activations that are subsequently passed through a softmax layer to produce the ten class probabilities.

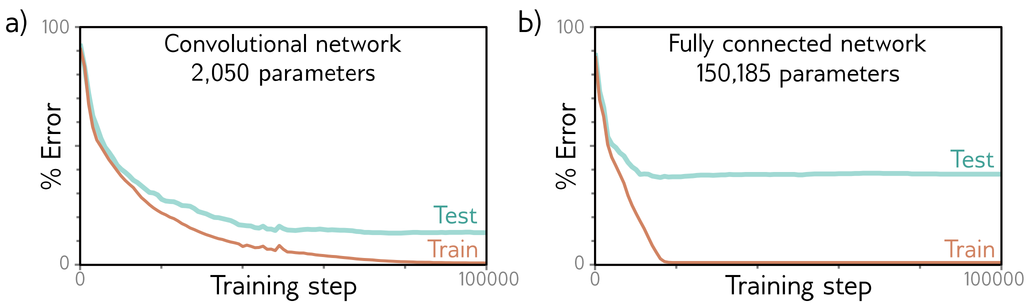

Figure 10.8 MNIST-1D results. a) The convolutional network from figure 10.7 eventually fits the training data perfectly and has ∼17% test error. b) A fully connected network with the same number of hidden layers and the number of hidden units in each learns the training data faster but fails to generalize well with ∼40% test error. The latter model can reproduce the convolutional model but fails to do so. The convolutional structure restricts the possible mappings to those that process every position similarly, and this restriction improves performance.

Notebook 10.2 Convolution for MNIST-1D

the logic of figure 10.4, the convolutional network is a special case of the fully connected one. The latter has enough flexibility to replicate the former exactly. Figure 10.8 shows both models fit the training data perfectly. However, the test error for the convolutional network is much less than for the fully connected network.

This discrepancy is probably not due to the difference in the number of parameters; we know overparameterization usually improves performance (section 8.4.1). The likely explanation is that the convolutional architecture has a superior inductive bias (i.e., interpolates between the training data better) because we have embodied some prior knowledge in the architecture; we have forced the network to process each position in the input in the same way. We know that the data were created by starting with a template that is (among other operations) randomly translated, so this is sensible.

The fully connected network has to learn what each digit template looks like at every position. In contrast, the convolutional network shares information across positions and hence learns to identify each category more accurately. Another way of thinking about this is that when we train the convolutional network, we search through a smaller family of input/output mappings, all of which are plausible. Alternatively, the convolutional structure can be considered a regularizer that applies an infinite penalty to most of the solutions that a fully connected network can describe.

10.3 Convolutional networks for 2D inputs

The previous section described convolutional networks for processing 1D data. Such networks can be applied to financial time series, audio, and text. However, convolutional networks are more usually applied to 2D image data. The convolutional kernel is now a 2D object. A 3×3 kernel $\boldsymbol{\Omega} \in \mathbb{R}^{3\times 3}$ applied to a 2D input comprising of elements x_{ij} computes a single layer of hidden units h_{ij} as:

$$h_{ij} \quad = \quad \mathrm{a}\left[\beta + \sum_{m=1}^{3}\sum_{n=1}^{3}\omega_{mn}x_{i+m-2,j+n-2}\right], \tag{10.6}$$

where ω_{mn} are the entries of the convolutional kernel. This is simply a weighted sum over a square 3×3 input region. The kernel is translated both horizontally and vertically across the 2D input (figure 10.9) to create an output at each position.

Problem 10.13

Often the input is an RGB image, which is treated as a 2D signal with three channels (figure 10.10). Here, a 3×3 kernel would have 3×3×3 weights and be applied to the three input channels at each of the 3×3 positions to create a 2D output that is the same height and width as the input image (assuming zero padding). To generate multiple output channels, we repeat this process with different kernel weights and append the results to form a 3D tensor. If the kernel is size $K \times K$, and there are C_i input channels. Each output channel is a weighted sum of $C_i \times K \times K$ quantities plus one bias. It follows that to compute C_o output channels, we need $C_i \times C_o \times K \times K$ weights and C_o biases.

Notebook 10.3 2D convolution

Problem 10.14

Appendix C.4.1 Tensors

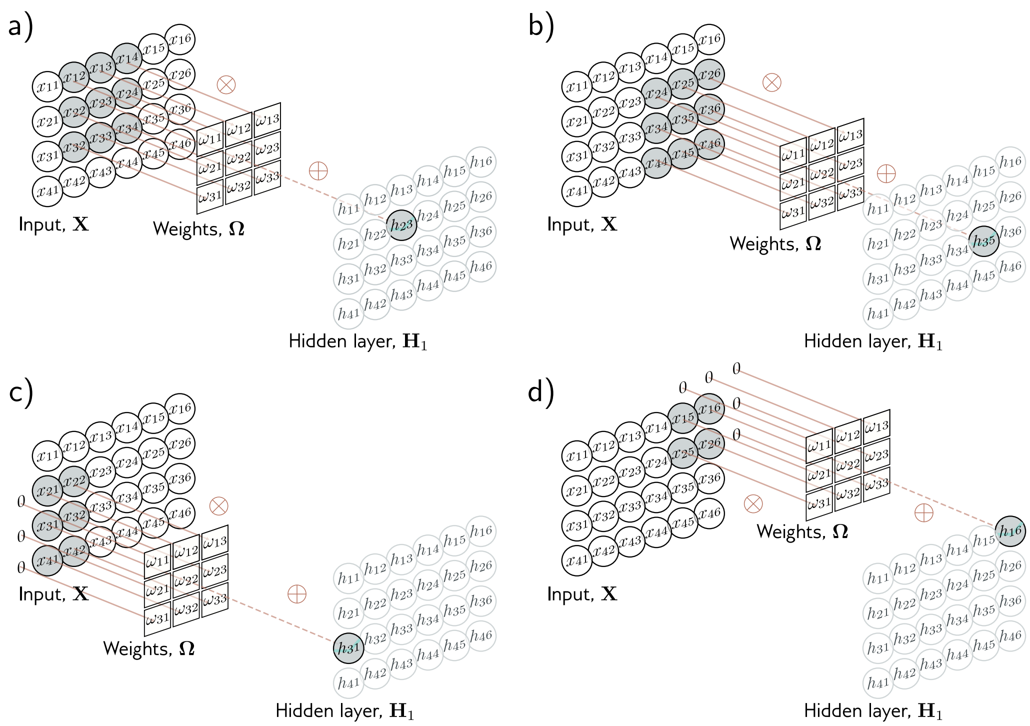

Figure 10.9 2D convolutional layer. Each output h_{ij} computes a weighted sum of the 3×3 nearest inputs, adds a bias, and passes the result through an activation function. a) Here, the output h_{23} (shaded output) is a weighted sum of the nine positions from x_{12} to x_{34} (shaded inputs). b) Different outputs are computed by translating the kernel across the image grid in two dimensions. c–d) With zero padding, positions beyond the image's edge are considered to be zero.

10.4 Downsampling and upsampling

The network in figure 10.7 increased receptive field size by scaling down the representation at each layer using stride two convolutions. We now consider methods for scaling down or *downsampling* 2D input representations. We also describe methods for scaling them back up (*upsampling*), which is useful when the output is also an image. Finally, we consider methods to change the number of channels between layers. This is helpful when recombining representations from two branches of a network (chapter 11).

10.4.1 Downsampling

There are three main approaches to scaling down a 2D representation. Here, we consider the most common case of scaling down both dimensions by a factor of two. First , we Problem 10.15

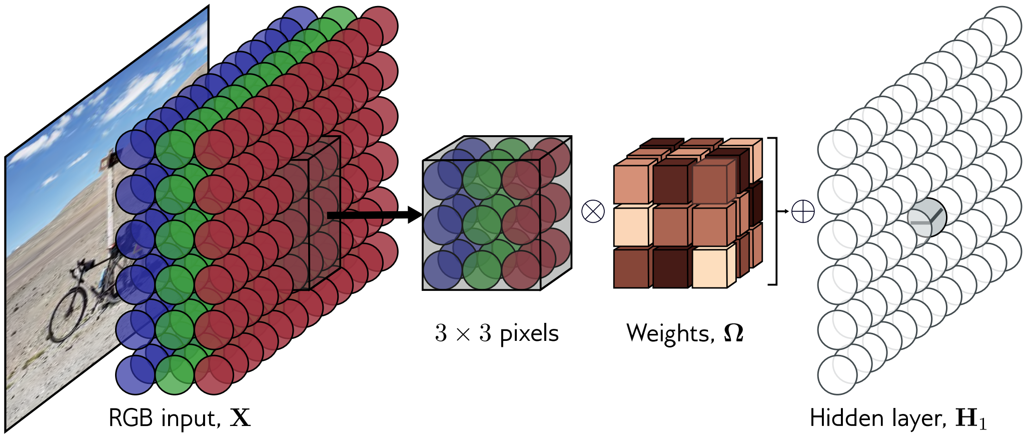

Figure 10.10 2D convolution applied to an image. The image is treated as a 2D input with three channels corresponding to the red, green, and blue components. With a 3×3 kernel, each pre-activation in the first hidden layer is computed by pointwise multiplying the 3×3×3 kernel weights with the 3×3 RGB image patch centered at the same position, summing, and adding the bias. To calculate all the pre-activations in the hidden layer, we "slide" the kernel over the image in both horizontal and vertical directions. The output is a 2D layer of hidden units. To create multiple output channels, we would repeat this process with multiple kernels, resulting in a 3D tensor of hidden units at hidden layer $\mathbf{H}_1$.

can sample every other position. When we use a stride of two, we effectively apply this method simultaneously with the convolution operation (figure 10.11a).

Second, *max pooling* retains the maximum of the 2×2 input values (figure 10.12b). This induces some invariance to translation; if the input is shifted by one pixel, many of these maximum values remain the same. Finally, *mean pooling* or *average pooling* averages the inputs. For all approaches, we apply downsampling separately to each channel, so the output has half the width and height but the same number of channels.

10.4.2 Upsampling

The simplest way to scale up a network layer to double the resolution is to duplicate all the channels at each spatial position four times (figure 10.12a). A second method is max-unpooling; this is used where we have previously used a max pooling operation for downsampling, and we distribute the values to the positions they originated from (figure 10.12b). A third approach uses bilinear interpolation to fill in the missing values between the points where we have samples. (figure 10.12c).

A fourth approach is roughly analogous to downsampling using a stride of two. In that method, there were half as many outputs as inputs and, for kernel size three, each

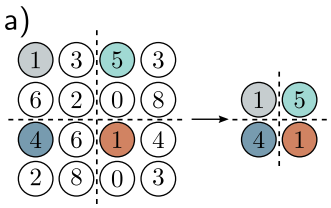

Figure 10.11 Methods for scaling down representation size (downsampling). a) Sub-sampling. The original 4×4 representation (left) is reduced to size 2×2 (right) by retaining every other input. Colors on the left indicate which inputs contribute to the outputs on the right. This is effectively what happens with a kernel of stride two, except that the intermediate values are never computed. b) Max pooling. Each output comprises the maximum value of the corresponding 2×2 block. c) Mean pooling. Each output is the mean of the values in the 2×2 block.

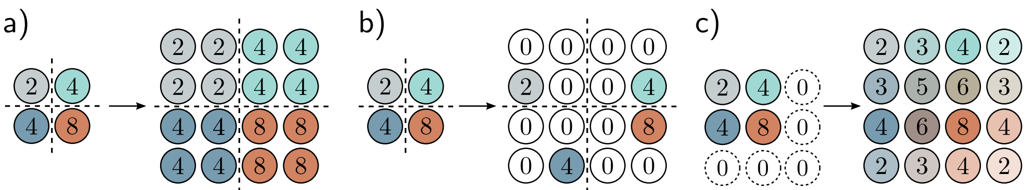

Figure 10.12 Methods for scaling up representation size (upsampling). a) The simplest way to double the size of a 2D layer is to duplicate each input four times. b) In networks where we have previously used a max pooling operation (figure 10.11b), we can redistribute the values to the same positions they originally came from (i.e., where the maxima were). This is known as max-unpooling. c) A third option is bilinear interpolation between the input values.

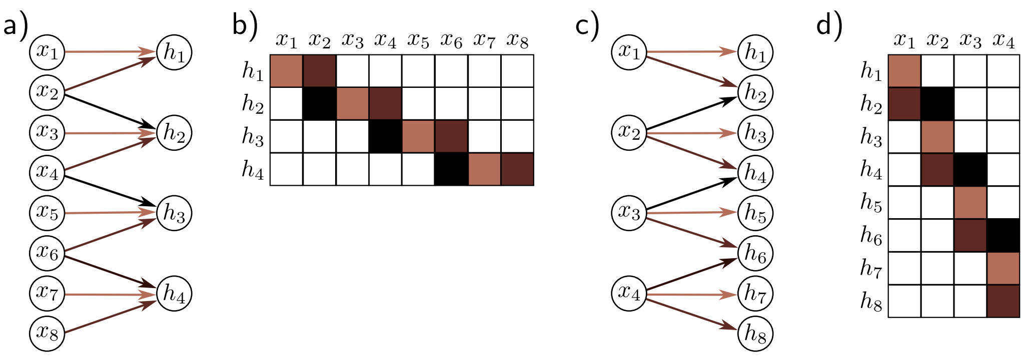

Figure 10.13 Transposed convolution in 1D. a) Downsampling with kernel size three, stride two, and zero padding. Each output is a weighted sum of three inputs (arrows indicate weights). b) This can be expressed by a weight matrix (same color indicates shared weight). c) In transposed convolution, each input contributes three values to the output layer, which has twice as many outputs as inputs. d) The associated weight matrix is the transpose of that in panel (b).

output was a weighted sum of the three closest inputs (figure 10.13a). In *transposed convolution*, this picture is reversed (figure 10.13c). There are twice as many outputs as inputs, and each input contributes to three of the outputs. When we consider the associated weight matrix of this upsampling mechanism (figure 10.13d), we see that it is the transpose of the matrix for the downsampling mechanism (figure 10.13b).

Notebook 10.4 Downsampling & upsampling

10.4.3 Changing the number of channels

Sometimes we want to change the number of channels between one hidden layer and the next without further spatial pooling. This is usually so we can combine the representation with another parallel computation (see chapter 11). To accomplish this, we apply a convolution with kernel size one. Each element of the output layer is computed by taking a weighted sum of all the channels at the same position (figure 10.14). We can repeat this multiple times with different weights to generate as many output channels as we need. The associated convolution weights have size $1 \times 1 \times C_i \times C_o$. Hence, this is known as *1×1 convolution*. Combined with a bias and activation function, it is equivalent to running the same fully connected network on the channels at every position.

10.5 Applications

We conclude by describing three computer vision applications. We describe convolutional networks for image classification where the goal is to assign the image to one of a predetermined set of categories. Then we consider object detection, where the goal is to identify multiple objects in an image and find the bounding box around each. Finally, we describe an early system for semantic segmentation where the goal is assign a label to each pixel according to which object is present.

10.5.1 Image classification

Much of the pioneering work on deep learning in computer vision focused on image classification using the ImageNet dataset (figure 10.15). This contains 1,281,167 training images, 50,000 validation images, and 100,000 test images, and every image is labeled as belonging to one of 1000 possible categories.

Most methods reshape the input images to a standard size; in a typical system, the input $\mathbf{x}$ to the network is a 224×224 RGB image and the output is a probability distribution over the 1000 classes. The task is challenging; there are a large number of classes, and they exhibit considerable variation (figure 10.15). In 2011, before deep networks were applied, the state-of-the-art method classified the test images with $\sim 25\%$ errors for the correct class being in the top five suggestions. Five years later, the best deep learning models eclipsed human performance.

In 2012, *AlexNet* was the first convolutional network to perform well on this task.

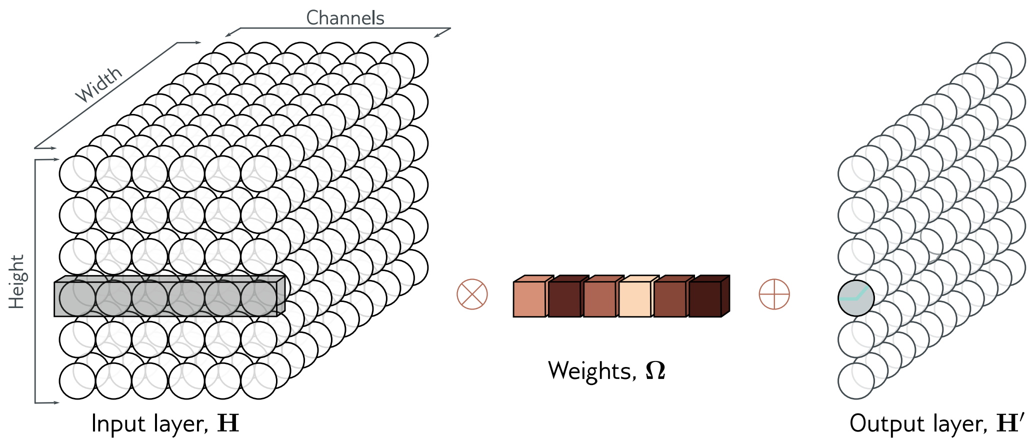

Figure 10.14 1×1 convolution. To change the number of channels without spatial pooling, we apply a 1×1 kernel. Each output channel is computed by taking a weighted sum of all of the channels at the same position, adding a bias, and passing through an activation function. Multiple output channels are created by repeating this operation with different weights and biases.

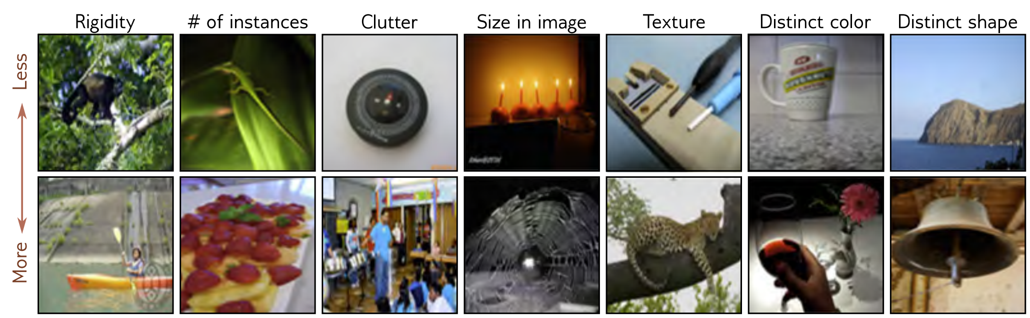

Figure 10.15 ImageNet classification task. The model assigns an input image to one of 1000 classes. The images vary greatly along different attributes (columns). These include rigidity (monkey < canoe), number of instances in image (lizard < strawberry), clutter (compass < steel drum), size (candle < spiderweb), texture (screwdriver < leopard), distinctiveness of color (mug < red wine), and distinctiveness of shape (headland < bell). Adapted from Russakovsky et al. (2015).

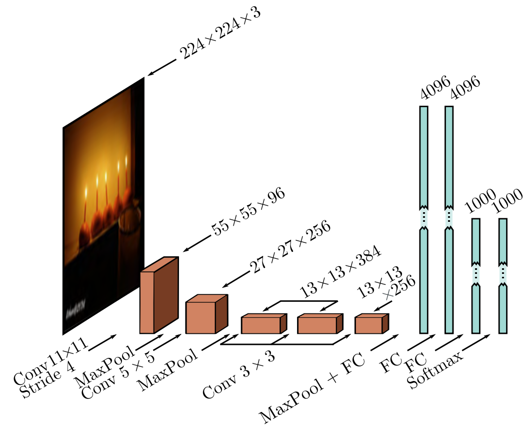

Figure 10.16 AlexNet (Krizhevsky et al., 2012). The input is a 224×224 color image, and the output is a 1000-dimensional vector representing class probabilities. The network first convolves with 11×11 kernels and stride 4 to create 96 channels. It decreases the resolution again using a max pool operation and applies a 5×5 convolutional layer. Another max pooling layer follows, and three 3×3 convolutional layers are applied. After a final max pooling operation, the result is vectorized and passed through three fully connected (FC) layers and finally the softmax layer.

It consists of eight hidden layers with ReLU activation functions, of which the first five are convolutional and the rest fully connected (figure 10.16). The network starts by downsampling the input using an 11×11 kernel with a stride of four to create 96 channels. It then downsamples again using a max pooling layer before applying a 5×5 kernel to create 256 channels. There are three more convolutional layers with kernel size 3×3, eventually resulting in a 13×13 representation with 256 channels. This is resized into a single vector of length $43,264$ and then passed through three fully connected layers containing 4096, 4096, and 1000 hidden units, respectively. The last layer is passed through the softmax function to generate probabilities for the 1000 classes. The complete network contains 60 million parameters, most of which are in the fully connected layers.

Problems 10.17–10.16

The dataset size was augmented by a factor of 2048 using (i) spatial transformations and (ii) modifications of the input intensities. At test time, five different cropped and mirrored versions of the image were run through the network, and their predictions averaged. The system was learned using SGD with a momentum coefficient of 0.9 and a batch size of 128. Dropout was applied in the fully connected layers, and an L2 (weight decay) regularizer was used. This system achieved a 16.4% top-5 error rate and a 38.1% top-1 error rate. At the time, this was an enormous leap forward in performance at a task considered far beyond the capabilities of contemporary methods.

Notebook 10.5 Convolution for MNIST

The *VGG network* was also targeted at classification in the ImageNet task and achieved a considerably better performance of 6.8% top-5 error rate and a 23.7% top-1 error rate. This network is similarly composed of a series of interspersed convolutional and max pooling layers, followed by three fully connected layers (figure 10.17). It was also trained using data augmentation, weight decay, and dropout.

Although there were various minor differences in the training regime, the most important change between AlexNet and VGG was the depth of the network. The latter used 19 hidden layers and 144 million parameters. The networks in figures 10.16 and 10.17 are depicted at the same scale for comparison. There was a general trend for several years for performance on this task to improve as the depth of the networks increased, and this is evidence that depth is important in neural networks.

Problem 10.18

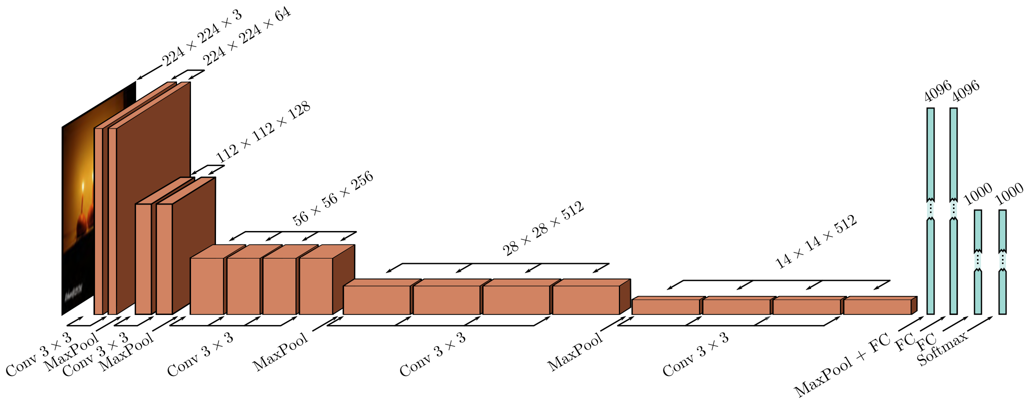

Figure 10.17 VGG network (Simonyan & Zisserman, 2014) depicted at the same scale as AlexNet (see figure 10.16). This network consists of a series of convolutional layers and max pooling operations, in which the spatial scale of the representation gradually decreases, but the number of channels gradually increases. The hidden layer after the last convolutional operation is resized to a 1D vector and three fully connected layers follow. The network outputs 1000 activations corresponding to the class labels that are passed through a softmax function to create class probabilities.

10.5.2 Object detection

In *object detection*, the goal is to identify and localize multiple objects within the image. An early method based on convolutional networks was *You Only Look Once*, or *YOLO* for short. The input to the YOLO network is a 448×448 RGB image. This is passed through 24 convolutional layers that gradually decrease the representation size using max pooling operations while concurrently increasing the number of channels, similarly to the VGG network. The final convolutional layer is of size 7×7 and has 1024 channels. This is reshaped to a vector, and a fully connected layer maps it to 4096 values. One further fully connected layer maps this representation to the output.

The output values encode which class is present at each of a 7×7 grid of locations (figure 10.18a). For each location, the output values also encode a fixed number of bounding boxes (figure 10.18b). Five parameters define each box: the x- and y-positions of the center, the height and width of the box, and the confidence of the prediction (figure 10.18c). The confidence estimates the overlap between the predicted and ground truth bounding boxes. The system is trained using momentum, weight decay, dropout, and data augmentation. Transfer learning is employed; the network is initially trained on the ImageNet classification task and is then fine-tuned for object detection.

After the network is run, a heuristic process is used to remove rectangles with low confidence and to suppress predicted bounding boxes that correspond to the same object so only the most confident one is retained.

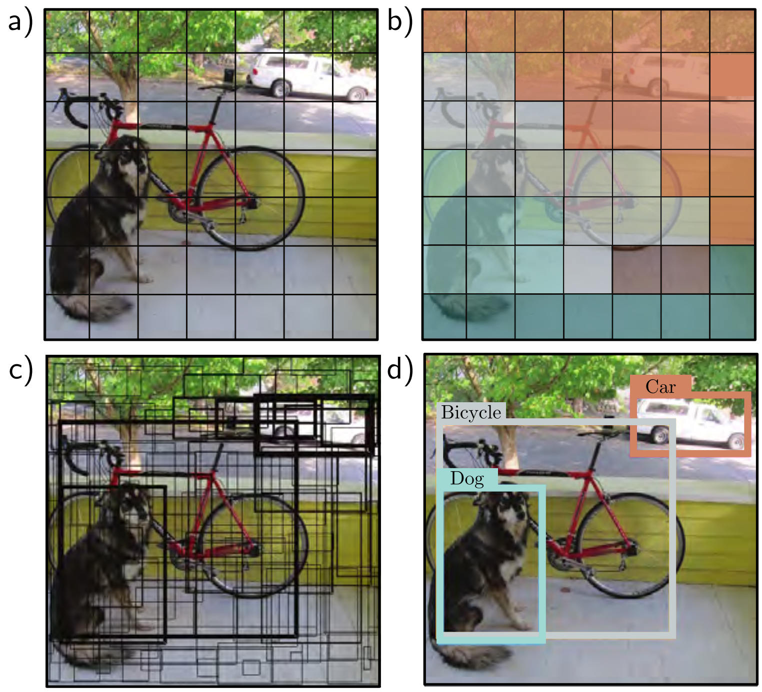

Figure 10.18 YOLO object detection. a) The input image is reshaped to 448×448 and divided into a regular 7×7 grid. b) The system predicts the most likely class at each grid cell. c) It also predicts two bounding boxes per cell, and a confidence value (represented by thickness of line). d) During inference, the most likely bounding boxes are retained, and boxes with lower confidence values that belong to the same object are suppressed. Adapted from Redmon et al. (2016).

10.5.3 Semantic segmentation

The goal of semantic segmentation is to assign a label to each pixel according to the object that it belongs to or no label if that pixel does not correspond to anything in the training database. An early network for semantic segmentation is depicted in figure 10.19. The input is a 224×224 RGB image, and the output is a 224×224×21 array that contains the probability of each of 21 possible classes at each position.

The first part of the network is a smaller version of VGG (figure 10.17) that contains thirteen rather than fifteen convolutional layers and downsizes the representation to size 14×14. There is then one more max pooling operation, followed by two fully connected layers that map to two 1D representations of size 4096. These layers do not represent spatial position but instead combine information from across the whole image.

Here, the architecture diverges from VGG. Another fully connected layer reconstitutes the representation into 7×7 spatial positions and 512 channels. This is followed

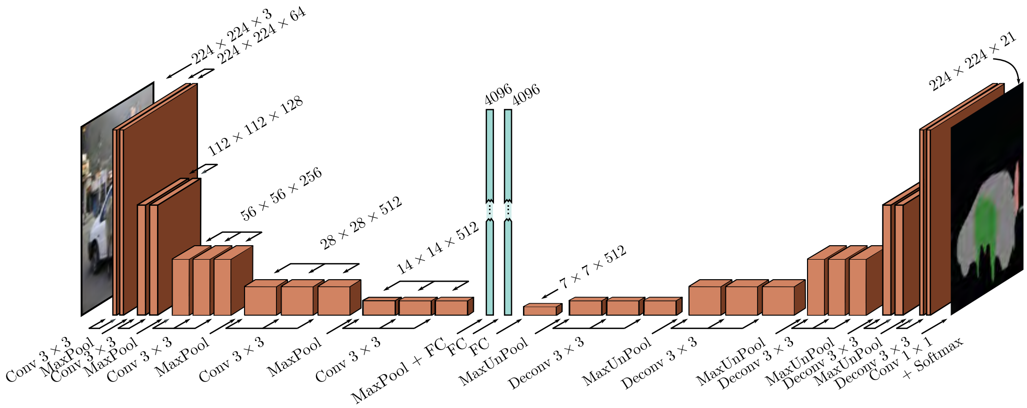

Figure 10.19 Semantic segmentation network of Noh et al. (2015). The input is a 224×224 image, which is passed through a version of the VGG network and eventually transformed into a representation of size 4096 using a fully connected layer. This contains information about the entire image. This is then reformed into a representation of size 7×7 using another fully connected layer, and the image is upsampled and deconvolved (transposed convolutions without upsampling) in a mirror image of the VGG network. The output is a 224×224×21 representation that gives the output probabilities for the 21 classes at each position.

by a series of max-unpooling layers (see figure 10.12b) and *deconvolution* layers. These are transposed convolutions (see figure 10.13) but in 2D and without the upsampling. Finally, there is a 1×1 convolution to create 21 channels representing the possible classes and a softmax operation at each spatial position to map the activations to class probabilities. The downsampling side of the network is sometimes referred to as an *encoder*, and the upsampling side as a *decoder*, so networks of this type are sometimes called *encoder-decoder networks* or *hourglass networks* due to their shape.

The final segmentation is generated using a heuristic method that greedily searches for the class that is most represented and infers its region, taking into account the probabilities but also encouraging connectedness. Then the next most-represented class is added where it dominates at the remaining unlabelled pixels. This continues until there is insufficient evidence to add more (figure 10.20).

10.6 Summary

In convolutional layers, each hidden unit takes a weighted sum of the nearby inputs, adds a bias, and applies an activation function. The weights and the bias are the same at every spatial position, so there are far fewer parameters than in a fully connected network, and the parameters don't increase with the input image size. To ensure that

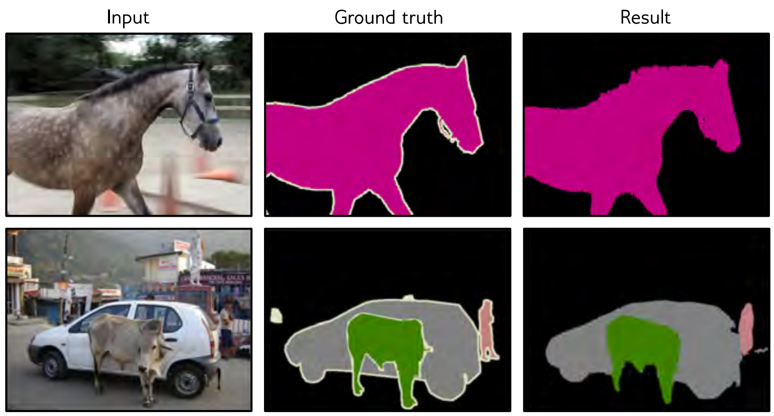

Figure 10.20 Semantic segmentation results. The final result is created from the 21 probability maps by greedily selecting the best class and using a heuristic method to find a sensible binary map based on the probabilities and their spatial proximity. If there is enough evidence, subsequent classes are added, and their segmentation maps are combined. Adapted from Noh et al. (2015).

information is not lost, this operation is repeated with different weights and biases to create multiple channels at each spatial position.

Typical convolutional networks consist of convolutional layers interspersed with layers that downsample by a factor of two. As the network progresses, the spatial dimensions usually decrease by factors of two, and the number of channels increases by factors of two. At the end of the network, there are typically one or more fully connected layers that integrate information from across the entire input and create the desired output. If the output is an image, a mirrored "decoder" upsamples back to the original size.

The translational equivariance of convolutional layers imposes a useful inductive bias that increases performance for image-based tasks relative to fully connected networks. We described image classification, object detection, and semantic segmentation networks. Image classification performance was shown to improve as the network became deeper. However, subsequent experimental evidence has shown that increasing the network depth indefinitely doesn't continue to help; after a certain depth, the system becomes difficult to train. This issue was partially resolved by *residual connections*, which are the topic of the next chapter.

Notes

Dumoulin & Visin (2016) present an overview of the mathematics of convolutions that expands on the brief treatment in this chapter.

Convolutional networks: Early convolutional networks were developed by Fukushima & Miyake (1982), LeCun et al. (1989a), and LeCun et al. (1989b). Initial applications included handwriting recognition (LeCun et al., 1989a; Martin, 1993), face recognition (Lawrence et al., 1997), phoneme recognition (Waibel et al., 1989), spoken word recognition (Bottou et al., 1990), and signature verification (Bromley et al., 1993). However, convolutional networks were popularized by LeCun et al. (1998), who built a system called LeNet for classifying 28×28 grayscale images of handwritten digits. This is immediately recognizable as a precursor of modern networks; it uses a series of convolutional layers, followed by fully connected layers, sigmoid activations rather than ReLUs, and average pooling rather than max pooling. AlexNet (Krizhevsky et al., 2012) is widely considered the starting point for modern deep convolutional networks.

ImageNet Challenge: The ImageNet classification challenge drove progress in deep learning for several years after the dramatic improvements of AlexNet. Notable subsequent winners of this challenge include the *network-in-network* architecture (Lin et al., 2014), which alternated convolutions with fully connected layers that operated independently on all of the channels at each position (i.e., 1×1 convolutions). Zeiler & Fergus (2014) and Simonyan & Zisserman (2014) made progress by training larger and deeper architectures that were fundamentally similar to AlexNet. Szegedy et al. (2017) developed an architecture called *GoogLeNet*, which introduced *inception blocks*. These use several parallel paths with different filter sizes, which are then recombined. This effectively allowed the system to learn the filter size.

The trend was for performance to improve with increasing depth; however, it ultimately became difficult to train deeper networks without modifications; these include residual connections and normalization layers, both of which are described in the next chapter. Progress in the ImageNet challenges is summarized in Russakovsky et al. (2015). A more general survey of image classification using convolutional networks can be found in Rawat & Wang (2017). The progress of image classification networks over time is visualized in figure 10.21.

Types of convolutional layers: Atrous or dilated convolutions were introduced by Chen et al. (2018c) and Yu & Koltun (2015). Transposed convolutions were introduced by Long et al. (2015). Odena et al. (2016) pointed out that they can lead to checkerboard artifacts and should be used with caution. Lin et al. (2014) is an early example of convolution with 1×1 filters.

Many variants of the standard convolutional layer aim to reduce the number of parameters. These include *depthwise* or *channel-separate convolution* (Howard et al., 2017; Tran et al., 2018), in which a different filter convolves each channel separately to create a new set of channels. For a kernel size of $K \times K$ with C input channels and C output channels, this requires $K \times K \times C$ parameters rather than the $K \times K \times C \times C$ parameters in a regular convolutional layer. A related approach is *grouped convolutions* (Xie et al., 2017), where each convolution kernel is only applied to a subset of the channels with a commensurate reduction in the parameters. In fact, grouped convolutions were used in AlexNet for computational reasons; the whole network could not run on a single GPU, so some channels were processed on one GPU and some on another, with limited interaction points. *Separable convolutions* treat each kernel as an outer product of 1D vectors; they use $C + K + K$ parameters for each of the C channels. *Partial convolutions* (Liu et al., 2018a) are used when inpainting missing pixels and account for the partial masking of the input. *Gated convolutions* learn the mask from the previous layer (Yu et al., 2019; Chang et al., 2019b). Hu et al. (2018b) propose squeeze-and-excitation networks which re-weight the channels using information pooled across all spatial positions.

Downsampling and upsampling: Average pooling dates back to at least LeCun et al. (1989a) and max pooling to Zhou & Chellappa (1988). Scherer et al. (2010) compared these methods

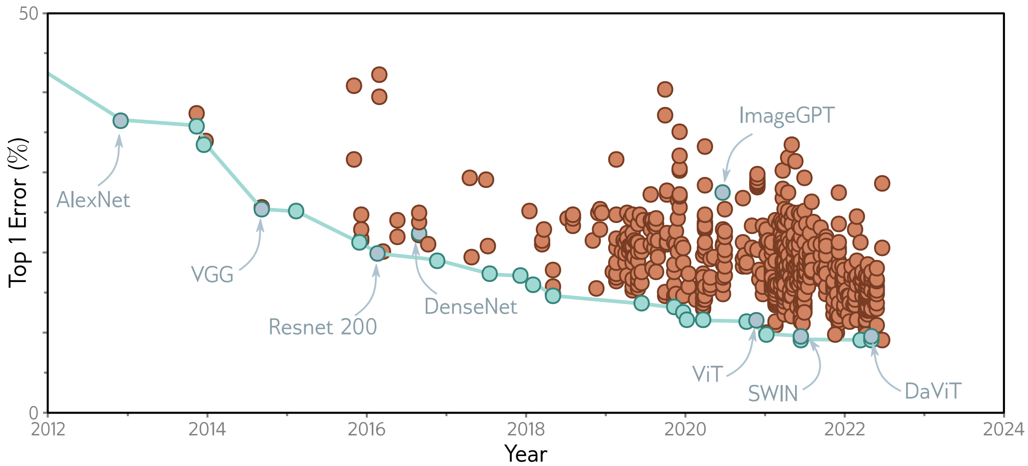

Figure 10.21 ImageNet performance. Each circle represents a different published model. Blue circles represent models that were state-of-the-art. Models discussed in this book are also highlighted. The AlexNet and VGG networks were remarkable for their time but are now far from state of the art. ResNet 200 and DenseNet are discussed in chapter 11. ImageGPT, ViT, SWIN, and DaViT are discussed in chapter 12. Adapted from https://paperswithcode.com/sota/image-classification-on-imagenet.

Appendix C.5.6 Vector norms

and concluded that max pooling was superior. The max unpooling method was introduced by Zeiler et al. (2011) and Zeiler & Fergus (2014). Max pooling can be thought of as applying an L_∞ norm to the hidden units that are to be pooled. This led to applying other L_k norms (Springenberg et al., 2015; Sainath et al., 2013), although these require more computation and are not widely used. Zhang (2019) introduced *max-blur-pooling*, in which a low-pass filter is applied before downsampling to prevent aliasing and showed that this improves generalization over translation of the inputs and also makes the network less susceptible to adversarial attacks (see section 20.4.6).

Shi et al. (2016) introduced *PixelShuffle*, which used convolutional filters with a stride of $1/s$ to scale up 1D signals by a factor of s. Only the weights that lie exactly on positions are used to create the outputs, and the ones that fall between positions are discarded. This can be implemented by multiplying the number of channels in the kernel by a factor of s, where the s^{th} output position is computed from just the s^{th} subset of channels. This can be trivially extended to 2D convolution, which requires s^2 channels.

Convolution in 1D and 3D: Convolutional networks are usually applied to images but have also been applied to 1D data in applications that include speech recognition (Abdel-Hamid et al., 2012), sentence classification (Zhang et al., 2015; Conneau et al., 2017), electrocardiogram classification (Kiranyaz et al., 2015), and bearing fault diagnosis (Eren et al., 2019). A survey of 1D convolutional networks can be found in Kiranyaz et al. (2021). Convolutional networks have also been applied to 3D data, including video (Ji et al., 2012; Saha et al., 2016; Tran et al., 2015) and volumetric measurements (Wu et al., 2015b; Maturana & Scherer, 2015).

Invariance and equivariance: Part of the motivation for convolutional layers is that they are approximately equivariant with respect to translation, and part of the motivation for max pooling is to induce invariance to small translations. Zhang (2019) considers the degree to which convolutional networks really have these properties and proposes the max-blur-pooling modification that demonstrably improves them. There is considerable interest in making networks equivariant or invariant to other types of transformations, such as reflections, rotations, and scaling. Sifre & Mallat (2013) constructed a system based on wavelets that induced both translational and rotational invariance in image patches and applied this to texture classification. Kanazawa et al. (2014) developed locally scale-invariant convolutional neural networks. Cohen & Welling (2016) exploited group theory to construct *group CNNs*, which are equivariant to larger families of transformations, including reflections and rotations. Esteves et al. (2018) introduced *polar transformer networks*, which are invariant to translations and equivariant to rotation and scale. Worrall et al. (2017) developed *harmonic networks*, the first example of a group CNN that was equivariant to continuous rotations.

Initialization and regularization: Convolutional networks are typically initialized using Xavier initialization (Glorot & Bengio, 2010) or He initialization (He et al., 2015), as described in section 7.5. However, the *ConvolutionOrthogonal* initializer (Xiao et al., 2018a) is specialized for convolutional networks (Xiao et al., 2018a). Networks of up to 10,000 layers can be trained using this initialization without the need for residual connections. Problem 10.19

Dropout is effective for fully connected networks but less so for convolutional layers (Park & Kwak, 2016). This may be because neighboring image pixels are highly correlated, so if a hidden unit drops out, the same information is passed on via adjacent positions. This is the motivation for spatial dropout and cutout. In spatial dropout (Tompson et al., 2015), entire feature maps are discarded instead of individual pixels. This circumvents the problem of neighboring pixels carrying the same information. Similarly, DeVries & Taylor (2017b) propose *cut-out*, in which a square patch of each input image is masked at training time. Wu & Gu (2015) modified max pooling for dropout layers using a method that involves sampling from a probability distribution over the constituent elements rather than always taking the maximum.

Adaptive Kernels: The *inception block* (Szegedy et al., 2017) applies convolutional filters of different sizes in parallel and, as such, provides a crude mechanism by which the network can learn the appropriate filter size. Other work has investigated learning the scale of convolutions as part of the training process (e.g., Pintea et al., 2021; Romero et al., 2021) or the stride of downsampling layers (Riad et al., 2022).

In some systems, the kernel size is changed adaptively based on the data. This is sometimes in the context of guided convolution, where one input is used to help guide the computation from another input. For example, an RGB image might be used to help upsample a low-resolution depth map. Jia et al. (2016) directly predicted the filter weights themselves using a different network branch. Xiong et al. (2020b) change the kernel size adaptively. Su et al. (2019a) moderate weights of fixed kernels by a function learned from another modality. Dai et al. (2017) learn offsets of weights so that they do not have to be applied in a regular grid.

Object detection and semantic segmentation: Object detection methods can be divided into *proposal-based* and *proposal-free* schemes. In the former case, processing occurs in two stages. A convolutional network ingests the whole image and proposes regions that might contain objects. These proposal regions are then resized, and a second network analyzes them to establish whether there is an object there and what it is. An early example of this approach was *R-CNN* (Girshick et al., 2014). This was subsequently extended to allow end-to-end training

(Girshick, 2015) and to reduce the cost of the region proposals (Ren et al., 2015). Subsequent work on *feature pyramid networks* improved both performance and speed by combining features across multiple scales Lin et al. (2017b). In contrast, proposal-free schemes perform all the processing in a single pass. YOLO Redmon et al. (2016), which was described in section 10.5.2, is the most celebrated example of a proposal-free scheme. The most recent iteration of this framework at the time of writing is YOLOv7 (Wang et al., 2022a). A recent review of object detection can be found in Zou et al. (2023).

The semantic segmentation network described in section 10.5.3 was developed by Noh et al. (2015). Many subsequent approaches have been variations of U-Net (Ronneberger et al., 2015), which is described in section 11.5.3. Recent surveys of semantic segmentation can be found in Minaee et al. (2021) and Ulku & Akagündüz (2022).

Visualizing Convolutional Networks The dramatic success of convolutional networks led to a series of efforts to visualize the information they extract from the image (see Qin et al., 2018, for a review). Erhan et al. (2009) visualized the optimal stimulus that activated a hidden unit by starting with an image containing noise and then optimizing the input to make the hidden unit most active using gradient ascent. Zeiler & Fergus (2014) trained a network to reconstruct the input and then set all the hidden units to zero except the one they were interested in; the reconstruction then provides information about what drives the hidden unit. Mahendran & Vedaldi (2015) visualized an entire layer of a network. Their *network inversion* technique aimed to find an image that resulted in the activations at that layer but also incorporates prior knowledge that encourages this image to have similar statistics to natural images.

Finally, Bau et al. (2017) introduced *network dissection*. Here, a series of images with known pixel labels capturing color, texture, and object type are passed through the network, and the correlation of a hidden unit with each property is measured. This method has the advantage that it only uses the forward pass of the network and does not require optimization. These methods did provide some partial insight into how the network processes images. For example, Bau et al. (2017) showed that earlier layers correlate more with texture and color and later layers with the object type. However, it is fair to say that fully understanding the processing of networks containing millions of parameters is currently not possible.

Problems

Problem 10.1* Show that the operation in equation 10.4 is equivariant with respect to translation.

Problem 10.2 Equation 10.3 defines 1D convolution with a kernel size of three, stride of one, and dilation zero. Write out the equivalent equation for the 1D convolution with a kernel size of three and a stride of two as pictured in figure 10.3a–b.

Problem 10.3 Write out the equation for the 1D dilated convolution with a kernel size of three and a dilation rate of one, as pictured in figure 10.3d.

Problem 10.4 Write out the equation for a 1D convolution with kernel size seven, dilation rate of two, and stride of three.

Problem 10.5 Draw weight matrices in the style of figure 10.4d for (i) the strided convolution in figure 10.3a–b, (ii) the convolution with kernel size 5 in figure 10.3c, and (iii) the dilated convolution in figure 10.3d.

Problem 10.6* Draw a 6×12 weight matrix in the style of figure 10.4d relating the inputs $x_1, \ldots, x_6$ to the outputs $h_1, \ldots, h_{12}$ in the multi-channel convolution as depicted in figures 10.5a–b.

Problem 10.7* Draw a 12×6 weight matrix in the style of figure 10.4d relating the inputs $h_1, \ldots, h_{12}$ to the outputs $h'_1, \ldots, h'_6$ in the multi-channel convolution in figure 10.5c.

Problem 10.8 Consider a 1D convolutional network where the input has three channels. The first hidden layer is computed using a kernel size of three and has four channels. The second hidden layer is computed using a kernel size of five and has ten channels. How many biases and how many weights are needed for each of these two convolutional layers?

Problem 10.9 A network consists of three 1D convolutional layers. At each layer, a zero-padded convolution with kernel size three, stride one, and dilation zero is applied. What size is the receptive field of the hidden units in the third layer?

Problem 10.10 A network consists of three 1D convolutional layers. At each layer, a zero-padded convolution with kernel size seven, stride one, and dilation zero is applied. What size is the receptive field of hidden units in the third layer?

Problem 10.11 Consider a convolutional network with 1D input $\mathbf{x}$. The first hidden layer $\mathbf{H}_1$ is computed using a convolution with kernel size five, stride two, and a dilation rate of zero. The second hidden layer $\mathbf{H}_2$ is computed using a convolution with kernel size three, stride one, and a dilation rate of zero. The third hidden layer $\mathbf{H}_3$ is computed using a convolution with kernel size three, stride one, and a dilation rate of one. What are the receptive field sizes at each hidden layer?

Problem 10.12 The 1D convolutional network in figure 10.7 was trained using stochastic gradient descent with a learning rate of 0.01 and a batch size of 100 on a training dataset of 4,000 examples for 100,000 steps. How many epochs was the network trained for?

Problem 10.13 Draw a weight matrix in the style of figure 10.4d that shows the relationship between the 24 inputs and the 24 outputs in figure 10.9.

Problem 10.14 Consider a 2D convolutional layer with kernel size 5×5 that takes 3 input channels and returns 10 output channels. How many convolutional weights are there? How many biases?

Problem 10.15 Draw a weight matrix in the style of figure 10.4d that samples every other variable in a 1D input (i.e., the 1D analog of figure 10.11a). Show that the weight matrix for 1D convolution with kernel size and stride two is equivalent to composing the matrices for 1D convolution with kernel size one and this sampling matrix.

Problem 10.16* Consider the AlexNet network (figure 10.16). How many parameters are used in each convolutional and fully connected layer? What is the total number of parameters?

Problem 10.17 What is the receptive field size at each of the first three layers of AlexNet (figure 10.16)?

Problem 10.18 How many weights and biases are there at each convolutional layer and fully connected layer in the VGG architecture (figure 10.17)?

Problem 10.19* Consider two hidden layers of size 224×224 with C_1 and C_2 channels, respectively, connected by a 3×3 convolutional layer. Describe how to initialize the weights using He initialization.

Chapter 11

Residual networks

The previous chapter described how image classification performance improved as the depth of convolutional networks was extended from eight layers (AlexNet) to eighteen layers (VGG). This led to experimentation with even deeper networks. However, performance decreased again when many more layers were added.

This chapter introduces *residual blocks*. Here, each network layer computes an additive change to the current representation instead of transforming it directly. This allows deeper networks to be trained but causes an exponential increase in the activation magnitudes at initialization. To compensate for this, residual blocks employ *batch normalization*, which re-centers and re-scales the activations at each layer.

Residual blocks with batch normalization allow much deeper networks to be trained, and these networks improve performance across a variety of tasks. Architectures that combine residual blocks to tackle image classification, medical image segmentation, and human pose estimation are described.

11.1 Sequential processing

Every network we have seen so far processes the data sequentially; each layer receives the output of the previous layer and passes the result to the next (figure 11.1). For example, a three-layer network is defined by:

$$\begin{aligned} \mathbf{h}_1 &= \mathbf{f}_1[\mathbf{x}, \boldsymbol{\phi}_1] \\ \mathbf{h}_2 &= \mathbf{f}_2[\mathbf{h}_1, \boldsymbol{\phi}_2] \\ \mathbf{h}_3 &= \mathbf{f}_3[\mathbf{h}_2, \boldsymbol{\phi}_3] \\ \mathbf{y} &= \mathbf{f}_4[\mathbf{h}_3, \boldsymbol{\phi}_4], \end{aligned} \tag{11.1}$$

where $\mathbf{h}_1$, $\mathbf{h}_2$, and $\mathbf{h}_3$ denote the intermediate hidden layers, $\mathbf{x}$ is the network input, $\mathbf{y}$ is the output, and the functions $\mathbf{f}_k[\bullet, \boldsymbol{\phi}_k]$ perform the processing.

In a standard neural network, each layer consists of a linear transformation followed by an activation function, and the parameters $\boldsymbol{\phi}_k$ comprise the weights and biases of the

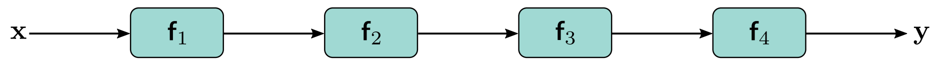

Figure 11.1 Sequential processing. Standard neural networks pass the output of each layer directly into the next layer.

linear transformation. In a convolutional network, each layer consists of a set of convolutions followed by an activation function, and the parameters comprise the convolutional kernels and biases.

Since the processing is sequential, we can equivalently think of this network as a series of nested functions:

$$\mathbf{y} = \mathbf{f}_4\Bigl[\mathbf{f}_3\Bigl[\mathbf{f}_2\bigl[\mathbf{f}_1[\mathbf{x}, \boldsymbol{\phi}_1], \boldsymbol{\phi}_2\bigr], \boldsymbol{\phi}_3\Bigr], \boldsymbol{\phi}_4\Bigr]. \tag{11.2}$$

11.1.1 Limitations of sequential processing

In principle, we can add as many layers as we want, and in the previous chapter we saw that adding more layers to a convolutional network does improve performance; the VGG network (figure 10.17), which has eighteen layers, outperforms AlexNet (figure 10.16), which has eight layers. However, image classification performance decreases again as further layers are added (figure 11.2). This is surprisingly, since generally models perform better as more capacity is added (figure 8.10). Indeed, the decrease is present for the training set as well as the test set, which implies that the problem is training deeper networks, rather than the inability of deeper networks to generalize.

This phenomenon is not completely understood but one conjecture is that at initialization, the loss gradients change unpredictably when we modify parameters in an early network layer. With appropriate initialization of the weights (see section 7.5), the gradient of the loss with respect to these parameters will be reasonable (i.e., no exploding or vanishing gradients). However, the derivative assumes an infinitesimal change in the parameter whereas optimization algorithms change the parameter by a finite step size. It may be that any reasonable choice of step size moves to a place with a completely different and unrelated gradient; the loss surface looks like an enormous range of tiny mountains, rather than a single relatively smooth structure that is easy to descend. Consequently, the algorithm does not make progress in the way that it does when the loss function gradient changes more slowly.

This conjecture is supported by empirical observations of the gradients in networks with a single input and a single output. For a shallow network, the gradient of the output with respect to the input changes relatively slowly as we change the input (figure 11.3a). However, for a deep network with 24 layers, a tiny change in the input results in a completely different gradient (figure 11.3b). This is captured by the autocorrelation function of the gradient (figure 11.3c). For shallow networks, the gradients stay highly

Appendix C.3.3 Autocorrelation function

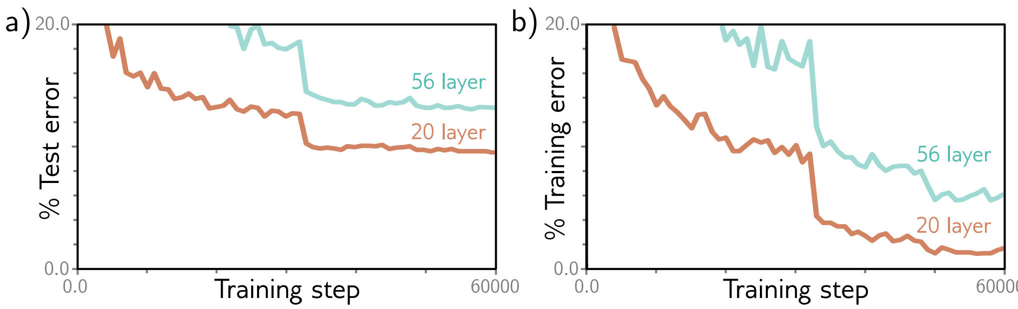

Figure 11.2 Decrease in performance when adding more convolutional layers. a) A 20-layer convolutional network outperforms a 56-layer neural network for image classification on the test set of the CIFAR-10 dataset (Krizhevsky & Hinton, 2009). b) This is also true for the training set, which suggests that the problem relates to training the original network, rather than a failure to generalize to new data. Adapted from He et al. (2016a).

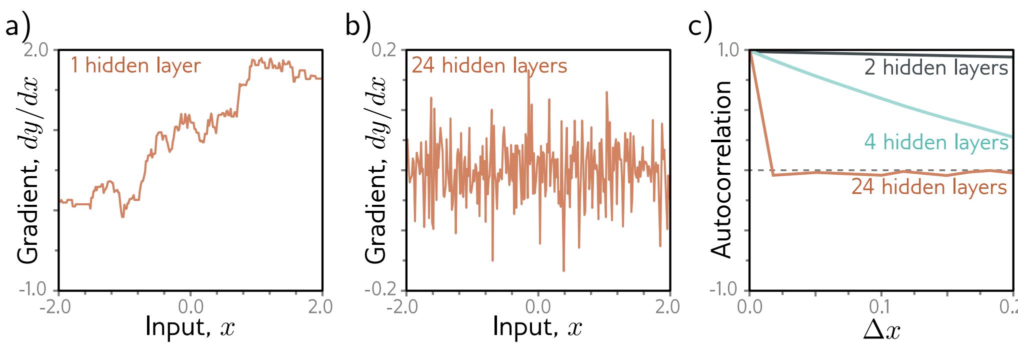

Figure 11.3 Shattered gradients. a) Consider a shallow network with 200 hidden units and Glorot initialization (He initialization without the factor of two) for both the weights and biases. The gradient $\partial y/\partial x$ of the scalar network output y with respect to the scalar input x changes relatively slowly as we change the input x. b) For a deep network with 24 layers and 200 hidden units per layer, this gradient changes very quickly and unpredictably. c) The autocorrelation function of the gradient shows that nearby gradients become unrelated (have autocorrelation close to zero) for deep networks. This *shattered gradients* phenomenon may explain why it is hard to train deep networks. Gradient descent algorithms rely on the loss surface being relatively smooth, so the gradients should be related before and after each update step. Adapted from Balduzzi et al. (2017).

correlated as the input changes, but for deep networks, their correlation quickly drops to zero. This is termed the *shattered gradients* phenomenon.

Shattered gradients presumably arise because changes in early network layers modify the output in an increasingly complex way as the network becomes deeper. The derivative of the output $\mathbf{y}$ with respect to the first layer $\mathbf{f}_1$ of the network in equation 11.1 is:

$$\frac{\partial \mathbf{y}}{\partial \mathbf{f}_1} = \frac{\partial \mathbf{f}_4}{\partial \mathbf{f}_3}\frac{\partial \mathbf{f}_3}{\partial \mathbf{f}_2}\frac{\partial \mathbf{f}_2}{\partial \mathbf{f}_1}. \tag{11.3}$$

When we change the parameters that determine $\mathbf{f}_1$, *all* of the derivatives in this sequence can change, since layers $\mathbf{f}_2, \mathbf{f}_3$ and $\mathbf{f}_4$ are themselves computed from $\mathbf{f}_1$. Consequently, the updated gradient at each training example may be completely different, and the loss function becomes badly behaved.[1]

11.2 Residual connections and residual blocks

Residual or *skip connections* are branches in the computational path, whereby the input to each network layer $\mathbf{f}[\bullet]$ is added back to the output (figure 11.4a). By analogy to equation 11.1, the residual network is defined as:

$$\begin{aligned} \mathbf{h}_1 &= \mathbf{x} + \mathbf{f}_1[\mathbf{x}, \boldsymbol{\phi}_1] \\ \mathbf{h}_2 &= \mathbf{h}_1 + \mathbf{f}_2[\mathbf{h}_1, \boldsymbol{\phi}_2] \\ \mathbf{h}_3 &= \mathbf{h}_2 + \mathbf{f}_3[\mathbf{h}_2, \boldsymbol{\phi}_3] \\ \mathbf{y} &= \mathbf{h}_3 + \mathbf{f}_4[\mathbf{h}_3, \boldsymbol{\phi}_4], \end{aligned} \tag{11.4}$$

where the first term on the right-hand side of each line corresponds to the residual connection. Each function $\mathbf{f}_k$ learns an additive change to the current representation. It follows that their outputs must be the same size as their inputs. Each additive combination of the input and the processed output is known as a *residual block*.

Problem 11.1

Once more, we can write this as a single function by substituting in the expressions for the intermediate quantities $\mathbf{h}_k$:

$$\begin{aligned} \mathbf{y} = \mathbf{x} \; + & \; \mathbf{f}_1[\mathbf{x}] \\ + & \; \mathbf{f}_2\big[\mathbf{x} + \mathbf{f}_1[\mathbf{x}]\big] \\ + & \; \mathbf{f}_3\Big[\mathbf{x} + \mathbf{f}_1[\mathbf{x}] + \mathbf{f}_2\big[\mathbf{x} + \mathbf{f}_1[\mathbf{x}]\big]\Big] \\ + & \; \mathbf{f}_4\bigg[\mathbf{x} + \mathbf{f}_1[\mathbf{x}] + \mathbf{f}_2\big[\mathbf{x} + \mathbf{f}_1[\mathbf{x}]\big] + \mathbf{f}_3\Big[\mathbf{x} + \mathbf{f}_1[\mathbf{x}] + \mathbf{f}_2\big[\mathbf{x} + \mathbf{f}_1[\mathbf{x}]\big]\Big]\bigg], \end{aligned} \tag{11.5}$$

where we have omitted the parameters $\boldsymbol{\phi}_\bullet$ for clarity. We can think of this equation as "unraveling" the network (figure 11.4b). We see that the final network output is a sum

[1] In equations 11.3 and 11.6 we overload notation to define $\mathbf{f}_k$ as the output of the function $\mathbf{f}_k[\bullet]$.

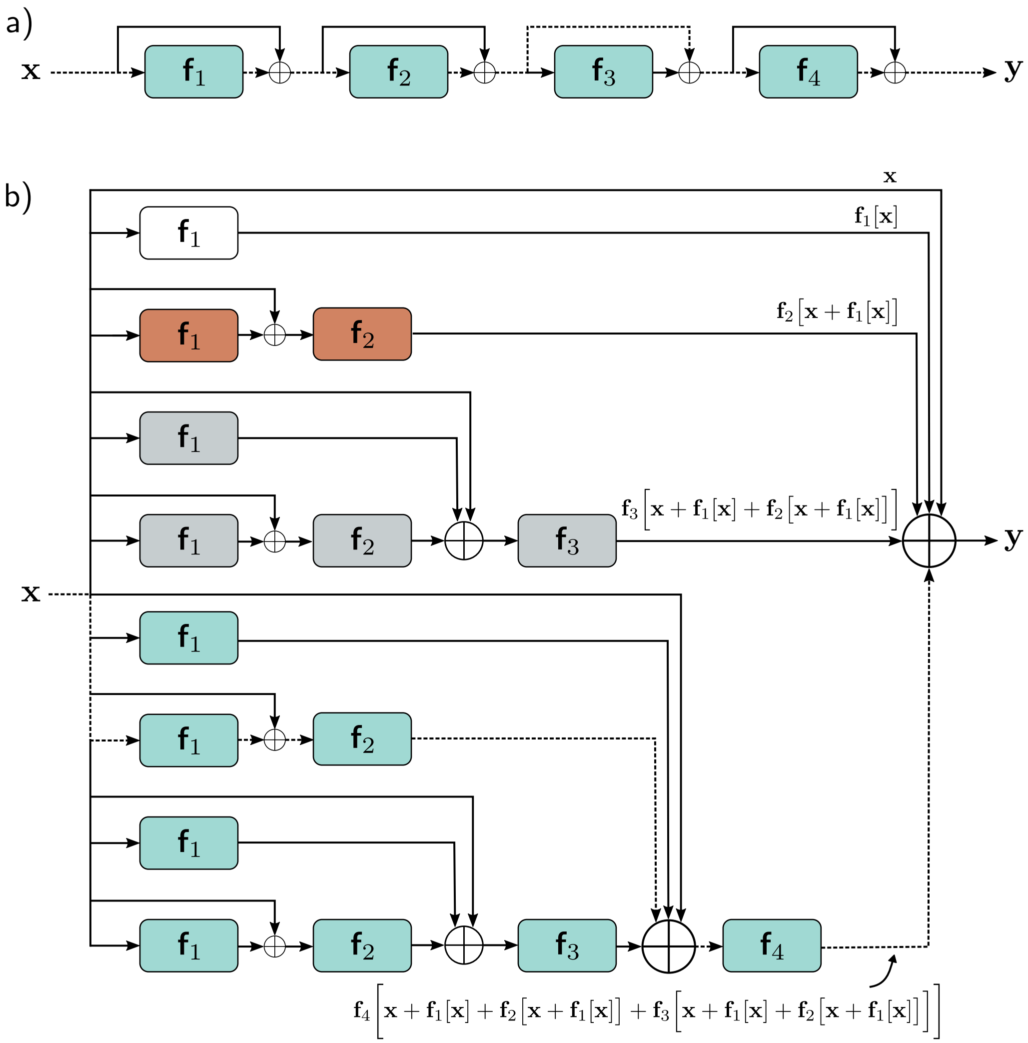

Figure 11.4 Residual connections. a) The output of each function $\mathbf{f}_k[\mathbf{x}, \boldsymbol{\phi}_k]$ is added back to its input, which is passed via a parallel computational path called a residual or skip connection. Hence, the function computes an additive change to the representation. b) Upon expanding (unraveling) the network equations, we find that the output is the sum of the input plus four smaller networks (depicted in white, orange, gray, and cyan, respectively, and corresponding to terms in equation 11.5); we can think of this as an ensemble of networks. Moreover, the output from the cyan network is itself a transformation $\mathbf{f}_4[\bullet, \boldsymbol{\phi}_4]$ of another ensemble and so on. Alternatively, we can consider the network as a combination of 16 different paths through the computational graph. One example is the dashed path from input $\mathbf{x}$ to output $\mathbf{y}$ which is the same in both panels (a) and (b).

of the input and four smaller networks, corresponding to each line of the equation; one interpretation is that residual connections turn the original network into an ensemble of these smaller networks whose outputs are summed to compute the result.

Problem 11.2

Problem 11.3

A complementary way of thinking about this residual network is that it creates sixteen paths of different lengths from input to output. For example, the first function $\mathbf{f}_1[\mathbf{x}]$ occurs in eight of these sixteen paths, including as a direct additive term, (i.e., a path length of one) and the analogous derivative to equation 11.3 is:

$$\frac{\partial \mathbf{y}}{\partial \mathbf{f}_1} = \mathbf{I} + \frac{\partial \mathbf{f}_2}{\partial \mathbf{f}_1} + \left(\frac{\partial \mathbf{f}_3}{\partial \mathbf{f}_1} + \frac{\partial \mathbf{f}_3}{\partial \mathbf{f}_2}\frac{\partial \mathbf{f}_2}{\partial \mathbf{f}_1}\right) + \left(\frac{\partial \mathbf{f}_4}{\partial \mathbf{f}_1} + \frac{\partial \mathbf{f}_4}{\partial \mathbf{f}_2}\frac{\partial \mathbf{f}_2}{\partial \mathbf{f}_1} + \frac{\partial \mathbf{f}_4}{\partial \mathbf{f}_3}\frac{\partial \mathbf{f}_3}{\partial \mathbf{f}_1} + \frac{\partial \mathbf{f}_4}{\partial \mathbf{f}_3}\frac{\partial \mathbf{f}_3}{\partial \mathbf{f}_2}\frac{\partial \mathbf{f}_2}{\partial \mathbf{f}_1}\right), \quad (11.6)$$

where there is one term for each of the eight paths. The identity term on the right-hand side shows that changes in the parameters $\boldsymbol{\phi}_1$ in the first layer $\mathbf{f}_1[\mathbf{x}, \boldsymbol{\phi}_1]$ contribute directly to changes in the network output $\mathbf{y}$. They also contribute indirectly through the other chains of derivatives of varying lengths. In general, gradients through shorter paths will be better behaved. Since both the identity term and various short chains of derivatives will be present in the derivative for each layer, networks with residual links suffer less from shattered gradients.

11.2.1 Order of operations in residual blocks

Until this point, we have implied that the additive functions $\mathbf{f}[\mathbf{x}]$ could be any valid network layer (e.g., fully connected, or convolutional). This is technically true, but the order of operations in these functions is important. They must contain a nonlinear activation function like a ReLU or the entire network will be linear. However, in a typical network layer (figure 11.5a), the ReLU function is at the end, and so the output is non-negative. If we adopt this convention, then each residual block we will only be able to increase the input values.

Hence, it is typical to change the order of operations so that the activation function is applied followed by the linear transformation (figure 11.5b). Sometimes there may be several layers of processing within the residual block (figure 11.5c) but these usually terminate with a linear transformation. Finally, we note that if we start each of these blocks with a ReLU operation, then they will do nothing if the initial network input is negative since the ReLU will clip the entire signal to zero. Hence, it's typical to start the network with a linear transformation, rather than a residual block as in figure 11.5b.

11.2.2 Deeper networks with residual connections

As a rule of thumb, adding residual connections roughly doubles the depth of a network that can be practically trained before performance starts to degrade. However, we would like to be able to increase the depth further. To understand why residual connections do not allow us to increase the depth arbitrarily, we must consider how the variance of the activations changes during the forward pass, and how the magnitude of the gradients changes during the backward pass.

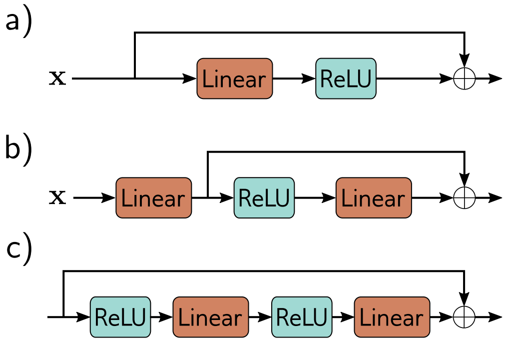

Figure 11.5 Order of operations in residual blocks. a) The usual order of linear transformation or convolution followed by a ReLU nonlinearity means that each residual block can only add non-negative quantities. b) With the reverse order, both positive and negative quantities can be added. However, we must add a linear transformation at the start of the network in case the input is all negative. c) In practice, it's common for a residual block to contain several network layers.

11.3 Exploding gradients in residual networks

In section 7.5 we saw that initializing the network parameters is critical. Without careful initialization, the magnitudes of the intermediate values during the forward pass of backpropagation can increase or decrease exponentially. Similarly, the gradients during the backward pass can explode or vanish as we move backward through the network.

The standard approach is to initialize the network parameters so that the expected variance of the activations (in the forward pass) and gradients (in the backward pass) remains the same between layers. He initialization (section 7.5) achieves this for ReLU activations by initializing the biases $\boldsymbol{\beta}$ to zero and choosing normally distributed weights $\boldsymbol{\Omega}$ with mean zero and variance $2/D_h$ where D_h is the number of hidden units in the previous hidden layer (see figure 7.7).

Now consider a residual network. We do not have to worry about the intermediate values or gradients vanishing with network depth since there exists a path whereby each layer directly contributes to the network output (equation 11.5 and figure 11.4b). However, even if we use He initialization within the residual block, the values in the forward pass increase exponentially as we move through the network.

To see why, consider that we add the result of the processing in the residual block back to the input. Each of the two branches has some (independent) variability. Hence, the overall variance increases when we recombine them. With ReLU activations and He initialization, the expected variance is unchanged by the processing in each block. Consequently, when we recombine with the input, the variance doubles (figure 11.6a), and so grows exponentially with the number of residual blocks. This limits the possible network depth before floating point precision is exceeded in the forward pass. A similar argument applies to the gradients in the backward pass of the backpropagation algorithm.

Problem 11.4

Hence, residual networks still suffer from unstable forward propagation and exploding gradients even with He initialization. One approach that would stabilize the forward and backward passes would be to use He initialization and then multiply the combined output of each residual block by $1/\sqrt{2}$ to compensate for the doubling (figure 11.6b). However, it is more usual to use *batch normalization*.

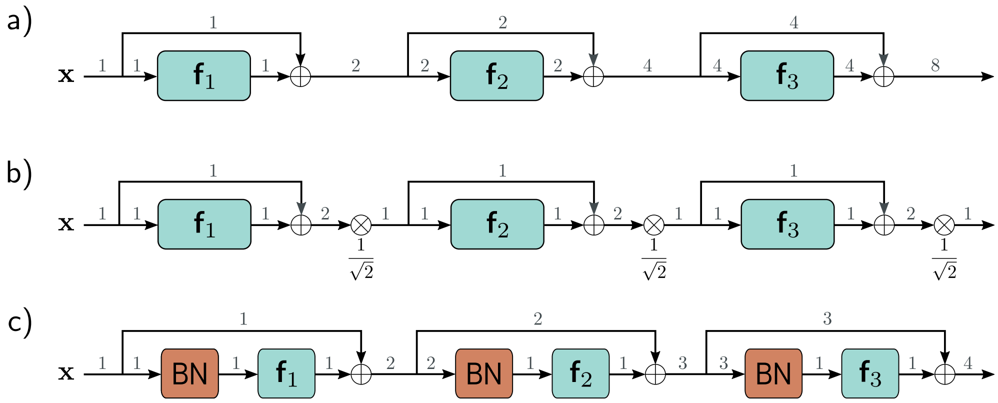

Figure 11.6 Variance in residual networks. a) He initialization ensures that the expected variance remains the same after a linear plus ReLU layer $\mathbf{f}_k$. Unfortunately, in residual networks, the output of each block is added back to the input, and so the variance doubles at each layer (gray numbers indicate variance) and grows exponentially. b) One approach would be to rescale the signal by $1/\sqrt{2}$ between each residual block. c) A second method is to use batch normalization (BN) as the first step in the residual block and initialize the associated offset δ to zero and scale γ to one. This transforms the input to each layer to have variance one, and with He initialization, the output variance will also be one. Now the variance increases linearly with the number of residual blocks. A side-effect is that at initialization, later layers of the network are dominated by the skip connection, and are hence close to computing the identity.

11.4 Batch normalization

Batch normalization or *BatchNorm* shifts and rescales each activation h so that its mean and variance across the batch $\mathcal{B}$ become values which are learned during training. First, the empirical mean m_h and standard deviation s_h are computed:

$$\begin{aligned} m_h &= \frac{1}{|\mathcal{B}|}\sum_{i\in\mathcal{B}} h_i \\ s_h &= \sqrt{\frac{1}{|\mathcal{B}|}\sum_{i\in\mathcal{B}}(h_i - m_h)^2} \end{aligned} \tag{11.7}$$

Appendix B.2.4 Standardization

where all quantities are scalars. Then we use these statistics to normalize the batch activations to have mean zero and variance one:

$$h_i \leftarrow \frac{h_i - m_h}{s_h + \epsilon} \qquad \forall i \in \mathcal{B}, \tag{11.8}$$

where ϵ is a small number that prevents division by zero if h_i is the same for every member of the batch and $s_h = 0$.

Finally, the normalized variable is scaled by γ and shifted by δ:

$$h_i \leftarrow \gamma h_i + \delta \qquad\qquad \forall i \in \mathcal{B}. \tag{11.9}$$

After this operation, the activations have mean δ and standard deviation γ across all members of the batch. Both of these quantities are parameters of the model and are learned during training.

Problem 11.5

Batch normalization is applied independently to each hidden unit, so in a standard neural network with K layers each containing D hidden units, there would be KD learned offsets δ and KD learned scales γ. In a convolutional network, the normalizing statistics are computed over both the batch and the spatial position, so if there were K layers each containing C channels, there would be KC offsets and KC scales. At test time, we do not have a batch from which we can gather statistics. To resolve this, the statistics m_h and σ_h are calculated across the whole training dataset (rather than just a batch) and frozen in the final network.

Problem 11.6

11.4.1 Costs and benefits of batch normalization

Batch normalization makes the network invariant to rescaling the weights and biases that contribute to each activation; if these are doubled, then the activations also double, the estimated standard deviation s_h doubles, and the normalization in equation 11.8 compensates for these changes. This happens separately for each hidden unit. Consequently, there will be a large family of weights and biases that all produce the same effect. Batch normalization also adds two parameters γ and δ at every hidden unit which makes the model somewhat larger. Hence, it both creates redundancy in the weight parameters and adds extra parameters to compensate for that redundancy. This is obviously inefficient, but batch normalization also provides several benefits:

Stable forward propagation: If we initialize the offsets δ to zero and the scales γ to one, then each output activation will have variance one. In a regular network, this ensures that the variance is stable during forward propagation at initialization. In a residual network, the variance must still increase as we are adding a new source of variation to the input at each layer. However, it will increase linearly with each residual block; the k^{th} layer adds one unit of variance to the existing variance of k (figure 11.6c).

This has the side-effect that later layers make a smaller change to the overall variation than earlier ones at initialization. Hence, the network is effectively less deep at the start of training, since later layers are close to computing the identity. As training proceeds, the network can increase the scales γ in the later layers, and so the network can easily control its own effective depth.

Higher learning rates: Empirical studies and theory both show that batch normalization makes the loss surface and its gradient change more smoothly (i.e., reduces shattered gradients). This means that we can use higher learning rates as the surface is more predictable. We saw in section 9.2 that higher learning rates can improve test performance.

Regularization: We also saw in chapter 9 that adding noise to the training process can improve generalization. Batch normalization injects noise because the normalization depends on the batch statistics. The activations for a given training example are normalized by an amount that depends on the other members of the batch, and so will be slightly different at each training iteration.

11.5 Common residual architectures

Residual connections are now a standard part of deep learning pipelines. This section reviews some well-known architectures that incorporate them.

11.5.1 ResNet

Residual blocks were first used in convolutional networks for image classification. The resulting networks are known as residual networks or *ResNets* for short. In ResNets each residual block contains a batch normalization operation, then the ReLU activation function, and a convolutional layer. This is followed by the same sequence again before being added back to the input (figure 11.7a). Trial and error has shown that this order of operations works well for image classification.

Problem 11.7

For very deep networks, the number of parameters may become undesirably large. *Bottleneck residual blocks* make more efficient use of parameters using three convolutions. The first has a 1×1 kernel and reduces the number of channels. The second is a regular 3×3 kernel and the third is another 1×1 kernel to increase the number of channels back to the original amount (figure 11.7b). In this way, we can integrate information over a 3×3 pixel area using fewer parameters.

Problem 11.8

The ResNet-200 model (figure 11.8) contains 200 layers and is intended for image classification on the ImageNet database (figure 10.15). The architecture is similar to AlexNet and VGG but it uses bottleneck residual blocks instead of vanilla convolutional layers. As with AlexNet and VGG, these are periodically interspersed with decreases in spatial resolution and simultaneous increases in the number of channels. Here, the resolution is decreased by downsampling using convolutions with stride two, and the number of channels is increased either by appending zeros to the representation or using an extra 1×1 convolution. At the start of the network is a 7×7 convolutional layer, followed by a downsampling operation. At the end, there is a fully connected layer that maps the block to a vector of length 1000. This is then passed through a softmax layer to generate the class probabilities.

The ResNet-200 model achieved a remarkable 4.8% error rate for the correct class being in the top five and 20.1% for identifying the correct class correctly. This compares favorably with AlexNet (16.4%, 38.1%) and VGG (6.8%, 23.7%) and was one of the first

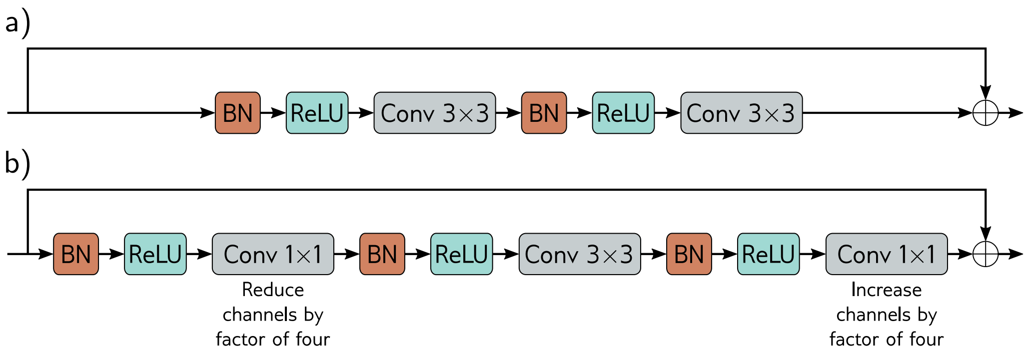

Figure 11.7 ResNet blocks. a) A standard block in the ResNet architecture contains a batch normalization operation, followed by an activation function, and then a 3×3 convolutional layer. Then, this sequence is repeated. b). A bottleneck ResNet block still integrates information over a 3×3 region but uses fewer parameters. It contains three convolutions. The first 1×1 convolution reduces the number of channels. The second 3×3 convolution is applied to the smaller representation. A final 1×1 convolution increases the number of channels again so that it can be added back to the input.

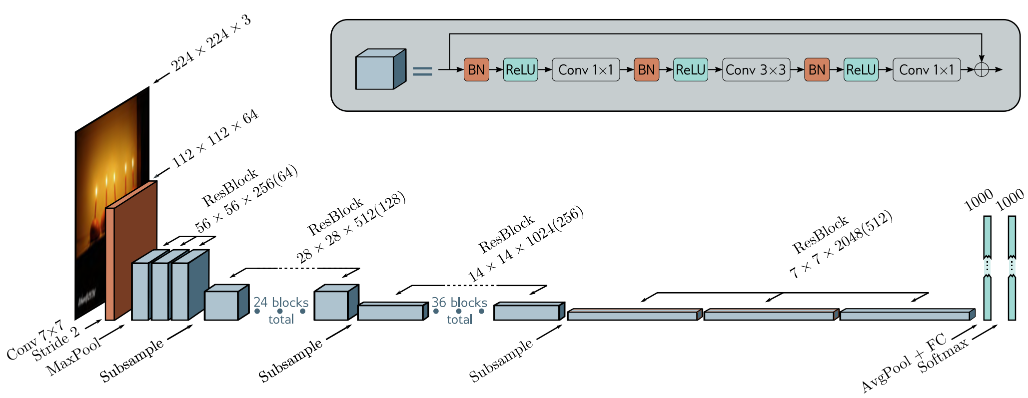

Figure 11.8 ResNet 200 model. A standard 7×7 convolutional layer with stride two is applied, followed by a MaxPool operation. A series of bottleneck residual blocks follow (number in brackets is channels after first 1×1 convolution), with periodic downsampling, and accompanying increases in the number of channels. The network concludes with average pooling across all spatial positions and a fully connected layer that maps to pre-softmax activations.

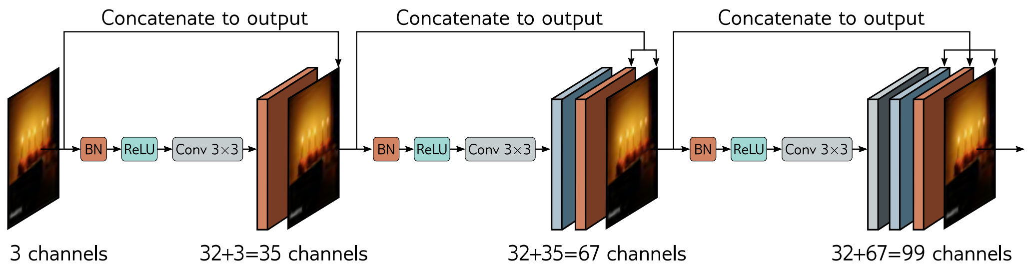

Figure 11.9 DenseNet. This architecture uses residual connections to concatenate the outputs of earlier layers to later ones. Here, the three-channel input image is processed to form a 32-channel representation. The input image is concatenated to this to give a total of 35 channels. This combined representation is processed to create another 32-channel representation and both earlier representations are concatenated to this to create a total of 67 channels and so on.

networks to exceed human performance (5.1% for being in the top five guesses). However, this model was conceived in 2016 and is now far from state-of-the-art. At the time of writing, the best-performing model on this task has a 9.0% error for identifying the class correctly (see figure 10.21). This and all the other current top-performing models for image classification are now based on transformers (see chapter 12).

11.5.2 DenseNet

Residual blocks receive the output from the previous layer, modify it, and add it back to the original input. An alternative is to concatenate the modified and original signals. This increases the representation size (in terms of channels for a convolutional network), but an optional subsequent linear transformation can map back to the original size (a 1×1 convolution for a convolutional network). This allows the model to add the representations together, take a weighted sum, or combine them in a more complex way.

The DenseNet architecture uses concatenation so that the input to a layer comprises the concatenated outputs from *all* previous layers (figure 11.9). These are processed to create a new representation that is itself concatenated with the previous representation and passed to the next layer. This concatenation means that there is a direct contribution from earlier layers to the output, and so the loss surface behaves reasonably.

Problem 11.9

In practice, this can only be sustained for a few layers because the number of channels (and hence the number of parameters required to process them) becomes increasingly large. This problem can be alleviated by applying a 1×1 convolution to reduce the number of channels before the next 3×3 convolution is applied. In a convolutional network, the input is periodically downsampled; concatenation of the representation across the downsampling makes no sense since the representations are of different sizes. Consequently, the chain of concatenation is broken at this point and a smaller representation starts a new chain. In addition, another bottleneck 1×1 convolution can be applied when the downsampling occurs to further control the representation size.

This network performs competitively with ResNet models on image classification benchmarks (see figure 10.21); indeed for a comparable parameter count, the DenseNet model can perform better. This is presumably because it has the option of reusing processing from earlier layers more flexibly.

11.5.3 U-Nets and hourglass networks

Section 10.5.3 described a network for semantic segmentation that had an encoder-decoder or hourglass structure. The encoder repeatedly downsamples the image until the receptive fields cover large areas and information is integrated from across the image. Then the decoder upsamples it again until it is the same size as the original image. The final output is a probability over possible object classes at each pixel. One drawback of this architecture is that the low-resolution representation in the middle of the network has to remember the high-resolution details of the original image to make the final result accurate. This is not necessary if residual connections add or concatenate the representations from the encoder to their partner in the decoder.

The *U-Net* (figure 11.10) is an encoder-decoder architecture where the earlier representations are concatenated to the later ones. The original implementation used "valid" convolutions, so the spatial size decreases by two pixels each time a 3×3 convolutional layer is applied. This means that the upsampled version is smaller than its counterpart in the encoder, which must be cropped before concatenation. Subsequent implementations have used zero-padding, so this cropping is not necessary. Note that the U-Net is completely convolutional, so after training it can be run on an image of *any size*.

Problem 11.10

The U-Net was intended for segmenting medical images (figure 11.11) but has found many other uses in computer graphics and vision. *Hourglass networks* are similar, but apply further convolutional layers in the skip connections and add the result back to the decoder rather than concatenating it. A series of these models forms a *stacked hourglass network* that alternates between considering the image at local and global levels. Stacked hourglass networks can be used for human pose estimation (figure 11.12). The system is trained to predict one "heatmap" for each joint, and the estimated joint position is derived from the maximum of each heatmap.

11.6 Why do nets with residual connections perform so well?

Residual networks allow much deeper networks to be trained; in fact, it's possible to extend the ResNet architecture to 1000 layers and still train effectively. The improvement in image classification performance was initially attributed to the additional depth of the network but two pieces of evidence have emerged that contradict this viewpoint.

First, shallower, wider residual networks sometimes outperform deeper, narrower ones with a comparable parameter count. In other words, better performance can sometimes be achieved with a network with fewer layers but more channels per layer. Second, there

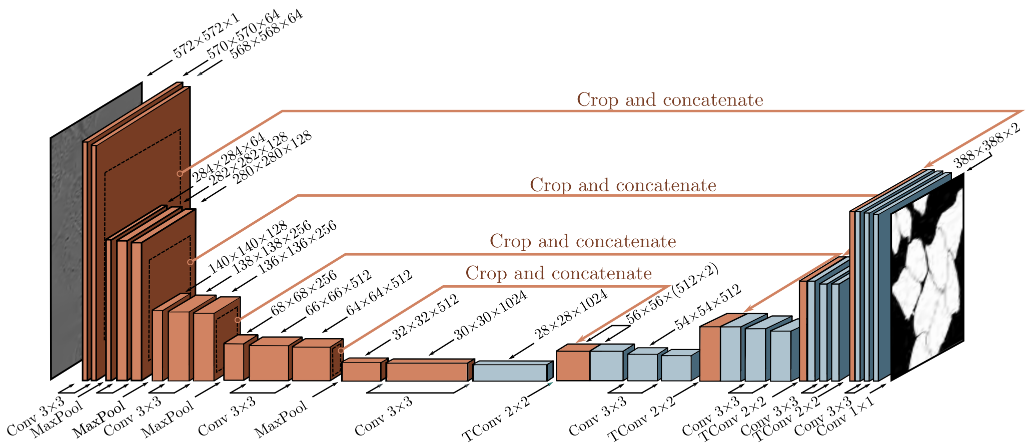

Figure 11.10 U-Net for segmenting HeLa cells. The network follows an encoder-decoder structure, in which the representation is downsampled (orange blocks) and then re-upsampled again (blue blocks). The encoder uses regular convolutions and the decoder uses transposed convolutions. Residual connections append the last representation at each scale on the left-hand side to the first representation at the same scale on the right-hand side (orange arrows). The U-Net uses "valid" convolutions, so the size decreases slightly with each layer even without downsampling. This means that the representations from the left-hand side must be cropped (dashed squares) before appending to the right-hand side. Adapted from Ronneberger et al. (2015).

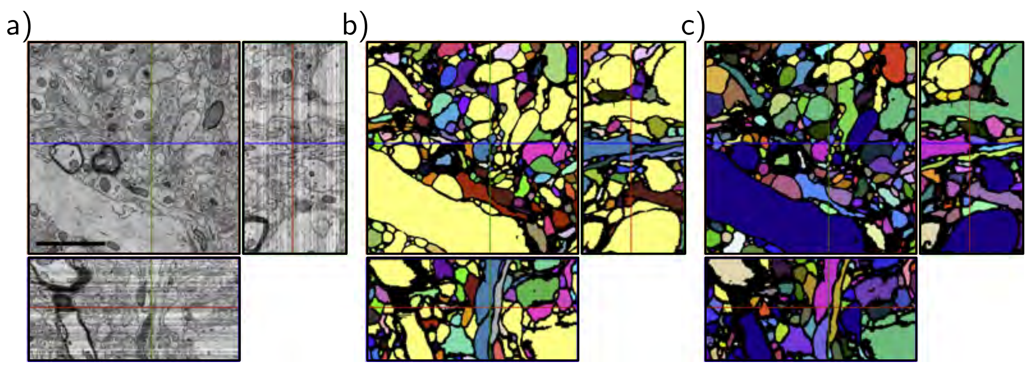

Figure 11.11 Segmentation using U-Net in 3D. a) Three slices through a 3D volume of mouse cortex taken by scanning electron microscope. b) A single U-Net is used to classify voxels as being inside or outside neurites. Connected regions are identified with different colors. c) For a better result, an ensemble of five U-Nets is trained and a voxel is only classified as belonging to the cell if all five networks agree. Adapted from Falk et al. (2019).

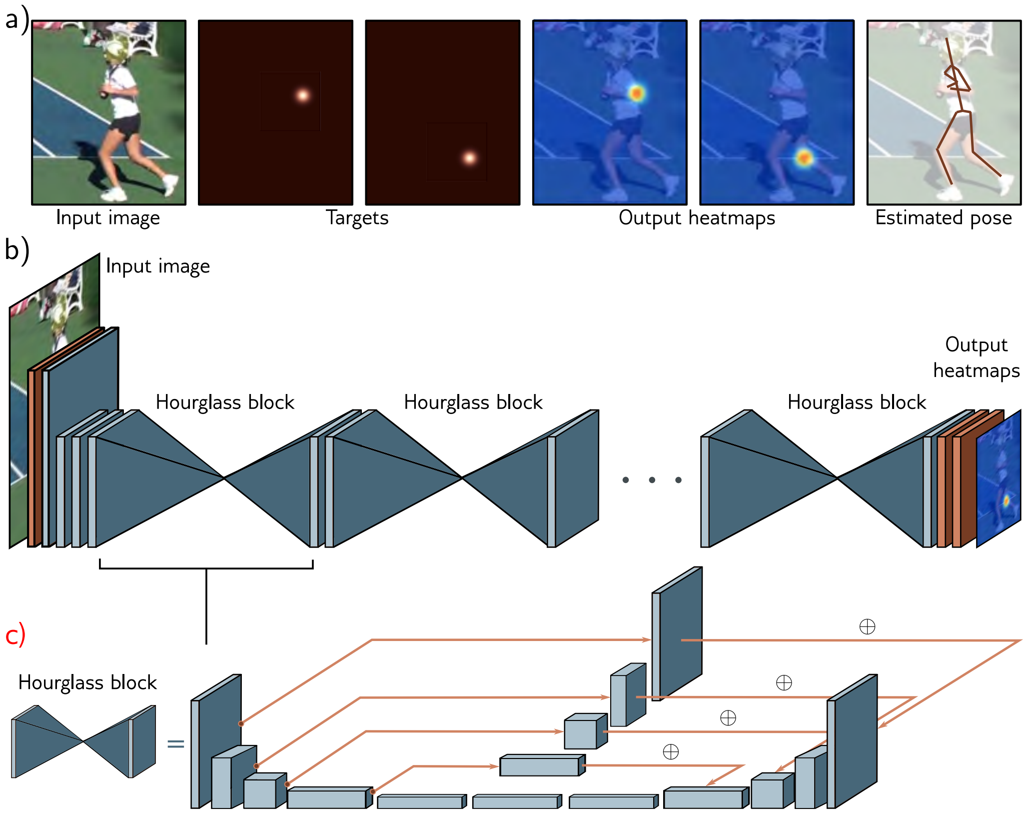

Figure 11.12 Stacked hourglass networks for pose estimation. a) The network input is an image containing a person and the output is a set of heatmaps, where there is one heatmap for each joint. This is formulated as a regression problem where the targets are heatmap images with small highlighted regions at the ground-truth joint positions. The peak of the estimated heatmap is used to establish each final joint position. b) The architecture consists of initial convolutional and residual layers followed by a series of hourglass blocks. c) Each hourglass block consists of an encoder-decoder network similar to the U-Net except that the convolutions use zero-padding, some further processing is done in the residual links, and these links add this processed representation rather than concatenate it. Each blue cuboid is itself a bottleneck residual block (figure 11.7b). Adapted from Newell et al. (2016).

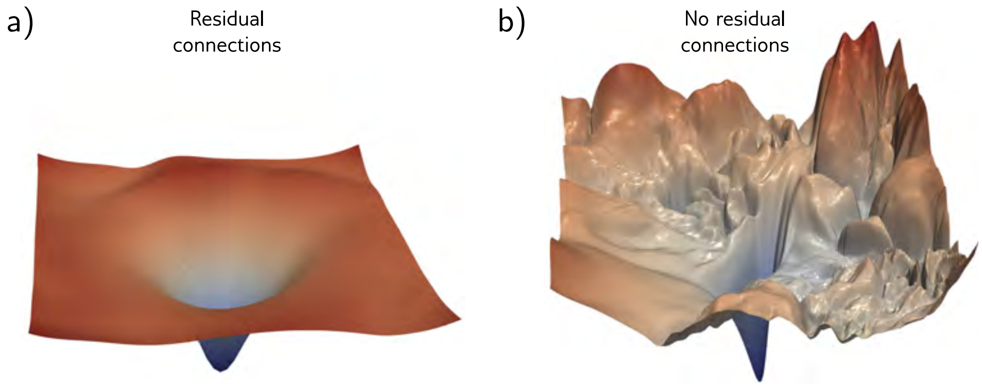

Figure 11.13 Visualizing neural network loss surfaces. Each plot shows the loss surface in two random directions in parameter space around the minimum found by SGD for an image classification task on the CIFAR-10 dataset. These directions are normalized to facilitate side-by-side comparison. a) Residual net with 56 layers. b) Results from the same network without skip connections. The surface is clearly smoother with the skip connections. This facilitates learning and makes the final network performance more robust to small errors in the parameters so that it will likely generalize better. Adapted from Li et al. (2018b).

is evidence that the gradients during training do not propagate effectively through very long paths in the unraveled network (figure 11.4b). In effect, a very deep network may be acting more like a combination of shallower networks.

The current view is that residual connections add some value of their own, as well as allowing training of deeper networks. This perspective is supported by the fact that the loss surfaces of residual networks around a minimum tend to be smoother and more predictable than those for the same network when the skip connections are removed (figure 11.13). This may make it easier to learn a good solution that generalizes well.

11.7 Summary

Increasing network depth indefinitely causes both training and test performance for image classification to decrease. This may be because the gradient of the loss with respect to parameters early in the network changes quickly and unpredictably relative to the update step size. Residual connections add the processed representation back to their own input. Now each layer contributes directly to the output as well as indirectly, so propagating gradients through many layers is not mandatory and the loss surface is smoother.

Residual networks do not suffer from vanishing gradients but introduce an exponential increase in the variance of the activations during forward propagation through the network, and corresponding problems with exploding gradients. This is usually handled by adding batch normalization layers to the network. These normalize by the empirical mean and variance of the batch and then shift and rescale using parameters that are learned. If these parameters are initialized judiciously, then very deep networks can be trained. There is evidence that both residual links and batch normalization make the loss surface smoother, which permits larger learning rates. Moreover, the variability in the batch statistics adds a source of regularization.

Residual blocks have been incorporated into convolutional networks. They allow deeper networks to be trained with commensurate increases in image classification performance. Variations of residual networks include the DenseNet architecture, which concatenates outputs of all prior layers to feed into the current layer, and U-Nets, which incorporate residual connections into encoder-decoder models.

Notes

Residual connections: Residual connections were introduced by He et al. (2016a) who built a network with 152 layers, which was eight times larger than VGG (figure 10.17), and which achieved state-of-the-art performance on the ImageNet classification task. Each residual block consisted of a convolutional layer followed by batch normalization, a ReLU activation, a second convolutional layer, and second batch normalization. A second ReLU function was then applied after this block was added back to the main representation. This architecture was termed *ResNet v1*. He et al. (2016b) investigated different variations of residual architectures, in which either (i) processing could also be applied along the skip connection or (ii) after the two branches had recombined. They concluded that neither of these was necessary leading to the architecture in figure 11.7, which is sometimes termed a *pre-activation residual block* and is the backbone of *ResNet v2*. They trained a network with 200 layers that improved further on the ImageNet classification task (see figure 11.8). Since this time, new methods for regularization, optimization, and data augmentation have been developed and Wightman et al. (2021) exploit these to present a more modern training pipeline for the ResNet architecture.

Why residual connections help: Residual networks certainly allow deeper networks to be trained. Presumably, this is related to reducing shattered gradients (Balduzzi et al., 2017) at the start of training and the smoother loss surface near the minima as depicted in figure 11.13 (Li et al., 2018b). Residual connections alone (i.e., without batch normalization) increase the trainable depth of a network by roughly a factor of two (Sankararaman et al., 2020). With batch normalization, very deep networks can be trained, but it is unclear that depth is critical for performance. Zagoruyko & Komodakis (2016) showed that wide residual networks with only 16 layers outperformed all residual networks of the time for image classification. Orhan & Pitkow (2017) propose a different explanation for why residual connections improve learning in terms of eliminating singularities (places on the loss surface where the Hessian is degenerate).

Related architectures: Residual connections are a special case of *highway networks* (Srivastava et al., 2015) which also split the computation into two branches and additively recombine. Highway networks use a gating function that weights the inputs to the two branches in a way that depends on the data itself, whereas residual networks send the data down both branches in a straightforward manner. Xie et al. (2017) introduced the ResNeXt architecture, which places a residual connection around multiple parallel convolutional branches.

Residual networks as ensembles: Veit et al. (2016) characterized residual networks as ensembles of shorter networks and depicted the “unraveled network” interpretation (figure 11.4b).

They provide evidence that this interpretation is valid by showing that deleting layers in a trained network (and hence a subset of paths) only has a modest effect on performance. Conversely, removing a layer in a purely sequential network like VGG is catastrophic. They also looked at the gradient magnitudes along paths of different lengths and showed that the gradient vanishes in longer paths. In a residual network consisting of 54 blocks, almost all of the gradient updates during training were from paths of length 5 to 17 blocks long, even though these only constitute 0.45% of the total paths. It seems that adding more blocks effectively adds more parallel shorter paths rather than creating a network that is truly deeper.

Regularization for residual networks: L2 regularization has a fundamentally different effect in vanilla networks and residual networks without BatchNorm. In the former, it encourages the output of the layer to be a constant function determined by the bias. In the latter, it encourages the output of the residual block to compute the identity, since only the "skip" connection remains when all the weights and biases are zero.

Several regularization methods have been developed that are targeted specifically at residual architectures. ResDrop (Yamada et al., 2016), stochastic depth (Huang et al., 2016), and RandomDrop (Yamada et al., 2019) all regularize residual networks by randomly dropping residual blocks during the training process. In the latter case, the propensity for dropping a block is determined by a Bernouilli variable, whose parameter is linearly decreased during training. At test time, the residual blocks are added back in with their expected probability. These methods are effectively versions of Dropout, in which all the hidden units in a block are simultaneously dropped in concert. In the multiple paths view of residual networks (figure 11.4b), they simply remove some of the paths at each training step. Wu et al. (2018b) developed BlockDrop which analyzes an existing network and decides which residual blocks to use at runtime with the goal of improving the efficiency of inference.

Separate regularization procedures have been developed for networks like ResNeXt which have multiple paths inside the residual block. Shake-shake (Gastaldi, 2017a,b) randomly re-weights these paths differently during the forward and backward passes. In the forward pass, this can be viewed as synthesizing random data, and in the backward pass as injecting another form of noise into the training method. ShakeDrop (Yamada et al., 2019) also draws a Bernoulli variable that decides whether each block will be subject to Shake-Shake or behave like a normal residual unit on this training iteration.

Batch normalization: Batch normalization was introduced by Ioffe & Szegedy (2015) outside of the context of residual networks. They showed empirically that it allowed higher learning rates, increased speed of convergence, and made sigmoid activation functions more practical (since the distribution of outputs is controlled, and so examples are less likely to fall in the saturated extremes of the sigmoid). Balduzzi et al. (2017) investigated the activation of hidden units in later layers of deep networks with ReLU functions at initialization. They showed that many such hidden units were always active or always inactive regardless of the input, but that BatchNorm reduced this tendency.

Although batch normalization helps stabilize the forward propagation of signals through a network, Yang et al. (2019) showed that it causes gradient explosion in ReLU networks without skip connections, with each layer increasing the magnitude of the gradients by $\sqrt{\pi/(\pi-1)} \approx 1.21$. This argument is summarized by Luther (2020). Since a residual network can be seen as a combination of paths of different lengths (figure 11.4), this effect must be present in residual networks as well. Presumably, however, the benefit of removing the 2^K increases in magnitude in the forward pass of a network with K layers outweighs the harm done by increasing the gradients by 1.21^K in the backward pass, and so overall BatchNorm makes training more stable.

Problem 11.11

Variations of batch normalization: Several variants of BatchNorm have been proposed (figure 11.14). BatchNorm normalizes each channel separately based on statistics gathered across the batch. *Ghost batch normalization* or *GhostNorm* (Hoffer et al., 2017) uses only part of the batch to compute the normalization statistics, which makes them noisier and increases the amount of regularization when the batch size is very large (figure 11.14b).

When the batch size is very small, or the fluctuations within a batch are very large (as is often the case in natural language processing tasks), the statistics in BatchNorm may become unreliable. Ioffe (2017) proposed *batch renormalization*, which keeps a running average of the batch statistics and modifies the normalization of any batch to ensure that it is more representative. A second problem with batch normalization is that it is unsuitable for use in recurrent neural networks (networks for processing sequences, in which the last output is fed back as an additional input as we move through the sequence (see figure 12.19). This is because the statistics must be stored at each step in the sequence, and it's not clear what to do if a test sequence is longer than the training sequences. A third problem is that batch normalization needs access to the whole batch, but this may not be easily available if the training is distributed across several machines using data parallelism.

Layer normalization or *LayerNorm* (Ba et al., 2016) avoids using the batch statistics by normalizing each data example separately, using statistics gathered across the channels and spatial position (figure 11.14c). However, there is still a separate learned scale γ and offset δ per channel. *Group normalization* or *GroupNorm* (Wu & He, 2018) is similar to LayerNorm but divides the channels into groups and computes the statistics for each group separately, computing statistics across the within-group channels and spatial position (figure 11.14d). Again, there are still separate scale and offset parameters per channel. *Instance normalization* or *InstanceNorm* (Ulyanov et al., 2016) takes this to the extreme where the number of groups is the same as the number of channels, and so each channel is normalized separately (figure 11.14e), using statistics gathered across spatial position alone. Salimans & Kingma (2016) investigated normalizing the network weights rather than the activations, but this has been less empirically successful. Teye et al. (2018) introduced *Monte Carlo batch normalization*, which can provide meaningful estimates of uncertainty in the predictions of neural networks. A recent comparison of the properties of different normalization schemes can be found in Lubana et al. (2021).

Why BatchNorm helps: BatchNorm helps control the initial gradients in a residual network (figure 11.6c). However, the mechanism by which BatchNorm improves performance more generally is not well understood. The stated goal of Ioffe & Szegedy (2015) was to reduce problems caused by *internal covariate shift*, which is the change in the distribution of inputs to a layer caused by updating preceding layers during the backpropagation update. However, Santurkar et al. (2018) provided evidence against this view by artificially inducing covariate shift and showing that networks with and without BatchNorm performed equally well.

Motivated by this, they searched for another explanation as to why BatchNorm should improve performance. They showed empirically for the VGG network that adding batch normalization decreases the variation in both the loss and its gradient as we move in the gradient direction. In other words, the loss surface is both smoother and changes more slowly, which is why larger learning rates are possible. They also provide theoretical proofs for both these phenomena and show that for any parameter initialization, the distance to the nearest optimum is less for networks with batch normalization. Bjorck et al. (2018) also argue that BatchNorm improves the properties of the loss landscape and allows larger learning rates.

Other explanations of why BatchNorm improves performance include that it decreases the importance of tuning the learning rate (Ioffe & Szegedy, 2015; Arora et al., 2018). Indeed Li & Arora (2019) show that it's possible to use an exponentially increasing learning rate schedule with batch normalization. Ultimately, this is because batch normalization makes the network invariant to the scales of the weight matrices (see Huszár, 2019, for an intuitive visualization).

Hoffer et al. (2017) identified that BatchNorm has a regularizing effect due to fluctuations in statistics due to the random composition of the batch. They proposed manipulating this directly by using a *ghost batch size*, in which the mean and standard deviation statistics are computed

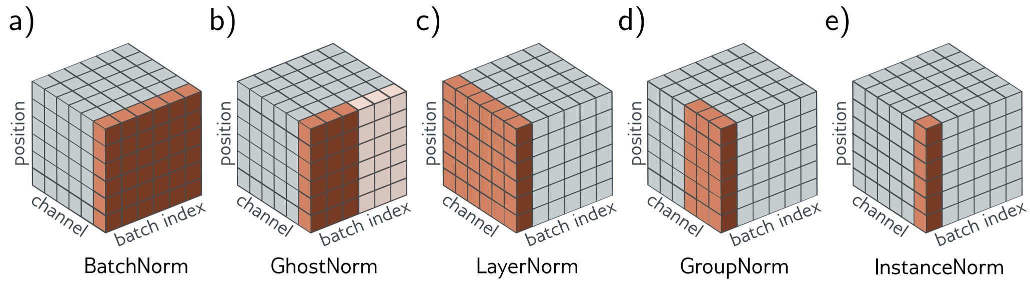

Figure 11.14 Normalization schemes. BatchNorm modifies each channel separately, but modifies each member of the batch in the same way based on statistics gathered across the batch and spatial position. Ghost BatchNorm computes these statistics from only part of the batch to make them more variable. LayerNorm computes statistics for each member of the batch separately, based on statistics gathered across the channels and spatial position. It retains a separate learned scaling factor for each channel. GroupNorm normalizes within each group of channels, and also retains a separate scale and offset parameter for each channel. InstanceNorm normalizes within each channel separately computing the statistics across spatial position only. Adapted from Wu & He (2018).

over a subset of the batch. In this way, large batches can be used, without losing the regularizing effect of the additional noise when the batch size is smaller. Luo et al. (2018) investigate the regularization effects of batch normalization.

Alternatives to batch normalization: Although BatchNorm is widely used, it is not strictly necessary to train deep residual nets; there are other ways of making the loss surface tractable. Balduzzi et al. (2017) proposed the rescaling by $\sqrt{1/2}$ in figure 11.6b; they argued that it prevents gradient explosion, but does not resolve the problem of shattered gradients.

Other work has investigated rescaling the output of the function in the residual block before addition back to the input. For example, De & Smith (2020) introduce SkipInit, in which a learnable scalar multiplier is placed at the end of each residual branch. This helps as long as this multiplier is initialized to less than $\sqrt{1/K}$, where K is the number of residual blocks. In practice, they suggest initializing this to zero. Similarly, Hayou et al. (2021) introduce Stable ResNet, which rescales the output of the function in the k^{th} residual block (before addition to the main branch) by a constant λ_k. They prove that in the limit of infinite width, the expected gradient norm of the weights in the first layer is lower bounded by the sum of squares of the scalings λ_k. They investigate setting these to a constant $\sqrt{1/K}$, where K is the number of residual blocks and show that it is possible to train networks with up to 1000 blocks.

Zhang et al. (2019a) introduce a method called *FixUp*, in which every layer is initialized using He normalization, but the last linear/convolutional layer of every residual block is set to zero. This means that the initial forward pass is stable (since each residual block contributes nothing) and the gradients do not explode in the backward pass (for the same reason). They also rescale the branches so that the magnitude of the total expected change in the parameters is constant regardless of the number of residual blocks. Although these methods allow training of deep residual networks, they do not generally achieve the same test performance as when using BatchNorm. This is probably because they do not benefit from the regularization induced by the noisy batch statistics. De & Smith (2020) modify their method to induce regularization via

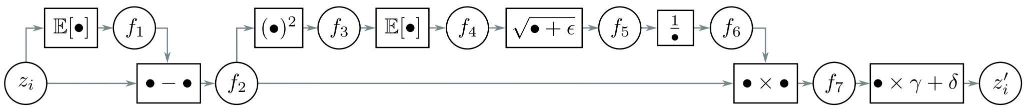

Figure 11.15 Computational graph for batch normalization (see problem 11.10).

dropout which helps close this gap.

DenseNet and U-Net: DenseNet was first introduced by Huang et al. (2017b), U-Net was developed by Ronneberger et al. (2015), and stacked hourglass networks by Newell et al. (2016). Of these architectures, U-Net has been most extensively adapted. Çiçek et al. (2016) introduced 3D U-Net and Milletari et al. (2016) introduced VNet, both of which extend U-Net to process 3D data. Zhou et al. (2018) combine the ideas of DenseNet and U-Net in an architecture that both downsamples and re-upsamples the image, but also repeatedly uses intermediate representations. U-Nets are commonly used in medical image segmentation and a review of this work can be found in Siddique et al. (2021). However, they have been applied to other areas including depth estimation (Garg et al., 2016), semantic segmentation (Iglovikov & Shvets, 2018), inpainting (Zeng et al., 2019), pansharpening (Yao et al., 2018), and image-to-image translation (Isola et al., 2017). U-Nets are also a key component in diffusion models (chapter 18).

Problems

Problem 11.1 Derive equation 11.5 from equations 11.4 by substituting in the expression for $\mathbf{h}_1, \mathbf{h}_2$, and $\mathbf{h}_3$.

Problem 11.2 The network in figure 11.4a has four residual blocks. When we unravel this network, we get one path of length zero, four paths of length one, six paths of length two, four paths of length three, and one path of length four. How many paths of each length would there be if there were (i) three residual blocks and (ii) five residual blocks? Deduce the rule for K residual blocks.

Problem 11.3 Show that the derivative of the network in equation 11.5 with respect to the first layer $\mathbf{f}_1[\mathbf{x}]$ is given by equation 11.6.

Problem 11.4 Consider a residual block, where the block contents comprise a standard linear transformation plus ReLU layer and we have used He initialization. Explain why the distributions of the activations in the block and the skip connection are independent.

Problem 11.5 The forward pass for batch normalization given a batch of scalar values $\{z_i\}_{i=1}^{I}$ consists of the following operations (figure 11.15):

$$
\begin{aligned}
f_1 &= \mathbb{E}[z_i] & f_5 &= \sqrt{f_4+\epsilon} \\
f_{2i} &= x_i - f_1 & f_6 &= 1/f_5 \\
f_{3i} &= f_{2i}^2 & f_{7i} &= f_{2i} \times f_6 \\
f_4 &= \mathbb{E}[f_{3i}] & z'_i &= f_{7i} \times \gamma + \delta,
\end{aligned} \tag{11.10}
$$

where $\mathbb{E}[z_i] = \frac{1}{I}\sum_i z_i$. Write Python code to implement the forward pass.

Now derive the algorithm for the backward pass. Work backward through the computational graph computing the derivatives to generate a set of operations that computes $\partial z'_i/\partial z_i$ for every element in the batch. Write Python code to implement the backward pass.

Problem 11.6 Consider a fully connected neural network with one input, one output, and ten hidden layers, each of which contains twenty hidden units. How many parameters does this network have? How many parameters will it have if we place a batch normalization operation between each linear transformation and ReLU?

Problem 11.7 Consider applying a L2 regularization penalty to the weights in the convolutional layers in figure 11.7a, but not to the scaling parameters of the subsequent BatchNorm layers. What do you expect will happen as training proceeds?

Problem 11.8 Consider a convolutional residual block that contains a batch normalization operation, followed by a ReLU activation function, and then a 3×3 convolutional layer. If the input has 512 channels, then how many parameters are needed to define this block? Now consider a bottleneck residual block that contains three batch normalization / activation / ReLU sequences. The first is a 1×1 convolutional layer that reduces the number of channels from 512 to 128. The second is a 3×3 convolutional layer with the same number of input and output channels. The third is a 1×1 convolutional layer that increases the number of channels from 128 to 512 (see figure 11.7b). How many parameters are needed to define this block?

Problem 11.9 The DenseNet architecture (figure 11.9) can be described by the equations:

$$
\begin{aligned}
\mathbf{h}_1 &= \mathbf{f}_1[\mathbf{x}] \\
\mathbf{h}_2 &= \mathbf{f}_2[\mathbf{concat}[\mathbf{x}, \mathbf{h}_1] \\
\mathbf{h}_3 &= \mathbf{f}_3[\mathbf{concat}[\mathbf{x}, \mathbf{h}_1, \mathbf{h}_2] \\
\mathbf{y} &= \mathbf{concat}[\mathbf{x}, \mathbf{h}_1, \mathbf{h}_2, \mathbf{h}_3]
\end{aligned}
\tag{11.11}
$$

Draw this network in the unraveled style (figure 11.4).

Problem 11.10 The U-Net is completely convolutional and can be run with any sized image after training. In principle, we could also train with a collection of arbitrary sized images. Why do you think this is not done in practice?

Problem 11.11 Figure 7.7 shows that the variance of the activations during the forward pass and the variance of the gradients during the backward pass in vanilla ReLU networks is stabilized by He initialization. Repeat this experiment, but with a BatchNorm layer with $\gamma = 1$ and $\delta = 0$ after each ReLU activation function. Write code to show that the gradients now increase as we move backward through the network at a rate of approximately 1.21 per layer.

Chapter 12

Transformers

Chapter 10 introduced convolutional networks. These are specialized for processing data that lie on a regular grid. They are particularly suited to processing images, which have a very large number of input variables (precluding the use of fully connected networks) and behave similarly at every position (leading to the idea of parameter sharing).

This chapter introduces transformers. These were originally targeted at natural language processing (NLP) problems, where the network input is a series of high-dimensional embeddings that represent words or word fragments. Language datasets share some of the characteristics of image data. The number of input variables can be very large, and the statistics are similar at every position; it's not sensible to re-learn the meaning of the word dog at every possible position in a body of text. However, language datasets have the complication that input sequences are of variable length, and unlike images, there is no way to easily resize them.

12.1 Processing text data

To motivate the transformer, consider the following passage:

The restaurant refused to serve me a ham sandwich because it only cooks vegetarian food. In the end, they just gave me two slices of bread. Their ambiance was just as good as the food and service.

The goal is to design a network that can process this text into a representation that is suitable for downstream tasks. For example, it might be used to classify the review as positive or negative, or answer questions such as “Does the restaurant serve steak?”.

We can make three immediate observations. First, the encoded input can be surprisingly large. In this case, each of the 37 words might be represented by an embedding vector of length 1024, so the input would be of length $37 \times 1024 = 37888$ even for this small passage. A more realistically sized input might have hundreds or even thousands of words, so fully connected neural networks are not practical.

Second, one of the defining characteristics of NLP problems is that each input (one or more sentences) is of a different length; hence, it's not even obvious how to apply a fully connected network. These first two observations both suggest that the network will need to share parameters across the words at different positions in the input in a similar way to the way that a convolutional network shares parameters across different positions in an image.

Third, language is fundamentally ambiguous; it is not clear from the syntax alone that the pronoun it refers to the restaurant and not to the ham sandwich. To understand the text, the word it should somehow be connected to the word restaurant. In the parlance of transformers, the former word should pay *attention* to the latter. This implies that there must be connections between the words and that the strength of these connections will depend on the words themselves. Moreover, these connections need to extend across large spans of the text; the word their in the last sentence also refers to the restaurant.

12.2 Dot-product self-attention

The previous section argued that a model for processing text will (i) use parameter sharing to cope with long input passages of differing lengths, and (ii) contain connections between word representations that depend on the words themselves. The transformer acquires both properties by using *dot-product self-attention*.

A standard neural network layer $\mathbf{f}[\mathbf{x}]$, takes a $D \times 1$ input $\mathbf{x}$, and applies a linear transformation followed by an activation function $\mathbf{a}[\bullet]$:

$$\mathbf{f}[\mathbf{x}] = \mathbf{a}[\boldsymbol{\beta} + \boldsymbol{\Omega}\mathbf{x}], \tag{12.1}$$

where $\boldsymbol{\beta}$ contains the biases and $\boldsymbol{\Omega}$ contains the weights.

A self-attention block $\mathbf{sa}[\bullet]$ takes N inputs $\mathbf{x}_n$, each of dimension $D\times 1$, and returns N output vectors of the same size. In the context of NLP, each of the inputs $\mathbf{x}_n$ will represent a word or word fragment. First, a set of *values* are computed for each input:

$$\mathbf{v}_n = \boldsymbol{\beta}_v + \boldsymbol{\Omega}_v \mathbf{x}_n, \tag{12.2}$$

where $\boldsymbol{\beta}_v$ and $\boldsymbol{\Omega}_v$ represent biases and weights respectively. Then the n^{th} output $\mathbf{sa}[\mathbf{x}_n]$ is a weighted sum of all the values $\mathbf{v}_n$:

$$\mathbf{sa}[\mathbf{x}_n] = \sum_{m=1}^{N} a[\mathbf{x}_m, \mathbf{x}_n]\mathbf{v}_m. \tag{12.3}$$

The scalar weight $a[\mathbf{x}_m, \mathbf{x}_n]$ is the *attention* that output $\mathbf{x}_n$ pays to input $\mathbf{x}_m$. The N weights $a[\bullet, \mathbf{x}_n]$ are non-negative and sum to one. Hence, self-attention can be thought of as *routing* the values in different proportions to create each output (figure 12.1).

The following sections examine dot-product self-attention in more detail by breaking it down into two parts. First, we consider the computation of the values and their subsequent weighting, as described in equation 12.3. Then we describe how to compute the attention weights $a[\mathbf{x}_m, \mathbf{x}_n]$ themselves.

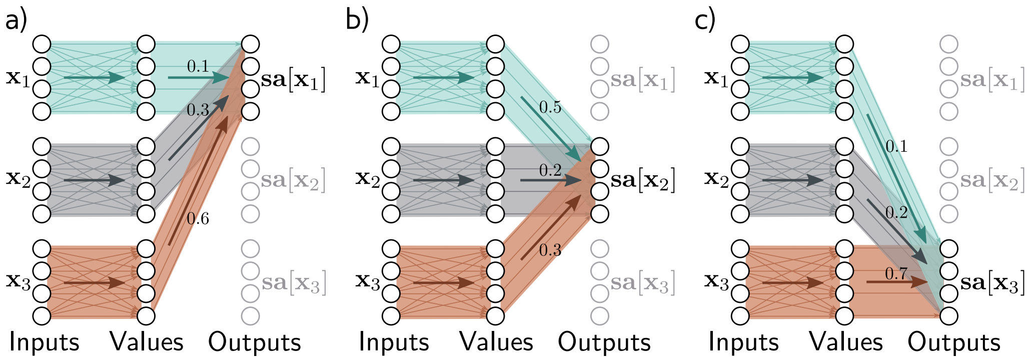

Figure 12.1 Self-attention as routing. The self-attention mechanism takes N inputs $\mathbf{x}_1, \ldots, \mathbf{x}_N$, each of size D (here $N = 3$ and $D = 4$) and processes each separately to compute N value vectors. The n^{th} output $\mathbf{sa}[\mathbf{x}_n]$ is then computed as a weighted sum of the N value vectors, where the weights are positive and sum to one. a) Output $\mathbf{sa}[\mathbf{x}_1]$ is computed as $a[1, 1] = 0.1$ times the first value vector, $a[1, 2] = 0.3$ times the second value vector, and $a[1, 3] = 0.6$ times the third value vector. b) Output $\mathbf{sa}[\mathbf{x}_2]$ is computed in the same way, but this time with weights of 0.5, 0.2, and 0.3. c) The weighting for output $\mathbf{sa}[\mathbf{x}_3]$ is different again. Each output can hence be thought of as a different routing of the N values.

12.2.1 Computing and weighting values

Equation 12.2 shows that the same weights $\boldsymbol{\Omega}_v \in \mathbb{R}^{D\times D}$ and biases $\boldsymbol{\beta}_v \in \mathbb{R}^D$ are applied to each input $\mathbf{x}_n \in \mathbb{R}^D$. This computation scales linearly with the sequence length N, and so requires fewer parameters than a fully connected network relating all DN inputs to all DN outputs. The value computation can be viewed as a sparse matrix operation with shared parameters (figure 12.2b).

The attention weights $a[\mathbf{x}_m, \mathbf{x}_n]$ combine the values from different inputs. They are also sparse in a sense, since there is only one weight for each ordered pair of inputs $(\mathbf{x}_m, \mathbf{x}_n)$, regardless of the size of these inputs (figure 12.2c). It follows that the number of attention weights has a quadratic dependence on the sequence length N, but is independent of the length D of each input $\mathbf{x}_n$. Problem 12.1

12.2.2 Computing attention weights

In the previous section, we saw that the outputs are the result of two chained linear transformations; the value vectors $\boldsymbol{\beta}_v + \boldsymbol{\Omega}_v\mathbf{x}_m$ are computed independently for each input $\mathbf{x}_m$ and these vectors are combined linearly by the attention weights $a[\mathbf{x}_m, \mathbf{x}_n]$. However, the overall self-attention computation is *nonlinear* because the attention weights are themselves nonlinear functions of the input. This is an example of a *hypernetwork*, in which one network is used to compute the weights of another.

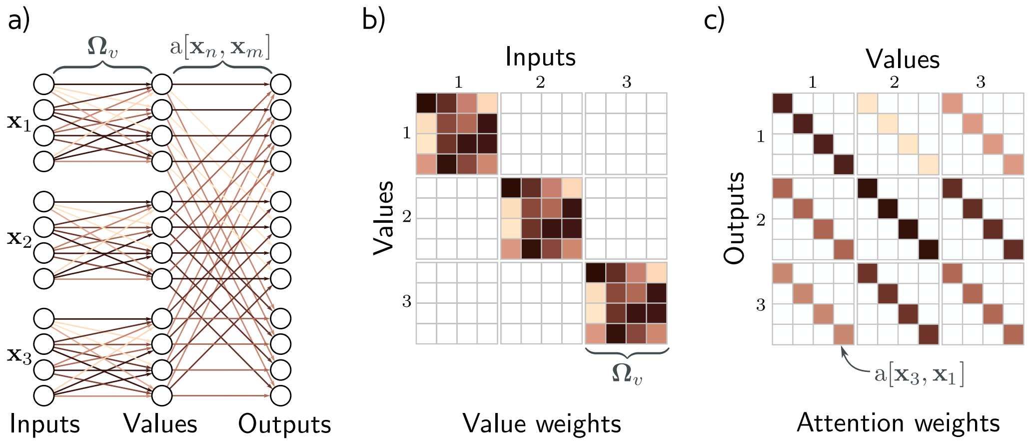

Figure 12.2 Self-attention for $N=3$ inputs $\mathbf{x}_n$, each with dimension $D=4$. a) Each input $\mathbf{x}_n$ is operated on independently by the same weights $\boldsymbol{\Omega}_v$ (same color equals same weight) and biases $\boldsymbol{\beta}_v$ (not shown) to form the values $\boldsymbol{\beta}_v + \boldsymbol{\Omega}_v\mathbf{x}_n$. Each output is a linear combination of the values, where there is a shared attention weight a$[\mathbf{x}_m, \mathbf{x}_n]$ that defines the contribution of the m^{th} value to the n^{th} output. b) Matrix showing block sparsity of linear transformation $\boldsymbol{\Omega}_v$ between inputs and values. c) Matrix showing sparsity of attention weights relating values and outputs (transposed as it will ultimately post-multiply the values).

To compute the attention, we apply two more linear transformations to the inputs:

$$\begin{aligned}\mathbf{q}_n &= \boldsymbol{\beta}_q + \boldsymbol{\Omega}_q\mathbf{x}_n \\ \mathbf{k}_n &= \boldsymbol{\beta}_k + \boldsymbol{\Omega}_k\mathbf{x}_n,\end{aligned} \tag{12.4}$$

where $\mathbf{q}_n$ and $\mathbf{k}_k$ are referred to as queries and keys, respectively. Then we compute dot products between the queries and keys and pass the results through a softmax function:

$$\begin{aligned}a[\mathbf{x}_m, \mathbf{x}_n] &= \text{softmax}_m\left[\mathbf{k}_\bullet^T\mathbf{q}_n\right] \\ &= \frac{\exp\left[\mathbf{k}_m^T\mathbf{q}_n\right]}{\sum_{m'=1}^N \exp\left[\mathbf{k}_{m'}^T\mathbf{q}_n\right]},\end{aligned} \tag{12.5}$$

so for each $\mathbf{x}_n$ they are positive and sum to one (figure 12.3). For obvious reasons, this is known as *dot-product self-attention*.

The names "queries" and "keys" were inherited from the field of information retrieval and have the following interpretation: the dot product operation returns a measure of similarity between its inputs, and so the weights $a[\mathbf{x}_\bullet, \mathbf{x}_n]$ depend on the relative similarities between each query and the keys. The softmax function means that we can

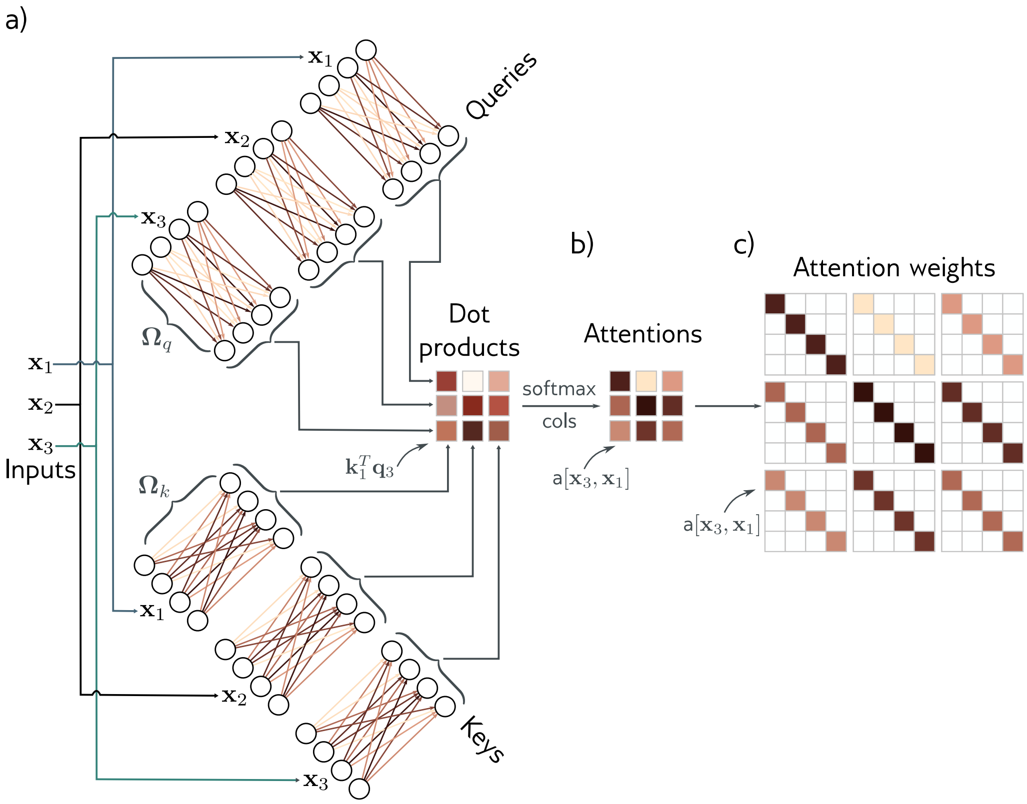

Figure 12.3 Computing attention weights. a) Query vectors $\mathbf{q}_n = \boldsymbol{\beta}_q + \boldsymbol{\Omega}_q\mathbf{x}_n$ and key vectors $\mathbf{k}_n = \boldsymbol{\beta}_k + \boldsymbol{\Omega}_k\mathbf{x}_n$ are computed for each input $\mathbf{x}_n$. b) The dot products between each query and the three keys are passed through a softmax function to form non-negative attentions that sum to one. c) These are used to route the value vectors (figure 12.1) via the sparse matrix from figure 12.2c.

think of the key vectors as "competing" with one another to contribute to the final result. The queries and keys must have the same dimensions. However, these can differ from the dimensions of the values, which are usually the same size as the input so that the representation does not change size. Problem 12.2

12.2.3 Self-attention summary

The n^{th} output is a weighted sum of the same linear transformation $\mathbf{v}_\bullet = \boldsymbol{\beta}_v + \boldsymbol{\Omega}_v\mathbf{x}_\bullet$ applied to all of the inputs, where these attention weights are positive and sum to one. The weights depend on a measure of similarity between input $\mathbf{x}_n$ and the other inputs.

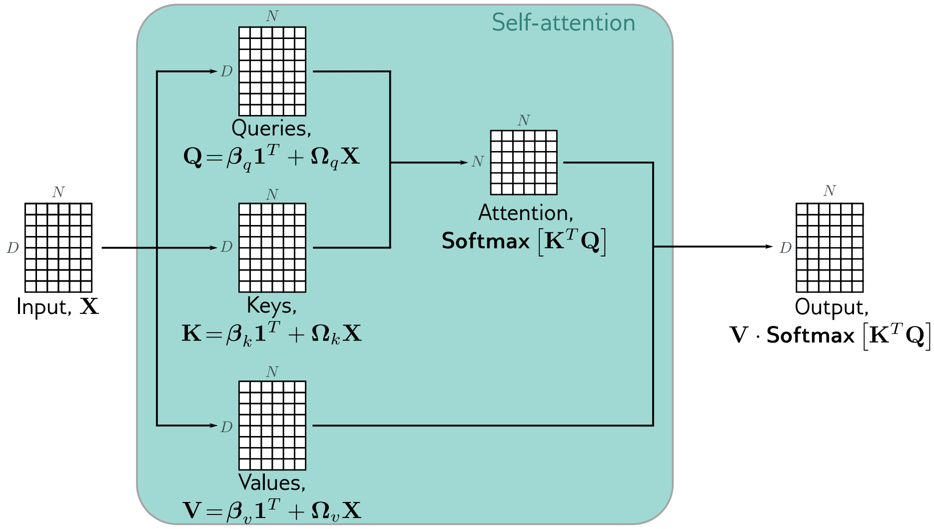

Figure 12.4 Self-attention in matrix form. Self-attention can be implemented efficiently if we store the N input vectors $\mathbf{x}_n$ in the columns of the $D \times N$ matrix $\mathbf{X}$. The input $\mathbf{X}$ is operated on separately by the query matrix $\mathbf{Q}$, key matrix $\mathbf{K}$, and value matrix $\mathbf{V}$. The dot products are then computed using matrix multiplication and a softmax operation is applied independently to each column of the resulting matrix to compute the attentions. Finally, the values are post-multiplied by the attentions to create an output of the same size as the input.

There is no activation function, but the mechanism is nonlinear due to the dot-product and a softmax operation used to compute the attention weights.

Note that this mechanism fulfills the initial requirements. First, there is a single shared set of parameters $\boldsymbol{\phi} = \{\boldsymbol{\beta}_v, \boldsymbol{\Omega}_v, \boldsymbol{\beta}_q, \boldsymbol{\Omega}_q, \boldsymbol{\beta}_k, \boldsymbol{\Omega}_k\}$. This is independent of the number of inputs N, and so the network can be applied to different sequence lengths. Second, the connections between the inputs (words) depend on the input representations themselves via the computed attention values.

12.2.4 Matrix form

Problem 12.3

The above computation can be written in a compact form if the N inputs $\mathbf{x}_n$ form the columns of the $D \times N$ matrix $\mathbf{X}$. The values, queries, and keys can be computed as:

$$
\begin{aligned}
\mathbf{V}[\mathbf{X}] &= \boldsymbol{\beta}_v \mathbf{1}^{\mathbf{T}} + \boldsymbol{\Omega}_{\mathbf{v}} \mathbf{X} \\
\mathbf{Q}[\mathbf{X}] &= \boldsymbol{\beta}_q \mathbf{1}^{\mathbf{T}} + \boldsymbol{\Omega}_{\mathbf{q}} \mathbf{X} \\
\mathbf{K}[\mathbf{X}] &= \boldsymbol{\beta}_k \mathbf{1}^{\mathbf{T}} + \boldsymbol{\Omega}_{\mathbf{k}} \mathbf{X},
\end{aligned}
\tag{12.6}
$$

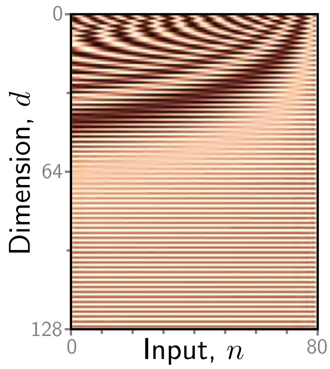

Figure 12.5 Position encodings. The self-attention architecture is equivariant to permutations of the inputs. To ensure that inputs at different positions are treated differently, a position embedding matrix $\mathbf{\Pi}$ can be added to the data matrix. Each column is different and so the positions can be distinguished. In this case, the position embeddings were predefined to be sinusoidal, but in other cases, they are learned.

where $\mathbf{1}$ is an $N \times 1$ vector containing ones. The self-attention computation is then:

$$\mathbf{Sa}[\mathbf{X}] = \mathbf{V}[\mathbf{X}] \cdot \mathbf{Softmax}\Big[\mathbf{K}[\mathbf{X}]^T \mathbf{Q}[\mathbf{X}]\Big], \tag{12.7}$$

where the function $\mathbf{Softmax}[\bullet]$ takes a matrix and performs the softmax operation independently on each of its columns (figure 12.4). In this formulation, we have explicitly included the dependence of the values, queries, and keys on the input $\mathbf{X}$ to emphasize the self-attention computes a kind of triple product based on the inputs. However, from now on we will drop this dependence and just write:

$$\mathbf{Sa}[\mathbf{X}] = \mathbf{V} \cdot \mathbf{Softmax}[\mathbf{K}^T \mathbf{Q}]. \tag{12.8}$$

12.3 Extensions to dot-product self-attention

In the previous section, we described the dot-product self-attention mechanism. Here, we introduce three extensions that are almost always used in practice.

12.3.1 Positional encoding

Observant readers will have noticed that the above mechanism loses some important information; the computation is the same regardless of the order of the inputs $\mathbf{x}_n$. More precisely, the self-attention mechanism is equivariant with respect to permutations of the inputs. However, when the inputs correspond to the words in a sentence, the order is important. The sentence The woman ate the raccoon has a quite different meaning to The raccoon ate the woman. There are two main approaches to incorporating position information. Problem 12.4

Absolute position embeddings: A matrix $\mathbf{\Pi}$ is added to the input $\mathbf{X}$ that encodes positional information (figure 12.5). Each column of $\mathbf{\Pi}$ is unique, and so contains information about the position in the input sequence. This matrix may either be chosen by hand or learned. It may be added to the network inputs or added at every network layer. Sometimes it is added to $\mathbf{X}$ in the computation of the queries and keys, but not for the values.

Relative position embeddings: The input to a self-attention mechanism may be an entire sentence, many sentences, or just a fragment of a sentence, and the absolute position of a word is much less important than the relative position between two inputs. Of course, this can be recovered if the system knows the absolute position of both, but relative position embeddings encode this information directly. Each element of the attention matrix corresponds to a particular offset between query position a and key position b. Relative position embeddings learn a parameter $\pi_{a,b}$ for each offset and use this to modify the attention matrix by adding these values, multiplying by them, or using them to modify the attention matrix in some other way.

12.3.2 Scaled dot product self-attention

The dot products in the attention computation can have very large magnitudes and move the arguments to the softmax function into a region where the largest value completely dominates. Now small changes to the inputs to the softmax function have little effect on the output (i.e., the gradients are very small) and the model becomes hard to train. To prevent this, the dot products are scaled by the square root of the dimension D_q of the queries and keys (i.e., the number of rows in $\boldsymbol{\Omega}_q$ and $\boldsymbol{\Omega}_k$, which must be the same):

Problem 12.5

$$\mathbf{Sa}[\mathbf{X}] = \mathbf{V} \cdot \mathbf{Softmax}\left[\frac{\mathbf{K}^T\mathbf{Q}}{\sqrt{D_q}}\right]. \tag{12.9}$$

This is known as *scaled dot product self-attention*.

12.3.3 Multiple heads

Multiple self-attention mechanisms are usually applied in parallel, and this is known as *multi-head self-attention*. Now H different sets of values, keys, and queries are computed:

$$\begin{aligned}
\mathbf{V}_h &= \boldsymbol{\beta}_{vh}\mathbf{1}^\mathbf{T} + \boldsymbol{\Omega}_{\mathbf{vh}}\mathbf{X} \\
\mathbf{Q}_h &= \boldsymbol{\beta}_{qh}\mathbf{1}^\mathbf{T} + \boldsymbol{\Omega}_{\mathbf{qh}}\mathbf{X} \\
\mathbf{K}_h &= \boldsymbol{\beta}_{kh}\mathbf{1}^\mathbf{T} + \boldsymbol{\Omega}_{\mathbf{kh}}\mathbf{X}.
\end{aligned} \tag{12.10}$$

The h^{th} self-attention mechanism or *head* can be written as:

$$\mathbf{Sa}_h[\mathbf{X}] = \mathbf{V}_h \cdot \mathbf{Softmax}\left[\frac{\mathbf{K}_h^T\mathbf{Q}_h}{\sqrt{D_q}}\right], \tag{12.11}$$

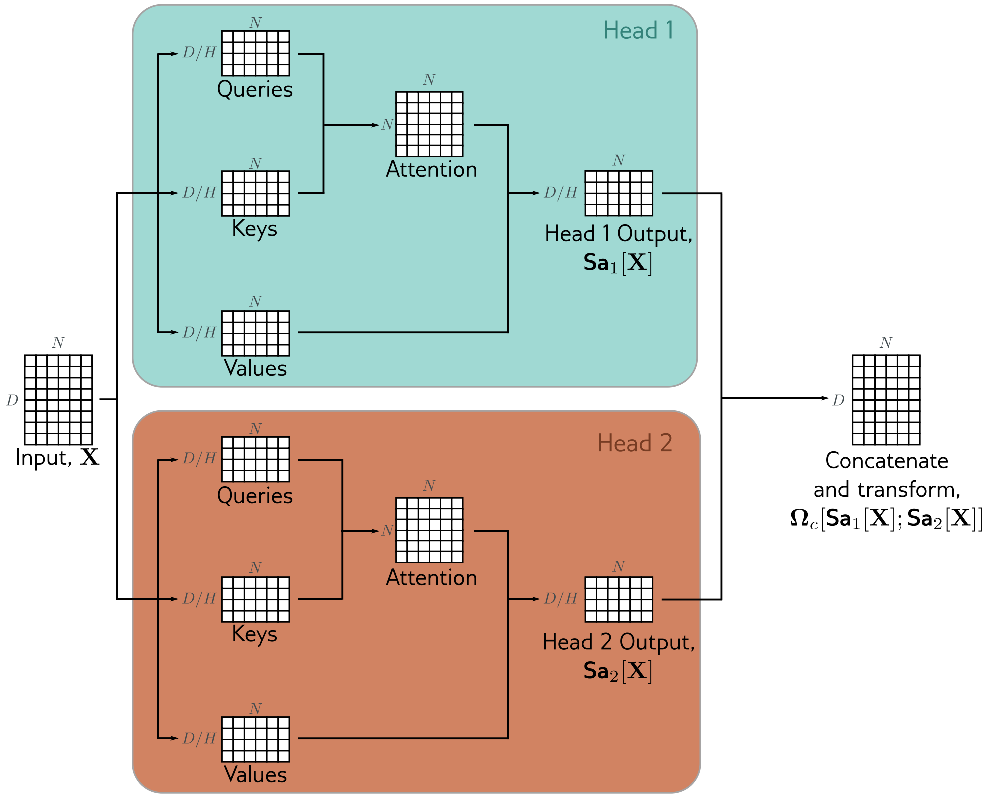

Figure 12.6 Multi-head self-attention. Self-attention occurs in parallel across multiple "heads". Each has its own queries, keys, and values. Here two heads are depicted, in the cyan and orange boxes, respectively. The outputs are vertically concatenated and another linear transformation $\mathbf{\Omega}_c$ is used to recombine them.

where we have different parameters $\{\boldsymbol{\beta}_{vh}, \mathbf{\Omega}_{vh}\}$, $\{\boldsymbol{\beta}_{qh}, \mathbf{\Omega}_{qh}\}$, and $\{\boldsymbol{\beta}_{kh}, \mathbf{\Omega}_{kh}\}$ for each head. Typically, if the dimension of the inputs $\mathbf{x}_m$ is D and there are H heads, then the values, queries, and keys will all be of size D/H, as this allows for an efficient implementation. The outputs of these self-attention mechanisms are vertically concatenated and another linear transform $\mathbf{\Omega}_c$ is applied to combine them (figure 12.6): Problem 12.6

$$\mathbf{MhSa}[\mathbf{X}] = \mathbf{\Omega}_c \left[\mathbf{Sa}_1[\mathbf{X}]; \mathbf{Sa}_2[\mathbf{X}]; \ldots; \mathbf{Sa}_H[\mathbf{X}]\right]. \tag{12.12}$$

Multiple heads seem to be necessary to make the transformer work well. It has been speculated that they make the self-attention network more robust to bad initializations.

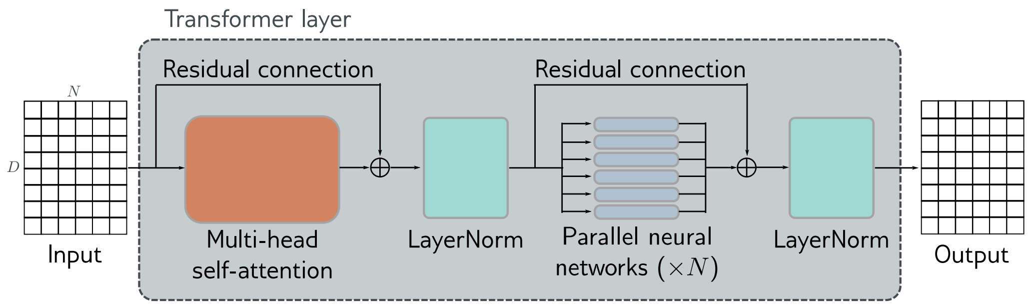

Figure 12.7 The transformer layer. The input consists of a $D \times N$ matrix containing the D-dimensional word embeddings for each of the N input tokens. The output is a matrix of the same size. The transformer layer consists of a series of operations. First, there is a multi-head attention block, which allows the word embeddings to interact with one another. This forms the processing of a residual block, so the inputs are added back to the output. Second, a LayerNorm operation is applied. Third, there is a second residual layer where the same two-layer fully connected neural network is applied to each word representation separately. Finally, LayerNorm is applied again.

12.4 Transformer layers

Self-attention is just one part of a larger *transformer layer*. This consists of a multi-head self-attention unit (which allows the word representations to interact with each other) followed by a fully connected network $\mathbf{mlp}[\mathbf{x}_\bullet]$ (that operates separately on each word). Both units are residual networks (i.e., their output is added back to the original input). In addition, it is typical to add a LayerNorm operation after both the self-attention and fully connected networks. This is similar to BatchNorm but uses statistics across the tokens within a single input sequence to perform the normalization (section 11.4 and figure 11.14). The complete layer can be described by the following series of operations:

$$
\begin{aligned}
\mathbf{X} &\leftarrow \mathbf{X} + \mathbf{MhSa}[\mathbf{X}] \\
\mathbf{X} &\leftarrow \mathbf{LayerNorm}[\mathbf{X}] \\
\mathbf{x}_n &\leftarrow \mathbf{x}_n + \mathbf{mlp}[\mathbf{x}_n] \qquad\qquad \forall\, n \in \{1, \ldots, N\} \\
\mathbf{X} &\leftarrow \mathbf{LayerNorm}[\mathbf{X}],
\end{aligned} \tag{12.13}
$$

where the column vectors $\mathbf{x}_n$ are separately taken from the full data matrix $\mathbf{X}$. In a real network, the data would pass through a series of these layers.

a) a_sailor_went_to_see_see_see_
to_see_what_he_could_see_see_see_
but_all_that_he_could_see_see_see_
was_the_bottom_of_the_deep_blue_sea_sea_sea_

_	e	s	a	t	o	h	l	u	b	d	w	c	f	i	m	n	p	r
33	28	15	12	11	8	6	6	4	3	3	3	2	1	1	1	1	1	1

b) a_sailor_went_to_see_see_see_
to_see_what_he_could_see_see_see_
but_all_that_he_could_see_see_see_
was_the_bottom_of_the_deep_blue_sea_sea_sea_

_	e	se	a	t	o	h	l	u	b	d	w	c	s	f	i	m	n	p	r
33	15	13	12	11	8	6	6	4	3	3	3	2	2	1	1	1	1	1	1

c) a_sailor_went_to_see_see_see_
to_see_what_he_could_see_see_see_
but_all_that_he_could_see_see_see_
was_the_bottom_of_the_deep_blue_sea_sea_sea_

_	se	a	e_	t	o	h	l	u	b	d	e	w	c	s	f	i	m	n	p	r
21	13	12	12	11	8	6	6	4	3	3	3	3	2	2	1	1	1	1	1	1

⋮ ⋮

d)

see_	sea_	e	b	l	w	a	could_	hat_	he_	o	t	t_	the_	to_	u	a_	d	f	m	n	p	s	sailor_	to
7	6	4	3	3	3	3	2	2	2	2	2	2	2	2	2	1	1	1	1	1	1	1	1	1

⋮ ⋮ ⋮

e)

see_	sea_	could_	he_	the_	a_	all_	blue_	bottom_	but_	deep_	of_	sailor_	that_	to_	was_	went_	what_
7	6	2	2	2	1	1	1	1	1	1	1	1	1	1	1	1	1

f)
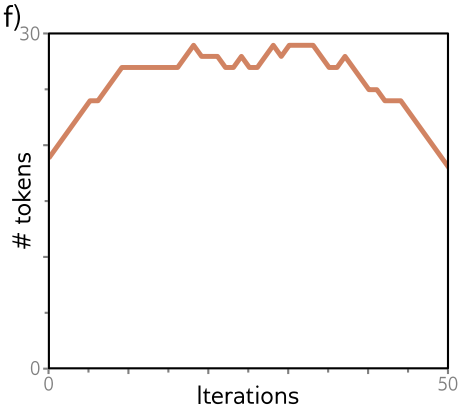

Figure 12.8 Sub-word tokenization. a) A passage of text from a nursery rhyme. The tokens are initially just the characters and whitespace (represented by an underscore), and their frequencies are displayed in the table. b) At each iteration, the sub-word tokenizer looks for the most commonly occurring adjacent pair of characters (in this case se) and merges them. This creates a new token and decreases the counts for the original tokens s and e. c) At the second iteration, the algorithm merges e and the whitespace character_. Note that the last character of the first token to be merged cannot be whitespace, which prevents merging across words. d) After 22 iterations, the tokens consist of a mix of letters, word fragments, and commonly occurring words. e) If we continue this process indefinitely, the tokens just represent the words. f) Over time, the number of tokens increases as we add word fragments to the letters, and then decreases again as we merge these fragments. In a real situation, there would be a very large number of words and the algorithm would terminate when the vocabulary size (number of tokens) reached a predetermined value. Punctuation and capital letters would also be treated as separate input characters.

12.5 Transformers for natural language processing

A typical natural language processing (NLP) pipeline starts with a *tokenize*r that splits the text into words or word fragments. Then each of these tokens is mapped to a learned embedding. These embeddings are passed through a series of transformer layers. We now consider each of these stages in turn.

12.5.1 Tokenization

A text processing pipeline begins with a *tokenizer*. This splits the text into a *vocabulary* of smaller constituent units (tokens) that can be processed by the subsequent network. In the discussion above, we have implied that these tokens represent words, but there are several difficulties with this.

- Inevitably, some words (e.g., names) will not be in the vocabulary.
- It's not clear how to handle punctuation but this is important. If a sentence ends in a question mark, then we need to encode this information.
- The vocabulary would need different tokens for versions of the same word with different suffixes (e.g., walk, walks, walked, walking) and there is no way to clarify that these variations are related.

One approach would be just to use letters and punctuation marks as the vocabulary, but this would mean splitting text into many very small parts and requiring the subsequent network to re-learn the relations between them.

In practice, a compromise between using letters and full words is used, and the final vocabulary includes both common words and word fragments from which larger and less frequent words can be composed. The vocabulary is computed using a *sub-word tokenizer* such as *byte pair encoding* (figure 12.8) that greedily merges commonly occurring substrings based on their frequency.

Problem 12.7

12.5.2 Embeddings

Each token in the vocabulary $\mathcal{V}$ is mapped to a *word embedding*. Importantly, the same token always maps to the same embedding. To accomplish this, the N input tokens are encoded in the matrix $\mathbf{T} \in \mathbb{R}^{|\mathcal{V}|\times N}$, where n^{th} column corresponds to the n^{th} token and is a $|\mathcal{V}| \times 1$ *one-hot vector* (i.e., a vector where every entry is zero except for the entry corresponding to the token, which is set to one). The embeddings for the whole vocabulary are stored in a matrix $\boldsymbol{\Omega}_e \in \mathbb{R}^{D\times|\mathcal{V}|}$. The input embeddings are then computed as $\mathbf{X} = \boldsymbol{\Omega}_e\mathbf{T}$, and $\boldsymbol{\Omega}_e$ is treated like any other network parameter (figure 12.9). A typical embedding size D is 1024 and a typical total vocabulary size $|\mathcal{V}|$ is 30,000, so even before the main network, there are many parameters in $\boldsymbol{\Omega}_e$ to learn.

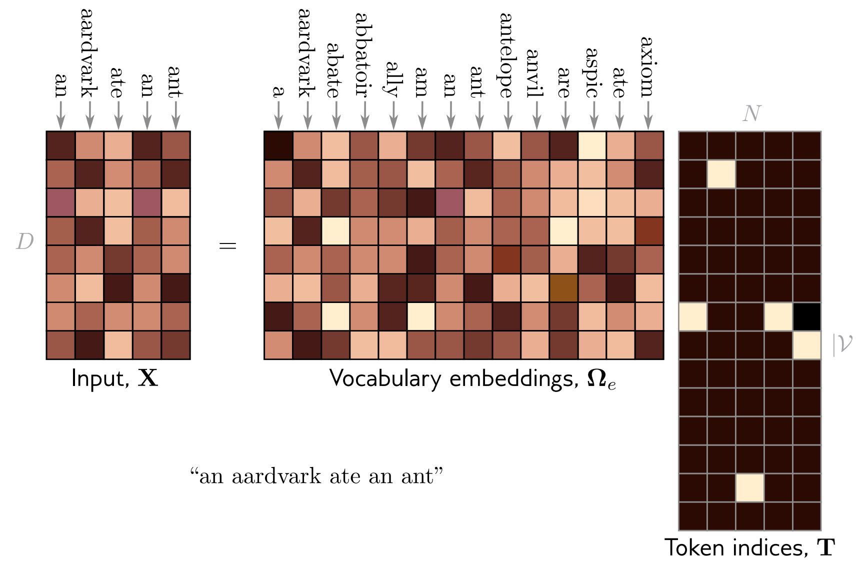

Figure 12.9 The input embedding matrix $\mathbf{X} \in \mathbb{R}^{D\times N}$ contains N embeddings of length D and is created by multiplying a matrix $\mathbf{\Omega}_e$ containing the embeddings for the entire vocabulary with a matrix containing one-hot vectors in its columns that correspond to the word or sub-word indices. The vocabulary matrix $\mathbf{\Omega}_e$ is considered a parameter of the model and is learned along with the other parameters. Note that the two embeddings for the word an in $\mathbf{X}$ are the same.

12.5.3 Transformer model

Finally, the input embedding matrix $\mathbf{X}$ is passed through a series of transformer layers, which we refer to as a *transformer model*. There are three types of transformer models. An *encoder* transforms the text into a representation that can support a variety of language tasks. A *decoder* generates a new token that continues the input text. *Encoder-decoder models* are used in *sequence-to-sequence tasks*, where one text string is converted into another (e.g., machine translation). These three variations are described in sections 12.6–12.8, respectively.

12.6 Encoder model example: BERT

BERT is an encoder model that uses a vocabulary of 30,000 tokens. The tokens are converted to 1024-dimensional word embeddings and passed through 24 transformer layers. Each contains a self-attention mechanism with 16 heads, and for each head, the queries, keys, and values are of dimension 64 (i.e., the matrices $\mathbf{\Omega}_{vh}, \mathbf{\Omega}_{qh}, \mathbf{\Omega}_{kh}$ are of

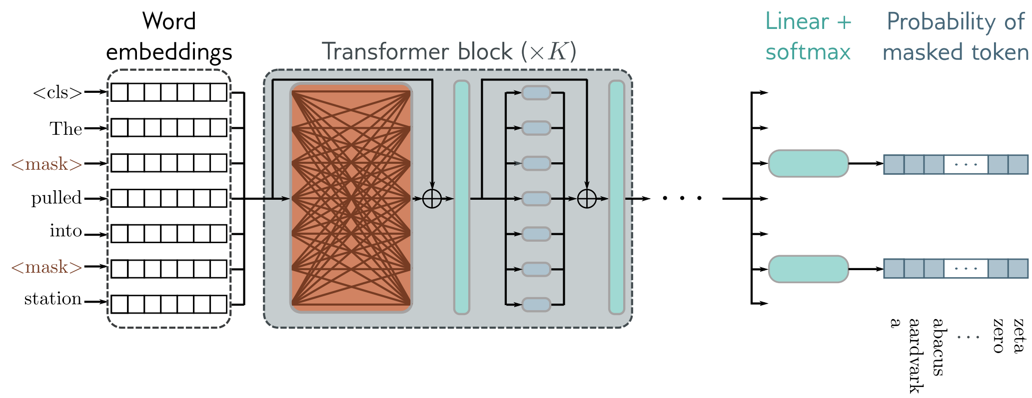

Figure 12.10 Pre-training for BERT-like encoder. The input tokens (and a special <cls> token denoting the start of the sequence) are converted to word embeddings. Here these are represented as rows rather than columns, and so the box labeled "word embeddings" is $\mathbf{X}^T$. These embeddings are passed through a series of transformer layers (orange connections indicate that every token attends to every other token in these layers) to create a set of output embeddings. A small fraction of the input tokens is replaced at random with a generic <mask> token. In pre-training, the goal is to predict the missing word from the associated output embedding. As such, the output embeddings are passed through a softmax function and the multiclass classification loss (section 5.24) is used. This task has the advantage that it uses both the left and right context to predict the missing word but has the disadvantage that it does not make efficient use of data; here, seven tokens need to be processed to add two terms to the objective function.

size 1024×64). The dimension of the hidden layer in the neural network layer of the transformer is 4096. The total number of parameters is ~ 340 million. When BERT was introduced, this was considered large but is now orders of magnitude smaller than state-of-the-art models.

Encoder models like BERT exploit transfer learning (section 9.3.6). During *pre-training*, the parameters of the transformer architecture are learned using *self-supervision* from a large corpus of text. The goal here is for the model to learn general information about the statistics of language. In the *fine-tuning stage*, the resulting network is adapted to solve a particular task, using a smaller body of supervised training data.

12.6.1 Pre-training

In the pre-training stage, the network is trained using self-supervision. This allows the use of enormous amounts of data without the need for manual labels. For BERT, the self-supervision task consisted of predicting missing words from sentences from a large

Problem 12.8

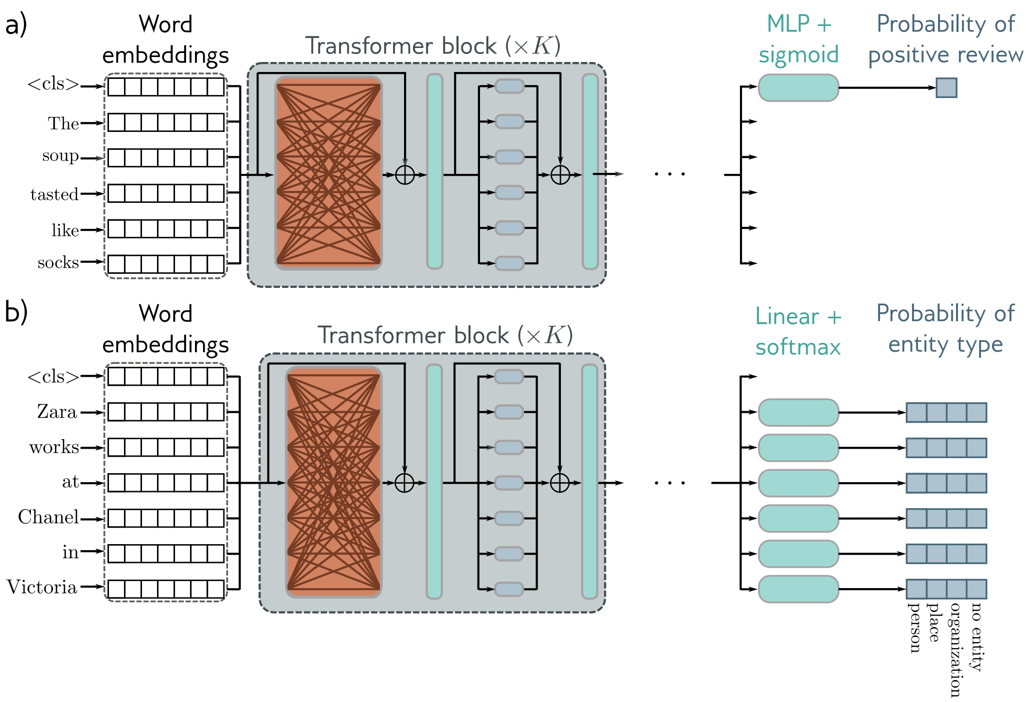

Figure 12.11 After pre-training, the encoder is fine-tuned using manually labeled data to solve a particular task. Usually, a linear transformation or a multi-layer perceptron (MLP) is appended to the encoder to produce whatever output is required for the task. a) Example text classification task. In this sentiment classification task, the <cls> token embedding is used to predict the probability that the review is positive. b) Example word classification task. In this named entity recognition problem, the embedding for each word is used to predict whether the word corresponds to a person, place, or organization, or is not an entity.

internet corpus (figure 12.10).[1] During training, the maximum input length was 512 tokens, and the batch size was 256. The system was trained for a million steps, which corresponded to roughly 50 epochs of the 3.3-billion word corpus.

Predicting missing words forces the transformer network to understand some syntax. For example, it might learn that the adjective red is often found before nouns like house or car but never before a verb like shout. It also allows the model to learn some superficial *common sense* about the world. For example, after training, the model will assign a higher probability to the missing word train in the sentence The <mask> pulled into the station, than it would to the word peanut. However, the degree of "understanding" that this type of model can ever have is limited.

[1]BERT also used a secondary task that involved predicting whether two sentences were originally adjacent in the text or not but this only marginally improved performance.

12.6.2 Fine-tuning

In the fine-tuning stage, the model parameters are adjusted to specialize the network to a particular task. An extra layer is appended onto the transformer network to convert the output vectors to the desired output format. Examples include:

Text classification: In BERT, there is a special token known as the classification or <cls> token that is placed at the start of each string during pre-training. For text classification tasks like *sentiment analysis* (in which the passage is labeled as having a positive or negative emotional tone), the vector associated with the <cls> token is mapped to a single number and passed through a logistic sigmoid (figure 12.11a). This contributes to a standard binary cross-entropy loss (section 5.4).

Word classification: The goal of *named entity recognition* is to classify each word as an entity type (e.g., person, place, organization, or no-entity). To this end, each input embedding $\mathbf{x}_n$ is mapped to a $K \times 1$ vector where K is the entity type. This is passed through a softmax function to create probabilities for each class, which contribute to a multiclass cross-entropy loss (figure 12.11b).

Text span prediction: In the SQuAD 1.1 question answering task, the question and a passage from Wikipedia containing the answer are concatenated and tokenized. BERT is then used to predict the text span in the passage that contains the answer. Each token maps to two numbers that indicate how likely it is that the text span begins and ends at this location. The resulting two sets of numbers are put through two softmax functions and the probability of any text span being the answer can then be derived by combining the probability of starting and ending at the appropriate places.

12.7 Decoder model example: GPT3

In this section, we present a high-level description of GPT3, which is an example of a decoder model. The basic architecture is extremely similar to the encoder model in that it consists of a series of transformer layers that operate on learned word embeddings. However, the goal is different. The encoder aimed to build a representation of the text that could be fine-tuned to solve a variety of more specific NLP tasks. Conversely, the decoder has one purpose, which is to generate the next token in a sequence. By feeding the extended sequence back into the model, it can generate a coherent text passage.

12.7.1 Language modeling

More formally, GPT3 constructs an autoregressive language model. For any sentence, it aims to model the joint probability $Pr(t_1, t_2, \ldots, t_N)$ of the N observed tokens and it does this by factorizing this joint probability into an autoregressive sequence:

$$Pr(t_1, t_2, \ldots, t_N) = Pr(t_1)\prod_{n=2}^{N} Pr(t_n|t_1, \ldots, t_{n-1}). \tag{12.14}$$

This is easiest to understand with a concrete example. Consider the sentence It takes great courage to let yourself appear weak. For simplicity, let's assume that the tokens are the full words. The probability of the full sentence is:

$$\begin{aligned} & Pr(\text{It takes great courage to let yourself appear weak}) \quad = \\ & Pr(\text{It}) \times Pr(\text{takes}|\text{It}) \times Pr(\text{great}|\text{It takes}) \times Pr(\text{courage}|\text{It takes great}) \times \\ & Pr(\text{to}|\text{It takes great courage}) \times Pr(\text{let}|\text{It takes great courage to}) \times \\ & Pr(\text{yourself}|\text{It takes great courage to let}) \times \\ & Pr(\text{appear}|\text{It takes great courage to let yourself}) \times \\ & Pr(\text{weak}|\text{It takes great courage to let yourself appear}). \end{aligned} \tag{12.15}$$

This demonstrates the connection between the probabilistic formulation of the loss function and the next token prediction task.

12.7.2 Masked self-attention

To train a decoder, we maximize the log probability of the input text under the autoregressive model. Ideally, we would pass in the whole sentence and compute all of the log probabilities and gradients simultaneously. However, this poses a problem; if we pass in the full sentence, then the term computing $\log[Pr(\text{great}|\text{It takes})]$ has access to both the answer great and the right context courage to let yourself appear weak.

Fortunately, in a transformer network, the tokens only interact in the self-attention layers. Hence, the problem can be resolved by ensuring that the attention to the answer and the right context is zero. This can be achieved by setting the corresponding dot products in the self-attention computation (equation 12.5) to negative infinity before they are passed through the $\mathbf{softmax}[\bullet]$ function. This is known as *masked self-attention*.

The full decoder network operates as follows. The input text is tokenized, and the tokens are converted to embeddings. The embeddings are passed into the transformer network, but now the transformer layers use masked self-attention so that they can only attend to the current and previous tokens. Each of the output embeddings can be thought of as representing a partial sentence, and for each, the goal is to predict the next token in the sequence. Consequently, after the transformer layers, a linear layer maps each word embedding to the size of the vocabulary, followed by a $\mathbf{softmax}[\bullet]$ function that converts these values to probabilities. We aim to maximize the sum of the log probabilities of the next token in the ground truth sequence at every position using a standard multiclass cross-entropy loss (figure 12.12).

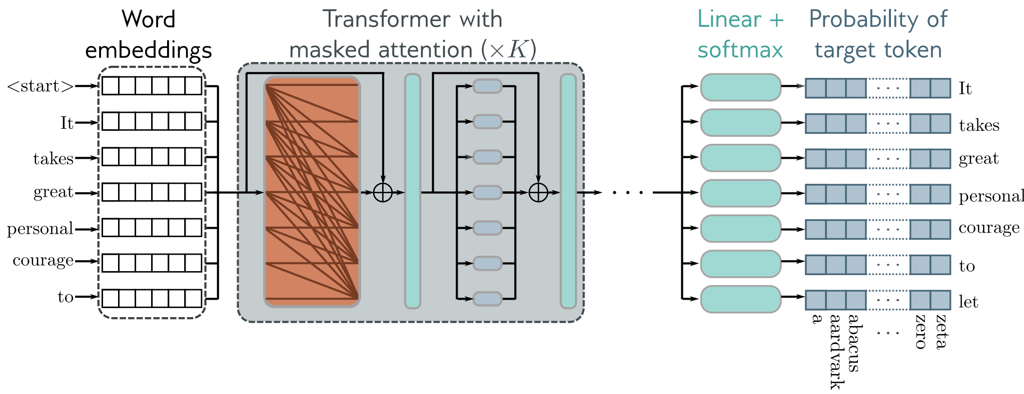

Figure 12.12 GPT3-type decoder network. The tokens are mapped to word embeddings with a special <start> token at the beginning of the sequence. The embeddings are passed through a series of transformers that use masked self-attention. Here, each position in the sentence can only attend to its own embedding and the embeddings of tokens earlier in the sequence (orange connections). The goal at each position is to maximize the probability of the next ground truth token in the sequence. In other words, at position one we want to maximize the probability of the token It, at position two we want to maximize the probability of the token takes, and so on. Masked self-attention is designed to ensure that the system cannot cheat by looking at subsequent inputs. This system has the advantage that it makes efficient use of the data since every word contributes a term to the loss function. However, it has the disadvantage that it only exploits the left context of each word.

12.7.3 Generating text from a decoder

The autoregressive language model is the first example of a *generative model* discussed in this book. Since it defines a probability model over text sequences, it can be used to sample new examples of plausible text. To generate from the model, we start with an input sequence of text (which might be just a special <start> token) and feed this into the network which then outputs the probabilities over possible next tokens. We can then either pick the most likely token or sample from this probability distribution. The new extended sequence can be fed back into the decoder network that outputs the probability distribution over the next token and in this way, we can generate large bodies of text. The computation can be made quite efficient as prior embeddings do not depend on subsequent ones due to the masked self-attention and hence much of the earlier computation can be recycled as we generate subsequent tokens.

In practice, many strategies can be employed to help make the output text more coherent. For example, *beam search* keeps track of multiple possible sentence completions with the aim of finding the overall most likely (which is not necessarily found by greedily choosing the most likely next word at each step). *Top-k sampling* randomly draws the next word from only the top-K most likely possibilities to prevent the system from accidentally choosing from the long tail of low probability tokens and leading to an unnecessary linguistic dead end.

12.7.4 GPT3 and few-shot learning

GPT3 applies these ideas on a massive scale. The sequence lengths are 2048 tokens long and since multiple spans of 2048 tokens are processed at once, the total batch size is 3.2 million tokens. There are 96 transformer layers (some of which implement a sparse version of attention), each of which processes a word embedding of size 12288. There are 96 heads in the self-attention layers and the value, query, and key dimension is 128. It is trained with 300 billion tokens and learns a total of 175 billion parameters.

Here's an example of completing text from the GPT3 model where the text provided to the model is in orange and the generated text is in cyan:

Understanding Deep Learning is a new textbook from MIT Press by Simon Prince that's designed to offer an accessible, broad introduction to the field. Deep learning is a branch of machine learning that is concerned with algorithms that learn from data that is unstructured or unlabeled. The book is divided into four sections:

1. Introduction to deep learning
2. Deep learning architecture
3. Deep learning algorithms
4. Applications of deep learning

The first section offers an introduction to deep learning, including its history and origins. The second section covers deep learning architecture, discussing various types of neural networks and their applications. The third section dives into deep learning algorithms, including supervised and unsupervised learning, reinforcement learning, and more. The fourth section applies deep learning to various domains, such as computer vision, natural language processing, and robotics.

This continuation is plausible, if not entirely accurate.

One surprising property of learning models on this scale is that they can perform many tasks without the need for fine-tuning. If we provide several examples of correct question/answer pairs, and then another question, they often answer the final question correctly by completing the sequence. One example is correcting English grammar:

Poor English input: I eated the purple berries.
Good English output: I ate the purple berries.
Poor English input: Thank you for picking me as your designer. I'd appreciate it.
Good English output: Thank you for choosing me as your designer. I appreciate it.
Poor English input: The mentioned changes have done. or I did the alteration that you requested. or I changed things you wanted and did the modifications.
Good English output: The requested changes have been made. or I made the alteration that

you requested. or I changed things you wanted and made the modifications.
Poor English input: I'd be more than happy to work with you in another project.
Good English output: I'd be more than happy to work with you on another project.

Here, the text containing the paired examples in orange was provided as context for GPT3 and the system then generated the correct answer in cyan. This phenomenon extends to many situations including generating code snippets based on natural language descriptions, arithmetic, translating between languages, and answering questions about text passages. Consequently, it is argued that enormous language models are *few-shot learners*; they can learn to do novel tasks based on just a few examples. However, in practice performance is erratic, and it is not clear the extent to which it is extrapolating from learned examples rather than merely interpolating, or copying verbatim.

12.8 Encoder-decoder model example: machine translation

Translation between languages is an example of a *sequence-to-sequence* task. This requires an encoder (to compute a good representation of the source sentence) and a decoder (to generate the sentence in the target language). This task can be tackled using an *encoder-decoder* model.

Consider the example of translating from English to French. The encoder receives the sentence in English and processes it through a series of transformer layers to create an output representation for each token. During training, the decoder receives the sentence in French and passes it through a series of transformer layers that use masked self-attention and produce the subsequent word at each position. However, the decoder layers also attend to the output of the encoder. Consequently, each French output word is conditioned not only on the previous output words but also on the entire English sentence that it is translating (figure 12.13).

This is achieved by modifying the transformer layers in the decoder. The original transformer layer in the decoder (figure 12.12) consisted of a masked self-attention layer followed by a neural network applied individually to each embedding. A new self-attention layer is added between these two components, in which the decoder embeddings attend to the encoder embeddings. This uses a version of self-attention known as *encoder-decoder attention* or *cross-attention* where the queries are computed from the decoder embeddings and the keys and values from the encoder embeddings (figure 12.14).

12.9 Transformers for long sequences

Since each token in a transformer encoder model interacts with every other token, the computational complexity scales quadratically with the length of the sequence. For a decoder model, each token only interacts with previous tokens, so there are roughly

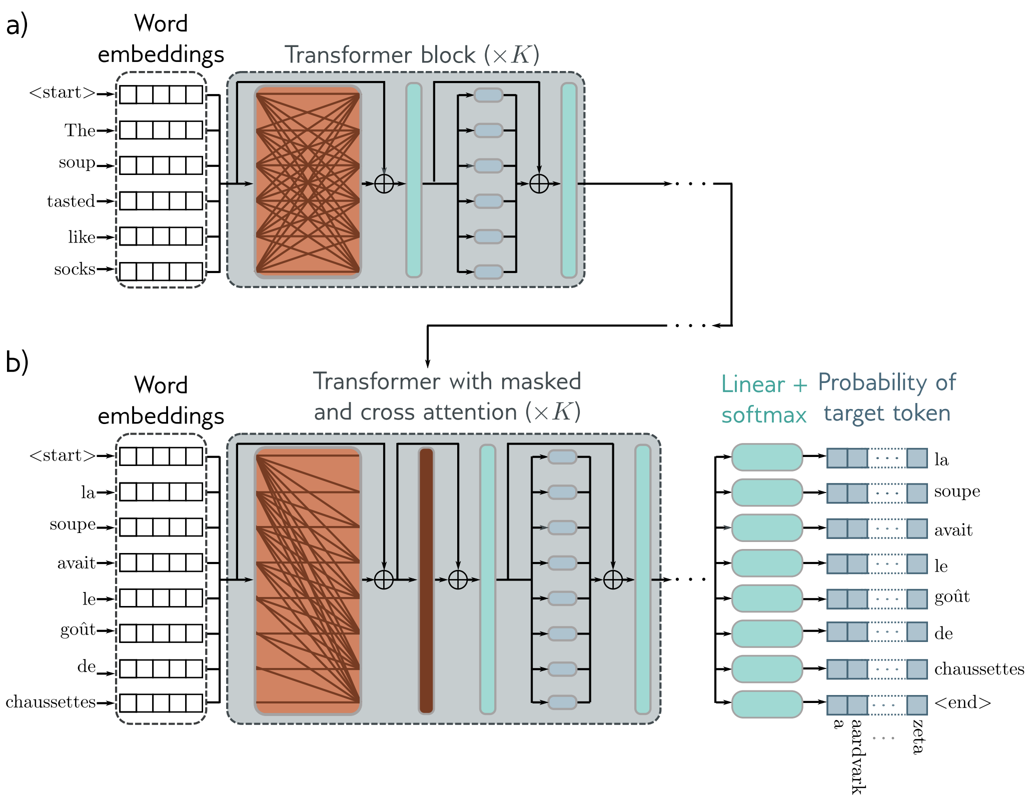

Figure 12.13 Encoder-decoder architecture. Two sentences are passed to the system with the goal of learning to translate the first into the second. The first sentence is passed through a standard encoder. The second sentence is passed through a decoder that uses masked self-attention but also attends to the output embeddings of the encoder using cross-attention (brown rectangle). The loss function is the same as for the decoder; we want to maximize the probability of the next word in the output sequence.

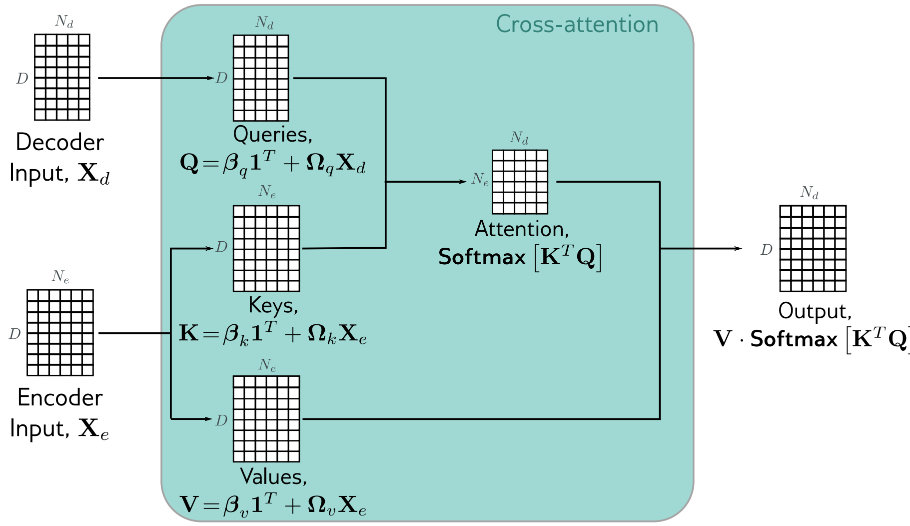

Figure 12.14 cross-attention. The flow of computation is the same as in standard self-attention. However, the queries are now calculated from the decoder embeddings $\mathbf{X}_d$, and the keys and values from the encoder embeddings $\mathbf{X}_e$.

half the number of interactions, but the complexity still scales quadratically. These relationships can be visualized as interaction matrices (figure 12.15a–b).

This quadratic increase in the amount of computation ultimately limits the length of sequences that can be used. Many methods have been developed to extend the transformer to cope with longer sequences. An important subset of these prunes the self-attention interactions, or equivalently sparsify the interaction matrix. One possibility is to use a convolutional structure so that each token only interacts with a few neighboring tokens. Across multiple layers, tokens still interact at larger distances as the receptive field expands. As for convolution in images, the kernel can vary in size and dilation rate.

A pure convolutional approach requires many layers to integrate information over large distances. One way to speed up this process is to allow select tokens (perhaps at the start of every sentence) to attend to all other tokens (encoder model) or all previous tokens (decoder model). A similar idea is to have a small number of global tokens that connect to all the other tokens and themselves. Like the <cls> token, these do not represent any word, but serve to provide long-distance connections.

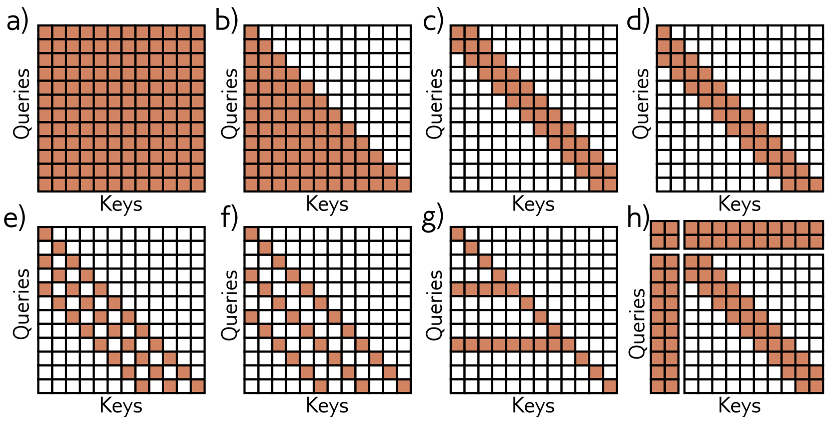

Figure 12.15 Interaction matrices for self-attention. a) In an encoder, every token interacts with every other token and computation expands quadratically with the number of tokens. b) In a decoder, each token only interacts with the previous tokens, but complexity is still quadratic. c) Complexity can be reduced by using a convolutional structure (encoder case) d) Convolutional structure for decoder case. e–f) Convolutional structure with dilation rate of two and three (decoder case). g) Another strategy is to allow selected tokens to interact with all the other tokens (encoder case) or all the previous tokens (decoder case pictured). h) Alternatively, global tokens can be introduced (left two columns and top two rows). These interact with all of the tokens as well as with each other.

12.10 Transformers for images

Transformers were initially developed for text data. Their enormous success in this area led to experimentation on images. This was not an obviously promising idea for two reasons. First, there are many more pixels in an image than words in a sentence, and so the quadratic complexity of self-attention poses a practical bottleneck. Second, convolutional nets are designed to have a good inductive bias because each layer is equivariant to spatial translation. However, this must be learned in a transformer network.

Regardless of these apparent disadvantages, transformer networks for images have now eclipsed the performance of convolutional networks for image classification and other tasks. This is partly because of the enormous scale at which they can be built, and the large amounts of data that can be used to pre-train the networks. This section describes transformer models for images.

12.10.1 ImageGPT

ImageGPT is a transformer decoder; it builds an autoregressive model of image pixels that ingests a partial image and predicts the subsequent pixel value. The quadratic

Figure 12.16 ImageGPT. a) Images generated from the autoregressive ImageGPT model. The top-left pixel is drawn from the estimated empirical distribution at this position. Subsequent pixels are generated in turn conditioned on the previous ones, working along the rows until the bottom-right of the image is reached. For each pixel, the transformer decoder generates a conditional distribution as in equation 12.14, and a sample is drawn. The extended sequence is then fed back into the network to generate the next pixel, and so on. b) Image completion. In each case, the lower half of the image is removed (top row) and ImageGPT completes the remaining part pixel by pixel (three different completions shown). Adapted from https://openai.com/blog/image-gpt/.

complexity of the transformer network means that the largest model (which contained 6.8 billion parameters) could still only operate on 64×64 images. Moreover, to make this tractable, the original 24-bit RGB color space had to be quantized into a nine-bit color space, so the system ingests (and predicts) one of 512 possible tokens at each position.

Images are naturally 2D objects, but ImageGPT simply learns a different position embedding at each pixel. Hence it must learn that each pixel not only has a close relationship with its preceding neighbors but also with nearby pixels in the row above. Figure 12.16 shows example generation results.

The internal representation of this decoder was used as a basis for image classification. The final pixel embeddings are averaged and a linear layer maps these to activations which are passed through a softmax layer to predict class probabilities. The system is pre-trained on a large corpus of web images and then fine-tuned on the ImageNet database resized to 48×48 pixels using a loss function that contains both a cross-entropy term for image classification and a generative loss term for predicting the pixels. Despite

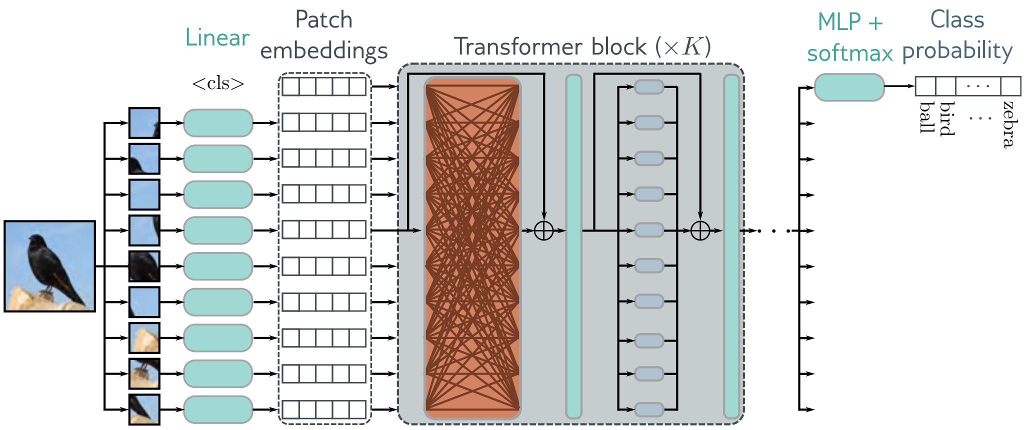

Figure 12.17 Vision transformer. The Vision Transformer (ViT) breaks the image into a grid of patches (16×16 in the original implementation) and each of these is projected via a learned linear transformation to become a patch embedding. These patch embeddings are fed into a transformer encoder network and the <cls> token is used to predict the class probabilities.

using a large amount of external training data, the system achieved only a 27.4% top-1 error rate on ImageNet (figure 10.15). This was less than convolutional architectures of the time (see figure 10.21) but is still impressive given the small input image size; it is unsurprising that it fails to classify images where the target object is small or thin.

12.10.2 Vision Transformer (ViT)

The *Vision Transformer* tackled the problem of image resolution by dividing the image into 16×16 patches (figure 12.17). Each of these is mapped to a lower dimension via a learned linear transformation and it is these representations that are fed into the transformer network. Once again, standard 1D position embeddings were learned. Problem 12.9

This is an encoder model with a <cls> token (see figures 12.10–12.11). However, unlike BERT it used *supervised* pre-training on a large database of 303 million labeled images from 18,000 classes. The <cls> token was mapped via a final network layer to create activations that are fed into a softmax function to generate class probabilities. After pre-training, the system is applied to the final classification task by replacing this final layer with one that maps to the desired number of classes and is fine-tuned.

For the ImageNet benchmark, this system achieved an 11.45% top-1 error rate. However, it did not perform as well as the best contemporary convolutional networks without supervised pre-training. It appears that the strong inductive bias of convolutional networks can only be superseded by employing extremely large amounts of training data.

12.10.3 Multi-scale vision transformers

The Vision Transformer differs from convolutional architectures in that it operates on a single scale. Many transformer models that process the image at multiple scales have subsequently been proposed. Similarly to convolutional networks, these generally start with high-resolution patches and few channels and gradually decrease the resolution, while simultaneously increasing the number of channels.

A representative example of a multi-scale transformer is the *shifted-window* or *SWIN* transformer. This is an encoder transformer that divides the image into patches and groups these patches into a grid of windows within which self-attention is applied independently (figure 12.18). These windows are shifted in adjacent transformer blocks, so the effective receptive field at a given patch can expand beyond the window border.

The scale is reduced periodically by concatenating features from non-overlapping 2×2 patches and applying a linear transformation that maps these concatenated features to twice the original number of channels. This architecture does not have a <cls> token but instead averages the output features at the last layer. These are then mapped via a linear layer to the desired number of classes and passed through a softmax function to output class probabilities. At the time of writing, the most sophisticated version of this architecture achieves a 9.89% top-1 error rate on the ImageNet database.

A related idea is to periodically integrate information from across the whole image. *Dual attention vision transformers* (DaVIT) achieve this by alternating two types of transformer blocks. In the first, different patches of the image attend to one another, and the self-attention computation uses all the channels. In the second, the different channels attend to one another, and the self-attention computation uses all of the spatial positions. This architecture reaches a 9.60% top-1 error rate on ImageNet and is close to the state-of-the-art at the time of writing.

Problem 12.10

12.11 Summary

This chapter introduced self-attention and then described how this contributes to the transformer architecture. The encoder, decoder, and encoder-decoder architectures were then described. The transformer operates on sets of high-dimensional embeddings. It has a low computational complexity per layer and much of the computation can be performed in parallel, using the matrix form. Since every input embedding interacts with every other, it can describe long-range dependencies in text. Ultimately though, the computation scales quadratically with the sequence length; one approach to reducing the complexity is to sparsify the interaction matrix.

One of the advantages of transformers is that they can be trained with extremely large unlabeled datasets. This is the first example of *unsupervised learning* (learning without labels) in this book. The encoder model trains a text representation that can be used for other tasks by predicting missing tokens. The decoder model builds an autoregressive probability model over the input tokens. This is the first example of a *generative model* in this book; sampling from generative models creates new data examples and examples

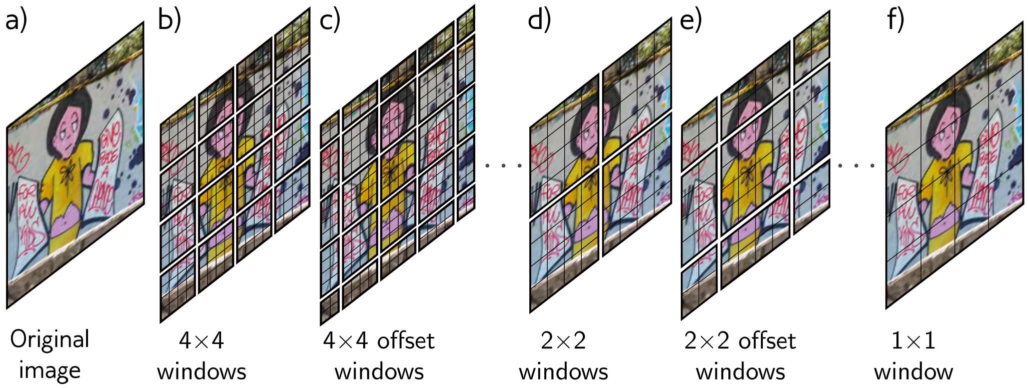

Figure 12.18 Shifted window (SWIN) transformer (Liu et al., 2021c). a) Original image. b) The SWIN transformer breaks the image into a grid of windows and each of these windows into a sub-grid of patches. The transformer network applies self-attention to the patches within each window independently. c) Each alternate layer shifts the windows so that the subsets of patches that interact with one another change and information can propagate across the whole image. d) After several layers, the 2×2 blocks of patch representations are concatenated so the effective patch (and window) size increase. e) Alternate layers use shifted windows at this new lower resolution. f) Eventually, the resolution is such that there is just a single window and the patches span the entire image.

of text and image generation were provided.

The next chapter considers networks for processing graph data. These have close connections with transformers in that they involve a series of network layers in which the nodes of the graph interact with each other. Chapters 14–18, return to unsupervised learning and generative models.

Notes

Natural language processing: Transformers were developed for natural language processing (NLP) tasks. This is an enormous area that deals with text analysis, categorization, generation, and manipulation. Example tasks include part of speech tagging, translation, text classification, entity recognition (people, places, companies, etc.), text summarization, question answering, word sense disambiguation, and document clustering. NLP was originally tackled by rule-based methods that exploited the structure and statistics of grammar. See Manning & Schutze (1999) and Jurafsky & Martin (2000) for early approaches.

Recurrent neural networks: Prior to the introduction of transformers, many state-of-the-art NLP applications used *recurrent neural networks*, or *RNNs* for short (figure 12.19). The term "recurrent" was introduced by Rumelhart et al. (1985), but the main idea dates to at least

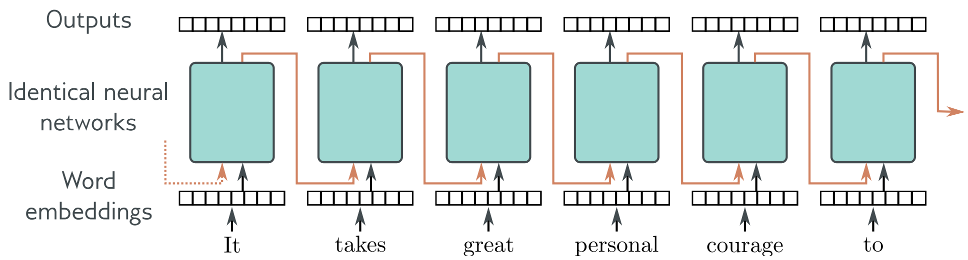

Figure 12.19 Recurrent neural networks. The word embeddings are passed sequentially through a series of identical neural networks. Each network has two outputs; one is the output embedding and the other (orange arrows) feeds back into the next neural network, along with the next word embedding. Each output embedding contains information about the word itself and its context in the preceding sentence fragment. In principle, the final output contains information about the entire sentence and could be used to support classification tasks in a similar way to the <cls> token in a transformer encoder model. However, the network sometimes gradually forgets about tokens that are further back in time.

Minsky & Papert (1969). RNNs ingest a sequence of inputs (words in NLP) one at a time. At each step, the network receives both the new input and a hidden representation computed from the previous time step (the recurrent connection). The final output contains information about the whole input. This representation can then be used to support NLP tasks like classification or translation. They have also been used in a decoding context in which generated tokens are fed back into the model to form the next input to the sequence. For example, the PixelRNN (Van den Oord et al., 2016c) used RNNs to build an autoregressive model of images.

From RNNs to transformers: One of the problems with RNNs is that they can forget information that is further back in the sequence. More sophisticated versions of this architecture such as *long short-term memory networks* or *LSTMs* (Hochreiter & Schmidhuber, 1997b) and *gated recurrent units* or *GRUs* (Cho et al., 2014; Chung et al., 2014) partially addressed this problem. However, in machine translation, the idea emerged that all of the intermediate representations in the RNN could be exploited to produce the output sentence. Moreover, certain output words should *attend* more to certain input words, according to their relation (Bahdanau et al., 2015). This ultimately led to dispensing with the recurrent structure altogether and replacing it with the encoder-decoder transformer (Vaswani et al., 2017). Here input tokens attend to one another (self-attention), output tokens attend to those earlier in the sequence (masked self-attention), and output tokens also attend to the input tokens (cross-attention). A formal algorithmic description of the transformer can be found in Phuong & Hutter (2022), and a survey of work can be found in Lin et al. (2022). The literature should be approached with caution, as many enhancements to transformers do not make meaningful performance improvements when carefully assessed in controlled experiments (Narang et al., 2021).

Applications: Models based on self-attention and/or the transformer architecture have been applied to text sequences (Vaswani et al., 2017), image patches (Dosovitskiy et al., 2021), protein sequences (Rives et al., 2021), graphs (Veličković et al., 2019), database schema (Xu et al., 2021b), speech (Wang et al., 2020c), mathematical integration which can be formulated as a translation problem (Lample & Charton, 2020), and time series (Wu et al., 2020b). However, their most celebrated successes have been in building language models, and more recently as a replacement for convolutional networks in computer vision.

Language models: The work of Vaswani et al. (2017) targeted translation tasks, but transformers are now more usually used to build either pure encoder or pure decoder models, the most famous of which are BERT (Devlin et al., 2019) and GPT2/GPT3 (Radford et al., 2019; Brown et al., 2020), respectively. These models are usually tested against benchmarks like GLUE (Wang et al., 2019b), which includes the SQuAD question-answering task (Rajpurkar et al., 2016) described in section 12.6.2, SuperGLUE (Wang et al., 2019a) and BIG-bench (Srivastava et al., 2022), which combine many NLP tasks to create an aggregate score for measuring language ability. Decoder models are generally not fine-tuned for these tasks but can perform well anyway when given a few examples of questions and answers and asked to complete the text from the next question. This is referred to as *few-shot learning* (Brown et al., 2020).

Since GPT3, many decoder language models have been released with steady improvement in few-shot results. These include GLaM (Du et al., 2022), Gopher (Rae et al., 2021), Chinchilla (Hoffmann et al., 2023), Megatron-Turing NLG (Smith et al., 2022), and LaMDa (Thoppilan et al., 2022). Most of the performance improvement is attributable to increased model size, using sparsely activated modules, and exploiting larger datasets. At the time of writing, the most recent model is PaLM (Chowdhery et al., 2022), which has 540 billion parameters and was trained on 780 billion tokens across 6144 processors. It is interesting to note that since text is highly compressible, this model has more than enough capacity to memorize the entire training dataset. This is true for many language models. Many bold statements have been made about how large language models exceed human performance. This is probably true for some tasks, but such statements should be treated with caution (see Ribeiro et al.,2021; McCoy et al., 2019; Bowman & Dahl, 2021; and Dehghani et al., 2021).

These models have considerable knowledge about the world. For example, in the example in section 12.7.4, the model knows key facts about deep learning, including that it is a type of machine learning, and that it has associated algorithms and applications. Indeed, one such model has been mistakenly identified as being sentient (Clark, 2022). However, there are persuasive arguments that the degree of "understanding" that this type of model can ever have is limited (Bender & Koller, 2020).

Tokenizers: Schuster & Nakajima (2012) and Sennrich et al. (2015) introduced *WordPiece* and *byte pair encoding* (*BPE*) respectively. Both of these methods greedily merge pairs of tokens based on their frequency of adjacency (figure 12.8), with the main difference being in how the initial tokens are chosen. For example, in BPE, the initial tokens are characters or punctuation with a special token to denote whitespace. The merges cannot occur over the whitespace. As the algorithm proceeds, new tokens are formed by combining characters recursively so that sub-word and word tokens emerge. The unigram language model (Kudo, 2018) generates several possible candidate merges and chooses the best one based on the likelihood in a language model. Provilkov et al. (2020) develop BPE dropout, which generates the candidates more efficiently by introducing randomness into the process of counting frequencies. Versions of both byte pair encoding and the unigram language model are included in the SentencePiece library (Kudo & Richardson, 2018), which works directly on Unicode characters, and so can work with any language. He et al. (2020) introduce a method that treats the sub-word segmentation as a latent variable that should be marginalized out for learning and inference.

Decoding algorithms: Transformer decoder models take a body of text and return a probability over the next token. This is then added to the preceding text and the model is run again. The process of choosing tokens from these probability distributions is known as *decoding*. Näive ways to do this would just be to either (i) greedily choose the most likely token or (ii) choose a token at random according to the distribution. However, neither of these methods works well in practice. In the former case, the results may be very generic, and the latter case may lead to degraded quality outputs (Holtzman et al., 2020). This is partly because during training the model was only exposed to sequences of ground truth tokens (known as *teacher forcing*) but sees its own output when deployed.

It is not computationally feasible to try every combination of tokens in the output sequence, but it is possible to maintain a fixed number of parallel hypotheses and choose the most likely overall sequence. This is known as *beam search*. Beam search tends to produce many similar hypotheses and has been modified to investigate more diverse sequences (Vijayakumar et al., 2016; Kulikov et al., 2018). One possible problem with random sampling is that there is a very long tail of unlikely following words that collectively have a significant probability. This has led to the development of *top-K sampling*, in which tokens are sampled from only the K most likely hypotheses (Fan et al., 2018). This still sometimes allows unreasonable token choices when there are only a few high-probability choices. To resolve this problem Holtzman et al. (2020) proposed *nucleus sampling*, in which tokens are sampled from a fixed proportion of the total probability mass. These issues are discussed in more depth by El Asri & Prince (2020).

Types of attention: Scaled dot-product attention (Vaswani et al., 2017) is just one of a family of attention mechanisms that includes additive attention (Bahdanau et al., 2015), multiplicative attention (Luong et al., 2015), key-value attention (Daniluk et al., 2017), and memory-compressed attention (Liu et al., 2019c). Other work (Zhai et al., 2021) has constructed "attention-free" transformers, in which the tokens interact in a way that does not have quadratic complexity. Multi-head attention was also introduced by Vaswani et al. (2017). Interestingly, it appears that most of the heads can be pruned after training without critically affecting the performance (Voita et al., 2019); it has been suggested that their role is to guard against bad initializations. Hu et al. (2018b) propose squeeze-and-excitation networks which are an attention-like mechanism which re-weights the channels in a convoluational layer based on globally computed features.

Relationship of self-attention to other models: The self-attention computation has close connections to other models. First, it is a case of a hypernetwork (Ha et al., 2017) in that it uses one part of the network to choose the weights of another part: the attention matrix forms the weights of a sparse network layer that maps the values to the outputs (figure 12.3). The *synthesizer* (Tay et al., 2021) simplifies this idea by simply using a neural network to create each row of the attention matrix from the corresponding input. Even though the input tokens no longer interact with each other to create the attention weights, this works surprisingly well. Wu et al. (2019) present a similar system that produces an attention matrix with a convolutional structure, so the tokens attend to their neighbors. The gated multi-layer perceptron (Wu et al., 2019) computes a matrix that pointwise multiplies the values, and so modifies them without mixing them. Transformers are also closely related to *fast weight memory systems*, which were the intellectual forerunners of hypernetworks (Schlag et al., 2021).

Self-attention can also be thought of as a routing mechanism (figure 12.1) and from this viewpoint, there is a connection to capsule networks (Sabour et al., 2017). These capture hierarchical relations in images so lower network levels might detect facial parts (noses, mouths), which are then combined (routed) in higher level capsules that represent a face. However, capsule networks use *routing by agreement*. In self-attention, the inputs compete with each other for how much they contribute to a given output (via the softmax operation). In capsule networks, the outputs of the layer compete with each other for inputs from earlier layers. Once we consider self-attention as a routing network, we can question whether it is necessary to make this routing dynamic (i.e., dependent on the data). The random synthesizer (Tay et al., 2021) removed the dependence of the attention matrix on the inputs entirely and either used predetermined random values or learned values. This performed surprisingly well across a variety of tasks.

Multi-head self-attention also has close connections to graph neural networks (see chapter 13), convolution (Cordonnier et al., 2020), recurrent neural networks (Choromanski et al., 2020), and memory retrieval in Hopfield networks (Ramsauer et al., 2021). For more information on the relationships between transformers and other models, consult Prince (2021a).

Position encoding: The original transformer paper (Vaswani et al., 2017) experimented with pre-defining the position embedding matrix $\mathbf{\Pi}$, and learning the position embedding $\mathbf{\Pi}$. It might seem odd to *add* the position embeddings to the $D \times N$ data matrix $\mathbf{X}$ rather than concatenate them. However, since the data dimension D is usually much greater than the number of tokens N, the position embedding lies in a subspace. The word embeddings in $\mathbf{X}$ are learned, and so it's possible in theory for the system to keep the two components in orthogonal subspaces and retrieve the position embeddings as required. The predefined embeddings chosen by Vaswani et al. (2017) were a family of sinusoidal components that had two attractive properties: (i) the relative position of two embeddings is easy to recover using a linear operation and (ii) their dot product generally decreased as the distance between positions increased (see Prince, 2021a, for more details). Many systems such as GPT3 and BERT used learned embedding matrices. Wang et al. (2020a) examined the cosine similarities of the learned position embeddings in these models and showed that they generally decline with relative distance, although they also have a periodic component.

Much subsequent work has modified just the attention matrix, so that in the scaled dot product self-attention equation:

$$\mathbf{Sa}[\mathbf{X}] = \mathbf{V} \cdot \mathbf{Softmax}\left[\frac{\mathbf{K}^T\mathbf{Q}}{\sqrt{D_q}}\right] \tag{12.16}$$

only the queries and keys contain position information:

$$\begin{aligned}
\mathbf{V} &= \boldsymbol{\beta}_v \mathbf{1}^\mathbf{T} + \boldsymbol{\Omega}_\mathbf{v}\mathbf{X} \\
\mathbf{Q} &= \boldsymbol{\beta}_q \mathbf{1}^\mathbf{T} + \boldsymbol{\Omega}_\mathbf{q}(\mathbf{X}+\mathbf{\Pi}) \\
\mathbf{K} &= \boldsymbol{\beta}_k \mathbf{1}^\mathbf{T} + \boldsymbol{\Omega}_\mathbf{k}(\mathbf{X}+\mathbf{\Pi}).
\end{aligned} \tag{12.17}$$

This has led to the idea of multiplying out the quadratic term in the numerator of equation 12.16 and retaining only some of the terms. For example, Ke et al. (2021) decouple or *untie* the content and position information by retaining only the content-content and position-position terms and using different projection matrices $\boldsymbol{\Omega}_\bullet$ for each.

Another modification is to directly inject information about the relative position. This is more important than absolute position since a batch of text can start at an arbitrary place in a document. Shaw et al. (2018), Raffel et al. (2020), and Huang et al. (2020b) all developed systems where a single term was learned for each relative position offset, and the attention matrix was modified in various ways using these *relative position embeddings.* Wei et al. (2019) investigated relative position embeddings based on predefined sinusoidal embeddings rather than learned values. DeBERTa (He et al., 2021) combines all of these ideas; they retain only a subset of terms from the quadratic expansion, apply different projection matrices to them, and use relative position embeddings. Other work has explored sinusoidal embeddings that encode absolute and relative position information in more complex ways (Su et al., 2021).

Wang et al. (2020a) compare the performance of transformers in BERT with different position embeddings. They found that relative position embeddings perform better than absolute position embeddings, but there was not much difference between using sinusoidal and learned embeddings. A survey of position embeddings can be found in Dufter et al. (2021).

Extending transformers to longer sequences: The complexity of the self-attention mechanism increases quadratically with the sequence length. Some tasks like summarization or question answering may require long inputs, and so this quadratic dependence limits performance. Three lines of work have attempted to address this problem. The first decreases the size of the attention matrix, the second makes the attention sparse, and the third modifies the attention mechanism to make it more efficient.

To decrease the size of the attention matrix, Liu et al. (2018b) introduced *memory compressed attention*. This applies strided convolution to the keys and values, which reduces the number of positions in a very similar way to a downsampling operation in a convolutional network. One way to think about this is that attention is applied between weighted combinations of neighboring positions, where the weights are learned. Along similar lines, Wang et al. (2020b) observed that the quantities in the attention mechanism are often low rank in practice and developed the *LinFormer*, which projects the keys and values onto a smaller subspace before computing the attention matrix.

To make attention sparse, Liu et al. (2018b) proposed *local attention*, in which neighboring blocks of tokens only attend to one another. This creates a block diagonal interaction matrix (see figure 12.15). Obviously this means that information cannot pass from block to block, and so such layers are typically alternated with full attention. Along the same lines, GPT3 (Brown et al., 2020) uses a convolutional interaction matrix and alternates this with full attention. Child et al. (2019) and Beltagy et al. (2020) experimented with various interaction matrices, including using convolutional structures with different dilation rates but allowing some queries to interact with every other key. Ainslie et al. (2020) introduced the *extended transformer construction* (figure 12.15h), which uses a set of global embeddings that interact with every other token. This can only be done in the encoder version, or these implicitly allow the system to "look ahead". When combined with relative position encoding, this scheme requires special encodings for mapping to, from, and between these global embeddings. *BigBird* (Ainslie et al., 2020) combined global embeddings and a convolutional structure with a random sampling of possible connections. Other work has investigated learning the sparsity pattern of the attention matrix (Roy et al., 2021; Kitaev et al., 2020; Tay et al., 2020).

Finally, it has been noted that the terms in the numerator and denominator of the softmax operation that computes attention have the form $\exp[\mathbf{k}^T\mathbf{q}]$. This can be treated as a kernel function and as such can be expressed as the dot product $\mathbf{g}[\mathbf{k}]^T\mathbf{g}[\mathbf{q}]$ where $\mathbf{g}[\bullet]$ is a nonlinear transformation. This formulation decouples the queries and keys and makes the attention computation more efficient. Unfortunately, to replicate the form of the exponential terms, the transformation $\mathrm{g}[\bullet]$ must map the inputs to the infinite space. The linear transformer (Katharopoulos et al., 2020) recognizes this and replaces the exponential term with a different measure of similarity. The *Performer* (Choromanski et al., 2020) approximates this infinite mapping with a finite-dimensional one.

Problem 12.11

More details about extending transformers to longer sequences can be found in Tay et al. (2023) and Prince (2021a).

Training transformers: Training transformers is challenging and requires both learning rate warm-up (Goyal et al., 2018) and Adam (Kingma & Ba, 2015). Indeed Xiong et al. (2020a) and Huang et al. (2020a) show experimentally that gradients vanish, and the Adam updates decrease in magnitude without learning rate warm-up. Several interacting factors cause these problems. The residual connections cause the gradients to explode (figure 11.6) and normalization layers are required to prevent this. Vaswani et al. (2017) used LayerNorm rather than BatchNorm because NLP statistics are highly variable between batches, although subsequent work has modified BatchNorm for transformers (Shen et al., 2020a). The positioning of the LayerNorm outside of the residual block causes gradients to shrink as they pass back through the network (Xiong et al., 2020a). In addition, the relative weight of the residual connections and main self-attention mechanism varies as we move through the network upon initialization (see figure 11.6c), and there is the additional complication that the gradients for the query and key parameter are much smaller than for the value parameters (Liu et al., 2020), and this necessitates the use of Adam. These factors interact in a complex way and make training unstable, necessitating the use of learning rate warm-up.

There have been various attempts to stabilize training including (i) a variation of FixUp called *TFixup* (Huang et al., 2020a) that allows the LayerNorm components to be removed, (ii) changing the position of the LayerNorm components in the network (Liu et al., 2020), and (iii) reweighting the two paths in the residual branches (Liu et al., 2020; Bachlechner et al., 2021). Xu et al. (2021b) introduce an initialization scheme called *DTFixup* that allows transformers to be trained with smaller datasets. A detailed discussion can be found in Prince (2021b).

Applications in vision: ImageGPT (Chen et al., 2020a) and the Vision Transformer (Dosovitskiy et al., 2021) were both early transformer architectures applied to images. Transformers have been used for image classification (Dosovitskiy et al., 2021; Touvron et al., 2021), object detection (Carion et al., 2020; Zhu et al., 2020b; Fang et al., 2021), semantic segmentation (Ye et al., 2019; Xie et al., 2021; Gu et al., 2022), super-resolution (Yang et al., 2020a), action recognition (Sun et al., 2019; Girdhar et al., 2019), image generation (Chen et al., 2021b; Nash et al., 2021), visual question answering (Su et al., 2019b; Tan & Bansal, 2019), inpainting (Wan et al., 2021; Zheng et al., 2021; Zhao et al., 2020b; Li et al., 2022), colorization (Kumar et al., 2021), and many other vision tasks. Surveys of transformers for vision can be found in Khan et al. (2022) and Liu et al. (2023b).

Transformers and convolutional networks: Transformers have been combined with convolutional neural networks to solve diverse computer vision tasks including image classification (Wu et al., 2020a), object detection (Hu et al., 2018a; Carion et al., 2020), video processing (Wang et al., 2018c; Sun et al., 2019), unsupervised object discovery (Locatello et al., 2020) and various text/vision tasks (Chen et al., 2020d; Lu et al., 2019; Li et al., 2019). Transformers can outperform convolutional networks for vision tasks but usually require large quantities of data to achieve superior performance. Often, they are pre-trained on enormous datasets like JRT (Sun et al., 2017) and LAION (Schuhmann et al., 2021). The transformer does not have the inductive bias of convolutional networks but it appears that by using gargantuan amounts of data they can surmount this disadvantage.

From pixels to video: Non-local networks (Wang et al., 2018c) were an early application of self-attention to image data. Transformers themselves were initially applied to pixels in local neighborhoods (Parmar et al., 2018; Hu et al., 2019; Parmar et al., 2019; Zhao et al., 2020a). ImageGPT (Chen et al., 2020a) scaled this to model all of the pixels in a (small) image. The Vision Transformer (ViT) (Dosovitskiy et al., 2021) used non-overlapping patches to analyze bigger images.

Since then, many multi-scale systems have been developed including the SWIN transformer (Liu et al., 2021c), SWINV2 (Liu et al., 2022), multi-scale transformers (MVIT) (Fan et al., 2021), and pyramid vision transformers (Wang et al., 2021). The Crossformer (Wang et al., 2022b) models interactions between spatial scales. Ali et al. (2021) introduced cross-covariance image transformers, in which the channels rather than spatial positions attend to one another, hence making the size of the attention matrix indifferent to the image size. The dual attention vision transformer was developed by Ding et al. (2022) and alternates between local spatial attention within sub-windows and spatially global attention between channels. Chu et al. (2021) similarly alternate between local attention within sub-windows and global attention by subsampling the spatial domain. Dong et al. (2022) adapt the ideas of figure 12.15, in which the interactions between elements are sparsified to the 2D image domain.

Transformers were subsequently adapted to video processing (Arnab et al., 2021; Bertasius et al., 2021; Liu et al., 2021c; Neimark et al., 2021; Patrick et al., 2021). A survey of transformers applied to video can be found in Selva et al. (2022).

Combining images and text: CLIP (Radford et al., 2021) learns a joint encoder for images and their captions using a contrastive pre-training task. The system ingests N images and their captions and produces a matrix of compatibility between images and captions. The loss function encourages the correct pairs to have a high score and the incorrect pairs to have a low score. Ramesh et al. (2021) and Ramesh et al. (2022) train a diffusion decoder to invert the CLIP image encoder for text-conditional image generation (see chapter 18).

Problems

Problem 12.1 Consider a self-attention mechanism that processes N inputs of length D to produce N outputs of the same size. How many weights and biases are used to compute the values? How many attention weights $a[\bullet, \bullet]$ will there be? How many weights and biases would there be if we build a fully connected network relating all DN inputs to all DN outputs?

Problem 12.2 Why might we want to ensure that the input to the self-attention mechanism is the same size as the output?

Problem 12.3 The self-attention mechanism is defined as:

$$\mathbf{X} = (\boldsymbol{\beta}_v \mathbf{1}^{\mathbf{T}} + \boldsymbol{\Omega}_{\mathbf{v}}\mathbf{X})^{\mathbf{T}}\mathbf{Softmax}[(\boldsymbol{\beta}_{\mathbf{q}}\mathbf{1}^{\mathbf{T}} + \boldsymbol{\Omega}_{\mathbf{q}}\mathbf{X})^{\mathbf{T}}(\boldsymbol{\beta}_{\mathbf{v}}\mathbf{1}^{\mathbf{T}} + \boldsymbol{\Omega}_{\mathbf{k}}\mathbf{X})]. \tag{12.18}$$

Find the derivatives of the output $\mathbf{X}$ with respect to the parameters $\boldsymbol{\beta}_v, \boldsymbol{\Omega}_v, \boldsymbol{\beta}_q, \boldsymbol{\Omega}_q, \boldsymbol{\beta}_k$ and $\boldsymbol{\Omega}_k$.

Problem 12.4 Show that the self-attention mechanism (equation 12.8) is invariant to a permutation $\mathbf{PX}$ of the data matrix $\mathbf{X}$.

Problem 12.5 Consider the softmax operation:

$$y_k = \text{softmax}_k[\mathbf{z}] = \frac{\exp[z_k]}{\sum_{k'=1}^{K} \exp[z_{k'}]}, \tag{12.19}$$

in the case where there are 5 inputs with values: $z_1 = -3$, $z_2 = 1$, $z_3 = 1000$, $z_4 = 5$, $z_5 = -1$. Compute the 25 derivatives, $\partial y_k[\mathbf{z}]/\partial z_j$ for all $j, k \in \{1, 2, 3, 4, 5\}$. What do you conclude?

Problem 12.6 Why is implementation more efficient if the values, queries, and keys in each of the H heads each have dimension D/H where D is the original dimension of the data?

Problem 12.7 Write Python code to create sub-word tokens for the nursery rhyme in figure 12.8 using byte-pair encoding.

Problem 12.8 BERT was pre-trained using two tasks. The first task requires the system to predict missing (masked) words. The second task requires the system to classify pairs of sentences as being adjacent or not in the original text. Identify whether each of these tasks is generative or contrastive (see section 9.3.6). Why do you think they used two tasks? Propose two novel contrastive tasks that could be used to pre-train a language model.

Problem 12.9 One problem with vision transformers is that the computation expands quadratically with the number of patches. Devise two methods to reduce the amount of computation using the principles from figure 12.15.

Problem 12.10 Consider representing an image with a grid of 16×16 patches, each of which is represented by a patch embedding of length 512. Compare the amount of computation required in the DaViT transformer to perform attention (i) between the patches, using all of the channels, and (ii) between the channels, using all of the patches.

Problem 12.11 Attention values are normally computed as:

$$\begin{aligned} a[\mathbf{x}_m, \mathbf{x}_n] &= \mathrm{softmax}_m\left[\mathbf{k}_{\bullet}\mathbf{q}_n\right] \\ &= \frac{\exp\left[\mathbf{k}_{\bullet}\mathbf{q}_n\right]}{\sum_{m'=1}^{N}\exp\left[\mathbf{k}_{m'}^T\mathbf{q}_n)\right]}. \end{aligned} \tag{12.20}$$

Consider replacing $\exp\left[\mathbf{k}_m^T\mathbf{q}_n\right]$ with the dot product $\mathbf{g}[\mathbf{k}_m]^T\mathbf{g}[\mathbf{q}_n]$ where $\mathbf{g}[\bullet]$ is a nonlinear transformation. Show how this makes the computation of the attention values more efficient.

Chapter 13

Graph neural networks

Chapter 10 described convolutional networks, which specialize in processing regular arrays of data (e.g., images). Chapter 12 described transformers, which specialize in processing sequences of variable length (e.g., text). This chapter describes *graph neural networks*. As the name suggests, these are neural architectures that process graphs (i.e., sets of nodes connected by edges).

There are three novel challenges associated with processing graphs. First, their topology is variable, and it is hard to design networks that are both expressive and can cope with this variation. Second, graphs may be enormous; a graph representing connections between users of a social network might have a billion nodes. Third, there may only be a single monolithic graph available, so the usual protocol of training with many data examples and testing with new data may not be appropriate.

This chapter starts by providing some examples of graphs and then describes how they are encoded and common problem formulations. The algorithmic requirements for processing graphs are discussed and this leads naturally to *graph convolutional networks*, which are a particular type of graph neural network.

13.1 What is a graph?

A graph is a very general structure and consists of a set of *nodes* or *vertices*, where pairs of nodes are connected by *edges* or *links*. Graphs are typically sparse; only a small subset of the possible edges are present.

Some objects in the real world naturally take the form of graphs. For example, road networks can be considered graphs in which the nodes are physical locations and the edges represent roads between them (figure 13.1a). Chemical molecules are small graphs in which the nodes represent atoms and the edges represent chemical bonds (figure 13.1b). Electrical circuits are graphs in which the nodes represent components and junctions, and the edges are electrical connections (figure 13.1c).

Furthermore, many datasets can also be represented by graphs, even if this is not their obvious surface form. For example:

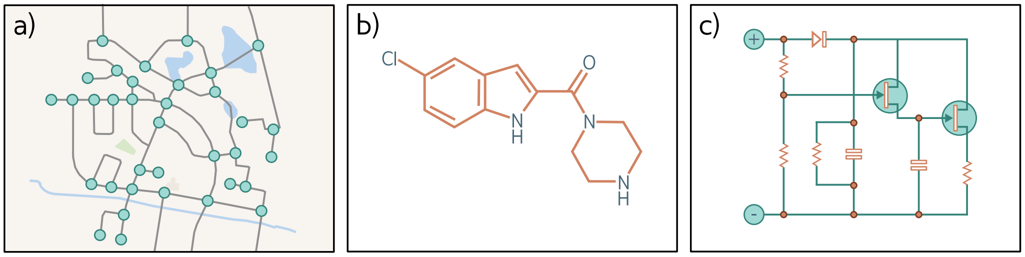

Figure 13.1 Real-world graphs. Some objects such as a) road networks, b) molecules, and c) electrical circuits are naturally structured as graphs.

- Social networks are graphs where nodes are people and the edges represent friendships between them.
- The scientific literature can be viewed as a graph in which the nodes are papers and the edges represent citations.
- Wikipedia can be thought of as a graph in which the nodes are articles and the edges represent hyperlinks between articles.
- Computer programs can be represented as graphs in which the nodes are syntax tokens (variables at different points in the program flow) and the edges represent computations involving these variables.
- Geometric point clouds can be represented as graphs. Here, each point is a node and has edges that connect to other nearby points.
- Protein interactions in a cell can be expressed as graphs, where the nodes are the proteins, and there is an edge between two proteins if they interact.

In addition, a set (an unordered list) can be treated as a graph in which every member is a node and connects to every other. Similarly, an image can be treated as a graph with regular topology, in which each pixel is a node and has edges to its eight adjacent neighbors.

13.1.1 Types of graphs

Graphs can be categorized in various ways. The social network in figure 13.2a contains *undirected edges*; each pair of individuals with a connection between them have mutually agreed to be friends, and so there is no sense that the relationship is directional. In contrast, the citation network in figure 13.2b contains *directed edges*. Each paper cites other papers, and this relationship is inherently one-way.

Figure 13.2c depicts a *knowledge graph* that encodes a set of facts about objects by defining relations between them. Technically, this is a *directed heterogeneous multigraph*. It is heterogeneous because the nodes can represent different types of entities (e.g., people,

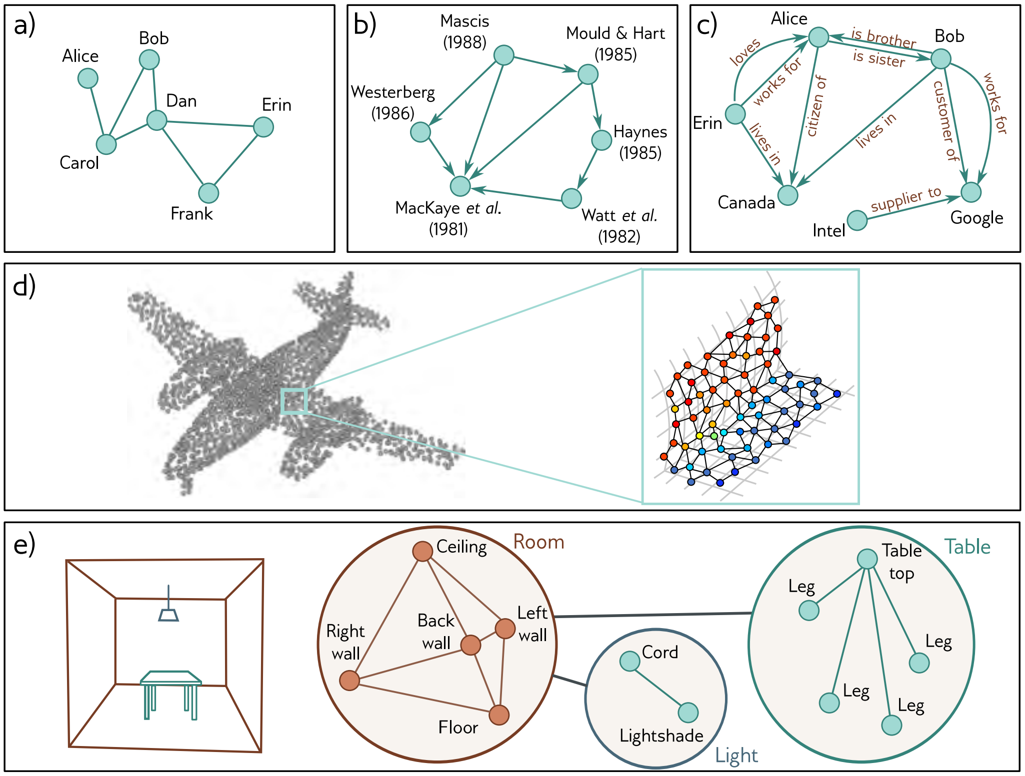

Figure 13.2 Types of graphs. a) A social network is an undirected graph; the connections between people are symmetric. b) A citation network is a directed graph; one publication cites another, so the relationship is asymmetric. c) A knowledge graph is a directed heterogeneous multigraph. The nodes are heterogeneous in that they represent different object types (people, places, companies) and there may be multiple edges representing different relations between each node. d) A point set can be converted to a graph by forming edges between nearby points. Each node has an associated position in 3D space and this is termed a geometric graph (adapted from Hu et al., 2022). e) The scene on the left can be represented by a hierarchical graph. The topology of the room, table, and light are all represented by graphs and these graphs form nodes in a larger graph representing object adjacency (adapted from Fernández-Madrigal & González, 2002).

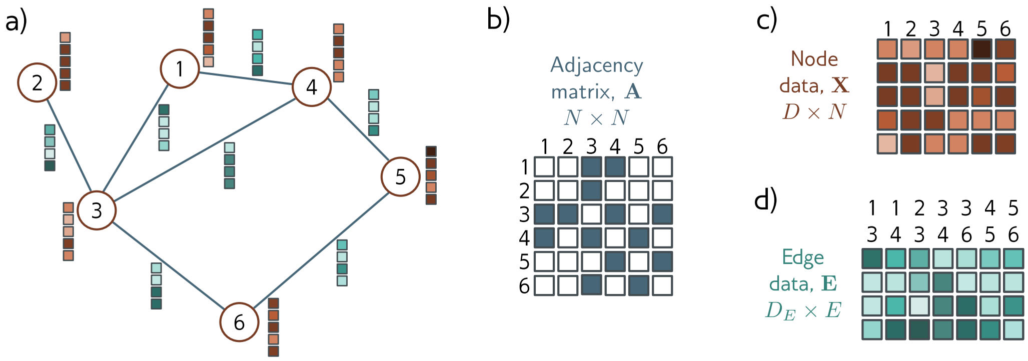

Figure 13.3 Graph representation. a) Example graph with six nodes and seven edges. Each node has an associated embedding of length five (brown vectors). Each edge has an associated embedding of length four (blue vectors). This graph can be represented by three matrices. b) The adjacency matrix is a binary matrix, where the element (m, n) is set to one if node m connects to node n. c) The node data matrix $\mathbf{X}$ contains the concatenated node embeddings. d) The edge data matrix $\mathbf{E}$ contains the edge embeddings.

countries, companies). It is a multigraph because there can be multiple edges of different types between any two nodes.

The point set representing the airplane in figure 13.2d can be converted into a graph by connecting each point to its K nearest neighbors. The result is a *geometric graph* where each point is associated with a position in 3D space. Figure 13.2e represents a *hierarchical graph*. The table, light, and room form three graphs, describing the adjacency of their respective components. These three graphs are themselves nodes in another graph that represents the topology of the objects in a larger model.

All types of graphs can be processed using deep learning. However, this chapter focuses on undirected graphs like the social network in figure 13.2a.

13.2 Graph representation

In addition to the graph structure itself, there is typically also information associated with each node. For example, in a social network, each individual might be characterized by a fixed length vector representing their interests. Sometimes, the edges also have information attached. For example, in the road network example each edge might be characterized by its length, number of lanes, frequency of accidents, and speed limit. The information at a node is stored in a *node embedding*, and the information at an edge is stored in an *edge embedding*.

More formally, a graph consists of a set of N nodes that are connected by a set of E

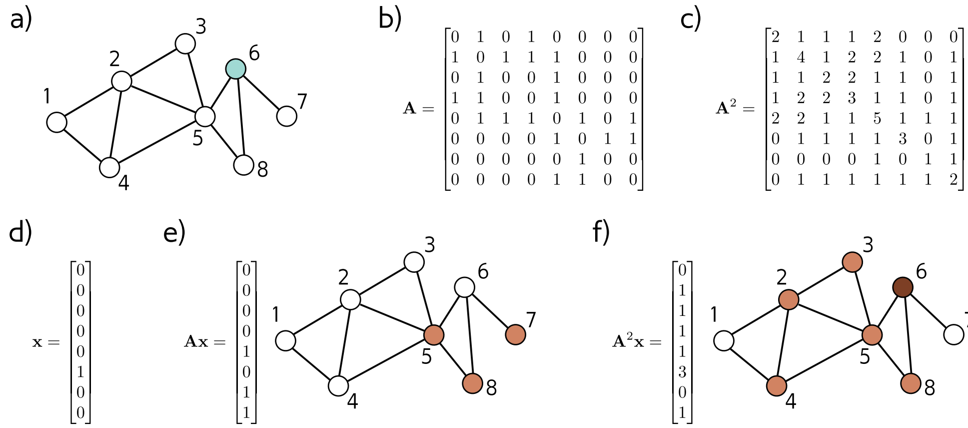

Figure 13.4 Properties of the adjacency matrix. a) Example graph. b) Position (m, n) of the adjacency matrix $\mathbf{A}$ contains the number of walks of length one from node m to node n. c) Position (m, n) of the squared adjacency matrix contains the number of walks of length two from node m to node n. d) One hot vector representing node six, which is highlighted in panel (a). e) When we pre-multiply this vector by $\mathbf{A}$, the result contains the number of walks of length one from node six to each node; we can reach nodes five, seven, and eight in one move. f) When we pre-multiply this vector by $\mathbf{A}^2$, the resulting vector contains the number of walks of length two from node six to each node; we can reach nodes two, three, four, five, and eight in two moves, and we can return to the original node in three different ways (via nodes five, seven, and eight).

edges. The graph is represented by three matrices $\mathbf{A}$, $\mathbf{X}$, and $\mathbf{E}$ representing the graph structure, node embeddings, and edge embeddings, respectively (figure 13.3).

Problems 13.1–13.2

The graph structure is represented by the *adjacency matrix*, $\mathbf{A}$. This is an $N \times N$ matrix where entry (m, n) is set to one if there is an edge between nodes m and n and zero otherwise. For undirected graphs, this matrix is always symmetric. For large sparse graphs, it can be stored as a list of connections (m, n) to save memory.

The n^{th} node has an associated node embedding $\mathbf{x}^{(n)}$ of length D. These embeddings are concatenated and stored in the $D \times N$ node data matrix $\mathbf{X}$. Similarly, the e^{th} edge has an associated edge embedding $\mathbf{e}^{(e)}$ of length D_E. These edge embeddings are collected into the $D_E \times E$ matrix $\mathbf{E}$. For simplicity, we initially consider graphs that only have node embeddings and return to edge embeddings in section 13.10.

13.2.1 Properties of the adjacency matrix

The adjacency matrix can be used to find the neighbors of a node using linear algebra. Consider encoding the n^{th} node as a one-hot column vector (a vector with only one non-zero entry at position n, which is set to one). When we pre-multiply this vector by the adjacency matrix, it extracts the n^{th} column of the adjacency matrix and returns a vector with ones at the positions of the neighbors (i.e., all the places we can reach in a walk of length one from the n^{th} node). If we repeat this procedure (i.e., pre-multiply by $\mathbf{A}$ again), then the resulting vector contains the number of walks of length two from node n to every node (figures 13.4d–f). Problems 13.3–13.4

In general, if we raise the adjacency matrix to the power of L, the entry at position (m, n) of $\mathbf{A}^L$ contains the number of unique "walks" of length L from node m to node n (figures 13.4a–c). This is not quite the same as the number of unique paths, since it includes routes that visit the same node more than once. Nonetheless, $\mathbf{A}^L$ still contains useful information about the graph connectivity; a non-zero entry at position (m, n) indicates that the distance from m to n must be less than or equal to L.

13.2.2 Permutation of node indices

Node indexing in graphs is arbitrary; permuting the node indices results in a permutation of the columns of the node data matrix $\mathbf{X}$ and a permutation of both the rows and columns of the adjacency matrix $\mathbf{A}$. However, the underlying graph is unchanged (figure 13.5). This is in contrast to images, where permuting the pixels creates a different image, and to text, where permuting the words creates a different sentence.

The operation of exchanging node indices can be expressed mathematically by a *permutation matrix*, $\mathbf{P}$. This is a matrix where exactly one entry in each row and column take the value one and the remaining values are zero. When position (m, n) of the permutation matrix is set to one, it indicates that node m will become node n after the permutation. To map from one indexing to another, we use the operations: Problem 13.5

$$
\begin{aligned}
\mathbf{X}' &= \mathbf{X}\mathbf{P} \\
\mathbf{A}' &= \mathbf{P}^T\mathbf{A}\mathbf{P}.
\end{aligned}
\tag{13.1}
$$

It follows that any processing applied to the graph should also be indifferent to these permutations. Otherwise, the result will depend on the particular choice of node indices.

13.3 Graph neural networks, tasks, and loss functions

A graph neural network is a model that takes the node embeddings $\mathbf{X}$ and the adjacency matrix $\mathbf{A}$ as inputs and passes the graph through a series of K layers. At each layer the node embeddings are updated to create intermediate "hidden" representations $\mathbf{H}_k$, before finally computing output embeddings $\mathbf{H}_K$.

At the start of this network, each column of the input node embeddings $\mathbf{X}$ just contains information about the node itself. At the end, each column of the model output $\mathbf{H}_K$ contains information about the node and its context within the graph. This is similar to word embeddings passing through a transformer network, which represent words at the start, but represent the word meanings in the context of the sentence at the end.

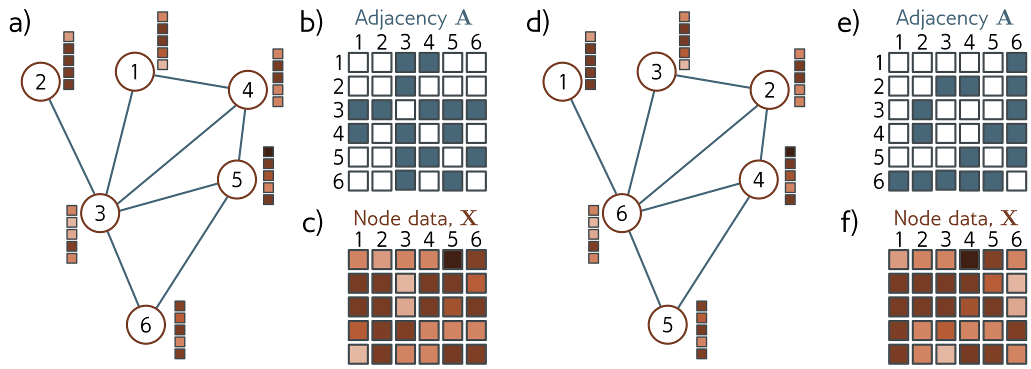

Figure 13.5 Permutation of node indices. a) Example graph, b) associated adjacency matrix, and c) node embeddings. d) The same graph where the (arbitrary) order of the indices has been changed. e) The adjacency matrix and f) node matrix are now different. Consequently, any network layer that operates on the graph should be indifferent to the ordering of the nodes.

13.4 Tasks and loss functions

We defer discussion of the model until section 13.5, and first describe the types of problems graph neural networks tackle and the loss functions associated with each. Typically, supervised graph problems fall into one of three categories (figure 13.6).

Graph-level tasks: The network assigns a label or estimates one or more values from the entire graph, exploiting both the structure and node embeddings. For example, we might want to predict the temperature at which a molecule becomes liquid (a regression task) or whether a molecule is poisonous to human beings or not (a classification task).

For graph-level tasks, the output node embeddings are combined (e.g., by averaging them) and the resulting vector is mapped via a linear transformation or neural network to a vector of fixed-size. For regression, the mismatch between the result and the ground truth values is computed using the least squares loss. For classification, the output is passed through a sigmoid or softmax function and the binary or multiclass cross-entropy loss is applied. For example, in binary classification, the output $y \in [0, 1]$ might be:

$$y = \text{sig}\left[\beta_K + \boldsymbol{\omega}_K \mathbf{H}_K \mathbf{1}/N\right], \tag{13.2}$$

where the scalar β_K and $1 \times D$ vector $\boldsymbol{\omega}_K$ are learned parameters. Post-multiplying the output embedding matrix $\mathbf{H}_K$ by the column vector $\mathbf{1}$ that contains ones has the effect of summing together all the embeddings and subsequently dividing by the number of nodes N computes the average. This is known as *mean pooling*.

Node-level tasks: The network assigns a label (classification) or one or more values (regression) to each node of the graph, using both the graph structure and node em-

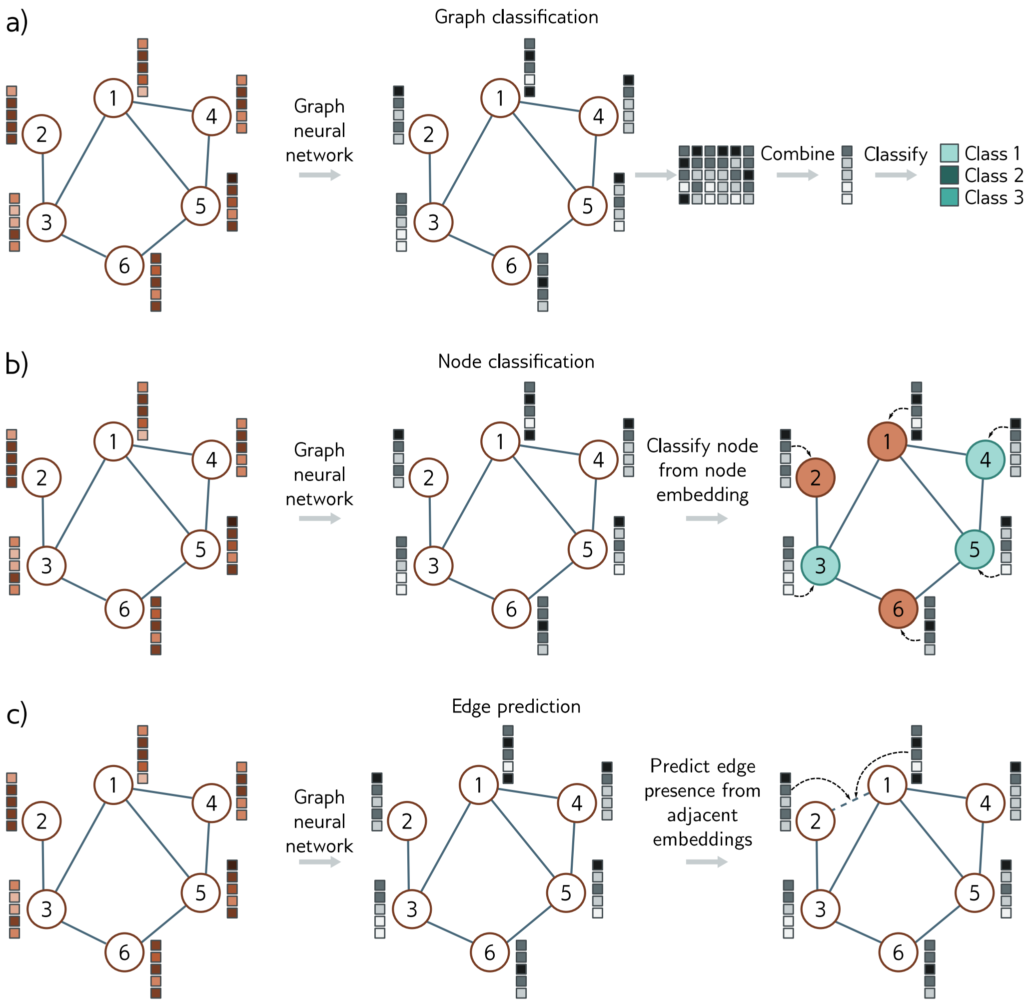

Figure 13.6 Common tasks for graphs. In each case, the input is a graph as represented by the adjacency matrix and node embeddings. The graph neural network processes the node embeddings by passing them through a series of layers. The node embeddings at the last layer contain information about both the node and its context in the graph. a) Graph classification. The node embeddings are combined (e.g., by averaging) and then mapped to a fixed-size vector that is passed through a softmax function to produce class probabilities. b) Node classification. Each node embedding is used individually as the basis for classification (cyan and orange colors represent assigned node classes). c) Edge prediction. Node embeddings adjacent to the edge are combined (e.g., by taking the dot product) to compute a single number that is mapped via a sigmoid function to produce a probability that a missing edge should be present.

beddings. For example, given a graph constructed from a 3D point cloud similar to figure 13.2d, the goal might be to classify the nodes according to whether they belong to the wing, fuselage, or engines. Loss functions are defined in exactly the same way as for graph-level tasks, except that now this is done independently at each node n:

$$y^{(n)} = \mathrm{sig}\left[\beta_K + \boldsymbol{\omega}_K \mathbf{h}_K^{(n)}\right]. \tag{13.3}$$

Edge prediction tasks: The network predicts whether there should be an edge or not between nodes n and m. For example, in the social network setting, the network might predict whether two people know and like each other and suggest that they connect if that is the case. This is a binary classification task where the two node embeddings must be mapped to a single number representing the probability that the edge is present. One possibility is to take the dot product of the node embeddings and pass the result through a sigmoid function to create the probability:

$$y^{(mn)} = \mathrm{sig}\left[\mathbf{h}^{(m)T}\mathbf{h}^{(n)}]\right]. \tag{13.4}$$

13.5 Graph convolutional networks

There are many types of graph neural networks but here we focus on *spatial-based convolutional graph neural networks* or *GCNs* for short. These models are convolutional in that they update each node by aggregating information from nearby nodes, and as such, they induce a *relational inductive bias* (i.e., a bias towards prioritizing information from neighbors). They are spatial-based because they do this in a straightforward manner using the original graph structure. This is in contrast to spectral-based methods that apply convolutions in the Fourier domain.

Each layer of the GCN is a function $\mathbf{F}[\bullet]$ with parameters $\boldsymbol{\Phi}$ that takes the node embeddings and adjacency matrix and outputs new node embeddings. The network can hence be written as:

$$\begin{aligned}
\mathbf{H}_1 &= \mathbf{F}[\mathbf{X}, \mathbf{A}, \boldsymbol{\phi}_0] \\
\mathbf{H}_2 &= \mathbf{F}[\mathbf{H}_1, \mathbf{A}, \boldsymbol{\phi}_1] \\
\mathbf{H}_3 &= \mathbf{F}[\mathbf{H}_2, \mathbf{A}, \boldsymbol{\phi}_2] \\
\vdots &= \vdots \\
\mathbf{H}_K &= \mathbf{F}[\mathbf{H}_{K-1}, \mathbf{A}, \boldsymbol{\phi}_{K-1}],
\end{aligned} \tag{13.5}$$

where $\mathbf{X}$ is the input, $\mathbf{A}$ is the adjacency matrix, $\mathbf{H}_k$ contains the modified node embeddings at the k^{th} layer, and $\boldsymbol{\phi}_k$ denotes the parameters associated with that layer.

13.5.1 Equivariance and invariance

We noted before that the indexing of the nodes in the graph is arbitrary and any permutation of the node indices does not change the graph. It is hence imperative that any model respects this property. It follows that each layer must be equivariant (see section 10.1) with respect to permutations of the node indices. In other words, if we permute the node indices, the node embeddings at each stage will be permuted in the same way. In mathematical terms, if $\mathbf{P}$ is a permutation matrix then we must have:

$$\mathbf{H}_{k+1}\mathbf{P} = \mathbf{F}[\mathbf{H}_k\mathbf{P}, \mathbf{P}^T\mathbf{A}\mathbf{P}, \boldsymbol{\phi}_k]. \tag{13.6}$$

For node classification and edge prediction tasks, the output should also be equivariant with respect to permutations of the node indices. However, for graph-level tasks, the final layer aggregates information from across the graph so the output is invariant to the order of the nodes. In fact, the output layer from equation 13.2 achieves this because:

Problem 13.6

$$y = \text{sig}\left[\beta_K + \boldsymbol{\omega}_K\mathbf{H}_K\mathbf{1}/N\right] = \text{sig}\left[\beta_K + \boldsymbol{\omega}_K\mathbf{H}_K\mathbf{P}\mathbf{1}/N\right], \tag{13.7}$$

for any permutation matrix $\mathbf{P}$ (problem 13.6).

This mirrors the case for images, where segmentation should be equivariant to image transformations and image classification should be invariant (figure 10.1). For images, convolutional and pooling layers partially achieve this with respect to translations, but there is no known way to guarantee these properties exactly. However, for graphs, it is possible to define networks that ensure equivariance or invariance to permutations.

13.5.2 Parameter sharing

Chapter 10 argued that it isn't sensible to apply fully connected networks to images because this requires the network to learn how to recognize an object separately at every image position. Instead, we used convolutional layers that processed every position in the image identically. This reduced the number of parameters and introduced an inductive bias that forced the model to treat every part of the image in the same way.

The same argument can be made about nodes in a graph. We could learn a model with separate parameters associated with each node. However, now the network must relearn the meaning of the connections in the graph at each position, and training would require many graphs with the same topology. Instead, we build a model that uses the same parameters at every node, reducing the number of parameters dramatically, and sharing what the network has learned at each node across the entire graph.

Recall that a convolution (equation 10.3) updates a variable by taking a weighted sum of information from its neighbors. One way to think of this is that each neighbor sends a message to the variable of interest, which aggregates these messages to form the update. When we considered images, the neighbors were pixels from a fixed-size square region around the current position, and so the spatial relationships at each position are the same. However, in a graph, each node may have a different number of neighbors and there are no consistent relationships; there is no sense that we can weight information from a node that is "above" this one differently from a node that is "below" it.

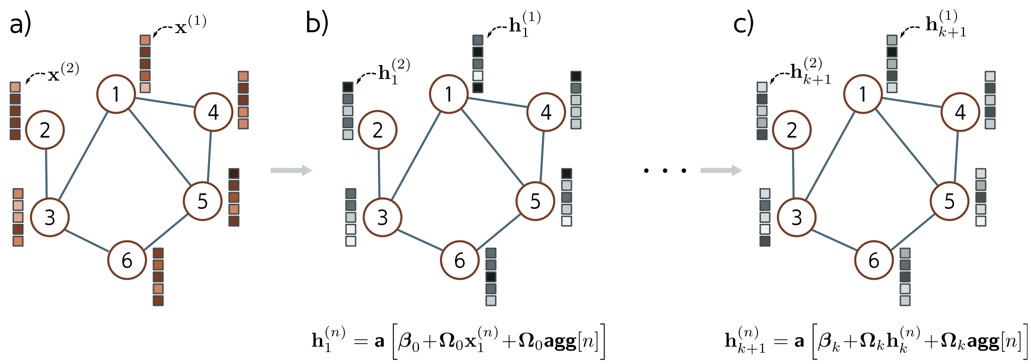

Figure 13.7 Simple Graph CNN layer. a) Input graph consists of structure (embodied in graph adjacency matrix $\mathbf{A}$, not shown) and node embeddings (stored in columns of $\mathbf{X}$). b) Each node in the first hidden layer is updated by (i) aggregating the neighboring nodes to form a single vector, (ii) applying a linear transformation $\boldsymbol{\Omega}_0$ to the aggregated nodes, (iii) applying the same linear transformation $\boldsymbol{\Omega}_0$ to the original node, (iv) adding these together with a bias $\boldsymbol{\beta}_0$, and finally (v) applying a nonlinear activation function $\mathbf{a}[\bullet]$ like a ReLU. This process is repeated at subsequent layers (but with different parameters for each layer) until we produce the final embeddings at the end of the network.

13.5.3 Example GCN layer

These considerations lead to a simple GCN layer (figure 13.7). At each node n in layer k we aggregate information from neighboring nodes by summing their node embeddings $\mathbf{h}_\bullet$:

$$\mathbf{agg}[n,k] = \sum_{m \in \mathrm{ne}[n]} \mathbf{h}_k^{(m)}, \tag{13.8}$$

where $\mathrm{ne}[n]$ returns the set of indices of the neighbors of node n. Then we apply a linear transformation $\boldsymbol{\Omega}_k$ to the embedding $\mathbf{h}_k^{(n)}$ at the current node and to this aggregated value, add a bias term $\boldsymbol{\beta}_k$, and pass the result through a nonlinear activation function $\mathbf{a}[\bullet]$, which is applied independently to every member of its vector argument:

$$\mathbf{h}_{k+1}^{(n)} = \mathbf{a}\left[\boldsymbol{\beta}_k + \boldsymbol{\Omega}_k \cdot \mathbf{h}_k^{(n)} + \boldsymbol{\Omega}_k \cdot \mathbf{agg}[n,k]\right]. \tag{13.9}$$

We can write this more succinctly by noting that post-multiplication of a matrix by a vector returns a weighted sum of its columns. The n^{th} column of the adjacency matrix $\mathbf{A}$ contains ones at the positions of the neighbors. Hence, if we collect the node embeddings into the $D \times N$ matrix $\mathbf{H}_k$ and post-multiply by the adjacency matrix $\mathbf{A}$, the n^{th} column of the result is $\mathbf{agg}[n,k]$. The update for the nodes is now:

$$\begin{aligned}\mathbf{H}_{k+1} &= \mathbf{a}\left[\boldsymbol{\beta}_k\mathbf{1}^T + \boldsymbol{\Omega}_k\mathbf{H}_k + \boldsymbol{\Omega}_k\mathbf{H}_k\mathbf{A}\right]\\ &= \mathbf{a}\left[\boldsymbol{\beta}_k\mathbf{1}^T + \boldsymbol{\Omega}_k\mathbf{H}_k(\mathbf{A}+\mathbf{I})\right],\end{aligned} \tag{13.10}$$

where $\mathbf{1}$ is an N×1 vector containing ones. Here, the nonlinear activation function $\mathbf{a}[\bullet]$ is applied independently to every member of its matrix argument.

This layer satisfies the design considerations: it is equivariant to permutations of the node indices, can cope with any number of neighbors, exploits the structure of the graph to provide a relational inductive bias, and shares parameters throughout the graph. Problem 13.7

13.6 Example: graph classification

We now combine these ideas to describe a network that classifies molecules as being toxic or harmless. The input to the network is the adjacency matrix $\mathbf{A}$ and node embedding matrix $\mathbf{X}$. The adjacency matrix derives directly from the molecular structure. Each node embedding takes one of 118 possible values corresponding to the 118 elements of the periodic table. These are encoded as one-hot vectors (i.e., vectors of length 118 where every position is zero except for the position corresponding to the relevant chemical element, which is set to one). These one-hot vectors form the columns of the data matrix $\mathbf{X} \in \mathbb{R}^{118\times N}$. The node embeddings can be transformed to an arbitrary size D by the first weight matrix $\boldsymbol{\Omega}_0 \in \mathbb{R}^{D\times 118}$.

The network equations are:

$$\begin{aligned}\mathbf{H}_1 &= \mathbf{a}\left[\boldsymbol{\beta}_0\mathbf{1}^T + \boldsymbol{\Omega}_0\mathbf{X}(\mathbf{A}+\mathbf{I})\right]\\ \mathbf{H}_2 &= \mathbf{a}\left[\boldsymbol{\beta}_1\mathbf{1}^T + \boldsymbol{\Omega}_1\mathbf{H}_1(\mathbf{A}+\mathbf{I})\right]\\ \vdots &= \vdots\\ \mathbf{H}_K &= \mathbf{a}\left[\boldsymbol{\beta}_{K-1}\mathbf{1}^T + \boldsymbol{\Omega}_{K-1}\mathbf{H}_{k-1}(\mathbf{A}+\mathbf{I})\right]\\ \mathrm{f}[\mathbf{X},\mathbf{A},\boldsymbol{\Phi}] &= \mathrm{sig}\left[\beta_K + \boldsymbol{\omega}_K\mathbf{H}_K\mathbf{1}/N\right],\end{aligned} \tag{13.11}$$

where the output $\mathrm{f}[\mathbf{X},\mathbf{A},\boldsymbol{\Phi}]$ of the network is a single value that determines the probability that the molecule is toxic (see equation 13.2).

13.6.1 Training with batches

Given I training graphs $\{\mathbf{X}_i, \mathbf{A}_i\}$ and their labels y_i, the parameters $\boldsymbol{\Phi} = \{\boldsymbol{\beta}_K, \boldsymbol{\Omega}_K\}_{k=0}^{K}$ can be learned using SGD and the binary cross-entropy loss (equation 5.19). Fully connected networks, convolutional, and transformers all exploited the parallelism of modern hardware to concurrently process an entire batch simultaneously. However, here each graph may have a different number of nodes. Hence, the matrices $\mathbf{X}_i$ and $\mathbf{A}_i$ have different sizes and there is no way to concatenate them into 3D tensors.

Luckily, there is a simple trick that allows us to perform the forward and backward passes in parallel. The graphs in the batch are treated as disjoint components of a single large graph. The network can then be run as a single instance of the network equations. The mean pooling is carried out only over the individual graphs to make a single representation per graph that can be fed into the loss function.

13.7 Inductive vs. transductive models

All of the models described so far in this book have been *inductive*: we exploit a training set of labeled data to learn the relation between the inputs and outputs. Then we apply this to new test data. One way to think of this is that we are learning the rule that maps inputs to outputs and then applying it elsewhere.

By contrast, a *transductive* model considers both the labeled and unlabeled data at the same time. It does not produce a rule, but merely a labeling for all of the unknown outputs. This is sometimes termed *semi-supervised learning*. It has the advantage that it can use patterns in the unlabeled data to help make its decisions. However, it has the disadvantage that when extra unlabeled data are added, the model should be retrained.

Both problem types are commonly encountered for graphs (figure 13.8). Sometimes we have many labeled graphs and learn a mapping between the graph and the labels. For example, we might have many molecules, each of which is labeled according to whether it is toxic to humans. We learn the rule that maps the graph to the toxic/non-toxic label and then apply this rule to new molecules. However, sometimes there is a single monolithic graph. In the graph of scientific paper citations we might have labels indicating the field (physics, biology, etc.) for some of the nodes, and wish to label the remaining nodes. Here, the training and test data are irrevocably connected.

Graph-level tasks only occur in the inductive setting where there are training and test graphs. However, node-level tasks and edge prediction tasks can occur in either setting. In the transductive case, the loss function minimizes the mismatch between the model output and the ground truth where this is known. New predictions are computed by running the forward pass and retrieving the results where the ground truth is unknown.

13.8 Transductive learning example: node classification

As a second example, consider a binary node classification task in a transductive setting. We start with a commercial-sized graph with millions of nodes. Some of these nodes have ground truth binary labels and the goal is to label the remaining unlabeled nodes. The body of the network will be the same as in the previous example (equation 13.11) but with a different final layer that produces an output vector of size $1 \times N$:

$$\mathbf{f}[\mathbf{X}, \mathbf{A}, \boldsymbol{\Phi}] = \mathbf{sig}\left[\beta_K \mathbf{1}^T + \boldsymbol{\omega}_K \mathbf{H}_K\right], \tag{13.12}$$

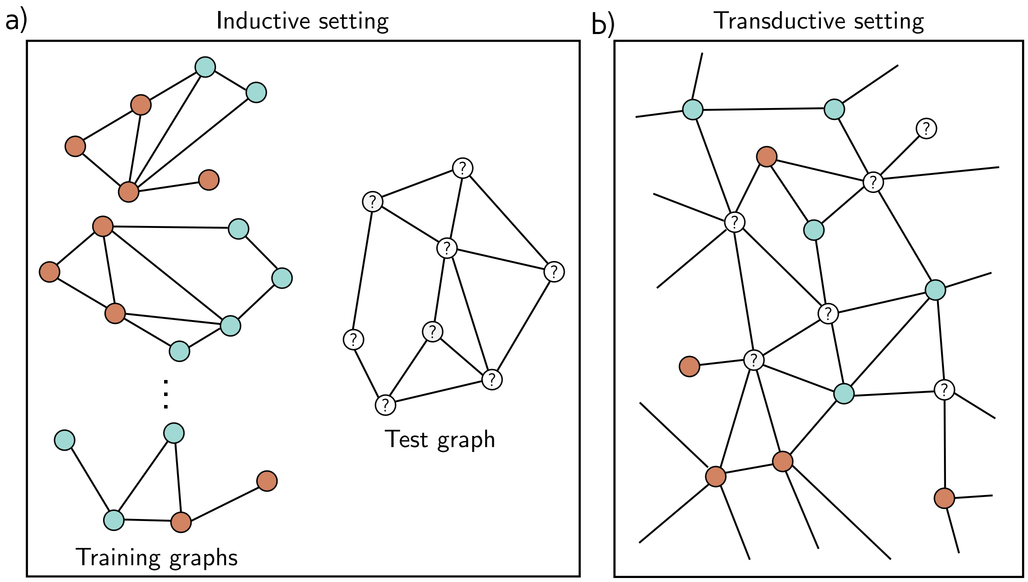

Figure 13.8 Inductive vs. transductive problems. a) Node classification task in inductive setting. We are given a set of I training graphs, where the node labels (orange and cyan colors) are known. After training, we are given a test graph and must assign labels to each node. b) Node classification in transductive setting. There is one large graph in which some of the nodes have labels (orange and cyan colors) and others are unknown. We train the model to predict the known labels correctly and then examine the predictions at the unknown nodes.

where the function $\mathbf{sig}[\bullet]$ applies the sigmoid function independently to every element of the row vector input. As usual, we use the binary cross-entropy loss, but now only at nodes where we know the ground truth label y. Note that equation 13.12 is just a vectorized version of the node classification loss from equation 13.3.

Training this network raises two problems. First, it is logistically difficult to train a graph neural network of this size. Consider that in the forward pass, we will have to store the node embeddings at every layer of the network. This will involve both storing and processing a structure that is several times the size of the entire graph, which may not be practical. Second, we have only a single graph, so it's not obvious how to perform stochastic gradient descent. How can we form a batch if there is only a single object?

13.8.1 Choosing batches

One way to form a batch is just to choose a random subset of the labeled nodes at each step of training. Each of these nodes depends on its neighbors in the previous layer.

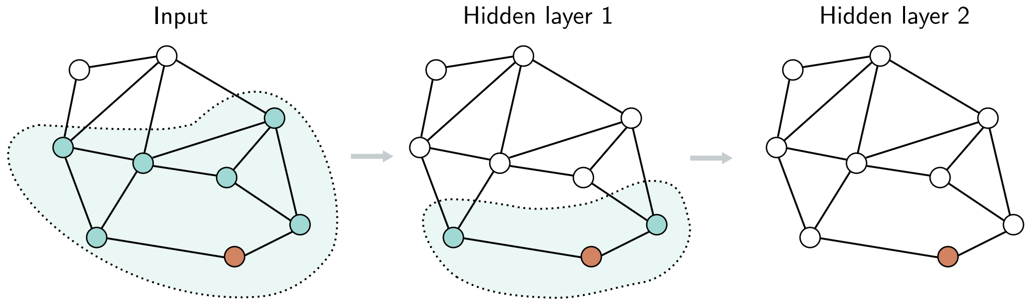

Figure 13.9 Receptive fields in graph neural networks. Consider the orange node in hidden layer two (right). This receives input from the nodes in the 1-hop neighborhood in hidden layer one (shaded region in center). These nodes in hidden layer one receive inputs from their neighbors in turn and the orange node in layer two receives inputs from all the input nodes in the 2-hop neighborhood (shaded region on left). The region of the graph that contributes to a given node is equivalent to the notion of a receptive field in convolutional neural networks

These in turn depend on their neighbors in the layer before that, so we can think of each node as having the equivalent of a receptive field (figure 13.9). The size of the receptive field is referred to as the *k-hop neighborhood*. We can hence perform a gradient descent step using the graph that forms the union of the k-hop neighborhoods of the nodes in the batch; the remaining inputs do not contribute.

Unfortunately, this only works if there are relatively few layers and the graph is sparse. For densely connected networks with many layers, every input node may be in the receptive field of every output, and so this may not reduce the graph size at all. This is known as the *graph expansion problem*. Two approaches that tackle this problem are *neighborhood sampling* and *graph partitioning*.

Neighborhood sampling: The full graph that feeds into the batch of nodes is sampled, thereby reducing the possible number of connections at each network layer (figure 13.10). For example, we might start with the batch nodes and randomly sample a fixed number of their neighbors in the previous layer. Then, we randomly sample a fixed number of *their* neighbors in the layer before, and so on. The graph still increases in size with each layer, but in a way that is much more controlled. This is done anew for each batch, so even if the same batch is drawn twice, the contributing neighbors differ. This is also reminiscent of dropout (section 9.3.3) and adds some regularization.

Graph partitioning: A second approach is to cluster the original graph into disjoint subsets of nodes (i.e., smaller graphs that are not connected to one another) before processing (figure 13.11). There are standard algorithms to choose these subsets so that the number of internal links is maximized. These smaller graphs can each be treated as

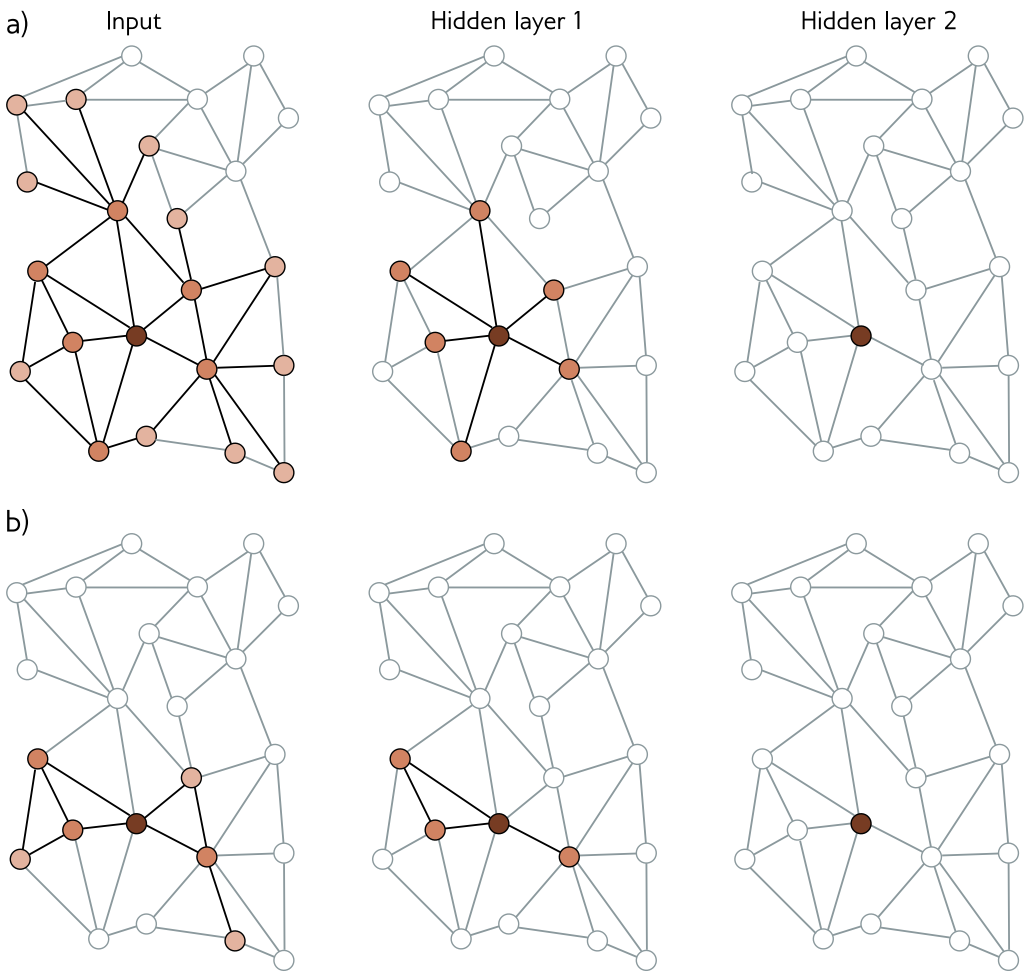

Figure 13.10 Neighborhood sampling. a) One way of forming batches on large graphs is to choose a subset of labeled nodes in the output layer (here just one node in layer two, right) and then work back to find all of the nodes in the K-hop neighborhood (receptive field). Only this sub-graph is needed to train this batch. Unfortunately, if the graph is densely connected, this may retain a large proportion of the graph. b) One solution is neighborhood sampling. As we work back from the final layer, we select a subset of neighbors (here three) in the layer before, and a subset of the neighbors of these in the layer before that. This restricts the size of the graph for training the batch.

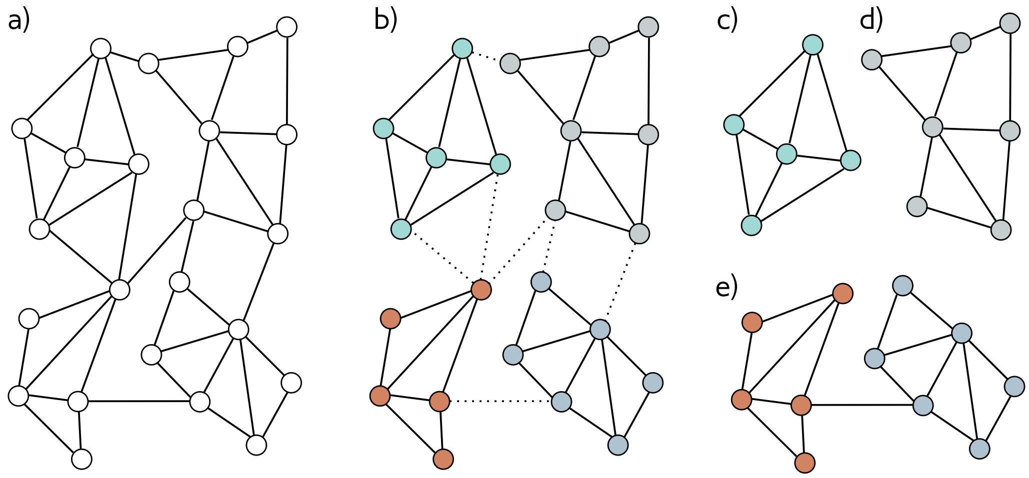

Figure 13.11 Graph partitioning. a) Input graph. b) The input graph is partitioned into smaller subgraphs using a principled method that removes the fewest edges. c-d) We can now use these subgraphs as batches to train in a transductive setting, so here there are four possible batches. e) Alternatively, we can use combinations of the subgraphs as batches, reinstating the edges between them. If we use pairs of subgraphs, there would be six possible batches here.

batches, or a random combination of them can be combined to form a batch (reinstating any links between them from the original graph).

Given one of the above methods to form batches, we can now train the network parameters in the same way as for the inductive setting, dividing the labeled nodes into train, test, and validation sets as desired; we have effectively converted a transductive problem to an inductive one. To perform inference, we compute predictions for the unknown nodes based on their k-hop neighborhood. Unlike training, this does not require storing the intermediate representations, and so is much more memory efficient.

13.9 Layers for graph convolutional networks

In the previous examples, we combined messages from adjacent nodes by summing them together with the transformed current node. This was accomplished by post-multiplying the node embedding matrix $\mathbf{H}$ by $\mathbf{A}+\mathbf{I}$ (the adjacency matrix plus the identity). We now consider different approaches to both (i) the combination of the current embedding with the aggregated neighbors and (ii) the aggregation process itself.

13.9.1 Combining current node and aggregated neighbors

In the example GCN layer above, we combined the aggregated neighbors $\mathbf{HA}$ with the current nodes $\mathbf{H}$ by just summing them:

$$\mathbf{H}_{k+1} = \mathbf{a}\left[\boldsymbol{\beta}_k \mathbf{1}^T + \boldsymbol{\Omega}_k \mathbf{H}_k(\mathbf{A}+\mathbf{I})\right]. \tag{13.13}$$

In another variation, the current node is multiplied by a factor of $(1+\epsilon_k)$ before contributing to the sum, where ϵ_k is a learned scalar that is different for each layer:

$$\mathbf{H}_{k+1} = \mathbf{a}\left[\boldsymbol{\beta}_k \mathbf{1}^T + \boldsymbol{\Omega}_k \mathbf{H}_k(\mathbf{A}+(1+\epsilon_k)\mathbf{I})\right]. \tag{13.14}$$

This is known as *diagonal enhancement*. A further possibility is to treat the current node differently from the aggregated neighbors by applying a different linear transform $\boldsymbol{\Psi}_k$ to the current node:

$$\begin{aligned}\mathbf{H}_{k+1} &= \mathbf{a}\left[\boldsymbol{\beta}_k \mathbf{1}^T + \boldsymbol{\Psi}_k \mathbf{H}_k + \boldsymbol{\Omega}_k \mathbf{H}_k \mathbf{A}\right] \\ &= \mathbf{a}\left[\boldsymbol{\beta}_k \mathbf{1}^T + \begin{bmatrix}\boldsymbol{\Omega}_k & \boldsymbol{\Psi}_k\end{bmatrix}\begin{bmatrix}\mathbf{H}_k\mathbf{A} \\ \mathbf{H}_k\end{bmatrix}\right] \\ &= \mathbf{a}\left[\boldsymbol{\beta}_k \mathbf{1}^T + \boldsymbol{\Omega}'_k\begin{bmatrix}\mathbf{H}_k\mathbf{A} \\ \mathbf{H}_k\end{bmatrix}\right],\end{aligned} \tag{13.15}$$

where we have defined $\boldsymbol{\Omega}'_k = \begin{bmatrix}\boldsymbol{\Omega}_k & \boldsymbol{\Psi}_k\end{bmatrix}$ in the third line. Problem 13.9

13.9.2 Residual connections

With residual connections, the aggregated representation from the neighbors is transformed and passed through the activation function before summation or concatenation with the current node. For the latter case, the associated network equations are:

$$\mathbf{H}_{k+1} = \begin{bmatrix}\mathbf{a}\left[\boldsymbol{\beta}_k \mathbf{1}^T + \boldsymbol{\Omega}_k \mathbf{H}_k \mathbf{A}\right] \\ \mathbf{H}_k\end{bmatrix}. \tag{13.16}$$

13.9.3 Mean aggregation

The above methods aggregate the neighbors by summing the node embeddings. However, it's possible to combine the node embeddings in different ways. Sometimes it's better to take the average of the neighbors rather than the sum; this might be superior if the embedding information is more important and the structural information is less important since the magnitude of the neighborhood contributions will not depend on the number of neighbors:

$$\mathbf{agg}[n] = \frac{1}{|\mathrm{ne}[n]|}\sum_{m\in\mathrm{ne}[n]} \mathbf{h}_m, \tag{13.17}$$

where as before ne$[n]$ denotes a set containing the indices of the neighbors of the n^{th} node. Equation 13.17 can be computed neatly in matrix form by introducing the diagonal $N \times N$ degree matrix $\mathbf{D}$. Each non-zero element of this matrix contains the number of neighbors for the associated node. It follows that each diagonal element in the inverse matrix $\mathbf{D}^{-1}$ contains the denominator that we need to compute the average. The new GCN layer can be written as:

Problem 13.8

$$\mathbf{H}_{k+1} = \mathbf{a}\left[\boldsymbol{\beta}_k \mathbf{1}^T + \boldsymbol{\Omega}_k \mathbf{H}_k(\mathbf{A}\mathbf{D}^{-1} + \mathbf{I})\right]. \tag{13.18}$$

13.9.4 Kipf normalization

There are many variations of graph neural networks based on mean aggregation. Sometimes the current node is included with its neighbors in the mean computation, rather than treated separately. In Kipf normalization, the sum of the node representations is normalized as:

Problem 13.9

$$\mathbf{agg}[n] = \sum_{m \in \text{ne}[n]} \frac{\mathbf{h}_m}{\sqrt{|\text{ne}[n]||\text{ne}[m]|}}, \tag{13.19}$$

with the logic that information coming from nodes with a very large number of neighbors should be downweighted since there are many connections and they provide less unique information. This can also be expressed in matrix form using the degree matrix:

$$\mathbf{H}_{k+1} = \mathbf{a}\left[\boldsymbol{\beta}_k \mathbf{1}^T + \boldsymbol{\Omega}_k \mathbf{H}_k(\mathbf{D}^{-1/2}\mathbf{A}\mathbf{D}^{-1/2} + \mathbf{I})\right]. \tag{13.20}$$

13.9.5 Max pooling aggregation

An alternative operation that is also invariant to permutation is computing the maximum of a set of objects. The *max pooling* aggregation operator is:

$$\mathbf{agg}[n] = \max_{m \in \text{ne}[n]} [\mathbf{h}_m], \tag{13.21}$$

where the operator $\mathbf{max}[\bullet]$ returns the element-wise maximum of the vectors $\mathbf{h}_m$ that are neighbors to the current node n.

13.9.6 Aggregation by attention

The aggregation methods discussed so far either weight the contribution of the neighbors equally or in a way that depends on the graph topology. Conversely, in *graph attention layers*, the weights depend on the data at the nodes. A linear transform is applied to the current node embeddings so that:

$$\mathbf{H}'_k = \boldsymbol{\beta}_k \mathbf{1}^T + \boldsymbol{\Omega}_k \mathbf{H}. \tag{13.22}$$

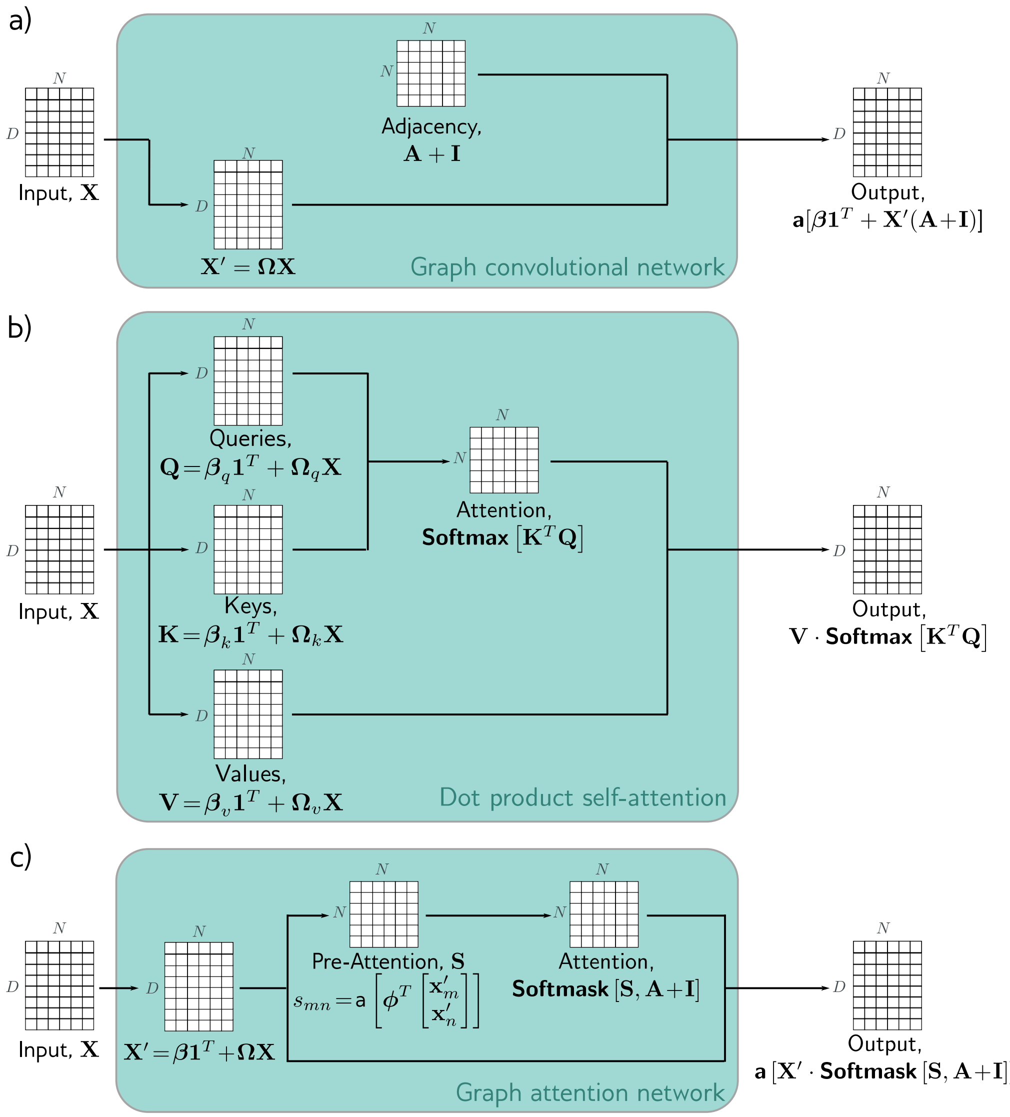

Figure 13.12 Comparison of graph convolutional network, dot product attention, and graph attention network. In each case, the mechanism maps N embeddings of size D stored in a $D \times N$ matrix $\mathbf{X}$ to an output of the same size. The graph convolutional network applies a linear transformation $\mathbf{X}' = \boldsymbol{\Omega}\mathbf{X}$ to the data matrix. It then computes a weighted sum of the transformed data, where the weighting is based on the adjacency matrix. A bias $\boldsymbol{\beta}$ is added and the result is passed through an activation function. b) The outputs of the self-attention mechanism are also weighted sums of the transformed inputs, but this time the weights depend on the data itself via the attention matrix. c) The graph attention network combines both of these mechanisms; the weights are both computed from the data and based on the adjacency matrix.

Then the similarity s_{mn} of each transformed node embedding $\mathbf{h}'_m$ to the transformed node embedding $\mathbf{h}'_n$ is computed by concatenating the pairs, taking a dot product with the column vector $\boldsymbol{\phi}_k$, and applying an activation function:

$$s_{mn} = \mathrm{a}\left[\boldsymbol{\phi}_k^T \begin{bmatrix}\mathbf{h}'_m \\ \mathbf{h}'_n\end{bmatrix}\right]. \tag{13.23}$$

These variables are stored in an $N \times N$ matrix $\mathbf{S}$, where each element represents the similarity of every node to every other. However, only those values corresponding to the current node and its neighbors are required. This can be achieved by pointwise multiplying $\mathbf{S}$ with $\mathbf{A}+\mathbf{I}$. As in dot-product self-attention, the attention weights that contribute to each output embedding are normalized to be positive and sum to one using the softmax operation. These weights are applied to the transformed embeddings:

$$\mathbf{H}_{k+1} = \mathbf{a}\left[\mathbf{H}'_k \cdot \mathbf{Softmask}[\mathbf{S}, \mathbf{A}+\mathbf{I}]\right], \tag{13.24}$$

where $\mathbf{a}[\bullet]$ is a second activation function. The function $\mathbf{Softmask}[\bullet,\bullet]$ applies the softmax operation separately to each column of its first argument, setting values where the second argument is zero to negative infinity. This has the effect of ensuring that the attention to non-neighboring nodes is zero.

This is very similar to the self-attention computation in transformers (figure 13.12), except that (i) the keys, queries, and values are all the same (ii) the measure of similarity is different, and (iii) the attentions are masked so that each node only attends to itself and its neighbors. As in transformers, this system can be extended to use multiple heads that are run in parallel and recombined.

Problem 13.10

13.10 Edge graphs

Until now, we have focused on processing node embeddings, which evolve as they are passed through the network so that by the end of the network they represent both the node and its context in the graph. We now consider the case where the information is associated with the edges of the graph.

It is easy to adapt the machinery for node embeddings to process edge embeddings using the *edge graph* (also known as the *adjoint graph* or *line graph*). This is a complementary graph, in which each edge in the original graph becomes a node, and every two edges that have a node in common in the original graph create an edge in the new graph (figure 13.13). In general, a graph can be recovered from its edge graph, and so it's possible to swap between these two representations.

Problems 13.11–13.13

To process edge embeddings, the graph is translated to its edge graph and we use exactly the same techniques, aggregating information at each new node from its neighbors and combining this with the current representation. When both node and edge embeddings are present, we can translate back and forth between the two graphs. Now there are four possible updates (nodes update nodes, nodes update edges, edges update nodes, and edges update edges) and these can be alternated as desired, or with minor modifications, nodes can be updated simultaneously from both nodes and edges.

Problem 13.14

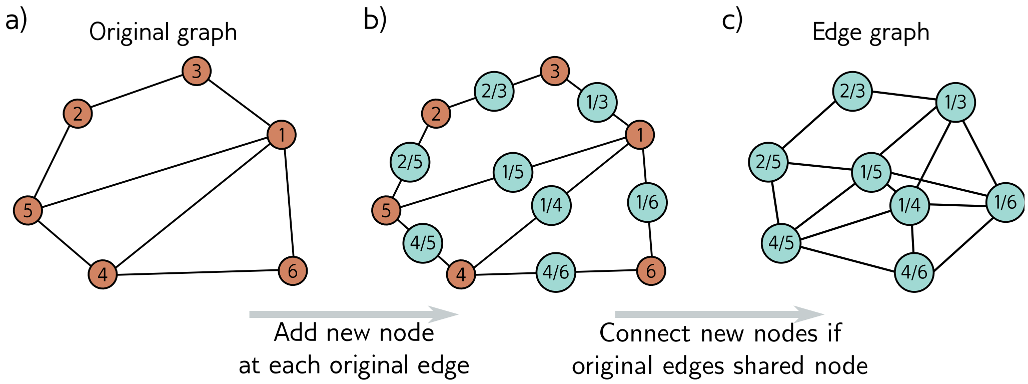

Figure 13.13 Edge graph. a) Graph with six nodes. b) To create the edge graph, we assign one node for each original edge (cyan circles), and c) connect the new nodes if the edges they represent connect to the same node in the original graph.

13.11 Summary

Graphs consist of a set of nodes, where pairs of these nodes are connected by edges. Both nodes and edges can have data attached and these are referred to as node embeddings and edge embeddings, respectively. Many real-world problems can be framed in terms of graphs, where the goal is to establish a property of the entire graph, properties of each node or edge, or the presence of additional edges in the graph.

Graph neural networks are deep learning models that are applied to graphs. Since the node order in graphs is arbitrary, the layers of graph neural networks must be equivariant to permutations of the node indices. Spatial-based convolutional networks are a family of graph neural networks that aggregate information from the neighbors of a node and then use this to update the node embeddings.

One challenge of processing graphs is that they often occur in the transductive setting, where there is only one partially labeled graph rather than sets of training and test graphs. This graph is often extremely large, which adds further challenges in terms of training, and has led to sampling and partitioning algorithms. The edge graph has a node for every edge in the original graph. By converting to this representation, graph neural networks can be used to update the edge embeddings.

Notes

Sanchez-Lengeling et al. (2021) and Daigavane et al. (2021) present good introductory articles on graph processing using neural networks. Recent surveys of research in graph neural networks can be found in articles by Zhou et al. (2020a) and Wu et al. (2020c) and the books of Hamilton

(2020) and Ma & Tang (2021). GraphEDM (Chami et al., 2020) unifies many existing graph algorithms into a single framework. In this chapter, we have related graphs to convolutional networks following Bruna et al. (2013), but there are also strong connections with belief propagation (Dai et al., 2016) and graph isomorphism tests (Hamilton et al., 2017a). Zhang et al. (2019c) provide a review that focuses specifically on graph convolutional networks. Bronstein et al. (2021) provide a general overview of geometric deep learning including learning on graphs.

Applications: Applications include graph classification (Zhang et al., 2018b, e.g.,), node classification (e.g., Kipf & Welling, 2017), edge prediction (e.g., Zhang & Chen, 2018), graph clustering (e.g., Tsitsulin et al., 2020), and recommender systems (e.g., Wu et al., 2023). Node classification methods are reviewed in Xiao et al. (2022a), graph classification methods in Errica et al. (2019), and edge prediction methods in Mutlu et al. (2020) and Kumar et al. (2020a).

Graph neural networks: Graph neural networks were introduced by Gori et al. (2005) and Scarselli et al. (2008) who formulated them as a generalization of recursive neural networks. The latter model used the iterative update:

$$\mathbf{h}_n \leftarrow \mathbf{f}\left[\mathbf{x}_n, \mathbf{x}_{m\in \text{ne}[n]}, \mathbf{e}_{e\in \text{nee}[n]}, \mathbf{h}_{m\in \text{ne}[n]}, \boldsymbol{\phi}\right], \tag{13.25}$$

in which each node embedding $\mathbf{h}_n$ is updated from the initial embedding $\mathbf{x}_n$, initial embeddings $\mathbf{x}_{m\in \text{ne}[n]}$ at the neighboring nodes, initial embeddings $\mathbf{e}_{e\in \text{nee}[n]}$ at the neighboring edges, and neighboring node embeddings $\mathbf{h}_{m\in \text{ne}[n]}$. For convergence, the function $\mathbf{f}[\bullet, \bullet, \bullet, \bullet, \boldsymbol{\phi}]$ must be a contraction mapping (see figure 16.9). If we unroll this equation in time for K steps and allow different parameters $\boldsymbol{\phi}_k$ at each time K, then equation 13.25 becomes similar to the graph convolutional network formulation. Subsequent work extended graph neural networks to use gated recurrent units (Li et al., 2016b) and long short-term memory networks (Selsam et al., 2019).

Spectral methods: Bruna et al. (2013) applied the convolution operation in the Fourier domain. The Fourier basis vectors can be found by taking the eigendecomposition of the *graph Laplacian matrix*, $\mathbf{L} = \mathbf{D} - \mathbf{A}$ where $\mathbf{D}$ is the degree matrix and $\mathbf{A}$ is the adjacency matrix. This has the disadvantages that the filters are not localized and the decomposition is prohibitively expensive for large graphs. Henaff et al. (2015) tackled the first problem by forcing the Fourier representation to be smooth (and hence the spatial domain to be localized). Defferrard et al. (2016) introduced ChebNet, which approximates the filters efficiently by making use of the recursive properties of Chebyshev polynomials. This both provides spatially localized filters and reduces the computation. Kipf & Welling (2017) simplified this further to construct filters that use only a 1-hop neighborhood, resulting in a formulation that is similar to the spatial methods described in this chapter and providing a bridge between spectral and spatial methods.

Spatial methods: Spectral methods are ultimately based on the Graph Laplacian, and so if the graph changes, the model must be retrained. This problem spurred the development of spatial methods. Duvenaud et al. (2015) defined convolutions in the spatial domain, using a different weight matrix to combine the adjacent embeddings for each node degree. This has the disadvantage that it becomes impractical if some nodes have a very large number of connections. Diffusion convolutional neural networks (Atwood & Towsley, 2016) use powers of the normalized adjacency matrix to blend features across different scales, sum these, pointwise multiply by weights, and pass through an activation function to create the node embeddings. Gilmer et al. (2017) introduced *message passing neural networks*, which defined convolutions on the graph as propagating messages from spatial neighbors. The "aggregate and combine" formulation of *GraphSAGE* (Hamilton et al., 2017a) fits into this framework.

Aggregate and combine: Graph convolutional networks (Kipf & Welling, 2017) take a weighted average of the neighbors and current node and then apply a linear mapping and ReLU. GraphSAGE (Hamilton et al., 2017a) applies a neural network layer to each neighbor and then takes the elementwise maximum to aggregate. Chiang et al. (2019) propose *diagonal enhancement* in which the previous embedding is weighted more than the neighbors. Kipf & Welling (2017) introduced Kipf normalization, which normalizes the sum of the neighboring embeddings based on the degrees of the current node and its neighbors (see equation 13.19).

The *mixture model network* or *MoNet* (Monti et al., 2017) takes this one step further by *learning* a weighting based on these two quantities. They associate a pseudo-coordinate system with each node, where the positions of the neighbors depend on the degrees of the current node and the neighbor. They then learn a continuous function based on a mixture of Gaussians and sample this at the pseudo-coordinates of the neighbors to get the weights. In this way, they can learn the weightings for nodes and neighbors with arbitrary degrees. Pham et al. (2017) use a linear interpolation of the node embedding and neighbors with a different weighted combination for each dimension. The weight of this gating mechanism is generated as a function of the data.

Higher-order convolutional layers: Zhou & Li (2017) used higher-order convolutions by replacing the adjacency matrix $\mathbf{A}$ with $\tilde{\mathbf{A}} = \mathbf{Min}[\mathbf{A}^L + \mathbf{I}, \mathbf{1}]$ where L is the maximum walk-length, $\mathbf{1}$ is a matrix containing only ones and $\mathbf{Min}[\bullet]$ takes the pointwise minimum of its two matrix arguments; the updates now sum together contributions from any nodes where there is at least one walk of length L. Abu-El-Haija et al. (2019) proposed MixHop, which computes node updates from the neighbors (using the adjacency matrix $\mathbf{A}$), the neighbors of the neighbors (using $\mathbf{A}^2$), and so on. They concatenate these updates at each layer. Lee et al. (2018) combined information from nodes beyond the immediate neighbors using geometric *motifs*, which are small local geometric patterns in the graph (e.g., a fully connected clique of five nodes).

Residual connections: Kipf & Welling (2017) proposed a residual connection in which the original embeddings are added to the updated ones. Hamilton et al. (2017b) concatenate the previous embedding to the output of the next layer (see equation 13.16). Rossi et al. (2020) present an inception-style network, where the node embedding is concatenated to not only the aggregation of its neighbors but also the aggregation of all neighbors within a walk of two (via computing powers of the adjacency matrix). Xu et al. (2018) introduced *jump knowledge connections* in which the final output at each node consists of the concatenated node embeddings throughout the network. Zhang & Meng (2019) present a general formulation of residual embeddings called *GResNet* and investigate several variations, in which the embeddings from the previous layer are added, the input embeddings are added, or versions of these that aggregate information from their neighbors (without further transformation) are added.

Attention in graph neural networks: Veličković et al. (2019) developed the graph attention network (figure 13.12c). Their formulation uses multiple heads whose outputs are combined together symmetrically. *Gated Attention Networks* (Zhang et al., 2018a) weight the output of the different heads in a way that depends on the data itself. Graph-BERT (Zhang et al., 2020) performs node classification using self-attention alone; the structure of the graph is captured by adding position embeddings to the data in a similar way to how the absolute or relative position of words is captured in the transformer (chapter 12). For example, they add positional information that depends on the number of hops between nodes in the graph.

Permutation invariance: In *DeepSets*, Zaheer et al. (2017) presented a general permutation invariant operator for processing sets. Janossy pooling (Murphy et al., 2018) accepts that many functions are not permutation equivariant, and instead uses a permutation-sensitive function and averages the results across many permutations.

Edge graphs: The notation of the *edge graph*, *line graph*, or *adjoint graph* dates to Whitney (1932). The idea of "weaving" layers that update node embeddings from node embeddings, node embeddings from edge embeddings, edge embeddings from edge embeddings, and edge embeddings from node embeddings was proposed by Kearnes et al. (2016), although here the node-node and edge-edge updates do not involve the neighbors. Monti et al. (2018) introduced the dual-primal graph CNN, which is a modern formulation in a CNN framework that alternates between updating on the original graph and the edge graph.

Power of graph neural networks: Xu et al. (2019) argue that a neural network should be able to distinguish different graph structures; it is undesirable to map two graphs with the same initial node embeddings but different adjacency matrices to the same output. They identified graph structures that could not be distinguished by previous approaches such as GCNs (Kipf & Welling, 2017) and GraphSAGE (Hamilton et al., 2017a). They developed a more powerful architecture that has the same discriminative power as the Weifeiler-Lehman graph isomorphism test (Weisfeiler & Leman, 1968), which is known to discriminate a broad class of graphs. This resulting *graph isomorphism network* was based on the aggregation operation:

$$\mathbf{h}_{k+1}^{(n)} = \mathbf{mlp}\left[(1+\epsilon_k)\,\mathbf{h}_k^{(n)} + \sum_{m\in\mathrm{ne}[n]} \mathbf{h}_k^{(m)}\right]. \tag{13.26}$$

Batches: The original paper on graph convolutional networks (Kipf & Welling, 2017) used full-batch gradient descent. This has memory requirements that are proportional to the number of nodes, embedding size, and number of layers during training. Since then, three types of methods have been proposed to reduce the memory requirements, and create batches for SGD in the transductive setting: node sampling, layer sampling, and sub-graph sampling.

Node sampling methods start by randomly selecting a subset of target nodes and then work back through the network, adding a subset of the nodes in the receptive field at each stage. GraphSAGE (Hamilton et al., 2017a) proposed a fixed number of neighborhood samples as in figure 13.10b. Chen et al. (2018b) introduce a variance reduction technique but this uses historical activations of nodes, and so still has a high memory requirement. *PinSAGE* (Ying et al., 2018a) used random walks from the target nodes and chooses the top K nodes with the highest visit count. This prioritizes ancestors that are more closely connected.

Node sampling methods still require increasing numbers of nodes as we pass back through the graph. *Layer sampling methods* address this by directly sampling the receptive field in each layer independently. Examples of layer sampling include FastGCN (Chen et al., 2018a), adaptive sampling (Huang et al., 2018b), and layer-dependent importance sampling (Zou et al., 2019).

Subgraph sampling methods randomly draw subgraphs or divide the original graph into subgraphs. These are then trained as independent data examples. Examples of these approaches include GraphSAINT (Zeng et al., 2020), which samples sub-graphs during training using random walks, and then runs a full GCN on the subgraph, while also correcting for the bias and variance of the minibatch. Cluster GCN (Chiang et al., 2019) partitions the graph into clusters (by maximizing the embedding utilization or number of within-batch edges) in a pre-processing stage and randomly selects clusters to form minibatches. To create more randomness, they train random subsets of these clusters plus the edges between them (see figure 13.11).

Wolfe et al. (2021) propose a method for distributed training, which both partitions the graph and trains narrower GCNs in parallel by partitioning the feature space at different layers. More information about sampling graphs can be found in Rozemberczki et al. (2020).

Regularization and normalization: Rong et al. (2020) proposed *DropEdge*, which randomly drops edges from the graph during each iteration of training by masking the adjacency matrix.

This can be done for the whole neural network, or differently in each layer (layer-wise DropEdge). In a sense, this is similar to dropout in that it breaks connections in the flow of data, but it can also be considered an augmentation method since changing the graph is similar to perturbing the data. Schlichtkrull et al. (2018), Teru et al. (2020) and Veličković et al. (2019) also propose randomly dropping edges from the graph as a form of regularization similar to dropout. Node sampling methods (Hamilton et al., 2017a; Huang et al., 2018b; Chen et al., 2018a) can also be thought of as regularizers. Hasanzadeh et al. (2020) present a general framework called *DropConnect* that unifies many of the above approaches.

There are also many proposed normalization schemes for graph neural networks, including *PairNorm* (Zhao & Akoglu, 2020), weight normalization (Oono & Suzuki, 2019), differentiable group normalization (Zhou et al., 2020b), and GraphNorm (Cai et al., 2021).

Multi-relational graphs: Schlichtkrull et al. (2018) proposed a variation of graph convolutional networks for multi-relational graphs (i.e., graphs with more than one edge type). Their scheme separately aggregates information from each edge type, using different parameters. If there are many edge types, then the number of parameters may become large, and to combat this they propose that each edge type uses a different weighting of a basis set of parameters.

Hierarchical representations and pooling: CNNs for image classification gradually decrease the size of the representation, but increase the number of channels as the network progresses. However, the GCNs for graph classification in this chapter maintain the entire graph until the last layer and then combine all of the nodes to compute the final prediction. Ying et al. (2018b) propose *DiffPool*, which clusters graph nodes to make a graph that gets progressively smaller as the depth increases in a way that is differentiable, so can be learned. This can be done based on the graph structure alone, or adaptively based on the graph structure and the embeddings. Other pooling methods include SortPool (Zhang et al., 2018b) and self-attention graph-pooling (Lee et al., 2019). A comparison of pooling layers for graph neural networks can be found in Grattarola et al. (2022). Gao & Ji (2019) propose an encoder-decoder structure for graphs based on the U-Net (see figure 11.10).

Geometric graphs: MoNet (Monti et al., 2017) can be easily adapted to exploit geometric information because neighboring nodes have well-defined spatial positions. They learn a mixture of Gaussians function and sample from this based on the relative coordinates of the neighbor. In this way, they can weight neighboring nodes based on their relative positions as in standard convolutional neural networks even though these positions are not consistent. The geodesic CNN (Masci et al., 2015) and anisotropic CNN (Boscaini et al., 2016) both adapt convolution to manifolds (i.e., surfaces) as represented by triangular meshes. They locally approximate the surface as a plane and define a coordinate system on this plane around the current node.

Oversmoothing and suspended animation: Unlike other deep learning models, graph neural networks did not until recently benefit significantly from increasing depth. Indeed, the original GCN paper (Kipf & Welling, 2017) and GraphSAGE (Hamilton et al., 2017a) both only use two layers, and Chiang et al. (2019) trained a five-layer Cluster-GCN to get state-of-the-art performance on the PPI dataset. One possible explanation is *over-smoothing* (Li et al., 2018c); at each layer, the network incorporates information from a larger neighborhood and it may be that this ultimately results in the dissolution of (important) local information. Indeed (Xu et al., 2018) prove that the influence of one node on another is proportional to the probability of reaching that node in a K-step random walk, and this approaches the stationary distribution of walks over the graph with increasing K causing the local neighborhood to be washed out.

Alon & Yahav (2021) proposed another explanation for why performance doesn't improve with network depth. They argue that adding depth allows information to be aggregated from longer paths. However, in practice, the exponential growth in the number of neighbors means there is a bottleneck whereby too much information is "squashed" into the fixed-size node embeddings.

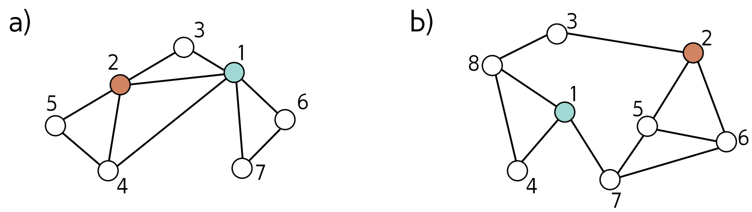

Figure 13.14 Graphs for problems 13.1, 13.3, and 13.8.

Ying et al. (2018a) also note that when the depth of the network exceeds a certain limit, the gradients no longer propagate back, and learning fails for both the training and test data. They term this effect *suspended animation*. This is very similar to what happens when many layers are naïvely added to convolutional neural networks (figure 11.2). They propose a family of residual connections that allow deeper networks to be trained. Vanishing gradients (section 7.5) have also been identified as a limitation by Li et al. (2021b).

It has recently become possible train to deeper graph neural networks using various forms of residual connection (Xu et al., 2018; Li et al., 2020a; Gong et al., 2020; Chen et al., 2020b; Xu et al., 2021a). Li et al. (2021a) train a state-of-the-art model with more than 1000 layers using an invertible network to reduce the memory requirements of training (see chapter 16).

Problems

Problem 13.1 Write out the adjacency matrices for the two graphs in figure 13.14.

Problem 13.2 Draw graphs that correspond to the following adjacency matrices:

$$\mathbf{A}_1 = \begin{bmatrix} 0 & 1 & 1 & 0 & 0 & 0 & 0 \\ 1 & 0 & 0 & 1 & 1 & 1 & 0 \\ 1 & 0 & 0 & 0 & 0 & 1 & 1 \\ 0 & 1 & 0 & 0 & 0 & 1 & 1 \\ 0 & 1 & 0 & 0 & 0 & 0 & 1 \\ 0 & 1 & 1 & 1 & 0 & 0 & 0 \\ 0 & 0 & 1 & 1 & 1 & 0 & 0 \end{bmatrix} \quad \text{and} \quad \mathbf{A}_2 = \begin{bmatrix} 0 & 0 & 1 & 1 & 0 & 0 & 1 \\ 0 & 0 & 0 & 1 & 1 & 0 & 0 \\ 1 & 0 & 0 & 0 & 0 & 1 & 0 \\ 1 & 1 & 0 & 0 & 1 & 1 & 1 \\ 0 & 1 & 0 & 1 & 0 & 0 & 1 \\ 0 & 0 & 1 & 1 & 0 & 0 & 1 \\ 1 & 0 & 0 & 1 & 1 & 1 & 0 \end{bmatrix}.$$

Problem 13.3 Consider the two graphs in figure 13.14. How many ways are there to walk from node one to node two in (i) three steps and (ii) seven steps?

Problem 13.4 The diagonal of $\mathbf{A}^2$ in figure 13.4c contains the number of edges that connect to each corresponding node. Explain this phenomenon.

Problem 13.5 What permutation matrix is responsible for the transformation between the graphs in figures 13.5a–c and figure 13.5d–f?

Problem 13.6 Prove that:

$$\mathrm{sig}\left[\beta_K + \boldsymbol{\omega}_K \mathbf{H}_K \mathbf{1}\right] = \mathrm{sig}\left[\beta_K + \boldsymbol{\omega}_K \mathbf{H}_K \mathbf{P} \mathbf{1}\right], \tag{13.27}$$

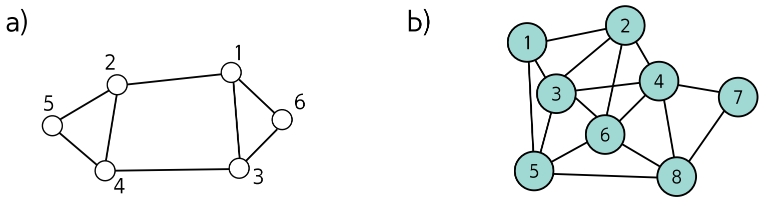

Figure 13.15 Graphs for problems 13.11–13.13.

where $\mathbf{P}$ is an $N \times N$ permutation matrix (a matrix which is all zeros except for exactly one entry in each row and each column which is one) and $\mathbf{1}$ is an $N \times 1$ vector of ones.

Problem 13.7 Consider the simple GNN layer:

$$\begin{aligned}\mathbf{H}_{k+1} &= \text{GraphLayer}[\mathbf{H}_k, \mathbf{A}] \\ &= \mathbf{a}\left[\boldsymbol{\beta}_k \mathbf{1}^T + \boldsymbol{\Omega}_k[\mathbf{H}_k; \mathbf{H}_k\mathbf{A}]\right],\end{aligned} \tag{13.28}$$

where $\mathbf{H}$ is a $D \times N$ matrix containing the N node embeddings in its columns, $\mathbf{A}$ is the $N \times N$ adjacency matrix, $\boldsymbol{\beta}$ is the bias vector and $\boldsymbol{\Omega}$ is the weight matrix. The notation $[\mathbf{H}_k; \mathbf{H}_k\mathbf{A}]$ indicates vertical concatenation of the matrices $\mathbf{H}_k$ and $\mathbf{H}_k\mathbf{A}$. Show that this layer is equivariant to permutations of the node order, so that:

$$\text{GraphLayer}[\mathbf{H}_k, \mathbf{A}]\mathbf{P} = \text{GraphLayer}[\mathbf{H}_k\mathbf{P}, \mathbf{P}^T\mathbf{A}\mathbf{P}], \tag{13.29}$$

where $\mathbf{P}$ is an $N \times N$ permutation matrix.

Appendix C.5.8
Permutation matrix

Problem 13.8 What is the degree matrix $\mathbf{D}$ for each of the graphs in figure 13.14?

Problem 13.9 The authors of GraphSAGE (Hamilton et al., 2017a) propose a pooling method, in which the node embedding is averaged together with its neighbors so that:

$$\mathbf{agg}[n] = \frac{1}{1 + |\text{ne}[n]|}\left(\mathbf{h}_n + \sum_{m \in \text{ne}[n]} \mathbf{h}_m\right). \tag{13.30}$$

Show how this operation can be computed simultaneously for all of the node embeddings in the $D \times N$ embedding matrix $\mathbf{H}$ using linear algebra. You will need to use both the adjacency matrix $\mathbf{A}$ and the degree matrix $\mathbf{D}$.

Problem 13.10 Devise a graph attention mechanism based on dot-product self-attention and draw its mechanism in the style of figure 13.12.

Problem 13.11 Draw the edge graph associated with the graph in figure 13.15a.

Problem 13.12 Draw the node graph that corresponds to the edge graph in figure 13.15b.

Problem 13.13 For a general undirected graph, describe how the adjacency matrix of the node graph relates to the adjacency matrix of the corresponding edge graph.

Problem 13.14 Design a layer that updates a node embedding $\mathbf{h}_n$ based on its neighboring node embeddings $\{\mathbf{h}_m\}_{m\in\text{ne}[n]}$ and neighboring edge embeddings $\{\mathbf{e}_m\}_{m\in\text{nee}[n]}$. You should consider the possibility that the edge embeddings are not the same size as the node embeddings.

Chapter 14

Unsupervised learning

Chapters 2–9 walked through the supervised learning pipeline. We defined models that mapped observed data $\mathbf{x}$ to output values $\mathbf{y}$, and introduced loss functions that measured the quality of that mapping for a training dataset $\{\mathbf{x}_i, \mathbf{y}_i\}$. Then we discussed how to fit and measure the performance of these models. Chapters 10–13 introduced more complicated model architectures that incorporated parameter sharing and allowed parallel computational paths.

The defining characteristic of *unsupervised learning models* is that they are learned from a set of observed data $\{\mathbf{x}_i\}$ without the presence of labels. All unsupervised models share this property, but they have diverse goals. They may be used to generate plausible new samples from the dataset, or to manipulate, denoise, interpolate between, or compress examples. They can also be used to reveal the internal structure of a dataset (e.g., by dividing it into coherent clusters) or used to distinguish whether new examples belong to the same data set or are outliers.

This chapter starts by introducing a taxonomy of unsupervised learning models and then discusses the desirable properties of models, and how to measure their performance. The four subsequent chapters discuss four particular models: generative adversarial networks, variational autoencoders, normalizing flows, and diffusion models.

14.1 Taxonomy of unsupervised learning models

Most unsupervised learning models define a mapping between the data $\mathbf{x}$ and a set of unseen *latent* variables $\mathbf{z}$. *Discriminative models* map from the data $\mathbf{x}$ to latent variables $\mathbf{z}$. *Generative models* map from the latent variables $\mathbf{z}$ to the data $\mathbf{x}$. The latent variables capture the underlying structure of the data and are usually of smaller dimension than the original data; in this sense, the latent variable $\mathbf{z}$ can be considered a compressed version of the data example $\mathbf{x}$ that captures its essential qualities (see figure 1.9).

This book focuses on generative latent variable models.[1] The four models in chap-

[1]Until this point, almost all of the relevant math has been embedded in the text. However, the next four chapters require a solid knowledge of probability. Appendix B covers the relevant material.

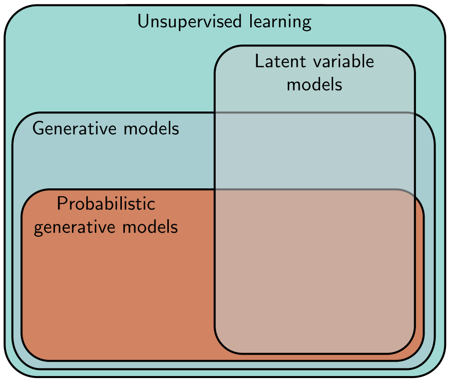

Figure 14.1 Unsupervised learning is a broad term that refers to any model applied to datasets without labels. Generative models can synthesize or generate new examples that have the same statistics as the dataset. A subset of generative models are probabilistic and also define a distribution over the data; to generate new data examples, we draw examples from this distribution. Latent variable models define a mapping between an underlying explanatory (latent) variable $\mathbf{z}$ and the data $\mathbf{x}$. They may fall into any of the above categories.

ters 15 to 18 all define a mapping from latent variables $\mathbf{z}$ to data examples $\mathbf{x}$. In each case, a probability distribution $Pr(\mathbf{z})$ is defined over the latent variable $\mathbf{z}$. New examples can be *generated* by drawing from this distribution and mapping the sample to the data space $\mathbf{x}$. *Generative adversarial networks* (chapter 15) learn to generate data examples $\mathbf{x}$ from latent variables $\mathbf{z}$, using a loss that encourages the generated examples to be indistinguishable from real examples (figure 14.2a).

Probabilistic generative models define a probability $Pr(\mathbf{x}|\boldsymbol{\phi})$ over the data $\mathbf{x}$ which depends on parameters $\boldsymbol{\phi}$. In training, we maximize the probability of the observed data $\{\mathbf{x}\}_i$ (figure 14.2b), and so the loss is the sum of the negative log-likelihoods:

$$L[\boldsymbol{\phi}] = -\sum_{i=1}^{I} \log\left[Pr(\mathbf{x}_i|\boldsymbol{\phi})\right]. \tag{14.1}$$

Since probability distributions must sum to one, this implicitly reduces the probability assigned to examples that are far from the observed data.

Variational autoencoders, normalizing flows, and diffusion models (chapters 17–18, respectively) are all probabilistic generative models.[2] In addition to generating new data, they can assign a probability to a data point, and this can be useful in its own right. For example, the probability can be thresholded to determine if an example belongs to the same dataset or is an *outlier*.

14.2 What makes a good generative model?

Generative models based on latent variables should have the following properties:

- **Efficient sampling:** Generating samples from the model should be computationally inexpensive and take advantage of the parallelism of modern hardware.

[2]Note that not all probabilistic generative models rely on latent variables. The transformer decoder (section 12.7) was learned without labels, can generate new examples, and can assign a probability to these examples but is based on an autoregressive formulation (equation 12.14).

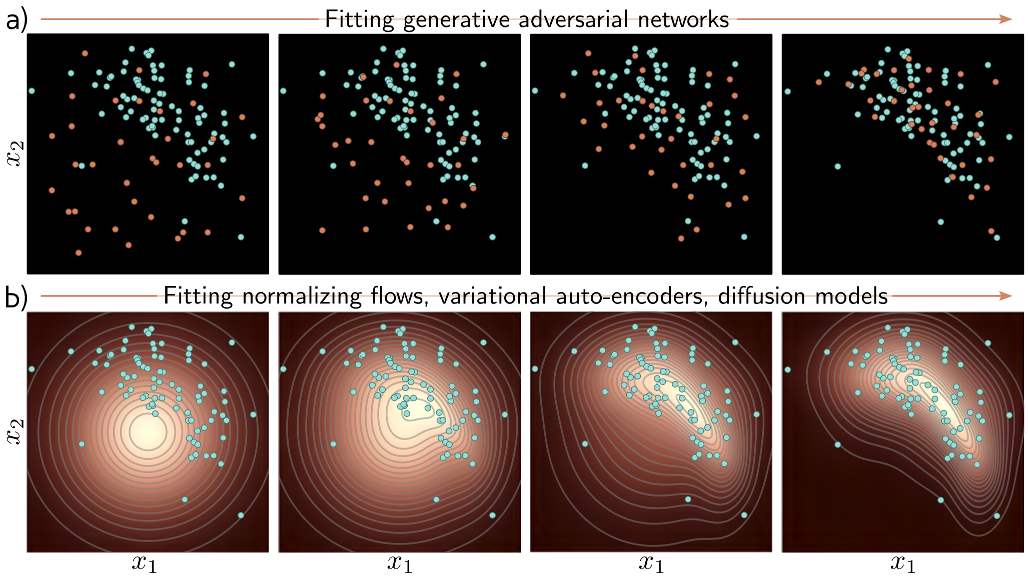

Figure 14.2 Fitting generative models a) Generative adversarial models (GANS) provide a mechanism for generating samples (orange points). During training (left to right), the GAN loss function encourages these samples to become progressively less distinguishable from real data. b) Probabilistic models (including variational autoencoders, normalizing flows, and diffusion models) learn a probability distribution over the training data (left to right). This distribution can be used to draw new samples, and assess the probability of new data points.

- **High-quality sampling:** The samples should be indistinguishable from the real data that the model was trained with.
- **Coverage:** Samples should represent the entire training distribution. It is insufficient to only generate samples that all look like a subset of the training data.
- **Well-behaved latent space:** Every latent variable $\mathbf{z}$ should correspond to a plausible data example $\mathbf{x}$ and smooth changes in $\mathbf{z}$ should correspond to smooth changes in $\mathbf{x}$.
- **Interpretable latent space:** Manipulating each dimension of $\mathbf{z}$ should correspond to changing an interpretable property of the data. For example, in a model of language, it might change the topic, tense, or verbosity.
- **Efficient likelihood computation:** If the model is probabilistic, we would like to be able to calculate the probability of new examples efficiently and accurately.

This naturally leads to the question of whether the generative models that we consider satisfy these properties. The answer is subjective, but figure 14.3 provides guidance. The precise assignments are disputable, but most practitioners would agree that there is no single model that satisfies all of these characteristics.

	GANs	VAEs	Flows	Diffusion
Efficient sampling	✓	✓	✓	✗
High quality	✓	✗	✗	✓
Coverage	✗	?	?	?
Well-behaved latent space	✓	✓	✓	✗
Interpretable latent space	?	?	?	✗
Efficient likelihood	n/a	✗	✓	✗

Figure 14.3 Properties of the generative models. Neither generative adversarial networks (GANs), variational auto-encoders (VAEs), normalizing flows (Flows), nor diffusion models (diffusion) have the full complement of desirable properties.

14.3 Quantifying performance

The previous section discussed desirable properties of generative models. We now consider quantitative measures of success for generative models. Much experimentation with generative models has used images, due to the widespread availability of that data, and the ease of qualitatively judging the samples. Consequently, some of these methods only apply to images.

Test likelihood: One way to compare probabilistic models is to measure the likelihood of a set of test data. It is not effective to measure the likelihood of the training data because a model could simply assign a very high probability to each training point and very low probabilities in between. This model would have a very high training likelihood but could only reproduce the training data. The test likelihood captures how well the model generalizes from the training data and also the coverage; if the model assigns a high probability to just a subset of the training data, it must assign lower probabilities elsewhere, and so a portion of the test examples will have low probability.

Test likelihood is a good way to quantify probabilistic models, but unfortunately, it is not relevant for generative adversarial models (which do not assign a probability), and is expensive to estimate for variational autoencoders and diffusion models (although it is possible to compute a lower bound on the log-likelihood). Normalizing flows are the only type of model for which the likelihood can be computed exactly and efficiently.

Inception score: The inception score (IS) is specialized for images, and ideally for generative models trained on the ImageNet database. The score is calculated using a pre-trained classification model – usually the "Inception" model, from which the name is derived. It is based on two criteria. First, each generated image should look like one and only one of the 1000 possible categories y. Hence, the model should classify it with high probability and $Pr(y|\mathbf{x}_n)$ should be highly peaked. Second, the entire set of generated images should be assigned to the classes with equal probability, so $Pr(y)$ should be flat when averaged over all generated examples.

The inception score measures the distance between these two distributions over the generated set. This distance will be large if one is peaked and the other flat. More precisely, it returns the exponential of the expected KL-divergence between $Pr(y|\mathbf{x}_n)$ and $Pr(y)$:

Appendix B.5.1 KL divergence

$$IS = \exp\left[\frac{1}{N}\sum_{n=1}^{N} D_{KL}\Big[Pr(y|\mathbf{x}_n)||Pr(y)\Big]\right], \tag{14.2}$$

where N is the number of generated examples and:

$$Pr(y) = \frac{1}{N}\sum_{n=1}^{N} Pr(y|\mathbf{x}=n). \tag{14.3}$$

Unfortunately, this model has some drawbacks; it is only sensible for generative models of the ImageNet database. It is very sensitive to the particular classification model, and retraining this model gives quite different numerical results. Moreover, it does not reward diversity within an object class; it would return a high value if the model could only generate one realistic example of each class.

Fréchet inception distance: This measure is also intended for images and computes a symmetric distance between the distributions of generated samples and real examples. This must be approximate since it is hard to characterize either distribution (indeed, characterizing the distribution of real examples is the job of generative models in the first place). Hence, the Fréchet inception distance approximates both distributions by multivariate Gaussians, and (as the name suggests) estimates the distance between them using the Fréchet distance.

Appendix ?? Fréchet distance

However, it does not model the distance with respect to the original data, but rather the activations in the deepest layer of the inception classification network. These hidden units are the ones most associated with object classes and so the comparison occurs at a semantic level, ignoring the more fine-grained details of the images. This metric does take account of diversity within classes, but relies heavily on the information retained by the features in the inception network; any information discarded by the network does not factor into the measure. Some of this discarded information may still be important to generate realistic samples.

Manifold precision/recall: Fréchet inception distance is sensitive both to the realism of the samples and the intra-class diversity, but does not distinguish between these two factors. To disentangle these factors, we can consider the overlap between the data *manifold* (i.e., the subset of the data space where the real examples lie) and the model manifold (i.e., where the generated examples lie). The *precision* is then the fraction of model samples that fall into the data manifold. This measures the proportion of generated samples that are realistic. The *recall* is the fraction of data samples that fall within the model manifold. This measures the proportion of the real data that can be generated by the model.

To estimate the manifold, a sphere is placed around each data example, where the radius of the sphere is the distance to the k^{th} nearest neighbor. The union of these spheres is an approximation of the manifold and it's easy to determine if a new point lies within it. This manifold is also typically computed in the feature space of a classifier with the advantages and disadvantages that entails.

14.4 Summary

Unsupervised models learn about the structure of a dataset in the absence of labels. A subset of these models is generative and can synthesize new data examples. A further subset is probabilistic, in that they can both generate new examples and assign a probability to observed data. The models considered in the next four chapters start with a latent variable $\mathbf{z}$ which has a known distribution. A deep neural network then maps from the latent variable to the observed data space. We considered desirable properties of generative models and we introduced several metrics that attempt to quantify their performance.

Notes

Popular generative models include generative adversarial networks (Goodfellow et al., 2014), variational autoencoders (Kingma & Welling, 2014), normalizing flows (Rezende & Mohamed, 2015), diffusion models (Sohl-Dickstein et al., 2015; Ho et al., 2020), auto-regressive models (Bengio et al., 2000; Van den Oord et al., 2016b) and energy-based models (LeCun et al., 2006). All except energy models are discussed in this book. Bond-Taylor et al. (2022) provide a recent survey of generative models.

Evaluation: Salimans et al. (2016) introduced the inception score and Heusel et al. (2017) introduced the Fréchet inception distance, both of which are based on the Pool-3 layer of the Inception V3 model (Szegedy et al., 2016). Nash et al. (2021) used earlier layers of the same network that retain more spatial information to ensure that the spatial statistics of images are also replicated. Kynkäänniemi et al. (2019) introduced the manifold precision/recall method. Barratt & Sharma (2018) discuss the inception score in detail and point out its weaknesses. Borji (2022) discusses the pros and cons of different methods for assessing generative models.

Chapter 15

Generative Adversarial Networks

A *generative adversarial network* or *GAN* is an unsupervised model that aims to generate new samples that are indistinguishable from a set of training examples. GANs are just mechanisms to create new samples; there is no easy way to assess how likely it is that a data point was generated from the model.

The underlying idea is simple; the main network generates samples by mapping random noise to the output data space. If a second network cannot discriminate between the generated samples and the real ones, then the samples must be plausible. If this network *can* tell the difference, then this provides a training signal that can be fed back to improve the quality of the samples. However, the practice of training GANs is more difficult: the learning algorithm can be unstable, and although they may learn to generate realistic samples, this does not imply that they learn to generate *all* possible samples.

GANs have been applied to many types of data including audio, 3D models, text, video, and graphs. However, they have found the most success in the image domain, where they can produce samples that are almost indistinguishable from real pictures. Accordingly, the examples in this chapter focus on synthesizing images.

15.1 Discrimination as a signal

We aim to generate new samples $\{\mathbf{x}_i^*\}$ that are statistically indistinguishable from a set of real training data $\{\mathbf{x}_i\}$. A single new sample $\mathbf{x}_j^*$ is generated by (i) choosing a *latent variable* $\mathbf{z}_j$ from a simple base distribution (e.g., a standard normal) and then (ii) passing this data through a network $\mathbf{x}_* = \mathbf{g}[\mathbf{z}_j, \boldsymbol{\theta}]$ with parameters $\boldsymbol{\theta}$. This network is known as the *generator*. During the learning process, the goal is to find parameters $\boldsymbol{\theta}$ so that the samples $\{\mathbf{x}_j^*\}$ look "similar" to the real data $\{\mathbf{x}_i\}$ (see figure 14.2a).

Similarity can be defined in many ways, but the GAN uses the principle that the samples should be indistinguishable from the true data. To this end, a second network $f[\bullet, \boldsymbol{\phi}]$ with parameters $\boldsymbol{\phi}$ called the *discriminator* is introduced. The goal of this network is to classify its input as being a real example or a generated sample. If this proves impossible, then the generated samples are indistinguishable from the real examples, and we

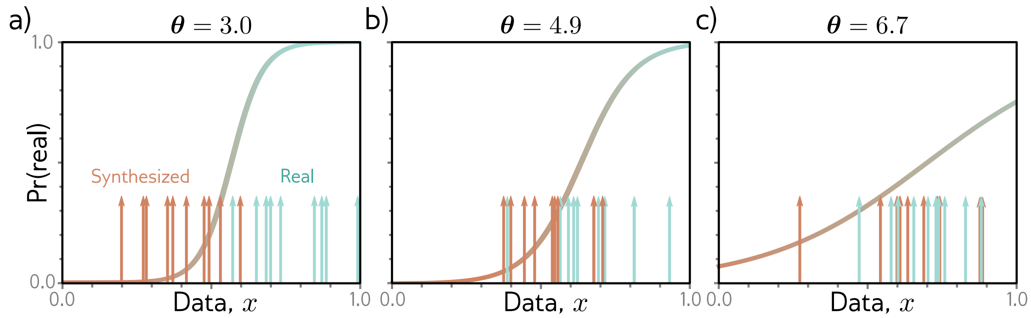

Figure 15.1 GAN mechanism. a) Given a parameterized function (a generator) that synthesizes samples (orange arrows) and a batch of real examples (cyan arrows), we train a discriminator to distinguish one from the other (sigmoid curve indicates the estimated probability that the data point is real). b) The generator is trained by modifying its parameters so that the discriminator becomes less certain the samples were synthetic (in this case, by moving the orange samples to the right). The discriminator is then updated. c) Alternating updates to the generator and discriminator cause the generated samples to become indistinguishable from real examples, and the impetus to change the generator (i.e., the slope of the sigmoid function) diminishes.

have succeeded. If it is possible, the discriminator provides a signal that can be used to improve the generation process.

Figure 15.1 shows the principle behind this scheme. We start with a database $\{x_i\}$ of real 1D examples. A different batch of ten of these examples $\{x_i\}_{i=1}^{10}$ is shown in each panel (cyan arrows). To create a batch of samples $\{x_j^*\}$, we use the simple generator:

$$x_j^* = \mathrm{g}[z_j, \theta] = z_j + \theta, \tag{15.1}$$

where latent variables $\{z_j\}$ are drawn from a standard normal distribution, and the parameter θ translates the generated samples along the x-axis (figure 15.1).

At initialization $\theta = 3.0$, and the generated samples (orange arrows) lie to the left of the true samples (cyan arrows). The discriminator is trained to distinguish the generated samples from the real examples (the sigmoid curve indicates the probability that a data point is real). During training, the generator parameters θ are manipulated to increase the probability that its samples are classified as real. In this case, this means increasing θ so that the samples move rightwards where the sigmoid curve is higher.

We alternate between retraining the discriminator and updating the generator. Figures 15.1b-c show two iterations of this process. It gradually becomes harder to classify the data, and so the impetus to change θ becomes weaker (i.e., the sigmoid becomes flatter). At the end of the process, there is no way to distinguish the two sets of data; the discriminator, which now has chance performance, is discarded and we are left with a generator that makes plausible samples.

15.1.1 GAN loss function

We now define the loss function for training GANs more precisely. We denote the discriminator by $\mathrm{f}[\mathbf{x}, \boldsymbol{\phi}]$. It takes a data example $\mathbf{x}$ as input, has parameters $\boldsymbol{\phi}$, and returns the probability that the data example was real. This is a binary classification problem and so we use the binary cross-entropy loss function (see section 5.4):

$$\hat{\boldsymbol{\phi}} = \underset{\boldsymbol{\phi}}{\operatorname{argmin}}\left[\sum_i -(1-y_i)\log\Big[1-\mathrm{sig}[\mathrm{f}[\mathbf{x}_i,\boldsymbol{\phi}]]\Big] - y_i\log\Big[\mathrm{sig}[\mathrm{f}[\mathbf{x}_i,\boldsymbol{\phi}]]\Big]\right], \tag{15.2}$$

where $y_i \in \{0,1\}$ is the label. As in figure 15.1, we assume that the real examples $\mathbf{x}$ have label $y=1$ and the generated samples $\mathbf{x}^*$ have label $y=0$ so that:

$$\hat{\boldsymbol{\phi}} = \underset{\boldsymbol{\phi}}{\operatorname{argmin}}\left[\sum_j -\log\Big[1-\mathrm{sig}[\mathrm{f}[\mathbf{x}^*_j,\boldsymbol{\phi}]]\Big] - \sum_i \log\Big[\mathrm{sig}[\mathrm{f}[\mathbf{x}_i,\boldsymbol{\phi}]]\Big]\right], \tag{15.3}$$

where i and j index the real and synthesized examples, respectively.

Now we substitute the definition for the generator $\mathbf{x}^*_j = \mathbf{g}[\mathbf{z}_j, \boldsymbol{\theta}]$ and note that we must maximize with respect to $\boldsymbol{\theta}$ since we want the generated samples to be misclassified (i.e., have low likelihood of being synthetic or high negative log-likelihood):

$$\hat{\boldsymbol{\phi}}, \hat{\boldsymbol{\theta}} = \underset{\boldsymbol{\theta}}{\operatorname{argmax}}\left[\min_{\boldsymbol{\phi}}\left[\sum_j -\log\Big[1-\mathrm{sig}[\mathrm{f}[\mathbf{g}[\mathbf{z}_j,\boldsymbol{\theta}],\boldsymbol{\phi}]]\Big] - \sum_i \log\Big[\mathrm{sig}[\mathrm{f}[\mathbf{x}_i,\boldsymbol{\phi}]]\Big]\right]\right]. \tag{15.4}$$

15.1.2 Training GANs

Equation 15.4 is a more complex loss function than we have seen before; the discriminator parameters $\boldsymbol{\phi}$ are manipulated to minimize the loss function and the generative parameters $\boldsymbol{\theta}$ are manipulated to maximize the loss function. GAN training is characterized as a *minimax game*; the generator tries to find new ways to fool the discriminator, which in turn searches for new ways to distinguish generated samples from real examples. Technically, the solution is a *Nash equilibrium* — the optimization algorithm searches for a position that is simultaneously a minimum of one function and a maximum of the other. If training proceeds as planned, then upon convergence $\mathbf{g}[\mathbf{z}, \boldsymbol{\theta}]$ will be drawn from the same distribution as the data, and $\mathbf{f}[\bullet, \boldsymbol{\phi}]$ will be at chance (i.e., 0.5).

To train the GAN, we can divide equation 15.4 into two loss functions:

$$\begin{aligned} L[\boldsymbol{\phi}] &= \sum_j -\log\Big[1-\mathrm{sig}[\mathrm{f}[\mathbf{g}[\mathbf{z}_j,\boldsymbol{\theta}],\boldsymbol{\phi}]]\Big] - \sum_i \log\Big[\mathrm{sig}[\mathrm{f}[\mathbf{x}_i,\boldsymbol{\phi}]]\Big] \\ L[\boldsymbol{\theta}] &= \sum_j \log\Big[1-\mathrm{sig}[\mathrm{f}[\mathbf{g}[\mathbf{z}_j,\boldsymbol{\theta}],\boldsymbol{\phi}]]\Big], \end{aligned} \tag{15.5}$$

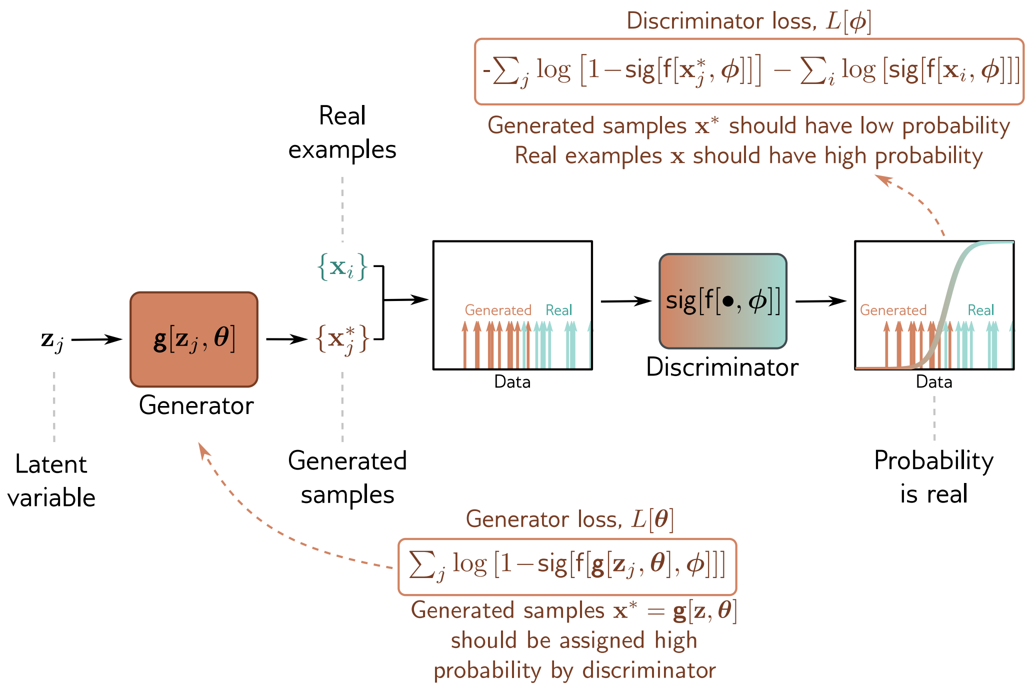

Figure 15.2 GAN loss functions. A latent variable $\mathbf{z}_j$ is drawn from the base distribution and passed through the generator to create a sample $\mathbf{x}^*$. A batch $\{\mathbf{x}^*_j\}$ of samples and a batch of real examples $\{\mathbf{x}_i\}$ are passed to the discriminator which assigns a probability that each is real. The discriminator parameters $\boldsymbol{\phi}$ are modified so that it assigns high probability to the real examples and low probability to the generated samples. The generator parameters $\boldsymbol{\theta}$ are modified to "fool" the discriminator into assigning the samples a high probability.

where we multiplied the second function by minus one to convert to a minimization problem and dropped the second term which has no dependence on $\boldsymbol{\theta}$. Minimizing the first loss function trains the discriminator. Minimizing the second trains the generator.

At each step, we draw a batch of latent variables $\mathbf{z}_j$ from the base distribution and pass these through the generator to create samples $\mathbf{x}^*_j = \mathbf{g}[\mathbf{z}_j,\boldsymbol{\theta}]$. Then we choose a batch of real training examples $\mathbf{x}_i$. Given the two batches, we can now perform one or more gradient descent steps on each loss function (figure 15.2).

15.1.3 Deep convolutional GAN

The *deep convolutional GAN* or *DCGAN* was an early GAN architecture specialized for generating images (figure 15.3). The input to the generator $\mathbf{g}[\mathbf{z},\boldsymbol{\theta}]$ is a 100D latent

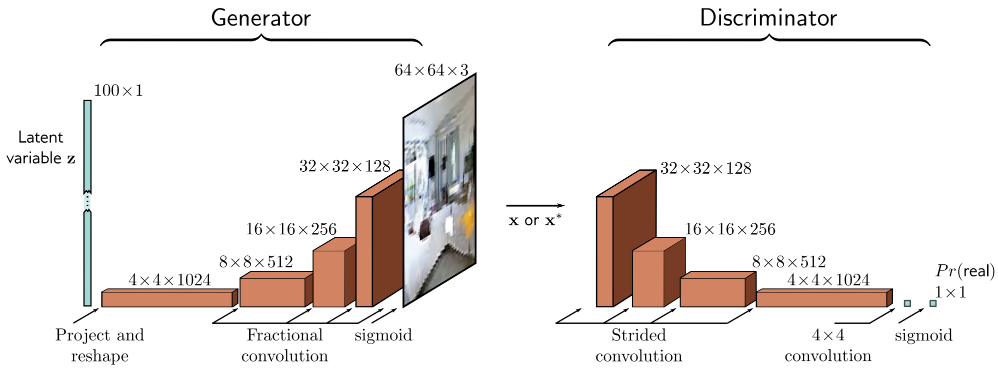

Figure 15.3 DCGAN architecture. In the generator, a 100D latent variable $\mathbf{z}$ is drawn from a uniform distribution and mapped by a linear transformation to a 4×4 representation with 1024 channels. This is then passed through a series of convolutional layers that gradually upsample the representation and decrease the number of channels. At the end is a sigmoid function that maps the 64×64×3 representation to a fixed range so that it can represent an image. The discriminator consists of a standard convolutional net that classifies the input as either a real example or a generated sample.

variable $\mathbf{z}$ sampled from a uniform distribution. This is then mapped to a 4×4 spatial representation with 1024 channels using a linear transformation. There follow four convolutional layers, each of which uses a fractionally-strided convolution that doubles the resolution (i.e., a convolution with a stride of 0.5). At the final layer, the 64×64×3 signal is passed through a sigmoid function to generate an image $\mathbf{x}^*$ in the range $[-1, 1]$. The discriminator $\mathrm{f}[\bullet, \phi]$ is a standard convolutional network where the final convolutional layer reduces the size to 1×1 with one channel. This single number is subsequently passed through a sigmoid function $\mathrm{sig}[\bullet]$ to create the output probability.

After training, the discriminator is discarded. To create new samples, latent variables $\mathbf{z}$ are drawn from the base distribution and passed through the generator. Example results are shown in figure 15.4.

15.1.4 Difficulty training GANs

Theoretically, the GAN is fairly straightforward. However, GANs are notoriously difficult to train. For example, to get the DCGAN to train reliably it was necessary to (i) use strided convolutions for upsampling and downsampling; (ii) use BatchNorm in both generator and discriminator except in the last and first layers, respectively; (iii) use the leaky ReLU activation function (figure 3.13) in the discriminator; and (iv) use the Adam optimizer but with a lower momentum coefficient than usual. This is unusual; most deep learning models are relatively robust to such choices.

Figure 15.4 Synthesized images from the DCGAN model. a) Random samples drawn from DGGAN trained on faces dataset. b) Random samples using ImageNet database (see figure 10.15). c) Random samples drawn from LSUN scene understanding dataset. Adapted from Radford et al. (2015).

Figure 15.5 Mode collapse. Synthesized images from a GAN trained on the LSUN scene understanding dataset using an MLP generator, but with a similar number of parameters and layers to the DCGAN. The samples are low quality and many are similar. Adapted from Arjovsky et al. (2017).

A common failure mode is that the generator makes plausible samples, but only those that represent a subset of the data (e.g., for faces, it might never generate faces with beards). This is known as *mode dropping*. An extreme version of this phenomenon can occur where the generator entirely or mostly ignores the input variables $\mathbf{z}$ and collapses all samples to one or a few points; this is known as *mode collapse* (figure 15.5).

15.2 Improving stability

To understand why GANs are difficult to train, it's necessary to understand exactly *what* the loss function represents.

15.2.1 Analysis of GAN loss function

If we divide the two sums in equation 15.3 by the numbers I, J of the constituent terms, then the loss function can be written in terms of expectations:

$$\begin{aligned} L[\boldsymbol{\phi}] &= \frac{1}{J}\sum_{j=1}^{J}\left(\log\left(1-\text{sig}[\text{f}[\mathbf{x}_j^*,\boldsymbol{\phi}]]\right)\right)+\frac{1}{I}\sum_{i=1}^{I}\left(\log\left[\text{sig}[\text{f}[\mathbf{x}_i,\boldsymbol{\phi}]]\right]\right) \\ &\approx \mathbb{E}_{\mathbf{x}^*}\left[\log\left[1-\text{sig}[\text{f}[\mathbf{x}^*,\boldsymbol{\phi}]]\right]\right]+\mathbb{E}_{\mathbf{x}}\left[\log\left[\text{sig}[\text{f}[\mathbf{x},\boldsymbol{\phi}]]\right]\right] \\ &= \int Pr(\mathbf{x}^*)\log\left[1-\text{sig}[\text{f}[\mathbf{x}^*,\boldsymbol{\phi}]]\right]d\mathbf{x}^*+\int Pr(\mathbf{x})\log\left[\text{sig}[\text{f}[\mathbf{x},\boldsymbol{\phi}]]\right]d\mathbf{x}, \end{aligned} \tag{15.6}$$

where $Pr(\mathbf{x}^*)$ is the probability distribution over the generated samples and $Pr(\mathbf{x})$ is the true probability distribution over the real examples.

The optimal discriminator should take the value:

$$Pr(\mathbf{x}\text{ is real}) = \text{sig}\left[\text{f}[\mathbf{x},\boldsymbol{\phi}]\right] = \frac{Pr(\mathbf{x})}{Pr(\mathbf{x}^*)+Pr(\mathbf{x})}. \tag{15.7}$$

Substituting this expression into equation 15.6, we get:

$$\begin{aligned} L[\boldsymbol{\phi}] &= \int Pr(\mathbf{x}^*)\log\left[1-\text{sig}[\text{f}[\mathbf{x}^*,\boldsymbol{\phi}]]\right]d\mathbf{x}^*+\int Pr(\mathbf{x})\log\left[\text{sig}[\text{f}[\mathbf{x},\boldsymbol{\phi}]]\right]d\mathbf{x} \\ &= \int Pr(\mathbf{x}^*)\log\left[1-\frac{Pr(\mathbf{x})}{Pr(\mathbf{x}^*)+Pr(\mathbf{x})}\right]d\mathbf{x}^*+\int Pr(\mathbf{x})\log\left[\frac{Pr(\mathbf{x})}{Pr(\mathbf{x}^*)+Pr(\mathbf{x})}\right]d\mathbf{x} \\ &= \int Pr(\mathbf{x}^*)\log\left[\frac{Pr(\mathbf{x}^*)}{Pr(\mathbf{x}^*)+Pr(\mathbf{x})}\right]d\mathbf{x}^*+\int Pr(\mathbf{x})\log\left[\frac{Pr(\mathbf{x})}{Pr(\mathbf{x}^*)+Pr(\mathbf{x})}\right]d\mathbf{x}. \end{aligned} \tag{15.8}$$

Disregarding additive and multiplicative constants, this is the *Jensen-Shannon divergence* between the synthesized distribution $Pr(x^*)$ and the true distribution $Pr(x)$:

Problems 15.1–15.2

Appendix B.5.2 Jensen-Shannon divergence

$$\begin{aligned} &D_{JS}\left[Pr(\mathbf{x}^*)\,||\,Pr(\mathbf{x})\right] \\ &\quad= \frac{1}{2}D_{KL}\left[Pr(\mathbf{x}^*)\,\middle|\middle|\,\frac{Pr(\mathbf{x}^*)+Pr(\mathbf{x})}{2}\right]+\frac{1}{2}D_{KL}\left[Pr(\mathbf{x})\,\middle|\middle|\,\frac{Pr(\mathbf{x}^*)+Pr(\mathbf{x})}{2}\right] \\ &\quad= \frac{1}{2}\int\underbrace{Pr(\mathbf{x}^*)\log\left[\frac{2Pr(\mathbf{x}^*)}{Pr(\mathbf{x}^*)+Pr(\mathbf{x})}\right]}_{\text{quality}}+\underbrace{Pr(\mathbf{x})\log\left[\frac{2Pr(\mathbf{x})}{Pr(\mathbf{x}^*)+Pr(\mathbf{x})}\right]}_{\text{coverage}}d\mathbf{x}. \end{aligned} \tag{15.9}$$

The first term states that the distance will be small if, wherever the sample density $Pr(\mathbf{x}^*)$ is high, the mixture $(Pr(\mathbf{x}^*)+Pr(\mathbf{x}))/2$ has high probability. In other words, it penalizes regions where there are samples, but no real examples; it enforces *quality*. The second term says that the distance will be small if, wherever the true density $Pr(\mathbf{x})$ is high, the mixture $(Pr(\mathbf{x}^*)+Pr(\mathbf{x}))/2$ has high probability. In other words,

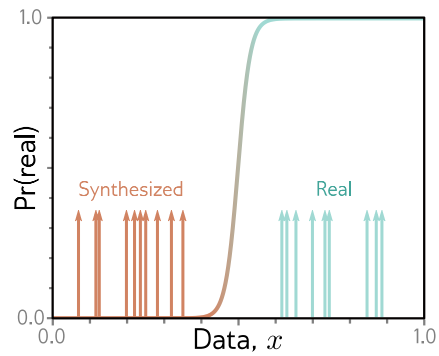

Figure 15.6 Problem with GAN loss function. If the generated samples (orange arrows) are easy to distinguish from the real examples (cyan arrows), then the discriminator (sigmoid) may have a very shallow slope at the positions of the samples; hence, the gradient to update the parameter of the generator may be very small.

it penalizes regions where there are real examples, but no samples. It enforces *coverage*. Referring back to equation 15.6 we see that the second term does not depend on the generator, which consequently doesn't care about coverage and is happy to generate a subset of possible examples accurately. This is the putative reason for mode dropping.

15.2.2 Vanishing gradients

In the previous section, we saw that when the discriminator is optimal, the loss function minimizes a measure of the distance between the generated and real samples. However, there is a potential problem with using this distance between probability distributions as the criterion for optimizing GANs. If the probability distributions are completely disjoint then this distance is infinite and any small change to the generator will not decrease the loss. The same phenomenon can be seen when we consider the original formulation; if the discriminator can separate the generated and real samples perfectly, then no small change to the generated data will change the classification score (figure 15.6).

Unfortunately, the distributions of generated samples and real examples may *really be* disjoint; at any point during the training, the generated samples lie in a subspace that is the size of the noise vector $\mathbf{z}$, and the real examples also lie in a low-dimensional subspace due to the physical processes that created the data (figure 1.9). There may be little or no overlap between these subspaces, and the result is very small or no gradients.

Figure 15.7 provides empirical evidence to support this hypothesis. If the DCGAN generator is frozen, and the discriminator is updated repeatedly so that its classification performance improves, then the generator gradients decrease. In short, there is a very fine balance between the quality of the discriminator and generator; if the discriminator becomes too good, then the training updates of the generator are attenuated.

15.2.3 Wasserstein distance

The previous sections showed that (i) the GAN loss can be interpreted in terms of distances between probability distributions and that (ii) the gradient of this distance becomes zero when the generated samples are too easy to distinguish from the real

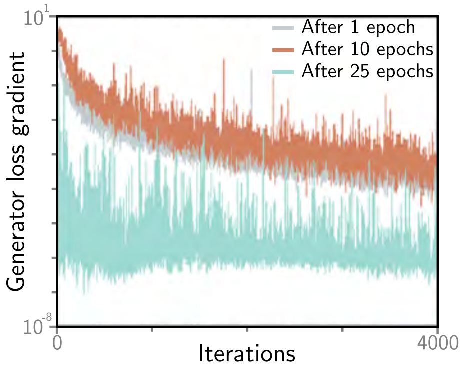

Figure 15.7 Vanishing gradients in the generator. The generator of a DCGAN is frozen after 1, 10, and 25 epochs and the discriminator is trained further. The gradient of the generator decreases very quickly (note log scale); if the discriminator accuracy becomes too high, then the gradients for the generator vanish. Adapted from Arjovsky & Bottou (2017).

examples. The obvious way forward is to choose a distance metric with better properties.

The *Wasserstein* or (for discrete distributions) *earth mover's* distance is the quantity of work required to transport the probability mass from one distribution to create the other. Here, "work" is defined as the mass multiplied by the distance moved. This immediately sounds more promising; the Wasserstein distance is well-defined even when the distributions are disjoint and decreases smoothly as they become closer to one another.

15.2.4 Wasserstein distance for discrete distributions

The Wasserstein distance is easiest to understand for discrete probability distributions. Consider distributions $Pr(x=i)$ and $q(x=j)$ defined over K bins. Assume that there is a cost P_{ij} associated with moving one unit of mass from bin i in the first distribution to bin j in the second; this cost might be the absolute difference $|i-j|$ between the indices. The masses moved collectively form the *transport plan* and are stored in a matrix $\mathbf{P}$.

The Wasserstein distance is defined as:

$$D_w\big[Pr(x)||q(x)\big] = \min_{\mathbf{P}} \left[\sum_{i,j} P_{ij}||i-j||\right], \tag{15.10}$$

subject to the constraints that:

$$\begin{array}{rcll} \sum_j P_{ij} & = & Pr(x=i) & \text{(initial distribution of } Pr(x)) \\ \sum_i P_{ij} & = & q(x=j) & \text{(initial distribution of } q(x)) \\ P_{ij} & \geq & 0 & \text{(non-negative masses).} \end{array} \tag{15.11}$$

In other words, the Wasserstein distance is the solution to a constrained minimization problem that maps the mass of one distribution to the other. This is inconvenient as we must solve this minimization problem over the elements P_{ij} every time that we want to compute the distance. Fortunately, this *linear programming problem* in its *primal form* is easily solved for small systems of equations:

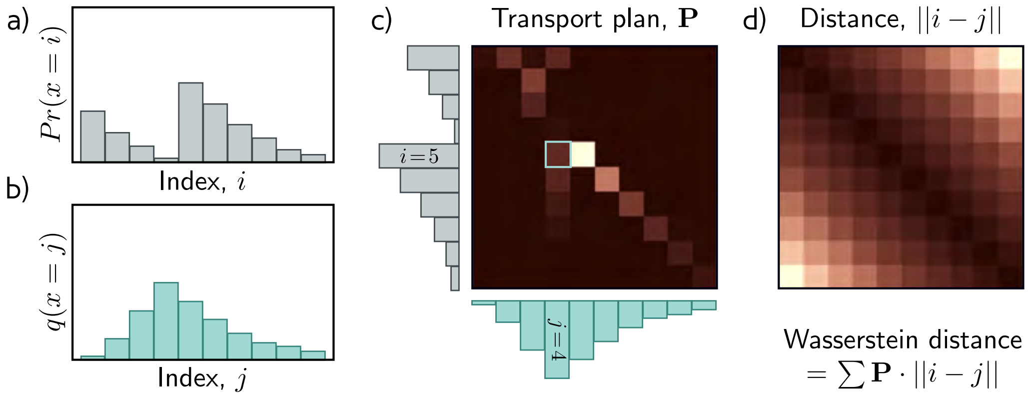

Figure 15.8 Wasserstein or earth mover's distance. a) Consider the discrete distribution $Pr(x=i)$. b) We wish to move the probability mass to create the target distribution $q(x=j)$. c) The transport plan $\mathbf{P}$ identifies how much mass will be moved from i to j. For example, the cyan highlighted square p_{54} indicates how much mass will be moved from $i=5$ to $j=4$. The elements of the transport plan must be non-negative, the sum over j must be $Pr(x=i)$, and the sum over i must be $q(x=j)$. Hence $\mathbf{P}$ is a joint probability distribution. d) The distance matrix between elements i and j. The optimal transport plan $\mathbf{P}$ minimizes the sum of the pointwise product of $\mathbf{P}$ and the distance matrix, which gives the Wasserstein distance. Hence, the elements of $\mathbf{P}$ tend to lie close to the diagonal where the distance cost is lowest. Adapted from Hermann (2017).

primal form:	**dual form:**
$\begin{array}{rlcl} \text{minimize} & \mathbf{c}^T\mathbf{p}, & & \\ \text{such that} & \mathbf{A}\mathbf{p} & = & \mathbf{b} \\ \text{and} & \mathbf{p} & \geq & \mathbf{0} \end{array}$	$\begin{array}{rlcl} \text{maximize} & \mathbf{b}^T\mathbf{q}, & & \\ \text{such that} & \mathbf{A}^T\mathbf{q} & \leq & \mathbf{c} \end{array}$

where $\mathbf{p}$ contains the vectorized elements P_{ij} that determine the amount of mass moved, $\mathbf{c}$ contains the distances, $\mathbf{A}\mathbf{p}=\mathbf{b}$ contains the initial distribution constraints, and $\mathbf{p}\geq 0$ ensures the masses moved are non-negative.

Problems 15.3-15.4

As for all linear programming problems, there is an equivalent *dual problem* with the same solution.[1] Here, we maximize with respect to a variable $\mathbf{q}$ that is applied to initial distributions, subject to constraints that depend on the distances $\mathbf{c}$. The solution is:

$$D_w\Big[Pr(x)||q(x)\Big] = \max_{f_\bullet}\left[\sum_i Pr(x=i)f_i - \sum_j q(x=i)f_j\right], \tag{15.12}$$

[1]The mathematical background is omitted due to space constraints. Linear programming is a standard problem with well-known algorithms for finding the minimum.

subject to the constraint that:

$$|f_{i+1} - f_i| < 1. \tag{15.13}$$

In other words, we optimize over a new set of variables $f_1 \ldots f_I$ where adjacent values cannot change by more than one.

15.2.5 Wasserstein distance for continuous distributions

Translating these results back to the continuous multi-dimensional domain, the equivalent of the primal form (equation 15.10) is:

Problems 15.5-15.7

$$D_w\Big[Pr(\mathbf{x}), q(\mathbf{x}^*)\Big] = \min_{\pi[\bullet,\bullet]} \int\int \pi(\mathbf{x}_1, \mathbf{x}_2)||\mathbf{x}_1 - \mathbf{x}_2||d\mathbf{x}_1 d\mathbf{x}_2, \tag{15.14}$$

where $\pi(\mathbf{x}_1, \mathbf{x}_2)$ is a joint probability distribution representing the mass moved from position $\mathbf{x}_1$ to $\mathbf{x}_2$. The equivalent of the dual form (equation 15.12) is:

$$D_w\Big[Pr(\mathbf{x}), q(\mathbf{x}^*)\Big] = \max_{\mathrm{f}[\mathbf{x}]} \left[\int Pr(\mathbf{x})\mathrm{f}[\mathbf{x}]d\mathbf{x} - \int Pr(\mathbf{x}^*)\mathrm{f}[\mathbf{x}]d\mathbf{x}\right], \tag{15.15}$$

subject to the constraint that the Lipschitz constant of the function $\mathrm{f}[\mathbf{x}]$ is less than one (i.e., the absolute gradient of the function never exceeds one).

15.2.6 Wasserstein GAN loss function

In the context of neural networks, we maximize over the space of functions $\mathrm{f}[\mathbf{x}]$ by optimizing the parameters $\boldsymbol{\phi}$ in a neural network $\mathrm{f}[\mathbf{x}, \boldsymbol{\phi}]$ and we approximate these integrals using generated samples $\mathbf{x}_i^*$ and real examples $\mathbf{x}_i$:

$$\begin{aligned} L[\boldsymbol{\phi}] &= \sum_j \mathrm{f}[\mathbf{x}_j^*, \boldsymbol{\phi}] - \sum_i \mathrm{f}[\mathbf{x}_i, \boldsymbol{\phi}] \\ &= \sum_j \mathrm{f}[\mathbf{g}[\mathbf{z}_j, \boldsymbol{\theta}], \boldsymbol{\phi}] - \sum_i \mathrm{f}[\mathbf{x}_i, \boldsymbol{\phi}], \end{aligned} \tag{15.16}$$

where we must constrain the neural network discriminator $\mathbf{f}[\mathbf{x}_i, \boldsymbol{\phi}]$ to have an absolute gradient norm of less than one at every position $\mathbf{x}$:

$$\left|\frac{\partial \mathrm{f}[\mathbf{x}, \boldsymbol{\phi}]}{\partial \mathbf{x}}\right| < 1. \tag{15.17}$$

One way to achieve this is to clip the discriminator weights to a small range (e.g., $[-0.01, 0.01]$). An alternative is the *gradient penalty Wasserstein GAN* or *WGAN-GP*, which adds a regularization term that increases as the gradient norm deviates from unity.

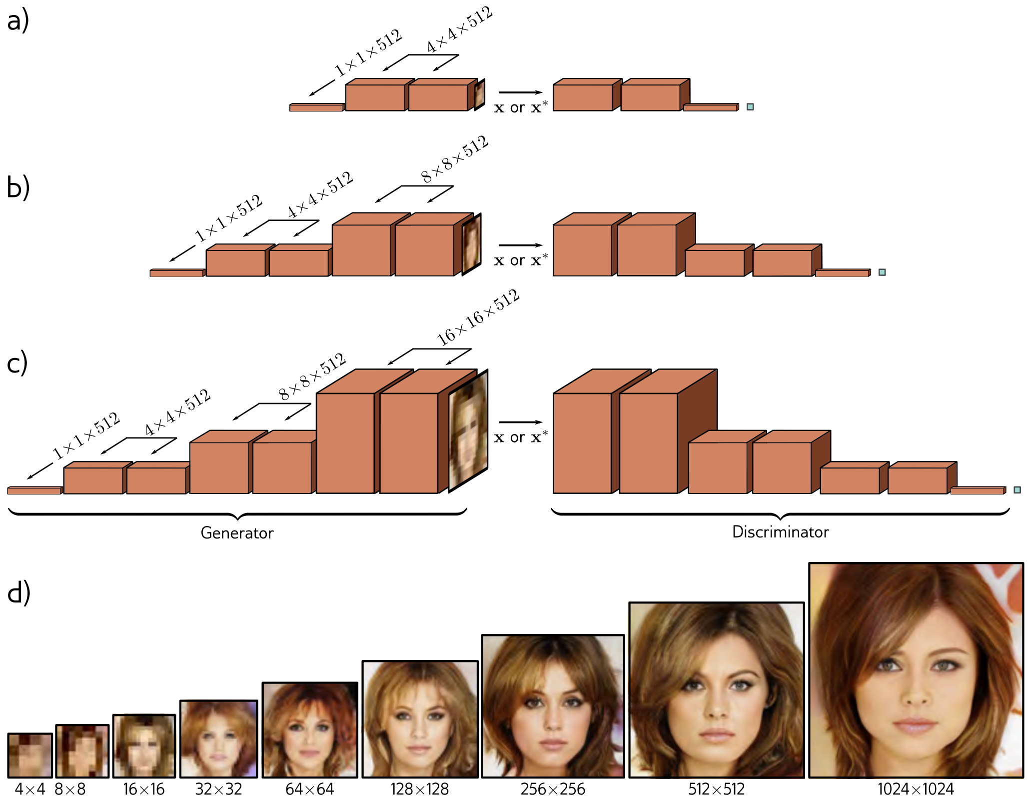

Figure 15.9 Progressive growing. a) The generator is initially trained to create very small (4×4) images, and the discriminator to identify if these images are synthesized or downsampled real images. b) After training at this low-resolution terminates, subsequent layers are then added to the generator to generate (8×8) images. Similar layers are added to the discriminator to downsample back again. c) This process continues to create (16×16) images and so on. In this way, a GAN that produces very realistic high-resolution images can be trained. d) Images of increasing resolution generated at different stages from the same latent variable. Adapted from Wolf (2021), using method of Karras et al. (2018).

15.3 Progressive growing, minibatch discrimination, and truncation

The Wasserstein formulation makes GAN training more stable. However, further machinery is needed to generate high-quality images. We now review *progressive growing*, *minibatch discrimination*, and *truncation*, which all improve output quality.

In *progressive growing* (figure 15.9), we first train a GAN that synthesizes 4×4 images, using an architecture similar to the DCGAN. Then we add subsequent layers to the generator which upsample the representation and perform further processing to create

Figure 15.10 Truncation. The quality of GAN samples can be traded off against diversity by rejecting samples from the latent variable $\mathbf{z}$ that fall further than τ standard deviations from the mean. a) If this threshold is large ($\tau = 2.0$), then the samples are visually varied but may have defects. b-c) As this threshold is decreased, the average visual quality improves, but the diversity decreases. d) With a very small threshold, the samples look almost identical. By judiciously choosing this threshold, it's possible to increase the average quality of GAN results. Adapted from Brock et al. (2016).

Figure 15.11 Progressive growing. This method generates realistic images of faces when trained on the CELEBA-HQ dataset, and more complex, variable objects when trained on LSUN categories. Adapted from Karras et al. (2018).

Figure 15.12 Traversing latent space of progressive GAN trained on LSUN cars. Moving in the latent space produces car images that change smoothly. This usually only works for short trajectories; eventually, the latent variable moves to somewhere that produces unrealistic images. Adapted from Karras et al. (2018).

an 8×8 image. The discriminator also has extra layers added to it, so that it can receive the higher-resolution images and classify them as either being generated samples or real examples. In practice, the higher-resolution layers are gradually "faded in" over time; initially, the higher-resolution image is an upsampled version of the previous result, passed via a residual connection and the new layers gradually take over.

Mini-batch discrimination ensures that the samples have sufficient variety and hence helps prevent mode collapse This can be done by computing feature statistics across the mini-batches of synthesized and real data. These can be summarized and added as a feature map (usually toward the end of the discriminator). This effectively allows the discriminator to send a signal back to the generator that encourages it to include a similar amount of variation in the synthesized data as in the original dataset.

Another trick to improve generation results is *truncation* (figure 15.10), in which only latent variables $\mathbf{z}$ with high probability (i.e., within a fixed distance from the mean) are chosen during sampling. This reduces the variation in the samples but improves their quality. Careful normalization and regularization schemes also improve sample quality. Using combinations of these methods, GANs can synthesize varied and realistic images (figure 15.11). Moving smoothly through the latent space can also sometimes produce realistic interpolations from one synthesized image to another (figure 15.12).

Problem 15.8

15.4 Conditional generation

GANs produce realistic images but we can't choose their attributes: we can't specify hair color, ethnicity, or age of face samples without training separate GANs for each combination of characteristics. *Conditional generation* allows us to specify such attributes.

15.4.1 Conditional GAN

The *conditional GAN* passes a vector $\mathbf{c}$ of attributes to both the generator and discriminator, which are now written as $\mathbf{g}[\mathbf{z}, \mathbf{c}, \boldsymbol{\theta}]$ and $\mathrm{f}[\mathbf{x}, \mathbf{c}, \boldsymbol{\phi}]$, respectively. The generator aims to transform the latent variable $\mathbf{z}$ into a data sample $\mathbf{x}$ with the correct attribute $\mathbf{c}$. The discriminator's goal is to distinguish between (i) the generated sample with the target attribute or (ii) a real example with the real attribute (figure 15.13a).

For the generator, the attribute $\mathbf{c}$ can be appended to the latent vector $\mathbf{z}$. For the discriminator, it may be appended to the input if the data is 1D. If the data is an image, then the attribute can be linearly transformed to a 2D representation and appended as an extra channel to the discriminator input, or to one of its intermediate hidden layers.

15.4.2 Auxiliary classifier GAN

The *auxiliary classifier GAN* or *ACGAN* simplifies conditional generation by requiring that the classifier correctly predicts the attribute (figure 15.13b). For a discrete attribute

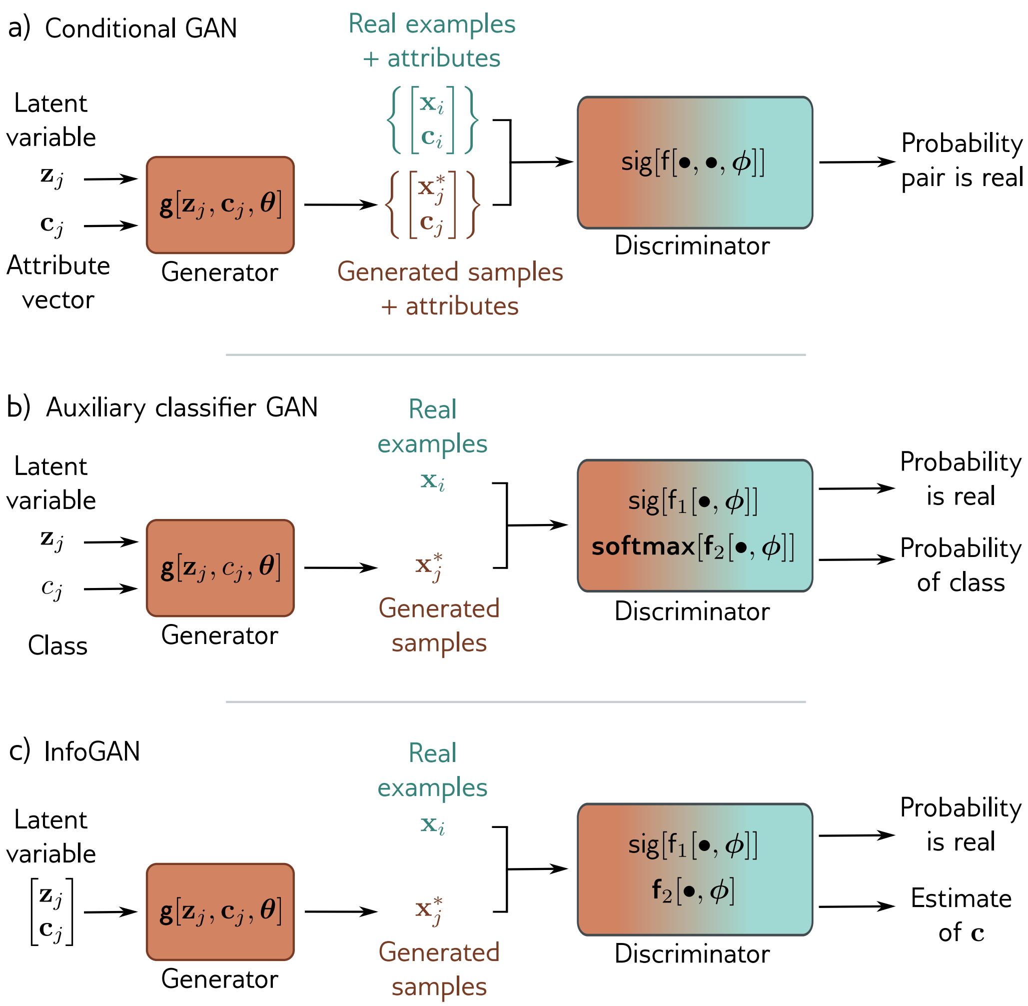

Figure 15.13 Conditional generation. a) The generator of the conditional GAN also receives an attribute vector $\mathbf{c}$ describing some aspect of the image. As usual, the input to the discriminator is either a real example or a generated sample, but now it also receives the attribute vector; this encourages the samples to be both realistic and compatible with the attribute. b) The generator of the auxiliary classifier GAN (ACGAN) takes a discrete attribute variable. The discriminator must both (i) determine if its input is real or synthetic and (ii) identify the class correctly. c) The InfoGAN splits the latent variable into noise $\mathbf{z}$ and unspecified random attributes $\mathbf{c}$. The discriminator must distinguish if its input is real, and also reconstruct these attributes. In practice, this means that the variables $\mathbf{c}$ correspond to salient aspects of the data that have real-world interpretations.

Figure 15.14 Auxiliary classifier GAN. The generator takes a class label as well as the latent vector. The discriminator must both identify if the data point is real *and* predict the class label. This model was trained on ten ImageNet classes. Left to right: generated examples of monarch butterflies, goldfinches, daisies, redshanks, and gray whales. Adapted from Odena et al. (2017).

with C categories, the discriminator takes the real/synthesized image as input, and has $C+1$ outputs; the first is passed through a sigmoid function and predicts if the sample is generated or real. The remaining outputs are passed through a softmax function to predict the probability that the data belongs to each of the C classes. Networks trained with this method can synthesize multiple classes from ImageNet (figure 15.14).

15.4.3 InfoGAN

The conditional GAN and ACGAN both generate samples that have predetermined attributes. By contrast, InfoGAN (figure 15.13c) attempts to identify important attributes automatically. The generator takes a vector that consists of random noise variables $\mathbf{z}$ and *random* attribute variables $\mathbf{c}$. The discriminator both predicts both whether the image is real or synthesized and estimates the attribute variables.

The insight is that interpretable real-world characteristics should be easiest to predict, and hence will be represented in the attribute variables $\mathbf{c}$. The attributes in $\mathbf{c}$ may be discrete (and a binary or multi-class cross-entropy loss would be used) or continuous (and a least squares loss would be used). The discrete variables identify categories in the data and the continuous ones identify gradual modes of variation (figure 15.15).

15.5 Image translation

Although the adversarial discriminator was first used in the context of the GAN for generating random samples, it can also be used as a prior that favors realism in tasks that translate one data example into another. This is most commonly done with images,

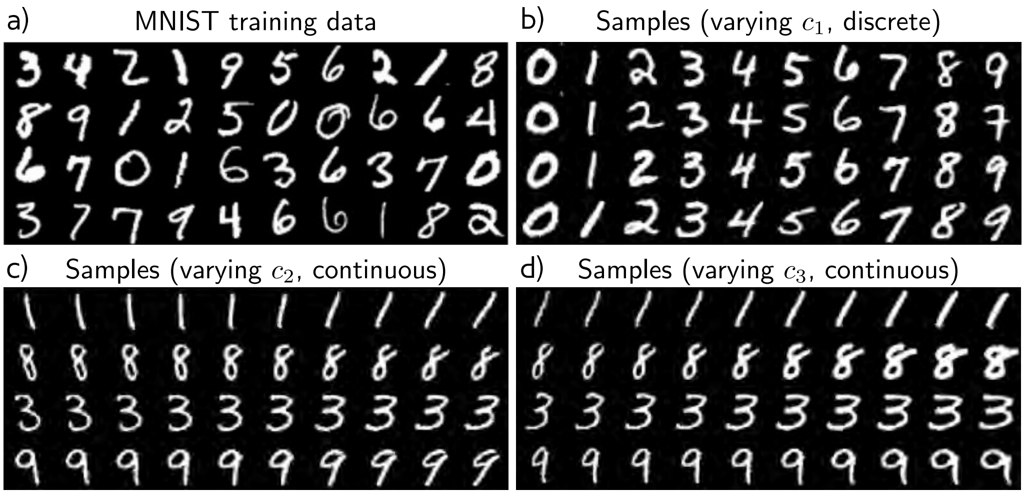

Figure 15.15 InfoGAN for MNIST. a) Training examples from the MNIST database, which consists of 32×32 pixel images of handwritten digits. b) The first attribute c_1 is categorical with 10 categories; each column shows samples generated with one of these categories. The InfoGAN recovers the ten digits. The attribute vectors c_2 and c_3 are continuous. c) Moving from left to right, each column represents a different value of c_2 while keeping the other latent variables constant. This attribute seems to correspond to the orientation of the character. d) The third attribute seems to correspond to the thickness of the stroke. Adapted from Chen et al. (2016b).

where we might want to translate a grayscale image to color, a noisy image to a clean one, a blurry image to a sharp one, or a sketch to a photo-realistic image.

This section discusses three image translation architectures that use different amounts of manual labeling. The Pix2Pix model uses before/after pairs for training. Models with adversarial losses use before/after pairs for the main model, but also exploit additional unpaired "after" images. The CycleGAN model uses unpaired images.

15.5.1 Pix2Pix

The Pix2Pix model is a network $\mathbf{x} = \mathbf{g}[\mathbf{c}, \boldsymbol{\theta}]$ that maps one image $\mathbf{c}$ to a different style image $\mathbf{x}$ using a U-Net (figure 11.10) with parameters $\boldsymbol{\theta}$ (figure 15.16). A typical use case would be colorization, where the input is grayscale and the output is color. The output should be similar to the input and this is encouraged using a *content loss* that penalizes the ℓ_1 norm $||\mathbf{x} - \mathbf{g}[\mathbf{c}, \boldsymbol{\theta}]||_1$ between the input and output

Appendix C.5.6 ℓ_1 norm

However, the output image should also look like a realistic conversion of the input, and this is encouraged by using an adversarial discriminator $\mathrm{f}[\mathbf{c}, \mathbf{x}, \boldsymbol{\phi}]$, which ingests the before and after images $\mathbf{c}$ and $\mathbf{x}$. At each step, the discriminator tries to distinguish between a real before/after pair and a before/synthesized pair. To the extent that these can be distinguished successfully, a feedback signal is provided to modify the U-Net to make its output more realistic. Since the content loss ensures that the large-scale image structure is correct, the discriminator is mainly needed to ensure that the local texture is plausible; to this end, the *PatchGAN* loss is based on a purely convolutional classifier. At the last layer, each hidden unit indicates whether the region within its receptive field is real or synthesized. These responses are averaged to provide the final output.

One way to think of this model is that it is a conditional GAN where the U-Net is the generator and is conditioned on an image rather than a label. Notice though that the U-Net input does not include noise, and so is not really a "generator" in the conventional sense. Interestingly, the original authors experimented with adding noise $\mathbf{z}$ to the U-Net in addition to the input image $\mathbf{c}$. However, the network just learned to ignore it.

15.5.2 Adversarial loss

The discriminator of the Pix2Pix model attempted to distinguish whether before/after pairs in an image translation task were plausible. This has the disadvantage that we need ground truth before/after pairs to exploit the discriminator loss. Fortunately, there is a simpler way to exploit the power of adversarial discriminators in the context of supervised learning, without the need for additional labeled training data.

An *adversarial loss* derives from a discriminator that tries to distinguish the output of a supervised network from a real example from its output domain. If this can be done, the discriminator sends feedback to the supervised model that changes its predictions. This may be done at the scale of the entire output or at the level of patches as in the Pix2Pix algorithm. This helps improve the *realism* of complex structured outputs. However, it doesn't necessarily decrease the original loss function.

The *super-resolution GAN* or *SRGAN* uses this approach (figure 15.17). The main model consists of a convolutional network with residual connections that ingests a low-resolution image and converts this via upsampling layers to a high-resolution image. The network is trained with three losses. The content loss measures the squared difference between the output and the true high-resolution image. The VGG loss passes the synthesized and ground truth outputs through the VGG network and measures the squared difference between their activations. This encourages the image to be semantically similar to the target. Finally, the adversarial loss uses a discriminator that attempts to distinguish whether this is a real high-resolution image, or an upsampled one. This encourages the output to be indistinguishable from real examples.

15.5.3 CycleGAN

The adversarial loss still assumes that we have labeled before/after images for the main supervised component of the network. The *CycleGAN* addresses the situation where we have two sets of data with distinct styles, but *no* matching pairs. A typical example might be to convert a photo to the artistic style of Monet. There exist many photos and

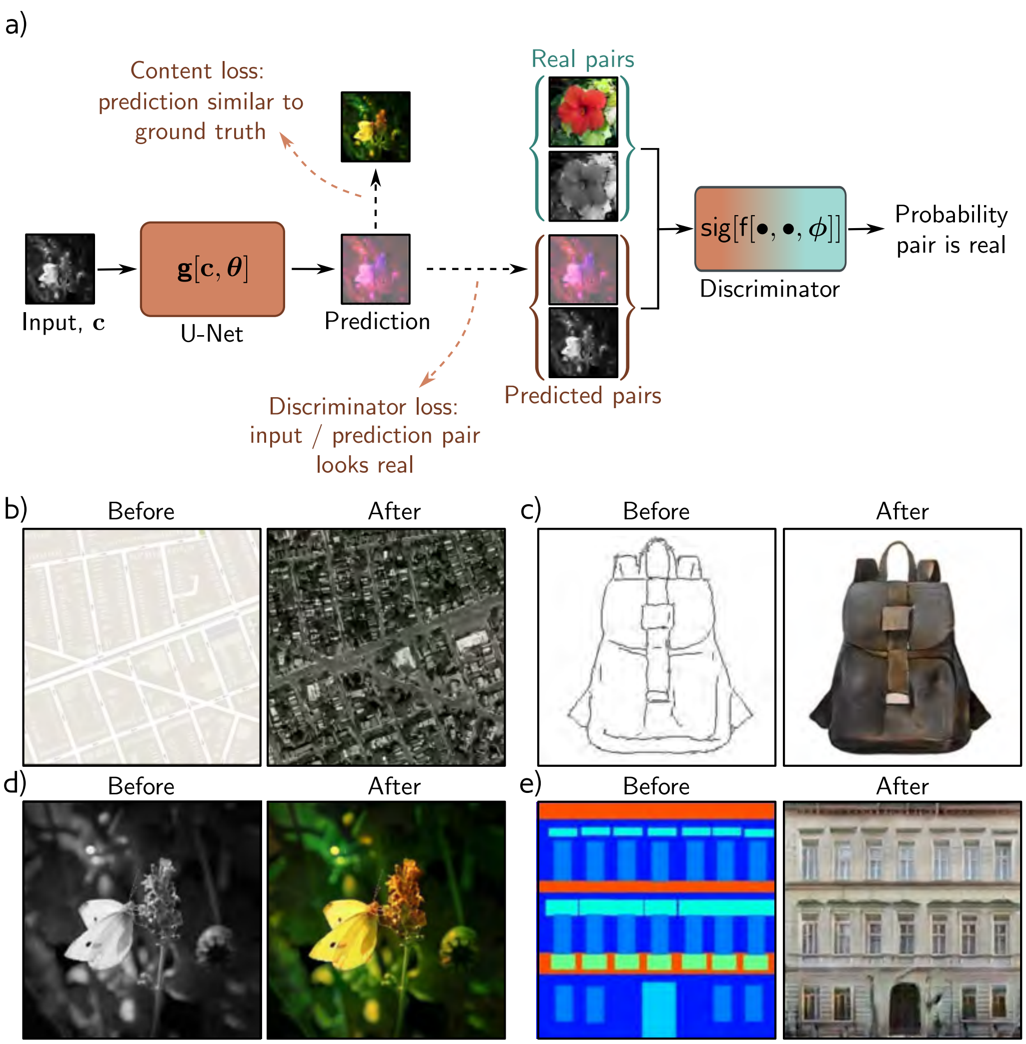

Figure 15.16 Pix2Pix model. a) The model translates an input image to a prediction in a different style using a U-Net (see figure 11.10). In this case, it maps a grayscale image to a plausibly colored version. The U-Net is trained with two losses. First, the content loss encourages the output image to have a similar structure to the input image. Second, the adversarial loss encourages the grayscale/color image pair to be indistinguishable from a real pair in each local region of these images. This framework can be adapted to many tasks, including b) translating maps to satellite imagery, c) converting sketches of bags to photorealistic examples, d) colorization, and e) converting label maps to photorealistic building facades. Adapted from Isola et al. (2017).

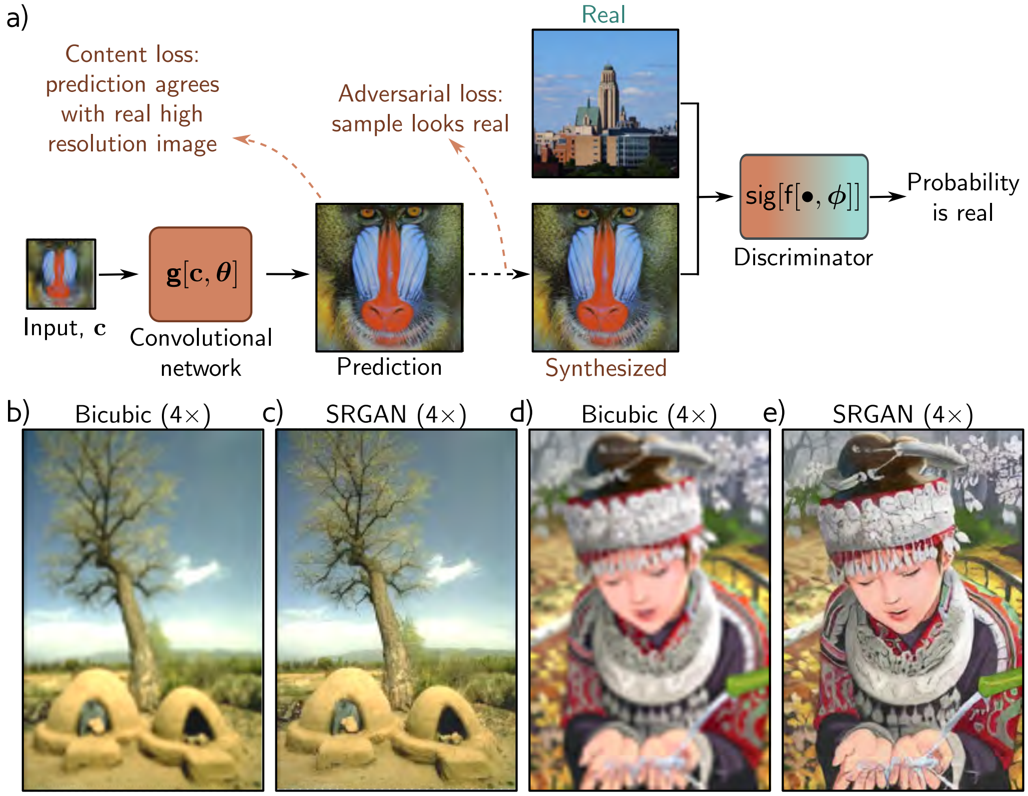

Figure 15.17 Super-resolution generative adversarial network (SRGAN). a) A convolutional network with residual connections is trained to increase the resolution of images by a factor of four. The model has losses that encourage the content to be close to the true high-resolution image. However, it also includes an adversarial loss, which penalizes results that can be distinguished from real high-resolution images. b) Upsampled image using bicubic interpolation. Upsampled image using SRGAN. d) Upsampled image using bicubic interpolation. e) Upsampled image using SRGAN. Adapted from Ledig et al. (2017)

many Monet paintings, but no correspondence between them.

The CycleGAN loss function is a weighted sum of three losses. The content loss encourages the before and after images to be similar and is based on the ℓ_1 norm. The adversarial loss uses a discriminator to encourage the output to be indistinguishable from examples of the target domain. Finally, the *cycle-consistency* loss encourages the mapping to be reversible; to this end, two models are trained simultaneously. One maps from the first domain to the second, and the other in the opposite direction. The cycle-consistency will be low if the translated image can be itself translated successfully back to the image in the original domain. The model combines these three losses to train networks to translate images from one style to another and back again.

15.6 StyleGAN

StyleGAN is a more contemporary GAN that partitions the variation in a dataset into meaningful components, each of which is controlled by a subset of the latent variables. In particular, StyleGAN controls the output image at different scales and separates style from noise. For face images, large-scale changes include face shape and head pose, medium-scale changes include the shape and details of facial features and fine-scale changes include hair and skin color. The style components represent aspects of the image which are salient to human beings and the noise aspects represent unimportant variation such as the exact placement of hairs, stubble, freckles, or skin pores.

The GANs that we have seen until now started from a latent variable $\mathbf{z}$ which is drawn from a standard base distribution. This was passed through a series of convolutional layers to produce the output image. However, the stochastic inputs to the generator can (i) be introduced at various points in the architecture, and (ii) modify the current representation at these points in different ways. StyleGAN makes these choices judiciously to control scale and to separate style from noise (figure 15.19).

The main generative branch of StyleGAN starts with a learned constant 4×4 representation with 512 channels. This passes through a series of convolutional layers that gradually upsample the representation to generate the image at its final resolution. Two sets of random latent variables representing style and noise are introduced at each scale; the closer that they are to the output, the finer scale details they represent.

The latent variables that represent noise are independently sampled Gaussian vectors $\mathbf{z}_1, \mathbf{z}_2 \ldots$ and are injected additively after each convolution operation in the main generative pipeline. They are the same spatial size as the main representation at the point that they are added but are multiplied by learned per-channel scaling factors $\boldsymbol{\psi}_1, \boldsymbol{\psi}_2 \ldots$ and so contribute in different amounts to each channel. As the resolution of the network increases, this noise contributes at finer scales.

The latent variables that represent style begin as a 512×512 noise vector, which is passed through a fully-connected network with seven hidden layers to create an intermediate variable $\mathbf{w}$. This allows the network to learn to decorrelate different aspects of style so that each dimension of $\mathbf{w}$ can represent an independent real-world factor such as head pose or hair color. The intermediate variable $\mathbf{w}$ is linearly transformed to a

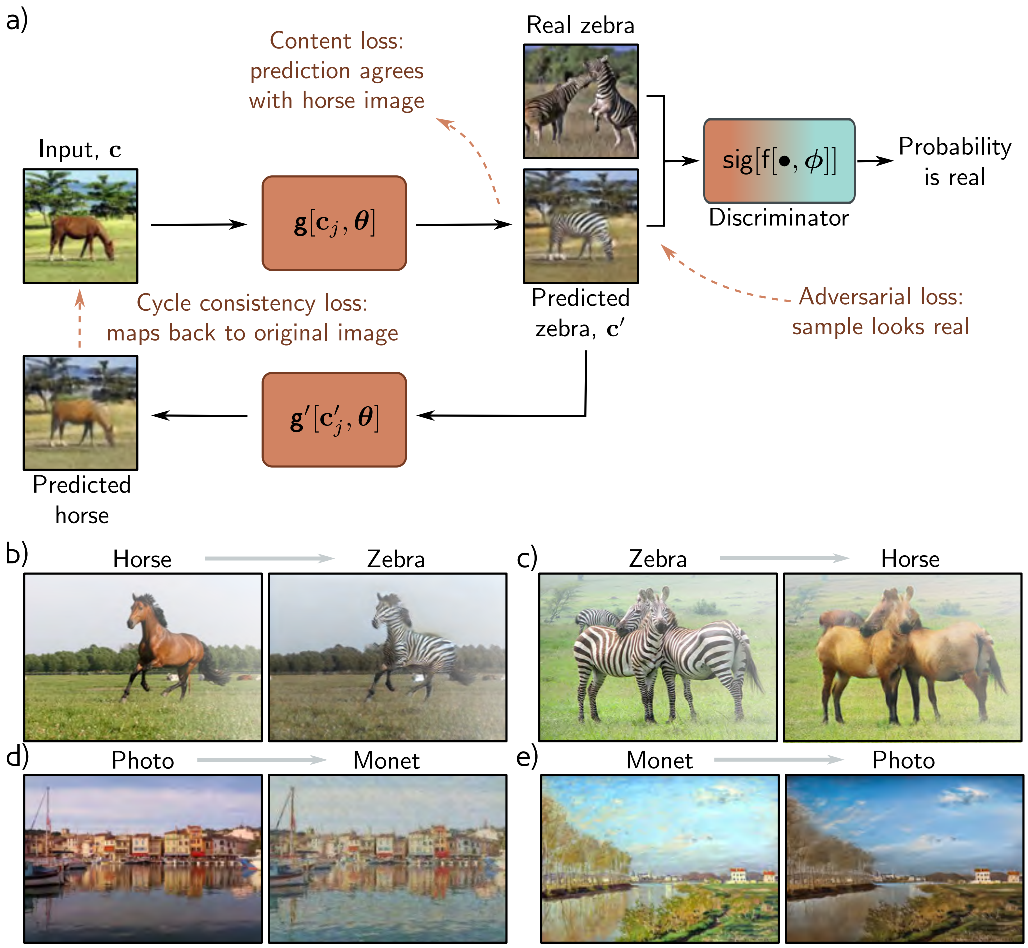

Figure 15.18 CycleGAN. Two models are trained simultaneously. The first $\mathbf{c}' = \mathbf{g}[\mathbf{c}_j, \boldsymbol{\theta}]$ translates from an image $\mathbf{c}$ in the first style (horse) to an image $\mathbf{c}'$ in the second style (zebra). The second model $\mathbf{c} = \mathbf{g}'[\mathbf{c}', \boldsymbol{\theta}]$ learns the opposite mapping. The cycle consistency loss penalizes each of these models if they cannot successfully convert an image to the other domain and back to the original. In addition, there are two adversarial losses, which encourage the translated images to look like realistic examples of the target domain (shown here for zebra only), and two content losses that encourage the images before and after each mapping to have similar content. Adapted from Zhu et al. (2017).

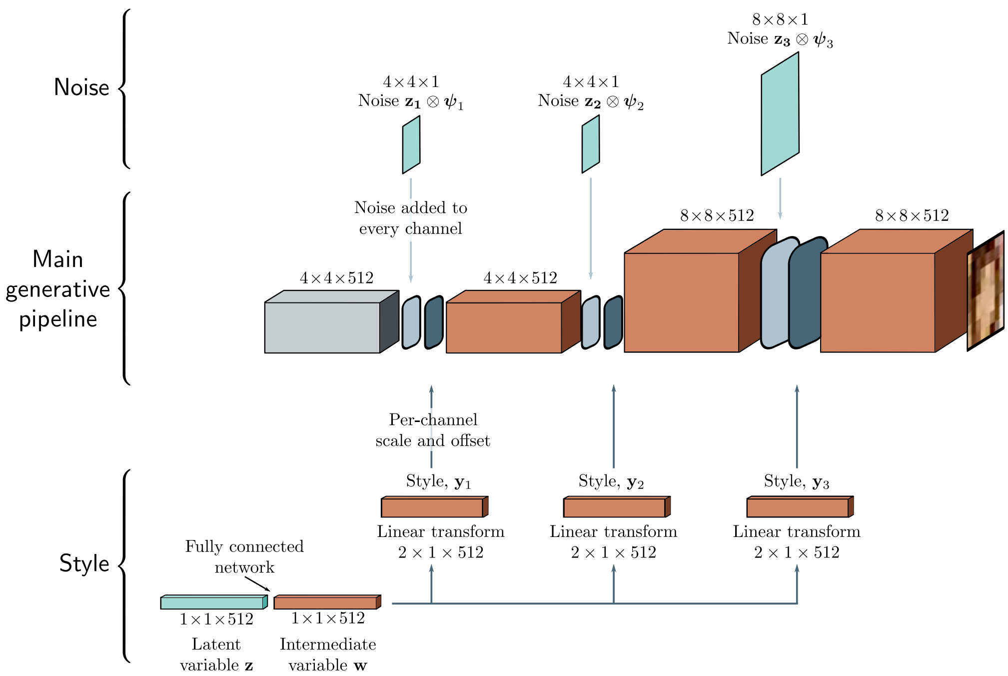

Figure 15.19 StyleGAN. The main pipeline (center row) starts with a constant learned representation (gray box). This is passed through a series of convolutional layers and gradually upsampled to create the output. Noise (top row) is added at different scales by periodically adding Gaussian variables $\mathbf{z}_\bullet$ with per-channel scaling $\boldsymbol{\psi}_\bullet$. The Gaussian style variable $\mathbf{z}$ is passed through a fully connected network to create intermediate variable $\mathbf{w}$ (bottom row). This is used to set the mean and variance of each channel at various points in the pipeline.

$2{\times}1{\times}512$ tensor $\mathbf{y}$. This is used to set the per-channel mean and standard deviation of the representation across spatial positions in the main generative branch after the noise addition step. This is termed *adaptive instance normalization* (see figure 11.14e). A series of style vectors $\mathbf{y}_1, \mathbf{y}_2 \ldots$ are injected in this way at several different points in the main branch so the same style contributes at different scales.

15.7 Summary

GANs learn a generator network that transforms random noise into data that is indistinguishable from a training set. To this end, the generator is trained using a discriminator

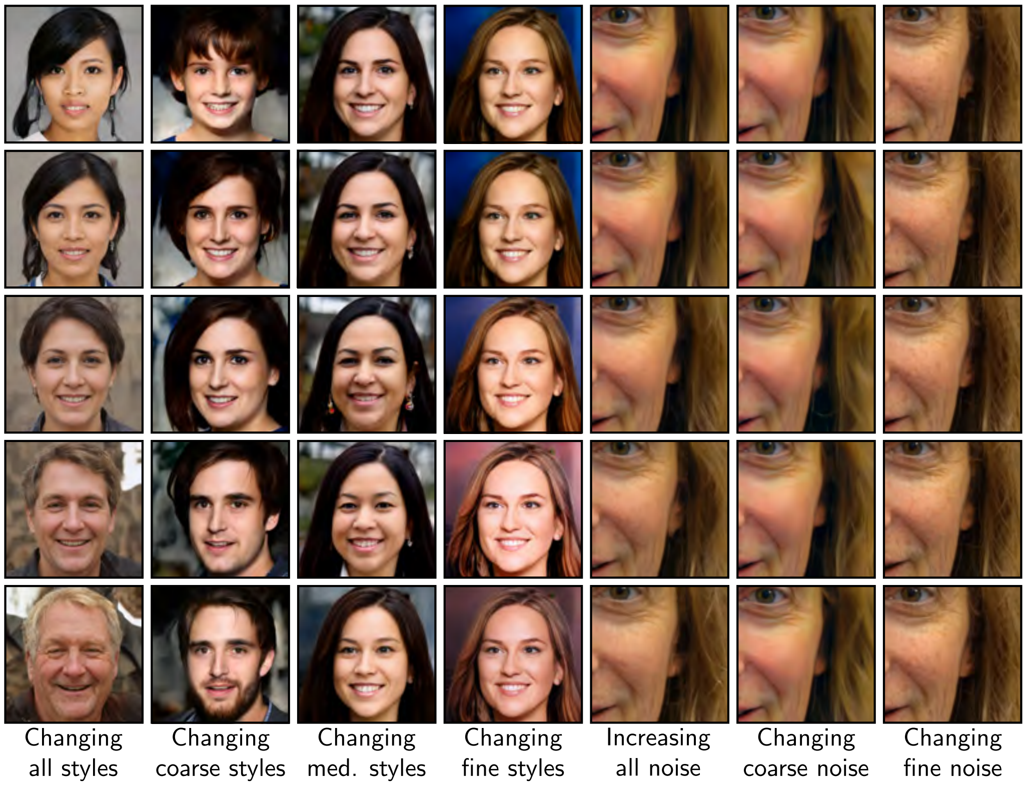

Figure 15.20 StyleGAN results. First four columns show systematic changes in style at various scales. Fifth column shows the effect of increasing noise magnitude. Last two columns show different noise vectors at two different scales.

network that tries to distinguish real data from generated data. The generator is then updated so that the data that it creates is identified as being more "real" by the discriminator. The original formulation of this idea has the flaw that the training signal is weak when it's easy to determine if the samples are real or generated. This led to the Wasserstein GAN which provides a more consistent training signal.

The chapter reviewed convolutional GANs for generating images, and a series of tricks that improve the quality of the generated images, including progressive growing, mini-batch discrimination, and truncation. Conditional GAN architectures introduce an auxiliary vector that allows control over the output (e.g., the choice of object class). In image translation tasks, we retain this conditional information in the form of an image but dispense with the initial random noise. The GAN discriminator now works as an additional loss term that favors "realistic" looking images. Finally, we described StyleGAN, which injects noise into the generator strategically to control the style and noise at different scales.

Notes

Goodfellow et al. (2014) introduced generative adversarial networks. An early review of progress can be found in Goodfellow (2016). More recent overviews include Creswell et al. (2018) and Gui et al. (2021). Park et al. (2021) present a review of GAN models that focuses on computer vision applications. Hindupur (2022) maintains a list of named GAN models (numbering 501 at the time of writing) from ABC-Gan (Susmelj et al., 2017) right through to ZipNet-GAN (Zhang et al., 2017b). Odena (2019) lists open problems concerning GANs.

Data: Most work on GANs has focused on image data including the deep convolutional GAN (Radford et al., 2015), progressive GAN (Karras et al., 2018), and StyleGAN (Karras et al., 2019) models presented in this chapter. For this reason, most GANs are based on convolutional layers, although more recently GANs that exploit transformers in the generator and discriminator to capture long-range correlations have been developed (e.g., SAGAN, Zhang et al., 2019b). However, GANs have also been used to generate molecular graphs (De Cao & Kipf, 2018), voice data (Saito et al., 2017; Donahue et al., 2018b; Kaneko & Kameoka, 2017; Fang et al., 2018), EEG data (Hartmann et al., 2018), text (Lin et al., 2017a; Fedus et al., 2018), music (Mogren, 2016; Guimaraes et al., 2017; Yu et al., 2017), 3D models (Wu et al., 2016), DNA (Killoran et al., 2017), and video data (Vondrick et al., 2016; Wang et al., 2018a).

GAN loss functions: Several studies (Arjovsky et al., 2017; Metz et al., 2017; Qi, 2020) identified that the original GAN loss function was unstable, and this led to different formulations. Mao et al. (2017) introduced the least squares GAN. For certain choices of parameters this implicitly minimizes the Pearson χ^2 divergence. Nowozin et al. (2016) argue that the Jensen-Shannon divergence is just a special case of a larger family of f-divergences and show that any f-divergence can be used for training generative neural networks Jolicoeur-Martineau (2019) introduce the relativistic GAN in which the discriminator estimates the probability that real data is more realistic than generated data, rather than the absolute probability that it is real. Zhao et al. (2017a) reformulate the GAN into a general energy-based framework in which the discriminator is a function that attributes low energies to real data and higher energies elsewhere. As an example, they use an autoencoder and base the energy on reconstruction error.

Arjovsky & Bottou (2017) analyzed vanishing gradients in GANs and this led to the Wasserstein GAN (Arjovsky et al., 2017) which is based on earth mover's distance/optimal transport. The Wasserstein formulation requires that the Lipschitz constant of the discriminator is less than one; the original paper proposed to clip the weights in the discriminator, but subsequent work imposed a gradient penalty (Gulrajani et al., 2016) or applied spectral normalization (Miyato et al., 2018) to limit the Lipschitz constant. Other variations of the Wasserstein GAN were introduced by Wu et al. (2018a), Bellemare et al. (2017b), and Adler & Lunz (2018). Hermann (2017) presents an excellent blog post discussing duality and the Wasserstein GAN. For more information about optimal transport, consult the book by Peyré et al. (2019). Lucic et al. (2018) present an empirical comparison of GAN loss functions of the time.

Tricks for training GANs: Many heuristics improve the stability of training GANs and the quality of the final results. Marchesi (2017) first used the truncation trick (figure 15.10) to trade off the variability of GAN outputs relative to their quality. This was also proposed by Pieters & Wiering (2018) and Brock et al. (2019), who added a regularizer that encourages the weight matrices in the generator to be orthogonal, which means that truncating the latent variable has a closer relationship to truncating the output variance and improves sample quality.

Other tricks include only using the gradients from the top K most realistic images (Sinha et al., 2020), label smoothing in the discriminator (Salimans et al., 2016), updating the discriminator using a history of generated images rather than the ones produced by the latest generator to avoid model "oscillation" (Salimans et al., 2016), and adding noise to the discriminator input

(Arjovsky & Bottou, 2017). Kurach et al. (2019) present an overview of normalization and regularization in GANs. Chintala et al. (2020) provide further suggestions for training GANs.

Sample diversity: The original GAN paper (Goodfellow et al., 2014) argued that given enough capacity, training samples, and computation time, a GAN can learn to minimize the Jensen-Shannon divergence between the generated samples and the true distribution. However subsequent work has cast doubt on whether this happens in practice. Arora et al. (2017) suggest that the finite capacity of the discriminator means that the GAN training objective can approach its optimum value even when the variation in the output distribution is limited. Wu et al. (2017) approximated the log-likelihoods of the distributions produced by GANs using annealed importance sampling and found that there was a mismatch between the generated and real distributions. Arora & Zhang (2017) ask human observers to identify GAN samples that are (near-)duplicates and infer the diversity of images from the frequency of these duplicates. They found that for DCGAN, a duplicate occurs with probability $>50\%$ with 400 samples; this implies that the support size was $\approx 400,000$, which is smaller than the training set. They also showed that the diversity increased as a function of the discriminator size. Bau et al. (2019) take a different approach and investigate the parts of the data space that GANs *cannot* generate.

Increasing diversity and preventing mode collapse: The extreme case of lack of diversity is *mode collapse*, in which the network repeatedly produces the same image (Salimans et al., 2016). This is a particular problem for conditional GANs, where the noise vector is sometimes completely ignored and the output depends only on the conditional information. Mao et al. (2019) introduce a regularization term to help prevent mode collapse in conditional GANs which maximizes the ratio of the distance between generated images with respect to the corresponding latent variables and hence encourages diversity in the outputs. Other work that aims to reduce mode collapse includes VEEGAN (Srivastava et al., 2017), which introduces a reconstruction network that maps the generated image back to the original noise and hence discourages many-to-one mappings from noise to images.

Salimans et al. (2016) suggested computing statistics across the mini-batch, and using the discriminator to ensure that these are indistinguishable from the statistics of batches of real images. This is known as *mini-batch discrimination* and is implemented by adding a layer towards the end of the discriminator that learns a tensor for each image that captures statistics of the batch. This was simplified by Karras et al. (2018) who compute a standard deviation for each feature in each spatial location over the mini-batch. Then they average over spatial locations and features to get a single estimate. This is replicated to get a single feature map which is appended to a layer near the end of the discriminator network. Lin et al. (2018) pass concatenated (real or generated) samples to the discriminator and provide a theoretical analysis of how presenting multiple samples to the discriminator increases diversity. MAD-GAN (Ghosh et al., 2018) increase the diversity of GAN samples by using multiple generators and requiring the single discriminator to identify which generator created the samples, thus providing a signal to help push the generators to create different samples from one another.

Multiple scales: Wang et al. (2018b) used multiple discriminators at different scales to help ensure that image quality is high in all frequency bands. Other work defined both generators and discriminators at different resolutions (Denton et al., 2015; Zhang et al., 2017d; Huang et al., 2017c). Karras et al. (2018) introduced the progressive growing method (figure 15.9), which is somewhat simpler and faster to train.

StyleGAN: Karras et al. (2019) introduced the StyleGAN framework (section 15.6). In subsequent work (Karras et al., 2020b), they improved the quality of generated images by (i) redesigning the normalization layers in the generator to remove blob artifacts and (ii) and reducing artifacts where fine details do not follow the coarse details by changing the progressive growing framework. Further improvements include developing methods to train GANs with limited amounts of data (Karras et al., 2020a) and fixing aliasing artifacts in the generated images (Karras et al., 2021). A large body of work finds and manipulates the latent variables in the StyleGAN to edit images (e.g., Abdal et al., 2021; Collins et al., 2020; Härkönen et al., 2020; Patashnik et al., 2021; Shen et al., 2020b; Tewari et al., 2020; Wu et al., 2021; Roich et al., 2022).

Conditional GANs: The conditional GAN was developed by Mirza & Osindero (2014), the auxiliary classifier GAN by Odena et al. (2017), and the InfoGAN by Chen et al. (2016b). The discriminators of these models usually append the conditional information to the discriminator input (Mirza & Osindero, 2014; Denton et al., 2015; Saito et al., 2017) or to an intermediate hidden layer in the discriminator (Reed et al., 2016a; Zhang et al., 2017d; Perarnau et al., 2016). However, Miyato & Koyama (2018) experimented with taking the inner product between embedded conditional information with a layer of the discriminator, motivated by the role of the class information in the underlying probabilistic model. Images generated by GANs have variously been conditioned on classes (e.g.(Odena et al., 2017)), input text (Reed et al., 2016a; Zhang et al., 2017d), attributes (Yan et al., 2016; Donahue et al., 2018a; Xiao et al., 2018b), bounding boxes and keypoints (Reed et al., 2016b), and images (e.g., Isola et al., 2017)).

Image translation: Isola et al. (2017) developed the Pix2Pix algorithm (figure 15.16), and a similar system with higher-resolution results was subsequently developed by Wang et al. (2018b). StarGAN (Choi et al., 2018) performs image-to-image translation across multiple domains using only a single model. The idea of cycle consistency loss was introduced by Zhou et al. (2016b) in DiscoGAN and Zhu et al. (2017) in CycleGAN (figure 15.18).

Adversarial loss: In many image translation tasks, there is no "generator"; these are supervised learning tasks, with an adversarial loss that encourages realism. The super-resolution algorithm of Ledig et al. (2017) is a good example of this (figure 15.17). Esser et al. (2021) used an autoencoder with an adversarial loss. This is a network that takes an image, reduces the representation size to create a "bottleneck" and then reconstructs the image from this reduced data space. In practice, the architecture is similar to encoder-decoder networks (e.g., figure 10.19). After training, the autoencoder reproduces something that is both close to the image and looks highly realistic. Esser et al. (2021) vector-quantize (discretize) the bottleneck of the autoencoder and then learn a probability distribution over the discrete variables using a transformer encoder. By sampling from this transformer encoder, they can produce extremely large high-quality images.

Inverting GANs: One way to edit real images is to project them to the latent space, manipulate the latent variable, and then re-project them to image space. This process is known as *resynthesis*. Unfortunately, GANs only map from the latent variable to the observed data and not vice versa. This has led to methods to *invert* GANs (i.e., find the latent variable that corresponds as closely as possible to an observed image). These methods fall into two classes. The first learns a network that maps in the opposite direction (Donahue et al., 2018b; Luo et al., 2017a; Perarnau et al., 2016; Dumoulin et al., 2017; Guan et al., 2020). This is known as an *encoder*. The second approach is to start with some latent variable $\mathbf{z}$ and optimize it until it reconstructs the image as closely as possible (Creswell & Bharath, 2018; Karras et al., 2020b; Abdal et al., 2019; Lipton & Tripathi, 2017). Zhu et al. (2020a) combine both approaches.

There has been particular interest in inversion for StyleGAN, both because it produces excellent results and because it can control the image at different scales. Unfortunately, Abdal et al. (2020) showed that it is not possible to invert StyleGan without artifacts but proposed inverting to an extended style space, and Richardson et al. (2021) trained an encoder that reliably maps to this space. Even after inverting to the extended space, editing images that are out of domain may still not work well. Roich et al. (2022) address this issue by fine-tuning the generator of StyleGAN so that it reconstructs the image exactly and show that the result can be edited well.

They also add extra terms that reconstruct nearby points exactly, so that the modification is local. This technique is known as *pivotal tuning*. A survey of GAN inversion techniques can be found in Xia et al. (2022).

Editing images with GANs: The iGAN (Zhu et al., 2016) allows users to make interactive edits by scribbling or warping parts of an existing image. The tool then adjusts the output image to be both realistic and to fit these new constraints. It does this by finding a latent vector that produces an image that is similar to the edited image and obeys the edge map of any added lines. It is typical to also add a mask so that only parts of the image close to the edits are changed. EditGAN (Ling et al., 2021) jointly models images and their semantic segmentation masks and allows edits to that mask.

Problems

Problem 15.1 What will the loss be in equation 15.8 when $q(\mathbf{x}) = Pr(\mathbf{x})$?

Problem 15.2 Write an equation relating the loss L in equation 15.8 to the Jensen-Shannon distance $D_{JS}[q(\mathbf{x})\,||\, Pr(\mathbf{x})]$ in equation 15.9.

Problem 15.3 Consider the case where the discrete distributions $Pr(x = i)$ and $q(x = j)$ are defined on $x = 1, 2, 3, 4$. If

$$\mathbf{b} = [Pr(x{=}1), Pr(x{=}2), Pr(x{=}3), Pr(x{=}4), q(x{=}1), q(x{=}2), q(x{=}3), q(x{=}4)]^T, \quad (15.18)$$

then write out the contents of the 8×8 matrix $\mathbf{A}$.

Problem 15.4 Consider the case where:

$$\begin{aligned} Pr(x=1) &= 0.18 & q(x=1) &= 0.4 \\ Pr(x=2) &= 0.1 & q(x=2) &= 0.05 \\ Pr(x=3) &= 0.5 & q(x=3) &= 0.1 \\ Pr(x=4) &= 0.22 & q(x=4) &= 0.45 \end{aligned} \quad (15.19)$$

and the distance between bins $Pr(x = i)$ and $q(x = j)$ is defined as $(i - j)^2$. Write Python code to find the optimal transport plan $\mathbf{P}$ using scipy.optimize.linprog.

Problem 15.5 Write Python code to compute (i) the KL divergence, (ii) the reverse KL divergence,(iii) the Jensen-Shannon divergence, and (iv) the Wasserstein distance between the distributions:

$$Pr(z) = \begin{cases} 0 & z < 0 \\ 1 & 0 \le z \le 1 \\ 0 & z > 1 \end{cases}, \quad (15.20)$$

and

$$Pr(z) = \begin{cases} 0 & z < a \\ 1 & a \leq z \leq a+1 \\ 0 & z > a \end{cases}. \tag{15.21}$$

for the range $-3 < a < 3$. To get a formula for the Wasserstein distance for this special case, think about the total "earth" (i.e., probability mass) that must be moved and multiply this by the squared distance it must move.

Problem 15.6 Write Python code to compute (i) the KL divergence, (ii) the reverse KL divergence, and (iii) the Jensen-Shannon divergence between the distributions:

$$Pr(z) = \begin{cases} 0 & z < 0 \\ 1 & 0 \leq z \leq 1 \\ 0 & z > 1 \end{cases}, \tag{15.22}$$

and

$$Pr(z) = \begin{cases} 0 & z < a \\ 0.5 & a \leq z \leq a+2 \\ 0 & z > a+2 \end{cases}. \tag{15.23}$$

for the range $-3 < a < 3$. What do you conclude about how the KL-divergence and reverse KL-divergence respond when parts of the distribution do not overlap?

Problem 15.7 The KL distance and Wasserstein distances between univariate Gaussian distributions are given by:

$$d_{kl} = \log\left[\frac{\sigma_2}{\sigma_1}\right] + \frac{\sigma_1^2 + (\mu_1 - \mu_2)^2}{2\sigma_2^2} - \frac{1}{2}, \tag{15.24}$$

and

$$d_w = (\mu_1 - \mu_2)^2 + \sigma_1 + \sigma_2 - 2\sqrt{\sigma_1 \sigma_2}, \tag{15.25}$$

respectively. Plot these distances as a function of $\mu_1 - \mu_2$ for the case when $\sigma_1 = \sigma_2 = 1$.

Problem 15.8 Consider a latent variable $\mathbf{z}$ with dimension 100. Consider truncating the values of this variable to (i) $\tau = 2.0$, (ii) $\tau = 1.0$, (iii) $\tau = 0.5$, (iv) $\tau = 0.04$ standard deviations. What proportion of the original probability distribution is disregarded in each case?

Chapter 16

Normalizing flows

Chapters 15 introduced generative adversarial networks (GANs). These are generative models that pass a latent variable through a deep network to create a new sample. GANs are trained using the principle that the samples should be indistinguishable from real data. However, they do not define a distribution over the data. Hence, it is not possible to assess the probability that a new data example was generated by the GAN.

In this chapter, we describe *normalizing flows*, which learn a probability model by using a deep network to transform a simple distribution into a more complicated one. Normalizing flows can both sample from the resulting distribution and evaluate the probability of new data examples. However, they require specialized architecture; each layer must be *invertible*; it must be able to transform data in both directions.

16.1 1D Normalizing flows example

Normalizing flows are probabilistic generative models in that they fit a complex probability distribution to training data (figure 14.2b). Consider a 1D distribution $Pr(x)$. Normalizing flows start with a simple tractable *base* distribution $Pr(z)$ over a latent variable z and apply a function $x = \mathrm{f}[z, \boldsymbol{\phi}]$, where the parameters $\boldsymbol{\phi}$ are chosen so that $Pr(x)$ has the desired distribution (figure 16.1). Generating a new example x^* is easy; we draw z^* from the base density and pass this through the function so that $x^* = \mathrm{f}[z^*, \boldsymbol{\phi}]$.

16.1.1 Measuring probability

Measuring the probability of a data point x is more challenging. Consider applying a function $\mathrm{f}[z, \boldsymbol{\phi}]$ to random variable z with known density $Pr(z)$. The probability density will decrease in areas that are stretched by the function, and increase in areas that are compressed so that the area under the new distribution remains one. The degree to which a function $\mathrm{f}[z, \boldsymbol{\phi}]$ stretches or compresses its input depends on the magnitude of its gradient. If a small change to the input causes a larger change in the output, then

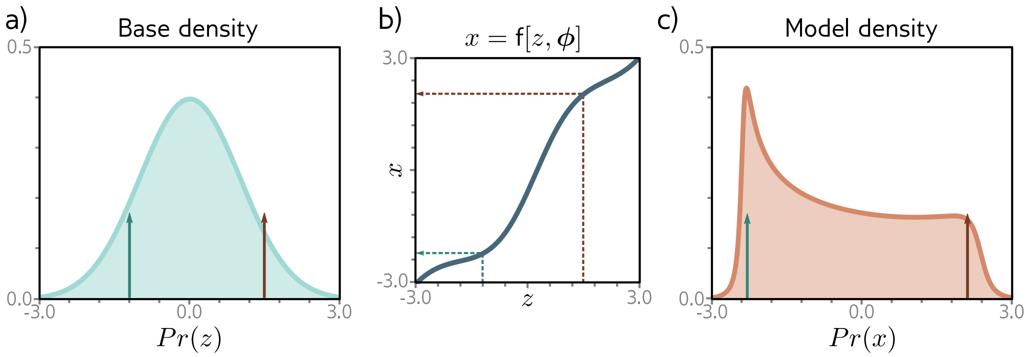

Figure 16.1 Transforming probability distributions. a) The base density is a standard normal defined on a latent variable z. b) This variable is transformed by a function $x = \mathrm{f}[z, \phi]$ to a new variable x, which c) has a new distribution. To sample from this model, we draw values z from the base density (green and brown arrows in panel (a) show two examples). We pass these through the function $\mathrm{f}[z, \phi]$ as shown by dotted arrows in panel (b) to generate the values of x, which are indicated as arrows in panel (c).

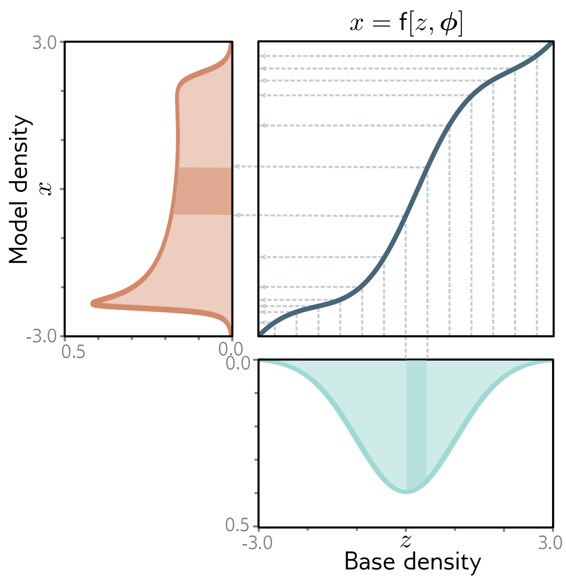

Figure 16.2 Transforming distributions. The base density (cyan, bottom) passes through a function (gray curve, top right) to create the model density (orange, left). Consider dividing the base density into equal intervals (gray vertical lines). The probability mass between adjacent lines must remain the same after transformation. The cyan-shaded region passes through a part of the function where the gradient is larger than one and so this region is stretched. Consequently, the height of the orange-shaded region must be lower so that it retains the same area as the cyan-shaded region. In other places (e.g., $z = -2$), the gradient is less than one, and the model density increases relative to the base density.

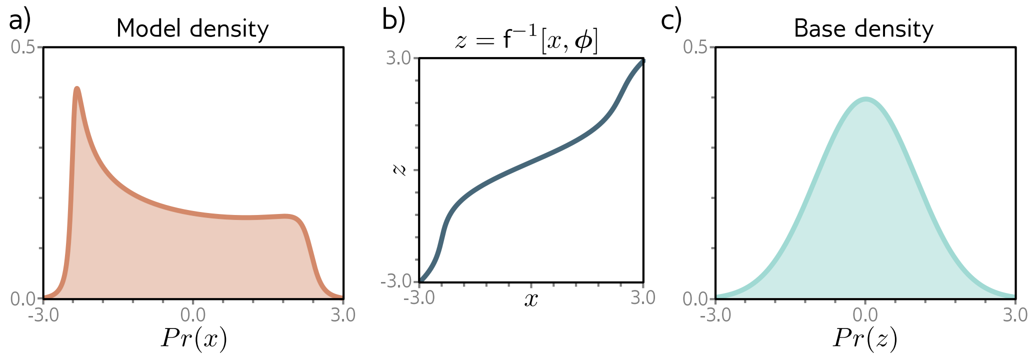

Figure 16.3 Inverse mapping (normalizing direction). If the function is invertible then it's possible to transform the model density back to the original base density. The probability of a point x under the model density depends in part on the probability of the equivalent point z under the base density (see equation 16.1).

it stretches the function. If a small change to the input causes a smaller change in the output, then it compresses the function (figure 16.2).

Hence, the probability of data x under the transformed distribution is:

$$Pr(x|\phi) = \left|\frac{\partial \mathrm{f}[z,\phi]}{\partial z}\right|^{-1} \cdot Pr(z), \tag{16.1}$$

where $z = \mathrm{f}^{-1}[x,\phi]$ is the latent variable that created x. The term $Pr(z)$ is the original probability of this latent variable under the base density. This is moderated according to the magnitude of the derivative of the function. If this is greater than one, then the probability decreases. If it is smaller, the probability increases.

16.1.2 Forward and inverse mappings

To draw samples from the distribution, we need the forward mapping $x = \mathrm{f}[z,\phi]$, but to measure the likelihood, we need to compute the inverse $z = \mathrm{f}^{-1}[x,\phi]$. Hence, we need to choose $\mathrm{f}[z,\phi]$ judiciously, so that it is *invertible*.

Problems 16.1-16.2

The forward mapping is sometimes termed the *generative direction*. The base density is usually chosen to be a standard normal distribution. Hence, the inverse mapping is termed the *normalizing direction*, since this takes the complex distribution over x and turns it into a normal distribution over z (figure 16.3).

16.1.3 Learning

To learn the distribution, we find parameters $\boldsymbol{\phi}$ that maximize the likelihood of the training data $\{x_i\}_{i=1}^I$ or equivalently minimize the negative log likelihood:

$$\begin{aligned}
\hat{\boldsymbol{\phi}} &= \underset{\boldsymbol{\phi}}{\operatorname{argmax}}\left[\prod_{i=1}^{I} Pr(x_i|\boldsymbol{\phi})\right] \\
&= \underset{\boldsymbol{\phi}}{\operatorname{argmin}}\left[\sum_{i=1}^{I} -\log\left[Pr(x_i|\boldsymbol{\phi})\right]\right] \\
&= \underset{\boldsymbol{\phi}}{\operatorname{argmin}}\left[\sum_{i=1}^{I} \log\left[\left|\frac{\partial \mathrm{f}[z_i,\boldsymbol{\phi}]}{\partial z_i}\right|\right] - \log\left[Pr(z_i)\right]\right],
\end{aligned} \tag{16.2}$$

where we have have assumed that the data are independent and identically distributed in the first line and used the likelihood definition from equation 16.1 in the third line.

16.2 General case

The previous section developed a simple 1D example that modeled a probability distribution $Pr(x)$ by transforming a simpler base density $Pr(z)$. We now extend this to multivariate distributions $Pr(\mathbf{x})$ and $Pr(\mathbf{z})$, and add the complication that the transformation is defined by a deep neural network.

Consider applying a function $\mathbf{x} = \mathbf{f}[\mathbf{z}, \boldsymbol{\phi}]$ to a base density $Pr(\mathbf{z})$, where $\mathbf{z} \in \mathbb{R}^D$ and $\mathbf{f}[\mathbf{z}, \boldsymbol{\phi}]$ is a deep neural network. The resulting variable $\mathbf{x} \in \mathbb{R}^D$ has a new distribution and a new sample $\mathbf{x}^*$ can be drawn from this distribution by (i) drawing a sample $\mathbf{z}^*$ from the base density and (ii) passing this through the neural network so that $\mathbf{x}^* = \mathbf{f}[\mathbf{z}^*, \boldsymbol{\phi}]$.

By analogy with equation 16.1, the likelihood of a sample under this distribution is:

$$Pr(\mathbf{x}|\boldsymbol{\phi}) = \left|\frac{\partial \mathbf{f}[\mathbf{z},\boldsymbol{\phi}]}{\partial \mathbf{z}}\right|^{-1} \cdot Pr(\mathbf{z}), \tag{16.3}$$

where $\mathbf{z} = \mathbf{f}^{-1}[\mathbf{x}, \boldsymbol{\phi}]$ is the latent variable $\mathbf{z}$ that created $\mathbf{x}$. The first term is the inverse of the determinant of the $D \times D$ Jacobian matrix $\partial \mathbf{f}[\mathbf{z}, \boldsymbol{\phi}]/\partial \mathbf{z}$ which contains terms $\partial \mathrm{f}_i[\mathbf{z}, \boldsymbol{\phi}]/\partial z_j$ at position (i, j). Just as the absolute derivative measured the change of area at a point on a 1D function when the function was applied, the absolute determinant measures the change in volume at a point in the multivariate function. The second term is probability of the latent variable under the base density.

Appendix C.5.5 Determinant

Appendix C.6.1 Jacobian

16.2.1 Forward mapping with a deep neural network

In practice, the forward mapping $\mathbf{f}[\mathbf{z}, \boldsymbol{\phi}]$ is usually defined by a neural network, consisting of a series of layers $\mathbf{f}_k[\bullet, \boldsymbol{\phi}_k]$ with parameters $\boldsymbol{\phi}_k$ which are composed together as:

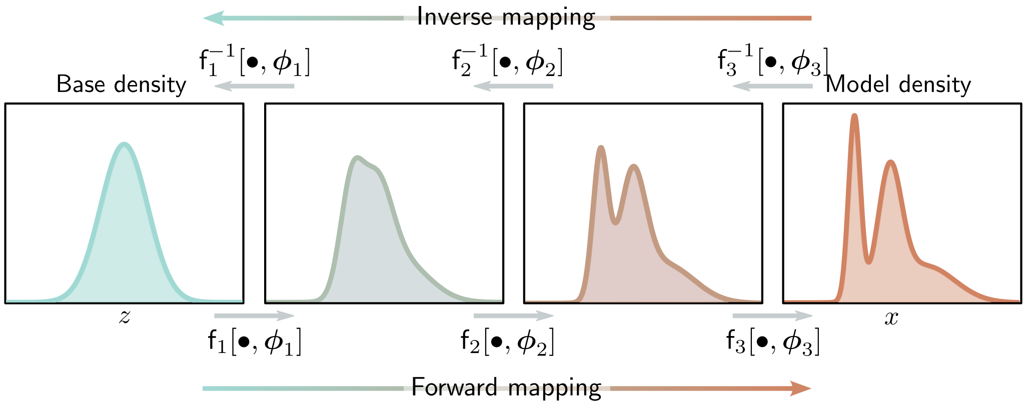

Figure 16.4 Forward and inverse mappings for a deep neural network. The base density (left) is gradually transformed by the network layers $f_1[\bullet, \phi_1], f_2[\bullet, \phi_2], \ldots$ to create the model density. Each layer is invertible and we can equivalently think of the inverse of the layers as gradually transforming (or "flowing") the model density back to the base density.

$$\mathbf{x} = \mathbf{f}[\mathbf{z}, \boldsymbol{\phi}] = \mathbf{f}_K\Big[\mathbf{f}_{K-1}\Big[\ldots \mathbf{f}_2\big[\mathbf{f}_1[\mathbf{z}, \boldsymbol{\phi}_1], \boldsymbol{\phi}_2\big], \ldots \boldsymbol{\phi}_{K-1}\Big], \boldsymbol{\phi}_K\Big]. \tag{16.4}$$

The inverse mapping (normalizing direction) is defined by the composition of the inverse of each layer $\mathbf{f}_k^{-1}[\bullet, \boldsymbol{\phi}_k]$ applied in the opposite order:

$$\mathbf{z} = \mathbf{f}^{-1}[\mathbf{x}, \boldsymbol{\phi}] = \mathbf{f}_1^{-1}\Big[\mathbf{f}_2^{-1}\Big[\ldots \mathbf{f}_{K-1}^{-1}\big[\mathbf{f}_K^{-1}[\mathbf{x}, \boldsymbol{\phi}_K], \boldsymbol{\phi}_{K-1}\big], \ldots \boldsymbol{\phi}_2\Big], \boldsymbol{\phi}_1\Big]. \tag{16.5}$$

The base density $Pr(\mathbf{z})$ is usually defined as a multivariate standard normal (i.e., with mean zero and identity covariance). Hence, the effect of each subsequent inverse layer is to gradually move or "flow" the data density toward the base density. Since the base density is usually normal, this gives rise to the name "normalizing flows".

The Jacobian of the forward mapping can be expressed as:

$$\frac{\partial \mathbf{f}[\mathbf{z}, \boldsymbol{\phi}]}{\partial \mathbf{z}} = \frac{\partial \mathbf{f}_K[\mathbf{f}_{K-1}, \boldsymbol{\phi}_K]}{\partial \mathbf{f}_{K-1}} \cdot \frac{\partial \mathbf{f}_{K-1}[\mathbf{f}_{K-2}, \boldsymbol{\phi}_{K-1}]}{\partial \mathbf{f}_{K-2}} \ldots \frac{\partial \mathbf{f}_2[\mathbf{f}_1, \boldsymbol{\phi}_2]}{\partial \mathbf{f}_1} \cdot \frac{\partial \mathbf{f}_1[\mathbf{z}, \boldsymbol{\phi}_1]}{\partial \mathbf{z}}, \tag{16.6}$$

where we have overloaded the notation to make $\mathbf{f}_k$ the output of the function $\mathbf{f}_k[\bullet, \boldsymbol{\phi}_k]$. The absolute determinant of this Jacobian can be computed by taking the product of the individual absolute determinants:

$$\left|\frac{\partial \mathbf{f}[\mathbf{z}, \boldsymbol{\phi}]}{\partial \mathbf{z}}\right| = \left|\frac{\partial \mathbf{f}_K[\mathbf{f}_{K-1}, \boldsymbol{\phi}_K]}{\partial \mathbf{f}_{K-1}}\right| \cdot \left|\frac{\partial \mathbf{f}_{K-1}[\mathbf{f}_{K-2}, \boldsymbol{\phi}_{K-1}]}{\partial \mathbf{f}_{K-2}}\right| \ldots \left|\frac{\partial \mathbf{f}_2[\mathbf{f}_1, \boldsymbol{\phi}_2]}{\partial \mathbf{f}_1}\right| \cdot \left|\frac{\partial \mathbf{f}_1[\mathbf{z}, \boldsymbol{\phi}_1]}{\partial \mathbf{z}}\right|. \tag{16.7}$$

The absolute determinant of the Jacobian of the inverse mapping is found by applying the same rule to equation 16.5. It is the reciprocal of the absolute determinant in the forward mapping.

Problem 16.3

We train normalizing flows with a dataset $\{\mathbf{x}_i\}$ of I training examples using the negative log-likelihood criterion:

$$
\begin{aligned}
\hat{\boldsymbol{\phi}} &= \operatorname*{argmax}\left[\prod_{i=1}^{I} Pr(\mathbf{z}_i)\cdot\left|\frac{\partial \mathbf{f}[\mathbf{z}_i,\boldsymbol{\phi}]}{\partial \mathbf{z}_i}\right|^{-1}\right]\\
&= \operatorname*{argmin}\left[\sum_{i=1}^{I}\log\left[\left|\frac{\partial \mathbf{f}[\mathbf{z}_i,\boldsymbol{\phi}]}{\partial \mathbf{z}_i}\right|\right]\right]-\log\left[Pr(\mathbf{z}_i)\right], \qquad (16.8)
\end{aligned}
$$

where $\mathbf{z}_i = \mathbf{f}^{-1}[\mathbf{x}_i,\boldsymbol{\phi}]$, $Pr(\mathbf{z}_i)$ is measured under the base distribution, and the absolute determinant $|\partial\mathbf{f}[\mathbf{z}_i,\boldsymbol{\phi}]/\partial\mathbf{z}_i|$ is given by equation 16.7.

16.2.2 Desiderata for network layers

The theory of normalizing flows is straightforward. However, for this to be practical, we need neural network layers $\mathbf{f}_k$ that have four properties.

1. Collectively, a set of network layers must be sufficiently *expressive* to map a multivariate standard normal distribution to an arbitrary density.

2. Each network layer must be *invertible*; each must define a unique one-to-one mapping from any point in the set of inputs to an output point (a *bijection*). If multiple inputs were mapped to the same output, then the inverse would be ambiguous.

Appendix C.1 Bijection

3. It must be possible to compute the *inverse* of each layer *efficiently*. We need to do this every time we evaluate the likelihood, this happens repeatedly during training, so there must be a closed-form solution or a fast algorithm for the inverse.

4. It also must be possible to evaluate the *determinant* of the Jacobian *efficiently* for either the forward or inverse mapping.

16.3 Invertible network layers

We now describe different invertible network layers or *flows* for use in these models. We start with linear and elementwise flows. These are easy to invert and it's possible to compute the determinant of their Jacobians but neither is sufficiently expressive to describe arbitrary transformations of the base density. However, they form the building blocks of coupling, autoregressive, and residual flows, which are all more expressive.

16.3.1 Linear flows

A linear flow has the form $\mathbf{f}[\mathbf{h}] = \boldsymbol{\beta} + \boldsymbol{\Omega}\mathbf{h}$. If the matrix $\boldsymbol{\Omega}$ is invertible then the linear transform is invertible. For $\boldsymbol{\Omega} \in \mathbb{R}^{D\times D}$, the computation of the inverse is $\mathcal{O}[D^3]$. The determinant of the Jacobian is just the determinant of $\boldsymbol{\Omega}$, which can also be computed in $\mathcal{O}[D^3]$. This means that linear flows become expensive as the dimension D increases.

Appendix C.7 Big O notation

If the matrix $\boldsymbol{\Omega}$ takes a special form, then inversion and computation of the determinant becomes more efficient but the transformation becomes less general. For example, diagonal matrices require only $\mathcal{O}[D]$ computation for the inversion and determinant, but the elements of $\mathbf{h}$ don't interact. Orthogonal matrices are also more efficient to invert, and their determinant is fixed, but they do not allow scaling of the individual dimensions. Triangular matrices are more practical; they are invertible using a process known as back-substitution which is $\mathcal{O}[D^2]$, and the determinant is just the product of the diagonal values.

Appendix C.5.7 Matrix types

Problem 16.4

One way to make a linear flow that is general, efficient to invert and for which the Jacobian can be computed efficiently is to parameterize it directly in terms of the LU decomposition. In other words, we use:

$$\boldsymbol{\Omega} = \mathbf{PL}(\mathbf{U} + \mathbf{D}), \tag{16.9}$$

where $\mathbf{P}$ is a predetermined permutation matrix, $\mathbf{L}$ is a lower diagonal matrix, $\mathbf{U}$ is an upper triangular matrix with zeros on the diagonal and $\mathbf{D}$ is a diagonal matrix that supplies those missing diagonal elements. This can be inverted in $\mathcal{O}[D^2]$ and the log determinant is just the sum of the log of the absolute values on the diagonal of $\mathbf{D}$.

Unfortunately, linear flows are not sufficiently expressive. When a linear function $\mathbf{f}[\mathbf{h}] = \boldsymbol{\beta} + \boldsymbol{\Omega}\mathbf{h}$ is applied to normally distributed input $\text{Norm}_{\mathbf{h}}[\boldsymbol{\mu}, \boldsymbol{\Sigma}]$, then the result is also normally distributed with mean and variance, $\boldsymbol{\beta} + \boldsymbol{\Omega}\boldsymbol{\mu}$ and $\boldsymbol{\Omega}\boldsymbol{\Sigma}\boldsymbol{\Omega}^T$, respectively. Hence, it is not possible to map a normal distribution to an arbitrary density using linear flows alone.

Problems 16.5-16.6

16.3.2 Elementwise flows

Since linear flows are not sufficiently expressive, we must turn to nonlinear flows. The simplest of these are elementwise flows, which apply a pointwise nonlinear function $\mathrm{f}[\bullet, \boldsymbol{\phi}]$ with parameters $\boldsymbol{\phi}$ to each element of the input so that:

$$\mathbf{f}[\mathbf{h}] = \left[\mathrm{f}[h_1, \boldsymbol{\phi}], \mathrm{f}[h_2, \boldsymbol{\phi}], \ldots \mathrm{f}[h_D, \boldsymbol{\phi}]\right]^T. \tag{16.10}$$

The Jacobian $\partial\mathbf{f}[\mathbf{h}]/\partial\mathbf{h}$ is diagonal since the d^{th} input to $\mathbf{f}[\mathbf{h}]$ only affects the d^{th} output. Its determinant is the product of the entries on the diagonal and so:

$$\left|\frac{\partial\mathbf{f}[\mathbf{h}]}{\partial\mathbf{h}}\right| = \prod_{d=1}^{D}\left|\frac{\partial\mathrm{f}[h_d]}{\partial h_d}\right|. \tag{16.11}$$

The function $\mathrm{f}[\bullet, \boldsymbol{\phi}]$ could be a fixed invertible nonlinearity like the leaky ReLU (figure 3.13) in which case there are no parameters, or it may be any parameterized

Problem 16.7

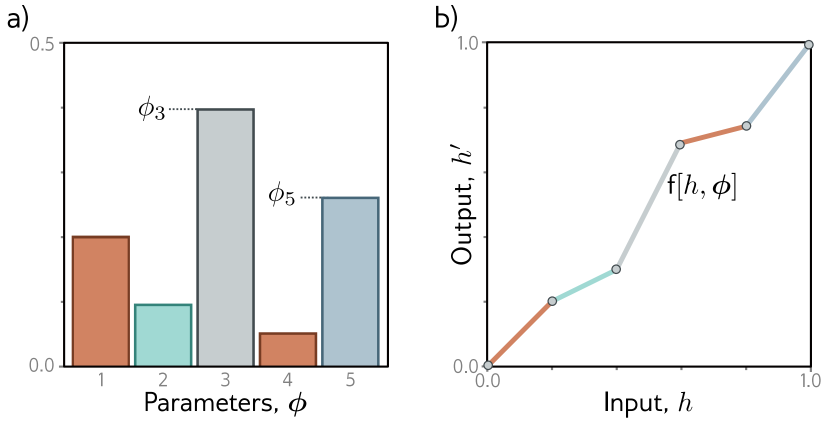

Figure 16.5 Piecewise-linear mapping. An invertible piecewise-linear mapping $h' = \mathrm{f}[h, \boldsymbol{\phi}]$ can be created by dividing the input domain $h \in [0, 1]$ into K equally sized regions (here $K = 5$). Each region has a slope with parameter $\boldsymbol{\phi}_k$. a) If these parameters are positive and sum to one, then b) the function will be invertible and map to the output domain $h' \in [0, 1]$.

invertible one-to-one mapping. A simple example is a piecewise-linear function with K regions (figure 16.5) which maps $[0, 1]$ to $[0, 1]$ as:

$$\mathrm{f}[h_d, \boldsymbol{\phi}] = \left(\sum_{k=1}^{b-1} \phi_k\right) + (Kh_d - b)\phi_b, \tag{16.12}$$

where the parameters $\phi_1, \phi_2, \ldots \phi_K$ are positive and sum to one, and $b = \lfloor Kh_d \rfloor$ is the index of the bin that contains h_d. The first term is the sum of all the preceding bins, and the second term represents the proportion of the way through the current bin that h_d lies. This function is easy to invert and its gradient can be calculated almost everywhere. There are many similar schemes for creating smooth functions, often using splines with parameters that ensure that the function is monotonic and hence invertible.

Problem 16.8-16.9

Elementwise flows are nonlinear but don't mix input dimensions, so they can't create correlations between variables. When alternated with linear flows (which do mix dimensions), more complex transformations can be modeled, but, in practice, elementwise flows are used as components of more complex layers like *coupling flows*.

16.3.3 Coupling flows

Coupling flows divide the input $\mathbf{h}$ into two parts so that $\mathbf{h} = [\mathbf{h}_1, \mathbf{h}_2]^T$ and define the flow $\mathbf{f}[\mathbf{h}, \boldsymbol{\phi}]$ as:

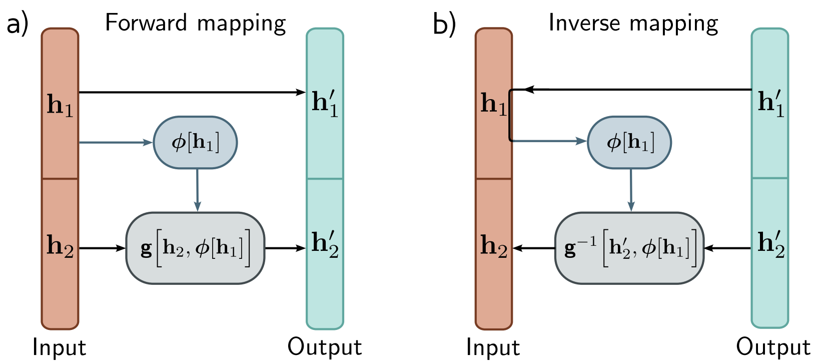

Figure 16.6 Coupling flows. a) The input (orange vector) is divided into $\mathbf{h}_1$ and $\mathbf{h}_2$. The first part $\mathbf{h}'_1$ of the output (cyan vector) is a copy of $\mathbf{h}_1$. The output $\mathbf{h}'_2$ is created by applying an invertible transformation $\mathbf{g}[\bullet, \boldsymbol{\phi}]$ to $\mathbf{h}_2$, where the parameters $\boldsymbol{\phi}$ are themselves a (not necessarily invertible) function of $\mathbf{h}_1$. b) In the inverse mapping, $\mathbf{h}_1 = \mathbf{h}'_1$. This allows us to calculate the parameters $\boldsymbol{\phi}[\mathbf{h}_1]$ and then apply the inverse $\mathbf{g}^{-1}[\mathbf{h}'_2, \boldsymbol{\phi}]$ to retrieve $\mathbf{h}_2$.

$$
\begin{aligned}
\mathbf{h}'_1 &= \mathbf{h}_1 \\
\mathbf{h}'_2 &= \mathbf{g}\Big[\mathbf{h}_2, \boldsymbol{\phi}[\mathbf{h}_1]\Big].
\end{aligned} \tag{16.13}
$$

Here $\mathbf{g}[\bullet, \boldsymbol{\phi}]$ is an elementwise flow (or other invertible layer) with parameters $\boldsymbol{\phi}[\mathbf{h}_1]$ that are themselves a nonlinear function of the inputs $\mathbf{h}_1$ (figure 16.6). The function $\boldsymbol{\phi}[\bullet]$ is usually a neural network of some kind and does not have to be invertible. The original variables can be recovered as:

$$
\begin{aligned}
\mathbf{h}_1 &= \mathbf{h}'_1 \\
\mathbf{h}_2 &= \mathbf{g}^{-1}\Big[\mathbf{h}'_2, \boldsymbol{\phi}[\mathbf{h}_1]\Big].
\end{aligned} \tag{16.14}
$$

If the function $\mathbf{g}[\bullet, \boldsymbol{\phi}]$ is an elementwise flow, then the Jacobian will be diagonal with the identity matrix in the top-left quadrant and the derivatives of the elementwise transformation in the bottom right. Its determinant is the product of these diagonal values.

The inverse and Jacobian can be computed efficiently, but this approach only transforms the second half of the parameters in a way that depends on the first half. To make a more general transformation, the elements of $\mathbf{h}$ are randomly shuffled using permutation matrices between layers so that ultimately, every variable is transformed by every other. In practice, these permutation matrices are difficult to learn and so they are initialized randomly and then frozen. For structured data like images, the channels are divided into two halves $\mathbf{h}_1$ and $\mathbf{h}_2$ and and permuted between layers using 1×1 convolutions.

Appendix C.5.8
Permutation matrix

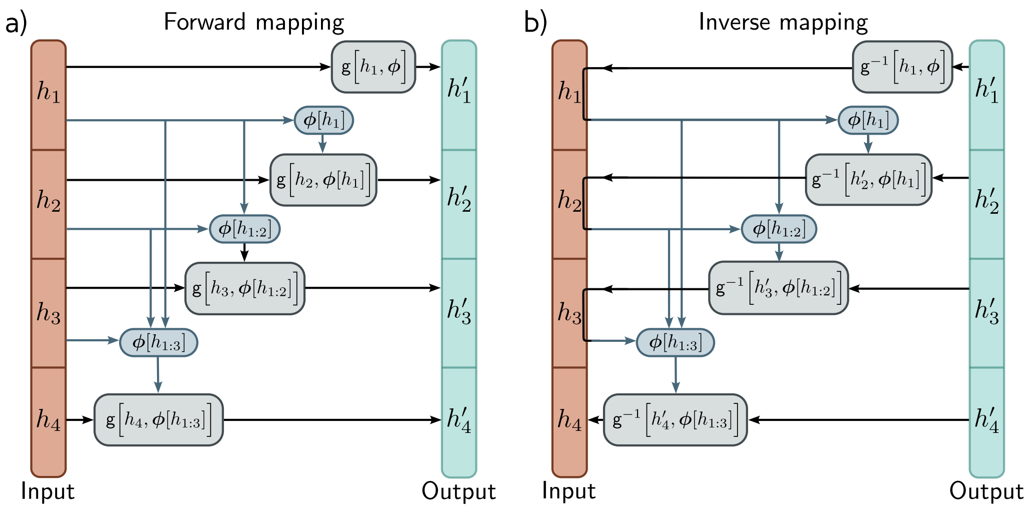

Figure 16.7 Autoregressive flows. This is a generalization of coupling flows in which the input $\mathbf{h}$ (orange column) and output $\mathbf{h}'$ (cyan column) are split into their constituent dimensions (here four dimensions). a) Output h_1' is an invertible transformation of input h_1. Output h_2' is an invertible function of input h_2 where the parameters depend on h_1. Output h_3' is an invertible function of input h_3 where the parameters depend on previous inputs h_1' and h_2' and so on. None of the outputs depend on one another, so they can be computed in parallel. b) The inverse of the autoregressive flow is computed using a similar method as for coupling flows. However, notice that to compute h_2' we must already know h_1', to compute h_2', we must already know h_1' and h_2' and so on. Consequently, the inverse cannot be computed in parallel.

16.3.4 Autoregressive flows

Autoregressive flows are a generalization of coupling flows that treat each input dimension as a separate "block" (figure 16.7). They compute the d^{th} dimension of the output $\mathbf{h}'$ based on the first $d-1$ dimensions of the input $\mathbf{h}$:

$$h_d' = \mathrm{g}\Bigl[h_d, \boldsymbol{\phi}[\mathbf{h}_{1:d-1}]\Bigr]. \tag{16.15}$$

The function $\mathrm{g}[\bullet,\bullet]$ is termed the *transformer*,[1] and the parameters $\boldsymbol{\phi}$, $\boldsymbol{\phi}[h_1]$, $\boldsymbol{\phi}[h_1, h_2]\ldots$ are termed *conditioners*. As for coupling flows, the transformer $\mathrm{g}[\bullet, \boldsymbol{\phi}]$ must be invertible, but $\boldsymbol{\phi}[\bullet]$ can take any form and is usually a neural network. If the transformer and conditioner are sufficiently flexible, then autoregressive flows are *universal approximators* in that they can represent any probability distribution.

It's possible to compute all of the entries of the output $\mathbf{h}'$ in parallel using a network with appropriate masks so that the parameters $\boldsymbol{\phi}$ at position d only depend on previous

[1]This is nothing to do with the transformer layers discussed in chapter 12.

positions. This is known as a *masked autoregressive flow*. The principle is very similar to masked self-attention (section 12.7.2); connections that relate inputs to previous outputs are pruned.

Inverting the transformation is less efficient. Consider the forward mapping:

$$
\begin{aligned}
h_1' &= \mathrm{g}\Big[h_1, \boldsymbol{\phi}\Big] \\
h_2' &= \mathrm{g}\Big[h_2, \boldsymbol{\phi}[h_1]\Big] \\
h_3' &= \mathrm{g}\Big[h_3, \boldsymbol{\phi}[h_{1:2}]\Big] \\
h_4' &= \mathrm{g}\Big[h_4, \boldsymbol{\phi}[h_{1:3}]\Big].
\end{aligned}
\tag{16.16}
$$

This must be inverted sequentially using a similar principle as for coupling flows:

$$
\begin{aligned}
h_1 &= \mathrm{g}^{-1}\Big[h_1', \boldsymbol{\phi}\Big] \\
h_2 &= \mathrm{g}^{-1}\Big[h_2', \boldsymbol{\phi}[h_1]\Big] \\
h_3 &= \mathrm{g}^{-1}\Big[h_3', \boldsymbol{\phi}[h_{1:2}]\Big] \\
h_4 &= \mathrm{g}^{-1}\Big[h_4', \boldsymbol{\phi}[h_{1:3}]\Big].
\end{aligned}
\tag{16.17}
$$

This can't be done in parallel as the computation for h_d depends on $h_{1:d-1}$ (i.e., the partial results so far). Hence, inversion is time-consuming when the input is large.

16.3.5 Inverse autoregressive flows

Masked autoregressive flows are defined in the normalizing (inverse) direction. This is required to evaluate the likelihood efficiently, and hence to learn the model. However, sampling requires the forward direction, in which each variable must be computed sequentially at each layer, which is slow. If we use an autoregressive flow for the forward (generative) transformation, then sampling is efficient, but computing the likelihood (and training) is slow. This is known as an *inverse autoregressive flow*.

A trick that allows fast learning and also fast (but approximate) sampling is to build a masked autoregressive flow to learn the distribution (the teacher), and then use this to train an inverse autoregressive flow from which we can sample efficiently (the student). This requires a different formuation of normalizing flows that learns to from another function rather than a set of samples (see section 16.5.3).

16.3.6 Residual flows: iRevNet

Residual flows take their inspiration from residual networks. They divide the input into two parts $\mathbf{h} = [\mathbf{h}_1^T, \mathbf{h}_2^T]^T$ (as for coupling flows) and define the outputs as:

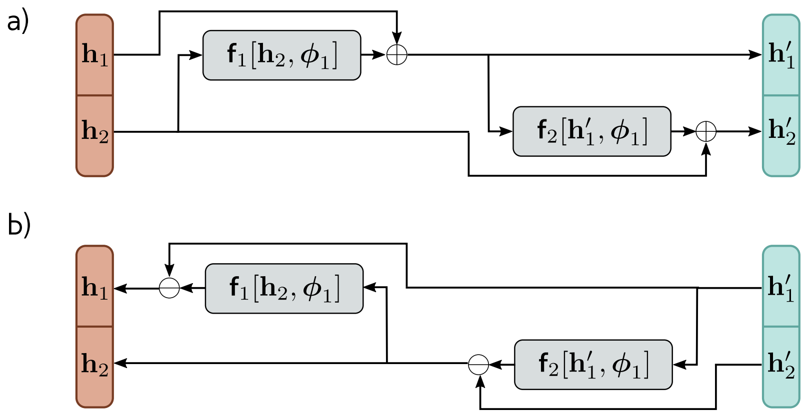

Figure 16.8 Residual flows. a) An invertible function is computed by splitting the input into $\mathbf{h}_1$ and $\mathbf{h}_2$ and creating two residual layers. In the first, $\mathbf{h}_2$ is processed and $\mathbf{h}_1$ is added. In the second, the result is processed and $\mathbf{h}_2$ is added. b) In the reverse mechanism the functions are computed in the opposite order and the addition operation becomes subtraction.

$$
\begin{aligned}
\mathbf{h}'_1 &= \mathbf{h}_1 + \mathbf{f}_1[\mathbf{h}_2, \boldsymbol{\phi}_1] \\
\mathbf{h}'_2 &= \mathbf{h}_2 + \mathbf{f}_2[\mathbf{h}'_1, \boldsymbol{\phi}_2],
\end{aligned}
\tag{16.18}
$$

where $\mathbf{f}_1[\bullet, \boldsymbol{\phi}_1]$ and $\mathbf{f}_2[\bullet, \boldsymbol{\phi}_2]$ are two functions that do not necessarily have to be invertible (figure 16.8). The inverse can be computed by reversing the order of computation:

$$
\begin{aligned}
\mathbf{h}_2 &= \mathbf{f}_2[\mathbf{h}'_1, \boldsymbol{\phi}_1] - \mathbf{h}'_2 \\
\mathbf{h}_1 &= \mathbf{f}_1[\mathbf{h}_2, \boldsymbol{\phi}_2] - \mathbf{h}'_1.
\end{aligned}
\tag{16.19}
$$

As for coupling flows, the division into blocks restricts the family of transformations that can be represented, and hence the inputs are permuted between layers so that the variables can mix in arbitrary ways.

This formulation can be inverted easily but for general functions $\mathbf{f}_1[\bullet, \boldsymbol{\phi}_1]$ and $\mathbf{f}_2[\bullet, \boldsymbol{\phi}_2]$, there is no efficient way to compute the Jacobian. This formulation is sometimes used to save memory when training residual networks; because the network is invertible, there is no need to store the activations at each layer in the forward pass. Problem 16.10

16.3.7 Residual flows and contraction mappings: iResNet

A different approach to exploiting residual networks is to utilize the *Banach fixed point theorem* or *contraction mapping theorem*, which states that every contraction mapping

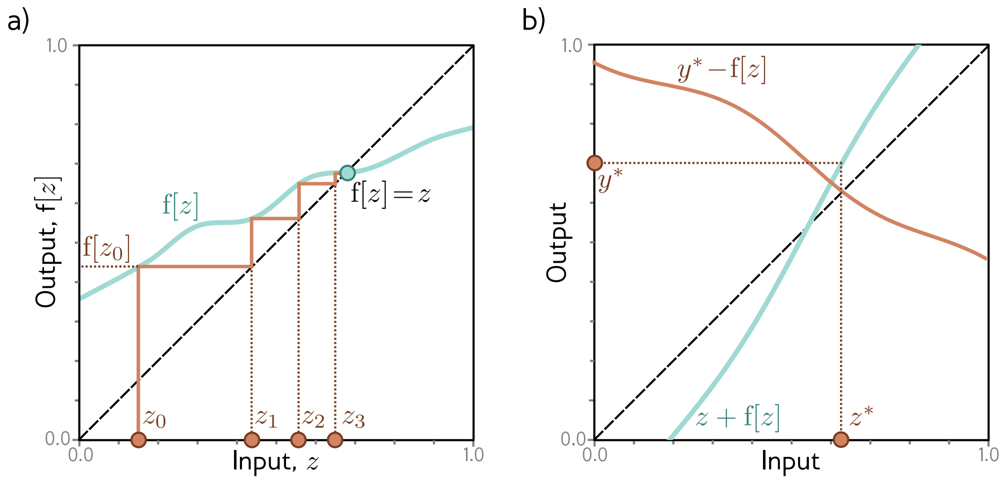

Figure 16.9 Contraction mappings. If a function has an absolute slope of less than one everywhere, then iterating the function converges to a fixed point $\mathrm{f}[z] = z$. a) Starting at z_0, we evaluate $z_1 = \mathrm{f}[z_0]$. We then pass z_1 back into the function and iterate. Eventually, the process converges to the point where $\mathrm{f}[z] = z$ (i.e., where the function crosses the dashed diagonal identity line). b) This can be used to invert equations of the form $y = z + \mathrm{f}[z]$ for a value y^* by noticing that the fixed point of $y - f[z]$ (where the orange line crosses the dashed identity line) is at the same position as where $y^* = z + \mathrm{f}[z]$.

has a fixed point. A contraction mapping $\mathrm{f}[\bullet]$ has the property that:

$$\mathrm{dist}\Big[\mathrm{f}[z'], \mathrm{f}[z]\Big] < \beta \cdot \mathrm{dist}\Big[z', z\Big] \qquad\qquad \forall\ z, z', \tag{16.20}$$

where $\mathrm{dist}[\bullet, \bullet]$ is a distance function and $0 < \beta < 1$. When a function with this property is iterated (i.e., the output is repeatedly passed back in as an input), the result converges to a fixed point where $\mathrm{f}[z] = z$ (figure 16.9). To understand this, consider applying the function to both the fixed point and the current position; the fixed point remains static, but the distance between the two must become smaller, and so the current position must get closer to the fixed point.

Problem 16.11

This theorem can be exploited to invert an equation of the form:

$$y = z + \mathrm{f}[z] \tag{16.21}$$

if $\mathrm{f}[z]$ is a contraction mapping. In other words, it can be used to find the z^* that maps to a given value y^*. This can be done by starting with any point y_0 and iterating $z = y^* - \mathrm{f}[z]$. This has a fixed point at $z + \mathrm{f}[z] = y^*$ (figure 16.9b).

The same principle can be used to invert residual network layers of the form $\mathbf{h}' = \mathbf{h} + \mathbf{f}[\mathbf{h}, \boldsymbol{\phi}]$ if we ensure that $\mathbf{f}[\mathbf{h}, \boldsymbol{\phi}]$ is a contraction mapping. In practice, this means that the Lipschitz constant must be less than one. Assuming that the slope of the activation

Appendix C.2 Lipschitz constant

functions is not greater than one, this is equivalent to ensuring the largest eigenvalue of each weight matrix $\boldsymbol{\Omega}$ must be less than one. A crude way to do this is to ensure that the absolute magnitudes of the weights $\boldsymbol{\Omega}$ are small by clipping them.

The Jacobian determinant cannot be computed easily, but its logarithm can be approximated by using a series of tricks.

$$
\begin{aligned}
\log\left[\left|\mathbf{I}+\frac{\partial\mathbf{f}[\mathbf{h},\boldsymbol{\phi}]}{\partial\mathbf{h}}\right|\right] &= \text{trace}\left[\log\left[\mathbf{I}+\frac{\partial\mathbf{f}[\mathbf{h},\boldsymbol{\phi}]}{\partial\mathbf{h}}\right]\right] \\
&= \sum_{k=1}^{\infty}(-1)^{k-1}\text{trace}\left[\frac{\partial\mathbf{f}[\mathbf{h},\boldsymbol{\phi}]}{\partial\mathbf{h}}\right]^k, \qquad (16.22)
\end{aligned}
$$

where we have used the identity $\log[|\mathbf{A}|]=\text{trace}[\log[\mathbf{A}]]$ in the first line and expanded this into a power series in the second line.

This series is truncated and the constituent terms can then be estimated using *Hutchinson's trace estimator*. Consider a normal random variable $\boldsymbol{\epsilon}$ with mean $\mathbf{0}$ and variance $\mathbf{I}$. The trace of a matrix $\mathbf{A}$ can be estimated as:

$$
\begin{aligned}
\text{trace}[\mathbf{A}] &= \text{trace}\left[\mathbf{A}\mathbb{E}\left[\boldsymbol{\epsilon}\boldsymbol{\epsilon}^T\right]\right] \\
&= \text{trace}\left[\mathbb{E}\left[\mathbf{A}\boldsymbol{\epsilon}\boldsymbol{\epsilon}^T\right]\right] \\
&= \mathbb{E}\left[\text{trace}\left[\mathbf{A}\boldsymbol{\epsilon}\boldsymbol{\epsilon}^T\right]\right] \\
&= \mathbb{E}\left[\text{trace}\left[\boldsymbol{\epsilon}^T\mathbf{A}\boldsymbol{\epsilon}\right]\right] \\
&= \mathbb{E}\left[\boldsymbol{\epsilon}^T\mathbf{A}\boldsymbol{\epsilon}\right], \qquad (16.23)
\end{aligned}
$$

where the first line is true because $\mathbb{E}[\boldsymbol{\epsilon}\boldsymbol{\epsilon}^T]=\mathbf{I}$. The second line derives from the properties of the expectation operator. The third line comes from the linearity of the trace operator. The fourth line is due to the invariance of the trace to cyclic permutation. The final line is true because the argument in the fourth line is now a scalar. We can now estimate the trace by drawing samples $\boldsymbol{\epsilon}_i$ from $Pr(\boldsymbol{\epsilon})$:

$$
\begin{aligned}
\text{trace}[\mathbf{A}] &= \mathbb{E}\left[\boldsymbol{\epsilon}^T\mathbf{A}\boldsymbol{\epsilon}\right] \\
&\approx \frac{1}{I}\sum_{i=1}^{I}\boldsymbol{\epsilon}_i^T\mathbf{A}\boldsymbol{\epsilon}_i. \qquad (16.24)
\end{aligned}
$$

In this way, we can approximate the trace of the powers of the Taylor expansion (equation 16.22) and evaluate the log probability.

16.4 Multi-scale flows

In normalizing flows, the latent space $\mathbf{z}$ must be the same size as the data space $\mathbf{x}$ but we know that natural datasets can often be described by fewer underlying variables. At

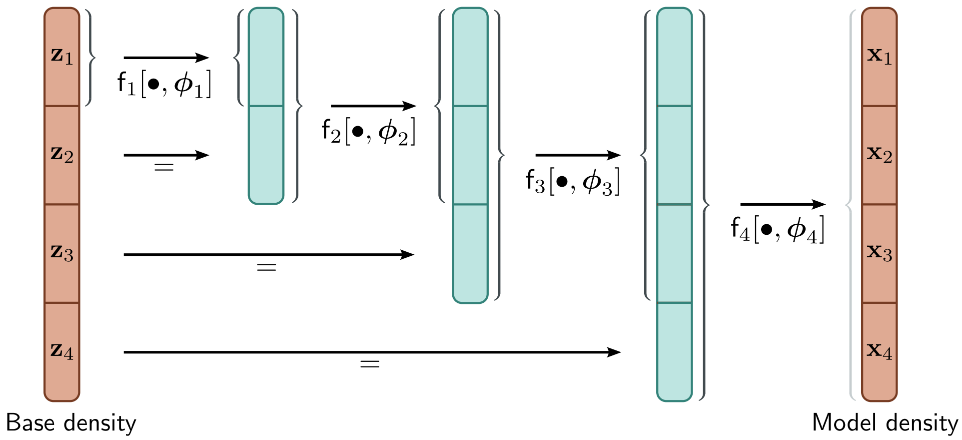

Figure 16.10 Multiscale flows. The latent space $\mathbf{z}$ must be the same size as the model density in normalizing flows. However, it can be partitioned into several components, and these can be gradually introduced at different layers. This makes both density estimation and sampling faster.

some point we have to introduce all of these variables, but it is inefficient to pass them through the entire network. The leads to the idea of *multi-scale flows* (figure 16.10).

In the generative direction, multi-scale flows partition the latent vector into $\mathbf{z} = [\mathbf{z}_1, \mathbf{z}_2, \ldots \mathbf{z}_N]$. The first partition $\mathbf{z}_1$ is processed by a series of reversible layers with the same dimension as $\mathbf{z}_1$, until at some point $\mathbf{z}_2$ is appended and is combined with the first partition. This continues until the network is the same size as the data $\mathbf{x}$. In the normalizing direction, the network starts at the full dimension of $\mathbf{x}$ but when it reaches the point where $\mathbf{z}_n$ was added, this is assessed against the base distribution.

16.5 Applications

In this section, we consider three applications of normalizing flows. First, we consider modeling probability densities. Second, we consider the GLOW model, which can be used to synthesize images. Finally, we discuss how normalizing flows can be used to approximate other distributions.

16.5.1 Modeling densities

Of the four generative models discussed in this book, normalizing flows is the only model that can compute the exact log-likelihood of a new sample. Generative adversarial

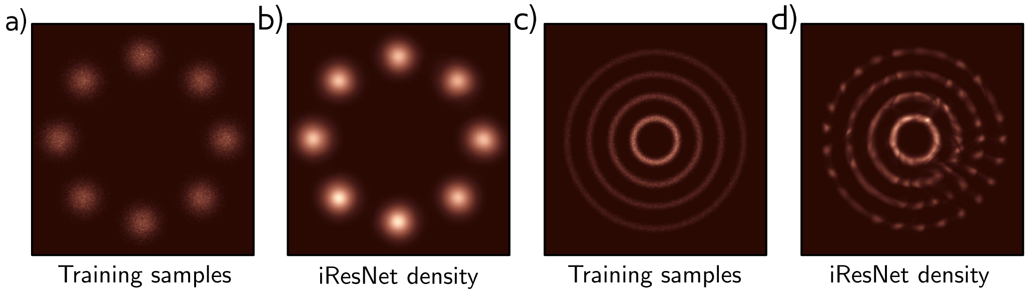

Figure 16.11 Modeling densities. a) Toy 2D data samples. b) Modeled density using iResNet. c-d) Second example. Adapted from Behrmann et al. (2019)

networks are not probabilistic, and both variational autoencoders and diffusion models can only return a lower bound on the likelihood.[2] Figure 16.11 depicts the estimated probability distributions in two toy problems using i-ResNet. One application of density estimation is anomaly detection; the data distribution of a clean dataset is described using a normalizing flow model. New examples with low probability are flagged as outliers. However, caution must be used as there may exist outliers with high probability that do not fall in the typical set (see figure 8.13).

16.5.2 Synthesis

Generative flows or *GLOW* is a normalizing flow model that can create high-fidelity images (figure 16.12) and uses many of the ideas from this chapter. It is easiest understood in the normalizing direction. GLOW starts with a $256 \times 256 \times 3$ tensor containing an RGB image. It uses coupling layers, in which the channels are partitioned into two halves. The second half is subject to a different affine transform at each spatial position, where the parameters of the affine transformation are computed by a 2D convolutional neural network run on the other half of the channels. The coupling layers are alternated with 1×1 convolutions, parameterized as LU decompositions which mix the channels.

Periodically, the resolution is halved by turning each 2×2 patch into a single position with four times as many channels. This is a multi-scale flow in which a portion of the channels are periodically removed and directly become part of the latent vector $\mathbf{z}$. Since images are discrete distributions (due to the quantization of RGB values), noise is added to the inputs to prevent the likelihood increasing without bound during learning. This is known as *dequantization*.

To sample more realistic images, the GLOW model samples from the base density raised to a positive power. This chooses examples that are closer to the center of the

[2]The lower bound for diffusion models can actually be better than the exact computation in normalizing flows, but computation is much slower (see chapter 18).

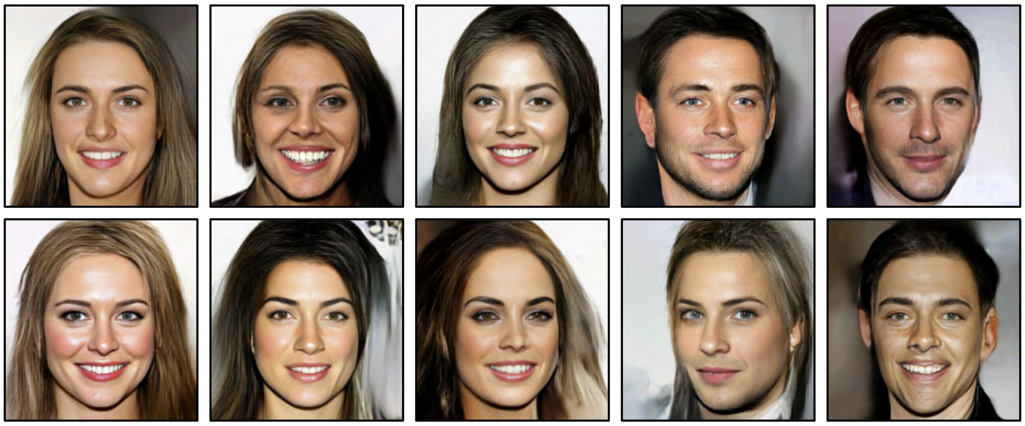

Figure 16.12 Samples from GLOW trained on the CelebA HQ dataset (Karras et al., 2018). The samples are of reasonable quality, although GANs and diffusion models produce superior results. Adapted from Kingma & Dhariwal (2018).

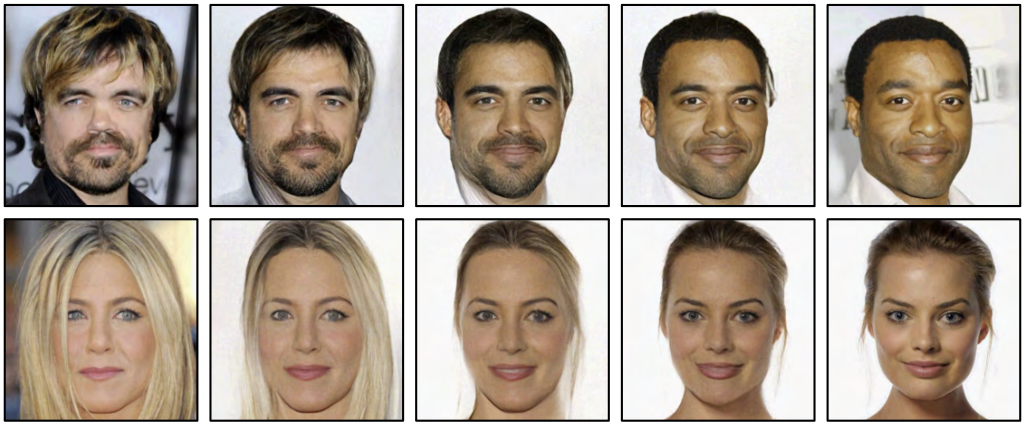

Figure 16.13 Interpolation using GLOW model. The left and right images are real people. The intermediate images were computed by projecting the real images to the latent space, interpolating, and then projecting the interpolated points back to image space. Adapted from Kingma & Dhariwal (2018).

density, rather than from the tails. This is a similar to the truncation trick in GANs (figure 15.10). Notably, the samples are not as good as those from GANs or diffusion models. It is unknown whether this is due to a fundamental restriction associated with invertible layers, or merely because less research effort has been invested in this goal.

Figure 16.13 shows an example of interpolation using GLOW. Two latent vectors are computed by transforming two real images in the normalizing direction. Intermediate points between these latent vectors are computed by linear interpolation, and these are projected back to image space using the network in the generative direction. The result is a set of images that interpolate realistically between the two real ones.

16.5.3 Approximating other density models

Normalizing flows can also learn to generate samples that approximate an existing density which is easy to evaluate but difficult to sample from. In this context, we denote the normalizing flow $Pr(\mathbf{x}|\boldsymbol{\phi})$ as the *student* and the target density $q(\mathbf{x})$ as the *teacher*.

To make progress, we generate samples $\mathbf{x}_i$ from the student. Since we generated these samples ourselves, we know their corresponding latent variables $\mathbf{z}_i$ and we can calculate their likelihood in the student model without inversion. Thus we can use a model like a masked-autoregressive flow where inversion is slow. We define a loss function based on the reverse KL divergence that encourages the student and teacher likelihood to be identical and use this to train the student model (figure 16.14):

$$\boldsymbol{\phi} = \text{argmin}\left[\text{KL}\left[\sum_{i=1}^{I} Pr(\mathbf{x}_i, \boldsymbol{\phi})\middle|\middle|\sum_{i=1}^{I} q(\mathbf{x}_i)\right]\right]. \tag{16.25}$$

This approach contrasts with the typical use of normalizing flows to build a probability model $Pr(\mathbf{x}_i, \boldsymbol{\phi})$ of data that came from an unknown distribution with samples $\mathbf{x}_i$ using maximum likelihood which relies on the cross-entropy term from the forward KL divergence (section 5.7):

$$\boldsymbol{\phi} = \text{argmin}\left[\text{KL}\left[\sum_{i=1}^{I} \delta[\mathbf{x}-\mathbf{x}_i]\middle|\middle|Pr(\mathbf{x}_i, \boldsymbol{\phi})\right]\right]. \tag{16.26}$$

A similar trick is used to exploit normalizing flows to model the posterior in variational auto-encoders (see chapter 17).

16.6 Summary

Normalizing flows transform a base distribution (usually a normal distribution) to create a new density. They have the advantage that they can both evaluate the likelihood of samples exactly and generate new samples. However, they have the architectural constraint that each layer must be invertible; we need the forward transformation to generate samples, and the backward transformation to evaluate the likelihoods.

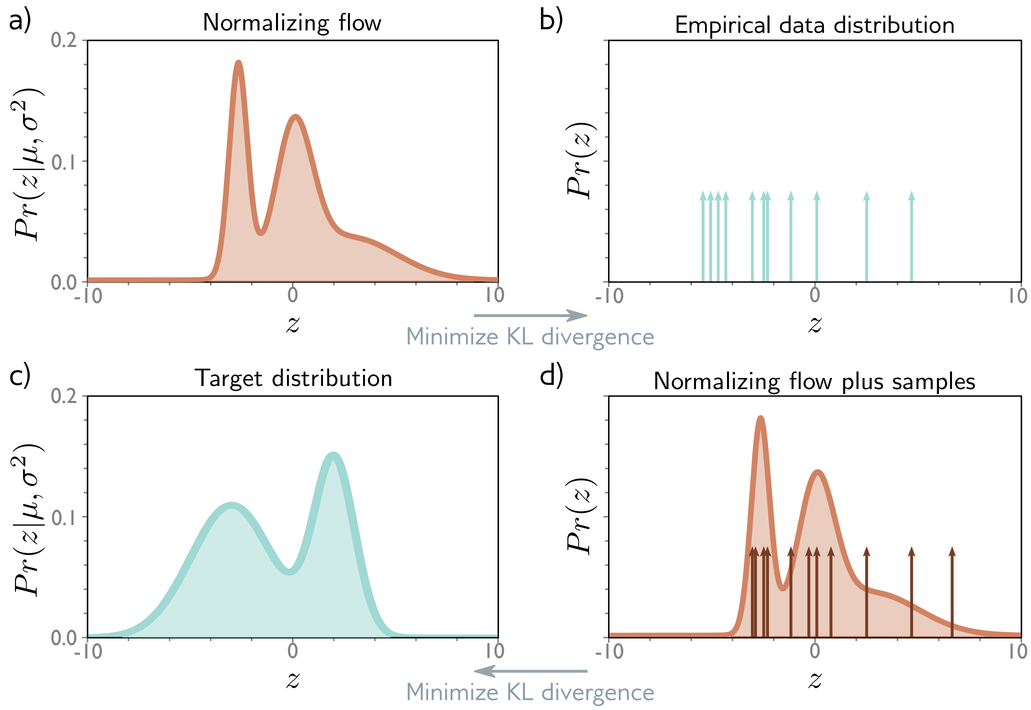

Figure 16.14 Approximating density models. a) Normally we modify the flow model to minimize the KL divergence to b) the empirical data distribution. This is equivalent to maximum likelihood fitting (see section 5.7). c) However, in some cases, we have a target model where we can evaluate the density (but perhaps not draw samples efficiently), and wish to train a normalizing flow to approximate it. d) Here we minimize the reverse KL divergence between samples from the normalizing flows model and the target density.

In practice, it's important that the Jacobian can be estimated efficiently to evaluate the likelihood. This is particularly important as the likelihood is used to learn the density. However, invertible layers are still useful in their own right even when the Jacobian cannot be estimated efficiently; they reduce the memory requirements of training a K-layer network from $\mathcal{O}[K]$ to $\mathcal{O}[1]$.

This chapter reviewed invertible network layers or flows. We considered linear flows and elementwise flows, which are simple but insufficiently expressive. Then we described more complex flows such as coupling flows, autoregressive flows, and residual flows. Finally, we showed how normalizing flows can be used to estimate likelihoods, generate and interpolate between images, and approximate other distributions.

Notes

Normalizing flows were first introduced by Rezende & Mohamed (2015), but had intellectual antecedents in the work of Tabak & Vanden-Eijnden (2010), Tabak & Turner (2013), and Rippel & Adams (2013). Reviews of normalizing flows can be found in Kobyzev et al. (2020) and Papamakarios et al. (2021). Kobyzev et al. (2020) presented a quantitative comparison of many normalizing flow approaches and concluded that the Flow++ model (a coupling flow with a novel elementwise transformation and other innovations) performed best at the time.

Invertible network layers: Invertible layers decrease the memory requirements of the back-propagation algorithm; the activations in the forward pass no longer need to be stored, since they can be recomputed in the backward pass. In addition to the regular network layers and residual layers (Gomez et al., 2017; Jacobsen et al., 2018) discussed in this chapter, invertible layers have been developed for graph neural networks (Li et al., 2021a), recurrent neural networks (MacKay et al., 2018), masked convolutions (Song et al., 2019), U-Nets (Brügger et al., 2019; Etmann et al., 2020), and transformers (Mangalam et al., 2022).

Radial and planar flows: The original normalizing flow paper (Rezende & Mohamed, 2015) used planar flows (which contract or expand the distribution along certain dimensions) and radial flows (which expand or contract around a certain point). Inverses for these flows can't be computed easily, but they are useful for approximating distributions where sampling is slow or where the likelihood can only be evaluated up to an unknown scaling factor (figure 16.14).

Applications: Applications include image generation (Ho et al., 2019; Kingma & Dhariwal, 2018), noise modeling (Abdelhamed et al., 2019), video generation (Kumar et al., 2019b), audio generation (Esling et al., 2019; Kim et al., 2018; Prenger et al., 2019), graph generation (Madhawa et al., 2019), image classification (Kim et al., 2021; Mackowiak et al., 2021), image steganography (Lu et al., 2021), super-resolution (Yu et al., 2020; Wolf et al., 2021; Liang et al., 2021), style transfer (An et al., 2021), motion style transfer (Wen et al., 2021), 3D shape modeling (Paschalidou et al., 2021), compression (Zhang et al., 2021b), sRGB to RAW image conversion (Xing et al., 2021), denoising (Liu et al., 2021b), anomaly detection (Yu et al., 2021), image-to-image translation (Ardizzone et al., 2020), synthesizing cell microscopy images under different molecular interventions (Yang et al., 2021), and light transport simulation (Müller et al., 2019b). For applications using image data, noise must be added before learning since the inputs are quantized and hence discrete (see Theis et al., 2016).

Rezende & Mohamed (2015) used normalizing flows to model the posterior in VAEs. Abdal et al. (2021) used normalizing flows to model the distribution of attributes in the latent space of StyleGAN and then used these distributions to systematically change specified attributes in real images. Wolf et al. (2021) use normalizing flows to learn the conditional image of a noisy input image given a clean one and hence simulate noisy data that can be used to train denoising or super-resolution models.

Normalizing flows have also found diverse uses in physics (Kanwar et al., 2020; Köhler et al., 2020; Noé et al., 2019; Wirnsberger et al., 2020; Wong et al., 2020), natural language processing (Tran et al., 2019; Ziegler & Rush, 2019; Zhou et al., 2019; He et al., 2018; Jin et al., 2019), and reinforcement learning (Schroecker et al., 2019; Haarnoja et al., 2018a; Mazoure et al., 2020; Ward et al., 2019; Touati et al., 2020).

Linear flows: Diagonal linear flows can represent normalization transformations like BatchNorm (Dinh et al., 2016) and ActNorm (Kingma & Dhariwal, 2018). Tomczak & Welling (2016) investigated combining triangular matrices and using orthogonal transformations parameterized by the Householder transform. Kingma & Dhariwal (2018) proposed the LU parameterization described in section 16.5.2. Hoogeboom et al. (2019b) proposed using the QR decomposition instead, which does not require pre-determined permutation matrices. Convolutions are linear transformations (figure 10.4) that are widely used in deep learning but their inverse and determinant are not straightforward to compute. Kingma & Dhariwal (2018) used 1×1 convolutions but this is effectively a full linear transformation that is applied separately at each position. Zheng et al. (2017) introduced ConvFlow, which was restricted to 1D convolutions. Hoogeboom et al. (2019b) provided more general solutions for modeling 2D convolutions either by stacking together masked autoregressive convolutions or by operating in the Fourier domain.

Elementwise flows and coupling functions: Elementwise flows transform each variable independently using the same function (but with different parameters for each variable). The same flows can be used to form the coupling functions in coupling and auto-regressive flows, in which case, their parameters depend on the preceding variables. To be invertible, these functions must be monotone.

An additive coupling function (Dinh et al., 2015) just adds an offset to the variable. Affine coupling functions scale the variable and add an offset and were used by Dinh et al. (2015), Dinh et al. (2016), Kingma & Dhariwal (2018), Kingma et al. (2016), and Papamakarios et al. (2017). Ziegler & Rush (2019) propose the nonlinear squared flow which is an invertible ratio of polynomials with five parameters. Continuous mixture CDFs (Ho et al., 2019) apply a monotone transformation based on the cumulative density function (CDF) of a mixture of K logistics, post-composed by an inverse logistic sigmoid, and scaled and offset.

The piecewise-linear coupling function (figure 16.5) was developed by Müller et al. (2019b). Since then, systems based on cubic splines (Durkan et al., 2019a), and rational quadratic splines (Durkan et al., 2019b) have been proposed. Huang et al. (2018a) introduced neural autoregressive flows, in which the function is represented by a neural network that produces a monotonic function. A sufficient condition is that the weights are all positive and the activation functions are monotone. Unfortunately, it is hard to train a network with the constraint that the weights are positive and this led to unconstrained monotone neural networks (Wehenkel & Louppe, 2019) which model strictly positive functions and then integrate them numerically to get a monotone function. Jaini et al. (2019) construct positive functions that can be integrated in closed-form based on a classic result that all positive single-variable polynomials are the sum of squares of polynomials. Finally, Dinh et al. (2019) investigated piecewise monotonic coupling functions.

Coupling flows: Dinh et al. (2015) introduced coupling flows in which the dimensions were split in half (figure 16.6). Dinh et al. (2016) introduced *RealNVP* which partitioned the image input by taking alternating pixels or blocks of channels. Das et al. (2019) proposed selecting features for the propagated part based on the magnitude of the derivatives. Dinh et al. (2016) interpreted multiscale flows (in which dimensions are gradually introduced) as coupling flows in which the parameters $\boldsymbol{\phi}$ have no dependence on the other half of the data. Kruse et al. (2021) introduce a hierarchical formulation of coupling flows in which each partition is recursively divided into two. GLOW (figures 16.12–16.13) was designed by Kingma & Dhariwal (2018) and uses coupling flows, as does NICE (Dinh et al., 2015), RealNVP (Dinh et al., 2016), FloWaveNet (Kim et al., 2018), WaveGlOW (Prenger et al., 2019), and Flow++ (Ho et al., 2019).

Autoregressive flows: Kingma et al. (2016) used autoregressive models for normalizing flows. Germain et al. (2015) developed a general method for masking previous variables and this was exploited by Papamakarios et al. (2017) to compute all of the outputs in the forward direction simultaneously in masked autoregressive flows. Kingma et al. (2016) introduced the inverse autoregressive flow. Parallel WaveNet (Van den Oord et al., 2018) distilled WaveNet (Van den Oord et al., 2016a), which is a different type of generative model for audio, into an inverse autoregressive flow so that sampling would be fast (see figure 16.14c-d).

Residual flows: Residual flows are based on residual networks (He et al., 2016a). RevNets (Gomez et al., 2017) and iRevNets (Jacobsen et al., 2018) divide the input into two sections (figure 16.8) each of which passes through a residual network. These networks are invertible, but the Jacobian cannot be computed easily. The residual connection can be interpreted as the discretization of an ordinary differential equation and this perspective led to different invertible architectures (Chang et al., 2018, 2019a). However, the Jacobian of these networks could still not be computed efficiently. Behrmann et al. (2019) noted that the network can be inverted using fixed point iterations if its Lipschitz constant was less than one. This led to iResNet, in which the Jacobian can be estimated using Hutchinson's trace estimator (Hutchinson, 1989). Chen et al. (2019) removed the bias induced by the truncation of the power series in equation 16.22 by using the Russian Roulette estimator.

Infinitesimal flows: If residual networks can be viewed as a discretization of an ordinary differential equation (ODE), then the next logical step is to represent the change in the variables directly by an ODE. The neural ODE was explored by Chen et al. (2018e) and exploits standard methods for forward and backward propagation in ODEs. The Jacobian is no longer required to compute the likelihood; this is represented by a different ODE in which the change in log probability is related to the trace of the derivative of the forward propagation. Grathwohl et al. (2019) used the Hutchinson estimator to estimate the trace and simplified this further. Finlay et al. (2020) added regularization terms to the loss function that make training easier, and Dupont et al. (2019) augmented the representation to allow the neural ODE to represent a broader class of diffeomorphisms. Tzen & Raginsky (2019) and Peluchetti & Favaro (2020) replaced the ODEs with stochastic differential equations.

Universality: The universality property refers to the ability of a normalizing flow to model any probability distribution arbitrarily well. Some flows (e.g., planar, elementwise) do not have this property. Autoregressive flows can be shown to have the universality property when the coupling function is a neural monotone network (Huang et al., 2018a), based on monotone polynomials (Jaini et al., 2020), or based on splines (Kobyzev et al., 2020). For dimension D, a series of D coupling flows can form an autoregressive flow. To understand why, note that the partitioning into two parts $\mathbf{h}_1$ and $\mathbf{h}_2$ means that at any given layer $\mathbf{h}_2$ depends only on the previous variables (figure 16.6). Hence, if we increase the size of $\mathbf{h}_1$ by one at every layer we can reproduce an autoregressive flow and the result is universal. It is not known whether coupling flows can be universal with less than D layers. However, they work well in practice (e.g., GLOW), without the need for this induced autoregressive structure.

Other work: Active areas of research in normalizing flows include the investigation of *discrete flows* (Hoogeboom et al., 2019a; Tran et al., 2019), normalizing flows on non-Euclidean manifolds (Gemici et al., 2016; Wang & Wang, 2019), and *equivariant flows* (Köhler et al., 2020; Rezende et al., 2019) which aim to create densities that are invariant to families of transformations.

Problems

Problem 16.1 Consider transforming a uniform base density defined on $z \in [0, 1]$ using the function $x = \mathrm{f}[z] = z^2$. Find an expression for the transformed distribution $Pr(x)$.

Problem 16.2 Consider transforming a standard normal distribution:

$$Pr(z) = \frac{1}{\sqrt{2\pi}} \exp\left[\frac{x^2}{2}\right], \tag{16.27}$$

with the function:

$$x = \mathrm{f}[z] = \frac{1}{1+\exp[-z]}. \tag{16.28}$$

Find an expression for the transformed distribution $Pr(x)$.

Problem 16.3 Write expressions for the Jacobian of the inverse mapping $\mathbf{z} = \mathbf{f}^{-1}[\mathbf{x}, \boldsymbol{\phi}]$ and the absolute determinant of that Jacobian in forms similar to equation 16.6 and 16.7.

Problem 16.4 Compute the inverse and the determinant of the following matrices by hand:

$$\boldsymbol{\Omega}_1 = \begin{bmatrix} 2 & 0 & 0 & 0 \\ 0 & -5 & 0 & 0 \\ 0 & 0 & 1 & 0 \\ 0 & 0 & 0 & 2 \end{bmatrix} \qquad\qquad \boldsymbol{\Omega}_2 = \begin{bmatrix} 1 & 0 & 0 & 0 \\ 2 & 4 & 0 & 0 \\ 1 & -1 & 2 & 0 \\ 4 & -2 & -2 & 1 \end{bmatrix}. \tag{16.29}$$

Problem 16.5 Consider a random variable $\mathbf{z}$ with mean $\boldsymbol{\mu}$ and variance $\boldsymbol{\Sigma}$ that is transformed as $\mathbf{x} = \mathbf{A}\mathbf{z} + \mathbf{b}$. Show that $\mathbb{E}[\mathbf{x}] = \mathbf{A}\boldsymbol{\mu} + \mathbf{b}$ and $\mathrm{Var}[\mathbf{x}] = \mathbf{A}\boldsymbol{\Sigma}\mathbf{A}^T$.

Problem 16.6 Prove that if $\mathbf{x} = \mathbf{f}[\mathbf{z}] = \mathbf{A}\mathbf{z} + \mathbf{b}$ and $Pr(\mathbf{z}) = \mathrm{Norm}_{\mathbf{z}}[\boldsymbol{\mu}, \boldsymbol{\Sigma}]$, then $Pr(\mathbf{x}) = \mathrm{Norm}_{\mathbf{x}}[\mathbf{A}\boldsymbol{\mu} + \mathbf{b}, \mathbf{A}\boldsymbol{\Sigma}\mathbf{A}^T]$ using the relation:

$$Pr(\mathbf{x}) = \mathrm{Pr}(\mathbf{z}) \cdot \left| \frac{\partial \mathbf{f}^{-1}[\mathbf{x}]}{\partial \mathbf{x}} \right|, \tag{16.30}$$

where $\mathbf{z} = \mathbf{f}^{-1}[\mathbf{x}, \boldsymbol{\phi}]$ and the result from problem 16.5.

Problem 16.7 The Leaky ReLU is defined as:

$$\mathrm{LReLU}[z] = \begin{cases} 0.1z & z < 0 \\ z & z \geq 0 \end{cases}. \tag{16.31}$$

Write an expression for the inverse of the leaky ReLU. Write an expression for the inverse absolute determinant of the Jacobian $|\partial \mathbf{f}[\mathbf{z}]/\partial \mathbf{z}|^{-1}$ for an elementwise transformation $\mathbf{x} = \mathbf{f}[z]$ of the multivariate variable $\mathbf{z}$ where:

$$\mathbf{f}[\mathbf{z}] = \Big[\mathrm{LReLU}[z_1, \boldsymbol{\phi}], \mathrm{LReLU}[z_2, \boldsymbol{\phi}], \ldots \mathrm{LReLU}[z_D, \boldsymbol{\phi}]\Big]^T. \tag{16.32}$$

Problem 16.8 Find the inverse $\mathrm{f}^{-1}[h', \boldsymbol{\phi}]$ of the piecewise linear function $\mathrm{f}[h, \boldsymbol{\phi}]$ defined in equation 16.12, for the domain $h' \in [0, 1]$. Consider applying this nonlinear function elementwise to an input $\mathbf{h} = [h_1, h_2, \ldots h_D]^T$ so that $\mathbf{f}[\mathbf{h}] = [\mathrm{f}[h_1, \boldsymbol{\phi}], \mathrm{f}[h_2, \boldsymbol{\phi}], \ldots, \mathrm{f}[h_D, \boldsymbol{\phi}]]$ What is the Jacobian $\partial \mathrm{f}[\mathbf{h}]/\partial \mathbf{h}$? What is the determinant of the Jacobian?

Problem 16.9 Consider constructing an element-wise flow based on a conical combination of sinusoids in equally spaced bins:

$$\mathbf{h}' = \mathrm{f}[h, \boldsymbol{\phi}] = \sin\left[\frac{Kh - b \times \pi}{2}\right] \phi_b + \sum_{k=1}^{b} \phi_k, \tag{16.33}$$

where $b = \lfloor Kh \rfloor$ is the bin that h falls into and the parameters $\boldsymbol{\phi}_k$ are positive and sum to one. Consider the case where $K = 5$ and $\phi_1 = 0.1, \phi_2 = 0.2, \phi_3 = 0.5, \phi_4 = 0.1, \phi_5 = 0.1$. Draw the function $\mathrm{f}[h, \boldsymbol{\phi}]$. Draw the inverse function $\mathrm{f}^{-1}[h', \boldsymbol{\phi}]$.

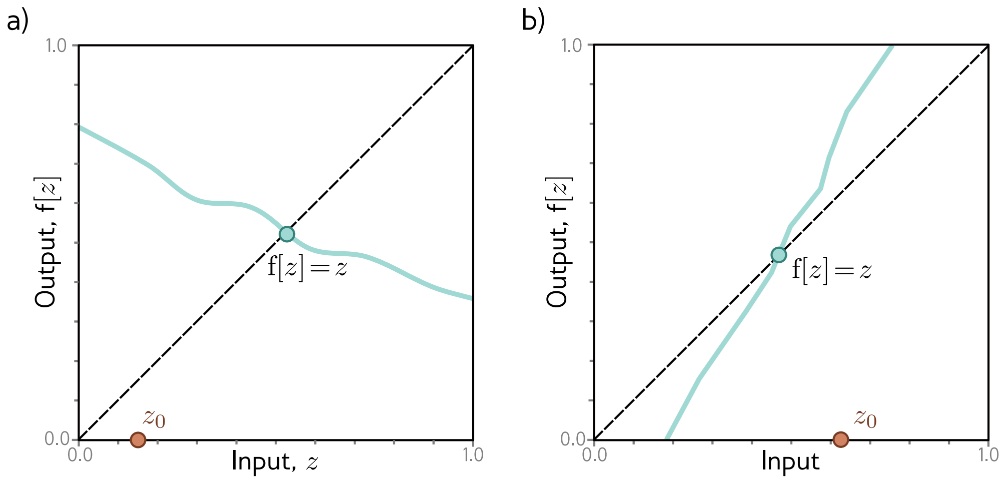

Figure 16.15 Functions for problem 16.11.

Problem 16.10 Draw a picture of the structure of the Jacobian for the forward mapping of the residual flow in figure 16.8 for the cases where $\mathbf{f}_1[\bullet, \boldsymbol{\phi}_1]$ and $\mathbf{f}_2[\bullet, \boldsymbol{\phi}_2]$ are (i) a fully connected neural network, (ii) an elementwise flow.

Problem 16.11 For each of the functions in figure 16.15, describe the behavior if we perform a fixed point iteration $z \leftarrow \mathrm{f}[z]$ starting at point z_0. For each case, indicate whether the iterations will converge to the fixed point $\mathrm{f}[z] = z$.

Problem 16.12 Write out the expression for the KL divergence in equation 16.25. Why does it not matter that we can only evaluate the posterior probability up to a scaling factor κ? Does the network have to be invertible to minimize this loss function? Explain your reasoning.

Chapter 17

Variational autoencoders

Generative adversarial networks learn a mechanism for creating samples that are statistically indistinguishable from the training data $\{\mathbf{x}_i\}$. In contrast, *variational autoencoders*, or *VAEs* are *probabilistic generative models*; like normalizing flows, they aim to learn a distribution $Pr(\mathbf{x})$ over the data (see figure 14.2). After training, it is possible to draw (generate) samples from this distribution. However, the properties of the VAE mean that it is unfortunately *not* possible to evaluate the probability of new examples $\mathbf{x}^*$ exactly.

It is common to talk about the VAE as if it *is* the model of $Pr(\mathbf{x})$ but this is misleading; the VAE is a neural architecture that is designed to help *learn* the model for $Pr(\mathbf{x})$. The final model for $Pr(\mathbf{x})$ contains neither the "variational" nor the "autoencoder" parts and might be better described as a *nonlinear latent variable model*.

This chapter starts by introducing latent variable models in general and then considers the specific case of the nonlinear latent variable model. It will become clear that maximum likelihood learning of this model is not straightforward. Nevertheless, it is possible to define a lower bound on the likelihood and the VAE architecture approximates this bound using a Monte Carlo (sampling) method. The chapter concludes by presenting some applications of the VAE.

17.1 Latent variable models

Latent variable models take an indirect approach to describing a probability distribution $Pr(\mathbf{x})$ over a multi-dimensional variable $\mathbf{x}$. Instead of directly writing the expression for $Pr(\mathbf{x})$, they model a joint distribution $Pr(\mathbf{x}, \mathbf{z})$ of the data $\mathbf{x}$ and an unobserved *hidden* or *latent variable* $\mathbf{z}$. They then describe the probability of $Pr(\mathbf{x})$ as a marginalization of this joint probability so that:

Appendix B.1.2 marginalization

$$Pr(\mathbf{x}) = \int Pr(\mathbf{x}, \mathbf{z}) d\mathbf{z}. \tag{17.1}$$

Appendix B.1.3 conditional probability

Typically, the joint probability $Pr(\mathbf{x}, \mathbf{z})$ is broken down into the product of the *likelihood* $Pr(\mathbf{x}|\mathbf{z})$ of the data with respect to the latent variables and the *prior* $Pr(\mathbf{z})$:

$$Pr(\mathbf{x}) = \int Pr(\mathbf{x}|\mathbf{z})Pr(\mathbf{z})d\mathbf{z}. \tag{17.2}$$

This is a rather indirect approach to describing $Pr(\mathbf{x})$ but it is useful because relatively simple expressions for $Pr(\mathbf{x}|\mathbf{z})$ and $Pr(\mathbf{z})$ can define complex distributions $Pr(\mathbf{x})$.

17.1.1 Example: mixture of Gaussians

The 1D mixture of Gaussians (figure 17.1a) is a simple latent variable model. Here the latent variable z is discrete and the prior $Pr(z)$ is a categorical distribution with one probability λ_n for each possible value of z. The likelihood $Pr(x|z=n)$ of the data x given that latent variable z takes value n is a Gaussian with a mean μ_n and variance σ_n^2:

Figure 5.9 categorical distribution

Problem 17.6

$$\begin{aligned} Pr(z=n) &= \lambda_n \\ Pr(x|z=n) &= \text{Norm}_x[\mu_n, \sigma_n^2]. \end{aligned} \tag{17.3}$$

As in equation 17.2, the likelihood $Pr(x)$ is given by the marginalization over the latent variable z (figure 17.1b). Here, the latent variable is discrete and so we sum over its possible values to marginalize:

$$\begin{aligned} Pr(x) &= \sum_{n=1}^{N} Pr(x, z=n) \\ &= \sum_{n=1}^{N} Pr(x|z=n)\cdot Pr(z=n) \\ &= \sum_{n=1}^{N} \lambda_n \cdot \text{Norm}_x[\mu_n, \sigma_n^2]. \end{aligned} \tag{17.4}$$

From simple expressions for the likelihood and prior, we describe a complex multi-modal probability distribution.

17.2 Nonlinear latent variable model

In the nonlinear latent variable model, both the data $\mathbf{x}$ and the latent variable $\mathbf{z}$ are continuous and multivariate. The prior $Pr(\mathbf{z})$ is a standard multivariate normal:

$$Pr(\mathbf{z}) = \text{Norm}_{\mathbf{z}}[\mathbf{0}, \mathbf{I}]. \tag{17.5}$$

The likelihood $Pr(\mathbf{x}|\mathbf{z}, \boldsymbol{\phi})$ is also normally distributed; its mean is a nonlinear function $\mathbf{f}[\mathbf{z}, \boldsymbol{\phi}]$ of the latent variable and its covariance $\sigma^2\mathbf{I}$ is spherical:

Appendix B.3.2 Multivariate normal

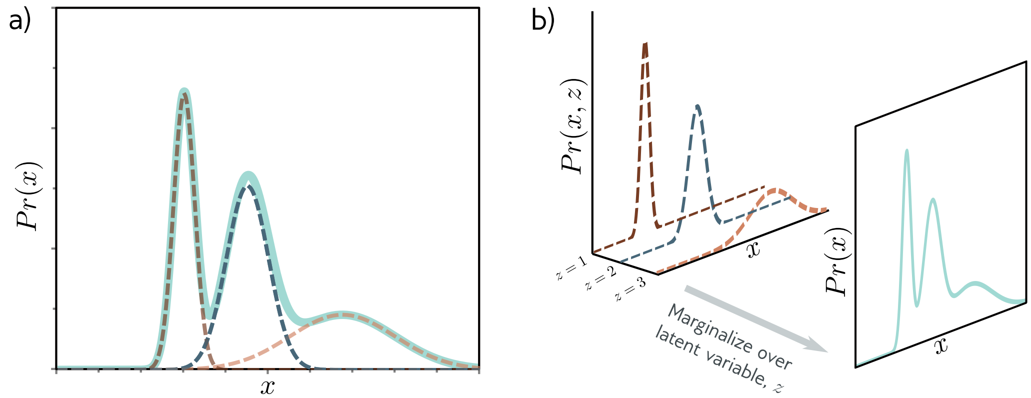

Figure 17.1 Mixture of Gaussians (MoG). a) The MoG describes a complex probability distribution (cyan curve) as a weights sum of Gaussian components (dashed curves). b) This weighted sum is the marginalization of the joint density $Pr(x, z)$ between the continuous observed data x and a discrete latent variable z.

$$Pr(\mathbf{x}|\mathbf{z}, \boldsymbol{\phi}) = \text{Norm}_{\mathbf{x}}[\mathbf{f}[\mathbf{z}, \boldsymbol{\phi}], \sigma^2\mathbf{I}]. \tag{17.6}$$

The function $\mathbf{f}[\mathbf{z}, \boldsymbol{\phi}]$ is described by a deep network with parameters $\boldsymbol{\phi}$. The latent variable $\mathbf{z}$ is smaller than the data $\mathbf{x}$. The model $\mathbf{f}[\mathbf{z}, \boldsymbol{\phi}]$ describes the important aspects of the data and the remaining unmodeled aspects are ascribed to the noise $\sigma^2\mathbf{I}$.

The data probability $Pr(\mathbf{x}|\boldsymbol{\phi})$ is found by marginalizing over the latent variable $\mathbf{z}$:

$$\begin{aligned} Pr(\mathbf{x}|\boldsymbol{\phi}) &= \int Pr(\mathbf{x}, \mathbf{z}|\boldsymbol{\phi}) d\mathbf{z} \\ &= \int Pr(\mathbf{x}|\mathbf{z}, \boldsymbol{\phi}) \cdot Pr(\mathbf{z}) d\mathbf{z} \\ &= \int \text{Norm}_{\mathbf{x}}\left[\mathbf{f}[\mathbf{z}, \boldsymbol{\phi}], \sigma^2\mathbf{I}\right] \cdot \text{Norm}_{\mathbf{z}}\left[\mathbf{0}, \mathbf{I}\right] d\mathbf{z}. \end{aligned} \tag{17.7}$$

This can be viewed as an infinite weighted sum (i.e., an infinite mixture) of Gaussians with different means, where the weights are $Pr(\mathbf{z})$ and the means are $\mathbf{f}[\mathbf{z}, \boldsymbol{\phi}]$ (figure 17.2).

17.2.1 Generation

Appendix B.4.2 Ancestral sampling

A new example $\mathbf{x}^*$ can be generated using *ancestral sampling* (figure 17.3). We draw $\mathbf{z}^*$ from the prior $Pr(\mathbf{z})$, pass this through the network $\mathbf{f}[\mathbf{z}^*, \boldsymbol{\phi}]$ to compute the mean of the likelihood $Pr(\mathbf{x}|\mathbf{z}^*, \boldsymbol{\phi})$ (equation 17.6), from which we draw $\mathbf{x}^*$. Both the prior and likelihood are normal distributions and so this is straightforward. [1]

[1] Note that this procedure can be modified to improve the sample quality by using the aggregate posterior instead of the prior (see section 17.8.2).

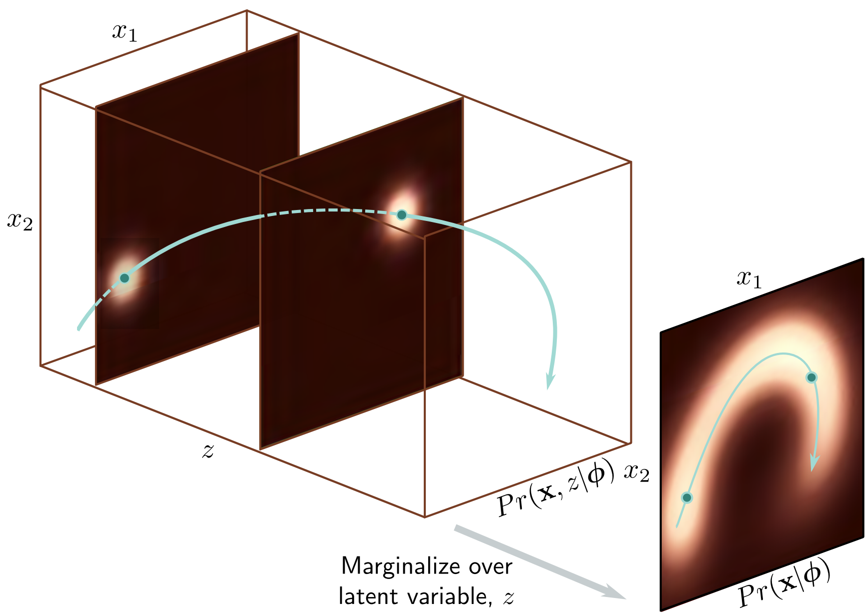

Figure 17.2 Nonlinear latent variable model. A complex 2D density $Pr(\mathbf{x})$ (right) is created as the marginalization of the joint distribution $Pr(\mathbf{x}, z)$ (left) over the latent variable z; to create $Pr(\mathbf{x})$, we integrate the 3D volume over the dimension z. For each z the distribution over $\mathbf{x}$ is a spherical Gaussian (two slices shown) with a mean $\mathbf{f}[z, \boldsymbol{\phi}]$ that is a nonlinear function of z and depends on parameters $\boldsymbol{\phi}$. The distribution $Pr(\mathbf{x})$ is a weighted sum of these spherical Gaussians.

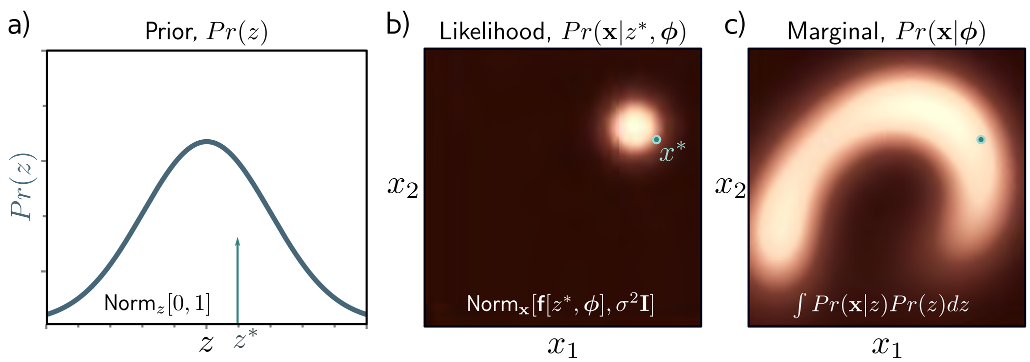

Figure 17.3 Generation from nonlinear latent variable model. a) We draw a sample z^* from the prior probability $Pr(z)$ over the latent variable. b) A sample $\mathbf{x}^*$ is then drawn from $Pr(\mathbf{x}|z^*, \boldsymbol{\phi})$. This is a spherical Gaussian with a mean that is a nonlinear function $\mathbf{f}[z, \boldsymbol{\phi}]$ of z^* and a fixed variance $\sigma^2\mathbf{I}$. c) If we repeat this process a very large number of times, we recover the density $Pr(\mathbf{x}|\boldsymbol{\phi})$.

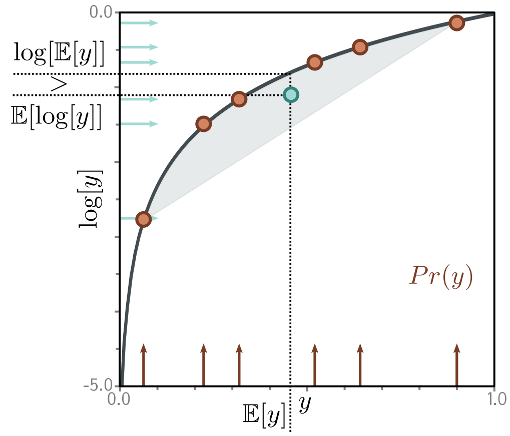

Figure 17.4 Jensen's inequality (discrete case). The logarithm (black curve) is a concave function; you can draw a straight line between any two points on the curve and this line will always lie underneath it. It follows that any convex combination (weighted sum with positive weights that sum to one) of the six points on the log function must lie in the gray region under the curve. Here, we have weighted the points equally (i.e., taken the mean) to yield the cyan point. Since this point lies below the curve, $\log[\mathbb{E}[y]] > \mathbb{E}[\log[y]]$.

17.3 Training

To train the model, we maximize the log likelihood over a training dataset $\{\mathbf{x}_i\}_{i=1}^I$ with respect to the model parameters. For simplicity, we assume that the variance term σ^2 in the likelihood expression is known and concentrate on learning $\boldsymbol{\phi}$:

$$\hat{\boldsymbol{\phi}} \quad = \quad \underset{\boldsymbol{\phi}}{\operatorname{argmax}} \left[\sum_{i=1}^{I} \log\Big[Pr(\mathbf{x}_i|\boldsymbol{\phi}) \Big] \right], \tag{17.8}$$

where:

$$Pr(\mathbf{x}_i|\boldsymbol{\phi}) \quad = \quad \int \text{Norm}_{\mathbf{x}_i}[\mathbf{f}[\mathbf{z}, \boldsymbol{\phi}], \sigma^2\mathbf{I}] \cdot \text{Norm}_{\mathbf{z}}[\mathbf{0}, \mathbf{I}] d\mathbf{z}. \tag{17.9}$$

Unfortunately, this is intractable. There is no way to integrate this expression, or to compute the value of the integral for a particular value of $\mathbf{x}$.

17.3.1 Evidence lower bound (ELBO)

To make progress, we define a *lower bound* on the log likelihood. This is a function that is always less than or equal to the log likelihood for a given value of $\boldsymbol{\phi}$ and will also depend on some other parameters $\boldsymbol{\theta}$. Eventually, we will build a network to compute this lower bound and optimize it. To define this lower bound, we need *Jensen's inequality.*

17.3.2 Jensen's inequality

Appendix C.3
Concave functions

Jensen's inequality says that a *concave* function $g[\bullet]$ of the expectation of the data y is

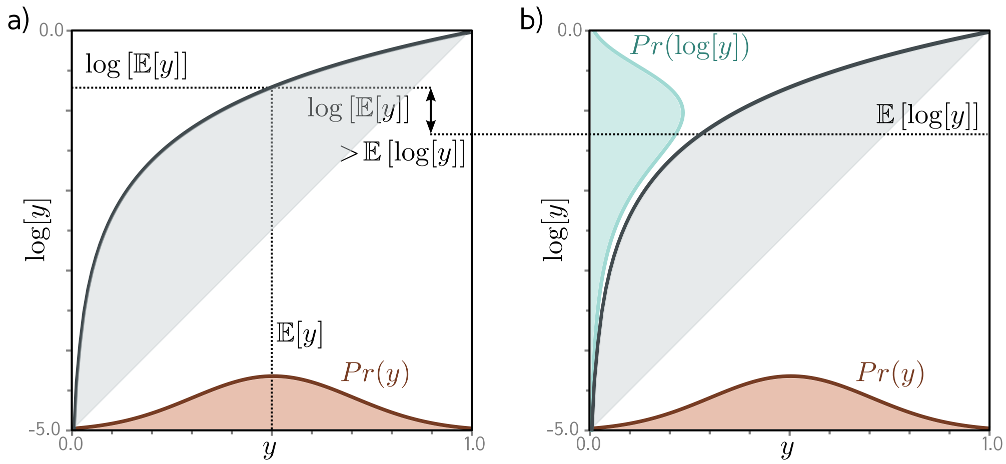

Figure 17.5 Jensen's inequality (continuous case). More generally, Jensen's inequality says that, for a concave function, computing the expectation of a distribution $Pr(y)$ and passing it through the function gives a result that is always greater than or equal to transforming the variable y by the function and then computing the expectation of the new variable. In the case of the logarithm we have $\log[\mathbb{E}[y]] \geq \mathbb{E}[\log[y]]$. The left-hand side of the figure corresponds to the left-hand side of this inequality and the right-hand side of the figure to the right-hand side. One way of thinking about this is to consider taking a convex combination of all of the points in the orange probability distribution over y. By the logic of figure 17.4, this must lie under the curve. Alternately, we can think about the concave function as compressing the high values of y relative to the low values, so the expected value is lower when we pass y through the function first.

greater than or equal to the expectation of the function of the data:

$$g[\mathbb{E}[y]] \geq \mathbb{E}[g[y]]. \tag{17.10}$$

In our case, the concave function is the logarithm so we have:

Problems 17.1-17.2

$$\log[\mathbb{E}[y]] \geq \mathbb{E}[\log[y]], \tag{17.11}$$

or writing out the expression for the expectation in full we have:

$$\log\left[\int Pr(y)y dy\right] \geq \int Pr(y)\log[y]dy. \tag{17.12}$$

This is explored in figures 17.4-17.5. In fact, the slightly more general statement is true:

$$\log\left[\int Pr(y)h[y]dy\right] \geq \int Pr(y)\log[h[y]]dy. \tag{17.13}$$

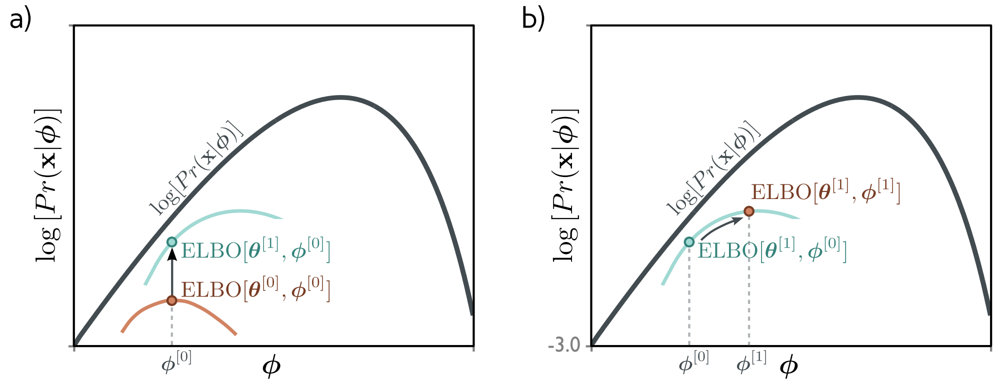

Figure 17.6 Evidence lower bound (ELBO). The goal is to maximize the log likelihood $\log[Pr(\mathbf{x}|\boldsymbol{\phi})]$ (black curve) with respect to the parameters $\boldsymbol{\phi}$. The ELBO is a function that lies everywhere below the log likelihood. It is a function of both $\boldsymbol{\phi}$ and a second set of parameters $\boldsymbol{\theta}$. For fixed $\boldsymbol{\theta}$ we get a function of $\boldsymbol{\phi}$ (two colored curves for different values of $\boldsymbol{\theta}$). Consequently, we can get increase the log likelihood by either improving the ELBO with respect to a) the new parameters $\boldsymbol{\theta}$ (moving from colored curve to colored curve) or b) the original parameters $\boldsymbol{\phi}$ (moving along the current colored curve).

where $h[y]$ is a function of y. This follows because $h[y]$ is another random variable with a new distribution. Since we never specified $Pr(y)$, the relation remains true.

17.3.3 Deriving the bound

We now use Jensen's inequality to derive the lower bound for the log likelihood. We start by multiplying and dividing the log likelihood by an arbitrary probability distribution $q(\mathbf{z})$ over the latent variables:

$$\begin{aligned}\log[Pr(\mathbf{x}|\boldsymbol{\phi})] &= \log\left[\int Pr(\mathbf{x},\mathbf{z}|\boldsymbol{\phi})d\mathbf{z}\right] \\ &= \log\left[\int q(\mathbf{z})\frac{Pr(\mathbf{x},\mathbf{z}|\boldsymbol{\phi})}{q(\mathbf{z})}d\mathbf{z}\right], \end{aligned} \tag{17.14}$$

We then use Jensen's inequality for the logarithm (equation 17.13) to find a lower bound:

$$\log\left[\int q(\mathbf{z})\frac{Pr(\mathbf{x},\mathbf{z}|\boldsymbol{\phi})}{q(\mathbf{z})}d\mathbf{z}\right] \geq \int q(\mathbf{z})\log\left[\frac{Pr(\mathbf{x},\mathbf{z}|\boldsymbol{\phi})}{q(\mathbf{z})}\right]d\mathbf{z}, \tag{17.15}$$

where the right-hand side is termed the *evidence lower bound* or *ELBO*. It gets this name because $Pr(\mathbf{x}|\boldsymbol{\phi})$ is called the *evidence* in the context of Bayes' rule (equation 17.19).

In practice, the distribution $q(\mathbf{z})$ has parameters $\boldsymbol{\theta}$, so the ELBO can be written as:

$$\mathrm{ELBO}[\boldsymbol{\theta}, \boldsymbol{\phi}] = \int q(\mathbf{z}|\boldsymbol{\theta}) \log\left[\frac{Pr(\mathbf{x}, \mathbf{z}|\boldsymbol{\phi})}{q(\mathbf{z}|\boldsymbol{\theta})}\right] d\mathbf{z}. \tag{17.16}$$

To learn the nonlinear latent variable model, we maximize this quantity as a function of both $\boldsymbol{\phi}$ and $\boldsymbol{\theta}$. The neural architecture that computes this quantity is the VAE.

17.4 ELBO properties

When first encountered, the ELBO is a somewhat mysterious object and so we now provide some intuition about its properties. Consider that the original log likelihood of the data is a function of the parameters $\boldsymbol{\phi}$ and that we want to find its maximum. For any fixed $\boldsymbol{\theta}$, the ELBO is still a function of the parameters, but one that must lie below the original likelihood function. When we change $\boldsymbol{\theta}$ we modify this function and depending on our choice, the lower bound may move closer or further from the log likelihood. When we change $\boldsymbol{\phi}$ we move along the lower bound function (figure 17.6).

17.4.1 Tightness of bound

The ELBO is *tight* when, for a fixed value of $\boldsymbol{\phi}$, the ELBO and the likelihood function coincide. To find the distribution $q(\mathbf{z}|\boldsymbol{\theta})$ that makes the bound tight, we factor the numerator of the log term in the ELBO using the definition of conditional probability:

Appendix B.1.3 Conditional probability

$$\begin{aligned}
\mathrm{ELBO}[\boldsymbol{\theta}, \boldsymbol{\phi}] &= \int q(\mathbf{z}|\boldsymbol{\theta}) \log\left[\frac{Pr(\mathbf{x}, \mathbf{z}|\boldsymbol{\phi})}{q(\mathbf{z}|\boldsymbol{\theta})}\right] d\mathbf{z} \\
&= \int q(\mathbf{z}|\boldsymbol{\theta}) \log\left[\frac{Pr(\mathbf{z}|\mathbf{x}, \boldsymbol{\phi})Pr(\mathbf{x}|\boldsymbol{\phi})}{q(\mathbf{z}|\boldsymbol{\theta})}\right] d\mathbf{z} \\
&= \int q(\mathbf{z}|\boldsymbol{\theta}) \log\left[Pr(\mathbf{x}|\boldsymbol{\phi})\right] d\mathbf{z} + \int q(\mathbf{z}|\boldsymbol{\theta}) \log\left[\frac{Pr(\mathbf{z}|\mathbf{x}, \boldsymbol{\phi})}{q(\mathbf{z}|\boldsymbol{\theta})}\right] d\mathbf{z} \\
&= \log[Pr(\mathbf{x}|\boldsymbol{\phi})] + \int q(\mathbf{z}|\boldsymbol{\theta}) \log\left[\frac{Pr(\mathbf{z}|\mathbf{x}, \boldsymbol{\phi})}{q(\mathbf{z}|\boldsymbol{\theta})}\right] d\mathbf{z} \\
&= \log[Pr(\mathbf{x}|\boldsymbol{\phi})] - \mathrm{D}_{KL}\big[q(\mathbf{z}|\boldsymbol{\theta})||Pr(\mathbf{z}|\mathbf{x}, \boldsymbol{\phi})\big].
\end{aligned} \tag{17.17}$$

Here, the first integral disappears between lines three and four since $\log[Pr(\mathbf{x}|\boldsymbol{\phi})]$ does not depend on $\mathbf{z}$ and the integral of the probability distribution $q(\mathbf{z}|\boldsymbol{\theta})$ is one. In the last line, we have just used the definition of the Kullback-Leibler (KL) divergence.

Appendix B.5.1 KL divergence

This equation shows that the ELBO is the original log likelihood minus the KL divergence $\mathrm{D}_{KL}\left[q(\mathbf{z}|\boldsymbol{\theta})||Pr(\mathbf{z}|\mathbf{x}, \boldsymbol{\phi})\right]$. The KL divergence is a measure of "distance" between distributions and can only take non-negative values. It follows the ELBO is a lower bound on $\log[Pr(\mathbf{x}|\boldsymbol{\phi})]$. The KL distance will be zero and the bound will be *tight* when $q(\mathbf{z}|\boldsymbol{\theta}) = Pr(\mathbf{z}|\mathbf{x}, \boldsymbol{\phi})$. This is the posterior distribution over the latent variables $\mathbf{z}$

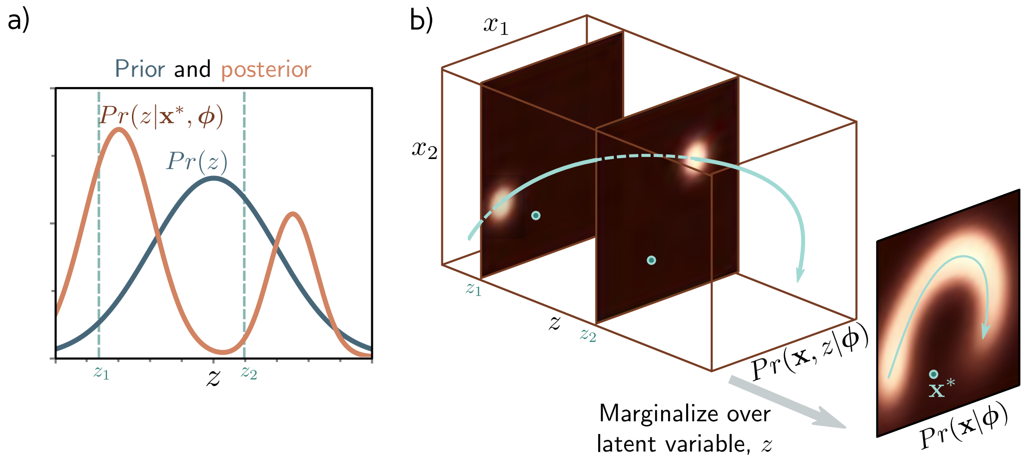

Figure 17.7 Posterior distribution over latent variable. a) The posterior distribution $Pr(z|\mathbf{x}^*, \boldsymbol{\phi})$ is the distribution over the values of the latent variable z that could be responsible for a data point $\mathbf{x}^*$. We calculate this via Bayes' rule $Pr(z|\mathbf{x}^*, \boldsymbol{\phi}) \propto Pr(\mathbf{x}^*|z, \boldsymbol{\phi})Pr(z)$. b) We compute the first term on the right-hand side (the likelihood) by assessing the probability of $\mathbf{x}^*$ against the symmetric Gaussian associated with each value of z. Here, it was more likely to have been created from z_1 than z_2. The second term is the prior probability $Pr(z)$ over the latent variable. Combining these two factors and normalizing so the distribution sums to one gives us the posterior $Pr(z|\mathbf{x}^*, \boldsymbol{\phi})$.

given observed data $\mathbf{x}$; it indicates which values of the latent variable could have been responsible for the data point (figure 17.7).

17.4.2 ELBO as reconstruction loss minus KL distance to prior

Equations 17.16 and 17.17 are two different ways to express the ELBO. A third way is to consider the bound as reconstruction error minus the distance to the prior:

$$\begin{aligned}
\text{ELBO}[\boldsymbol{\theta}, \boldsymbol{\phi}] &= \int q(\mathbf{z}|\boldsymbol{\theta}) \log \left[\frac{Pr(\mathbf{x}, \mathbf{z}|\boldsymbol{\phi})}{q(\mathbf{z}|\boldsymbol{\theta})}\right] d\mathbf{z} \\
&= \int q(\mathbf{z}|\boldsymbol{\theta}) \log \left[\frac{Pr(\mathbf{x}|\mathbf{z}, \boldsymbol{\phi})Pr(\mathbf{z})}{q(\mathbf{z}|\boldsymbol{\theta})}\right] d\mathbf{z} \\
&= \int q(\mathbf{z}|\boldsymbol{\theta}) \log \left[Pr(\mathbf{x}|\mathbf{z}, \boldsymbol{\phi})\right] d\mathbf{z} + \int q(\mathbf{z}|\boldsymbol{\theta}) \log \left[\frac{Pr(\mathbf{z})}{q(\mathbf{z}|\boldsymbol{\theta})}\right] d\mathbf{z} \\
&= \int q(\mathbf{z}|\boldsymbol{\theta}) \log \left[Pr(\mathbf{x}|\mathbf{z}, \boldsymbol{\phi})\right] d\mathbf{z} - \text{D}_{KL}\big[q(\mathbf{z}|\boldsymbol{\theta})||Pr(\mathbf{z})\big], \qquad (17.18)
\end{aligned}$$

where the joint distribution $Pr(\mathbf{x}, \mathbf{z}|\boldsymbol{\phi})$ has been factored into conditional probability $Pr(\mathbf{x}|\mathbf{z}, \boldsymbol{\phi})Pr(\mathbf{z})$ between the first and second lines and the definition of KL divergence used again in the last line.

Problem 17.3

In this formulation, the first term measures the average agreement $Pr(\mathbf{x}|\mathbf{z}, \boldsymbol{\phi})$ of the latent variable and the data. This is termed the *reconstruction loss*. The second term measures the degree to which the auxiliary distribution $q(\mathbf{z}, \boldsymbol{\theta})$ matches the prior. This formulation is the one that will be used in the variational autoencoder.

17.5 Variational approximation

We saw in equation 17.17 that the ELBO is tight when $q(\mathbf{z}|\boldsymbol{\theta})$ is the posterior $Pr(\mathbf{z}|\mathbf{x}, \boldsymbol{\phi})$. In principle, we can compute the posterior using Bayes's theorem:

$$Pr(\mathbf{z}|\mathbf{x}, \boldsymbol{\phi}) = \frac{Pr(\mathbf{x}|\mathbf{z}, \boldsymbol{\phi})Pr(\mathbf{z})}{Pr(\mathbf{x}|\boldsymbol{\phi})}, \tag{17.19}$$

but in practice this is intractable because we can't evaluate the data likelihood in the denominator (see section 17.3).

One solution is to make a variational approximation: we choose a simple parametric form for $q(\mathbf{z}|\boldsymbol{\theta})$ and use this as an approximation to the true posterior. Here, we choose a multivariate normal distribution with mean $\boldsymbol{\mu}$ and diagonal covariance $\boldsymbol{\Sigma}$. This will not always match the posterior well but will be better for some values of $\boldsymbol{\mu}$ and $\boldsymbol{\Sigma}$ than others. During training, we will find the normal distribution that is "closest" to the true posterior $Pr(\mathbf{z}|\mathbf{x})$ (figure 17.8). This corresponds to minimizing the KL divergence in equation 17.17 and moving the colored curves in figure 17.6 upwards.

Appendix B.3.2 multivariate normal

Since the optimal choice for $q(\mathbf{z}|\boldsymbol{\theta})$ was the posterior $Pr(\mathbf{z}|\mathbf{x})$ and this depends on the data example $\mathbf{x}$, our variational approximation should do the same, so we choose:

$$q(\mathbf{z}|\mathbf{x}, \boldsymbol{\theta}) = \text{Norm}_{\mathbf{z}}[\mathbf{g}_{\boldsymbol{\mu}}[\mathbf{x}, \boldsymbol{\theta}], \mathbf{g}_{\boldsymbol{\Sigma}}[\mathbf{x}, \boldsymbol{\theta}]], \tag{17.20}$$

where $\mathbf{g}[\mathbf{x}, \boldsymbol{\theta}]$ is a second neural network with parameters $\boldsymbol{\theta}$ that predicts the mean $\boldsymbol{\mu}$ and variance $\boldsymbol{\Sigma}$ of the normal variational approximation.

17.6 The variational autoencoder

Finally, we can describe the VAE. We build a network that computes the ELBO:

$$\text{ELBO}[\boldsymbol{\theta}, \boldsymbol{\phi}] = \int q(\mathbf{z}|\mathbf{x}, \boldsymbol{\theta}) \log\left[Pr(\mathbf{x}|\mathbf{z}, \boldsymbol{\phi})\right] d\mathbf{z} - \text{D}_{KL}[q(\mathbf{z}|\mathbf{x}, \boldsymbol{\theta})||Pr(\mathbf{z})], \tag{17.21}$$

where the distribution $q(\mathbf{z}|\mathbf{x}, \boldsymbol{\theta})$ is the approximation from equation 17.20.

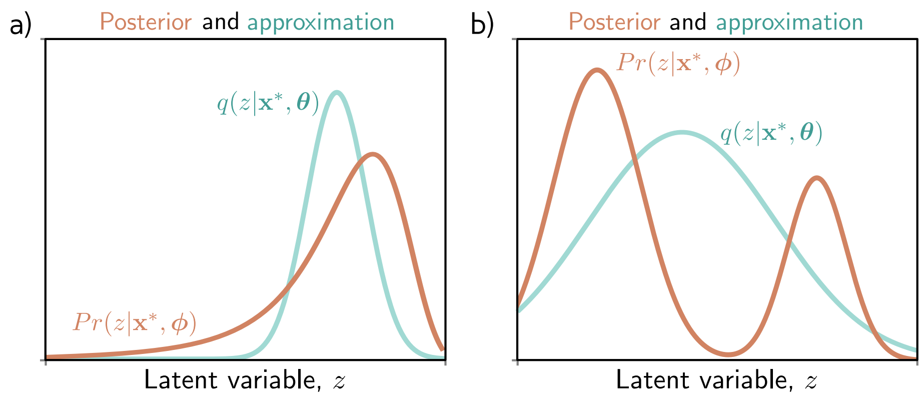

Figure 17.8 Variational approximation. The posterior $Pr(\mathbf{z}|\mathbf{x}^*, \boldsymbol{\phi})$ can't be computed in closed form. The variational approximation chooses a family of distributions $q(\mathbf{z}|\mathbf{x}, \boldsymbol{\theta})$ (here Gaussians) and tries to find the closest member of this family to the true posterior. a) Sometimes the approximation (cyan curve) is good and lies close to the true posterior (orange curve). b) However, if the posterior is multi-modal (as in figure 17.7), then the Gaussian approximation will be poor.

Appendix B.2 Expectation

Problem 17.4

The first term still involves an intractable integral, but since it is an expectation with respect to $q(\mathbf{z}|\mathbf{x}, \boldsymbol{\theta})$, we can approximate it by sampling. For any function $\mathrm{a}[\bullet]$ we have:

$$\mathbb{E}_{\mathbf{z}}\big[\mathrm{a}[\mathbf{z}]\big] = \int \mathrm{a}[\mathbf{z}]Pr(\mathbf{z})d\mathbf{z} \approx \frac{1}{N}\sum_{n=1}^{N}\mathrm{a}[\mathbf{z}_N^*], \tag{17.22}$$

where $\mathbf{z}_n^*$ is the n^{th} sample from $Pr(\mathbf{z})$. This is known as a *Monte Carlo estimate*. For a very approximate estimate, we can just use a single sample $\mathbf{z}^*$ from $q(\mathbf{z}|\mathbf{x}, \boldsymbol{\theta})$:

$$\mathrm{ELBO}[\boldsymbol{\theta}, \boldsymbol{\phi}] \quad \approx \quad \log\left[Pr(\mathbf{x}|\mathbf{z}^*, \boldsymbol{\phi})\right] - \mathrm{D}_{KL}\big[q(\mathbf{z}|\mathbf{x}, \boldsymbol{\theta})||Pr(\mathbf{z})\big]. \tag{17.23}$$

The second term is the KL divergence between the variational distribution $q(\mathbf{z}|\mathbf{x}, \boldsymbol{\theta}) = \mathrm{Norm}_{\mathbf{z}}[\boldsymbol{\mu}, \boldsymbol{\Sigma}]$ and the prior $Pr(\mathbf{z}) = \mathrm{Norm}_{\mathbf{z}}[\mathbf{0}, \mathbf{I}]$. The KL divergence between two normal distributions can be calculated in closed form. For the case where one distribution has parameters $\boldsymbol{\mu}, \boldsymbol{\Sigma}$ and the other is a standard normal, it is given by:

Appendix B.5.4 KL divergence between normal distributions

$$\mathrm{D}_{KL}[q(\mathbf{z}|\mathbf{x}, \boldsymbol{\theta})||Pr(\mathbf{z})] = \frac{1}{2}\left(\mathrm{Tr}[\boldsymbol{\Sigma}] + \boldsymbol{\mu}^T\boldsymbol{\mu} - D_{\mathbf{z}} - \log\Big[\det[\boldsymbol{\Sigma}]\Big]\right). \tag{17.24}$$

where $D_{\mathbf{z}}$ is the dimensionality of the latent space.

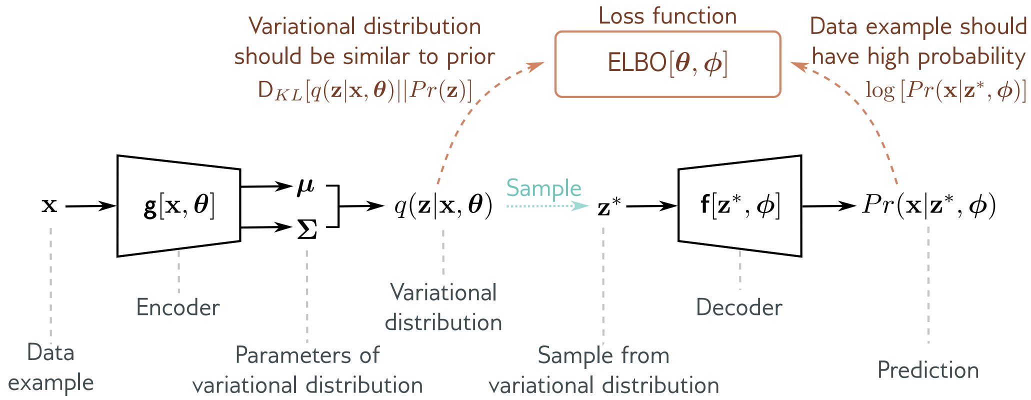

Figure 17.9 Variational autoencoder. The encoder takes a training example $\mathbf{x}$ and predicts the parameters $\boldsymbol{\mu}, \boldsymbol{\Sigma}$ of the variational distribution $q(\mathbf{z}|\mathbf{x},\boldsymbol{\theta})$. We sample from this distribution and then use the decoder to predict the data $\mathbf{x}$. The loss function is the negative ELBO, which depends on how good this prediction is and how similar the variational distribution is to the prior (equation 17.21).

17.6.1 VAE algorithm

To summarize, our goal is to build a model that computes the evidence lower bound for a point $\mathbf{x}$. Then we use automatic differentiation to maximize this lower bound and hence improve the log likelihood of the model. To compute the ELBO we:

- compute the mean $\boldsymbol{\mu}$ and variance $\boldsymbol{\Sigma}$ of the variational posterior distribution $q(\mathbf{z}|\boldsymbol{\theta},\mathbf{x})$ for this data point $\mathbf{x}$ using the network $\mathbf{g}[\mathbf{x},\boldsymbol{\theta}]$,
- draw a sample $\mathbf{z}^*$ from this distribution, and finally
- compute the ELBO using equation 17.23.

The associated architecture is shown in figure 17.9. It should now be clear why this is called a variational autoencoder. It is variational because it computes a Gaussian approximation to the posterior distribution. It is an autoencoder because it starts with a data point $\mathbf{x}$, computes a lower-dimensional latent vector $\mathbf{z}$ from this, and then uses this vector to recreate the data point $\mathbf{x}$ as closely as possible. In this context, the mapping from the data to the latent variable by the network $\mathbf{g}[\mathbf{x},\boldsymbol{\theta}]$ is called the *encoder*, and the mapping from the latent variable to the data by the network $\mathbf{f}[\mathbf{z},\boldsymbol{\phi}]$ is called the *decoder*.

The VAE computes the ELBO as a function of both $\boldsymbol{\phi}$ and $\boldsymbol{\theta}$. To maximize this bound we run mini-batches of samples through the network and update these parameters using SGD or Adam. We are both moving between the colored curves (changing $\boldsymbol{\theta}$) and along them (changing $\boldsymbol{\phi}$) in figure 17.10. During this process, the parameters $\boldsymbol{\phi}$ change to assign the data a higher likelihood in the nonlinear latent variable model.

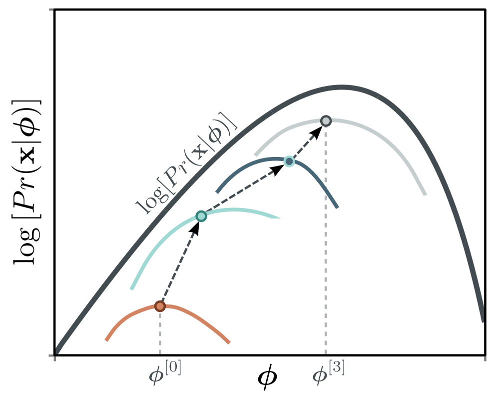

Figure 17.10 The VAE updates both of the factors that determine the lower bound at each iteration. Both the parameters $\boldsymbol{\phi}$ of the decoder and the parameters $\boldsymbol{\theta}$ of the encoder are manipulated to increase this lower bound.

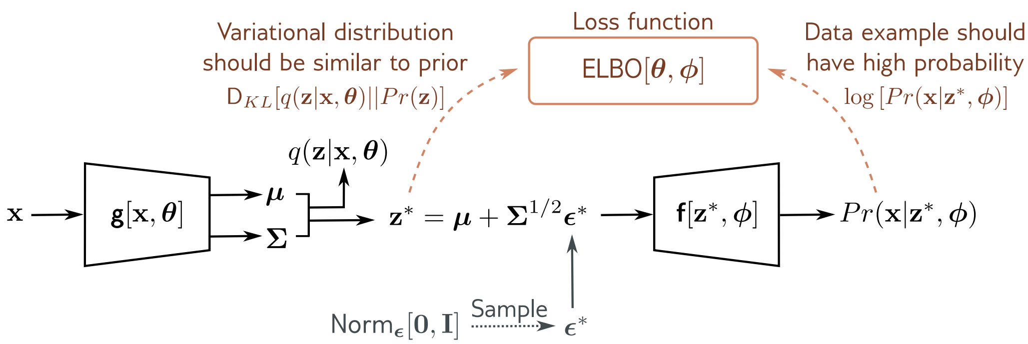

Figure 17.11 Reparameterization trick. With the original architecture (figure 17.9), we cannot easily backpropagate through the sampling step. The reparameterization trick removes the sampling step from the main pipeline; we draw from a standard normal and combine this with the predicted mean and covariance to get a sample from the variational distribution.

17.7 The reparameterization trick

There is one more complication; the network involves a sampling step and it is difficult to differentiate through this stochastic component. However, differentiating past this step is necessary to make updates to the parameters $\boldsymbol{\theta}$ that precede it in the network.

Fortunately, there is a simple solution; we can move the stochastic part into a branch of the network which draws a sample $\boldsymbol{\epsilon}^*$ from $\text{Norm}_{\epsilon}[\mathbf{0},\mathbf{I}]$ and then use the relation:

$$\mathbf{z}^* = \boldsymbol{\mu} + \boldsymbol{\Sigma}^{1/2}\boldsymbol{\epsilon}^*, \tag{17.25}$$

to draw from the intended Gaussian. Now we can compute the derivatives as usual because the backpropagation algorithm does not need to pass down the stochastic branch. This is known as the *reparameterization trick* (figure 17.11).

17.8 Applications

Variational autoencoders have many uses, including denoising, anomaly detection, and compression. This section reviews several applications for image data.

17.8.1 Approximating sample probability

In section 17.3, we argued that it is not possible to evaluate the probability of a sample with the VAE, which describes this probability as:

$$\begin{aligned} Pr(\mathbf{x}) &= \int Pr(\mathbf{x}|\mathbf{z})Pr(\mathbf{z}) \\ &= \mathbb{E}_{\mathbf{z}}\Big[Pr(\mathbf{x}|\mathbf{z})\Big]d\mathbf{z} \\ &= \mathbb{E}_{\mathbf{z}}\Big[\text{Norm}_{\mathbf{x}}[\mathbf{f}[\mathbf{z},\boldsymbol{\phi}],\sigma^2\mathbf{I}]\Big]. \end{aligned} \tag{17.26}$$

In principle, we could *approximate* this probability using equation 17.22 by drawing samples from $Pr(\mathbf{z}) = \text{Norm}_{\mathbf{z}}[\mathbf{0},\mathbf{I}]$ and computing:

$$Pr(\mathbf{x}) \approx \frac{1}{N}\sum_{n=1}^{N} Pr(\mathbf{x}|\mathbf{z}_n). \tag{17.27}$$

However, the curse of dimensionality means that almost all values of $\mathbf{z}_n$ that we draw would have a very low probability and we would have to draw an enormous number of samples to get a reliable estimate. A better approach is to use *importance sampling*. Here, we sample $\mathbf{z}$ from an auxiliary distribution $q(\mathbf{z})$, evaluate $Pr(\mathbf{x}|\mathbf{z}_n)$, and re-scale the resulting values by the probability $q(\mathbf{z})$ under the new distribution:

$$\begin{aligned} Pr(\mathbf{x}) &= \int Pr(\mathbf{x}|\mathbf{z})Pr(\mathbf{z})d\mathbf{z} \\ &= \int \frac{Pr(\mathbf{x}|\mathbf{z})Pr(\mathbf{z})}{q(\mathbf{z})}q(\mathbf{z})d\mathbf{z} \\ &= \mathbb{E}_{q(\mathbf{z})}\Big[\frac{Pr(\mathbf{x}|\mathbf{z})Pr(\mathbf{z})}{q(\mathbf{z})}\Big] \\ &\approx \frac{1}{N}\sum_{n=1}^{N}\frac{Pr(\mathbf{x}|\mathbf{z}_n)Pr(\mathbf{z}_n)}{q(\mathbf{z}_n)}, \end{aligned} \tag{17.28}$$

where now we draw the samples from $q(\mathbf{z})$. If $q(\mathbf{z})$ is close to the region of $\mathbf{z}$ where the $Pr(\mathbf{x}|\mathbf{z})$ has high likelihood, then we will focus our sampling on the relevant area of space and estimate $Pr(\mathbf{x})$ much more efficiently. Problem 17.5

The product $Pr(\mathbf{x}|\mathbf{z})Pr(\mathbf{z})$ that we are trying to integrate is proportional to the posterior distribution $Pr(\mathbf{z}|\mathbf{x})$ (by Bayes' rule). Hence, a sensible choice of auxiliary distribution $q(\mathbf{z})$ is the variational posterior $q(\mathbf{z}|\mathbf{x})$, which is computed by the encoder.

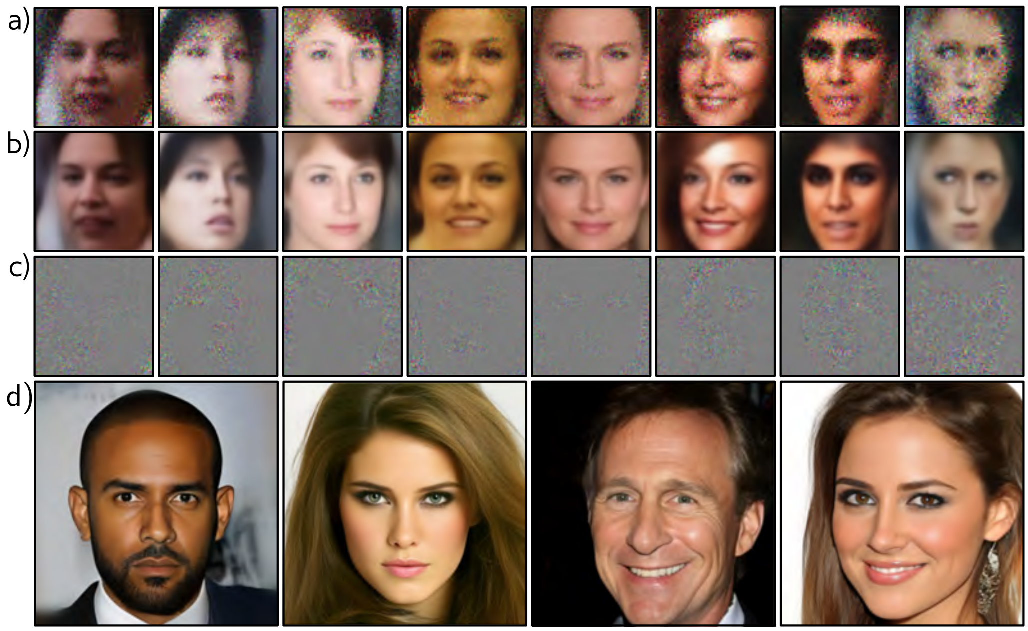

Figure 17.12 Sampling from a standard VAE trained on CELEBA. In each column, a latent variable $\mathbf{z}^*$ is drawn and passed through the model to predict the mean $\mathbf{f}[\mathbf{z}^*, \phi]$ before adding independent Gaussian noise (see figure 17.3). a) A set of samples which are the sum of b) the predicted means and c) spherical Gaussian noise vectors. The images look too smooth before we add the noise and too noisy afterwards. This is typical and usually the noise-free version is shown since the noise is considered to represent aspects of the image that are not modeled. Adapted from Dorta et al. (2018). d) It is now possible to generate high-quality images from VAEs using hierarchical priors, specialized architecture and careful regularization. Adapted from Vahdat & Kautz (2020).

In this way, we can approximate the probability of new samples. With sufficient samples, this will provide a better estimate than the lower bound and could be used to evaluate the quality of the model by evaluating the log likelihood of test data. Alternatively, it could be used as a criterion for determining whether new examples belong to the distribution or are anomalous.

17.8.2 Generation

VAEs build a probabilistic model and it's easy to sample from this model by drawing from the prior $Pr(\mathbf{z})$ over the latent variable, passing this result through the decoder $\mathbf{f}[\mathbf{z}, \phi]$, and adding noise according to $Pr(\mathbf{x}|\mathbf{f}[\mathbf{z}, \phi])$. Unfortunately, samples from vanilla VAEs are generally low-quality (figure 17.12a-c). This is partly because of the naïve spherical Gaussian noise model, but also partly because of the Gaussian models used for the prior and variational posterior. One trick to improves generation quality is to sample from the *aggregated posterior* $q(\mathbf{z}) = (1/I)\sum_i q(\mathbf{z}|\mathbf{x}_i, \boldsymbol{\theta})$ rather than the prior; this is a mixture of Gaussians that is more representative of true distribution in latent space.

Modern VAEs can produce high-quality samples (figure 17.12d), but only by using hierarchical priors and specialized network architecture and regularization techniques. Diffusion models (chapter 18) can be viewed as a VAE with a hierarchical prior and also create very high quality samples.

17.8.3 Resynthesis

VAEs can also be used to modify real data. A data point $\mathbf{x}$ can be projected into the latent space by either (i) taking the mean of the distribution predicted by the encoder, or (ii) by using an optimization procedure to find the latent variable $\mathbf{z}$ that maximizes the posterior probability, which Bayes' rule tells us is proportional to $Pr(\mathbf{x}|\mathbf{z})Pr(\mathbf{z})$.

In figure 17.13, multiple images that have been labeled as "neutral" or "smiling" are projected into latent space, and the vector representing this change is estimated by taking the difference in latent space between the means of these two groups. A second vector is estimated to represent "mouth closed" versus "mouth open".

Now the image of interest is projected into the latent space, and then the representation is modified by adding or subtracting these vectors. To generate intermediate images, *spherical linear interpolation* or *Slerp* is used rather than linear interpolation. In 3D, this would be the difference between interpolating along the surface of a sphere versus digging a straight tunnel through its body. Problem 17.7

The process of encoding (and possibly modifying) input data before decoding again is known as *resynthesis*. This can also be done with GANs and normalizing flows. However, in GANs there is no encoder, and so a separate procedure must be used to find the latent variable that corresponds to the observed data.

17.8.4 Disentanglement

In the resynthesis example above, the directions in space that represent interpretable properties had to be estimated using labeled training data. Other work attempts to improve the characteristics of the latent space so that its coordinate directions correspond to real-world properties. When each dimension represents an independent real-world factor, the latent space is described as *disentangled*. For example, when modeling face images, we might hope to uncover head pose or hair color as independent factors.

Methods to encourage disentanglement typically add regularization terms to the loss function based on either (i) the posterior $q(\mathbf{z}|\mathbf{x}, \boldsymbol{\theta})$ over the latent variables $\mathbf{z}$, or (ii) the aggregated posterior $q(\mathbf{z}) = (1/I)\sum_i q(\mathbf{z}|\mathbf{x}_i, \boldsymbol{\theta})$:

$$L_{\text{new}} = -\text{ELBO}[\boldsymbol{\theta}, \boldsymbol{\phi}] + \lambda_1 \mathbb{E}_{Pr(\mathbf{x})}\bigl[\mathrm{r}_1\bigl[q(\mathbf{z}|\mathbf{x}, \boldsymbol{\theta})\bigr]\bigr] + \lambda_2 \mathrm{r}_2\bigl[q(\mathbf{z})\bigr]. \tag{17.29}$$

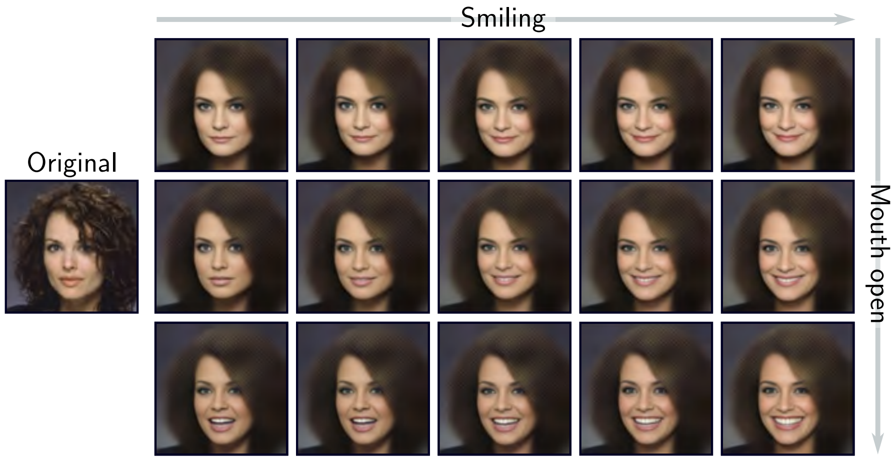

Figure 17.13 Resynthesis. The original image on the left is projected into the latent space using the encoder and the mean of the predicted Gaussian is chosen to represent the image. The center-left image in the grid is the reconstruction of the input. The other images are reconstructions after manipulating the latent space in directions that represent smiling/neutral (horizontal) and mouth open/closed (vertical). Adapted from White (2016).

Here the regularization term $\mathrm{r}_1[\bullet]$ is a function of the posterior and weighted by λ_1. The term $\mathrm{r}_2[\bullet]$ is a function of the aggregated posterior (i.e., the average posterior over all samples) and is weighted by λ_2.

For example, the *Beta VAE* upweights the second term in the ELBO (equation 17.18):

$$\mathrm{ELBO}[\boldsymbol{\theta}, \boldsymbol{\phi}] \approx \log\bigl[Pr(\mathbf{x}|\mathbf{z}^*, \boldsymbol{\phi})\bigr] - \beta \cdot \mathrm{D}_{KL}\Bigl[q(\mathbf{z}|\mathbf{x}, \boldsymbol{\theta})||Pr(\mathbf{z})\Bigr], \tag{17.30}$$

where $\beta > 1$ determines how much more the deviation from the prior $Pr(\mathbf{z})$ is weighted relative to the reconstruction error. Since the prior is usually a multivariate normal with a spherical covariance matrix, its dimensions are independent. Hence, up-weighting this term encourages the posterior distributions to be less correlated. Another variant is the total correlation VAE, which adds a term to decrease the total correlation between variables in the latent space (figure 17.14) and maximizes the mutual information between a small subset of the latent variables and the observations.

17.9 Summary

The VAE is an architecture that helps to learn a nonlinear latent variable model over $\mathbf{x}$. This model can generate new examples by sampling from the latent variable, passing the

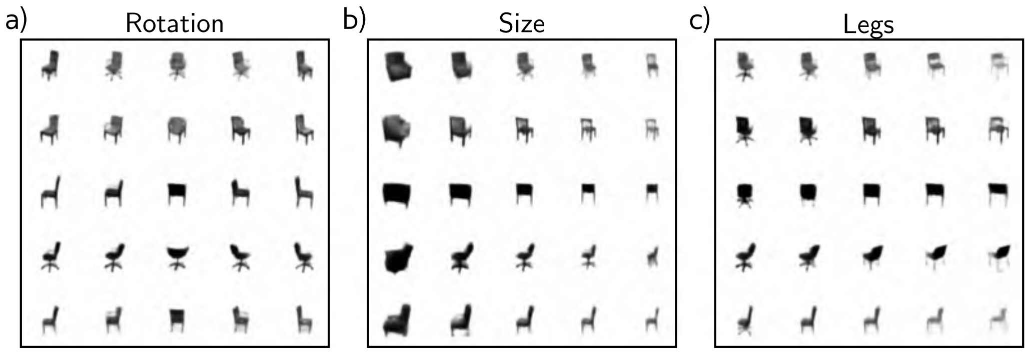

Figure 17.14 Disentanglement in the total correlation VAE. The VAE model is modified so that the loss function encourages the total correlation of the latent variables to be minimized and hence encourages disentanglement. When trained on a dataset of images of chairs, several of the latent dimensions have clear real-world interpretations including a) rotation, b) overall size, and c) legs (swivel chair versus normal). In each case, the central column depicts samples from the model, and as we move left to right we are subtracting or adding a coordinate vector in latent space. Adapted from Chen et al. (2018d).

result through a deep network, and then adding independent Gaussian noise.

It is not possible to compute the likelihood of a data point in closed form, and this poses problems for training with maximum likelihood. However, we can define a lower bound on the likelihood and maximize this bound. Unfortunately, for the bound to be tight, we need to compute the posterior probability of the latent variable given the observed data, which is also intractable. The solution is to make a variational approximation. This is a simpler distribution (usually a Gaussian) that approximates the posterior and whose parameters are computed by a second encoder network.

To create high quality samples from the VAE, it seems to be necessary to model the latent space with more sophisticated probability distributions than the Gaussian prior and posterior. One option is to use hierarchical priors (in which one latent variable generates another). Diffusion models, which are discussed in chapter 18 also produce very high-quality examples, can be viewed as hierarchical VAEs.

Notes

The VAE was originally introduced by Kingma & Welling (2014). A comprehensive introduction to variational autoencoders can be found in Kingma et al. (2019).

Applications: The VAE and variants thereof have been applied to images (Kingma & Welling, 2014; Gregor et al., 2016; Gulrajani et al., 2016; Akuzawa et al., 2018), speech (Hsu et al., 2017b), text (Bowman et al., 2015; Hu et al., 2017; Xu et al., 2020), molecules (Gómez-Bombarelli et al., 2018; Sultan et al., 2018), graphs (Kipf & Welling, 2016; Simonovsky & Komodakis, 2018), robotics (Hernández et al., 2018; Inoue et al., 2018; Park et al., 2018), reinforcement learning (Heess et al., 2015; Van Hoof et al., 2016), 3D scenes (Eslami et al., 2016, 2018; Rezende Jimenez et al., 2016), and handwriting (Chung et al., 2015).

Applications include resynthesis and interpolation (White, 2016; Bowman et al., 2015), collaborative filtering (Liang et al., 2018), and compression (Gregor et al., 2016). Gómez-Bombarelli et al. (2018) use the VAE to construct a continuous representation of chemical structures that can then be optimized for desirable properties. Ravanbakhsh et al. (2017) simulate astronomical observations for calibrating measurements.

Relation to other models: The autoencoder (Rumelhart et al., 1985; Hinton & Salakhutdinov, 2006) passes data through an encoder to a bottleneck layer and then reconstructs it using a decoder. The bottleneck is similar to latent variables in the VAE, but the motivation differs. Here, the goal is not to learn a probability distribution but to create a low-dimensional representation that captures the essence of the data. Autoencoders also have various applications including denoising (Vincent et al., 2008) and anomaly detection (Zong et al., 2018).

If the encoder and decoder are linear transformations, then the autoencoder is just principal component analysis (PCA). Hence, the non-linear autoencoder is a generalization of PCA. There are also probabilistic forms of PCA. Probabilistic PCA (Tipping & Bishop, 1999) adds spherical Gaussian noise to the reconstruction to create a probability model and factor analysis adds diagonal Gaussian noise (see Rubin & Thayer, 1982). If we make the encoder and decoder of these probabilistic variants nonlinear, then we return to the variational autoencoder.

Architectural variations: The conditional VAE (Sohn et al., 2015) passes class information c into both the encoder and decoder. The result is that the latent space does not need to encode the class information. For example, when MNIST data is conditioned on the digit label, the latent variables might encode the orientation and width of the digit, rather than the digit category itself. Sønderby et al. (2016a) introduced ladder variational autoencoders which recursively correct the generative distribution with a data-dependent approximate likelihood term.

Modifying likelihood: Other work investigates more sophisticated likelihood models $Pr(\mathbf{x}|\mathbf{z})$. The PixelVAE (Gulrajani et al., 2016) used an auto-regressive model over the output variables and Dorta et al. (2018) modeled the covariance as well as the mean. Lamb et al. (2016) improved the quality of reconstruction by adding extra regularization terms that encourage the reconstruction to be similar to the original image in the space of activations of a layer of an image classification model. This encourages semantic information to be retained and was the model used to generate the results in figure 17.13. Larsen et al. (2016) use an adversarial loss for reconstruction which also improves results.

Latent space, prior, and posterior: Many different forms for the variational approximation to the posterior have been investigated including normalizing flows (Rezende & Mohamed, 2015; Kingma et al., 2016), directed graphical models (Maaløe et al., 2016), undirected models (Vahdat et al., 2020), and recursive models for temporal data (Gregor et al., 2016, 2019).

Other authors have investigated using a discrete latent space (Van Den Oord et al., 2017; Razavi et al., 2019b; Rolfe, 2017; Vahdat et al., 2018a,b) For example, Razavi et al. (2019b) use a vector quantized latent space, and model the prior with an autoregressive model (equation 12.14). This is slow to sample from but can describe very complex distributions.

Jiang et al. (2016) use a mixture of Gaussians for the posterior, allowing clustering. This is a hierarchical latent variable model that adds a discrete latent variable that improves the flexibility of the posterior. Other authors (Salimans et al., 2015; Ranganath et al., 2016; Maaløe et al., 2016; Vahdat & Kautz, 2020) have experimented with hierarchical models that use continuous variables. These have a close connection with diffusion models (chapter 18).

Combination with other models: Gulrajani et al. (2016) combined VAEs with an autoregressive model to produce more realistic images. Chung et al. (2015) combine the VAE with recurrent neural networks to model time-varying measurements.

As discussed above, adversarial losses have been used to directly inform the likelihood term. However, other models have combined ideas from generative adversarial networks (GANs) with VAEs in different ways. Makhzani et al. (2015) use an adversarial loss in the latent space; the idea is that the discriminator will ensure that the aggregated posterior distribution $q(\mathbf{z})$ is indistinguishable from the prior distribution $Pr(\mathbf{z})$. Tolstikhin et al. (2018) generalize this to a broader family of distances between the prior and aggregated posterior. Dumoulin et al. (2017) introduced adversarially learned inference which uses an adversarial loss to distinguish two pairs of latent/observed data points. In one case, the latent variable is drawn from the latent posterior distribution and, in the other drawn from the prior. Other hybrids of VAEs and GANs were proposed by Larsen et al. (2016), Brock et al. (2016), and Hsu et al. (2017a).

Posterior collapse: One potential problem in training is *posterior collapse*, in which the encoder always predicts the prior distribution. This was identified by Bowman et al. (2015) and can be mitigated by using an optimization schedule that gradually increases the term that encourages the KL distance between the posterior and the prior to be small. Several other methods have been proposed to prevent posterior collapse (Razavi et al., 2019a; Lucas et al., 2019b,a), and this also part of the motivation for using a discrete latent space (Van Den Oord et al., 2017).

Blurry reconstructions: Zhao et al. (2017c) provide evidence that the blurry reconstructions are partly due to Gaussian noise, but also because of the sub-optimal posterior distributions induced by the variational approximation. It is perhaps not coincidental that some of the best synthesis results have come from using a discrete latent space, that is modeled by a sophisticated auto-regressive model (Razavi et al., 2019b), or from using hierarchical latent spaces (Vahdat & Kautz, 2020; see figure 17.12d). Figure 17.12a-c used a VAE that was trained on the CELEBA database (Liu et al., 2015). Figure 17.12d uses a hierarchical VAE that was trained on the CELEBA HQ dataset (Karras et al., 2018).

Other problems: Chen et al. (2017) noted that when more complex likelihood terms are used such as the PixelCNN (Van den Oord et al., 2016c), the output can cease to depend on the latent variables at all. They term this the *information preference* problem. This was addressed by Zhao et al. (2017b) in the InfoVAE which added an extra term that maximized the mutual information between the latent and observed distributions.

Another problem with the VAE is that there can be "holes" in the latent space that do not correspond to any realistic sample. Xu et al. (2020) introduce the constrained posterior VAE, which helps prevent these vacant regions in latent space by adding a regularization term. This allows for better interpolation from real samples.

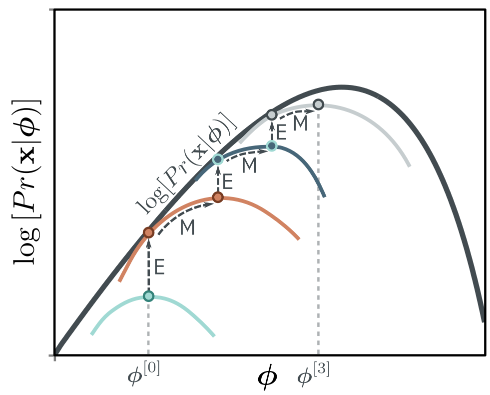

Figure 17.15 Expectation maximization (EM) algorithm. The EM algorithm, alternately adjusts the auxiliary parameters $\boldsymbol{\theta}$ (moves between colored curves) and model parameters $\boldsymbol{\phi}$ (moves along colored curves) until the overall maximum of the likelihood is reached. These adjustments are known as the E-step and the M-step, respectively. Because the E-Step uses the posterior distribution $Pr(h|\mathbf{x}, \boldsymbol{\phi})$ for $q(h|\mathbf{x}, \boldsymbol{\theta})$, the bound is tight and the colored curve touches the black likelihood curve after each E-Step.

Disentangling latent representation: Methods to "disentangle" the latent representation include the Beta VAE (Higgins et al., 2017) and others (e.g., Kim & Mnih, 2018; Kumar et al., 2018). Chen et al. (2018d) further decomposed the ELBO to show the existence of a term measuring the total correlation between the latent variables. They use this to motivate the total correlation VAE, which attempts to minimize this quantity.

Lower bound and the EM algorithm: VAE training is based on optimizing the evidence lower bound (sometimes also referred to as the variational lower bound or negative variational free energy). Hoffman & Johnson (2016) and Lücke et al. (2020) re-express this lower bound in several ways that elucidate its properties. Other work has aimed to make this bound tighter (Burda et al., 2016; Li & Turner, 2016; Bornschein et al., 2016; Masrani et al., 2019). For example, Burda et al. (2016) use a modified bound based on using multiple importance-weighted samples from the approximate posterior to form the objective function.

The evidence lower bound is tight when the distribution $q(\mathbf{z}|\boldsymbol{\theta})$ matches the posterior $Pr(\mathbf{z}|\mathbf{x}, \boldsymbol{\phi})$. This observation is also the basis of the *expectation maximization* (*EM*) algorithm (Dempster et al., 1977). Here, we alternately (i) choose $\boldsymbol{\theta}$ so that $q(\mathbf{z}|\boldsymbol{\theta})$ equals the posterior $Pr(\mathbf{z}|\mathbf{x}, \boldsymbol{\phi})$ and (ii) change $\boldsymbol{\phi}$ to maximize the lower bound (figure 17.15). This is viable for models like the mixture of Gaussians where we can compute the posterior distribution in closed-form. Unfortunately, for the nonlinear latent variable model, there is no closed-form expression, and so this method cannot be used.

Problem 17.8

Problems

Problem 17.1 A function is concave if its second derivative is negative everywhere. Show that this is true for the function $\mathrm{g}[x] = \log[x]$.

Problem 17.2 For convex functions, Jensen's inequality works the other way around.

$$g[\mathbb{E}[y]] \leq \mathbb{E}[g[y]]. \tag{17.31}$$

A function is convex if its second derivative is positive everywhere. Show that the function $g[x] = x^{2n}$ is convex for arbitrary $n \in [1, 2, 3, \ldots]$. Use this relation to show that the square of the mean of a distribution $Pr(x)$ must be less than or equal to its second moment $\mathbb{E}[x^2]$.

Problem 17.3 Show that the ELBO as expressed in equation 17.18 can alternatively be derived from the KL divergence between the variational distribution $q(\mathbf{z}|\mathbf{x})$ and the true posterior distribution $Pr(\mathbf{z}|\mathbf{x}, \boldsymbol{\phi})$:

$$D_{KL}\Big[q(\mathbf{z}|\mathbf{x})||Pr(\mathbf{z}|\mathbf{x},\boldsymbol{\phi})\Big] = \int q(\mathbf{z}|\mathbf{x}) \log\left[\frac{q(\mathbf{z}|\mathbf{x})}{Pr(\mathbf{z}|\mathbf{x},\boldsymbol{\phi})}\right] d\mathbf{z}. \tag{17.32}$$

Start by using Bayes's rule (equation 17.19).

Problem 17.4 Write code to use equation 17.22 to approximate the expectation:

$$\mathbb{E}\big[\sin^2[y]\big] = \int \sin^2[y] Pr(y) dy, \tag{17.33}$$

where $Pr(y) = \text{Norm}_y[0,1]$. Show how the variation of this approximation decreases as we increase the number of samples N.

Problem 17.5
Consider the function

$$f[y] = 5\exp\left[-(y-3)^4\right], \tag{17.34}$$

which decreases very rapidly as we move away from the position $y = 3$. Now consider estimating the expectation:

$$\mathbb{E}_y\left[\text{f}[y]\right] = \int \text{f}[y] Pr(y) dy, \tag{17.35}$$

where $Pr(y) = \text{Norm}_y[0,1]$ using the sampling approach from equation 17.22. Make 100 different estimates using 50 samples each. What do you notice about the variance of the estimates? Now repeat this experiment, but this time use importance sampling with auxiliary distribution $q(y) = \text{Norm}_y[3,1]$. Explain your findings.

Problem 17.6 How many parameters are needed to create a 1D mixture of Gaussians with $n = 5$ components (equation 17.4)? State the possible range of values that each parameter could take.

Problem 17.7 Why is it better to use spherical linear interpolation rather than regular linear interpolation when moving between points in the latent space? Hint: consider figure 8.13.

Problem 17.8 Derive the EM algorithm for the 1D mixture of Gaussians algorithm with N components. To do this you need to (i) find an expression for the posterior distribution over the latent variable z for a data point x and (ii) find an expression that updates the evidence lower bound given the posterior distributions for all of the data points. You will need to use Lagrange multipliers to ensure that the weights $\lambda_1, \ldots, \lambda_N$ of the Gaussians sum to one.

Chapter 18

Diffusion models

Chapter 15 described generative adversarial models, which generate plausible looking samples but do not define a probability distribution over the data. Chapter 16 discussed normalizing flows, which can assign a probability but which place architectural constraints on the network; each layer must be invertible and the determinant of its Jacobian must be easy to calculate. Chapter 17 introduced variational autoencoders, which also have a solid probabilistic foundation, but where computation of the likelihood is intractable and but can be approximated by a lower bound.

This chapter introduces diffusion models. Like normalizing flows, these are probabilistic models that define a nonlinear mapping from latent variables to the observed data where both quantities have the same dimension. Like variational autoencoders they approximate the data likelihood using a lower bound based on an encoder that maps *to* the latent variable. However, in diffusion models this encoder is predetermined; the goal is to learn a decoder that is the inverse of this process and can be used to produce samples. Diffusion models are easy to train and can produce very high quality samples, that exceed the realism of those produced by GANs. The reader should be familiar with variational autoencoders (chapter 17) before reading this chapter.

18.1 Overview

A diffusion model consists of an *encoder* and a *decoder*. The encoder takes a data sample $\mathbf{x}$ and maps it through a series of intermediate latent variables $\mathbf{z}_1 \ldots \mathbf{z}_T$. The decoder reverses this process; it starts with $\mathbf{z}_T$ and maps back through $\mathbf{z}_{T-1}, \ldots, \mathbf{z}_1$ until it finally (re-)creates a data point $\mathbf{x}$. In both encoder and decoder, the mappings are stochastic rather than deterministic.

The encoder is predetermined; it gradually blends the input with samples of white noise (figure 18.1). With enough steps, the conditional distribution $q(\mathbf{z}_T|\mathbf{x})$ and marginal distribution $q(\mathbf{z}_T)$ of the final latent variable both become the standard normal distribution. Since this process is pre-specified, all the learned parameters are in the decoder.

In the decoder, a series of networks are trained to map backwards between each

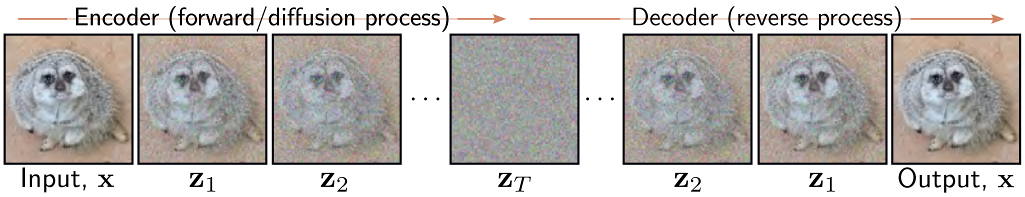

Figure 18.1 Diffusion models. The encoder (forward, or diffusion process) maps the input $\mathbf{x}$ through a series of latent variables $\mathbf{z}_1 \ldots \mathbf{z}_T$. This process is predetermined and gradually mixes the data with noise until only noise remains. The decoder (reverse process) is learned and passes the data back through the latent variables, removing noise at each stage. After training, new examples are generated by sampling noise vectors $\mathbf{z}_T$ and passing them through the decoder.

adjacent pair of latent variables $\mathbf{z}_t$ and $\mathbf{z}_{t-1}$. The loss function encourages each network to invert the corresponding decoder step. The result is that noise is gradually removed from the representation until a realistic looking data example remains. To generate a new data example $\mathbf{x}$, we draw a sample from $q(\mathbf{z}_T)$ and pass it through the decoder.

In section 18.2, we consider the encoder in detail. Its properties are non-obvious, but are critical for the learning algorithm. In section 18.3 we discuss the decoder. Section 18.4 derives the training algorithm and section 18.5 reformulates it to be more practical. Section 18.6 discusses implementation details, including how to make the generation conditional on text prompts.

18.2 Encoder (forward process)

The *diffusion* or *forward* process[1] (figure 18.2) maps a data example $\mathbf{x}$ through a series of intermediate variables $\mathbf{z}_1, \mathbf{z}_2, \ldots, \mathbf{z}_T$ with the same size as $\mathbf{x}$ according to:

$$\begin{aligned}\mathbf{z}_1 &= \sqrt{1-\beta_1}\mathbf{x} + \sqrt{\beta_1}\boldsymbol{\epsilon}_1 \\ \mathbf{z}_t &= \sqrt{1-\beta_t}\mathbf{z}_{t-1} + \sqrt{\beta_t}\boldsymbol{\epsilon}_t \qquad \forall\, t \in 2, \ldots, T,\end{aligned} \tag{18.1}$$

where $\boldsymbol{\epsilon}_t$ is noise drawn from a standard normal distribution. The first term attenuates the data plus any noise added so far, and the second adds more noise. The hyperparameters $\{\beta_t\} \in [0, 1]$ determine how quickly the noise is blended and are collectively known as the *noise schedule*. This can equivalently be written as:

[1]Note, this is the opposite nomenclature to normalizing flows, where the inverse mapping moves from the data to the latent variable, and the forward mapping moves back again.

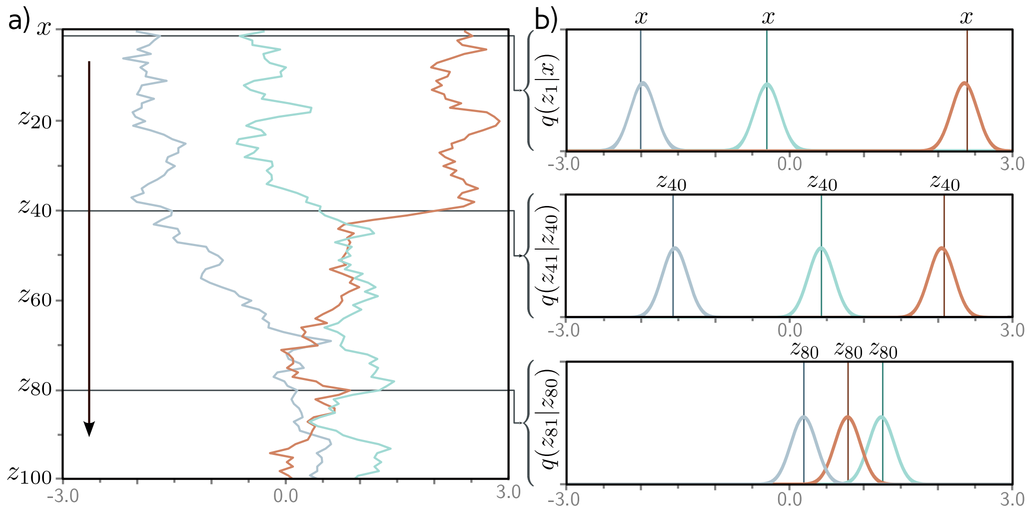

Figure 18.2 Forward process. a) We consider one-dimensional data x with $T = 100$ latent variables $z_1, \ldots, z_{100}$ and a $\beta = 0.03$ at all steps. Three values of x (orange, green, and gray) are initialized (top row). These are propagated through $z_1, \ldots, z_{100}$. At each step, the variable is updated by attenuating its value by $\sqrt{1-\beta}$ and adding noise with variance β (equation 18.1). Accordingly, the three examples noisily propagate through the variables with a tendency to move towards zero. b) The conditional probabilities $Pr(z_1|x)$ and $Pr(z_t|z_{t-1})$ are normal distributions with a mean that is slightly closer to zero than the current point and a fixed variance β_t (equation 18.2).

$$
\begin{aligned}
q(\mathbf{z}_1|\mathbf{x}) &= \mathrm{Norm}_{\mathbf{z}_1}\left[\sqrt{1-\beta_1}\mathbf{x}, \beta_1\mathbf{I}\right] \\
q(\mathbf{z}_t|\mathbf{z}_{t-1}) &= \mathrm{Norm}_{\mathbf{z}_t}\left[\sqrt{1-\beta_t}\mathbf{z}_{t-1}, \beta_t\mathbf{I}\right] \qquad \forall\, t \in 2, \ldots, T.
\end{aligned}
\tag{18.2}
$$

Problem 18.1

With sufficient steps T, all traces of the original data are removed, and $q(\mathbf{z}_T|\mathbf{x}) = q(\mathbf{z}_T)$ becomes a standard normal distribution.

The joint distribution of all of the latent variables $\mathbf{z}_1, \mathbf{z}_2, \ldots, \mathbf{z}_T$ given input $\mathbf{x}$ is:

$$
q(\mathbf{z}_{1\ldots T}|\mathbf{x}) = q(\mathbf{z}_1|\mathbf{x}) \prod_{t=2}^{T} q(\mathbf{z}_t|\mathbf{z}_{t-1}). \tag{18.3}
$$

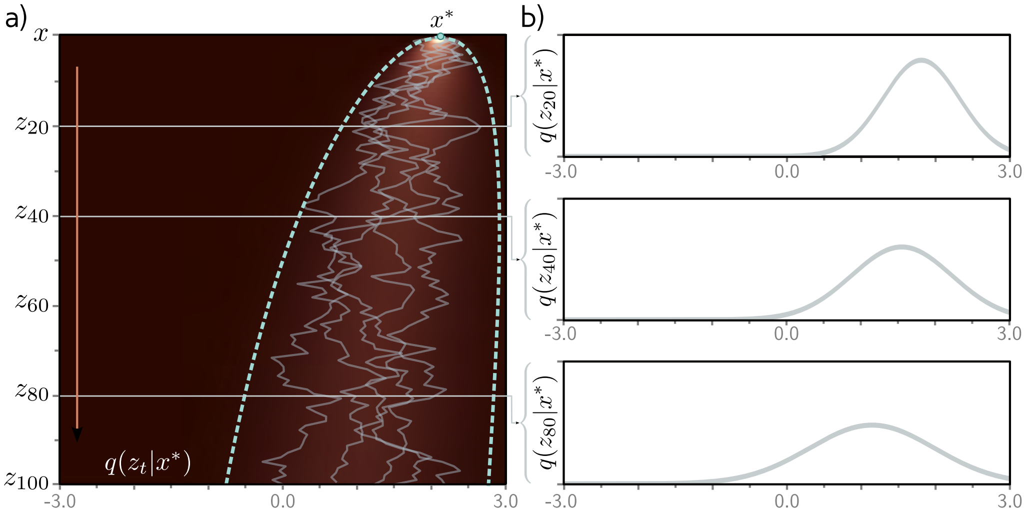

Figure 18.3 Diffusion kernel. a) The point $x^* = -2.0$ is propagated through the latent variables using equation 18.1 (five paths shown in gray). The diffusion kernel $q(z_t|x^*)$ is the probability distribution over variable z_t given that we started from x^*. It can be computed in closed-form and is a normal distribution whose mean moves towards zero and whose variance increases as t increases. Heatmap shows $q(z_t|x^*)$ for each variable. Cyan lines show ± 2 standard deviations of the normal. b) The diffusion kernel $q(z_t|x^*)$ is shown explicitly for $t = 20, 40, 80$. In practice, this means its easy to sample a latent variable z_t corresponding to a given x^* without computing the intermediate variables $z_1, \ldots, z_{t-1}$.

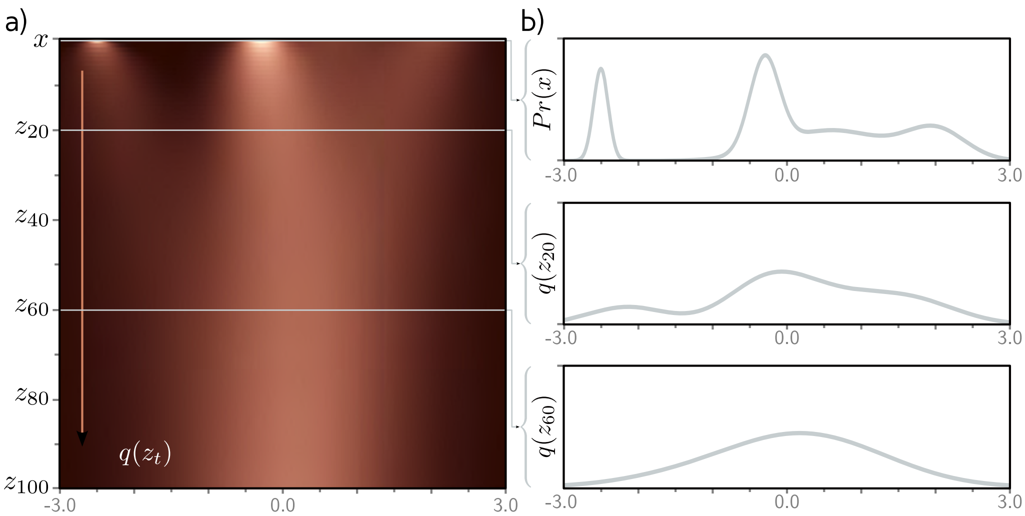

Figure 18.4 Marginal distributions. a) Given an initial density $Pr(x)$ with mean zero and standard deviation one, the diffusion process gradually blurs the distribution as it passes through the latent variables z_t and moves it towards a standard normal distribution. Each horizontal line of heatmap represents marginal distribution $Pr(x)$ (top row) or $q(z_t)$ (remaining rows). b) The top graph shows the initial distribution $Pr(x)$. The other two graphs show the marginal distributions $q(z_{20})$ and $q(z_{60})$, respectively.

18.2.1 Diffusion kernel $q(\mathbf{z}_t|\mathbf{x})$

To train the decoder to invert this process, we will use multiple samples $\mathbf{z}_t$ for the same example $\mathbf{x}$. However, generating these sequentially using equation 18.1 is time-consuming when t is large. Fortunately, there is a closed-form expression for $q(\mathbf{z}_t|\mathbf{x})$, which allows us to directly draw samples $\mathbf{z}_t$ given initial data point $\mathbf{x}$ without computing the intermediate variables. This is known as the *diffusion kernel* (figure 18.3).

To derive an expression for $q(\mathbf{z}_t|\mathbf{x})$, consider the first two steps of the forward process:

$$\begin{aligned}\mathbf{z}_1 &= \sqrt{1-\beta_1}\cdot\mathbf{x}+\sqrt{\beta_1}\cdot\boldsymbol{\epsilon}_1\\ \mathbf{z}_2 &= \sqrt{1-\beta_2}\cdot\mathbf{z}_1+\sqrt{\beta_2}\cdot\boldsymbol{\epsilon}_2.\end{aligned}\tag{18.4}$$

Substituting the first equation into the second, we get:

$$\begin{aligned}\mathbf{z}_2 &= \sqrt{1-\beta_2}\left(\sqrt{1-\beta_1}\cdot\mathbf{x}+\sqrt{\beta_1}\cdot\boldsymbol{\epsilon}_1\right)+\sqrt{\beta_2}\cdot\boldsymbol{\epsilon}_2 \qquad (18.5)\\ &= \sqrt{1-\beta_2}\left(\sqrt{1-\beta_1}\cdot\mathbf{x}+\sqrt{1-(1-\beta_1)}\cdot\boldsymbol{\epsilon}_1\right)+\sqrt{\beta_2}\cdot\boldsymbol{\epsilon}_2\\ &= \sqrt{(1-\beta_2)(1-\beta_1)}\cdot\mathbf{x}+\sqrt{1-\beta_2-(1-\beta_2)(1-\beta_1)}\cdot\boldsymbol{\epsilon}_1+\sqrt{\beta_2}\cdot\boldsymbol{\epsilon}_2.\end{aligned}$$

Problem 18.2

The last two terms are independent samples from mean zero normal distributions with variances $1-\beta_2-(1-\beta_2)(1-\beta_1)$ and β_2, respectively. The mean of this sum is zero, and its variance is the sum of the component variances (see problem 18.2), so:

$$\mathbf{z}_2 = \sqrt{(1-\beta_2)(1-\beta_1)}\cdot\mathbf{x}+\sqrt{1-(1-\beta_2)(1-\beta_1)}\cdot\boldsymbol{\epsilon},\tag{18.6}$$

where $\boldsymbol{\epsilon}$ is also a sample from a standard normal distribution.

Problem 18.3

If we continue this process by substituting this equation into the expression for $\mathbf{z}_3$ and so on, we can show that:

$$\mathbf{z}_t = \sqrt{\alpha_t}\cdot\mathbf{x}+\sqrt{1-\alpha_t}\cdot\boldsymbol{\epsilon},\tag{18.7}$$

where $\alpha_t=\prod_{s=1}^{t}1-\beta_s$. We can equivalently write this in probabilistic form:

$$q(\mathbf{z}_t|\mathbf{x}) = \text{Norm}_{\mathbf{z}_t}\left[\sqrt{\alpha_t}\cdot\mathbf{x},(1-\alpha_t)\mathbf{I}\right].\tag{18.8}$$

For any starting data point $\mathbf{x}$, variable $\mathbf{z}_t$ is normally distributed with a known mean and variance. Consequently, if we don't care about the history of the evolution through the intermediate variables, it is easy to generate samples from $q(\mathbf{z}_t|\mathbf{x})$.

18.2.2 Marginal distributions $q(\mathbf{z}_t)$

The marginal distribution $q(\mathbf{z}_t)$ is the probability of observing a value of $\mathbf{z}_t$ given the distribution of possible starting points $\mathbf{x}$ and the possible diffusion paths for each starting point (figure 18.4). It can be computed by considering the joint distribution $q(\mathbf{x}, \mathbf{z}_{1...t})$ and marginalizing over all the variables except $\mathbf{z}_t$:

$$\begin{aligned} q(\mathbf{z}_t) &= \iint q(\mathbf{z}_{1...t}, \mathbf{x}) d\mathbf{z}_{1...t-1} d\mathbf{x} \\ &= \iint q(\mathbf{z}_{1...t}|\mathbf{x}) Pr(\mathbf{x}) d\mathbf{z}_{1...t-1} d\mathbf{x}, \end{aligned} \tag{18.9}$$

where $q(\mathbf{z}_{1...t}|\mathbf{x})$ was defined in equation 18.3.

However, since we now have an expression for the diffusion kernel $q(\mathbf{z}_t|\mathbf{x})$ that "skips" the intervening variables, we can equivalently write:

$$q(\mathbf{z}_t) = \int q(\mathbf{z}_t|\mathbf{x}) Pr(\mathbf{x}) d\mathbf{x}. \tag{18.10}$$

Hence, if we sample repeatedly from the data distribution $Pr(\mathbf{x})$, and superimpose the diffusion kernel $q(\mathbf{z}_t|\mathbf{x})$ on each sample, the result is the marginal distribution $q(\mathbf{z}_t)$ (figure 18.4). However, the marginal distribution cannot be written in closed from because we don't know the original data distribution $Pr(\mathbf{x})$.

18.2.3 Conditional distribution $q(\mathbf{z}_{t-1}|\mathbf{z}_t)$

We defined the conditional probability $q(\mathbf{z}_t|\mathbf{z}_{t-1})$ as the mixing process (equation 18.2). To reverse this process we apply Bayes' rule:

$$q(\mathbf{z}_{t-1}|\mathbf{z}_t) = \frac{q(\mathbf{z}_t|\mathbf{z}_{t-1})q(\mathbf{z}_{t-1})}{q(\mathbf{z}_t)}. \tag{18.11}$$

This is intractable since we cannot compute the marginal distribution $q(\mathbf{z}_{t-1})$. This matches our intuition; we are mixing the original data example with noise at each stage, and there is no way to reverse this unless we knew the starting point.

For this simple 1D example, it's possible to evaluate these distributions numerically (figure 18.5). In general, their form is complex, but in many cases they are well-approximated by a normal distribution. This is important because when we build the decoder, we will approximate the reverse process using a normal distribution.

18.2.4 Conditional diffusion distribution $q(\mathbf{z}_{t-1}|\mathbf{z}_t, \mathbf{x})$

There is one final distribution related to the encoder to consider. We noted above that we could not find the conditional distribution $q(\mathbf{z}_{t-1}|\mathbf{z}_t)$ because we do not know the marginal distribution $q(\mathbf{z}_{t-1})$. However, if we know the starting variable $\mathbf{x}$, then we *do* know the distribution $q(\mathbf{z}_{t-1}|\mathbf{x})$ at the time before. This is just the diffusion kernel (figure 18.3) and it is normally distributed.

Hence, it is possible to compute the conditional diffusion distribution $q(\mathbf{z}_{t-1}|\mathbf{z}_t, \mathbf{x})$ in closed form (figure 18.6): This distribution is used to train the decoder. It is the

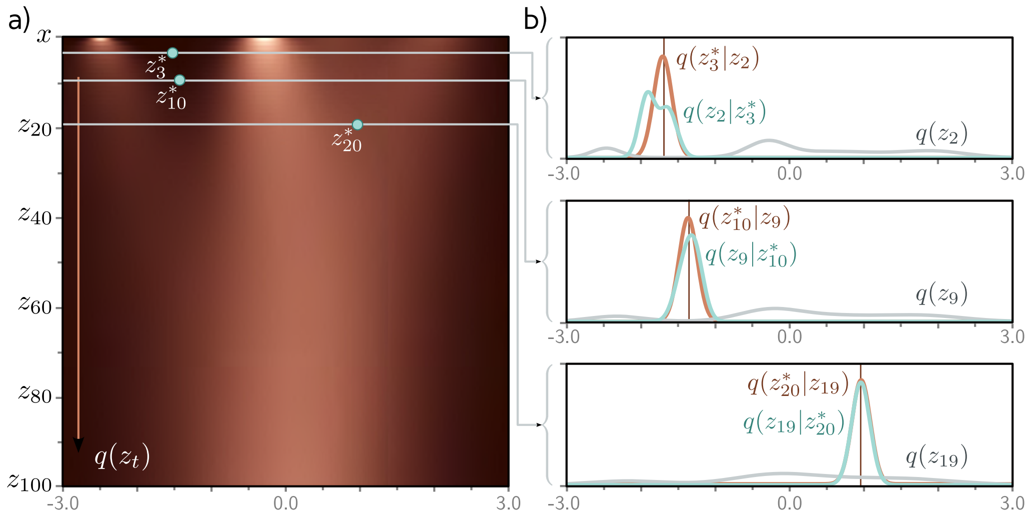

Figure 18.5 Conditional distribution $q(z_{t-1}|z_t)$. a) The marginal densities $q(z_t)$ with three points z_t^* highlighted. b) The probability $q(z_{t-1}|z_t^*)$ (cyan curves) is computed via Bayes' rule and is proportional to $q(z_t^*|z_{t-1})q(z_{t-1})$. In general, it is not normally distributed (top graph), although often the normal is a good approximation (bottom two graphs). The first contributing term $q(z_t^*|z_{t-1})$ is normal (equation 18.2) with a mean that is slightly further from zero than z_t^* (brown curves). The second term is the marginal density $q(z_{t-1})$ (gray curves).

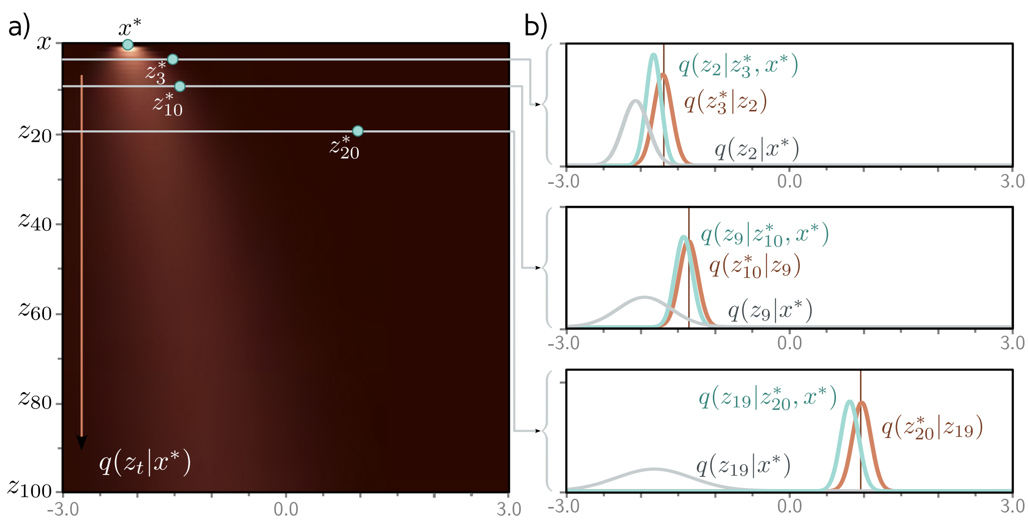

Figure 18.6 Conditional distribution $q(z_{t-1}|z_t, x)$. a) Diffusion kernel for $x^* = -2.1$ with three points z_t^* highlighted. b) The probability $q(z_{t-1}|z_t^*, x^*)$ is computed via Bayes' rule and is proportional to $q(z_t^*|z_{t-1})q(z_{t-1}|x^*)$. This *is* normally distributed and can be computed in closed form. The first term $q(z_t^*|z_{t-1})$ is normal with a mean that is slightly further from zero than z_t^* (brown curves). The second term is the diffusion kernel $q(z_{t-1}|x^*)$ (gray curves).

distribution over $\mathbf{z}_{t-1}$ when we know the current latent variable $\mathbf{z}_t$ and the training data example $\mathbf{x}$ (which, of course, we do when training). To compute an expression for $q(\mathbf{z}_{t-1}|\mathbf{z}_t,\mathbf{x})$ we start with Bayes' rule:

$$\begin{aligned} q(\mathbf{z}_{t-1}|\mathbf{z}_t,\mathbf{x}) &= \frac{q(\mathbf{z}_t|\mathbf{z}_{t-1},\mathbf{x})q(\mathbf{z}_{t-1}|\mathbf{x})}{q(\mathbf{z}_t|\mathbf{x})} \qquad (18.12)\\ &\propto q(\mathbf{z}_t|\mathbf{z}_{t-1})q(\mathbf{z}_{t-1}|\mathbf{x})\\ &= \text{Norm}_{\mathbf{z}_t}\left[\sqrt{1-\beta_t}\cdot\mathbf{z}_{t-1},\beta_t\mathbf{I}\right]\text{Norm}_{\mathbf{z}_{t-1}}\left[\sqrt{\alpha_{t-1}}\cdot\mathbf{x},(1-\alpha_{t-1})\mathbf{I}\right]\\ &= \text{Norm}_{\mathbf{z}_{t-1}}\left[\frac{1}{\sqrt{1-\beta_t}}\mathbf{z}_t,\frac{\beta_t}{1-\beta_t}\mathbf{I}\right]\text{Norm}_{\mathbf{z}_{t-1}}\left[\sqrt{\alpha_{t-1}}\cdot\mathbf{x},(1-\alpha_{t-1})\mathbf{I}\right] \end{aligned}$$

where between the first two lines we have used the fact that $q(\mathbf{z}_t|\mathbf{z}_{t-1},\mathbf{x}) = q(\mathbf{z}_t|\mathbf{z}_{t-1})$ because the diffusion process is Markov and all information about $\mathbf{z}_t$ is captured by $\mathbf{z}_{t-1}$. Between lines three and four we use the Gaussian identity

Problem 18.4

$$\text{Norm}_{\mathbf{v}}\left[\mathbf{A}\mathbf{w},\mathbf{B}\right]\propto\text{Norm}_{\mathbf{w}}\left[\left(\mathbf{A}^T\mathbf{B}^{-1}\mathbf{A}\right)^{-1}\mathbf{A}^T\mathbf{B}^{-1}\mathbf{v},\left(\mathbf{A}^T\mathbf{B}^{-1}\mathbf{A}\right)^{-1}\right], \qquad (18.13)$$

to rewrite the first distribution in terms of $\mathbf{z}_{t-1}$. We then use a second Gaussian identity:

Problem 18.5

$$\begin{aligned} \text{Norm}_{\mathbf{w}}[\mathbf{a},\mathbf{A}]\cdot\text{Norm}_{\mathbf{w}}[\mathbf{b},\mathbf{B}] \quad &\propto \qquad (18.14)\\ &\text{Norm}_{\mathbf{w}}\left[\left(\mathbf{A}^{-1}+\mathbf{B}^{-1}\right)^{-1}(\mathbf{A}^{-1}\mathbf{a}+\mathbf{B}^{-1}\mathbf{b}),\left(\mathbf{A}^{-1}+\mathbf{B}^{-1}\right)^{-1}\right], \end{aligned}$$

to combine the two normal distributions in $\mathbf{z}_{t-1}$ which gives:

$$q(\mathbf{z}_{t-1}|\mathbf{z}_t,\mathbf{x}) = \text{Norm}_{\mathbf{z}_{t-1}}\left[\frac{(1-\alpha_{t-1})}{1-\alpha_t}\sqrt{1-\beta_t}\mathbf{z}_t+\frac{\sqrt{\alpha_{t-1}}\beta_t}{1-\alpha_t}\mathbf{x},\frac{\beta_t(1-\alpha_{t-1})}{1-\alpha_t}\mathbf{I}\right]. \qquad (18.15)$$

Note that the constants of proportionality in equations 18.12, 18.13, and 18.14 must cancel out, since the final result is already a correctly normalized probability distribution.

18.3 Decoder model (reverse process)

When we learn a diffusion model, we learn the *reverse process*. In other words, we learn a series of probabilistic mappings back from latent variable $\mathbf{z}_T$ to $\mathbf{z}_{T-1}$, from $\mathbf{z}_{T-1}$ to $\mathbf{z}_{T-2}$ and so on until we reach the data $\mathbf{x}$. The true reverse distributions $q(\mathbf{z}_{t-1}|\mathbf{z}_t)$ of the diffusion process are complex multi-modal distributions (figure 18.5) that depend on the data distribution $Pr(\mathbf{x})$. We approximate these as normal distributions:

$$\begin{aligned} Pr(\mathbf{z}_T) &= \text{Norm}_{\mathbf{z}_T}[\mathbf{0},\mathbf{I}]\\ Pr(\mathbf{z}_{t-1}|\mathbf{z}_t,\boldsymbol{\phi}_t) &= \text{Norm}_{\mathbf{z}_{t-1}}\left[\mathbf{f}_t[\mathbf{z}_t,\boldsymbol{\phi}_t],\sigma_t^2\mathbf{I}\right]\\ Pr(\mathbf{x}|\mathbf{z}_1,\boldsymbol{\phi}_1) &= \text{Norm}_{\mathbf{x}}\left[\mathbf{f}_1[\mathbf{z}_1,\boldsymbol{\phi}_1],\sigma_t^1\mathbf{I}\right], \qquad (18.16) \end{aligned}$$

where $\mathbf{f}_t[\mathbf{z}_t, \boldsymbol{\phi}_1]$ is a neural network that computes the mean of the normal distribution in the estimated mapping from $\mathbf{z}_{t-1}$ to the subsequent latent variable $\mathbf{z}_t$. The terms $\{\sigma_t^2\}$ are predetermined. If the hyperparameters β_t in the diffusion process are close to one (and the number of time steps T is large), then this normal approximation will be reasonable.

We generate new examples from $Pr(\mathbf{x})$ using ancestral sampling. We start by drawing $\mathbf{z}_T$ from $Pr(\mathbf{z}_T)$. Then we sample $\mathbf{z}_{T-1}$ from $Pr(\mathbf{z}_{T-1}|\mathbf{z}_T, \boldsymbol{\phi}_T)$, $\mathbf{z}_{T-2}$ from $Pr(\mathbf{z}_{T-2}|\mathbf{z}_{T-1}, \boldsymbol{\phi}_{T-1})$ and so on until we finally generate $\mathbf{x}$ from $Pr(\mathbf{x}|\mathbf{z}_1, \boldsymbol{\phi}_1)$.

18.4 Training

The joint distribution of the observed variable $\mathbf{x}$ and the latent variables $\{\mathbf{z}_t\}$ is:

$$Pr(\mathbf{x}, \mathbf{z}_{1\ldots T}|\boldsymbol{\phi}_{1\ldots T}) = Pr(\mathbf{x}|\mathbf{z}_1, \boldsymbol{\phi}_1) \prod_{t=2}^{T} Pr(\mathbf{z}_{t-1}|\mathbf{z}_t, \boldsymbol{\phi}_t) \cdot Pr(\mathbf{z}_T). \tag{18.17}$$

Appendix B.1.2 Marginalization

The likelihood of the parameters $Pr(\mathbf{x}|\boldsymbol{\phi}_{1\ldots T})$ is found by marginalizing over the latent variables:

$$Pr(\mathbf{x}|\boldsymbol{\phi}_{1\ldots T}) = \int Pr(\mathbf{x}, \mathbf{z}_{1\ldots T}|\boldsymbol{\phi}_{1\ldots T}) d\mathbf{z}_{1\ldots T}. \tag{18.18}$$

To train the model, we maximize the log likelihood of the training data $\{\mathbf{x}_i\}$ with respect to the parameters $\boldsymbol{\phi}$:

$$\hat{\boldsymbol{\phi}}_{1\ldots t} = \underset{\boldsymbol{\phi}_{1\ldots T}}{\operatorname{argmax}} \left[\sum_{i=1}^{I} \Bigl[\log\bigl[Pr(\mathbf{x}_i|\boldsymbol{\phi}_{1\ldots T})\bigr] \Bigr] \right]. \tag{18.19}$$

We can't maximize this directly because the marginalization in equation 18.18 is intractable. Hence, we use Jensen's inequality to define a lower bound on the likelihood and optimize the parameters $\{\boldsymbol{\phi}_t\}$ with respect to this bound exactly as we did for the VAE (see section 17.3.1).

18.4.1 Evidence lower bound (ELBO)

To derive the lower bound, we multiply and divide the log likelihood by the encoder distribution $q(\mathbf{z}_{1\ldots T}|\mathbf{x})$ and apply Jensen's inequality for the concave logarithm function:

$$\begin{aligned}\log\left[Pr(\mathbf{x}, \boldsymbol{\phi}_{1\ldots T})\right] &= \log\left[\int Pr(\mathbf{x}, \mathbf{z}_{1\ldots T}|\boldsymbol{\phi}_{1\ldots T})d\mathbf{z}_{1\ldots T}\right] \\ &= \log\left[\int q(\mathbf{z}_{1\ldots T}|\mathbf{x})\frac{Pr(\mathbf{x}, \mathbf{z}_{1\ldots T}|\boldsymbol{\phi}_{1\ldots T})}{q(\mathbf{z}_{1\ldots T}|\mathbf{x})}d\mathbf{z}_{1\ldots T}\right] \\ &\geq \int q(\mathbf{z}_{1\ldots T}|\mathbf{x})\log\left[\frac{Pr(\mathbf{x}, \mathbf{z}_{1\ldots T}|\boldsymbol{\phi}_{1\ldots T})}{q(\mathbf{z}_{1\ldots T}|\mathbf{x})}\right]d\mathbf{z}_{1\ldots T}. \end{aligned} \tag{18.20}$$

This gives us the evidence lower bound (ELBO):

$$\text{ELBO}[\boldsymbol{\phi}_{1\ldots T}] = \int q(\mathbf{z}_{1\ldots T}|\mathbf{x})\log\left[\frac{Pr(\mathbf{x}, \mathbf{z}_{1\ldots T}|\boldsymbol{\phi}_{1\ldots T})}{q(\mathbf{z}_{1\ldots T}|\mathbf{x})}\right]d\mathbf{z}_{1\ldots T}. \tag{18.21}$$

In the VAE, the encoder $q(\boldsymbol{\phi})$ approximates the posterior distribution over the latent variables to make the bound tight, and the decoder maximizes this bound (figure 17.10). In diffusion models, the decoder must do all the work, since the encoder has no parameters. It makes the bound tighter by both (i) changing its parameters so that the static encoder does approximate the posterior $Pr(\mathbf{z}_{1\ldots T}|\mathbf{x}, \boldsymbol{\phi}_{1\ldots T})$, and (ii) optimizing its parameters with respect to that bound (see figure 17.6).

18.4.2 Simplifying the ELBO

We now manipulate the log term from the ELBO into the final form that we will optimize. We first substitute in the definitions for the numerator and denominator, from equations 18.17 and 18.3, respectively:

$$\begin{aligned}\log\left[\frac{Pr(\mathbf{x}, \mathbf{z}_{1\ldots T}|\boldsymbol{\phi}_{1\ldots T})}{q(\mathbf{z}_{1\ldots T}|\mathbf{x})}\right] &= \log\left[\frac{Pr(\mathbf{x}|\mathbf{z}_1, \boldsymbol{\phi}_1)\prod_{t=2}^{T}Pr(\mathbf{z}_{t-1}|\mathbf{z}_t, \boldsymbol{\phi}_t)\cdot Pr(\mathbf{z}_T)}{q(\mathbf{z}_1|\mathbf{x})\prod_{t=2}^{T}q(\mathbf{z}_t|\mathbf{z}_{t-1})}\right] \\ &= \log\left[\frac{Pr(\mathbf{x}|\mathbf{z}_1, \boldsymbol{\phi}_1)}{q(\mathbf{z}_1|\mathbf{x})}\right]+\log\left[\frac{\prod_{t=2}^{T}Pr(\mathbf{z}_{t-1}|\mathbf{z}_t, \boldsymbol{\phi}_t)}{\prod_{t=2}^{T}q(\mathbf{z}_t|\mathbf{z}_{t-1})}\right]+\log\Big[Pr(\mathbf{z}_T)\Big]. \end{aligned} \tag{18.22}$$

Then we expand the denominator of the second term:

$$q(\mathbf{z}_t|\mathbf{z}_{t-1}) = q(\mathbf{z}_t|\mathbf{z}_{t-1}, \mathbf{x}) = \frac{q(\mathbf{z}_{t-1}|\mathbf{z}_t, \mathbf{x})q(\mathbf{z}_t|\mathbf{x})}{q(\mathbf{z}_{t-1}|\mathbf{x})}, \tag{18.23}$$

where the first equality follows because all of the information about variable $\mathbf{z}_t$ is encompassed in $\mathbf{z}_{t-1}$ and so the extra conditioning on the data $\mathbf{x}$ is irrelevant. The second equality is a straightforward application of Bayes' rule.

Appendix B.1.4
Bayes' rule

Substituting this result back in, we have:

$$
\begin{aligned}
&\log\left[\frac{Pr(\mathbf{x},\mathbf{z}_{1\ldots T}|\boldsymbol{\phi}_{1\ldots T})}{q(\mathbf{z}_{1\ldots T}|\mathbf{x})}\right]\\
&\qquad= \log\left[\frac{Pr(\mathbf{x}|\mathbf{z}_1,\boldsymbol{\phi}_1)}{q(\mathbf{z}_1|\mathbf{x})}\right] + \log\left[\frac{\prod_{t=2}^{T} Pr(\mathbf{z}_{t-1}|\mathbf{z}_t,\boldsymbol{\phi}_t)}{\prod_{t=2}^{T} q(\mathbf{z}_{t-1}|\mathbf{z}_t,\mathbf{x})}\cdot\frac{q(\mathbf{z}_{t-1}|\mathbf{x})}{q(\mathbf{z}_t|\mathbf{x})}\right] + \log\Big[Pr(\mathbf{z}_t)\Big]\\
&\qquad= \log\left[Pr(\mathbf{x}|\mathbf{z}_1,\boldsymbol{\phi}_1)\right] + \log\left[\frac{\prod_{t=2}^{T} Pr(\mathbf{z}_{t-1}|\mathbf{z}_t,\boldsymbol{\phi}_t)}{\prod_{t=2}^{T} q(\mathbf{z}_{t-1}|\mathbf{z}_t,\mathbf{x})}\right] + \log\left[\frac{Pr(\mathbf{z}_t)}{q(\mathbf{z}_T|\mathbf{x})}\right]\\
&\qquad\approx \log\left[Pr(\mathbf{x}|\mathbf{z}_1,\boldsymbol{\phi}_1)\right] + \sum_{t=2}^{T}\log\left[\frac{Pr(\mathbf{z}_{t-1}|\mathbf{z}_t,\boldsymbol{\phi}_t)}{q(\mathbf{z}_{t-1}|\mathbf{z}_t,\mathbf{x})}\right], \qquad (18.24)
\end{aligned}
$$

where all but two of the terms in the sum of the ratio $q(\mathbf{z}_{t-1}|\mathbf{x})/q(\mathbf{z}_t|\mathbf{x})$ cancel out between lines two and three leaving only $q(\mathbf{z}_1|\mathbf{x})$ and $q(\mathbf{z}_T|\mathbf{x})$. The last term in the third line is approximately $\log[1]=0$, since the result of the forward process $q(\mathbf{z}_T|\mathbf{x})$ should be a standard normal distribution and so is the prior $Pr(\mathbf{z}_T)$.

The simplified ELBO is hence:

$$
\begin{aligned}
\mathrm{ELBO}[\boldsymbol{\phi}_{1\ldots T}] &= \int q(\mathbf{z}_{1\ldots T}|\mathbf{x})\log\left[\frac{Pr(\mathbf{x},\mathbf{z}_{1\ldots T}|\boldsymbol{\phi}_{1\ldots T})}{q(\mathbf{z}_{1\ldots T}|\mathbf{x})}\right]d\mathbf{z}_{1\ldots T} \qquad (18.25)\\
&\approx \int q(\mathbf{z}_{1\ldots T}|\mathbf{x})\left(\log\left[Pr(\mathbf{x}|\mathbf{z}_1,\boldsymbol{\phi}_1)\right] + \sum_{t=2}^{T}\log\left[\frac{Pr(\mathbf{z}_{t-1}|\mathbf{z}_t,\boldsymbol{\phi}_t)}{q(\mathbf{z}_{t-1}|\mathbf{z}_t,\mathbf{x})}\right]\right)d\mathbf{z}_{1\ldots T}\\
&= \mathbb{E}_{q(\mathbf{z}_1|\mathbf{x})}\Big[\log\left[Pr(\mathbf{x}|\mathbf{z}_1,\boldsymbol{\phi}_1)\right]\Big] - \sum_{t=2}^{T}\mathrm{D}_{KL}\Big[Pr(\mathbf{z}_{t-1}|\mathbf{z}_t,\boldsymbol{\phi}_t)||q(\mathbf{z}_{t-1}|\mathbf{z}_t,\mathbf{x})\Big].
\end{aligned}
$$

Appendix B.5.1 KL divergence

where we have substituted in the definition of $q(\mathbf{z}_{1\ldots T}|\mathbf{x})$ from equation 18.3 between lines two and three and integrated out the irrelevant terms. The second term results from the definition of KL-divergence.

18.4.3 Analyzing the ELBO

The first probability term in the ELBO was defined in equation 18.16:

$$
Pr(\mathbf{x}|\mathbf{z}_1,\boldsymbol{\phi}_1) = \mathrm{Norm}_{\mathbf{x}}\left[\mathbf{f}_1[\mathbf{z}_1,\boldsymbol{\phi}_1],\sigma_t^2\mathbf{I}\right], \qquad (18.26)
$$

and is equivalent to the reconstruction term in the VAE. The ELBO will be larger if the model prediction matches the observed data. As for the VAE, we will approximate the expectation over the log of this quantity using a Monte-Carlo estimate (see equations 17.22–17.23), in which we estimate the expectation with a sample from $q(\mathbf{z}_1|\mathbf{x})$.

The KL-divergence terms in the ELBO measure the distance between $Pr(\mathbf{z}_{t-1}|\mathbf{z}_t,\boldsymbol{\phi}_t)$ and $q(\mathbf{z}_{t-1}|\mathbf{z}_t,\mathbf{x})$ which were defined in equations 18.16 and 18.15, respectively:

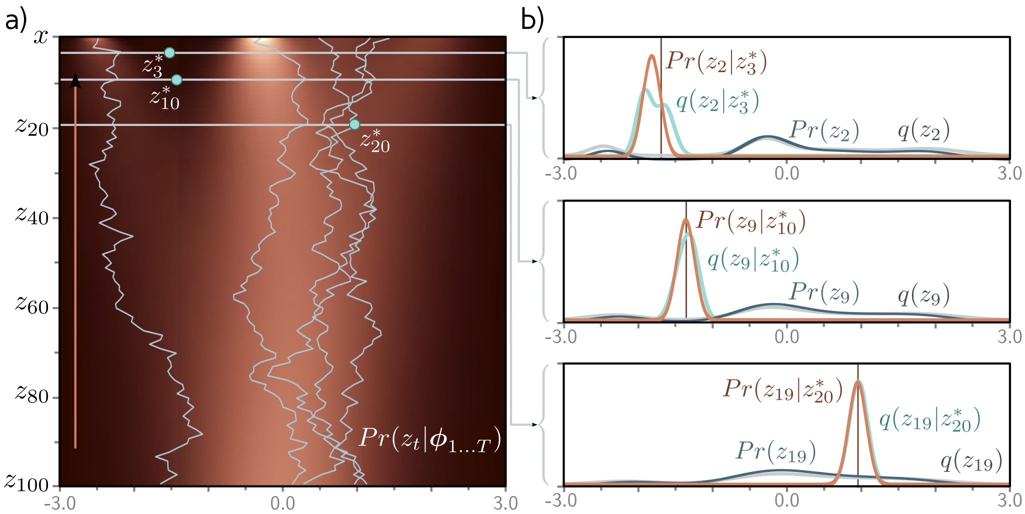

Figure 18.7 Fitted Model. a) Individual samples can be generated by sampling from the standard normal distribution $Pr(z_T)$ and then sampling z_{T-1} from $Pr(z_{T-1}|z_T) = \text{Norm}_{\mathbf{z}_{T-1}}[\text{f}_T[z_T, \boldsymbol{\phi}_T], \sigma_T^2\mathbf{I}]$ and so on until we reach x (five paths shown). The estimated marginal densities (heatmap) are the aggregation of these samples, and are similar to the true marginal densities (figure 18.4). b) The estimated distribution $Pr(z_{t-1}|z_t)$ (brown curve) is a reasonable approximation to the true posterior of the diffusion model $q(z_{t-1}|z_t)$ (cyan curve) from figure 18.5. The marginal distributions $Pr(z_t)$ and $q(z_t)$ of the estimated and true models (dark blue and gray curves, respectively) are also similar.

$$
\begin{aligned}
Pr(\mathbf{z}_{t-1}|\mathbf{z}_t, \boldsymbol{\phi}_t) &= \text{Norm}_{\mathbf{z}_{t-1}}\left[\mathbf{f}_t[\mathbf{z}_t, \boldsymbol{\phi}_t], \sigma_t^2\mathbf{I}\right] \\
q(\mathbf{z}_{t-1}|\mathbf{z}_t, \mathbf{x}) &= \text{Norm}_{\mathbf{z}_{t-1}}\left[\frac{(1-\alpha_{t-1})}{1-\alpha_t}\sqrt{1-\beta_t}\mathbf{z}_t + \frac{\sqrt{\alpha_{t-1}}\beta_t}{1-\alpha_t}\mathbf{x}, \frac{\beta_t(1-\alpha_{t-1})}{1-\alpha_t}\mathbf{I}\right].
\end{aligned}
\tag{18.27}
$$

The KL-divergence between two normal distributions has a closed form expression. Moreover, many of the terms in this expression do not depend on $\boldsymbol{\phi}$ (see problem 18.6), and the expression simplifies to the squared difference between the means:

Appendix B.5.4 KL divergence between normal distributions

Problem 18.6

$$
\begin{aligned}
D_{KL}\Big[Pr(\mathbf{z}_{t-1}|\mathbf{z}_t, \boldsymbol{\phi}_t)||q(\mathbf{z}_{t-1}|\mathbf{z}_t, \mathbf{x})\Big] &= \\
\frac{1}{2\sigma_t^2}\left\|\frac{(1-\alpha_{t-1})}{1-\alpha_t}\sqrt{1-\beta_t}\mathbf{z}_t + \frac{\sqrt{\alpha_{t-1}}\beta_t}{1-\alpha_t}\mathbf{x} - \mathbf{f}_t[\mathbf{z}_t, \boldsymbol{\phi}_t]\right\|^2 &+ C,
\end{aligned}
\tag{18.28}
$$

where C is a constant.

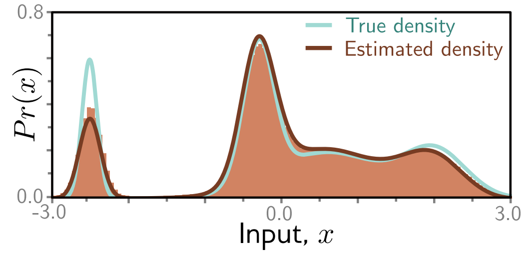

Figure 18.8 Fitted model results. Cyan and brown curves are original and estimated densities and correspond to the top rows of figures 18.5 and 18.7, respectively. Vertical bars are binned samples from the model, generated by propagating back samples $Pr(\mathbf{z}_T)$ as shown for the five paths in figure 18.7.

18.4.4 Diffusion loss function

To fit the model, we maximize the ELBO with respect to the parameters $\boldsymbol{\phi}_{1...T}$. We recast this as a minimization by multiplying with minus one to give the loss function:

$$\begin{aligned} L[\boldsymbol{\phi}] &= \sum_{i=1}^{I}\Bigg(\overbrace{-\log\Big[\text{Norm}_{\mathbf{x}_i}\big[\mathbf{f}_1[\mathbf{z}_{i1},\boldsymbol{\phi}_1],\sigma_1^2\mathbf{I}\big]\Big]}^{\text{reconstruction term}} \\ &\quad + \sum_{t=2}^{T}\frac{1}{2\sigma_t^2}\Bigg\|\underbrace{\left(\frac{(1-\alpha_{t-1})}{1-\alpha_t}\sqrt{1-\beta_t}\mathbf{z}_{it}+\frac{\sqrt{\alpha_{t-1}}\beta_t}{1-\alpha_t}\mathbf{x}_i\right)}_{\text{mean of } q(\mathbf{z}_{t-1}|\mathbf{z}_t,\mathbf{x})} - \underbrace{\mathbf{f}_t[\mathbf{z}_{it},\boldsymbol{\phi}_t]}_{\text{predicted } \mathbf{z}_{t-1}}\Bigg\|^2\Bigg), \end{aligned} \tag{18.29}$$

where $\mathbf{x}_i$ is the i^{th} data point and $\mathbf{z}_{it}$ is the associated latent variable at diffusion step t.

18.4.5 Training procedure

This loss function can be used to train a network for each diffusion time step. It minimizes the difference between the estimate $\mathbf{f}_t[\mathbf{z}_t,\boldsymbol{\phi}_t]$ of the hidden variable at the previous time step and the most likely value that it took given the ground truth de-noised data $\mathbf{x}$.

Figures 18.7 and 18.8 show the fitted reverse process for the simple 1D example. This model was trained by (i) taking a large dataset of examples $\mathbf{x}$ from the original density, (ii) using the diffusion kernel to predict many corresponding values for the latent variable at time $\mathbf{z}_t$, and then (iii) training a series of models $\mathbf{f}_t[\mathbf{z}_t,\boldsymbol{\phi}_t]$ to minimize the loss function in equation 18.29. These models were nonparametric (i.e., lookup tables relating 1D input to 1D output), but more typically they would be deep neural networks.

18.5 Reparameterization of loss function

Although the loss function in equation 18.29 can be used, diffusion models have been found to work better with a different parameterization; the loss function is modified so that the model aims to predict the noise that was mixed with the original data example to create the current variable. Section 18.5.1 discusses reparameterizing the target (first two terms in second line of equation 18.29) and section 18.5.2 discusses reparameterizing the network (last term in second line of equation 18.29).

18.5.1 Reparameterization of target

The original diffusion update was given by:

$$\mathbf{z}_t = \sqrt{\alpha_t}\mathbf{x} + \sqrt{1-\alpha_t}\boldsymbol{\epsilon}, \tag{18.30}$$

and so the data term $\mathbf{x}$ in equation 18.28, can be expressed as the diffused image minus the noise that was added to it:

$$\mathbf{x} = \frac{1}{\sqrt{\alpha_t}}\mathbf{z}_t - \frac{\sqrt{1-\alpha_t}}{\sqrt{\alpha_t}}\boldsymbol{\epsilon}. \tag{18.31}$$

Substituting this into the target terms from equation 18.29 gives:

$$\begin{aligned}
\frac{(1-\alpha_{t-1})}{1-\alpha_t}\sqrt{1-\beta_t}\mathbf{z}_t + \frac{\sqrt{\alpha_{t-1}}\beta_t}{1-\alpha_t}\mathbf{x} \quad &= \\
&\frac{(1-\alpha_{t-1})}{1-\alpha_t}\sqrt{1-\beta_t}\mathbf{z}_t + \frac{\sqrt{\alpha_{t-1}}\beta_t}{1-\alpha_t}\left(\frac{1}{\sqrt{\alpha_t}}\mathbf{z}_t - \frac{\sqrt{1-\alpha_t}}{\sqrt{\alpha_t}}\boldsymbol{\epsilon}\right) \\
&\frac{(1-\alpha_{t-1})}{1-\alpha_t}\sqrt{1-\beta_t}\mathbf{z}_t + \frac{\beta_t}{1-\alpha_t}\left(\frac{1}{\sqrt{1-\beta_t}}\mathbf{z}_t - \frac{\sqrt{1-\alpha_t}}{\sqrt{1-\beta_t}}\boldsymbol{\epsilon}\right),
\end{aligned} \tag{18.32}$$

where we have used the fact that $\sqrt{\alpha_t}/\sqrt{\alpha_{t-1}} = \sqrt{1-\beta_t}$ between the second and third lines. Simplifying further, we get: Problem 18.7

$$\begin{aligned}
\frac{(1-\alpha_{t-1})}{1-\alpha_t}\sqrt{1-\beta_t}\mathbf{z}_t + \frac{\sqrt{\alpha_{t-1}}\beta_t}{1-\alpha_t}\mathbf{x} \quad &= \\
&\left(\frac{(1-\alpha_{t-1})\sqrt{1-\beta_t}}{1-\alpha_t} + \frac{\beta_t}{(1-\alpha_t)\sqrt{1-\beta_t}}\right)\mathbf{z}_t - \frac{\beta_t}{\sqrt{1-\alpha_t}\sqrt{1-\beta_t}}\boldsymbol{\epsilon} \\
&\left(\frac{(1-\alpha_{t-1})(1-\beta_t)}{(1-\alpha_t)\sqrt{1-\beta_t}} + \frac{\beta_t}{(1-\alpha_t)\sqrt{1-\beta_t}}\right)\mathbf{z}_t - \frac{\beta_t}{\sqrt{1-\alpha_t}\sqrt{1-\beta_t}}\boldsymbol{\epsilon} \\
&\frac{(1-\alpha_{t-1})(1-\beta_t)+\beta_t}{(1-\alpha_t)\sqrt{1-\beta_t}}\mathbf{z}_t - \frac{\beta_t}{\sqrt{1-\alpha_t}\sqrt{1-\beta_t}}\boldsymbol{\epsilon} \\
&\frac{1-\alpha_t}{(1-\alpha_t)\sqrt{1-\beta_t}}\mathbf{z}_t - \frac{\beta_t}{\sqrt{1-\alpha_t}\sqrt{1-\beta_t}}\boldsymbol{\epsilon} \\
&\frac{1}{\sqrt{1-\beta_t}}\mathbf{z}_t - \frac{\beta_t}{\sqrt{1-\alpha_t}\sqrt{1-\beta_t}}\boldsymbol{\epsilon},
\end{aligned} \tag{18.33}$$

where we have multiplied the numerator and denominator of the first term by $\sqrt{1-\beta_t}$ between lines two and three, and multiplied out the terms and simplified the numerator in the first term between lines three and four.

Problem 18.8

Substituting this back into the loss function we have:

$$
\begin{aligned}
L[\boldsymbol{\phi}] &= \sum_{i=1}^{I} -\log\Bigl[\mathrm{Norm}_{\mathbf{x}_i}\left[\mathbf{f}_1[\mathbf{z}_{i1},\boldsymbol{\phi}_1],\sigma_1^2\mathbf{I}\right]\Bigr] \\
&\quad + \sum_{t=2}^{T}\frac{1}{2\sigma_t^2}\left\|\left(\frac{1}{\sqrt{1-\beta_t}}\mathbf{z}_{it}-\frac{\beta_t}{\sqrt{1-\alpha_t}\sqrt{1-\beta_t}}\boldsymbol{\epsilon}\right)-\mathbf{f}_t[\mathbf{z}_{it},\boldsymbol{\phi}_t]\right\|^2.
\end{aligned}
\tag{18.34}
$$

18.5.2 Reparameterization of network

Now we replace the model $\hat{\mathbf{z}}_{t-1} = \mathbf{f}_t[\mathbf{z}_t,\boldsymbol{\phi}_t]$, with a new model $\hat{\boldsymbol{\epsilon}} = \mathbf{g}_t[\mathbf{z}_t,\boldsymbol{\phi}_t]$, which predicts the noise $\boldsymbol{\epsilon}$ that was mixed with $\mathbf{x}$ to create $\mathbf{z}_t$:

$$
\mathbf{f}_t[\mathbf{z}_t,\boldsymbol{\phi}_t] = \frac{1}{\sqrt{1-\beta_t}}\mathbf{z}_t - \frac{\beta_t}{\sqrt{1-\alpha_t}\sqrt{1-\beta_t}}\mathbf{g}_t[\mathbf{z}_t,\boldsymbol{\phi}_t]. \tag{18.35}
$$

Substituting the new model into equation 18.34 produces the criterion:

$$
L[\boldsymbol{\phi}] = \sum_{i=1}^{I} -\log\Bigl[\mathrm{Norm}_{\mathbf{x}_i}\left[\mathbf{f}_1[\mathbf{z}_{i1},\boldsymbol{\phi}_1],\sigma_1^2\mathbf{I}\right]\Bigr] + \sum_{t=2}^{T}\frac{\beta_t^2}{(1-\alpha_t)(1-\beta_t)2\sigma_t^2}\left\|\mathbf{g}_t[\mathbf{z}_{it},\boldsymbol{\phi}_t]-\boldsymbol{\epsilon}_{it}\right\|^2. \tag{18.36}
$$

The log normal can equivalently be written as a least squares loss plus a constant C_i:

$$
L[\boldsymbol{\phi}] = \sum_{i=1}^{I}\frac{1}{2\sigma_1^2}\left\|\mathbf{x}_i-\mathbf{f}_1[\mathbf{z}_{i1},\boldsymbol{\phi}_1]\right\|^2 + \sum_{t=2}^{T}\frac{\beta_t^2}{(1-\alpha_t)(1-\beta_t)2\sigma_t^2}\left\|\mathbf{g}_t[\mathbf{z}_{it},\boldsymbol{\phi}_t]-\boldsymbol{\epsilon}_{it}\right\|^2 + C_i.
$$

Problem 18.9

Substituting in the definitions of $\mathbf{x}$ and $\mathbf{f}_t[\mathbf{z}_t,\boldsymbol{\phi}_t]$ from equations 18.31 and 18.35, respectively, the first term simplifies to:

$$
\frac{1}{2\sigma_1^2}\left\|\mathbf{x}_i-\mathbf{f}_1[\mathbf{z}_{i1},\boldsymbol{\phi}_1]\right\|^2 = \frac{1}{2\sigma_1^2}\left\|\frac{\beta_1}{\sqrt{1-\alpha_1}\sqrt{1-\beta_1}}\mathbf{g}_1[\mathbf{z}_{i1},\boldsymbol{\phi}_1] - \frac{\beta_1}{\sqrt{1-\alpha_1}\sqrt{1-\beta_1}}\boldsymbol{\epsilon}_{i1}\right\|^2. \tag{18.37}
$$

Adding this back to the final loss function yields:

$$
L[\boldsymbol{\phi}] = \sum_{i=1}^{I}\sum_{t=1}^{T}\frac{\beta_t^2}{(1-\alpha_t)(1-\beta_t)2\sigma_t^2}\left\|\mathbf{g}_t[\mathbf{z}_{it},\boldsymbol{\phi}_t]-\boldsymbol{\epsilon}_{it}\right\|^2, \tag{18.38}
$$

where we have disregarded the additive constants C_i.

Algorithm 18.1: Diffusion model training

Input: Training data $\mathbf{x}$
Output: Model parameters $\boldsymbol{\phi}_t$
repeat
  for $i \in \mathcal{B}$ **do** // For every training example index in batch
    $t \sim \text{Uniform}[1, \ldots T]$ // Sample random timestep
    $\boldsymbol{\epsilon} \sim \text{Norm}[\mathbf{0}, \mathbf{I}]$ // Sample noise
    $\ell_i = \left\|\mathbf{g}_t\left[\sqrt{\alpha_t}\mathbf{x}_i + \sqrt{1-\alpha_t}\boldsymbol{\epsilon}, \boldsymbol{\phi}_t\right] - \boldsymbol{\epsilon}\right\|^2$ // Compute individual loss
  Accumulate losses for batch and take gradient step
until converged

where the log normal has been replaced by a least squares term plus an additive constant C (see section 5.3.1). In practice, the scaling factors (which might be different at each time step) are ignored giving an even simpler formulation:

$$
\begin{aligned}
L[\boldsymbol{\phi}] &= \sum_{i=1}^{I}\sum_{t=1}^{T}\left\|\mathbf{g}_t[\mathbf{z}_{it}, \boldsymbol{\phi}_t] - \boldsymbol{\epsilon}_{it}\right\|^2 \\
&= \sum_{i=1}^{I}\sum_{t=1}^{T}\left\|\mathbf{g}_t\left[\sqrt{\alpha_t}\mathbf{x}_i + \sqrt{1-\alpha_t}\boldsymbol{\epsilon}_{it}, \boldsymbol{\phi}_t\right] - \boldsymbol{\epsilon}_{it}\right\|^2,
\end{aligned}
\tag{18.39}
$$

where we have rewritten $\mathbf{z}_t$ using the diffusion kernel (equation 18.30) in the second line.

18.6 Implementation

This leads to straightforward algorithms for both training the model (algorithm 18.1) and sampling (algorithm 18.2). The training algorithm has the advantages that it is (i) simple to implement and (ii) naturally augments the dataset; we can reuse every original data point $\mathbf{x}_i$ as many times as we want at each time step with different noise instantiations $\boldsymbol{\epsilon}$. The sampling algorithm has the disadvantage that it requires serial processing of many neural networks $\mathbf{g}_t[\mathbf{z}_t, \boldsymbol{\phi}_t]$, and is hence time consuming.

18.6.1 Application to images

The early successes of diffusion models were in modeling image data. Here, we need to construct models that can take a noisy image and predict the noise that was added to it at each stage. The obvious architectural choice for this image-to-image mapping is an encoder-decoder model similar to the U-Net.

Algorithm 18.2: Sampling

Input: Model, $\mathbf{g}_t[\bullet, \boldsymbol{\phi}_t]$
Output: Sample, $\mathbf{x}$
$\mathbf{z}_T \sim \text{Norm}_{\mathbf{z}}[\mathbf{0}, \mathbf{I}]$ `// Sample last latent variable`
for $t = T \ldots 2$ **do**
  $\hat{\mathbf{z}}_{t-1} = \frac{1}{\sqrt{1-\beta_t}}\mathbf{z}_t - \frac{\beta_t}{\sqrt{1-\alpha_t}\sqrt{1-\beta_t}}\mathbf{g}_t[\mathbf{z}_t, \boldsymbol{\phi}_t]$ `// Predict previous latent variable`
  $\boldsymbol{\epsilon} \sim \text{Norm}_{\boldsymbol{\epsilon}}[\mathbf{0}, \mathbf{I}]$ `// Draw new noise vector`
  $\mathbf{z}_{t-1} = \hat{\mathbf{z}}_{t-1} + \sigma_t \boldsymbol{\epsilon}$ `// Add noise to previous latent variable`
$\mathbf{x} = \frac{1}{\sqrt{1-\beta_1}}\mathbf{z}_1 - \frac{\beta_1}{\sqrt{1-\alpha_1}\sqrt{1-\beta_1}}\mathbf{g}_1[\mathbf{z}_1, \boldsymbol{\phi}_1]$ // Generate sample from $\mathbf{z}_1$ without noise

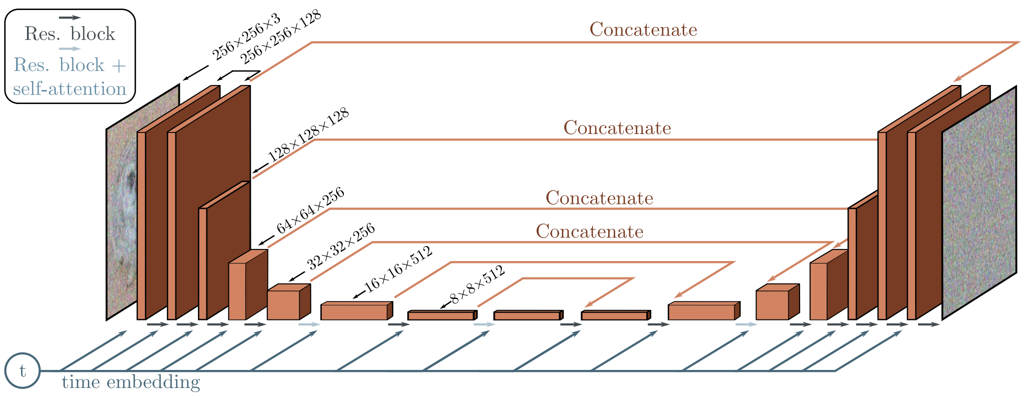

Figure 18.9 U-Net as used in diffusion models for images. The network aims to predict the noise that was added to the image. It consists of an encoder which reduces the scale and increases the number of channels and a decoder which increases the scale and reduces the number of channels. The encoder representations are concatenated to their partner in the decoder. Connections between adjacent representations consist of residual blocks, and periodic global self-attention in which every spatial position interacts with every other spatial position. A single network is used for all time steps, by passing a sinusoidal time embedding (figure 12.5) through a shallow neural network and adding the result to the channels at every spatial position at every stage of the U-Net.

However, there may be a very large number of diffusion steps, and training and storing this many U-Nets is inefficient. The solution is to train a single U-Net that also takes a predetermined vector representing the time step as input (figure 18.9). In practice, this is resized to match the number of channels at each stage of the U-Net and used to offset and/or scale the representation at each spatial position.

The logic for having so many time steps is that the conditional probabilities $q(\mathbf{z}_{t-1}|\mathbf{z}_t)$ become closer to normally distributed when the hyperparameters β_t are close to zero and so the variational approximation is closer. However, in practice, this makes sampling very

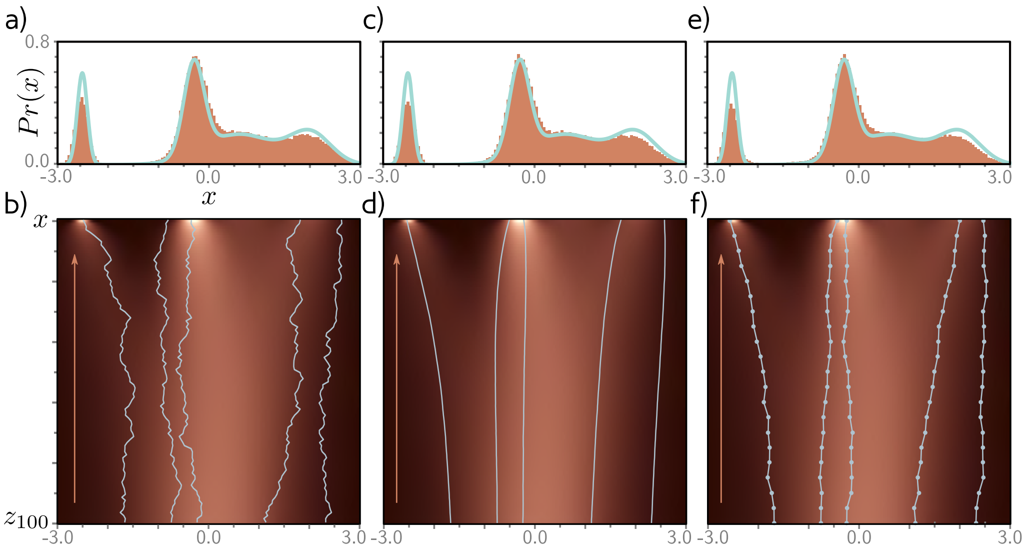

Figure 18.10 Different diffusion processes that are all compatible with the same model. a) Histogram of samples generated from re-parameterized model plotted alongside ground truth density curve. b) Five sampled trajectories superimposed on ground truth marginal distributions (figure 18.5) The same trained model is compatible with a family of diffusion models (and corresponding updates in the opposite direction), including the denoising diffusion implicit (DDIM) model, which is deterministic and does not add noise at each step. c) Histogram of samples from DDIM model. d) Five trajectories from DDIM model. The same model is also compatible with accelerated diffusion models that skip inference steps for increased sampling speed. e) Histogram of samples from accelerated model. f) Five trajectories from accelerated model.

slow. We might have to run the U-Net model through $T = 1000$ steps to generate good images.

18.6.2 Improving generation speed

The loss function (equation 18.39) requires the diffusion kernel to have the form $q(\mathbf{z}_t|\mathbf{x}) = \text{Norm}[\sqrt{\alpha_t}\mathbf{x}, \sqrt{1-\alpha_t}\cdot\mathbf{I}]$. The same loss function will be valid for *any* forward process with this relation and there are a family of such compatible processes. These are all optimized by the same loss function, but have different rules for the forward process, and different corresponding rules for how to use the estimated noise $\text{g}[\mathbf{z}_t, \boldsymbol{\phi}_t]$ to estimate $\mathbf{z}_{t-1}$ from $\mathbf{z}_t$ in the reverse process (figure 18.10).

Among this family are *denoising diffusion implicit models*, which are no longer stochastic after the first step from $\mathbf{x}$ to $\mathbf{z}_1$ and *accelerated sampling* models where the forward process is defined only on a sub-sequence of time steps. This allows a reverse process that skips time steps and hence makes sampling much more efficient; good samples can be created with 50 time steps when the forward process is no longer stochastic. This is much faster than before but still slower than most other generative models.

18.6.3 Conditional generation

If the data has associated labels c, then these can be exploited to control the generation. Sometimes this can improve generation results in GANs and we might expect this to be the case in diffusion models as well; it's easier to denoise an image if you have some information about what that image contains. One approach to conditional synthesis in GANs is *classifier guidance*. This modifies the denoising update from $\mathbf{z}_t$ to $\mathbf{z}_{t-1}$ to take into account additional information c. In practice, this means adding an extra term into the final update step in algorithm 18.2 to:

$$\mathbf{z}_{t-1} = \hat{\mathbf{z}}_{t-1} + \sigma_t^2 \frac{\partial \log\big[\Pr(c|\mathbf{z}_t)\big]}{\partial \mathbf{z}_t} + \sigma_t \boldsymbol{\epsilon}. \tag{18.40}$$

The new term depends on the gradient of a classifier $Pr(c|\mathbf{z}_t)$ that is based on the latent variable $\mathbf{z}_t$. This maps features from the downsampling half of the U-Net to the class c. Like the U-Net , it is usually shared across all time-steps and takes time as an input. The update from $\mathbf{z}_t$ to $\mathbf{z}_{t-1}$ now makes the class c more likely.

Classifier-free guidance avoids learning a separate classifier $Pr(c|\mathbf{z}_t)$, but instead incorporates class information into the main model $\mathbf{g}_t[\mathbf{z}_t, \boldsymbol{\phi}_t, c]$. In practice, this usually takes the form of adding an embedding based on c to the layers of the U-Net in a similar way to how the time step is added (see figure 18.9). This model is jointly trained on conditional and unconditional objectives by randomly dropping the class information during training. Hence, it can both generate unconditional or conditional data examples at test time or any weighted combination of the two. This brings a surprising advantage; if the conditioning information is over-weighted, then the model tends to produce very high quality, but slightly stereotypical examples. This is somewhat analogous to the use of truncation in GANs (figure 15.10).

18.6.4 Improving generation quality

As for other generative models, the highest quality results result from applying a combination of tricks and extensions to the basic model. First, it's been noted that it also helps to estimate the variances σ_t^2 of the reverse process as well as the mean (i.e., the widths of the brown normal distributions in figure 18.7). This particularly improves the results when sampling with fewer steps. Second, it's possible to modify the noise schedule in the forward process so that β_t varies at each step, and this can improve results.

Third, to generate high resolution images, a cascade of diffusion models is used. The first creates a low resolution image (possibly guided by class information). The subsequent diffusion models generate progressively higher resolution images. They condition

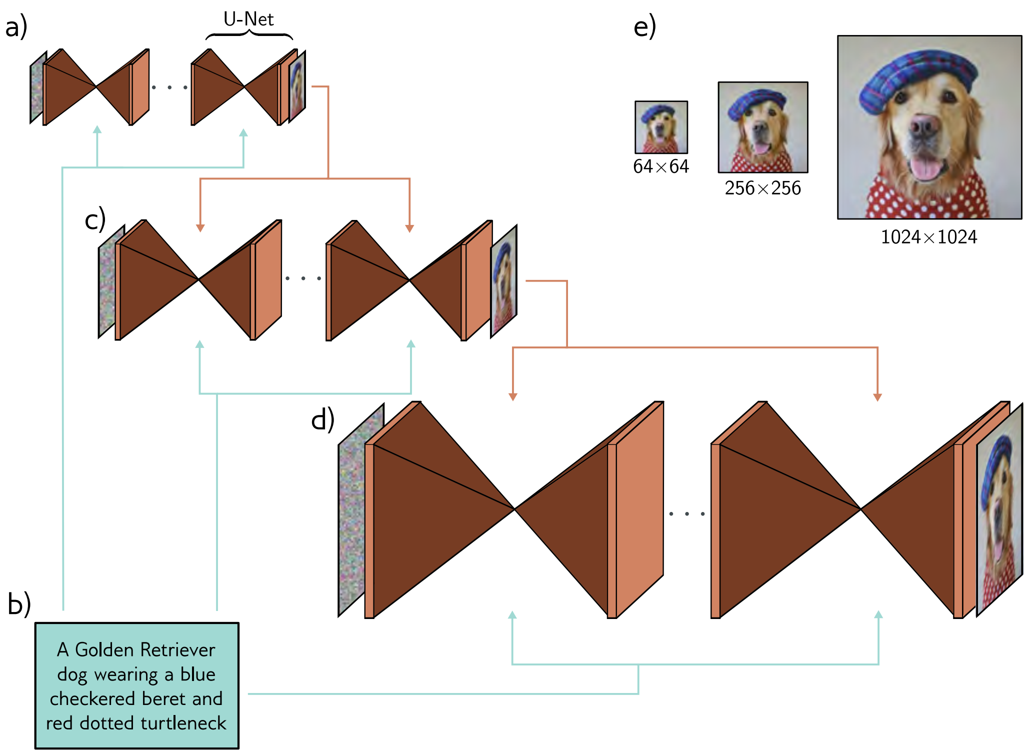

Figure 18.11 Cascaded conditional generation based on a text prompt. a) A diffusion model consisting of a series of U-Nets is used to generate a 64×64 image. b) This generation is conditioned on a sentence embedding computed by a language model. c) A higher resolution 256×256 image is generated and conditioned on the smaller image *and* the text encoding. d) This is repeated to create a 1024×1024 image. e) Final image sequence. Adapted from Saharia et al. (2022b).

on the lower resolution image by resizing this and appending it to the layers of the constituent U-Net, as well as any other class information (figure 18.11).

Combining all of these techniques allows generation of very high quality images. Figure 18.12 shows examples of images generated from a model conditioned on the ImageNet class. It is particularly impressive that the same model can learn to generate such diverse classes. Figure 18.13 shows images generated from a model that is trained to condition on text captions encoded by a language model like BERT, which are inserted into the model in the same way as the time step and lower resolution images (figures 18.9 and 18.11). This results in very realistic images that agree with the caption. Since the diffusion model is by its nature stochastic, it's possible to generate multiple images that are conditioned on the same caption.

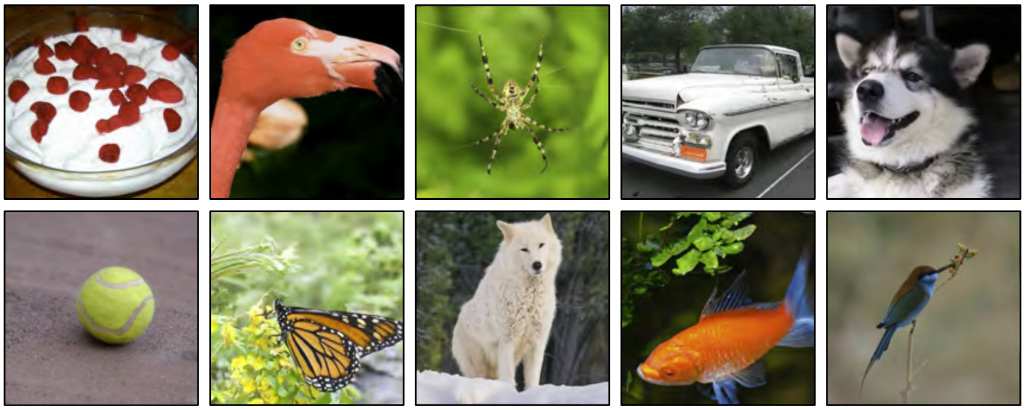

Figure 18.12 Conditional generation using classifier guidance. Image samples conditioned on different ImageNet classes. The same model produces high quality samples of highly varied image classes. Adapted from Dhariwal & Nichol (2021).

Figure 18.13 Conditional generation using text prompts. Synthesized images from a cascaded generation framework, conditioned on a text prompt encoded by a large language model. The stochastic model can produce many different images compatible with the prompt. The model can count objects, and incorporate text into images. Adapted from Saharia et al. (2022b).

18.7 Summary

Diffusion models map the data examples through a series of latent variables by repeatedly blending the current representation with random noise. After sufficient steps, the representation becomes indistinguishable from white noise. Since these steps are small, the reverse denoising process at each step can be approximated with a normal distribution, and predicted by a deep learning model. The loss function is based on the evidence lower bound (ELBO), and ultimately results in a simple least-squares formulation.

For image generation, each denoising step is implemented using a U-Net, so sampling is slow compared to other generative models. To improve generation speed, it's possible to change the diffusion model to a deterministic formulation and here sampling with fewer steps works well. Several methods have been proposed to condition generation on class information, images, and text information. Combining these methods produces very impressive text-to-image synthesis.

Notes

Denoising diffusion models were introduced by Sohl-Dickstein et al. (2015), and early related work based on score-matching was carried out by Song & Ermon (2019). Ho et al. (2020) produced image samples that were competitive with GANs and kick-started a wave of interest in this area. Most of the exposition in this chapter including the original formulation and the reparameterization is derived from this paper. Dhariwal & Nichol (2021) improved on the quality of these results and showed for the first time that images from diffusion models were quantitatively superior to GAN models in terms of Fréchet Inception Distance. At the time of writing, the state-of-the-art results for conditional image synthesis have been achieved by Karras et al. (2022). Surveys of denoising diffusion models can be found in Croitoru et al. (2022), Cao et al. (2022), Luo (2022), and Yang et al. (2022).

Applications for images: Applications of diffusion models include text-to-image generation (Nichol et al., 2022; Ramesh et al., 2022; Saharia et al., 2022b), image-to-image tasks such as colorization, inpainting, uncropping and restoration (Saharia et al., 2022a), super-resolution (Saharia et al., 2022c), image editing (Hertz et al., 2022; Meng et al., 2021), removing adversarial perturbations (Nie et al., 2022), semantic segmentation (Baranchuk et al., 2022), and medical imaging (Song et al., 2021b; Chung & Ye, 2022; Chung et al., 2022; Peng et al., 2022; Xie & Li, 2022; Luo et al., 2022) where the diffusion model is sometimes used as a prior.

Different data types: Diffusion models have also been applied to video data (Ho et al., 2022b; Harvey et al., 2022; Yang et al., 2022; Höppe et al., 2022; Voleti et al., 2022) for generation, past and future frame prediction, and interpolation. They have been used for 3D shape generation (Zhou et al., 2021; Luo & Hu, 2021), and recently a technique has been introduced to generate 3D models using only a 2D text-to-image diffusion model (Poole et al., 2023). Austin et al. (2021) and Hoogeboom et al. (2021) investigated diffusion models for discrete data. Kong et al. (2021) and Chen et al. (2021d) applied diffusion models to audio data.

Alternatives to denoising: The diffusion models in this chapter mix noise with the data and build a model to gradually denoise the result. However, degrading the image using noise is not necessary. Rissanen et al. (2022) devised a method that progressively blurred the image and

Bansal et al. (2022) show that the same ideas work with a large family of degradations which do not have to be stochastic. These include masking, morphing, blurring, and pixelating.

Comparison to other generative models: Diffusion models synthesize higher quality images than other generative models and are simple to train. They can be thought of as a special case of a hierarchical VAE (Vahdat & Kautz, 2020; Sønderby et al., 2016b) where the encoder is fixed and the latent space is the same size as the data. They are probabilistic, but like the VAE can only compute a lower bound on the likelihood of a data point. However, Kingma et al. (2021) show that this lower bound improves on the exact log likelihoods for test data from normalizing flows and autoregressive models. The main disadvantages of diffusion models is that they are slow and that the latent space has no semantic interpretation.

Improving quality: Many techniques have been proposed to improve image quality. These include the reparameterization of the network described in section 18.5 and the equal-weighting of the subsequent terms (Ho et al., 2020). Choi et al. (2022) subsequently investigated different weightings of terms in the loss function.

Kingma et al. (2021) improved the test log-likelihood of the model by learning the denoising weights β_t. Conversely, Nichol & Dhariwal (2021) improved performance by learning separate variances σ^2 of the denoising estimate at each time step in addition to the mean. Bao et al. (2022) show how to learn the variances *after* training the model.

Ho et al. (2022a) developed the cascaded method for producing very high resolution images (figure 18.11). To prevent artifacts in lower resolution images being propagated the higher resolutions, they introduced *noise conditioning augmentation*; here, the lower resolution image is degraded by adding noise to the conditioning image at each training step. This reduces the reliance on the exact details of the lower resolution image during training. It is done during inference, and here where the best noise level is chosen by sweeping over different values.

Improving speed: One of the major drawbacks of diffusion models is that they take a long time to train and sample from. Stable diffusion (Rombach et al., 2022) projects the original data to a smaller latent space using a conventional VAE and then runs the diffusion process in this smaller space. This has the advantages of reducing the dimensionality of the training data for the diffusion process, and allowing other data types (text, graphs, etc.) to be described by diffusion models. Vahdat et al. (2021) applied a similar approach.

Song et al. (2021a) showed that an entire family of diffusion processes are compatible with the training objective. Most of these processs are non-Markovian (i.e., the diffusion step does not only depend on the results of the previous step). One of these models is the denoising diffusion implicit model (DDIM) in which the updates are not stochastic (figure 18.10b). This model is amenable to taking larger steps (figure 18.10b) without inducing large errors. It effectively converts the model into an ordinary differential equation (ODE) in which the trajectories have low curvature, and allows efficient numerical methods for solving ODEs to be applied.

Song et al. (2021c) propose converting the underlying stochastic differential equations into a *probability flow* ODE which has the same marginal distributions as the original process. Vahdat et al. (2021), Xiao et al. (2022b), and Karras et al. (2022) all exploit techniques for solving ODEs to speed up synthesis. Karras et al. (2022) identified the best-performing time discretization for sampling, and evaluated different sampler schedules. The results of these and other improvements has been a significant drop in steps required during synthesis.

Sampling is slow because many small diffusion steps are required to ensure that the posterior distribution $Pr(\mathbf{z}_{t-1}|\mathbf{z}_t)$ is close to Gaussian (figure 18.5), and so the variational Gaussian distribution is appropriate. If we use a model that describes a more complex distribution at each denoising step, then we can use fewer diffusion steps in the first place. To this end, Xiao et al. (2022b) have investigated using conditional GAN models and Gao et al. (2021) investigated using conditional energy based models. Although these models cannot describe the original data distribution, they suffice to predict the (much simpler) reverse diffusion step.

Salimans & Ho (2022) distilled adjacent steps of the denoising process into a single step to speed up synthesis. Dockhorn et al. (2022) introduced momentum into the diffusion process. This makes the trajectories smoother and so more amenable to coarse sampling.

Conditional generation: Dhariwal & Nichol (2021) introduced classifier guidance, in which a classifier learned to identify the category of object being synthesized at each step, and this is used to bias the denoising update towards that class. This works well, but training a separate classifier is expensive. *Classifier free guidance* (Ho & Salimans, 2022) concurrently trains conditional and unconditional denoising models by dropping the class information some proportion of the time in a process akin to dropout. This technique allows control of the relative contributions of the conditional and unconditional components. By over-weighting the conditional component, the model produces more typical and realistic samples.

The standard technique for conditioning on images is to append the (resized) image to the different layers of the U-Net. For example, this was used in the cascaded generation process for super-resolution (Ho et al., 2022a). Choi et al. (2021) provide a method for conditioning on images in an unconditional diffusion model by matching the latent variables with those of a conditioning image. The standard technique for conditioning on text is to linearly transform the text to the same size as the U-Net layer and then add it to the representation in the same way that the time embedding is introduced (figure 18.9).

Text-to-image: Before diffusion models, state-of-the-art text-to-image systems were based on transformers (Ramesh et al., 2021). GLIDE (Nichol et al., 2022) and Dall·E 2 (Ramesh et al., 2022) both conditioned on embeddings from the CLIP model (Radford et al., 2021) which generates joint embeddings for text and image data. Imagen (Saharia et al., 2022b) showed that text embeddings from a large language model could produce even better results (see figure 18.13). The same authors introduced a benchmark (DrawBench) which is designed to evaluate the ability of a model to render colors, numbers of objects, spatial relations and other characteristics. Feng et al. (2022) have developed a Chinese text-to-image model.

Connections to other models: This chapter described diffusion models as hierarchical variational autoencoders because this approach connects most closely with the other parts of this book. However, diffusion models also have close connections with stochastic differential equations (consider the paths in figure 18.5) and with score matching (Song & Ermon, 2019, 2020). Song et al. (2021c) presented a framework based on stochastic differential equations that encompasses both the denoising and score matching interpretations. Diffusion models also have close connections to normalizing flows (Zhang & Chen, 2021). Yang et al. (2022) present an overview of the relation between diffusion models and other generative approaches.

Problems

Problem 18.1 Show that if $\mathrm{Var}[\mathbf{x}_{t-1}] = \mathbf{I}$ and we use the update:

$$\mathbf{x}_t = \sqrt{1-\beta_t}\cdot\mathbf{x}_{t-1} + \sqrt{\beta_t}\cdot\boldsymbol{\epsilon}_t, \tag{18.41}$$

then $\mathrm{Var}[\mathbf{x}_t] = \mathbf{I}$ and so the variance stays the same.

Problem 18.2 Consider the variable:

$$z = a \cdot \epsilon_1 + b \cdot \epsilon_2, \tag{18.42}$$

where both ϵ_1 and ϵ_2 are drawn from independent standard normal distributions with mean zero and unit variance. Show that:

$$\begin{aligned} \mathbb{E}[z] &= 0 \\ \text{Var}[z] &= a^2 + b^2, \end{aligned} \tag{18.43}$$

and so we could equivalently compute $z = \sqrt{a^2+b^2} \cdot \epsilon$ where ϵ is also drawn from a standard normal distribution.

Problem 18.3 Continue the process in equation 18.5 to show that:

$$\mathbf{x}_3 = \prod_{s=1}^{3} \sqrt{1-\beta_s} \cdot \mathbf{x} + \sqrt{1 - \prod_{s=1}^{3} (1-\beta_s)} \cdot \boldsymbol{\epsilon}. \tag{18.44}$$

Problem 18.4 Prove the relation:

$$\text{Norm}_{\mathbf{v}}\left[\mathbf{A}\mathbf{w}, \mathbf{B}\right] \propto \text{Norm}_{\mathbf{w}}\Big[(\mathbf{A}^T\mathbf{B}^{-1}\mathbf{A})^{-1}\mathbf{A}^T\mathbf{B}^{-1}\mathbf{v}, (\mathbf{A}^T\mathbf{B}^{-1}\mathbf{A})^{-1}\Big]. \tag{18.45}$$

Problem 18.5 Prove the relation:

$$\begin{aligned} \text{Norm}_{\mathbf{x}}[\mathbf{a}, \mathbf{A}]\text{Norm}_{\mathbf{x}}[\mathbf{b}, \mathbf{B}] \quad &\propto \\ &\text{Norm}_{\mathbf{x}}\Big[(\mathbf{A}^{-1}+\mathbf{B}^{-1})^{-1}(\mathbf{A}^{-1}\mathbf{a}+\mathbf{B}^{-1}\mathbf{b})(\mathbf{A}^{-1}+\mathbf{B}^{-1})^{-1}\Big]. \end{aligned} \tag{18.46}$$

Problem 18.6

The KL-divergence between two normal distributions is given by:

$$\begin{aligned} D_{KL}\Big[\text{Norm}_{\mathbf{w}}[\mathbf{a}, \mathbf{A}]\Big|\Big|\text{Norm}_{\mathbf{w}}[\mathbf{b}, \mathbf{B}]\Big] \quad &= \\ &\frac{1}{2}\left(\text{tr}\left[\mathbf{B}^{-1}\mathbf{A}\right] - d + (\mathbf{a}-\mathbf{b})^T\mathbf{B}^{-1}(\mathbf{a}-\mathbf{b}) + \log\left[\frac{|\mathbf{B}|}{|\mathbf{A}|}\right]\right). \end{aligned} \tag{18.47}$$

Substitute the definitions from equation 18.27 into this expression and show that the only term that depends on the parameters $\boldsymbol{\phi}$ is the first term from equation 18.28.

Problem 18.7 If $\alpha_t = \prod_{s=1}^{t} 1 - \beta_s$, then show that:

$$\sqrt{\frac{\alpha_{t-1}}{\alpha_t}} = \sqrt{1-\beta_t}. \tag{18.48}$$

Problem 18.8 If $\alpha_t = \prod_{s=1}^{t} 1 - \beta_s$, then show that:

$$\frac{(1-\alpha_{t-1})(1-\beta_t)+\beta_t}{(1-\alpha_t)\sqrt{1-\beta_t}} = \frac{1-\alpha_t}{(1-\alpha_t)\sqrt{1-\beta_t}}. \tag{18.49}$$

Problem 18.9 Prove equation 18.37.

Chapter 19

Reinforcement learning

Reinforcement learning (RL) is a sequential decision-making framework in which agents learn to perform actions in an environment with the goal of maximizing rewards. For example, an RL algorithm might control the moves (actions) of a character (the agent) in a video game (the environment) and aim to maximize the score (the reward). In robotics, an RL algorithm might control the motor movements (actions) of a robot (the agent) in the real world (the environment) to achieve a goal (the reward). In finance, an RL algorithm might control a virtual trader (the agent) who buys or sells assets (the actions) on a trading platform (the environment) to try to make money (the reward).

Consider learning to play chess. Here, there is a single positive reward at the end of the game if the agent wins and zero at every other time step. This illustrates the challenges of RL. First, the reward is sparse; we must play an entire game to get a single bit of information for training. Second, the reward is temporally offset from the action that caused it; a decisive advantage might be gained thirty moves before victory. We must associate the reward with this critical action. This is termed the *temporal credit assignment problem*. Third, the environment is stochastic; the opponent doesn't always make the same move in the same situation, so it's hard to know if an action was truly good or just lucky. Finally, the agent must balance exploring the environment (e.g., trying new opening moves) with exploiting what it already knows (e.g., sticking to a previously successful opening). This is termed the *exploration/exploitation trade-off*.

Reinforcement learning is a framework that is neutral to the type of machine learning model. However, in practice, state-of-the-art systems often use deep networks. They encode the environment (the video game display, robot sensors, financial time series, or chessboard) and map this directly or indirectly to the next action (figure 1.13).

19.1 Markov decision processes, returns, and policies

Reinforcement learning maps observations of an environment to actions with the goal of maximizing a numerical quantity. In this book, we consider the most common case, in which we learn a *policy* that maximizes the expected *return* in a *Markov decision process*. This section explains these terms.

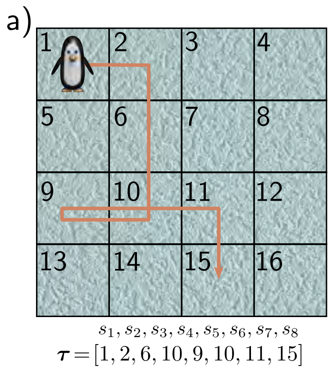

b)

$$
\begin{array}{cc}
 & s_t \\
s_{t+1} & \begin{bmatrix}
0 & 0.33 & 0 & 0 & 0.33 & 0 & 0 & 0 & 0 & 0 & 0 & 0 & 0 & 0 & 0 & 0 \\
0.5 & 0 & 0.33 & 0 & 0 & 0.25 & 0 & 0 & 0 & 0 & 0 & 0 & 0 & 0 & 0 & 0 \\
0 & 0.33 & 0 & 0.5 & 0 & 0 & 0.25 & 0 & 0 & 0 & 0 & 0 & 0 & 0 & 0 & 0 \\
0 & 0 & 0.33 & 0 & 0 & 0 & 0 & 0.33 & 0 & 0 & 0 & 0 & 0 & 0 & 0 & 0 \\
0.5 & 0 & 0 & 0 & 0 & 0.25 & 0 & 0 & 0.33 & 0 & 0 & 0 & 0 & 0 & 0 & 0 \\
0 & 0.33 & 0 & 0 & 0.33 & 0 & 0.25 & 0 & 0 & 0.25 & 0 & 0 & 0 & 0 & 0 & 0 \\
0 & 0 & 0.33 & 0 & 0 & 0.25 & 0 & 0.33 & 0 & 0 & 0.25 & 0 & 0 & 0 & 0 & 0 \\
0 & 0 & 0 & 0.5 & 0 & 0 & 0.25 & 0 & 0 & 0 & 0 & 0.33 & 0 & 0 & 0 & 0 \\
0 & 0 & 0 & 0 & 0.33 & 0 & 0 & 0 & 0 & 0.25 & 0 & 0 & 0.5 & 0 & 0 & 0 \\
0 & 0 & 0 & 0 & 0 & 025 & 0 & 0 & 0.33 & 0 & 0.25 & 0 & 0 & 0.33 & 0 & 0 \\
0 & 0 & 0 & 0 & 0 & 0 & 0.25 & 0 & 0 & 0.25 & 0 & 0.33 & 0 & 0 & 0.33 & 0 \\
0 & 0 & 0 & 0 & 0 & 0 & 0 & 0.33 & 0 & 0 & 0.25 & 0 & 0 & 0 & 0 & 0.5 \\
0 & 0 & 0 & 0 & 0 & 0 & 0 & 0 & 0.33 & 0 & 0 & 0 & 0 & 0.33 & 0 & 0 \\
0 & 0 & 0 & 0 & 0 & 0 & 0 & 0 & 0 & 0.25 & 0 & 0 & 0.5 & 0 & 0.33 & 0 \\
0 & 0 & 0 & 0 & 0 & 0 & 0 & 0 & 0 & 0 & 0.25 & 0 & 0 & 0.33 & 0 & 0.5 \\
0 & 0 & 0 & 0 & 0 & 0 & 0 & 0 & 0 & 0 & 0 & 0.33 & 0 & 0 & 0.33 & 0
\end{bmatrix} \\
 & Pr(s_{t+1}|s_t)
\end{array}
$$

Figure 19.1 Markov process. A Markov process consists of a set of states and transition probabilities $Pr(s_{t+1}|s_t)$ that define the probability of moving to state s_{t+1} given the current state is s_t. a) The penguin can potentially visit 16 different positions (states) on the ice. b) The ice is slippery, so at each time, it has an equal probability of moving to any adjacent state. For example, in position 6, it has a 25% chance of moving to states 2, 5, 7, and 10. A trajectory $\tau = [s_1, s_2, s_3, \ldots]$ from this process consists of a sequence of states.

19.1.1 Markov process

A *Markov process* assumes that the world is always in one of a set of possible states. The term *Markov* means that the probability of being in a state depends only on the previous state and not on the states before. The changes between states are captured by the *transition probabilities* $Pr(s_{t+1}|s_t)$ of moving to the next state s_{t+1} given the current state s_t, where t indexes the time step. Hence, a Markov process is an evolving system that produces a time series $s_1, s_2, s_3 \ldots$ of states (figure 19.1)

19.1.2 Markov reward process

Problem 19.1

A *Markov reward process* also includes a distribution $Pr(r_{t+1}|s_t)$ over the possible rewards r_{t+1} received at the next time step, given that we are in state s_t. This produces a time series $s_1, r_2, s_2, r_3, s_3, r_4 \ldots$ of states and the associated rewards (figure 19.2).

The Markov reward process also includes a *discount factor* $\gamma \in [0, 1]$ that is used to compute the *return* G_t at time t:

$$G_t = \sum_{k=0}^{\infty} \gamma^k r_{t+k+1}. \tag{19.1}$$

The return is the sum of the cumulative discounted future rewards; it measures the future benefit of being on this trajectory. The discount factor makes rewards that are closer in time more valuable than rewards that are further away.

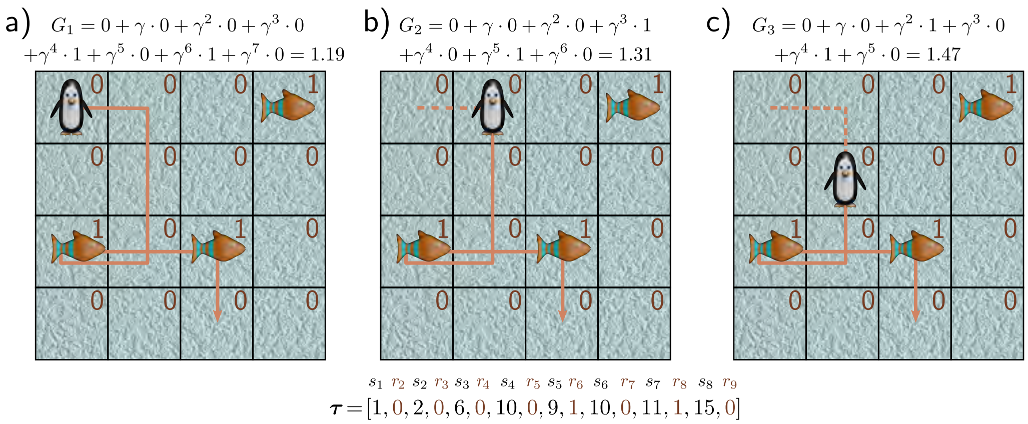

Figure 19.2 Markov reward process. This associates a distribution $Pr(r_{t+1}|s_t)$ of rewards r_{t+1} with each state s_t. a) Here, the rewards are deterministic; the penguin will receive a reward of one if it lands on a fish and zero otherwise. The trajectory τ now consists of a sequence $s_1, r_2, s_2, r_3, s_3, r_4 \ldots$ of alternating states and rewards. The return G_t of the sequence is the sum of discounted future rewards, where here the discount factor $\gamma = 0.9$. b-c) As the penguin proceeds along the trajectory and gets closer to reaching the rewards, the return increases.

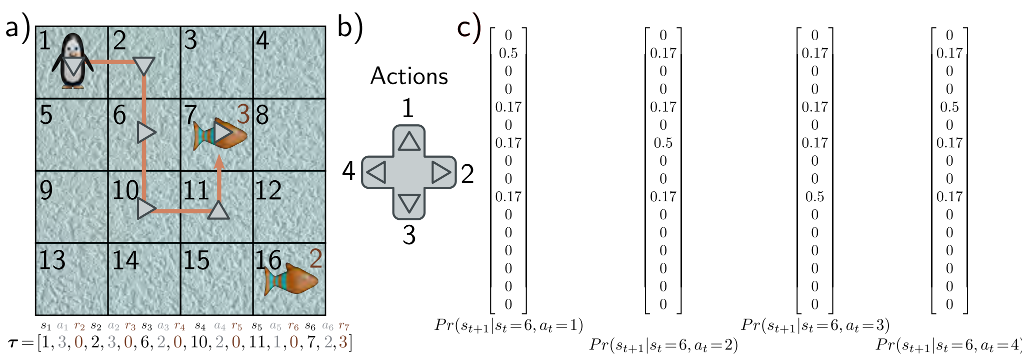

Figure 19.3 Markov decision process. The agent (penguin) can perform one of a set of actions in each state. The action influences both the probability of moving to the successor state and the probability of receiving rewards. b) Here, the four actions correspond to moving up, right, down, and left. c) For any state (here, state 6), the action changes the probability of moving to the next state. The penguin moves in the intended direction with 50% probability, but the ice is slippery, so it might accidentally move one of the other adjacent positions with equal probability. Accordingly, in panel (a), the action taken (gray triangles) does not always line up with the trajectory (orange line). Here, the action does not affect the reward, so $Pr(r_{t+1}|s_t, a_t) = Pr(r_{t+1}|s_t)$. The trajectory $\boldsymbol{\tau}$ from an MDP consists of a sequence $s_1, a_1, r_2, s_2, a_2, r_3, s_3, a_3, r_4 \ldots$ of alternating states s_t, actions a_t, and rewards, r_{t+1}. Note that the penguin receives the reward when it *leaves* a state with a fish (i.e., the reward is received for landing on the fish square, regardless of whether the penguin arrived there intentionally or not).

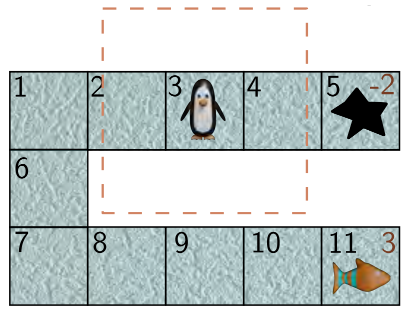

Figure 19.4 Partially observed Markov decision process (POMDP). In a POMDP, the agent does not have access to the entire state. Here, the penguin is in state three and can only see the region in the dashed box. This is indistinguishable from what it would see in state nine. In the first case, moving right leads to the hole in the ice (with -2 reward) and, in the latter, to the fish (with +3 reward).

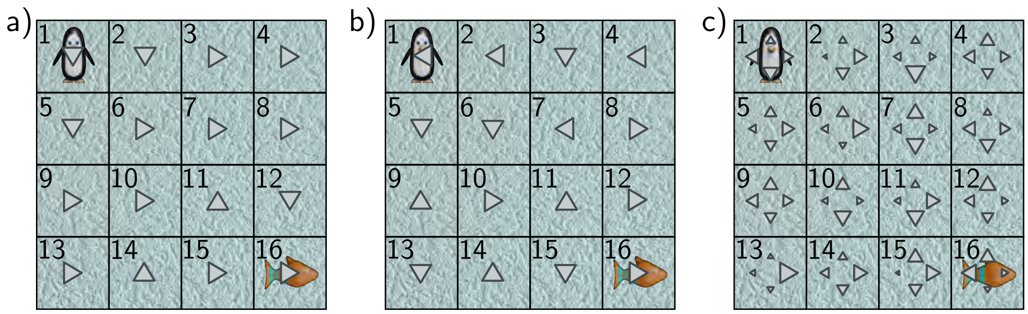

Figure 19.5 Policies. a) A deterministic policy chooses a certain action in each state (indicated by arrow). Some policies are better than others. This policy is not optimal but still generally steers the penguin from top-left to bottom-right where the reward lies. b) This policy is more random. c) A stochastic policy has a probability distribution over actions for each state (probability indicated by size of arrows). This has the advantage that the agent naturally explores the states and can be necessary for optimal performance in partially observed Markov decision processes.

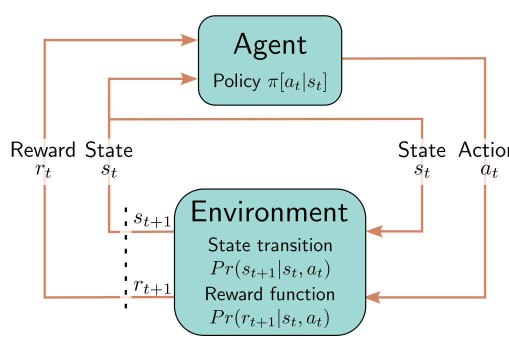

Figure 19.6 Reinforcement learning loop. The agent takes an action a_t at time t based on the state s_t, according to the policy $\pi[a_t|s_t]$. This triggers the generation of a new state s_{t+1} (via the state transition function) and a reward r_{t+1} (via the reward function). Both are passed back to the agent, which then chooses a new action.

19.1.3 Markov decision processes

A *Markov decision process* or *MDP* adds a set of possible *actions* at each time step. The action a_t changes the transition probabilities, which are now written as $Pr(s_{t+1}|s_t, a_t)$. The rewards can also depend on the action and are now written as $Pr(r_{t+1}|s_t, a_t)$. An MDP produces a sequence $s_1, a_1, r_2, s_2, a_2, r_3, s_3, a_3, r_4 \ldots$ of states, actions, and rewards (figure 19.3). The entity that performs the actions is known as the *agent*.

19.1.4 Partially observed Markov decision process

In a *partially observed Markov decision process* or *POMDP*, the state is not directly visible (figure 19.4). Instead, the agent receives an observation o_t drawn from $Pr(o_t|s_t)$. Hence, a POMDP generates a sequence $s_1, o_1, a_1, r_2, s_2, o_2, a_2, r_3, o_3, a_3, s_3, r_4, \ldots$ of states, rewards, observations, and actions. In general, each observation will be more compatible with some states than others but insufficient to identify the state uniquely.

19.1.5 Policy

The rules that determine the agent's action for each state are known as the *policy* $\pi[a|s]$ (figure 19.5). The policy may be deterministic (the agent always takes the same action in a given state) or stochastic (the policy defines a distribution over actions for each state). A *stationary* policy depends only on the current state. A *non-stationary* policy depends on the time step or previous history.

The MDP and policy form a loop (figure 19.6). The agent receives the state s_t and reward r_t from the previous time step. Based on this, it can modify the policy $\pi[a_t|s_t]$ if desired and choose the next action a_t. The environment then returns the next state according to $Pr(s_{t+1}|s_t, a_t)$ and the reward according to $Pr(r_{t+1}|s_t, a_t)$. We assume in this chapter that the rewards are deterministic and can be written as $r[s_t, a_t]$.

19.2 Expected returns

The previous section introduced the Markov decision process and the idea of an agent carrying out actions according to a policy. We want to choose a policy that maximizes the expected returns. In this section, we make this idea mathematically precise. To do that, we assign a *value* to each state s_t and state/action pair $\{s_t, a_t\}$.

19.2.1 Values of state and values of action

The return G_t depends on the initial state s_t and the policy $\pi[a|s]$. From this state, the agent will pass through a sequence of subsequent states taking actions and receiving rewards. This sequence differs every time the agent starts in the same place since, in

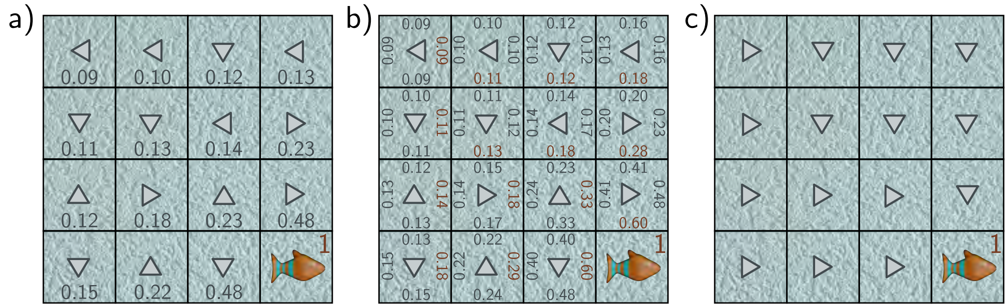

Figure 19.7 Values of state and action. a) The value $v[s_t|\pi]$ of a state s_t (number at each position) is the expected return for this state for a given policy π (gray arrows). It is the average sum of discounted rewards received over many trajectories started from this state. In this case, states closer to the fish are more valuable. b) The value $q[a_t|s_t, \pi]$ of an action a_t in state s_t is the expected return given that this particular action is taken in this state. In this case, it gets larger as we get closer to the fish and is larger for actions that head in the direction of the fish. c) If we know the value of the actions for a state, then the policy can be modified so that it chooses the maximum of these values.

general, the policy $\pi[a_t|s_t]$, the state transitions $Pr(s_{t+1}|s_t, a_t)$, and the rewards issued $Pr(r_{t+1}|s_t, a_t)$ are all stochastic.

We can characterize how "good" a state is by considering the expected return $\mathrm{v}[s_t]$. This is the average return that would be received over many sequences and is termed the *value of state* (figure 19.7a):

$$\mathrm{v}[s_t|\pi] = \mathbb{E}\Big[G_t|s_t, \pi\Big]. \tag{19.2}$$

The value can be thought of as the expected *long-term* rewards associated with that state for the chosen policy. It is highest for states where it's probable that subsequent transitions will bring high rewards soon.

Similarly, the *value of action* or *action-state value function* $q[s_t, a_t|\pi]$ is the expected return from executing action a in state s (figure 19.7b):

$$q[s_t, a_t|\pi] = \mathbb{E}\Big[G_t|s_t, a_t, \pi\Big]. \tag{19.3}$$

This can be thought of as the expected *long-term* rewards associated with taking action a_t in the state s_t, given the current policy. Through this quantity, reinforcement learning algorithms connect future rewards to current actions (i.e., resolve the temporal credit assignment problem).

19.2.2 Optimal policy

We want a policy that maximizes the expected return. For MDPs (but not POMDPs), there is always a deterministic, stationary policy that maximizes the value of every state. If we know this optimal policy, then we get the optimal expected return $v^*[s_t]$:

$$\mathrm{v}^*[s_t] = \underset{\pi}{\operatorname{argmax}}\Big[\mathbb{E}\Big[G_t|s_t,\pi\Big]\Big]. \tag{19.4}$$

Similarly, the optimal values of action are obtained under the best policy:

$$q^*[s_t,a_t] = \underset{\pi}{\operatorname{argmax}}\Big[\mathbb{E}\Big[G_t|s_t,a_t,\pi\Big]\Big]. \tag{19.5}$$

Turning this on its head, if we knew the optimal values of action, then we would know the optimal policy, which is to select a_t to maximize the value of action (figure 19.7c):

$$\boldsymbol{\pi}[a_t|s_t] = \underset{a_t}{\operatorname{argmax}}\Big[\mathbb{E}\Big[q^*[s_t,a_t]\Big]\Big]. \tag{19.6}$$

Indeed, some reinforcement learning algorithms are based on alternately estimating these two quantities (see section 19.3).

19.2.3 Bellman equations

We may not know the values of state or values of action for any policy. However, we know that they must be consistent with one another, and it's easy to write relations between these quantities. The value of state $v[s_t]$ can be found by taking a weighted sum of the values of each action $q[s_t,a_t]$, where the weights depend on the probability under the policy $\pi[a_t|s_t]$ of taking that action (figure 19.9a):

$$v[s_t|\pi] = \sum_{a_t}\pi[a_t|s_t]q[s_t,a_t|\pi]. \tag{19.7}$$

Similarly, the value of an action is the immediate reward $r_{t+1}=r[a_t,s_t]$ generated by taking the action, plus the value $v[s_{t+1}]$ of being in the subsequent state s_{t+1} discounted by γ (figure 19.9b). Since the assignment of s_{t+1} is not not deterministic, we weight the values $v[s_{t+1}]$ according to the transition probabilities $Pr(s_{t+1}|s_t,a_t)$:

$$q[s_t,a_t|\pi] = r[a_t,s_t] + \gamma\cdot\sum_{s_{t+1}}Pr(s_{t+1}|s_t,a_t)v[s_{t+1}|\pi]. \tag{19.8}$$

Substituting equation 19.8 into equation 19.7 provides a relation between the value of the state at time t and $t+1$:

$$v[s_t|\pi] = \sum_{a_t}\pi[a_t|s_t]\left(r[a_t,s_t] + \gamma\cdot\sum_{s_{t+1}}Pr(s_{t+1}|s_t,a_t)v[s_{t+1}|\pi]\right). \tag{19.9}$$

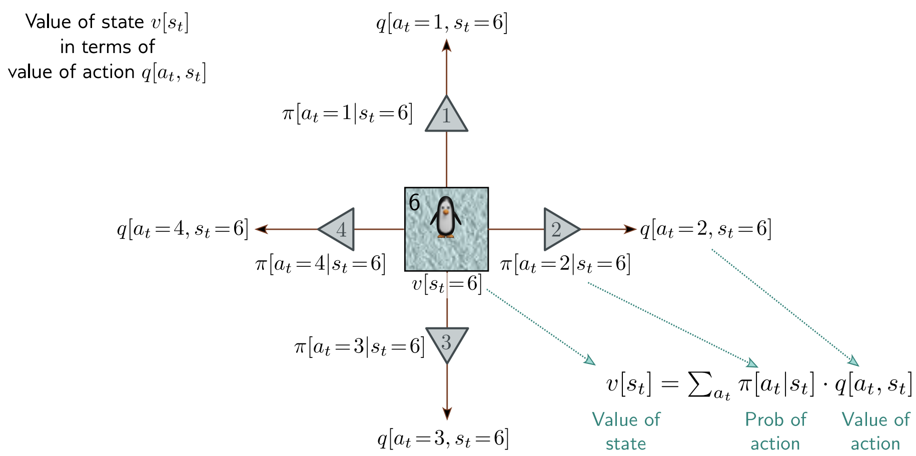

Figure 19.8 Relationship between values of state and action. The value of state six $v[s_t = 6]$ is a weighted sum of the values of action $q[a_t, s_t = 6]$ at state six, where the weights are the policy probabilities $\pi[a_t|s_t=6]$ of taking that action.

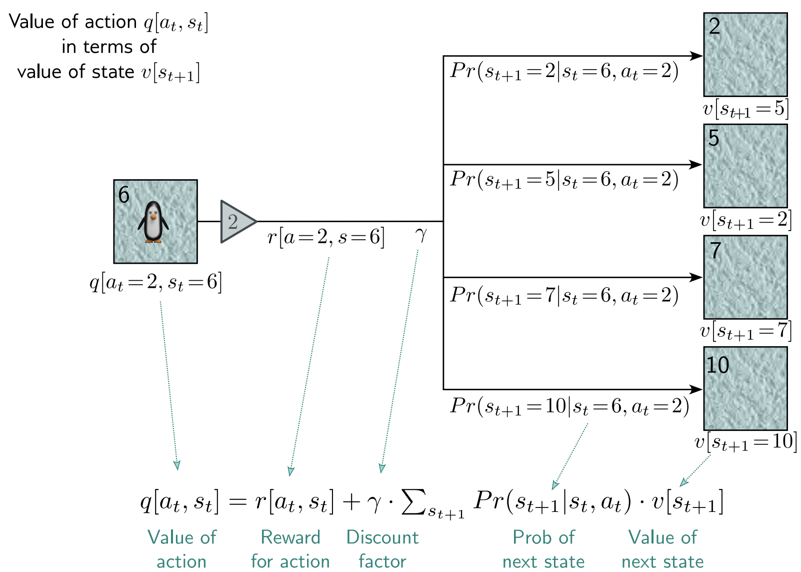

Figure 19.9 Relationship between values of action and state. The value $q[a_t = 2, s_t = 6]$ of taking action two in state six is the reward $r[a_t = 2, s_t = 6]$ from taking that action plus a weighted sum of the discounted values $v[s_{t+1}]$ of being in successor states, where the weights are the transition probabilities $Pr(s_{t+1}|s_t = 6, a_t = 2)$. The Bellman equations chain these relations to link the current and next values of (i) state and (ii) action.

Similarly, substituting equation 19.7 into equation 19.8 provides a relation between the value of the action at time t and $t+1$:

$$q[s_t, a_t|\pi] = r[a_t, s_t] + \gamma \cdot \sum_{s_{t+1}} Pr(s_{t+1}|s_t, a_t) \left(\sum_{a_{t+1}} \pi[a_{t+1}|s_{t+1}] q[s_{t+1}, a_{t+1}|\pi] \right). \quad (19.10)$$

The latter two relations are the *Bellman equations* and are the backbone of many RL methods. In short, they say that the values of state (action) have to be self-consistent. Consequently, when we update an estimate of one value of state (action), this will have a ripple effect that causes modifications to all the others.

19.3 Classical reinforcement learning

This section presents a brief overview of "classical" RL algorithms (i.e., methods that do not rely on deep learning). They can be divided into *model-based* and *model-free* methods. *Model-based methods* use the MDP structure explicitly and find the best policy from the transition matrix $Pr(s_{t+1}|s_t, a_t)$ and reward probabilities $Pr(r_{t+1}|a_t, s_t)$. If these distributions are known, this is a straightforward optimization problem that can be tackled using *dynamic programming*. If they are unknown, they must be estimated from observed MDP trajectories before applying dynamic programming.

Conversely, *model-free* methods eschew a model of the MDP and fall into two classes:

1. *Value estimation* methods estimate the values of action for each state and then assign the policy according to the action with the greatest value.
2. *Policy estimation* methods directly estimate the policy using a gradient descent technique without the intermediate steps of estimating the model or values.

We focus initially on value estimation methods. Within this family, *Monte Carlo* methods simulate many trajectories through the MDP for a given policy to gather information from which this policy can be improved. Sometimes it is not feasible or practical to simulate many trajectories before updating the policy. *Temporal difference (TD)* methods update the policy *while* the agent traverses the MDP.

The following three sections give a brief overview of dynamic programming (which estimates the optimal policy in a known MDP) and Monte-Carlo and temporal difference methods (which both estimate the values of action in an unknown MDP).

19.3.1 Dynamic programming

Dynamic programming algorithms assume that we can access the transition and reward probabilities. Here, we assume that the rewards are deterministic and can be written as $r[s, a]$. The values of state $v[s]$ are initialized (usually to zero). The deterministic

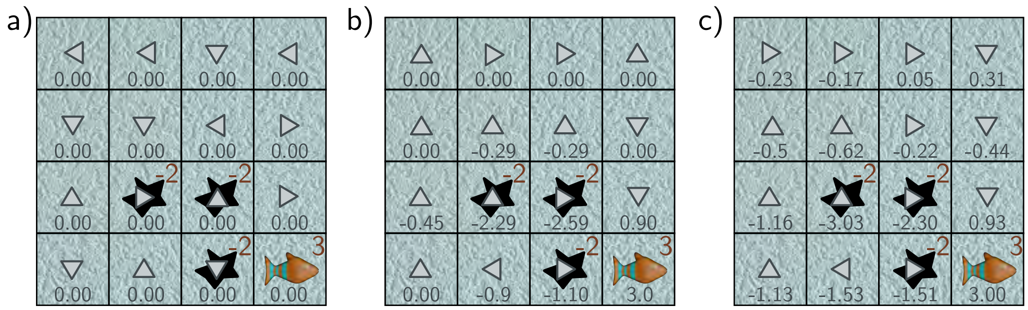

Figure 19.10 Dynamic programming. a) The values of state are initialized to zero, and the policy (arrows) is chosen randomly. b) The values of state are updated so they are compatible with their neighbors (equation 19.11, shown after two iterations). The policy is updated to move the agent to states with a higher value (equation 19.12). c) After several iterations, the algorithm converges to the optimal policy, in which the penguin tries to avoid the holes and reach the fish.

policy $\pi[a|s]$ is also initialized (usually by choosing a random action for each state). The algorithm then alternates between iteratively computing the values of state for the current policy (*policy evaluation*) and improving that policy (*policy improvement*).

Policy evaluation: We sweep through possible values of s_t updating their values:

$$v[s_t] \leftarrow \sum_{a_t} \pi[a_t|s_t] \sum_{s_{t+1}} Pr(s_{t+1}|s_t, a_t)\Big(r[s_t, a_t] + \gamma \cdot v[s_{t+1}]\Big), \tag{19.11}$$

where s_{t+1} is the successor state and $Pr(s_{t+1}|s_t, a_t)$ is the state transition probability. Each update makes $v[s_t]$ consistent with the value at the successor state s_{t+1} using the Bellman equation for values (equation 19.9). This is termed *bootstrapping*.

Policy improvement: To update the policy, we greedily choose the action that maximizes the value for each state:

$$\pi[a_t|s_t] \leftarrow \underset{a_t}{\operatorname{argmax}}\Big[Pr(s_{t+1}|s_t, a_t)\Big(r[s_t, a_t] + \gamma \cdot v[s_{t+1}]\Big)\Big]. \tag{19.12}$$

This is guaranteed to improve the policy according to the *policy improvement theorem*.

Problems 19.2-19.3

These two steps are iterated until the policy converges (figure 19.10).

There are many variations to this approach. In *policy iteration*, the policy evaluation step is iterated until convergence before policy improvement. The values of state can be updated either in place or synchronously in each sweep. In *value iteration*, the policy evaluation procedure sweeps through the values just once before policy improvement. *Asynchronous* dynamic programming algorithms do not systematically sweep through all the values at each step.

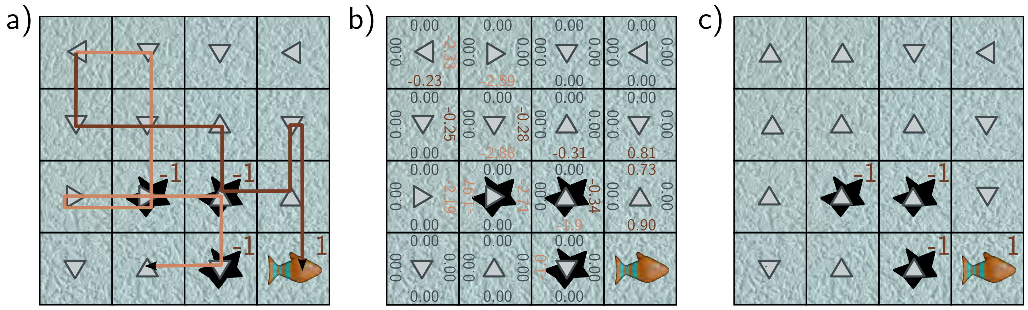

Figure 19.11 Monte-Carlo methods. a) The policy (arrows) is initialized randomly. The MDP is repeatedly simulated the trajectories of these episodes are stored (orange and brown paths represent two trajectories). b) The values of action are empirically estimated based on the observed returns averaged over these trajectories. In this case, the values of action were all initially zero and have been updated where an action was observed. c) The policy can then be updated according to the action which received the best (or least bad) reward.

19.3.2 Monte Carlo methods

Monte Carlo methods don't assume knowledge of the MDP's transition probabilities and reward structure. Instead, they gain experience by repeatedly simulating the MDP and observing the rewards. They alternate between computing the values of action (based on this experience) and updating the policy (based on the values).

To estimate the values of action $q[s, a]$, a series of *episodes* are run[1]. Each starts with a given state and action and thereafter follows the current policy, producing a series of actions, states, and returns (figure 19.11a). The value of action for a given state-action pair under the current policy is estimated as the average of the empirical returns that follow after each time this pair is observed (figure 19.11b). Then the policy is updated by choosing the action with the maximum value at every state (figure 19.11c):

$$\pi[a|s] \leftarrow \underset{a}{\operatorname{argmax}}\Big[q[s, a]\Big]. \tag{19.13}$$

This is an *on-policy* method; the current best policy is used to guide the agent through the environment. This policy is based on the observed values of action in every state, but of course, it's not possible to estimate the value of actions that haven't been used, and there is nothing to encourage the algorithm to explore these. One solution is to use *exploring starts*. Here, episodes with all possible state/action pairs are initiated, so every combination is observed at least once. However, this is not practical if the number of states is large or the starting point cannot be controlled.

[1]In RL, the term *episode* is used semi-interchangeably with the terms *rollout* or *trajectory*. All refer to an observed sequence of states, rewards, and actions.

In *off-policy* methods, the policy π' that generates the episodes is not the estimate π of the optimal policy. For example, the episodes might be generated by an *epsilon greedy* policy, in which a random action is taken with probability ϵ, and the optimal action is allotted the remaining probability. The choice of ϵ trades off exploitation and exploration. Some off-policy methods explicitly use importance sampling (section 17.8.1) to estimate the value of action under policy π using samples from π'. Others, such as Q-learning (described in the next section), estimate the values based on the greedy action even though this is not necessarily what is chosen.

19.3.3 Temporal difference methods

Temporal difference (TD) methods assume that the transition probabilities and reward structure are unknown. Unlike Monte Carlo methods, they update the values and policy *while* the agent traverses the states of the MDP instead of afterward. Similarly to dynamic programming, a bootstrapping process updates the values to make them self-consistent under the current policy.

SARSA (State-Action-Reward-State-Action) is an on-policy algorithm with update:

$$q[s_t, a_t] \leftarrow q[s_t, a_t] + \alpha\Big(r[a_t, s_t] + \gamma \cdot q[s_{t+1}, a_{t+1}] - q[s_t, a_t]\Big), \tag{19.14}$$

where $\alpha \in (0, 1]$ is the learning rate. The bracketed term measures the consistency between the value of action $q[s_t, a_t]$ and the predicted value $r[a_t, s_t] + \gamma \cdot q[s_{t+1}, a_{t+1}]$ from looking ahead one step.

By contrast, *Q-Learning* is an off-policy algorithm with update:

$$q[s_t, a_t] \leftarrow q[s_t, a_t] + \alpha\Big(r[a_t, s_t] + \gamma \cdot \max_{a_{t+1}}\big[q[s_{t+1}, a_{t+1}]\big] - q[s_t, a_t]\Big). \tag{19.15}$$

In both cases, the policy is updated by taking the maximum of the values of action at each state (equation 19.13). It can be shown that these updates are contraction mappings (see equation 16.20); the values of action will eventually converge assuming that every state-action pair is visited an infinite number of times.

Problem 19.4

19.4 Fitted Q-learning

Temporal difference methods rely on repeatedly traversing the entire MDP and updating the values of action. However, this is only practical if the state-action space is small. Unfortunately, this is rarely the case; even for the constrained environment of a chessboard, there are more than 10^{40} possible legal states.

The principle of *fitted Q-learning* is that the discrete representation $q[s_t, a_t]$ of the values of action should be replaced by a machine learning model $\mathrm{q}[s_t, a_t, \boldsymbol{\phi}]$. We then define a least squares loss function based on the consistency of adjacent values of action similar to the original Q-learning update (equation 19.15):

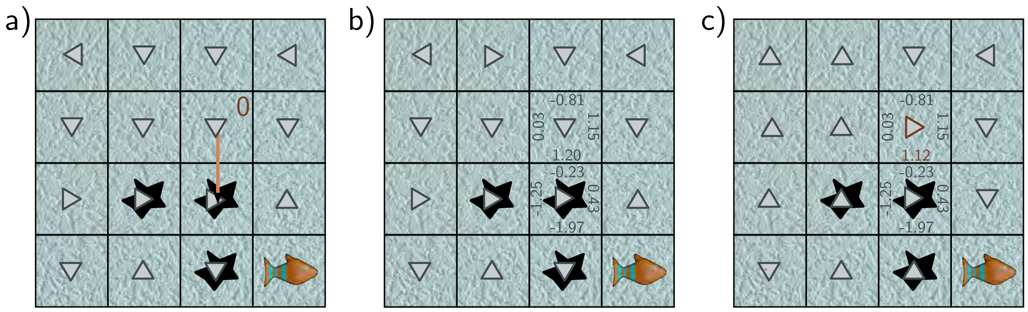

$$q[s_t, a_t] \leftarrow q[s_t, a_t] + \alpha\Big(r[s_t, a_t] + \gamma \cdot \max_a\big[q[s_{t+1}, a_{t+1}]\big] - q[s_t, a_t]\Big)$$

$$1.12 \leftarrow 1.20 + 0.1\Big(0.0 + 0.9 \cdot \max\big[-0.23, 0.43, -1.97, -1.25\big]\big] - 1.20\Big)$$

Figure 19.12 Temporal difference learning. a) The agent starts in state s_t and takes action $a_t = 2$ according to the policy. It does not slip on the ice and moves downward, receiving reward $r[a_t, s_t] = 0$ for leaving the original state. b) The maximum value of action at the new state is found (here 0.43). c) The value of action for action 2 in the original state is updated to 1.12 based on the current estimate of the maximum value of action at the subsequent state, the reward, discount factor $\gamma = 0.9$, and learning rate $\alpha = 0.1$. This changes the highest value of action at the original state, so the policy changes.

$$L[\boldsymbol{\phi}] = \left(r[a_t, s_t] + \gamma \cdot \max_{a_{t+1}}\Big[\mathrm{q}[s_{t+1}, a_{t+1}, \boldsymbol{\phi}]\Big] - \mathrm{q}[s_t, a_t, \boldsymbol{\phi}]\right)^2, \tag{19.16}$$

which in turn leads to the update:

$$\boldsymbol{\phi} \leftarrow \boldsymbol{\phi} + \alpha\left(r[a_t, s_t] + \gamma \cdot \max_{a_{t+1}}\Big[\mathrm{q}[s_{t+1}, a_{t+1}, \boldsymbol{\phi}]\Big] - \mathrm{q}[s_t, a_t, \boldsymbol{\phi}]\right)\frac{\partial \mathrm{q}[s_t, a_t, \boldsymbol{\phi}]}{\partial \boldsymbol{\phi}}. \tag{19.17}$$

Fitted Q-learning differs from Q-Learning in that convergence is no longer guaranteed. A change to the parameters potentially modifies both the target $r[a_t, s_t] + \gamma \cdot \max_{a_{t+1}}\left[\mathrm{q}[s_{t+1}, a_{t+1}, \boldsymbol{\phi}]\right]$ (the maximum value may change) and the prediction $\mathrm{q}[s_t, a_t, \boldsymbol{\phi}]$. This can be shown both theoretically and empirically to damage convergence.

19.4.1 Deep Q-networks for playing ATARI games

Deep networks are ideally suited to making predictions from a high-dimensional state space, so are a natural choice for the model in fitted Q-learning. In principle, they could take both state and action as input and predict the values but in practice, the network takes only the state and simultaneously predicts the values for each action.

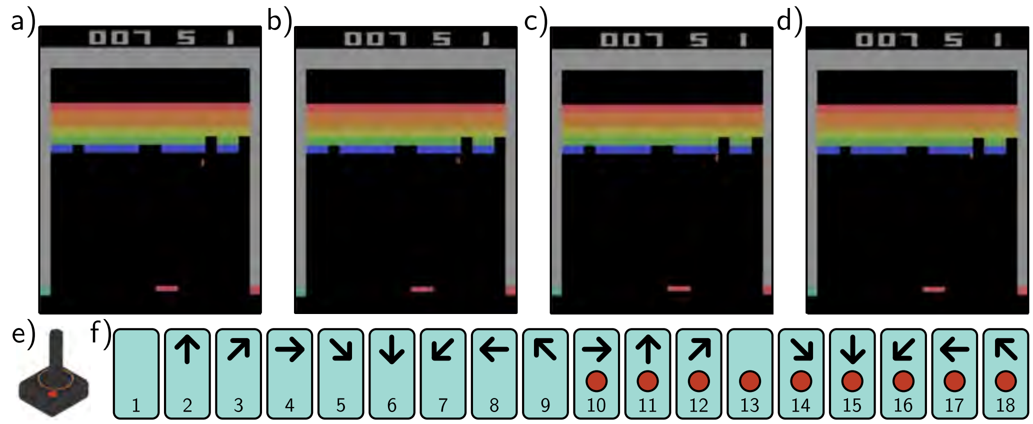

Figure 19.13 Atari Benchmark. The Atari benchmark consists of 49 Atari 2600 games, including Breakout (pictured), Pong, and various shoot-em-up, platform, and other types of games. a-d) Even for games with a single screen, the state is not fully observable from a single frame because the velocity of the objects is unknown. Consequently, it is usual to use several adjacent frames (here, 4) to represent the state. e) The action simulates the user input via a joystick. f) There are eighteen actions corresponding to 8 directions of movement or no movement, and for each of these nine cases, the button is pressed or not.

The *Deep Q-Network* was a breakthrough reinforcement learning architecture that exploited deep networks to learn to play ATARI 2600 games. The observed data consists of 220×160 images with 128 possible colors at each pixel (figure 19.13). This was reshaped to size 84×84, and only the brightness value was retained. Unfortunately, the full state is not observable from a single frame. For example, the velocity of game objects is unknown. To help resolve this problem, the network ingests the last four frames at each time step. It maps these frames through three convolutional layers followed by a fully connected layer to predict the value of every action (figure 19.14).

Several modifications were made to the standard training procedure. First, the rewards (which were driven by the score in the game) were clipped to -1 for a negative change and $+1$ for a positive change. This compensates for the wide variation in scores between different games and allows the same learning rate to be used. Second, the system exploited *experience replay*. Rather than update the network based on the tuple $< s, a, r, s' >$ at the current step or with a batch of the last I tuples, all recent tuples were stored in a buffer. This buffer was sampled randomly to generate a batch at each step. This approach reuses data samples many times and reduces correlations between the samples in the batch that arise due to the similarity of adjacent frames.

Finally, the issue of convergence in fitted Q-Networks was tackled by fixing the target parameters to values $\boldsymbol{\phi}^{-}$ and only updating them periodically. This gives the update:

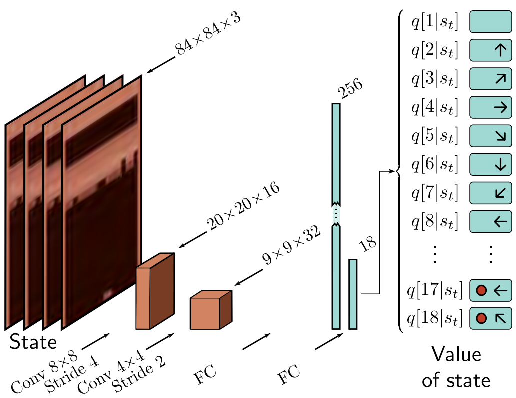

Figure 19.14 Deep Q-network architecture. The input consists of four adjacent frames of the ATARI game. Each is resized to 84×84 and converted to grayscale. These frames are represented as four channels and processed by an 8×8 convolution with stride four, followed by a 4×4 convolution with stride 2, followed by two fully connected layers. The final output predicts the value of action for each of the 18 actions in this state.

$$\boldsymbol{\phi} \leftarrow \boldsymbol{\phi} + \alpha\left(r[a_t, s_t] + \gamma \cdot \max_{a_{t+1}}\Big[\mathrm{q}[s_{t+1}, a_{t+1}, \boldsymbol{\phi}^-]\Big] - \mathrm{q}[s_t, a_t, \boldsymbol{\phi}]\right)\frac{\partial \mathrm{q}[s_t, a_t, \boldsymbol{\phi}]}{\partial \boldsymbol{\phi}}. \tag{19.18}$$

Now the network no longer chases a moving target and is less prone to oscillation.

Using these and other heuristics and with an ϵ-greedy policy, Deep Q-Networks performed at a level comparable to a professional game tester across a set of 49 games using the same network (trained separately for each game). It should be noted that the training process was data-intensive. It took around 38 full days of experience to learn each game. In some games, the algorithm exceeded human performance. On other games like "Montezuma's Revenge," it barely made any progress. This game features sparse rewards and multiple screens with quite different appearances.

19.4.2 Double Q-learning and double deep Q-networks

One potential flaw of Q-Learning is that the maximization over the actions in the update:

$$q[s_t, a_t] \leftarrow q[s_t, a_t] + \alpha\Big(r[a_t, s_t] + \gamma \cdot \max_{a_{t+1}}\big[q[s_{t+1}, a_{t+1}]\big] - q[s_t, a_t]\Big) \tag{19.19}$$

leads to a systematic bias in the estimated values of state $q[s_t, a_t]$. Consider two actions that provide the same average reward, but one is stochastic and the other deterministic. The stochastic reward will exceed the average half of the time and be chosen by the maximum operation, causing the corresponding value of action $q[s_t, a_t]$ to be overestimated. A similar argument can be made about random inaccuracies in the output of the network $\mathrm{q}[s_t, a_t, \boldsymbol{\phi}]$ or random initializations of the q-function.

The underlying problem is that the same network both selects the target (by the maximization operation) and updates the value. Double Q-Learning tackles this problem by training two models $q_1[s_t, a_t]$ and $q_2[s_t, a_t]$ simultaneously:

$$
\begin{aligned}
q_1[s_t, a_t] &\leftarrow q_1[s_t, a_t] + \alpha\Bigl(r[a_t, s_t] + \gamma \cdot q_2\left[s_{t+1}, \underset{a_{t+1}}{\operatorname{argmax}}\bigl[q_1[s_{t+1}, a_{t+1}]\bigr]\right] - q_1[s_t, a_t]\Bigr)\\
q_2[s_t, a_t] &\leftarrow q_2[s_t, a_t] + \alpha\Bigl(r[a_t, s_t] + \gamma \cdot q_1\left[s_{t+1}, \underset{a_{t+1}}{\operatorname{argmax}}\bigl[q_2[s_{t+1}, a_{t+1}]\bigr]\right] - q_2[s_t, a_t]\Bigr).
\end{aligned}
\tag{19.20}
$$

Now the choice of the target and the target itself are decoupled, which helps prevent these biases. In practice, new tuples $< s, a, r, s' >$ are randomly assigned to update one model or another. This is known as *double Q-learning*. *Double deep Q-networks* or *double DQNs* use deep networks $\mathrm{q}[s_t, a_t, \boldsymbol{\phi}_1]$ and $\mathrm{q}[s_t, a_t, \boldsymbol{\phi}_2]$ to estimate the values of action, and the update becomes:

$$
\begin{aligned}
\boldsymbol{\phi}_1 \leftarrow \boldsymbol{\phi}_1 + \alpha\left(r[a_t, s_t] + \gamma \cdot q\left[s_{t+1}, \underset{a_{t+1}}{\operatorname{argmax}}\Bigl[\mathrm{q}[s_{t+1}, a_{t+1}, \boldsymbol{\phi}_1]\Bigr], \boldsymbol{\phi}_2\right] - \mathrm{q}[s_t, a_t, \boldsymbol{\phi}_1]\right)\frac{\partial \mathrm{q}[s_t, a_t, \boldsymbol{\phi}_1]}{\partial \boldsymbol{\phi}_1}\\
\boldsymbol{\phi}_2 \leftarrow \boldsymbol{\phi}_2 + \alpha\left(r[a_t, s_t] + \gamma \cdot q\left[s_{t+1}, \underset{a_{t+1}}{\operatorname{argmax}}\Bigl[\mathrm{q}[s_{t+1}, a_{t+1}, \boldsymbol{\phi}_2]\Bigr], \boldsymbol{\phi}_1\right] - \mathrm{q}[s_t, a_t, \boldsymbol{\phi}_2]\right)\frac{\partial \mathrm{q}[s_t, a_t, \boldsymbol{\phi}_2]}{\partial \boldsymbol{\phi}_2}.
\end{aligned}
\tag{19.21}
$$

19.5 Policy gradient methods

Q-learning estimates the values of actions first and then use these to update the policy. Conversely, *policy-based methods* learn the policy directly. They usually estimate a stochastic policy (i.e., a distribution over possible actions from which we can sample). In MDPs, there is always a deterministic policy that can maximize the value of every state. However, there are three reasons to use a stochastic policy:

1. A stochastic policy naturally helps with exploration of the space; we are not obliged to take the best action at each time step.
2. The loss changes smoothly as we change a stochastic policy. This means we can use gradient descent methods even though the rewards are discrete. This is similar to how the loss for classification problems is based on likelihood. The loss changes smoothly as the model parameters change to make the true class more likely.
3. The MDP assumption is often incorrect; we usually don't have complete knowledge of the state. For example, consider an agent navigating in an environment where it can only observe nearby locations. If two locations look identical, but the nearby reward structure is different, a stochastic policy allows the possibility of taking different actions until this ambiguity is resolved (figure 19.4).

19.5.1 Derivation of gradient update

Consider a trajectory $\boldsymbol{\tau} = [\mathbf{s}_1, a_1, \mathbf{s}_2, a_2, \ldots, \mathbf{s}_T, a_T]$ through an MDP. The probability of this trajectory $Pr(\boldsymbol{\tau}|\boldsymbol{\theta})$ depends on both the state evolution function $Pr(s_{t+1}|s_t, a_t)$ and the current stochastic policy $\boldsymbol{\pi}[a_t|\mathbf{s}_t, \boldsymbol{\theta}]$:

$$Pr(\boldsymbol{\tau}|\boldsymbol{\theta}) = Pr(\mathbf{s}_1)\prod_{t=1}^{T}\boldsymbol{\pi}[a_t|\mathbf{s}_t,\boldsymbol{\theta}]Pr(\mathbf{s}_{t+1}|\mathbf{s}_t,a_t), \tag{19.22}$$

where the policy is now a machine learning model with parameters $\boldsymbol{\theta}$. Policy gradient algorithms aim to maximize the expected return $r[\boldsymbol{\tau}]$ over many such trajectories:

$$\boldsymbol{\theta} = \underset{\boldsymbol{\theta}}{\mathrm{argmax}}\left[\mathbb{E}_{\boldsymbol{\tau}}\Bigl[r[\boldsymbol{\tau}]\Bigr]\right] = \underset{\boldsymbol{\theta}}{\mathrm{argmax}}\left[\int Pr(\boldsymbol{\tau}|\boldsymbol{\theta})r[\boldsymbol{\tau}]d\boldsymbol{\tau}\right], \tag{19.23}$$

where the return is the sum of all the rewards received along the trajectory.

To maximize this quantity, we use the gradient ascent update:

$$\begin{aligned}\boldsymbol{\theta} &\leftarrow \boldsymbol{\theta} + \alpha\cdot\frac{\partial}{\partial\boldsymbol{\theta}}\int Pr(\boldsymbol{\tau}|\boldsymbol{\theta})r[\boldsymbol{\tau}]d\boldsymbol{\tau}\\ &= \boldsymbol{\theta} + \alpha\cdot\int\frac{\partial Pr(\boldsymbol{\tau}|\boldsymbol{\theta})}{\partial\boldsymbol{\theta}}r[\boldsymbol{\tau}]d\boldsymbol{\tau}.\end{aligned} \tag{19.24}$$

where α is the learning rate.

We want to approximate this integral with a sum over empirically observed trajectories. These are drawn from the distribution $Pr(\boldsymbol{\tau})$, so to make progress, we multiply and divide the integrand by this distribution:

$$\begin{aligned}\boldsymbol{\theta} &\leftarrow \boldsymbol{\theta} + \alpha\cdot\int\frac{\partial}{\partial\boldsymbol{\theta}}Pr(\boldsymbol{\tau}|\boldsymbol{\theta})r[\boldsymbol{\tau}]d\boldsymbol{\tau}\\ &= \boldsymbol{\theta} + \alpha\cdot\int Pr(\boldsymbol{\tau}|\boldsymbol{\theta})\frac{1}{Pr(\boldsymbol{\tau}|\boldsymbol{\theta})}\frac{\partial Pr(\boldsymbol{\tau}|\boldsymbol{\theta})}{\partial\boldsymbol{\theta}}r[\boldsymbol{\tau}]d\boldsymbol{\tau}\\ &\approx \boldsymbol{\theta} + \alpha\cdot\frac{1}{I}\sum_{i=1}^{I}\frac{1}{Pr(\boldsymbol{\tau}_i|\boldsymbol{\theta})}\frac{\partial Pr(\boldsymbol{\tau}_i|\boldsymbol{\theta})}{\partial\boldsymbol{\theta}}r[\boldsymbol{\tau}_i].\end{aligned} \tag{19.25}$$

This equation has a simple interpretation; the update changes the parameters $\boldsymbol{\theta}$ to increase the likelihood $Pr(\boldsymbol{\tau}_i|\boldsymbol{\theta})$ of an observed trajectory $\boldsymbol{\tau}_i$ in proportion to the reward $r[\boldsymbol{\tau}_i]$ from that trajectory. However, it also normalizes by the probability of observing that trajectory in the first place to compensate for the fact that some trajectories are observed more frequently than others. If a trajectory is already common and yields high rewards, then we don't need to change much. The biggest updates will come from trajectories that are quite rare but create large rewards.

We can simplify this expression using the *likelihood ratio trick*:

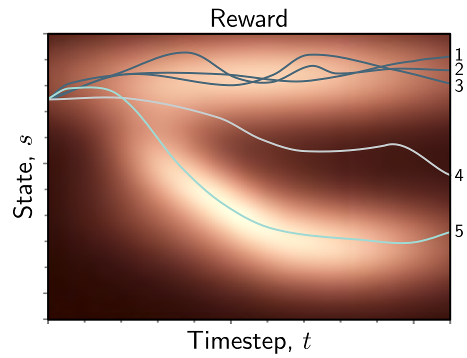

Figure 19.15 Policy gradients. Five episodes for the same policy. Trajectories 1, 2, and 3 generate consistently high rewards, but similar trajectories already frequently occur with this policy, so there is no impetus for change. Trajectory 4 receives low rewards, so the policy should be modified to avoid producing similar trajectories. Trajectory 5 receives high rewards *and* is unusual. This will cause the largest change to the policy under equation 19.25.

$$\frac{\partial \log[\mathrm{f}[z]]}{\partial z} = \frac{1}{f[z]}\frac{\partial \mathrm{f}[z]}{\partial z}, \tag{19.26}$$

which yields the update:

$$\boldsymbol{\theta} \leftarrow \boldsymbol{\theta} + \alpha \cdot \frac{1}{I}\sum_{i=1}^{I}\frac{\partial \log\bigl[Pr(\boldsymbol{\tau}_i|\boldsymbol{\theta})\bigr]}{\partial \boldsymbol{\theta}} r[\boldsymbol{\tau}_i], \tag{19.27}$$

The log probability $\log[Pr(\boldsymbol{\tau}|\boldsymbol{\theta})]$ of a trajectory is given by:

$$\begin{aligned}\log[Pr(\boldsymbol{\tau}|\boldsymbol{\theta})] &= \log\Bigl[Pr(\mathbf{s}_1)\prod_{t=1}^{T}\boldsymbol{\pi}[a_t|\mathbf{s}_t,\boldsymbol{\theta}]Pr(\mathbf{s}_{t+1}|\mathbf{s}_t,a_t)\Bigr] \qquad (19.28)\\ &= \log\bigl[Pr(\mathbf{s}_1)\bigr] + \sum_{t=1}^{T}\log\bigl[\boldsymbol{\pi}[a_t|\mathbf{s}_t,\boldsymbol{\theta}]\bigr] + \sum_{t=1}^{T}\log\bigl[Pr(\mathbf{s}_{t+1}|\mathbf{s}_t,a_t)\bigr],\end{aligned}$$

and noting that only the center term depends on $\boldsymbol{\theta}$, we can rewrite the update from equation 19.27 as:

$$\boldsymbol{\theta} \leftarrow \boldsymbol{\theta} + \alpha \cdot \frac{1}{I}\sum_{i=1}^{I}\sum_{t=1}^{T}\frac{\partial \log\bigl[\boldsymbol{\pi}[a_{it}|\mathbf{s}_{it},\boldsymbol{\theta}]\bigr]}{\partial \boldsymbol{\theta}} r[\boldsymbol{\tau}_i], \tag{19.29}$$

where $\mathbf{s}_{it}$ is the state at time t in episode i, and a_{it} is the action taken at time t on episode i. Note that since the terms relating to the state evolution $Pr(\mathbf{s}_{t+1}|\mathbf{s}_t, a_t)$ disappear, this parameter update does not assume a Markov time evolution process.

We can further simplify this by noting that:

$$r[\boldsymbol{\tau}_i] = \sum_{t=1}^{T} r_{it} = \sum_{k=1}^{t-1} r_{ik} + \sum_{k=t}^{T} r_{ik}, \tag{19.30}$$

where r_{it} is the reward at time t in the i^{th} episode. The first term (the rewards before time t) does not affect the update from time t, so we can write: Problem 19.5

$$\boldsymbol{\theta} \;\leftarrow\; \boldsymbol{\theta} + \alpha \cdot \frac{1}{I}\sum_{i=1}^{I}\sum_{t=1}^{T}\frac{\partial \log\big[\boldsymbol{\pi}[a_{it}|\mathbf{s}_{it},\boldsymbol{\theta}]\big]}{\partial \boldsymbol{\theta}}\sum_{k=t}^{T} r_{ik}. \tag{19.31}$$

19.5.2 REINFORCE algorithm

REINFORCE is an early policy gradient algorithm that exploits this result and incorporates discounting. It is a Monte Carlo method that generates episodes $\boldsymbol{\tau}_i = [s_{i1}, a_{i1}, r_{i2}, s_{i2}, a_{i2}, r_{i3}, \ldots, r_{iT}]$ based on the current policy $\boldsymbol{\pi}[a|\mathbf{s},\boldsymbol{\theta}]$. For discrete actions, this policy could be determined by a neural network $\boldsymbol{\pi}[\mathbf{s}|\boldsymbol{\theta}]$, which takes the current state $\mathbf{s}$ and returns one output for each possible action. These outputs are passed through a softmax function to create a distribution over actions, which is sampled at each time step.

For each episode i, we loop through each step t and calculate the empirical discounted return for the partial trajectory $\boldsymbol{\tau}_{it}$ that starts at time t:

$$r[\boldsymbol{\tau}_{it}] = \sum_{k=t+1}^{T} \gamma^{k-t-1} r_{ik}, \tag{19.32}$$

and then we update the parameters for each time step t in each trajectory:

$$\boldsymbol{\theta} \leftarrow \boldsymbol{\theta} + \alpha \cdot \gamma^{t}\frac{\partial \log\big[\boldsymbol{\pi}_{a_{it}}[\mathbf{s}_{it},\boldsymbol{\theta}]\big]}{\partial \boldsymbol{\theta}} r[\boldsymbol{\tau}_{it}] \qquad\qquad \forall\, i, t, \tag{19.33}$$

where $\boldsymbol{\pi}_{a_t}[s_t, \boldsymbol{\theta}]$ is the probability of a_t produced by the neural network given the current state $\mathbf{s}_t$ and parameters $\boldsymbol{\theta}$, and α is the learning rate. The extra term γ^t ensures that the rewards are discounted relative to the start of the sequence because we maximize the log probability of returns in the whole sequence (equation 19.23).

19.5.3 Baselines and advantage estimates

Policy gradient methods have the drawback that they exhibit high variance; many episodes may be needed to get stable updates of the derivatives. One way to reduce this variance is to subtract the trajectory returns $r[\boldsymbol{\tau}]$ from a baseline b:

$$\boldsymbol{\theta} \leftarrow \boldsymbol{\theta} + \alpha \cdot \frac{1}{I}\sum_{i=1}^{I}\sum_{t=1}^{T}\frac{\partial \log\big[\boldsymbol{\pi}_{a_{it}}[\mathbf{s}_{it},\boldsymbol{\theta}]\big]}{\partial \boldsymbol{\theta}}\left(r[\boldsymbol{\tau}_{it}] - b\right). \tag{19.34}$$

The difference between the empirically observed rewards and the baseline is known as the *advantage estimate*. As long as the baseline b doesn't depend on the actions, then: Problem 19.6

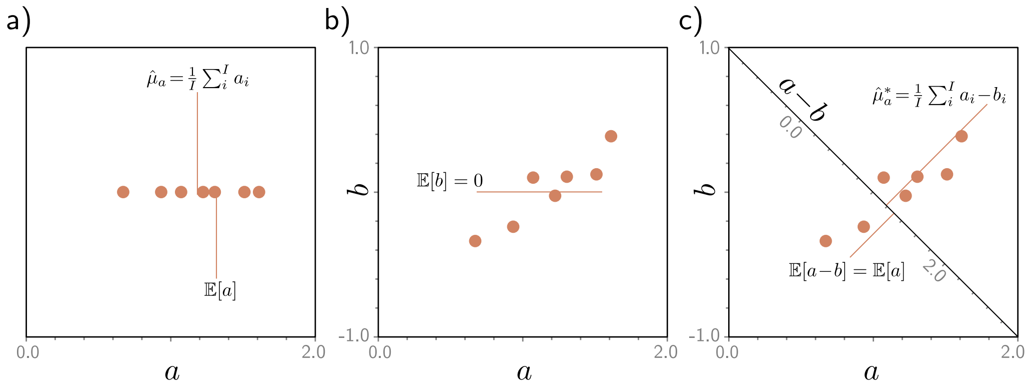

Figure 19.16 Decreasing variance of estimates using control variates. a) Consider trying to estimate $\mathbb{E}[a]$ from a small number of samples. The estimate (the mean of the samples) will vary based on the number of samples and the variance of those samples. b) Now consider observing another variable b that co-varies with a and has $\mathbb{E}[b] = 0$ and the same variance as a. c) The variance of the samples of $a - b$ is much less than that of a, but the expected value $\mathbb{E}[a - b] = \mathbb{E}[a]$ and so we get an estimator with lower variance.

$$\mathbb{E}_{\boldsymbol{\tau}}\left[\sum_{t=1}^{T}\frac{\partial \log\left[\boldsymbol{\pi}_{a_{it}}[\mathbf{s}_{it}, \boldsymbol{\theta}]\right]}{\partial \boldsymbol{\theta}} \cdot b\right] = 0, \tag{19.35}$$

and the expected value will not change. However, if the baseline co-varies with irrelevant factors that add uncertainty, then subtracting it reduces the variance (figure 19.16). This is a special case of the method of *control variates* (see problem 19.7). Problem 19.7

This raises the question of what we should choose b to be. We can find the value of b that minimizes the variance by writing an expression for the variance, taking the derivative with respect to b, setting the result to zero, and solving to yield: Problem 19.8

$$b = \sum_i \frac{\sum_{t=1}^{T}\left(\partial \log\left[\boldsymbol{\pi}_{a_{it}}[\mathbf{s}_{it}, \boldsymbol{\theta}]\right]/\partial\boldsymbol{\theta}\right)^2 r[\boldsymbol{\tau}_{it}]}{\sum_{t=1}^{T}\left(\partial \log\left[\boldsymbol{\pi}_{a_{it}}[\mathbf{s}_{it}, \boldsymbol{\theta}]\right]/\partial\boldsymbol{\theta}\right)^2}. \tag{19.36}$$

In practice, this is often approximated as:

$$b = \frac{1}{I}\sum_i r[\boldsymbol{\tau}_i]. \tag{19.37}$$

Subtracting this baseline factors out variance due to the returns $r[\boldsymbol{\tau}_i]$ from all trajectories being greater than is typical because they happen to pass through states with higher than average returns *whatever* actions we take.

19.5.4 State-dependent baselines

A better option is to use a baseline $b[\mathbf{s}_{it}]$ that depends on the current state $\mathbf{s}_{it}$.

$$\boldsymbol{\theta} \leftarrow \boldsymbol{\theta} + \alpha \cdot \frac{1}{I}\sum_{i=1}^{I}\sum_{t=1}^{T}\frac{\partial \log\big[\boldsymbol{\pi}_{a_{it}}[\mathbf{s}_{it},\boldsymbol{\theta}]\big]}{\partial \boldsymbol{\theta}}\left(r[\boldsymbol{\tau}_{it}] - b[\mathbf{s}_{it}]\right). \tag{19.38}$$

Here, we are compensating for variance introduced by some states having greater overall returns than others, whichever actions we take.

A sensible choice is the expected future reward based on the current state, which is just the value of state $v[\mathbf{s}]$. Since we are in a Monte-Carlo context, this can be parameterized by a neural network $b[s_t] = \mathrm{v}[\mathbf{s},\boldsymbol{\phi}]$ with parameters $\boldsymbol{\phi}$, which we can fit to the observed returns using least squares loss:

$$L[\boldsymbol{\phi}] = \sum_{i=1}^{I}\sum_{t=1}^{T}\left(\mathrm{v}[\mathbf{s},\boldsymbol{\phi}] - \sum_{t=1}^{T} r_{it}\right)^2. \tag{19.39}$$

19.6 Actor-critic methods

Actor-critic algorithms are temporal difference (TD) policy gradient algorithms. They can update the parameters of the policy network at each step. This contrasts with the Monte-Carlo REINFORCE algorithm, which *must* wait for one or more episodes to complete before updating the parameters.

In the TD approach, we do not have access to the future rewards $r[\boldsymbol{\tau}_t] = \sum_{k=t}^{T} r_k$ along this trajectory. Actor critic algorithms approximate the sum over all the future rewards with the observed current reward plus the discounted value of the next state:

$$\sum_{k=1}^{T} r[\boldsymbol{\tau}_{ik}] \approx r_{it} + \gamma \cdot \mathrm{v}[\mathbf{s}_{i,t+1},\boldsymbol{\phi}]. \tag{19.40}$$

Here the value $\mathrm{v}[\mathbf{s}_{i,t+1},\boldsymbol{\phi}]$ is estimated by a second neural network with parameters $\boldsymbol{\phi}$.

Substituting this into equation 19.38 gives the update:

$$\boldsymbol{\theta} \leftarrow \boldsymbol{\theta} + \alpha \cdot \frac{1}{I}\sum_{i=1}^{I}\sum_{t=1}^{T}\frac{\partial \log\big[Pr(a_{it}|\mathbf{s}_{it},\boldsymbol{\theta})\big]}{\partial \boldsymbol{\theta}}\Big(r_{it} + \gamma \cdot \mathrm{v}[\mathbf{s}_{i,t+1},\boldsymbol{\phi}] - \mathrm{v}[\mathbf{s}_{i,t},\boldsymbol{\phi}]\Big). \tag{19.41}$$

Concurrently, we update the parameters $\boldsymbol{\phi}$ by bootstrapping using the loss function:

$$L[\boldsymbol{\phi}] = \sum_{i=1}^{I}\sum_{t=1}^{T}\left(r_{it} + \gamma \cdot \mathrm{v}[\mathbf{s}_{i,t+1},\boldsymbol{\phi}] - \mathrm{v}[\mathbf{s}_{i,t},\boldsymbol{\phi}],\right)^2. \tag{19.42}$$

The policy network $\boldsymbol{\pi}[\mathbf{s}_t,\boldsymbol{\theta}]$ that predicts $Pr(a|\mathbf{s}_t)$ is known as the *actor*. The value network $\mathrm{v}[\mathbf{s}_t,\boldsymbol{\phi}]$ that estimates the future expected rewards of being in a state is termed the *critic*. Often the same network represents both actor and the critic, with two sets of outputs that predict the policy and the value of the state, respectively. Note that although actor-critic methods can update the parameters of the policy at each step, this is rarely done in practice. The agent typically collects a batch of experience over many time steps before the policy is updated.

19.7 Offline reinforcement learning

Interaction with the environment is at the core of reinforcement learning. However, there are some scenarios where it is not practical to send a naïve agent into an environment to explore the effect of different actions. This may be because erratic behavior in the environment is dangerous (e.g., driving autonomous vehicles) or because data collection is time-consuming or expensive (e.g., making financial trades).

However, it *is* possible to gather historical data from human agents in both cases. *Offline RL* or *batch RL* aims to learn how to take actions that maximize rewards on future episodes by observing past sequences $\mathbf{s}_1, a_1, r_2, \mathbf{s}_2, a_2, r_3, \ldots$, without ever interacting with the environment. It is distinct from *imitation learning*, a related technique that (i) does not have access to the rewards and (ii) attempts to replicate the performance of a historical agent rather than improve it.

Although there are offline RL methods based on Q-Learning and policy gradients, this paradigm opens up new possibilities. In particular, we can treat this as a sequence learning problem, in which the goal is to predict the next action, given the history of states, rewards, and actions. The *decision transformer* exploits a transformer decoder framework (section 12.7) to make these predictions (figure 19.17).

However, the goal is to predict actions based on *future rewards* and these are not captured in a standard $\mathbf{s}, a, r$ sequence. Hence, the decision transformer replaces the reward r_t with the *returns-to-go* $R_{t:T} = \sum_{t'=t}^{T} r_t$ (i.e., the sum of the empirically observed future rewards). The remaining framework is very similar to a standard transformer decoder. The states, actions, and returns-to-go are converted to fixed-size embeddings via learned mappings. For Atari games, the state embedding might be converted via a convolutional network similar to that in figure 19.14. The embeddings for the actions and returns-to-go can be learned in the same way as word embeddings (figure 12.9). The transformer is trained with masked self-attention and position embeddings.

This formulation is natural during training but poses a quandary during inference because we don't know the returns-to-go. This can be resolved by using the desired total return at the first step and decrementing this as rewards are received. For example, in an Atari game, the desired total return would be the total score required to win.

Decision transformers can also be fine-tuned from online experience and hence learn over time. They have the advantage of dispensing with most of the reinforcement learning machinery and its associated instability and replacing this with standard supervised learning. Transformers can learn from enormous quantities of data and integrate information across large time contexts (making the temporal credit assignment problem more tractable). This represents an intriguing new direction for reinforcement learning.

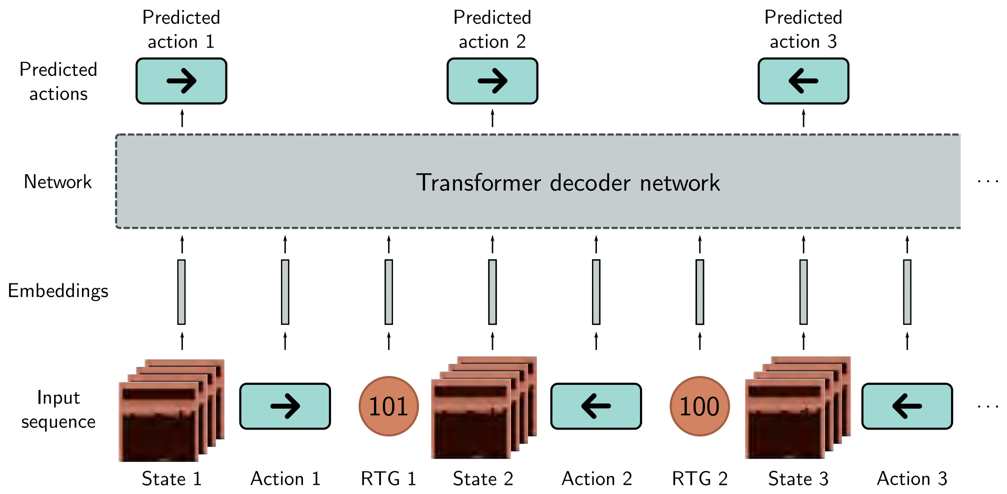

Figure 19.17 Decision transformer. The decision transformer treats offline reinforcement learning as a sequence prediction task. The input is a sequence of states, actions, and returns-to-go (remaining rewards in the episode), each of which is mapped to a fixed-size embedding. At each time step, the network predicts the next action. During testing, the returns-to-go are unknown; in practice, an initial estimate is made from which subsequent observed rewards are subtracted.

19.8 Summary

Reinforcement learning is a sequential decision-making framework for Markov decision processes and similar systems. This chapter reviewed classical approaches to RL, including dynamic programming (in which the environment model is known), Monte Carlo methods (in which multiple episodes are run and the values of actions and policy subsequently changed based on the rewards received), and temporal difference models (in which these values are updated while the episode is ongoing).

Deep Q-Learning is a temporal difference method where deep neural networks are used to predict the value of action for every state. It can train agents to perform Atari 2600 games at a level similar to humans. Policy gradient methods directly optimize the policy rather than assigning values to actions. They produce stochastic policies, which are important when the environment is partially observed. The updates are noisy, and many refinements have been made to reduce their variance.

Offline reinforcement learning is used when we cannot learn by interacting with the environment but must learn from historical data. The decision transformer leverages recent progress in deep learning to build a model of the state-action-reward sequence and predict the actions that will maximize the rewards.

Notes

Sutton & Barto (2018) cover classical reinforcement learning methods in depth. Li (2017), Arulkumaran et al. (2017), François-Lavet et al. (2018), and Wang et al. (2022c) all provide overviews of deep reinforcement learning. Graesser & Keng (2019) is an excellent introductory resource that includes Python code.

Landmarks in deep reinforcement learning: Most landmark achievements of reinforcement learning have been in either video games or real-world games since these provide constrained environments with limited actions and fixed rules. Deep Q-Learning (Mnih et al., 2015) achieved human-level performance across a benchmark of ATARI games. AlphaGo (Silver et al., 2016) beat the world champion at Go, a game that was previously considered very difficult for computers to play. Berner et al. (2019) built a system that beat the world champion team in the five vs. five-player game *Defence of the Ancients 2*, which requires cooperation across players. Ye et al. (2021) built a system that could beat humans on Atari games with limited data (in contrast to previous systems, which need much more experience than humans). More recently, the Cicero system demonstrated human-level performance in the game *Diplomacy* which requires natural language negotiations and coordination between players (FAIR, 2022).

RL has also been applied successfully to combinatorial optimization problems (see Mazyavkina et al., 2021). For example, Kool et al. (2019) learned a model that performed similarly to the best heuristics for the traveling salesman problem. Recently, AlphaTensor (Fawzi et al., 2022) treated matrix multiplication as a game and learned faster ways to multiply matrices using fewer multiplication operations. Since deep learning is heavily reliant on matrix multiplication, this is one of the first examples of self-improvement in AI.

Classical reinforcement learning methods: Very early contributions to the theory of MDPs were made by Thompson (1933) and Thompson (1935). The Bellman recursions were introduced by Bellman (1966). Howard (1960) introduced policy iteration. Sutton & Barto (2018) identify the work of Andreae (1969) as being the first to describe RL using the MDP formalism.

The modern era of reinforcement learning arguably originated in the Ph.D. theses of Sutton (1984) and Watkins (1989). Sutton (1988) introduced the term temporal difference learning. Watkins (1989) and Watkins & Dayan (1992) introduced Q-Learning and showed that it converges to a fixed point by Banach's theorem because the Bellman operator is a contraction mapping. Watkins (1989) made the first explicit connection between dynamic programming and reinforcement learning. SARSA was developed by Rummery & Niranjan (1994). Gordon (1995) introduced *fitted Q-learning* in which a machine learning model is used to predict the value of action for each state/action pair. Riedmiller (2005) introduced *neural-fitted Q-learning*, which used a neural network to predict all the values of action at once from a state. Early work on Monte Carlo methods was carried out by Singh & Sutton (1996), and the exploring starts algorithm was introduced by Sutton & Barto (1999). Note that this is an extremely cursory summary of more than fifty years of work. A much more thorough treatment can be found in Sutton & Barto (2018).

Deep Q-Networks: The deep Q-Learning algorithm was devised by Mnih et al. (2015) and is a direct intellectual descendent of neural-fitted Q-learning. It exploited the then-recent successes of convolutional networks to develop a fitted Q-Learning method that could achieve human-level performance on a benchmark of ATARI games. Deep Q-Learning suffers from the *deadly triad issue* (Sutton & Barto, 2018): training can be unstable in any scheme that incorporates (i) bootstrapping, (ii) off-policy learning, and (iii) function approximation. Consequently, much subsequent work aimed to make training more stable. Mnih et al. (2015) introduced the experience replay buffer, which was subsequently improved by Schaul et al. (2016) to favor more important tuples and hence increase learning speed. This is known as *prioritized experience replay*.

The original Q-Learning paper appended four frames to allow the network to observe the velocities of objects and make the underlying process closer to fully observable. Hausknecht & Stone (2015) introduced *deep recurrent Q-learning*, which used a recurrent neural network architecture that only ingested a single frame at a time because it could "remember" the previous states. Van Hasselt (2010) identified the systematic overestimation of the values of state due to the max operation and proposed the double Q-Learning approach in which two models are trained simultaneously to remedy this. This was subsequently applied in the context of deep Q-learning (Van Hasselt et al., 2016). Wang et al. (2016) introduced *deep dueling networks* in which two heads of the same network predict (i) the value of state and (ii) the *advantage* (relative value) of each action. The intuition here is that sometimes it is the value of state that is important, and it doesn't matter much which action is taken, and decoupling these estimates improves stability.

Fortunato et al. (2018) introduced *noisy deep Q-Networks*, in which some weights in the Q-Network are multiplied by noise to add stochasticity to the predictions and encourage exploration. The network can learn to decrease the magnitudes of the noise over time as it converges to sensible policy. Distributional DQN (Bellemare et al., 2017a; Dabney et al., 2018 following Morimura et al., 2010) aims to estimate more complete information about the distribution of return than just its expectation. This potentially allows the network to mitigate against worst-case outcomes but can also improve performance as predicting higher moments provides a richer training signal. *Rainbow* (Hessel et al., 2018) combined six improvements to the original deep Q-learning algorithm, including dueling networks, distributional DQN, and noisy DQN, to improve both the training speed and the final performance on the ATARI benchmark.

Policy gradients: Williams (1992) introduced the REINFORCE algorithm. The term "policy gradient method" dates to Sutton et al. (1999). Konda & Tsitsiklis (1999) introduced the actor-critic algorithm. In practice, policy gradient methods often use undiscounted state distributions (Thomas, 2014). Decreasing the variance by using different baselines is discussed in Greensmith et al. (2004) and Peters & Schaal (2008).

Policy gradients have been adapted to produce deterministic policies (Silver et al., 2014; Lillicrap et al., 2016; Fujimoto et al., 2018). The most direct approach is to maximize over the possible actions, but if the action space is continuous, this requires an optimization procedure at each step. The *deep deterministic policy gradient* algorithm (Lillicrap et al., 2016) moves the policy in the direction of the gradient of the value of action (implying the use of an actor-critic method).

Modern policy gradients: We introduced policy gradients in terms of the parameter update. However, they can also be viewed as optimizing a surrogate loss based on importance sampling of the expected rewards, using trajectories from the current policy parameters. This view allows us to take multiple optimization steps validly. However, this can cause very large policy updates. Overstepping is a minor problem in supervised learning, as the trajectory can be corrected later. However, in RL, it affects future data collection and can be extremely destructive.

Several methods have been proposed to moderate these updates. *Natural policy gradients* (Kakade, 2001) are based on natural gradients (Amari, 1998), which modify the descent direction by the Fisher information matrix. This provides a better update which is less likely to get stuck in local plateaus, but unfortunately, the Fisher matrix is impractical to compute in models with many parameters. In *trust-region policy optimization* or *TRPO* (Schulman et al., 2015), the surrogate objective is maximized subject to a constraint on the KL divergence between the old and new policies. Schulman et al. (2017) propose a simpler formulation in which this KL divergence appears as a regularization term. The regularization weight is adapted based on the distance between the KL divergence and a target indicating how much we want the policy to change. *Proximal policy optimization* or *PPO* (Schulman et al., 2017) is an even simpler approach in which the loss is clipped to ensure smaller updates.

Actor-critic: The actor-critic algorithm was introduced by Konda & Tsitsiklis (1999). In the actor-critic algorithm described in section 19.6, the critic used a 1-step estimator. It's also possible to use k-step estimators (in which we observe k discounted rewards and approximate the subsequent rewards with an estimate of the values of state). In general, as k increases, the variance of the estimate increases, but the bias decreases. *Generalized advantage estimation* (Schulman et al., 2016) weights together estimates from many steps and parameterizes the weighting by a single term that trades off the bias and the variance. Mnih et al. (2016) introduced *asynchronous actor-critic* or *A3C* in which multiple agents are run independently in parallel environments and update the same parameters. Both the policy and value function are updated every T time steps using a mix of k-step returns. Wang et al. (2017) introduce several methods designed to make asynchronous actor-critic more efficient. *Soft actor-critic* (Haarnoja et al., 2018b) adds an entropy term to the cost function, which encourages exploration and less overfitting since the policy is encouraged to be less confident.

Offline RL: In offline reinforcement learning, the policy is learned by observing the behavior of other agents, including the rewards they receive, *without* the ability to change the policy. It is related to imitation learning, where the goal is to copy the behavior of another agent without access to rewards (see Hussein et al., 2017). One approach is to treat offline RL in the same way as off-policy reinforcement learning. However, in practice, the distributional shift between the observed and applied policy manifests in overly optimistic value of action estimates and poor performance (see Fujimoto et al., 2019; Kumar et al., 2019a; Agarwal et al., 2020). Conservative Q-learning (Kumar et al., 2020b) learns conservative, lower-bound estimates of the value function by regularizing the Q-values. The decision transformer (Chen et al., 2021c) is a simple approach to offline learning that takes advantage of the well-studied self-attention architecture. It can subsequently be fine-tuned with online training (Zheng et al., 2022).

Other areas of RL: Reinforcement learning is an enormous area, which easily justifies its own book, and this literature review is extremely superficial. Other notable areas of RL that we have not discussed include *model-based RL*, in which the state transition probabilities and rewards function are modeled (see Moerland et al., 2023). This allows forward planning and has the advantage that the same model can be reused for different reward structures. *Hybrid methods* such as AlphaGo (Silver et al., 2016) and MuZero (Schrittwieser et al., 2020) have separate models for the dynamics of the states, the policy, and the value of future positions.

This chapter has only discussed simple methods for exploration, like the epsilon-greedy approach, noisy Q-learning, and adding an entropy term to penalize overconfident policies. *Intrinsic motivation* refers to methods that add rewards for exploration and thus imbue the agent with "curiosity" (see Barto, 2013; Aubret et al., 2019). *Hierarchical reinforcement learning* (see Pateria et al., 2021) refers to methods that break down the final objective into sub-tasks. *Multi-agent reinforcement learning* (see Zhang et al., 2021a) considers the case where multiple agents coexist in a shared environment. This may be in either a competitive or cooperative context.

Problems

Problem 19.1 Figure 19.18 shows a single trajectory through the example MDP. Calculate the return for each step in the trajectory given that the discount factor γ is 0.9.

Problem 19.2* Prove the policy improvement theorem. In other words show that $v[s|\pi] < v[s|\pi']$ where π' is the updated policy after a single iteration through equations 19.11 and 19.12.

Problem 19.3 Show that when the values of state and policy are initialized as in figure 19.10a, they become those in figure 19.10b after two iterations of (i) policy evaluation and (ii) policy

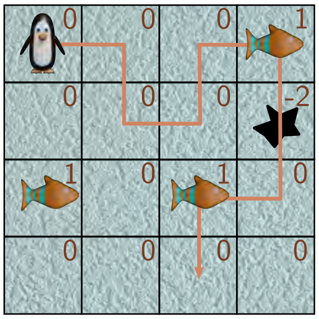

Figure 19.18 One trajectory through an MDP. The penguin receives a reward of +1 for eating the first fish, -2 for falling into the hole, and +1 for eating the second fish. The discount factor γ is 0.9.

improvement. The state transition allots 0.5 probability to the direction the policy indicates and divides the remaining probability equally between the other valid actions. The reward function returns -2 regardless of the action when the penguin leaves a hole. The reward function returns +3 regardless of the action when the penguin leaves the fish tile, and the episode ends, so the fish tile must have a value of +3.

Problem 19.4* The Q-Learning update for the values of action is given by:

$$q[s_t, a_t] \leftarrow q[s_t, a_t] + \alpha\Bigl(r[a_t, s_t] + \gamma \cdot q[s_{t+1}, a_{t+1}] - q[s_t, a_t]\Bigr). \tag{19.43}$$

Show that this is a contraction mapping (equation 16.20). It follows that a fixed point will exist by Banach's theorem and that the updates will eventually converge.

Problem 19.5 Show that:

$$\sum_{t=1}^{T} \frac{\partial \log\bigl[Pr(a_t|\mathbf{s}_t, \boldsymbol{\theta})\bigr]\bigr]}{\partial \boldsymbol{\theta}} \left(\sum_{k=1}^{t-1} r_t\right) = 0, \tag{19.44}$$

and so removing the past rewards from the policy gradient update at time t does not change the expected gradient update.

Problem 19.6 Show that:

$$\mathbb{E}_{\boldsymbol{\tau}}\left[\frac{\partial}{\partial \boldsymbol{\theta}} \log\bigl[Pr(\boldsymbol{\tau}|\boldsymbol{\theta})\bigr] b\right] = 0, \tag{19.45}$$

and so adding a baseline update doesn't change the expected policy gradient update.

Problem 19.7* Suppose that we want to estimate a quantity $\mathbb{E}[a]$ from samples $a_1, a_2 \ldots a_I$. Consider that we also have paired samples $b_1, b_2 \ldots b_I$ that are samples that co-vary with a where $\mathbb{E}[b] = \mu_b$. Show that the estimator:

$$\hat{\mu}'_a = \frac{1}{I}\sum_i a_i - c(b_i - \mathbb{E}[b]), \tag{19.46}$$

has a lower variance than the standard estimator

$$\hat{\mu}_a = \frac{1}{I}\sum_i a_i, \tag{19.47}$$

when the constant c is chosen judiciously. Find an expression for the optimal value of c.

Problem 19.8 The estimate of the gradient in equation 19.34 can be written as:

$$\mathbb{E}_{\boldsymbol{\tau}}\Big[g[\boldsymbol{\theta}](r[\boldsymbol{\tau}_t]-b)\Big], \tag{19.48}$$

where

$$g[\theta]=\sum_{t=1}^{T}\frac{\partial\log\big[Pr(a_t|\mathbf{s}_t,\boldsymbol{\theta})]\big]}{\partial\boldsymbol{\theta}}, \tag{19.49}$$

and

$$r[\boldsymbol{\tau}_t]=\sum_{k=t}^{T}r_k. \tag{19.50}$$

Show that the value of b that minimizes the variance of the gradient estimate is given by:

$$b=\frac{\mathbb{E}[g[\boldsymbol{\tau}]^2]r[\boldsymbol{\tau}]}{\mathbb{E}[g[\boldsymbol{\tau}]^2]}. \tag{19.51}$$

Chapter 20

Why does deep learning work?

The final chapter of this book differs from those that precede it. Instead of presenting established results, it poses questions about how and why deep learning works so well. These questions are rarely discussed in textbooks. However, it's important to realize that (despite the title of this book) our understanding of deep learning is still limited.

We argue that it is surprising that deep networks are easy to train and surprising that they generalize. Then we consider each of these topics in turn. We enumerate the factors that influence training success and discuss what is known about loss functions for deep networks. Then we consider the factors that influence generalization. We conclude with a discussion of whether networks need to be overparameterized and deep.

20.1 The case against deep learning

The MNIST-1D dataset (figure 8.1) has just forty input dimensions and ten output dimensions. With enough hidden units per layer, a two-layer fully connected network fits 10000 MNIST-1D training data points perfectly and generalizes reasonably to unseen examples (figure 8.10a). Indeed, we now take it for granted that with sufficient hidden units deep networks will classify almost any training set near-perfectly. We also take it as read that the fitted model will generalize to new data. However, it's not *at all* obvious either that the training process should succeed or that the resulting model should generalize. This section argues that both these phenomena are surprising.

20.1.1 Training

Performance of a two-layer fully-connected network on 10000 MNIST-1D training examples is perfect once there are 43 hidden units per layer ($\sim$4000 parameters). However, finding the global minimum of an arbitrary non-convex function is NP-hard (Murty & Kabadi, 1987), and this is also true for certain neural network loss functions (Blum & Rivest, 1992). It's remarkable that the fitting algorithm doesn't get trapped in local minima or stuck near saddle points, and that it can efficiently recruit spare model capacity to fit unexplained training data wherever they lie.

Perhaps this success is less surprising when there are far more parameters than training data. However, it's debatable whether this is generally the case. AlexNet had $\sim$60 million parameters and was trained with $\sim$1 million data points. However, to complicate matters, each training example was augmented with 2048 transformations. GPT-3 had 175 billion parameters and was trained with 300 billion tokens. There is not a clear-cut case that either model was overparameterized and yet they were successfully trained.

In short, it's surprising that we can fit deep networks reliably and efficiently. Either the data, the models, the training algorithms, or some combination of all three must have some special properties that make this possible.

20.1.2 Generalization

If the efficient fitting of neural networks is startling, their generalization to new data is *dumbfounding*. First, it's not obvious *a priori* that our datasets are sufficient to characterize the input/output mapping. The curse of dimensionality implies that the training dataset is tiny compared to the *possible* inputs; if each of the 40 inputs of the MNIST-1D data were quantized into 10 possible values, there would be 10^{40} possible inputs, which is a factor of 10^{35} more than the number of training examples.

Problem 20.1

Second, deep networks describe *very* complicated functions. A fully connected network for MNIST-1D with two hidden layers of width 400 can create mappings with up to 10^{42} linear regions. That's roughly 10^{37} regions per training example, so very few of these regions contain data at any stage during training; regardless, those regions that *do* encounter data points constrain the remaining regions to behave reasonably.

Third, generalization gets *better* with more parameters (figure 8.10). The model in the previous paragraph has 177,201 parameters. Assuming it can fit one training example per parameter, it has 167,201 spare degrees of freedom. This surfeit gives the model latitude to do *almost anything* between the training data, and yet it behaves sensibly.

20.1.3 The unreasonable effectiveness of deep learning

To summarize, it's neither obvious that we should be able to fit deep networks, nor that they should generalize. *A priori*, deep learning shouldn't work. And yet it does. This chapter investigates why. Sections 20.2–20.3 describe what we know about fitting deep networks and their loss functions. Sections 20.4–20.6 examine generalization.

20.2 Factors that influence fitting performance

Figure 6.4 showed that loss functions for nonlinear models can have both local minima and saddle points. However, we can reliably fit deep networks to complex training sets.

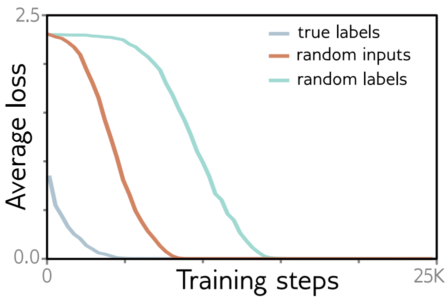

Figure 20.1 Fitting random data. Losses for AlexNet architecture trained on CIFAR10 dataset with SGD. When the pixels are drawn from Gaussian random distribution with the same mean and variance as the original data, the model can still be fit (albeit more slowly). When the labels are randomized, the model can still be fit (albeit even more slowly). Adapted from Zhang et al. (2017a).

For example, figure 8.10 shows perfect training performance on MNIST-1D, MNIST, and CIFAR-100. This section considers factors that might resolve this contradiction.

20.2.1 Dataset

It's important to realize that we can't learn *any* function. Consider a completely random mapping from every possible 28×28 binary image to one of ten categories. Since there is no structure to this function, the only recourse is to memorize the 2^{784} assignments. However, it's easy to train a model on the MNIST dataset (figures 8.10 and 15.15) which contains 60,000 examples of 28×28 images labelled with one of ten categories. One explanation for this contradiction could be that it is easy to find global minima because the real-world functions that we approximate are relatively simple.

This hypothesis was investigated by Zhang et al. (2017a) who trained AlexNet on the CIFAR10 image classification dataset when (i) the labels of the 10 classes were randomly permuted and (ii) each image was replaced with Gaussian noise (figure 20.1). These changes slowed down learning, but the network could still fit the data well. This implies that the properties of the dataset aren't critical. Problem 20.2

20.2.2 Regularization

Another possible explanation for the ease with which models are trained is that regularization makes the loss surface flatter and more convex. However, Zhang et al. (2017a) found that neither explicit regularization nor Dropout was required to fit random data. This does not eliminate implicit regularization due to the finite step size of the fitting algorithms (section 9.2). However, this effect increases with the learning rate (equation 9.9) and model-fitting does not get easier with larger learning rates.

20.2.3 Stochastic training algorithms

Chapter 6 argued that SGD algorithm potentially allows the optimization trajectory to move between "valleys" during training. However, Keskar et al. (2017) show that

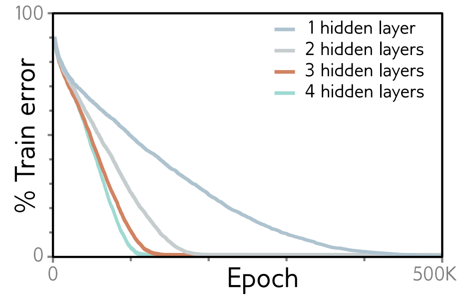

Figure 20.2 MNIST-1D training. Four fully connected networks were fit to 4000 MNIST-1D examples with random labels using full batch gradient descent, He initialization, no momentum or regularization, and learning rate 0.0025. Models with 1,2,3,4 layers had 298, 100, 75, 63 hidden units per layer and 15208, 15210, 15235, 15139 parameters, respectively. All models train successfully but deeper models require fewer epochs.

several models (including fully-connected and convolutional networks) can be fit to many datasets (including CIFAR100 and MNIST) almost perfectly with very large batches of 5000-6000 images. This eliminates most of the randomness but training still succeeds.

Figure 20.2 shows training results for four fully connected models fitted to 4000 MNIST-1D examples with randomized labels using full-batch (i.e., non-stochastic) gradient descent. There was no explicit regularization and the learning rate was set to a constant small value of 0.0025 to minimize implicit regularization. Here, the true mapping from data to labels has no structure, the training is deterministic, and there is no regularization and yet the training error *still* decreases to zero. This suggests that these loss functions may genuinely have no local minima.

Problem 20.3

20.2.4 Overparameterization

Overparameterization almost certainly *is* an important factor that contributes to the ease of training neural networks. It implies that there is a large family of degenerate solutions and so there may always be some direction in which the parameters can be modified to decrease the loss. Sejnowski (2020) suggests that "... the degeneracy of solutions changes the nature of the problem from finding a needle in a haystack to a haystack of needles."

In practice, networks are frequently overparameterized by one or two orders of magnitude (figure 20.3). However, data augmentation makes it difficult to make precise statements. Augmentation may increase the data by several orders of magnitude, but these are manipulations of existing examples rather than independent new data points. Moreover, figure 8.10 shows that neural networks can sometimes fit the training data well when there are the same number or fewer parameters than data points. This is presumably due to redundancy in training examples from the same underlying function.

Several theoretical convergence results show that, *under certain circumstances*, SGD converges to a global minimum when the network is sufficiently overparameterized. For example, Du et al. (2019b) show that randomly initialized SGD converges to a global minimum for shallow fully connected ReLU networks with a least squares loss with enough hidden units. Similarly, Du et al. (2019a) consider deep, residual, and convolutional networks when the activation function is smooth and Lipschitz. Zou et al. (2020) analyzed the convergence of gradient descent on deep fully connected networks using a

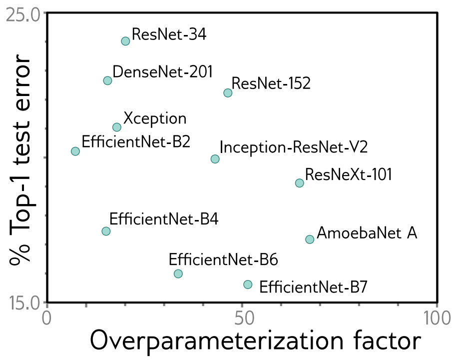

Figure 20.3 Overparameterization. ImageNet performance for convolutional nets as a function of overparameterization (in multiples of dataset size). Most models have 10–100 times more parameters than there were training examples. Models compared are ResNet (He et al., 2016a,b), DenseNet (Huang et al., 2017b), Xception (Chollet, 2017), EfficientNet (Tan & Le, 2019), Inception (Szegedy et al., 2017), ResNeXt (Xie et al., 2017), and AmoebaNet (Cubuk et al., 2019).

hinge loss. Allen-Zhu et al. (2019) considered deep networks with ReLU functions.

If a neural network is sufficiently overparameterized so that it can memorize any data set of a fixed size, then all stationary points become global minima (Livni et al., 2014; Nguyen & Hein, 2017, 2018). Other results show that if the network is wide enough, then local minima where the loss is higher than the global minimum are rare (see Choromanska et al., 2015; Pascanu et al., 2014; Pennington & Bahri, 2017). Kawaguchi et al. (2019) prove that as a network becomes deeper, wider, or both, the loss at local minima becomes closer to that at the global minima for squared loss functions.

These theoretical results are intriguing, but usually make unrealistic assumptions about the network structure. For example, Du et al. (2019a) show that residual networks converge to zero training loss when the width of the network D (i.e., the number of hidden units) is $\mathcal{O}[I^4K^2]$ where I is the amount of training data and K is the depth of the network. Similarly, Nguyen & Hein (2017) assume that the network's width is larger than the data set size, which is unrealistic in most practical scenarios. Overparameterization seems to be important, but theory cannot yet explain empirical fitting performance.

20.2.5 Activation functions

The activation function is also known to affect training difficulty. Networks where the activation only changes over a small part of the input range are harder to fit than ReLUs (which vary over half the input range), or Leaky ReLUs (which vary over the full range); For example, sigmoid and tanh nonlinearities (figure 3.13a) have shallow gradients in their tails; where the activation function is near-constant, the training gradient is near-zero, and so there is no mechanism to improve the model.

20.2.6 Initialization

Another potential explanation is that Xavier/He initialization set the parameters to values that are easy to optimize. Of course, for deeper networks, such initialization is necessary to avoid exploding and vanishing gradients, so in a trivial sense, it is critical

Figure 20.4 Effect of initialization on fitting. A three-layer fully connected network with 200 hidden units per layer was trained on 1000 MNIST examples with AdamW using one-hot targets and mean-squared error loss. It takes longer to fit networks when larger multiples of He initialization are used but this does not affect the outcome. This may just reflect the extra distance that the weights move. Adapted from Liu et al. (2023c).

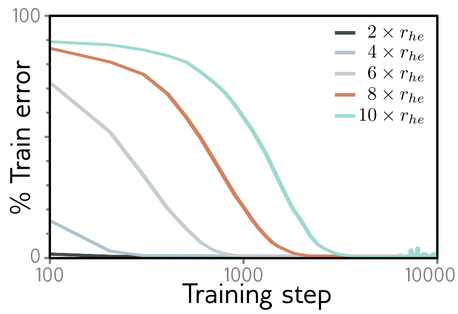

to training success. However, for shallower networks, the initial variance of the weights is less important. Liu et al. (2023c) trained a 3-layer fully connected network with 200 hidden units per layer on 1000 MNIST data points. They found that more iterations were required to fit the training data as the variance increased from that proposed by He (figure 20.4) but this did not ultimately impede fitting. Hence, initialization does not shed much light on why fitting neural networks is so easy, although exploding/vanishing gradients do reveal initializations that make training difficult with finite precision math.

20.2.7 Network depth

Neural networks are harder to fit when the depth becomes very large due to exploding and vanishing gradients (figure 7.7) and shattered gradients (figure 11.3). However, these are (arguably) practical numerical issues. There is no definitive evidence that the underlying loss function is fundamentally more or less convex as the network depth increases. Figure 20.2 does show that for MNIST data with randomized labels and He initialization, deeper networks train in fewer iterations. However, this might be because either (i) the gradients in deeper networks are steeper or (ii) He initialization just starts shallower networks further away from the optimal parameters.

Frankle & Carbin (2019) show that for small networks like VGG you can get the same or better performance if you (i) train the network, (ii) prune the weights with the smallest magnitudes and (iii) retrain from the same initial weights. This does not work if the weights are randomly re-initialised. They concluded that the original over-parameterised network contains small trainable sub-networks which are sufficient to provide the performance. They term this the *lottery ticket hypothesis* and denote the sub-networks as *winning tickets*. This suggests that the effective number of sub-networks may have a key role to play in fitting. This (perhaps) varies with the network depth for a fixed parameter count, but a precise characterization of this idea is lacking.

20.3 Properties of loss functions

The previous section discussed factors that contribute to the ease with which neural networks can be trained. The number of parameters (degree of overparameterization) and the choice of activation function are both important. Surprisingly, the choice of dataset, the randomness of the fitting algorithm, and the use of regularization don't seem important. There is no definitive evidence that (for a fixed parameter count) the depth of the network matters (other than numerical problems due to exploding/vanishing gradients and shattered gradients). This section tackles the same topic from a different angle by considering the empirical properties of loss functions.

20.3.1 Multiple global minima

We *expect* loss functions for deep networks to have a large family of equivalent global minima. In fully connected networks, the hidden units at each layer and their associated weights can be permuted without changing the output. In convolutional networks, permuting the channels and convolution kernels appropriately doesn't change the output. We can multiply the weight before any ReLU function and divide the weight after by a positive number without changing the output. Using BatchNorm induces another set of redundancies because the mean and variance of each hidden unit or channel are reset.

The above modifications all produce the same output for *every* input. However, the global minimum only depends on the output at the training data points. In overparameterized networks, there will also be families of solutions that behave identically at the data points, but differently between them. All of these are also global minima.

20.3.2 Route to the minimum

Goodfellow et al. (2015b) considered a straight line between the initial parameters and the final values. They show that the loss function along this line usually decreases monotonically (except for a small bump near the start sometimes). This phenomenon is observed for several different types of networks and activation functions (figure 20.5a).

Of course, real optimization trajectories do not proceed in a straight line. However, Li et al. (2018b) find that they do lie in low-dimensional subspaces. They attribute this to the existence of large, nearly convex regions in the loss landscape that capture the trajectory early on and funnel it in a few important directions. Surprisingly, Li et al. (2018a) showed that networks still train well if optimization is *constrained* to lie on a random low-dimensional hyperplane, as long its dimensionality is sufficient (figure 20.6).

Li & Liang (2018) show that as network width increases, the relative change in the parameters during training decreases; for large widths, the initial parameters take smaller values, change by a smaller proportion of those values, and converge in fewer steps.

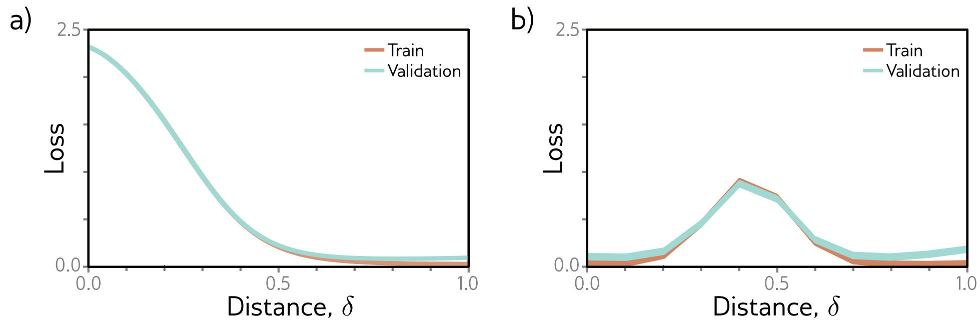

Figure 20.5 Linear slices through loss function. a) A two-layer fully connected ReLU network is trained on MNIST. The loss along a straight line starting at the initial parameters (δ=0) and finishing at the trained parameters (δ=1) descends monotonically to the final value. b) However, in this two-layer fully connected MaxOut network on MNIST, there is a significant increase in the loss along a straight line between one solution (δ=0) and another (δ=1).

Figure 20.6 Subspace training. A fully connected network with two hidden layers, each with 200 units was trained on MNIST. Parameters were initialized using a standard method but then constrained to lie within a random subspace. Performance reaches 90% of the unconstrained level when this subspace is 750D (termed the *intrinsic dimension*), which is 0.4% of the original parameters. Adapted from Li et al. (2018a).

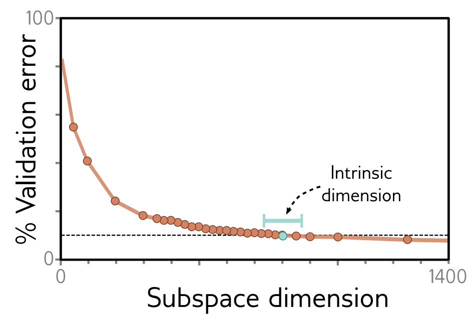

20.3.3 Connections between minima

Goodfellow et al. (2015b) examined the loss function along a straight line between two minima that were found independently. They saw a pronounced increase in the loss between them (figure 20.5b); good minima are not generally linearly connected. However, Frankle et al. (2020) showed that this increase vanishes if the networks are identically trained initially and later allowed to diverge by using different SGD noise and augmentation. This suggests that the solution is constrained early in training and that *some* families of minima are linearly connected.

Draxler et al. (2018) found minima with good (but different) performance on the CIFAR10 dataset. They then showed that it is possible to construct paths from one to the other, where the loss function remains low along this path. They conclude that there is a single connected manifold of low loss (figure 20.7). This seems to be increasingly true as the width and depth of the network increase. Garipov et al. (2018) and Fort & Jastrzebski (2019) present other schemes for connecting minima.

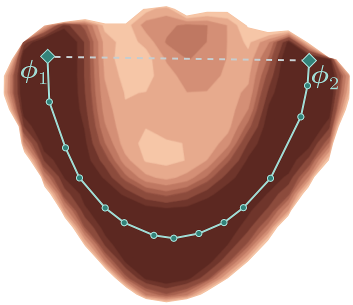

Figure 20.7 Connections between minima. A slice through the loss function of DenseNet on CIFAR10. Parameters $\boldsymbol{\phi}_1$ and $\boldsymbol{\phi}_2$ are two independently discovered minima. Linear interpolation between these parameters reveals an energy barrier (dashed line). However, for sufficiently deep and wide networks, it is possible to find a curved path of low energy between two minima (cyan line). Adapted from Draxler et al. (2018).

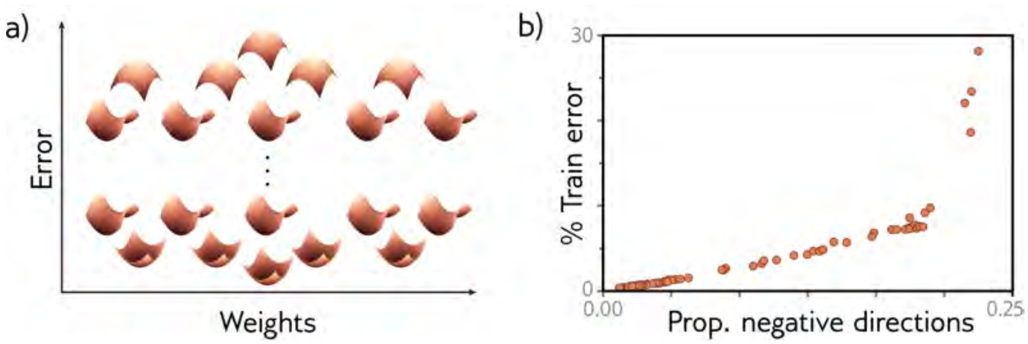

Figure 20.8 Critical points vs. loss. a) In random Gaussian functions, the number of directions in which the function curves down decreases with the height so minima all appear near the bottom of the function. b) Dauphin et al. (2014) found critical points on a neural network loss surface (i.e., points with zero gradient). They showed that the proportion of negative eigenvalues (directions that point down) decreases with the loss. The implication is that all minima (points with zero gradient where no directions point down) have low losses. Adapted from Dauphin et al. (2014) and Bahri et al. (2020).

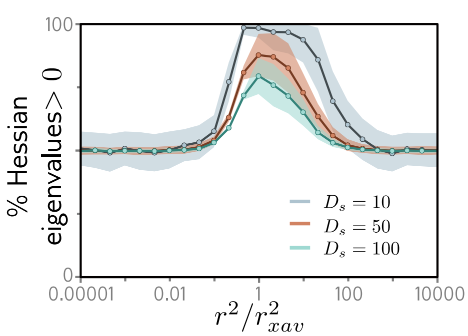

Figure 20.9 Goldilocks zone. The proportion of eigenvalues of the Hessian that are greater than zero (a measure of positive curvature / convexity) within a random subspace of dimension D_s in a two-layer fully-connected network with ReLU functions applied to MNIST as a function of the squared radius r^2 of the point relative to Xavier initialization. There is a pronounced region of positive curvature, known as the *Goldilocks zone.* Adapted from Fort & Scherlis (2019).

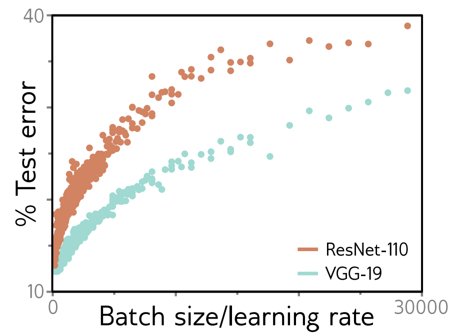

Figure 20.10 Batch size to learning rate ratio. Generalization of two models on the CIFAR 10 database depends on the ratio of batch size to learning rate. As the batch size increases, generalization decreases. As the learning rate increases, generalization increases. Adapted from He et al. (2019).

20.3.4 Curvature of loss surface

Random Gaussian functions (in which points are jointly distributed with covariance given by a kernel function of their distance) have an interesting property: for points where the gradient is zero, the fraction of directions where the function curves down decreases as the height decreases (see Bahri et al., 2020). Dauphin et al. (2014) searched for saddle points in a neural network loss function and similarly found a correlation between the loss and the number of negative eigenvalues (figure 20.8). Baldi & Hornik (1989) analyzed the error surface of a shallow network and found that there were *no local minima*, but only saddle points. These results suggest that there are few or no bad local minima.

Fort & Scherlis (2019) measure the curvature at random points on a neural network loss surface; they showed that the curvature of the surface is unusually positive when the ℓ_2 norm of the weights lies within a certain range (figure 20.9). He and Xavier initialization fall within this range, which they term the *Goldilocks zone*.

20.4 Factors that determine generalization

The last two sections considered factors that determine whether the network trains successfully, and what is known about neural network loss functions. This section considers factors that determine how well a trained network generalizes. This complements the discussion of regularization (chapter 9) which explicitly aims to encourage generalization.

20.4.1 Training algorithms

Since deep networks are usually overparameterized, the details of the training process determine which of the degenerate family of minima the algorithm converges to. Some of these details reliably improve generalization.

LeCun et al. (2012) show that SGD generalizes better than full-batch gradient descent. It has been argued that SGD generalizes better than Adam (e.g., Wilson et al., 2017; Keskar & Socher, 2017), but more recent studies suggest that there is little dif-

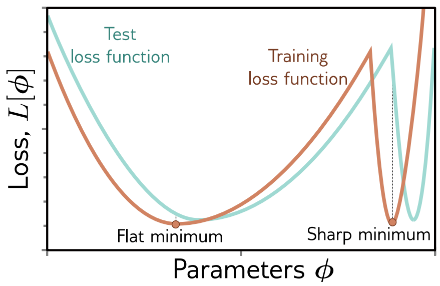

Figure 20.11 Flat vs. sharp minima. Flat minima are expected to generalize better. Small errors in estimating the parameters or in the alignment of the train and test loss functions are less problematic in flat regions. Adapted from Keskar et al. (2017).

ference when the hyperparameter search is done carefully (Choi et al., 2019). Keskar et al. (2017) show that deep nets generalize better with smaller batch-size when no other form of regularisation is used. It is also well-known that larger learning rates tend to generalize better (e.g., figure 9.5). He et al. (2019) argue that these two observations are related. They show a significant correlation between the batch size:learning rate ratio and the degree of generalization and prove a generalization bound for neural networks which has a positive correlation with this ratio (figure 20.10).

These observations are aligned with the discovery that SGD implicitly adds regularization terms to the loss function (section 9.2) and their magnitude depends on the learning rate. The trajectory of the parameters is changed by this regularization and they converge to a part of the loss function that generalizes well.

20.4.2 Flatness of minimum

There has been speculation dating at least to Hochreiter & Schmidhuber (1997a) that flat minima in the loss function generalize better than sharp minima (figure 20.11). Informally, if the minimum is flatter, then small errors in the estimated parameters are less important. This can also be motivated from various theoretical viewpoints. For example, minimum description length theory suggests models specified by fewer bits generalize better (Rissanen, 1983). For wide minima, the precision needed to store the weights is lower, so they should generalize better.

Flatness can be measured by (i) the size of the connected region around the minimum for which training loss is similar (Hochreiter & Schmidhuber, 1997a), (ii) the second-order curvature around the minimum (Chaudhari et al., 2019), or (iii) the maximum loss within a neighborhood of the minimum (Keskar et al., 2017). However, caution is required; estimated flatness can be affected by trivial reparameterizations of the network due to the non-negative homogeneity property of the ReLU function (Dinh et al., 2017).

Nonetheless, Keskar et al. (2017) varied the batch size and learning rate and showed that flatness correlates with generalization. Izmailov et al. (2018) average together weights from multiple points in a learning trajectory. This both results in flatter test and training surfaces at the minimum and improves generalization. Other regularization techniques can also be viewed through this lens. For example, averaging model outputs (ensembling) may also make the test loss surface flatter. Kleinberg et al. (2018) showed that large gradient variance during training helps avoid sharp regions. This may explain why reducing the batch size and adding noise helps generalization.

The above studies consider flatness for a single model and training set. However, sharpness is not a good criterion to predict generalization between datasets; when the labels in the CIFAR dataset are randomized (making generalization impossible), there is no commensurate decrease in the flatness of the minimum (Neyshabur et al., 2017).

20.4.3 Architecture

The inductive bias of a network is determined by its architecture and judicious choices of model can drastically improve generalization. Chapter 10 introduced convolutional networks, which are designed to process data on regular grids; they implicitly assume that the input statistics are the same across the input and so share parameters across position. Similarly, transformers are suited for modeling data that is invariant to permutations, and graph neural networks are suited to data represented on irregular graphs. Matching the architecture to the properties of the data improves generalization over generic fully-connected architectures (see figure 10.8).

20.4.4 Norm of weights

Section 20.3.4 reviewed the finding of Fort & Scherlis (2019) that the curvature of the loss surface is unusually positive when the ℓ_2 norm of the weights lies within a certain range. The same authors provided evidence that generalization is also good when the ℓ_2 weight norm falls within this Goldilocks zone. This is perhaps unsurprising. The norm of the weights is (indirectly) related to the Lipschitz constant of the model. If this norm is too small, then the model will not be able to change fast enough to capture the variation in the mapping. If the norm is too large, then the model will be unnecessarily variable between training points and will not interpolate smoothly.

This finding was used by Liu et al. (2023c) to explain the phenomenon of *grokking* (Power et al., 2022) in which a sudden improvement in generalization can occur many epochs after the training error is already zero (figure 20.13). It is proposed that grokking occurs when the norm of the weights is initially too large; the training data fits well, but the variation of the model between the data points is large. Over time, implicit or explicit regularization decreases the norm of the weights until they reach the Goldilocks zone and generalization suddenly improves.

20.4.5 Overparameterization

Figure 8.10 showed that generalization performance generally improves with the degree of overparameterization (figure 8.10). When combined with the bias/variance trade-off curve, this results in double descent. The putative explanation for this phenomenon is that the network has more latitude to become smoother *between* the training data points when the model is overparameterized.

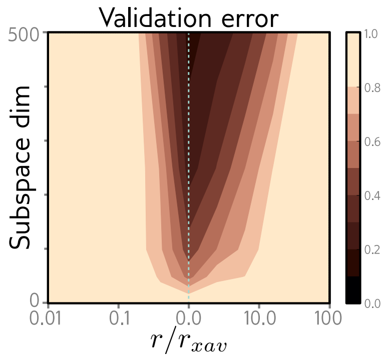

Figure 20.12 Generalization on hyperspheres. A fully connected network with two hidden layers, each with 200 units (198,450 parameters) was trained on the MNIST database. The parameters are initialized to a given ℓ_2 norm and then constrained to maintain this norm and to lie in a subspace (vertical direction). The network generalizes well in a small range around the radius r defined by Xavier initialization (cyan dotted line). Adapted from Fort & Scherlis (2019).

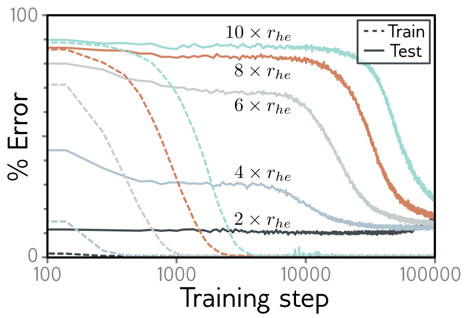

Figure 20.13 Grokking. When the ℓ_2 norm (radius) of the parameters is considerably larger than that proposed by He initialization training takes longer (dashed lines) and generalization takes *much* longer (solid lines). The lag in generalization is attributed to the time taken for the norm of the weights to decrease back to the Goldilocks zone. Adapted from Liu et al. (2023c).

It follows that the norm of the weights can also be used to explain double descent. The norm of the weights increases when the number of parameters is similar to the number of data points (as the model contorts itself to fit these points exactly) causing generalization to reduce. As the network width increases and the number of weights increases, the overall norm of these weights decreases; the weights are initialized with a variance that is inversely proportional to the width (i.e., with He or Glorot initialization), and the weights change very little from their original values.

20.4.6 Leaving the data manifold

Until this point, we have discussed how models generalize to new data that is drawn from the same distribution as the training data. This is a reasonable assumption for experimentation. However, systems deployed in the real world may encounter unexpected data, due to noise, changes in the data statistics over time, or deliberate attacks. Of course, it is harder to make definite statements about this scenario, but D'Amour et al. (2020) show that the variability of identical models trained with different seeds on corrupted data can be enormous and unpredictable.

Goodfellow et al. (2015a) showed that deep learning models are susceptible to *adversarial attacks*. Consider perturbing an image that is correctly classified by the network as "dog" so that the probability of the correct class decreases as fast as possible until the class flips. If this image is now classified as an airplane, you might expect the perturbed

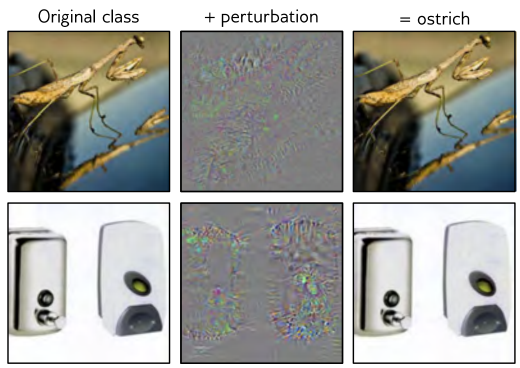

Figure 20.14 Adversarial examples. In each case, the left image is correctly classified by AlexNet. By considering the gradients of the network output with respect to the input, it's possible to find a small perturbation (center, magnified by 10 for visibility) that when added to the original image (right) causes the network to misclassify it as an ostrich. This is despite the fact that the original and perturbed images are almost indistinguishable to humans. Adapted from Szegedy et al. (2014).

image to look like a cross between a dog and an airplane. However, in practice, the perturbed image looks almost indistinguishable from the original dog image (figure 20.14).

The conclusion is that there are positions that are close to but not on the data manifold that are misclassified by the network. These are known as *adversarial examples*. Their existence is surprising; how can such a small change to the network input make such a drastic change to the output? The best current explanation is that adversarial examples are not demonstrating a lack of robustness to data that is not taken from the original training set. Instead, they are exploiting a source of information that is in the dataset but which has a small norm and is imperceptible to humans (Ilyas et al., 2019).

20.5 Do we need so many parameters?

Section 20.4 argued that models generalize better when over-parameterized. Indeed, there are almost no examples of state-of-the-art performance on complex datasets where the model has significantly fewer parameters than there were training data points.

However, section 20.2 reviewed evidence that training becomes easier as the number of parameters increases. Hence, it's not clear if some fundamental property of smaller models prevents them from performing as well, or whether our training algorithms can't find good solutions for small models. *Pruning* and *distilling* are two methods for reducing the size of trained models. This section examines whether these methods can produce under-parameterized models which retain the performance of overparameterized ones.

20.5.1 Pruning

Pruning trained models reduces their size and hence storage requirements (figure 20.15). The simplest approach is to remove individual weights. This can be done based on the second derivatives of the loss function (LeCun et al., 1990; Hassibi & Stork, 1993), or (more practically) based on the absolute value of the weight (Han et al., 2016, 2015).

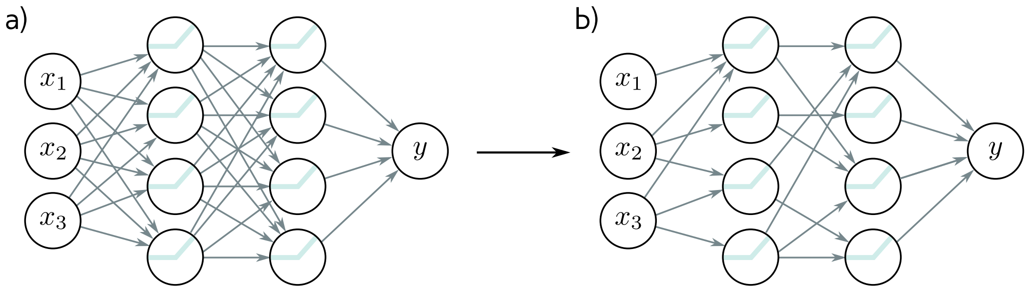

Figure 20.15 Pruning neural networks. The goal is to remove as many weights as possible without decreasing performance. This is often done just based on the magnitude of the weights. Typically, the network is fine-tuned after pruning. a) Example fully connected network. b) After pruning.

Other work prunes hidden units (Zhou et al., 2016a; Alvarez & Salzmann, 2016), channels in convolutional networks (Li et al., 2017a; Luo et al., 2017b; He et al., 2017; Liu et al., 2019a), or entire layers in residual nets (Huang & Wang, 2018). Often, the network is fine-tuned after pruning, and sometimes this process is repeated.

In general, the smaller the model, the more pruning can be done without significantly damaging performance. For example, Han et al. (2016) maintained good performance for the VGG network on ImageNet classification when only 8% of the weights were retained. This is a significant decrease in model size, but not enough to demonstrate that overparameterization is not required; the VGG network has ∼100 times as many parameters as there are training examples in ImageNet (disregarding augmentation).

Pruning can be considered a form of architecture search. In their work on lottery tickets (see section 20.2.7), Frankle & Carbin (2019) (i) trained a network, (ii) pruned the weights with the smallest magnitudes, and (iii) retrained the remaining network from the same initial weights. By iterating this procedure, they managed to reduce the size of VGG-19 network (originally 138 million parameters) by 98.5% on the CIFAR-10 database (60,000 examples) while maintaining good performance. For ResNet 50 (25.6 million parameters), they could reduce the parameters by 80% without reducing the performance on ImageNet (1.28 million examples). These demonstrations are impressive but (disregarding data augmentation) these networks are still over-parameterized after this pruning.

20.5.2 Knowledge distillation

The parameters can also be reduced by training a smaller network (the student) to replicate the performance of a larger one (the teacher). This is known as *knowledge distillation* and dates back to at least Buciluǎ et al. (2006). Hinton et al. (2015) showed that the pattern of information across the output classes is important and trained a

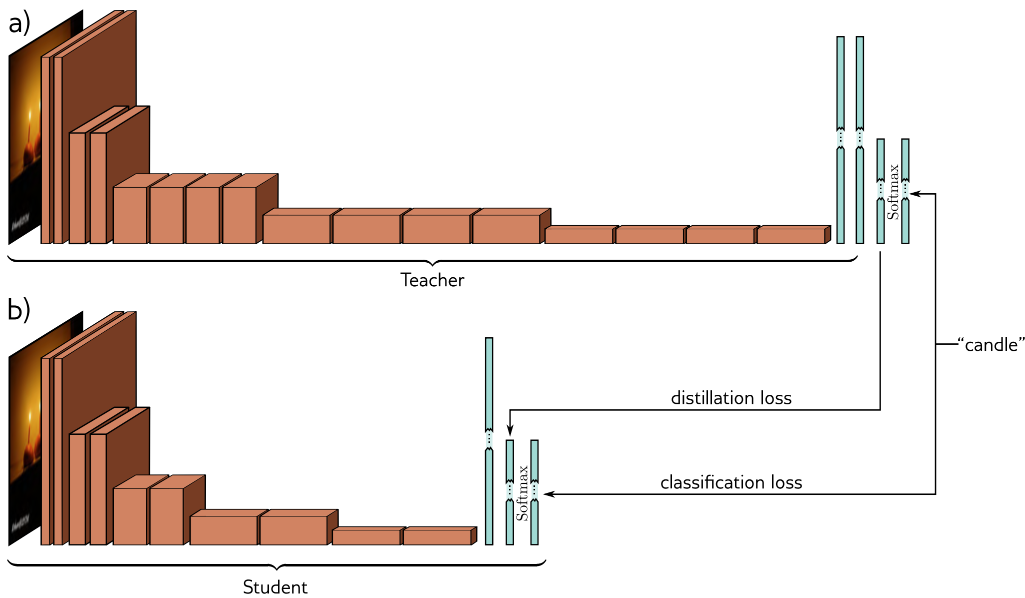

Figure 20.16 Knowledge distillation. a) A teacher network for image classification is trained as usual, using a multi-class cross-entropy classification loss. b) A smaller student network is trained with the same loss, plus also a distillation loss that encourages the pre-softmax activations to be the same as for the teacher.

smaller network to approximate the pre-softmax logits of the larger one (figure 20.16).

Zagoruyko & Komodakis (2017) further encouraged the spatial maps of the activations of the student network to be similar to the teacher network at various points. They use this *attention transfer* method to approximated the performance of a 34-layer residual networks ($\sim$63 million parameters) with an 18-layer residual network ($\sim$11 million parameters) on the ImageNet classification task. However, this is still larger than the number of training examples ($\sim$1 million images). Modern methods (e.g. Chen et al., 2021a) can improve on this result but distillation has not yet provided convincing evidence that under-parameterized models can perform well.

20.5.3 Discussion

Current evidence suggests that overparameterization *is* needed for generalization — at least for the size and complexity of datasets that are currently used. There are no demonstrations of state-of-the-art performance on complex datasets where there are significantly fewer parameters than training examples. Attempts to reduce model size by pruning or distilling trained networks have not changed this picture.

Moreover, recent theory shows that there is a trade-off between the model's Lipschitz constant and overparameterization; Bubeck & Sellke (2021) proved that in D dimensions, *smooth* interpolation requires D times more parameters than mere interpolation. They argue that current models for large datasets (e.g., ImageNet) aren't overparameterized *enough*; increasing model capacity further may be key to improving performance.

20.6 Do networks have to be deep?

Chapter 3 discussed the universal approximation theorem. This states that shallow neural networks can approximate any function to arbitrary accuracy given enough hidden units. This raises the obvious question of whether networks *need* to be deep.

First, let's consider the evidence that depth *is* required. Historically, there has been a definite correlation between performance and depth. For example, performance on the ImageNet benchmark initially improved as a function of network depth until training became difficult. Subsequently, residual connections and batch normalization (chapter 11) allowed training of deeper networks with commensurate gains in performance. At the time of writing, almost all state-of-the-art applications including image classification (e.g., the vision transformer), text generation (e.g., GPT3), and text-guided image synthesis (e.g., DALL·E-2) are based on deep networks with tens or hundreds of layers.

Despite this trend, there have been efforts to use shallower networks. Zagoruyko & Komodakis (2016) constructed shallower but wider residual neural networks and achieved similar performance to ResNet. More recently, Goyal et al. (2021) constructed a network that used parallel convolutional channels and achieved performance similar to deeper networks with only 12 layers. Furthermore, Veit et al. (2016) showed that it is predominantly shorter paths of 5–17 layers that drive performance in residual networks.

Nonetheless, the balance of evidence suggests that depth is critical; even the shallowest networks with good image classification performance require >10 layers. However, there is no definitive explanation for why. Three possible explanations are that (i) deep networks can represent more complex functions than shallow ones, (ii) deep networks are easier to train, and (iii) deep networks impose better inductive biases.

20.6.1 Complexity of modeled function

Chapter 4 showed that deep networks make functions with many more linear regions than shallow ones for the same parameter count. We also saw that "pathological" functions have been identified that require exponentially more hidden units to model with a shallow network than a deep one (e.g., Eldan & Shamir, 2016; Telgarsky, 2016). Indeed Liang & Srikant (2016) found quite general families of function that are more efficiently fit by deep networks. However, Nye & Saxe (2018) found that some of these functions cannot be fit by deep networks easily in practice. Moreover, there is little evidence that the real-world functions that we are describing have these pathological properties.

20.6.2 Tractability of training

An alternative explanation is that shallow networks with a practical number of hidden units could support state-of-the-art performance, but it is just difficult to find a good solution that both fits the training data well, and interpolates sensibly.

One way to show this is to distill successful deep networks into shallower (but wider) student models and see if performance can be maintained. Urban et al. (2017) distilled an ensemble of 16 convolutional networks for image classification on the CIFAR10 dataset into student models of varying depths. They found that shallow networks could not replicate the performance of the deeper teacher and that the student performance increased as a function of depth for a constant parameter budget.

20.6.3 Inductive bias

Most current models rely on convolutional blocks or transformers. These networks share parameters for local regions of the input data, and often they gradually integrate this information across the whole input. These constraints mean that the functions that these networks can represent are not general. One explanation for the supremacy of deep networks then is that (i) these constraints have a good inductive bias (ii) it is difficult to force shallow networks to obey these constraints.

Multi-layer convolutional architectures seem to be inherently helpful even without training. Ulyanov et al. (2018) demonstrated that the structure of an untrained CNN can be used as a prior in low-level tasks such as denoising and super-resolution. Frankle et al. (2021) achieved good performance in image classification by initializing the kernels randomly, fixing their values, and just training the batch normalization offset and scaling factors. Zhang et al. (2017a) show that features from randomly initialized convolutional filters can support subsequent image classification using a kernel model.

Additional evidence that convolutional networks provide a useful inductive bias comes from Urban et al. (2017) who attempted to distill convolutional networks into shallower networks. They found that distilling into convolutional architectures systematically worked better than distilling into fully-connected networks. This suggests that the convolutional architecture has some inherent advantages. Since the sequential local processing of convolutional networks cannot easily be replicated by shallower networks, this argues that depth is indeed important.

20.7 Summary

This chapter has made the case that the success of deep learning is surprising. We discussed the challenges of optimizing high-dimensional loss functions and argued that overparameterization, and the choice of activation function are the most two important factors that make this tractable in deep networks. We saw that in training the parameters move through a low-dimensional subspace to one of a family of connected global minima and that local minima are not apparent.

Generalization of neural networks also improves with overparameterization, although other factors such as the flatness of the minimum and the inductive bias of the architecture are also important. It appears that both a large number of parameters and multiple network layers are required for good generalization, although we do not yet know why.

Many questions remain unanswered. We do not currently have any prescriptive theory that will allow us to predict the circumstances in which training and generalization will succeed or fail. We do not know the limits of learning in deep networks or whether much more efficient models are possible. We do not know if there are parameters that would generalize better within the same model. The study of deep learning is still driven by empirical demonstrations. These are undeniably impressive but they are not yet matched by our understanding of deep learning mechanisms.

Problems

Problem 20.1 Consider the ImageNet image classification task in which the input images contain $224\times224\times3$ RGB values. Consider coarsely quantizing these inputs into 10 bins per RGB value and training with $\sim 10^7$ training examples. How many possible inputs are there per training data point.

Problem 20.2 Consider figure 20.1. Why do you think that the algorithm fits the data faster when the pixels are randomized relative to when the labels are randomized?

Problem 20.3 Figure 20.2 shows a non-stochastic fitting process with a fixed learning rate successfully fitting random data. Does this imply that the loss function has no local minima? Does this imply that the function is convex? Justify your answer and give a counter-example if you think either statement is false.

Appendix A

Notation

This appendix details the notation used in this book. Most of this is standard in computer science, but deep learning is applicable to many different areas, so the conventions are written out in full. In addition, there are several conventions that are unique to this book, including the notation for functions, Jacobians, and the systematic differentiation between parameters and variables.

Scalars, vectors, matrices and tensors

Scalars (i.e., real numbers) are denoted by either small or capital letters a, A, α, column vectors (i.e., 1D arrays of numbers) by bold small letters $\mathbf{a}, \boldsymbol{\phi}$, and row vectors as the transpose of column vectors $\mathbf{a}^T, \boldsymbol{\phi}^T$. Matrices and tensors (i.e., 2D and ND arrays of numbers, respectively) are both represented by bold capital letters $\mathbf{B}, \boldsymbol{\Phi}$.

Variables and parameters

Variables (usually the inputs and outputs of functions, or intermediate calculations) are always denoted by Roman letters $a, \mathbf{b}, \mathbf{C}$. Parameters (which are internal to functions or probability distributions) are always denoted by Greek letters $\alpha, \boldsymbol{\beta}, \boldsymbol{\Gamma}$. Generic unspecified parameters are denoted by $\boldsymbol{\phi}$. This distinction is retained throughout the book except for the policy in reinforcement learning which is denoted by π according to the usual convention.

Sets

Sets are denoted by curly brackets, so $\{0, 1, 2\}$ denotes the collection of numbers 0,1, and 2. The notation $\{0, 1, 2, \ldots, \}$ denotes the set of positive integers. Sometimes, we want to specify a set of variables and $\{\mathbf{x}_i\}_{i=1}^{I}$ denotes the I variables $\mathbf{x}_1, \ldots \mathbf{x}_I$. When it's not necessary to specify how many items are in the set, this is sometimes shortened to $\{\mathbf{x}_i\}$. The notation $\{\mathbf{x}_i, \mathbf{y}_i\}_{i=1}^{I}$ denotes the set of I pairs x_i, y_i. The convention for naming sets is to use calligraphic letters. Notable $\mathcal{B}_t$ is used to denote the set of indices in the batch at iteration t during training.

Sets of real numbers are defined using blackboard fonts. The set $\mathbb{R}$ denotes the set of real numbers. The set $\mathbb{R}^+$ denotes the set of non-negative numbers. The notation $\mathbb{R}^D$

denotes the set of D-dimensional vectors containing real numbers. The notation $\mathbb{R}^{D_1 \times D_2}$ denotes the set of matrices of dimension $D_1 \times D_2$. The notation $\mathbb{R}^{D_1 \times D_2 \times D_3}$ denotes the set of tensors of size $D_1 \times D_2 \times D_3$ and so on.

The notation $[a, b]$ denotes the real numbers from a to b including a and b themselves. When the square brackets are replaced by round brackets, this means that the adjacent value is not included in the set. For example, the set $(-\pi, \pi]$ denotes the real numbers from $-\pi$ to π, but excluding $-\pi$.

Membership of sets is denoted by the symbol $\in$, so $x \in \mathbb{R}^+$ means that the variable x is a non-negative real number and the notation $\boldsymbol{\Sigma} \in \mathbb{R}^{D \times D}$ denotes that $\boldsymbol{\Sigma}$ is a matrix of size $D \times D$. Sometimes, we want to work through each element of a set systematically, and the notation $\forall \ \{1, \ldots K\}$ means "for all" the integers from 1 to K.

Functions

Functions are expressed as a name, followed by square brackets that contain the arguments of the function. For example, $\log[x]$ returns the logarithm of the variable x. When the function returns a vector, it is written in bold and starts with a small letter. For example, the function $\mathbf{y} = \mathbf{mlp}[\mathbf{x}, \boldsymbol{\phi}]$ returns a vector $\mathbf{y}$ and has arguments $\mathbf{x}$ and $\boldsymbol{\phi}$. When a function returns a matrix or tensor, it is written in bold and starts with a capital letter. For example, the function $\mathbf{Y} = \mathbf{Sa}[\mathbf{X}, \boldsymbol{\phi}]$ returns a matrix $\mathbf{Y}$ and has arguments $\mathbf{X}$ and $\boldsymbol{\phi}$. When we want to leave the arguments of a function deliberately ambiguous, we use the bullet symbol (e.g., $\mathbf{mlp}[\bullet, \boldsymbol{\phi}]$).

Minimizing and maximizing

Some special functions are used repeatedly throughout the text:

- The function $\min_x[\mathrm{f}[x]]$ returns the minimum value of the function $\mathrm{f}[x]$ over all possible values of the variable x. This notation is often used without specifying the details of how this minimum function might be found.
- The function $\mathrm{argmin}_x[\mathrm{f}[x]]$ returns the value of x that minimizes $f[x]$, so if $y = \mathrm{argmin}_x[\mathrm{f}[x]]$, then $\min_x[\mathrm{f}[x]] = \mathrm{f}[y]$.
- The functions $\max_x[\mathrm{f}[x]]$ and $\mathrm{argmax}_x[\mathrm{f}[x]]$ perform the equivalent operations for maximizing functions.

Probability distributions

Probability distributions should be written as $Pr(X = x)$ denoting that the random variable X takes the value of x but this notation is cumbersome. Hence, we simplify this and just write $Pr(x)$, where x denotes either the random variable or the value it takes according to the sense of the equation. The conditional probability of y given x is written as $Pr(y|x)$. The joint probability of y and x is written as $Pr(y, x)$. These two forms can be combined so $Pr(\mathbf{y}|\mathbf{x}, \boldsymbol{\phi})$ denotes the probability of the variable $\mathbf{y}$ given that we know $\mathbf{x}$ and $\boldsymbol{\phi}$. Similarly, $Pr(\mathbf{y}, \mathbf{x}|\boldsymbol{\phi})$ denotes the probability of variables $\mathbf{y}$ and $\mathbf{x}$ given that we know $\boldsymbol{\phi}$. When we need two probability distributions over the same variable, we write $Pr(x)$ for the first distribution and $q(x)$ for the second. More information about probability distribution can be found in appendix B.

Derivatives and Jacobians

Derivatives and Jacobians are written variously as:

$$\frac{\partial x}{\partial y}, \frac{\partial \mathbf{x}}{\partial y}, \frac{\partial \mathbf{x}}{\partial \mathbf{y}}, \text{ and } \frac{\partial \mathbf{X}}{\partial \mathbf{y}} \tag{A.1}$$

The first case denotes the derivative of a scalar quantity x with a scalar quantity y (i.e., how a small change in y affects x). The second case is the derivative of the vector $\mathbf{x}$ with respect to y (i.e., a vector where each element represents how a small change in y effects each element of $\mathbf{x}$).

Similarly, the Jacobian $\frac{\partial \mathbf{x}}{\partial \mathbf{y}}$ is the derivative $\mathbf{x}$ with respect to $\mathbf{y}$. This is a matrix where each element indicates how each a small change in each element of $\mathbf{y}$ affects each element of $\mathbf{x}$. Sometimes this is written as $\nabla_{\mathbf{y}}\mathbf{x}$ in other documents. Finally, the notation $\frac{\partial \mathbf{X}}{\partial \mathbf{y}}$ where $\mathbf{X} \in \mathcal{R}^{D_1 \times D_2}$ denotes the 3D tensor that represents how the a small change to each of the elements in the vector $\mathbf{y}$ changes the elements of the matrix $\mathbf{X}$.

Miscellaneous

A small dot in a mathematical equation is intended to improve easy of reading and has no real meaning (or just implies multiplication). For example $\alpha \cdot \mathrm{f}[x]$ is the same as $\alpha\mathrm{f}[x]$, but is easier to read. A left arrow symbol $\leftarrow$ denotes assignment, so $x \leftarrow x + 2$ means that we are adding two to the current value of x.

Appendix B

Probability

Probability is critical to deep learning. In supervised learning, deep networks implicitly rely on a probabilistic formulation via the loss function. In unsupervised learning, generative models aim to produce samples that are drawn from the same distribution as the training data. Reinforcement learning is usually framed in terms of Markov decision processes, and these are defined in terms of probability distributions. This appendix provides a primer for probability as used in machine learning.

B.1 Random variables and probability distributions

A random variable x denotes a quantity that is uncertain. It may be *discrete* (take only certain values) or *continuous* (take any value within a certain range). If we observe several instances of a random variable x, it will take different values, and the relative propensity to take different values is described by a *probability distribution* $Pr(z)$.

For a discrete variable, this distribution associates a non-negative *probability* $Pr(x = k) \in [0, 1]$ with each potential outcome k and the sum of these probabilities is one. For a continuous variable, there is a non-negative *probability density* $Pr(x = a) \geq 0$ associated with each value a in the domain of x, and the integral of this probability density function (PDF) over this domain must be one. This density can be greater than one for any point a.

From here on, we assume that the random variables are continuous. The main ideas are the same for discrete distributions, but with sums replacing integrals. We also drop the distinction between the random variable x and the value a that it takes and just write $Pr(x)$ instead of $Pr(x = a)$.

B.1.1 Joint probability

Consider the case where we have two random variables x and y. The *joint distribution* $Pr(x, y)$ tells us about the propensity that x and y take particular combinations of values. Now there is a non-negative probability density $Pr(x = a, y = b)$ associated with each pair of values x and y and this must satisfy:

$$\iint Pr(x, y) \cdot dxdy = 1. \tag{B.1}$$

This idea extends to multiple variables. Sometimes, we store multiple random variables in a vector $\mathbf{x}$ and the write the joint density as $Pr(\mathbf{x})$.

B.1.2 Marginalization

If we know the joint distribution $Pr(x, y)$ over two variables, then we can recover the *marginal* distributions $Pr(x)$ and $Pr(y)$ by integrating over the other variable:

$$\begin{aligned}\int Pr(x, y)dx &= Pr(y) \\ \int Pr(x, y)dy &= Pr(x).\end{aligned} \tag{B.2}$$

This process is called *marginalization*. It extends to higher dimensions. For example, if we have a joint distribution $Pr(x, y, z)$ we can recover the joint distribution $Pr(x, z)$ of x and z by integrating over y.

B.1.3 Conditional probability and likelihood

The *conditional probability* $Pr(x|y)$ of variable x taking a certain value *given* that we know the value of of y can be found by taking a slice through the joint distribution $Pr(x, y)$ for a fixed y. This slice is then divided by the probability of that value y occurring so that the conditional distribution sums to one:

$$Pr(x|y) = \frac{Pr(x, y)}{Pr(y)}. \tag{B.3}$$

Similarly,

$$Pr(y|x) = \frac{Pr(x, y)}{Pr(x)}. \tag{B.4}$$

The vertical line in the conditional probability is read as the English word "given" so $Pr(x|y)$ is the probability of x given y.

When we consider the conditional probability $Pr(x|y)$ as a function of x, it must sum to one. When we consider the same quantity $Pr(x|y)$ as a function of y, it is termed the *likelihood* and does not have to sum to one.

B.1.4 Bayes' theorem

From equations B.3 and B.4, we get two expressions for the joint probability $Pr(x, y)$:

$$Pr(x, y) = Pr(x|y)Pr(y) = Pr(y|x)Pr(x), \tag{B.5}$$

which we can rearrange to get:

$$Pr(x|y) = \frac{Pr(y|x)Pr(x)}{Pr(y)}. \tag{B.6}$$

This expression relates conditional probability $Pr(x|y)$ of x given y to the the conditional probability $Pr(y|x)$ of y given x and is known as *Bayes' theorem*.

B.1.5 Independence

If the value of the random variable variable y tells us nothing about x and vice-versa then we say that x and y are *independent*, and we can write $Pr(x|y) = Pr(x)$ and $Pr(y|x) = Pr(y)$. Starting from the first expression for the joint probability in equation B.5, we see that the joint distribution becomes the product of the marginal distributions:

$$Pr(x, y) \quad = \quad Pr(x|y)Pr(y) = Pr(x)Pr(y) \tag{B.7}$$

when the variables are independent.

B.2 Expectation

Consider a function $\mathrm{f}[x]$ and a probability distribution $Pr(x)$ defined over x. If we drew a large number of samples from $Pr(x)$, calculated $\mathrm{f}[x]$ for each sample and took the average of these values, the result would approximate the *expectation* $\mathbb{E}[\mathrm{f}[x]]$ of the function. More precisely, the expected value of a function $\mathrm{f}[\bullet]$ of a random variable x with respect to the probability distribution $Pr(x)$ is defined as:

$$\mathbb{E}_x\Big[\mathrm{f}[x]\Big] \quad = \quad \int \mathrm{f}[x]Pr(x)dx. \tag{B.8}$$

This idea generalizes to functions $\mathbf{g}[\bullet]$ of more than one random variable:

$$\mathbb{E}_{x,y}\Big[\mathrm{f}[x, y]\Big] \quad = \quad \iint f[x, y]Pr(x, y)dxdy. \tag{B.9}$$

An expectation is always taken with respect to a distribution over one or more variables. However, when this is obvious, we don't usually make this explicit, so instead of writing $\mathbb{E}_x[\mathrm{f}[x]]$, we write $\mathbb{E}[\mathrm{f}[x]]$.

B.2.1 Rules for manipulating expectations

There are four rules for manipulating expectations:

$$
\begin{aligned}
\mathbb{E}\Big[k\Big] &= k \\
\mathbb{E}\Big[k\cdot \mathrm{f}[x]\Big] &= k\cdot\mathbb{E}\Big[\mathrm{f}[x]\Big] \\
\mathbb{E}\Big[\mathrm{f}[x]+\mathrm{g}[x]\Big] &= \mathbb{E}\Big[\mathrm{f}[x]\Big]+\mathbb{E}\Big[\mathrm{g}[x]\Big] \\
\mathbb{E}_{x,y}\Big[\mathrm{f}[x]\cdot\mathrm{g}[y]\Big] &= \mathbb{E}_{x}\Big[\mathrm{f}[x]\Big]\cdot\mathbb{E}_{y}\Big[\mathrm{g}[y]\Big] \qquad \text{if } x,y \text{ independent,} \qquad \text{(B.10)}
\end{aligned}
$$

where k is an arbitrary constant. These are proven below for the continuous case.

Rule 1: The expectation $\mathbb{E}[k]$ of a constant value k is just k.

$$
\begin{aligned}
\mathbb{E}\Big[k\Big] &= \int k\cdot Pr(x)dx \\
&= k\cdot\int Pr(x)dx \\
&= k.
\end{aligned}
$$

Rule 2: The expectation $\mathbb{E}[k\cdot \mathrm{f}[x]]$ of a constant k times a function of the variable x is k times the expectation $\mathbb{E}[\mathrm{f}[x]]$ of the function:

$$
\begin{aligned}
\mathbb{E}\Big[k\cdot [x]\Big] &= \int k\cdot \mathrm{f}[x]Pr(x)dx \\
&= k\cdot\int \mathrm{f}[x]Pr(x)dx \\
&= k\cdot\mathbb{E}\Big[\mathrm{f}[x]\Big].
\end{aligned}
$$

Rule 3: The expectation of a sum $\mathbb{E}[\mathrm{f}[x]+\mathrm{g}[x]]$ of terms is the sum $\mathbb{E}[\mathrm{f}[x]]+\mathbb{E}[\mathrm{g}[x]]$ of the expectations:

$$
\begin{aligned}
\mathbb{E}\Big[\mathrm{f}[x]+\mathrm{g}[x]\Big] &= \int (\mathrm{f}[x]+\mathrm{g}[x])\cdot Pr(x)dx \\
&= \int\Big(\mathrm{f}[x]\cdot Pr(x)+\mathrm{g}[x]\cdot Pr(x)\Big)dx \\
&= \int \mathrm{f}[x]\cdot Pr(x)dx+\int \mathrm{g}[x]\cdot Pr(x)dx \\
&= \mathbb{E}\Big[\mathrm{f}[x]\Big]+\mathbb{E}\Big[\mathrm{g}[x]\Big].
\end{aligned}
$$

Rule 4: The expectation of a product $\mathbb{E}[\mathrm{f}[x] \cdot \mathrm{g}[y]]$ of terms is the product $\mathbb{E}[\mathrm{f}[x]] \cdot \mathbb{E}[\mathrm{g}[y]]$ if x and y are independent.

$$\begin{aligned}
\mathbb{E}\Big[\mathrm{f}[x] \cdot \mathrm{g}[y]\Big] &= \int\int \mathrm{f}[x] \cdot \mathrm{g}[y] Pr(x,y) dx dy \\
&= \int\int \mathrm{f}[x] \cdot \mathrm{g}[y] Pr(x) Pr(y) dx dy \\
&= \int \mathrm{f}[x] Pr(x) dx \int \mathrm{g}[y] Pr(y) dy \\
&= \mathbb{E}\Big[\mathrm{f}[x]\Big]\mathbb{E}\Big[\mathrm{g}[y]\Big],
\end{aligned}$$

where we used the definition of independence (equation B.7) between the first two lines.

B.2.2 Mean, variance, and covariance

indexstandard deviation For some choices of the function $\mathrm{f}[\bullet]$, the expectation is given a special name. These quantities are often used to summarize the properties of complex distributions. For example, when $\mathrm{f}[x] = x$, the resulting expectation $\mathbb{E}[x]$ is termed the *mean*, μ. It is a measure of the center of a distribution. Similarly, the expected squared deviation from the mean $\mathbb{E}[(x-\mu)^2]$ is termed the *variance*, σ^2. This is a measure of the spread of the distribution. The *standard deviation* σ is the positive square root of the variance. It also measures the spread of the distribution, but has the merit that it is expressed in the same units as the variable x.

As the name suggests, the *covariance* $\mathbb{E}[(x-\mu_x)(y-\mu_y)]$ of two variables x and y measures the degree to which they co-vary. Here μ_x and μ_y represent the mean of the variables x and y, respectively. The covariance will be large when the variance of both variables is large, and when the value of x tends to increase when the value of y increases. The covariance of multiple random variables stored in a column vector $\mathbf{x}$ is captured by the matrix $\mathbb{E}[(\mathbf{x}-\boldsymbol{\mu}_x)(\mathbf{x}-\boldsymbol{\mu}_x)^T]$, where the vectors $\boldsymbol{\mu}_x$ and $\boldsymbol{\mu}_y$ contain the means $\mathbb{E}[\mathbf{x}]$ and $\mathbb{E}[\mathbf{y}]$ respectively.

B.2.3 Variance identity

The rules of expectation (appendix B.2.1) can be used to prove the following identity that allows us to write the variance in a different form:

$$\mathbb{E}\big[(x-\mu)^2\big] = \mathbb{E}\big[x^2\big] - \mathbb{E}\big[x\big]^2. \tag{B.11}$$

Proof:

$$\begin{aligned}
\mathbb{E}\big[(x-\mu)^2\big] &= \mathbb{E}\big[x^2 - 2\mu x + \mu^2\big] \\
&= \mathbb{E}\big[x^2\big] - \mathbb{E}\big[2\mu x\big] + \mathbb{E}\big[\mu^2\big] \\
&= \mathbb{E}\big[x^2\big] - 2\mu \cdot \mathbb{E}\big[x\big] + \mu^2 \\
&= \mathbb{E}\big[x^2\big] - 2\mu^2 + \mu^2 \\
&= \mathbb{E}\big[x^2\big] - \mu^2 \\
&= \mathbb{E}\big[x^2\big] - \mathbb{E}\big[x\big]^2,
\end{aligned} \tag{B.12}$$

where we have used rule 3 between lines 1 and 2, rules 1 and 2 between lines 2 and 3, and the definition $\mu = \mathbb{E}[x]$ in the remaining two lines.

B.2.4 Standardization

Setting the mean of a random variable to zero and the variance to one is known as *standardization*. This is acheived using the transformation:

$$x' = \frac{x-\mu}{\sigma}, \tag{B.13}$$

where μ is the mean of x and $\sigma[x]$ is the standard deviation.

Proof: The mean of the new distribution over x' is given by:

$$\begin{aligned}
\mathbb{E}[x'] &= \mathbb{E}\left[\frac{x-\mu}{\sigma}\right] \\
&= \frac{1}{\sigma}\mathbb{E}\big[x-\mu\big] \\
&= \frac{1}{\sigma}\left(\mathbb{E}\big[x\big] - \mathbb{E}\big[\mu\big]\right) \\
&= \frac{1}{\sigma}\left(\mu - \mu\right) = 0
\end{aligned} \tag{B.14}$$

where again, we have used the four rules for manipulating expectations. The variance of the new distribution is given by:

$$\begin{aligned}
\mathbb{E}\big[(x'-\mu'_x)^2\big] &= \mathbb{E}\big[x'^2\big] \\
&= \mathbb{E}\left[\left(\frac{x-\mu}{\sigma}\right)^2\right] \\
&= \frac{1}{\sigma^2}\cdot\mathbb{E}[(x-\mu)^2] \\
&= \frac{1}{\sigma^2}\cdot\sigma^2 = 1
\end{aligned} \tag{B.15}$$

B.3 Normal probability distributions

We use a number of probability distributions in this book, including the the Bernoulli distribution (figure 5.6), the categorical distribution (figure 5.9), the Poisson distribution (figure 5.15), the von Mises distribution (figure 5.13), and the mixture of Gaussians (figures 5.14 and 17.1). However, the most common distribution in machine learning is the normal distribution. This section details its properties.

B.3.1 Univariate normal distribution

The univariate normal distribution is defined by two parameters, the mean μ and the variance σ^2 and defined by:

$$\text{Norm}_x[\mu, \sigma^2] = \frac{1}{\sqrt{2\pi\sigma^2}} \exp\left[-\frac{(x-\mu)^2}{2\sigma^2}\right], \tag{B.16}$$

and is pictured in figure 5.3. When the mean is zero and the variance is one, we refer to this as a *standard normal distribution*.

The term $-(x-\mu)/2\sigma^2$ is a quadratic function that falls away from zero when $x = \mu$ at a rate that increases when σ becomes smaller. When we pass this through the exponential function (figure **??**), we get a bell-shaped curve which has a value of one at $x = \mu$ and falls away to either side. Dividing by the constant $\sqrt{2\pi\sigma^2}$ ensures that the function integrates to one and is a valid distribution.

B.3.2 Multivariate normal distribution

The multivariate normal distribution generalizes the normal distribution to describe the probability over a vector quantity $\mathbf{x}$ of length D. It is defined by a $D \times 1$ *mean vector* $\boldsymbol{\mu}$ and a positive definite $D \times D$ *covariance matrix* $\boldsymbol{\Sigma}$:

$$\text{Norm}_{\mathbf{x}}[\boldsymbol{\mu}, \boldsymbol{\Sigma}] = \frac{1}{(2\pi)^{D/2}|\Sigma|^{1/2}} \exp\left[-\frac{(\mathbf{x}-\boldsymbol{\mu})^T\boldsymbol{\Sigma}^{-1}(\mathbf{x}-\boldsymbol{\mu})}{2}\right]. \tag{B.17}$$

The interpretation is similar to the univariate case. The quadratic term $-(\mathbf{x}-\boldsymbol{\mu})^T\boldsymbol{\Sigma}^{-1}(\mathbf{x}-\boldsymbol{\mu})/2$ returns a scalar that decreases as $\mathbf{x}$ grows further from the mean $\boldsymbol{\mu}$, at a rate that depends on the matrix $\boldsymbol{\Sigma}$. This is turned into a bell-curve shape by the exponential and dividing by $(2\pi)^{D/2}|\Sigma|^{1/2}$ ensures that the function integrates to one and represents a distribution.

The covariance matrix can take spherical, diagonal, and full forms:

$$\boldsymbol{\Sigma}_{spher} = \begin{bmatrix} \sigma^2 & 0 \\ 0 & \sigma^2 \end{bmatrix} \quad \boldsymbol{\Sigma}_{diag} = \begin{bmatrix} \sigma_1^2 & 0 \\ 0 & \sigma_2^2 \end{bmatrix} \quad \boldsymbol{\Sigma}_{full} = \begin{bmatrix} \sigma_{11}^2 & \sigma_{12}^2 \\ \sigma_{21}^2 & \sigma_{22}^2 \end{bmatrix}. \tag{B.18}$$

When $D = 2$, (figure B.1), the spherical covariances produce circular iso-density contours, and diagonal covariances produce ellipsoidal iso-contours that are aligned with the

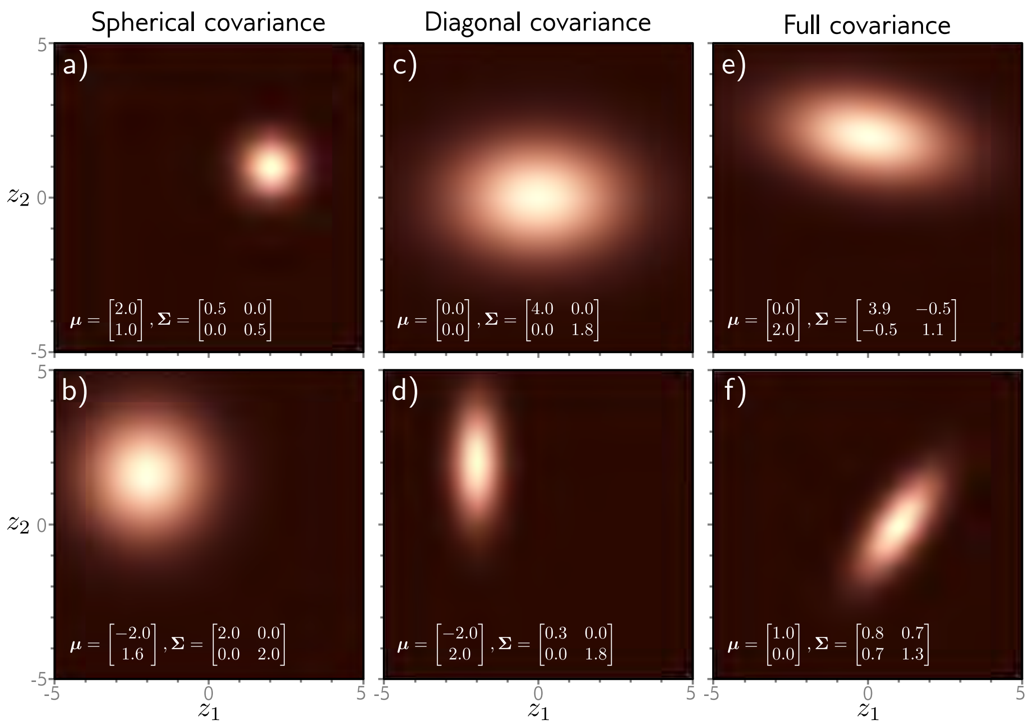

Figure B.1 Bivariate normal distribution. a–b) When the covariance matrix is a multiple of the diagonal matrix, the isocontours are circle, and we refer to this as spherical covariance. c–d) When the covariance is an arbitrary diagonal matrix, the isocontours are axis-aligned ellipses, and we refer to this as diagonal covariance e–f) When the covariance is an arbitrary positive definite matrix, the iso-contours are general ellipses, and we refer to this as full covariance.

coordinate axes. Full covariances also produce general ellipsoidal iso-density contours. When the covariance is spherical or diagonal, the individual variables are independent:

$$
\begin{aligned}
Pr(x_1, x_2) &= \frac{1}{2\pi\sqrt{|\mathbf{\Sigma}|}} \exp\left[-0.5 \begin{pmatrix} x_1 & x_2 \end{pmatrix} \mathbf{\Sigma}^{-1} \begin{pmatrix} x_1 \\ x_2 \end{pmatrix}\right] \\
&= \frac{1}{2\pi\sigma_1\sigma_2} \exp\left[-0.5 \begin{pmatrix} x_1 & x_2 \end{pmatrix} \begin{pmatrix} \sigma_1^{-2} & 0 \\ 0 & \sigma_2^{-2} \end{pmatrix} \begin{pmatrix} x_1 \\ x_2 \end{pmatrix}\right] \\
&= \frac{1}{\sqrt{2\pi\sigma_1^2}} \exp\left[-\frac{x_1^2}{2\sigma_1^2}\right] \frac{1}{\sqrt{2\pi\sigma_2^2}} \cdot \exp\left[-\frac{x_2^2}{2\sigma_2^2}\right] \\
&= Pr(x_1) \cdot Pr(x_2).
\end{aligned}
\tag{B.19}
$$

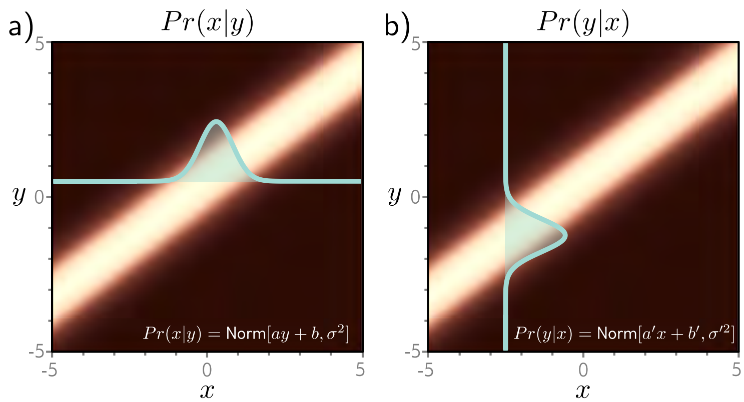

Figure B.2 Change of variables. a) The conditional probability $Pr(x|y)$ is a normal distribution where the mean is a linear function of y. For any given y, the distribution over x is a normal distribution with a constant variance, but a different mean. Cyan distribution shows one example for $y = 0.5$. b) This is proportional to the conditional probability $Pr(y|x)$, which is a normal distribution where the mean is a different linear function of x. For any given value of x, the distribution over y is a normal distribution with a constant variance and a mean that depends on x. Cyan distribution shows one example for $x = -2.5$.

B.3.3 Change of variable

When the mean of a multivariate normal in $\mathbf{x}$ is a linear function $\mathbf{Az} + \mathbf{b}$ of a second variable $\mathbf{y}$, this is proportional to another normal distribution in $\mathbf{y}$, where the mean is a linear function of $\mathbf{x}$:

$$\text{Norm}_{\mathbf{x}}\left[\mathbf{Ay} + \mathbf{b}, \boldsymbol{\Sigma}\right] \propto \text{Norm}_{\mathbf{y}}[(\mathbf{A}^T\boldsymbol{\Sigma}^{-1}\mathbf{A})^{-1}\mathbf{A}^T\boldsymbol{\Sigma}^{-1}(\mathbf{x} - \mathbf{b}), (\mathbf{A}^T\mathbf{B}^{-1}\mathbf{A})^{-1}]. \tag{B.20}$$

This change of variables formula was exploited when we discussed diffusion models. The proof is provided as the answer to problem 18.4. At first sight, this relation is rather opaque, but figure B.2 shows the case for scalar x and y which is easy to understand.

B.4 Sampling

To sample from a univariate distribution $Pr(x)$, we first compute the cumulative distribution $f[x]$ (the integral of $Pr(x)$). Then we draw a sample z^* from a uniform distribution over the range $[0, 1]$ and evaluate this against the inverse of the cumulative distribution, so the sample x^* is created as:

$$x^* = \mathrm{f}^{-1}[z^*]. \tag{B.21}$$

B.4.1 Reparameterization

Generating a sample $\mathbf{x}$ from multivariate normal distribution is easy when the covariance matrix is the identity: we sample each dimension independently from a standard normal distribution. To generate a sample $\mathbf{x}'$ from a multivariate normal distribution with mean $\boldsymbol{\mu}$ and covariance $\boldsymbol{\Sigma}$, we simple transform the variable using the relation:

$$\mathbf{x}'^* = \boldsymbol{\mu} + \boldsymbol{\Sigma}^{1/2}\mathbf{x}. \tag{B.22}$$

The rules for manipulating expectations can be used to confirm that the mean and variance of $\mathbf{x}'$ are as desired.

B.4.2 Ancestral sampling

When the joint distribution can be factored into a series of conditional probabilities, we can generate samples using *ancestral sampling*. The basic idea is to generate a sample from the root variable(s) and then sample from the subsequent conditional distributions based on this instantiation. This process is known as *ancestral sampling* and is easiest to understand with an example. Consider a joint distribution over three variables, x, y, and z where the distribution factors as:

$$Pr(x, y, z) = Pr(x)Pr(y|x)Pr(z|y). \tag{B.23}$$

To sample from this joint distribution, we first draw a sample x^* from $Pr(x)$. Then we draw a sample y^* from $Pr(y|x^*)$. Finally, we draw a sample z^* from $Pr(z^*|y^*)$.

B.5 Distances between probability distributions

Supervised learning can be framed in terms of minimizing the distance between the probability distribution implied by the model and the discrete probability distribution implied by the samples (section 5.7). Unsupervised learning can often be framed as trying to minimize the distance between the probability distribution of real examples and the distribution of samples from the model. In both cases, we need a measure of distance between two probability distributions. This section considers the properties of several different measures of distance between distributions (see also figure 15.8 for a discussion of the Wasserstein or earth mover's distance).

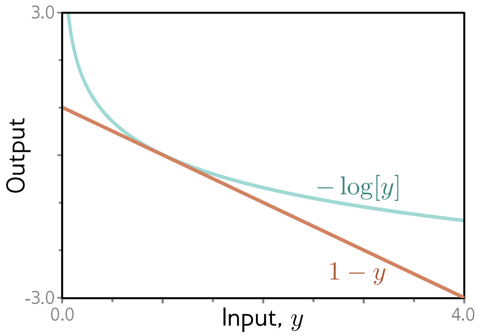

Figure B.3 Lower bound on negative logarithm. The function $1-y$ is always less than the function $-\log[y]$. This relation is used to show that the Kullback-Leibler divergence is always greater than one.

B.5.1 Kullback-Leibler divergence

The most common measure of distance between probability distributions $p(x)$ and $q(x)$ is *Kullback-Leibler* or KL divergence and is defined as:

$$D_{KL}\Big[p(x)||q(x)\Big] = \int p(x)\log\left[\frac{p(x)}{q(x)}\right]dx. \tag{B.24}$$

This distance is always greater than or or equal to zero, which is easily demonstrated by noting that $-\log[y] \geq 1-y$ so:

$$\begin{aligned} D_{KL}\Big[p(x)||q(x)\Big] &= \int p(x)\log\left[\frac{p(x)}{q(x)}\right]dx \\ &= -\int p(x)\log\left[\frac{q(x)}{p(x)}\right]dx \\ &\geq \int p(x)\left(1-\frac{q(x)}{p(x)}\right)dx \\ &= \int p(x)-q(x)dx \\ &= 1-1=0. \end{aligned} \tag{B.25}$$

The KL divergence is infinite if there are places where $q(x)$ is zero but $p(x)$ is non-zero. This can make it quite unstable as a distance metric.

B.5.2 Jensen-Shannon divergence

Another disadvantage of the KL divergence is that it is not symmetric (i.e., $D_{KL}[p(x)||q(x)] \neq D_{KL}[q(x)||p(x)]$). The Jensen-Shannon divergence is a measure of distance that is symmetric by construction as it is an average of the forward and reverse KL divergences:

$$D_{JS}\Big[p(x)||q(x)\Big] = \frac{1}{2}D_{KL}\Big[p(x)||q(x)\Big] + \frac{1}{2}D_{KL}\Big[q(x)||p(x)\Big]. \tag{B.26}$$

B.5.3 Fréchet distance

The Fréchet distance D_{FR} between two distributions $p(x)$ and $q(x)$ is given by:

$$D_{fr}\Big[p(y)||q(y)\Big] = \sqrt{\min_{x,y}\left[\int\int p(x)q(y)|x-y|^2 dxdy\right]}, \tag{B.27}$$

and is a measure of the maximum distance between the cumulative probability curves.

B.5.4 Distances between normal distributions

Often we want to compute the distance between two multivariate normal distributions with means $\boldsymbol{\mu}_1$ and $\boldsymbol{\mu}_2$ and covariances $\boldsymbol{\Sigma}_1$ and $\boldsymbol{\Sigma}_2$. In this case, various measures of distance can be written in closed form.

The KL divergence can be computed as:

$$\begin{aligned} D_{fr}\Big[\text{Norm}[\boldsymbol{\mu}_1,\boldsymbol{\Sigma}_1]||\text{Norm}[\boldsymbol{\mu}_2,\boldsymbol{\Sigma}_2]\Big] &= \\ \frac{1}{2}\left(\log\left[\frac{|\boldsymbol{\Sigma}_2|}{|\boldsymbol{\Sigma}_1|}\right.\right. - D + \text{trace}\left[\boldsymbol{\Sigma}_2^{-1}\boldsymbol{\Sigma}\right] &+ \left.\left.(\boldsymbol{\mu}_2-\boldsymbol{\mu}_1)\boldsymbol{\Sigma}_2^{-1}(\boldsymbol{\mu}_2-\boldsymbol{\mu}_1)\right]\right). \end{aligned} \tag{B.28}$$

The Frećhet distance can be computed as:

$$\begin{aligned} D_{fr}\Big[\text{Norm}[\boldsymbol{\mu}_1,\boldsymbol{\Sigma}_1]||\text{Norm}[\boldsymbol{\mu}_2,\boldsymbol{\Sigma}_2]\Big] &= \\ ||\boldsymbol{\mu}_1-\boldsymbol{\mu}_2||^2 + \text{trace}\left[\boldsymbol{\Sigma}_1+\boldsymbol{\Sigma}_2-2\left(\boldsymbol{\Sigma}_1^{1/2}\boldsymbol{\Sigma}_2\boldsymbol{\Sigma}_1^{1/2}\right)^{1/2}\right]&. \end{aligned} \tag{B.29}$$

Appendix C

Maths

This appendix reviews mathematical concepts that are used in the main text and that some readers may be unfamiliar with. It can be read in full, or just referred to as and when it is flagged in the main text.

C.1 Functions

A *function* defines a mapping from a set $\mathcal{X}$ (e.g., the set of real numbers) to another set $\mathcal{Y}$. An *injection* is a function where every element in the first set maps to a position in the second set (but there may be elements of the second set that are not mapped to). A *surjection* is a function where every element in the second set receives a mapping from the first (but there may be elements of the first set that are not mapped). A *bijection* or *bijective mapping* is a function that is both injective and surjective. It has a one-to-one correspondence between members of the two sets. A *diffeomorphism* is a special case of a bijection where the both the forward and reverse mapping are differentiable.

C.2 Lipschitz constant

A function $\mathrm{f}[z]$ is *Lipschitz continuous* if for all z_1, z_2:

$$||\mathrm{f}[z_1] - \mathrm{f}[z_2]|| \leq \beta||z_1 - z_2||, \tag{C.1}$$

where β is known as the Lipschitz constant and determines the maximum gradient of the function (i.e., how fast the function can change) with respect to the distance metric. If the Lipschitz constant is less than one then the function is a contraction mapping, and we can use Banach's theorem to find the inverse for any point (see figure 16.9).

Composing two functions with Lipschitz constants β_1 and β_2 creates a new Lipschitz continuous function with a constant that is less than or equal to $\beta_1\beta_2$. Adding two functions with Lipschitz constants β_1 and β_2 creates a new Lipschitz continuous function with a constant that is less than or equal to $\beta_1 + \beta_2$. The Lipschitz constant of a linear transformation $\mathrm{f}[\mathbf{z}] = \mathbf{Az} + \mathbf{b}$ is equal to the maximum eigenvalue of the matrix $\mathbf{A}$.

C.3 Convexity

A function is *convex* if we can draw a straight line between any two points on the function, and this line always lies above the function. Similarly, a function is *concave* if we can draw a straight line between any two points on the function and the line always lies below the function. By definition, convex (concave) functions have a single global minimum (maximum).

A region of $\mathbb{R}^D$ is convex if we can draw a straight line between any two points on the boundary of the region without intersecting the boundary in another place. Gradient descent can be used to find the global minimum of function that are convex and defined on convex regions.

C.3.1 Special functions

The following functions are used in the main text:

- The *exponential function* $y = \exp[x]$ maps a real variable $x \in \mathbb{R}$ to a non-negative number $y \in \mathcal{R}^+$ as $y = e^x$ (figure **??**a).
- The *logarithm* is the inverse of the exponential function $x = \log[y]$ and maps a non-negative number $y \in \mathcal{R}^+$ to a real variable $x \in \mathbb{R}$ (figure **??**b). Note that all logarithms in this book are in base e.
- The *gamma function* is defined as:

$$\Gamma[z] = \int_0^\infty t^{z-1}e^{-t}dt, \tag{C.2}$$

  It extends the factorial function to continuous values so that $\Gamma[x] = (x-1)!$.
- The *Dirac delta function* $\delta[\mathbf{z}]$ has a total area of one, all of which is at position $\mathbf{z} = \mathbf{0}$. A dataset with N elements can be thought of as a probability distribution consisting of a sum of delta functions centered at each data point $\mathbf{x}_i$ and scaled by $1/N$. The delta function is usually drawn as an arrow (e.g., figure 5.12). The delta function has the key property that $\int \mathrm{f}[\mathbf{x}]\delta[\mathbf{x}-\mathbf{x}_0]d\mathbf{x} = \mathrm{f}[x]$.

C.3.2 Stirling's formula

C.3.3 Autocorrelation

The autocorrelation $r[\tau]$ of a continuous function $\mathrm{f}[z]$ is defined as:

$$r[\tau] = \int_{-\infty}^{\infty} \mathrm{f}[t+\tau] f[t] dt, \tag{C.3}$$

where τ is the time lag. Sometimes, this is normalized by $r[0]$ so that the autocorrelation at time lag zero is one. The autocorrelation function is a measure of the correlation of the function with itself as a function of an offset (i.e.the time lag). If a function changes slowly and predictably, then autocorrelation function will decrease slowly as the time lag increases from zero. If the function changes fast and unpredictably, then it will decrease quickly to zero.

C.4 Linear algebra

Linear algebra is the mathematics of linear functions $\mathrm{f}[z_1, z_2, \ldots z_n]$, which have the form:

$$\mathrm{f}[z_1, z_2, \ldots z_n] = \phi_1 z_1 + \phi_2 z_2 + \ldots \phi_D z_D, \tag{C.4}$$

where $\phi_1, \ldots, \phi_D$ are parameters that define the function. In machine learning, we often add a constant term ϕ_0 to the right hand side. This is technically an *affine* function, but is often referred to as linear in machine learning. We adopt this convention throughout.

C.4.1 Vector, matrices, and tensors

In machine learning, a vector $\mathbf{x}$ is a one-dimensional array of numbers. Similarly, a matrix $\mathbf{Y}$ is a two-dimensional array of numbers, and a tensor $\mathbf{z}$ is an N-dimensional array of numbers. Confusingly, all three of these quantities are stored in objects known as "tensors" in modern deep learning APIs such as PyTorch and TensorFlow.

C.4.2 Linear equations in matrix form

Consider a collection of linear functions:

$$\begin{aligned} y_1 &= \phi_{10} + \phi_{11} z_1 + \phi_{12} z_2 + \phi_{13} z_3 \\ y_2 &= \phi_{20} + \phi_{21} z_1 + \phi_{22} z_2 + \phi_{23} z_3 \\ y_3 &= \phi_{20} + \phi_{31} z_1 + \phi_{32} z_2 + \phi_{33} z_3 \end{aligned} \tag{C.5}$$

can be written in matrix form as:

$$\begin{bmatrix} y_1 \\ y_2 \\ y_3 \end{bmatrix} = \begin{bmatrix} \phi_{10} \\ \phi_{20} \\ \phi_{30} \end{bmatrix} + \begin{bmatrix} \phi_{11} & \phi_{12} & \phi_{13} \\ \phi_{21} & \phi_{22} & \phi_{23} \\ \phi_{31} & \phi_{32} & \phi_{33} \end{bmatrix} \begin{bmatrix} z_1 \\ z_2 \\ z_3 \end{bmatrix}, \tag{C.6}$$

or as $\mathbf{y} = \boldsymbol{\phi}_0 + \boldsymbol{\Phi}\mathbf{z}$ for short, where $y_i = \phi_{i0} + \sum_{j=1}^{3} \phi_{ij} z_j$.

C.5 Properties of matrices

The product of two matrices $\mathbf{C} = \mathbf{AB}$ is a third matrix where:

$$C_{ij} = \sum_{k=1}^{K} A_{ik} B_{kj} \tag{C.7}$$

C.5.1 Transpose

The transpose of a matrix $\mathbf{A}$ is written as $\mathbf{A}^T$ and is formed by reflecting it around the principal diagonal, so that the k^{th} column becomes the k^{th} row and vice-versa. If we take the transpose of a matrix product $\mathbf{AB}$, then we take the transpose of the original matrices but reverse the order so that

$$(\mathbf{AB})^T = \mathbf{B}^T\mathbf{A}^T. \tag{C.8}$$

C.5.2 Inverse

A square matrix $\mathbf{A}$ may or may not have an inverse $\mathbf{A}^{-1}$ such that $\mathbf{A}^{-1}\mathbf{A} = \mathbf{AA}^{-1} = \mathbf{I}$. If a matrix does not have an inverse, it is called *singular*.

Diagonal matrices are particularly easy to invert: the inverse is also a diagonal matrix, with each diagonal value d_{ii} replaced by $1/d_{ii}$. Hence, any diagonal matrix which has non-zero values on the diagonal is invertible. It follows that the inverse of the identity matrix is the identity matrix itself.

If we take the inverse of a matrix product $\mathbf{AB}$ then we can equivalently take the inverse of each matrix individually, and reverse the order of multiplication

$$(\mathbf{AB})^{-1} = \mathbf{B}^{-1}\mathbf{A}^{-1}. \tag{C.9}$$

C.5.3 Subspaces

Consider a matrix $\mathbf{Z} \in \mathbb{R}^{I\times J}$. If the number of rows I of the matrix is greater than the number of columns J (i.e., the matrix is "portrait", then the product $\mathbf{Zx}$ cannot reach all possible positions in the I-dimensional output space. This product consists of the J columns of $\mathbf{Z}$ weighed by the J elements of x, and can only reach the *linear subspace* that is spanned by these columns. The remaining part of space that cannot be reached (i.e., where $\mathbf{Zx} = 0$ for all $\mathbf{x}$) is termed the *nullspace* of the matrix.

C.5.4 Eigenspectrum

If we multiply all the 2D points on a unit circle by a given 2 matrix $\mathbf{A}$, then the result is an ellipse. The diameters of the major and minor axes of this ellipse (i.e., the longest and shortest directions) are the *eigenvalues* λ_1 and λ_2 of the matrix. The same idea applies in higher dimensions. A $D-$dimensional sphere is mapped by a $D \times D$ matrix $\mathbf{A}$ to a $D-$dimensional ellipsoid. The diameters of the D principle axes of this ellipsoid are the eigenvalues.

They set of eigenvalues are sometimes called the eigenspecturam and they tell us something about the magnitude of the scaling applied by the matrix. This information is commonly summarized using the *determinant*, and *trace*, and the *spectral norm* of the matrix.

C.5.5 Determinant and trace

Every square matrix $\mathbf{A}$ has a scalar associated with it called the determinant and denoted by $|\mathbf{A}|$ or $\det[\mathbf{A}]$, which is the product of the eigenvalues. It is hence related to the average scaling applied by the matrix for different inputs. Matrices with small determinants tend to make vectors smaller upon multiplication. Matrices with large determinants tend to make them larger. If a matrix is *singular*, the determinant will be zero and there will be at least one direction in space that is mapped to the origin when the matrix is applied. For a diagonal matrix the determinant is the product of the diagonal values. It follows that the determinant of the identity matrix is 1. Determinants of matrix expressions can be computed using the following rules:

$$
\begin{aligned}
|\mathbf{A}^T| &= |\mathbf{A}| && \text{(C.10)}\\
|\mathbf{AB}| &= |\mathbf{A}||\mathbf{B}| && \text{(C.11)}\\
|\mathbf{A}^{-1}| &= 1/|\mathbf{A}|. && \text{(C.12)}
\end{aligned}
$$

The trace of a square matrix is the sum of the diagonal values (the matrix itself need not be diagonal), or alternately, the sum of the eigenvalues. The traces of compound terms are bound by the following rules:

$$
\begin{aligned}
\mathrm{tr}[\mathbf{A}^{\mathbf{T}}] &= \mathrm{tr}[\mathbf{A}] && \text{(C.13)}\\
\mathrm{tr}[\mathbf{AB}] &= \mathrm{tr}[\mathbf{BA}] && \text{(C.14)}\\
\mathrm{tr}[\mathbf{A}+\mathbf{B}] &= \mathrm{tr}[\mathbf{A}]+\mathrm{tr}[\mathbf{B}] && \text{(C.15)}\\
\mathrm{tr}[\mathbf{ABC}] &= \mathrm{tr}[\mathbf{BCA}] = \mathrm{tr}[\mathbf{CAB}]. && \text{(C.16)}
\end{aligned}
$$

where in the last relation the trace is invariance for cyclic permutations only, so that in general $\mathrm{tr}[\mathbf{ABC}] \neq \mathrm{tr}[\mathbf{BAC}]$.

C.5.6 Vector and matrix norms

The spectral norm of a square matrix is the largest eigenvalue. It captures the largest possible change in magnitude when the matrix is applied to a vector of unit length. As such, it tells us about the Lipschitz constant of the transformation.

Sometimes we want measures of the overall "magnitude" of a vector or matrix. For a vector $\mathbf{z}$, the ℓ_p norm is defined as:

$$||\mathbf{z}||_p = \left(\sum_{d=1}^{D} |z_d|^p \right)^{1/2}. \tag{C.17}$$

When $p = 2$, this is known as the *Euclidean norm*. It is this case that is most commonly used in deep learning, and often the exponent p is omitted and the Euclidean norm just written as $||\mathbf{z}||$.

Norms can be computed in a similar way for matrices. The ℓ_2 norm of a matrix $\mathbf{Z}$ is known as the *Frobenius norm* and is calculated as:

$$||\mathbf{Z}||_F = \left(\sum_{i=1}^{I} \sum_{j=1}^{J} |z_{ij}|^2 \right)^{1/2}. \tag{C.18}$$

C.5.7 Special types of matrix

C.5.8 Permutation matrices

C.6 Matrix calculus

C.6.1 Jacobian

C.7 Complexity

C.8 Biniomial coefficients

Appendix D

Ethics further reading

Bibliography

Abdal, R., Qin, Y., & Wonka, P. (2019). Image2StyleGAN: How to embed images into the stylegan latent space? *IEEE/CVF International Conference on Computer Vision*, 4432–4441. 305

Abdal, R., Qin, Y., & Wonka, P. (2020). Image2StyleGAN++: How to edit the embedded images? *IEEE/CVF Computer Vision & Pattern Recognition*, 8296–8305. 305

Abdal, R., Zhu, P., Mitra, N. J., & Wonka, P. (2021). StyleFlow: Attribute-conditioned exploration of StyleGAN-generated images using conditional continuous normalizing flows. *ACM Transactions on Graphics (ToG)*, *40*(3), 1–21. 305, 327

Abdel-Hamid, O., Mohamed, A.-r., Jiang, H., & Penn, G. (2012). Applying convolutional neural networks concepts to hybrid NN-HMM model for speech recognition. *IEEE International Conference on Acoustics, Speech and Signal Processing*, 4277–4280. 182

Abdelhamed, A., Brubaker, M. A., & Brown, M. S. (2019). Noise flow: Noise modeling with conditional normalizing flows. *IEEE/CVF International Conference on Computer Vision*, 3165–3173. 327

Abeßer, J., Mimilakis, S. I., Gräfe, R., Lukashevich, H., & Fraunhofer, I. (2017). Acoustic scene classification by combining autoencoder-based dimensionality reduction and convolutional neural networks. *Workshop on Detection and Classification of Acoustic Scenes and Events*, 7–11. 159

Abu-El-Haija, S., Perozzi, B., Kapoor, A., Alipourfard, N., Lerman, K., Harutyunyan, H., Ver Steeg, G., & Galstyan, A. (2019). MixHop: Higher-order graph convolutional architectures via sparsified neighborhood mixing. *International Conference on Machine Learning*, 21–29. 267

Adler, J., & Lunz, S. (2018). Banach Wasserstein GAN. *Neural Information Processing Systems*, *31*, 6755–6764. 303

Agarwal, R., Schuurmans, D., & Norouzi, M. (2020). An optimistic perspective on offline reinforcement learning. *International Conference on Machine Learning*, 104–114. 404

Aggarwal, C. C., Hinneburg, A., & Keim, D. A. (2001). On the surprising behavior of distance metrics in high dimensional space. *International Conference on Database Theory*, 420–434. 135

Aiken, M., & Park, M. (2010). The efficacy of round-trip translation for MT evaluation. *Translation Journal*, *14*(1). 160

Ainslie, J., Ontañón, S., Alberti, C., Cvicek, V., Fisher, Z., Pham, P., Ravula, A., Sanghai, S., Wang, Q., & Yang, L. (2020). ETC: Encoding long and structured inputs in transformers. *ACL Empirical Methods in Natural Language Processing*, 268–284. 240

Akuzawa, K., Iwasawa, Y., & Matsuo, Y. (2018). Expressive speech synthesis via modeling expressions with variational autoencoder. *INTERPSPEECH*, 3067–3071. 349

Ali, A., Touvron, H., Caron, M., Bojanowski, P., Douze, M., Joulin, A., Laptev, I., Neverova, N., Synnaeve, G., Verbeek, J., et al. (2021). XCiT: Cross-covariance image transformers. *Neural Information Processing Systems*, *34*, 20014–20027. 241

Allen-Zhu, Z., Li, Y., & Song, Z. (2019). A convergence theory for deep learning via over-parameterization. *International Conference on Machine Learning*, *97*, 242–252. 411

Alon, U., & Yahav, E. (2021). On the bottleneck of graph neural networks and its practical implications. *International Conference on Learning Representations*. 269

Alvarez, J. M., & Salzmann, M. (2016). Learning the number of neurons in deep networks. *Neu-*

ral Information Processing Systems, *29*, 2262–2270. 421

Amari, S.-I. (1998). Natural gradient works efficiently in learning. *Neural Computation*, *10*(2), 251–276. 403

An, G. (1996). The effects of adding noise during backpropagation training on a generalization performance. *Neural Computation*, *8*(3), 643–674. 158

An, J., Huang, S., Song, Y., Dou, D., Liu, W., & Luo, J. (2021). ArtFlow: Unbiased image style transfer via reversible neural flows. *IEEE/CVF Computer Vision & Pattern Recognition*, 862–871. 327

Andreae, J. (1969). Learning machines: A unified view. *Encyclopaedia of Linguistics, Information and Control*, 261–270. 402

Ardizzone, L., Kruse, J., Lüth, C., Bracher, N., Rother, C., & Köthe, U. (2020). Conditional invertible neural networks for diverse image-to-image translation. *DAGM German Conference on Pattern Recognition*, 373–387. 327

Arjovsky, M., & Bottou, L. (2017). Towards principled methods for training generative adversarial networks. *International Conference on Learning Representations*. 287, 303, 304

Arjovsky, M., Chintala, S., & Bottou, L. (2017). Wasserstein generative adversarial networks. *International Conference on Machine Learning*, 214–223. 284, 303

Arnab, A., Dehghani, M., Heigold, G., Sun, C., Lučić, M., & Schmid, C. (2021). ViVit: A video vision transformer. *IEEE/CVF International Conference on Computer Vision*, 6836–6846. 241

Arora, R., Basu, A., Mianjy, P., & Mukherjee, A. (2016). Understanding deep neural networks with rectified linear units. *arXiv:1611.01491*. 52

Arora, S., Ge, R., Liang, Y., Ma, T., & Zhang, Y. (2017). Generalization and equilibrium in generative adversarial nets (GANs). *International Conference on Machine Learning*, 224–232. 304

Arora, S., Li, Z., & Lyu, K. (2018). Theoretical analysis of auto rate-tuning by batch normalization. *arXiv:1812.03981*. 205

Arora, S., & Zhang, Y. (2017). Do GANs actually learn the distribution? An empirical study. *arXiv:1706.08224*. 304

Arulkumaran, K., Deisenroth, M. P., Brundage, M., & Bharath, A. A. (2017). Deep reinforcement learning: A brief survey. *IEEE Signal Processing Magazine*, *34*(6), 26–38. 402

Atwood, J., & Towsley, D. (2016). Diffusion-convolutional neural networks. *Neural Information Processing Systems*, *29*, 1993–2001. 266

Aubret, A., Matignon, L., & Hassas, S. (2019). A survey on intrinsic motivation in reinforcement learning. *arXiv:1908.06976*. 404

Austin, J., Johnson, D. D., Ho, J., Tarlow, D., & van den Berg, R. (2021). Structured denoising diffusion models in discrete state-spaces. *Neural Information Processing Systems*, *34*, 17981–17993. 375

Ba, J. L., Kiros, J. R., & Hinton, G. E. (2016). Layer normalization. *arXiv:1607.06450*. 205

Bachlechner, T., Majumder, B. P., Mao, H., Cottrell, G., & McAuley, J. (2021). ReZero is all you need: Fast convergence at large depth. *Uncertainty in Artificial Intelligence*, 1352–1361. 241

Bahdanau, D., Cho, K., & Bengio, Y. (2015). Neural machine translation by jointly learning to align and translate. *International Conference on Learning Representations*. 236, 238

Bahri, Y., Kadmon, J., Pennington, J., Schoenholz, S. S., Sohl-Dickstein, J., & Ganguli, S. (2020). Statistical mechanics of deep learning. *Annual Review of Condensed Matter Physics*, *11*, 501–528. 415, 416

Baldi, P., & Hornik, K. (1989). Neural networks and principal component analysis: Learning from examples without local minima. *Neural networks*, *2*(1), 53–58. 416

Balduzzi, D., Frean, M., Leary, L., Lewis, J., Ma, K. W.-D., & McWilliams, B. (2017). The shattered gradients problem: If ResNets are the answer, then what is the question? *International Conference on Machine Learning*, 342–350. 189, 203, 204, 206

Bansal, A., Borgnia, E., Chu, H.-M., Li, J. S., Kazemi, H., Huang, F., Goldblum, M., Geiping, J., & Goldstein, T. (2022). Cold diffusion: Inverting arbitrary image transforms without noise. *arXiv:2208.09392*. 376

Bao, F., Li, C., Zhu, J., & Zhang, B. (2022). Analytic-DPM: An analytic estimate of the optimal reverse variance in diffusion probabilistic models. *International Conference on Learning Representations*. 376

Baranchuk, D., Rubachev, I., Voynov, A., Khrulkov, V., & Babenko, A. (2022). Label-efficient semantic segmentation with diffusion models. *International Conference on Learning Representations*. 375

Barber, D., & Bishop, C. (1997). Ensemble learning for multi-layer networks. *Neural Information Processing Systems*, *10*, 395–401. 159

Barratt, S., & Sharma, R. (2018). A note on the inception score. *Workshop on Theoretical Foundations and Applications of Deep Generative Models*. 278

Barrett, D. G. T., & Dherin, B. (2021). Implicit gradient regularization. *International Conference on Learning Representations*. 157

Barron, J. T. (2019). A general and adaptive robust loss function. *IEEE/CVF Computer Vision & Pattern Recognition*, 4331–4339. 73

Bartlett, P. L., Foster, D. J., & Telgarsky, M. J. (2017). Spectrally-normalized margin bounds for neural networks. *Neural Information Processing Systems*, vol. 30, 6240–6249. 156

Bartlett, P. L., Harvey, N., Liaw, C., & Mehrabian, A. (2019). Nearly-tight VC-dimension and pseudodimension bounds for piecewise linear neural networks. *Journal of Machine Learning Research*, *20*(1), 2285–2301. 134

Barto, A. G. (2013). Intrinsic motivation and reinforcement learning. *Intrinsically Motivated Learning in Natural and Artificial Systems*, 17–47. 404

Bau, D., Zhou, B., Khosla, A., Oliva, A., & Torralba, A. (2017). Network dissection: Quantifying interpretability of deep visual representations. *IEEE/CVF Computer Vision & Pattern Recognition*, 6541–6549. 184

Bau, D., Zhu, J.-Y., Wulff, J., Peebles, W., Strobelt, H., Zhou, B., & Torralba, A. (2019). Seeing what a GAN cannot generate. *IEEE/CVF International Conference on Computer Vision*, 4502–4511. 304

Baydin, A. G., Pearlmutter, B. A., Radul, A. A., & Siskind, J. M. (2018). Automatic differentiation in machine learning: A survey. *Journal of Marchine Learning Research*, *18*, 1–43. 113

Bayer, M., Kaufhold, M.-A., & Reuter, C. (2022). A survey on data augmentation for text classification. *ACM Computing Surveys*, *55*(7), 1–39. 160

Behrmann, J., Grathwohl, W., Chen, R. T., Duvenaud, D., & Jacobsen, J.-H. (2019). Invertible residual networks. *International Conference on Machine Learning*, 573–582. 323, 329

Belinkov, Y., & Bisk, Y. (2018). Synthetic and natural noise both break neural machine translation. *International Conference on Learning Representations*. 160

Belkin, M., Hsu, D., Ma, S., & Mandal, S. (2019). Reconciling modern machine-learning practice and the classical bias–variance trade-off. *Proceedings of the National Academy of Sciences*, *116*(32), 15849–15854. 130, 134

Bellemare, M. G., Dabney, W., & Munos, R. (2017a). A distributional perspective on reinforcement learning. *International Conference on Machine Learning*, 449–458. 403

Bellemare, M. G., Danihelka, I., Dabney, W., Mohamed, S., Lakshminarayanan, B., Hoyer, S., & Munos, R. (2017b). The Cramer distance as a solution to biased Wasserstein gradients. *arXiv:1705.10743*. 303

Bellman, R. (1966). Dynamic programming. *Science*, *153*(3731), 34–37. 402

Beltagy, I., Peters, M. E., & Cohan, A. (2020). Longformer: The long-document transformer. *arXiv:2004.05150*. 240

Bender, E. M., & Koller, A. (2020). Climbing towards NLU: On meaning, form, and understanding in the age of data. *Meeting of the Association for Computational Linguistics*, 5185–5198. 237

Bengio, Y., Ducharme, R., & Vincent, P. (2000). A neural probabilistic language model. *Neural Information Processing Systems*, *13*, 932–938. 278

Bergstra, J., & Bengio, Y. (2012). Random search for hyper-parameter optimization. *Journal of Machine Learning Research*, *13*(10), 281–305. 136

Bergstra, J. S., Bardenet, R., Bengio, Y., & Kégl, B. (2011). Algorithms for hyper-parameter optimization. *Neural Information Processing Systems*, vol. 24, 2546–2554. 136

Berner, C., Brockman, G., Chan, B., Cheung, V., Dębiak, P., Dennison, C., Farhi, D., Fischer, Q., Hashme, S., Hesse, C., et al. (2019). DOTA 2 with large scale deep reinforcement learning. *arXiv:1912.06680*. 402

Bertasius, G., Wang, H., & Torresani, L. (2021). Is space-time attention all you need for video understanding? *International Conference on Machine Learning*, 3, 813–824. 241

Beyer, K., Goldstein, J., Ramakrishnan, R., & Shaft, U. (1999). When is "nearest neighbor" meaningful? *International Conference on Database Theory*, 217–235. 135

Binns, R. (2018). Algorithmic accountability and public reason. *Philosophy & Technology*, *31*(4), 543–556. 14

Bishop, C. (1995). Regularization and complexity control in feed-forward networks. *International Conference on Artificial Neural Networks*, 141–148. 157, 158

Bishop, C. M. (1994). Mixture density networks. *Aston University Technical Report*. 73

Bishop, C. M. (2006). *Pattern recognition and machine learning*. Springer. 15, 159

Bjorck, N., Gomes, C. P., Selman, B., & Weinberger, K. Q. (2018). Understanding batch normalization. *Neural Information Processing Systems*, *31*, 7705–7716. 205

Blum, A. L., & Rivest, R. L. (1992). Training a 3-node neural network is NP-complete. *Neural Networks*, *5*(1), 117–127. 407

Blundell, C., Cornebise, J., Kavukcuoglu, K., & Wierstra, D. (2015). Weight uncertainty in neural network. *International Conference on Machine Learning*, 1613–1622. 159

Bond-Taylor, S., Leach, A., Long, Y., & Willcocks, C. G. (2022). Deep generative modelling: A comparative review of VAEs, GANs, normalizing flows, energy-based and autoregressive models. *IEEE Transactions on Pattern Analysis & Machine Intelligence*, *44*(11), 7327–7347. 278

Borji, A. (2022). Pros and cons of GAN evaluation measures: New developments. *Computer Vision & Image Understanding*, *215*, 103329. 278

Bornschein, J., Shabanian, S., Fischer, A., & Bengio, Y. (2016). Bidirectional Helmholtz machines. *International Conference on Machine Learning*, 2511–2519. 352

Boscaini, D., Masci, J., Rodolà, E., & Bronstein, M. (2016). Learning shape correspondence with anisotropic convolutional neural networks. *Neural Information Processing Systems*, *29*, 3189–3197. 269

Bottou, L. (2012). Stochastic gradient descent tricks. *Neural Networks: Tricks of the Trade: Second Edition*, 421–436. 91

Bottou, L., Curtis, F. E., & Nocedal, J. (2018). Optimization methods for large-scale machine learning. *SIAM Review*, *60*(2), 223–311. 91

Bottou, L., Soulié, F. F., Blanchet, P., & Liénard, J.-S. (1990). Speaker-independent isolated digit recognition: Multilayer perceptrons vs. dynamic time warping. *Neural Networks*, *3*(4), 453–465. 181

Bousselham, W., Thibault, G., Pagano, L., Machireddy, A., Gray, J., Chang, Y. H., & Song, X. (2021). Efficient self-ensemble framework for semantic segmentation. *arXiv:2111.13280*. 162

Bowman, S. R., & Dahl, G. E. (2021). What will it take to fix benchmarking in natural language understanding? *ACL Human Language Technologies*, 4843–4855. 237

Bowman, S. R., Vilnis, L., Vinyals, O., Dai, A. M., Jozefowicz, R., & Bengio, S. (2015). Generating sentences from a continuous space. *ACL Conference on Computational Natural Language Learning*, 10–21. 350, 351

Brock, A., Donahue, J., & Simonyan, K. (2019). Large scale GAN training for high fidelity natural image synthesis. *International Conference on Learning Representations*. 303

Brock, A., Lim, T., Ritchie, J. M., & Weston, N. (2016). Neural photo editing with introspective adversarial networks. *International Conference on Learning Representations*. 291, 351

Bromley, J., Guyon, I., LeCun, Y., Säckinger, E., & Shah, R. (1993). Signature verification using a "Siamese" time delay neural network. *Neural Information Processing Systems*, *6*, 737–744. 181

Bronstein, M. M., Bruna, J., Cohen, T., & Veličković, P. (2021). Geometric deep learning: Grids, groups, graphs, geodesics, and gauges. *arXiv:2104.13478*. 266

Brown, T., Mann, B., Ryder, N., Subbiah, M., Kaplan, J. D., Dhariwal, P., Neelakantan, A., Shyam, P., Sastry, G., Askell, A., et al. (2020). Language models are few-shot learners. *Neural Information Processing Systems*, *33*, 1877–1901. 9, 159, 237, 240

Brügger, R., Baumgartner, C. F., & Konukoglu, E. (2019). A partially reversible U-Net for memory-efficient volumetric image segmentation. *International Conference on Medical Image Computing and Computer-Assisted Intervention*, 429–437. 327

Bruna, J., Zaremba, W., Szlam, A., & LeCun, Y. (2013). Spectral networks and locally connected networks on graphs. *International Conference on Learning Representations*. 266

Bryson, A., Ho, Y.-C., & Siouris, G. (1979). Applied optimal control: Optimization, estimation, and control. *IEEE Transactions on Systems, Man & Cybernetics*, *9*, 366–367. 113

Bubeck, S., & Sellke, M. (2021). A universal law of robustness via isoperimetry. *Neural Infor-*

mation Processing Systems, *34*, 28811–28822. 135, 423

Buciluǎ, C., Caruana, R., & Niculescu-Mizil, A. (2006). Model compression. *ACM SIGKDD International Conference on Knowledge Discovery and Data Mining*, 535–541. 421

Burda, Y., Grosse, R. B., & Salakhutdinov, R. (2016). Importance weighted autoencoders. *International Conference on Learning Representations*. 73, 352

Buschjäger, S., & Morik, K. (2021). There is no double-descent in random forests. *arXiv:2111.04409*. 134

Cai, T., Luo, S., Xu, K., He, D., Liu, T.-y., & Wang, L. (2021). GraphNorm: A principled approach to accelerating graph neural network training. *International Conference on Machine Learning*, 1204–1215. 269

Calimeri, F., Marzullo, A., Stamile, C., & Terracina, G. (2017). Biomedical data augmentation using adversarial neural networks. *International Conference on Artificial Neural Networks*, 626–634. 159

Cao, H., Tan, C., Gao, Z., Chen, G., Heng, P.-A., & Li, S. Z. (2022). A survey on generative diffusion model. *arXiv:2209.02646*. 375

Cao, Z., Qin, T., Liu, T.-Y., Tsai, M.-F., & Li, H. (2007). Learning to rank: From pairwise approach to listwise approach. *International Conference on Machine Learning*, 129–136. 73

Carion, N., Massa, F., Synnaeve, G., Usunier, N., Kirillov, A., & Zagoruyko, S. (2020). End-to-end object detection with transformers. *European Conference on Computer Vision*, 213–229. 241

Cauchy, A. (1847). Methode generale pour la resolution des systemes d'equations simultanees. *Comptes Rendus de l'Académie des Sciences*, *25*. 91

Chami, I., Abu-El-Haija, S., Perozzi, B., Ré, C., & Murphy, K. (2020). Machine learning on graphs: A model and comprehensive taxonomy. *arXiv:2005.03675*. 266

Chang, B., Chen, M., Haber, E., & Chi, E. H. (2019a). AntisymmetricRNN: A dynamical system view on recurrent neural networks. *International Conference on Learning Representations*. 329

Chang, B., Meng, L., Haber, E., Ruthotto, L., Begert, D., & Holtham, E. (2018). Reversible architectures for arbitrarily deep residual neural networks. *AAAI Conference on Artificial Intelligence*, 2811–2818. 329

Chang, Y.-L., Liu, Z. Y., Lee, K.-Y., & Hsu, W. (2019b). Free-form video inpainting with 3D gated convolution and temporal PatchGAN. *IEEE/CVF International Conference on Computer Vision*, 9066–9075. 181

Chaudhari, P., Choromanska, A., Soatto, S., LeCun, Y., Baldassi, C., Borgs, C., Chayes, J., Sagun, L., & Zecchina, R. (2019). Entropy-SGD: Biasing gradient descent into wide valleys. *Journal of Statistical Mechanics: Theory and Experiment*, *12*, 124018. 158, 417

Chen, D., Mei, J.-P., Zhang, Y., Wang, C., Wang, Z., Feng, Y., & Chen, C. (2021a). Cross-layer distillation with semantic calibration. *AAAI Conference on Artificial Intelligence*, 7028–7036. 422

Chen, H., Wang, Y., Guo, T., Xu, C., Deng, Y., Liu, Z., Ma, S., Xu, C., Xu, C., & Gao, W. (2021b). Pre-trained image processing transformer. *IEEE/CVF Computer Vision & Pattern Recognition*, 12299–12310. 241

Chen, J., Ma, T., & Xiao, C. (2018a). FastGCN: Fast learning with graph convolutional networks via importance sampling. *International Conference on Learning Representations*. 268, 269

Chen, J., Zhu, J., & Song, L. (2018b). Stochastic training of graph convolutional networks with variance reduction. *International Conference on Machine Learning*, 941–949. 268

Chen, L., Lu, K., Rajeswaran, A., Lee, K., Grover, A., Laskin, M., Abbeel, P., Srinivas, A., & Mordatch, I. (2021c). Decision transformer: Reinforcement learning via sequence modeling. *Neural Information Processing Systems*, *34*, 15084–15097. 404

Chen, L.-C., Papandreou, G., Kokkinos, I., Murphy, K., & Yuille, A. L. (2018c). DeepLab: Semantic image segmentation with deep convolutional nets, atrous convolution, and fully connected CRFs. *IEEE Transactions on Pattern Analysis & Machine Intelligence*, *40*(4), 834—–848. 181

Chen, M., Radford, A., Child, R., Wu, J., Jun, H., Luan, D., & Sutskever, I. (2020a). Generative pretraining from pixels. *International Conference on Machine Learning*, 1691–1703. 241

Chen, M., Wei, Z., Huang, Z., Ding, B., & Li, Y. (2020b). Simple and deep graph convolutional networks. *International Conference on Machine Learning*, 1725–1735. 270

Chen, N., Zhang, Y., Zen, H., Weiss, R. J., Norouzi, M., Dehak, N., & Chan, W. (2021d).

WaveGrad 2: Iterative refinement for text-to-speech synthesis. *INTERSPEECH*, 3765–3769. 375

Chen, R. T., Behrmann, J., Duvenaud, D. K., & Jacobsen, J.-H. (2019). Residual flows for invertible generative modeling. *Neural Information Processing Systems*, *32*, 9913–9923. 329

Chen, R. T., Li, X., Grosse, R. B., & Duvenaud, D. K. (2018d). Isolating sources of disentanglement in variational autoencoders. *Neural Information Processing Systems*, *31*, 2615–2625. 349, 352

Chen, R. T., Rubanova, Y., Bettencourt, J., & Duvenaud, D. K. (2018e). Neural ordinary differential equations. *Neural Information Processing Systems*, *31*, 6572–6583. 329

Chen, T., Fox, E., & Guestrin, C. (2014). Stochastic gradient Hamiltonian Monte Carlo. *International Conference on Machine Learning*, 1683–1691. 159

Chen, T., Kornblith, S., Norouzi, M., & Hinton, G. (2020c). A simple framework for contrastive learning of visual representations. *International Conference on Machine Learning*, 1597–1607. 159

Chen, T., Xu, B., Zhang, C., & Guestrin, C. (2016a). Training deep nets with sublinear memory cost. *arXiv:1604.06174*. 114

Chen, W., Liu, T.-Y., Lan, Y., Ma, Z.-M., & Li, H. (2009). Ranking measures and loss functions in learning to rank. *Neural Information Processing Systems*, *22*, 315–323. 73

Chen, X., Duan, Y., Houthooft, R., Schulman, J., Sutskever, I., & Abbeel, P. (2016b). InfoGAN: Interpretable representation learning by information maximizing generative adversarial nets. *Neural Information Processing Systems*, *29*, 2172–2180. 295, 305

Chen, X., Kingma, D. P., Salimans, T., Duan, Y., Dhariwal, P., Schulman, J., Sutskever, I., & Abbeel, P. (2017). Variational lossy autoencoder. *International Conference on Learning Representations*. 351

Chen, Y.-C., Li, L., Yu, L., El Kholy, A., Ahmed, F., Gan, Z., Cheng, Y., & Liu, J. (2020d). UNITER: Universal image-text representation learning. *European Conference on Computer Vision*, 104–120. 241

Chiang, W.-L., Liu, X., Si, S., Li, Y., Bengio, S., & Hsieh, C.-J. (2019). Cluster-GCN: An efficient algorithm for training deep and large graph convolutional networks. *ACM SIGKDD International Conference on Knowledge Discovery & Data Mining*, 257–266. 267, 268, 269

Child, R., Gray, S., Radford, A., & Sutskever, I. (2019). Generating long sequences with sparse transformers. *arXiv:1904.10509*. 240

Chintala, S., Denton, E., Arjovsky, M., & Matheiu, M. (2020). How to train a GAN? Tips and tricks to make GANs work. `https://github.com/soumith/ganhacks`. 304

Cho, K., van Merrienboer, B., Bahdanau, D., & Bengio, Y. (2014). On the properties of neural machine translation: Encoder-decoder approaches. *ACL Workshop on Syntax, Semantics and Structure in Statistical Translation*, 103–111. 236

Choi, D., Shallue, C. J., Nado, Z., Lee, J., Maddison, C. J., & Dahl, G. E. (2019). On empirical comparisons of optimizers for deep learning. *arXiv:1910.05446*. 94, 417

Choi, J., Kim, S., Jeong, Y., Gwon, Y., & Yoon, S. (2021). ILVR: Conditioning method for denoising diffusion probabilistic models. *IEEE/CVF International Conference on Computer Vision*, 14347–14356. 377

Choi, J., Lee, J., Shin, C., Kim, S., Kim, H., & Yoon, S. (2022). Perception prioritized training of diffusion models. *IEEE/CVF Computer Vision & Pattern Recognition*, 11472–11481. 376

Choi, Y., Choi, M., Kim, M., Ha, J.-W., Kim, S., & Choo, J. (2018). StarGAN: Unified generative adversarial networks for multi-domain image-to-image translation. *IEEE/CVF Computer Vision & Pattern Recognition*, 8789–8797. 305

Chollet, F. (2017). Xception: Deep learning with depthwise separable convolutions. *IEEE/CVF Computer Vision & Pattern Recognition*, 1251–1258. 411

Choromanska, A., Henaff, M., Mathieu, M., Arous, G. B., & LeCun, Y. (2015). The loss surfaces of multilayer networks. *International Conference on Artificial Intelligence and Statistics*. 411

Choromanski, K., Likhosherstov, V., Dohan, D., Song, X., Gane, A., Sarlos, T., Hawkins, P., Davis, J., Mohiuddin, A., Kaiser, L., et al. (2020). Rethinking attention with Performers. *International Conference on Learning Representations*. 238, 240

Chorowski, J., & Jaitly, N. (2017). Towards better decoding and language model integration in sequence to sequence models. *INTERSPEECH*, 523–527. 158

Chowdhery, A., Narang, S., Devlin, J., Bosma, M., Mishra, G., Roberts, A., Barham, P., Chung, H. W., Sutton, C., Gehrmann, S., et al. (2022).

PaLM: Scaling language modeling with pathways. *arXiv:2204.02311*. 237

Chu, X., Tian, Z., Wang, Y., Zhang, B., Ren, H., Wei, X., Xia, H., & Shen, C. (2021). Twins: Revisiting the design of spatial attention in vision transformers. *Neural Information Processing Systems*, *34*, 9355–9366. 241

Chung, H., Sim, B., & Ye, J. C. (2022). Come-closer-diffuse-faster: Accelerating conditional diffusion models for inverse problems through stochastic contraction. *IEEE/CVF Computer Vision & Pattern Recognition*, 12413–12422. 375

Chung, H., & Ye, J. C. (2022). Score-based diffusion models for accelerated MRI. *Medical Image Analysis*, *80*, 102479. 375

Chung, J., Gulcehre, C., Cho, K., & Bengio, Y. (2014). Empirical evaluation of gated recurrent neural networks on sequence modeling. *Deep Learning and Representation Workshop*. 236

Chung, J., Kastner, K., Dinh, L., Goel, K., Courville, A. C., & Bengio, Y. (2015). A recurrent latent variable model for sequential data. *Neural Information Processing Systems*, *28*, 2980–2988. 350, 351

Çiçek, Ö., Abdulkadir, A., Lienkamp, S. S., Brox, T., & Ronneberger, O. (2016). 3D U-Net: Learning dense volumetric segmentation from sparse annotation. *International Conference on Medical Image Computing and Computer-Assisted Intervention*, 424–432. 207

Clark, M. (2022). The engineer who claimed a Google AI is sentient has been fired. The Verge, July 22, 2022. `https://www.theverge.com/2022/7/22/23274958/google-ai-engineer-blake-lemoine-chatbot-lamda-2-sentience`. 237

Clevert, D.-A., Unterthiner, T., & Hochreiter, S. (2015). Fast and accurate deep network learning by exponential linear units (ELUs). *arXiv:1511.07289*. 38

Cohen, N., Sharir, O., & Shashua, A. (2016). On the expressive power of deep learning: A tensor analysis. *PMLR Conference on Learning Theory*, 698–728. 53

Cohen, T., & Welling, M. (2016). Group equivariant convolutional networks. *International Conference on Machine Learning*, 2990–2999. 183

Collins, E., Bala, R., Price, B., & Susstrunk, S. (2020). Editing in style: Uncovering the local semantics of GANs. *IEEE/CVF Computer Vision & Pattern Recognition*, 5771–5780. 305

Conneau, A., Schwenk, H., Barrault, L., & Lecun, Y. (2017). Very deep convolutional networks for text classification. *Meeting of the Association for Computational Linguistics*, 1107–1116. 182

Cordonnier, J.-B., Loukas, A., & Jaggi, M. (2020). On the relationship between self-attention and convolutional layers. *International Conference on Learning Representations*. 238

Cordts, M., Omran, M., Ramos, S., Rehfeld, T., Enzweiler, M., Benenson, R., Franke, U., Roth, S., & Schiele, B. (2016). The Cityscapes dataset for semantic urban scene understanding. *IEEE/CVF Computer Vision & Pattern Recognition*, 1877–1901. 6, 153

Coulombe, C. (2018). Text data augmentation made simple by leveraging NLP cloud APIs. *arXiv:1812.04718*. 160

Creswell, A., & Bharath, A. A. (2018). Inverting the generator of a generative adversarial network. *IEEE Transactions on Neural Networks and Learning Systems*, *30*(7), 1967–1974. 305

Creswell, A., White, T., Dumoulin, V., Arulkumaran, K., Sengupta, B., & Bharath, A. A. (2018). Generative adversarial networks: An overview. *IEEE Signal Processing Magazine*, *35*(1), 53–65. 303

Cristianini, M., & Shawe-Taylor, J. (2000). *An Introduction to support vector machines*. CUP. 74

Croitoru, F.-A., Hondru, V., Ionescu, R. T., & Shah, M. (2022). Diffusion models in vision: A survey. *arXiv:2209.04747*. 375

Cubuk, E. D., Zoph, B., Mané, D., Vasudevan, V., & Le, Q. V. (2019). Autoaugment: Learning augmentation strategies from data. *IEEE/CVF Computer Vision & Pattern Recognition*, 113–123. 411

Cybenko, G. (1989). Approximation by superpositions of a sigmoidal function. *Mathematics of Control, Signals and Systems*, *2*(4), 303–314. 38

Dabney, W., Rowland, M., Bellemare, M., & Munos, R. (2018). Distributional reinforcement learning with quantile regression. *AAAI Conference on Artificial Intelligence*. 403

Dai, H., Dai, B., & Song, L. (2016). Discriminative embeddings of latent variable models for structured data. *International Conference on Machine Learning*, 2702–2711. 266

Dai, J., Qi, H., Xiong, Y., Li, Y., Zhang, G., Hu, H., & Wei, Y. (2017). Deformable convolutional networks. *IEEE/CVF International Conference on Computer Vision*, 764–773. 183

Daigavane, A., Balaraman, R., & Aggarwal, G. (2021). Understanding convolutions on graphs. Distill, `https://distill.pub/2021/understanding-gnns/`. 265

Daniluk, M., Rocktäschel, T., Welbl, J., & Riedel, S. (2017). Frustratingly short attention spans in neural language modeling. *International Conference on Learning Representations*. 238

Dao, D. (2021). *Awful AI*. Github. Retrieved January 17, 2023. `https://github.com/daviddao/awful-ai`. 15

Dar, Y., Muthukumar, V., & Baraniuk, R. G. (2021). A farewell to the bias-variance tradeoff? An overview of the theory of overparameterized machine learning. *arXiv:2109.02355*. 135

Das, H. P., Abbeel, P., & Spanos, C. J. (2019). Likelihood contribution based multi-scale architecture for generative flows. *arXiv:1908.01686*. 328

Dauphin, Y. N., Pascanu, R., Gülçehre, Ç., Cho, K., Ganguli, S., & Bengio, Y. (2014). Identifying and attacking the saddle point problem in high-dimensional non-convex optimization. *Neural Information Processing Systems*, vol. 27, 2933–2941. 415, 416

David, H. (2015). Why are there still so many jobs? The history and future of workplace automation. *Journal of Economic Perspectives*, *29*(3), 3–30. 14

De, S., & Smith, S. (2020). Batch normalization biases residual blocks towards the identity function in deep networks. *Neural Information Processing Systems*, *33*, 19964–19975. 206

De Cao, N., & Kipf, T. (2018). MolGAN: An implicit generative model for small molecular graphs. *ICML Workshop on Theoretical Foundations and Applications of Deep Generative Models*. 303

Dechter, R. (1986). Learning while searching in constraint-satisfaction-problems. *AAAI Conference on Artificial Intelligence*, 178—183. 52

Defferrard, M., Bresson, X., & Vandergheynst, P. (2016). Convolutional neural networks on graphs with fast localized spectral filtering. *Neural Information Processing Systems*, *29*, 3837–3845. 266

Dehghani, M., Tay, Y., Gritsenko, A. A., Zhao, Z., Houlsby, N., Diaz, F., Metzler, D., & Vinyals, O. (2021). The benchmark lottery. *arXiv:2107.07002*. 237

Deisenroth, M. P., Faisal, A. A., & Ong, C. S. (2020). *Mathematics for machine learning*. Cambridge University Press. 15

Dempster, A. P., Laird, N. M., & Rubin, D. B. (1977). Maximum likelihood from incomplete data via the EM algorithm. *Journal of the Royal Statistical Society: Series B*, *39*(1), 1–22. 352

Denton, E. L., Chintala, S., Fergus, R., et al. (2015). Deep generative image models using a Laplacian pyramid of adversarial networks. *Neural Information Processing Systems*, *28*, 1486–1494. 304, 305

Devlin, J., Chang, M., Lee, K., & Toutanova, K. (2019). BERT: pre-training of deep bidirectional transformers for language understanding. *ACL Human Language Technologies*, 4171–4186. 159, 237

DeVries, T., & Taylor, G. W. (2017a). Dataset augmentation in feature space. *arXiv:1702.05538*. 158

DeVries, T., & Taylor, G. W. (2017b). Improved regularization of convolutional neural networks with Cutout. *arXiv:1708.04552*. 183

Dhariwal, P., & Nichol, A. (2021). Diffusion models beat GANs on image synthesis. *Neural Information Processing Systems*, *34*, 8780–8794. 374, 375, 377

Ding, M., Xiao, B., Codella, N., Luo, P., Wang, J., & Yuan, L. (2022). DaViT: Dual attention vision transformers. *European Conference on Computer Vision*, 74–92. 241

Dinh, L., Krueger, D., & Bengio, Y. (2015). NICE: Non-linear independent components estimation. *International Conference on Learning Representations Workshop*. 328

Dinh, L., Pascanu, R., Bengio, S., & Bengio, Y. (2017). Sharp minima can generalize for deep nets. *International Conference on Machine Learning*, 1019–1028. 417

Dinh, L., Sohl-Dickstein, J., & Bengio, S. (2016). Density estimation using Real NVP. *International Conference on Learning Representations*. 327, 328

Dinh, L., Sohl-Dickstein, J., Larochelle, H., & Pascanu, R. (2019). A RAD approach to deep mixture models. *ICLR Workshop on Deep Generative Models for Highly Structured Data*. 328

Dockhorn, T., Vahdat, A., & Kreis, K. (2022). Score-based generative modeling with critically-damped Langevin diffusion. *International Conference on Learning Representations*. 377

Doersch, C., Gupta, A., & Efros, A. A. (2015). Unsupervised visual representation learning by context prediction. *IEEE International Conference on Computer Vision*, 1422–1430. 159

Domingos, P. (2000). A unified bias-variance decomposition. *International Conference on Machine Learning*, 231–238. 133

Domke, J. (2010). Statistical machine learning. `https://people.cs.umass.edu/~domke/`. 116

Donahue, C., Lipton, Z. C., Balsubramani, A., & McAuley, J. (2018a). Semantically decomposing the latent spaces of generative adversarial networks. *International Conference on Learning Representations*. 305

Donahue, C., McAuley, J., & Puckette, M. (2018b). Adversarial audio synthesis. *International Conference on Learning Representations*. 303, 305

Dong, X., Bao, J., Chen, D., Zhang, W., Yu, N., Yuan, L., Chen, D., & Guo, B. (2022). CSWin transformer: A general vision transformer backbone with cross-shaped windows. *IEEE/CVF Computer Vision & Pattern Recognition*, 12124–12134. 241

Dorta, G., Vicente, S., Agapito, L., Campbell, N. D., & Simpson, I. (2018). Structured uncertainty prediction networks. *IEEE/CVF Computer Vision & Pattern Recognition*, 5477–5485. 73, 346, 350

Dosovitskiy, A., Beyer, L., Kolesnikov, A., Weissenborn, D., Zhai, X., Unterthiner, T., Dehghani, M., Minderer, M., Heigold, G., Gelly, S., et al. (2021). An image is worth 16x16 words: Transformers for image recognition at scale. *International Conference on Learning Representations*. 236, 241

Dozat, T. (2016). Incorporating Nesterov momentum into Adam. *International Conference on Learning Representations — Workshop track*. 93

Draxler, F., Veschgini, K., Salmhofer, M., & Hamprecht, F. A. (2018). Essentially no barriers in neural network energy landscape. *International Conference on Machine Learning*, 1308–1317. 414, 415

Du, N., Huang, Y., Dai, A. M., Tong, S., Lepikhin, D., Xu, Y., Krikun, M., Zhou, Y., Yu, A. W., Firat, O., et al. (2022). GLaM: Efficient scaling of language models with mixture-of-experts. *International Conference on Machine Learning*, 5547–5569. 237

Du, S. S., Lee, J. D., Li, H., Wang, L., & Zhai, X. (2019a). Gradient descent finds global minima of deep neural networks. *International Conference on Machine Learning*, 1675–1685. 410, 411

Du, S. S., Zhai, X., Poczos, B., & Singh, A. (2019b). Gradient descent provably optimizes over-parameterized neural networks. *International Conference on Learning Representations*. 410

Duchi, J., Hazan, E., & Singer, Y. (2011). Adaptive subgradient methods for online learning and stochastic optimization. *Journal of Machine Learning Research*, *12*, 2121–2159. 93

Dufter, P., Schmitt, M., & Schütze, H. (2021). Position information in transformers: An overview. *Computational Linguistics*, 1–31. 239

Dumoulin, V., Belghazi, I., Poole, B., Mastropietro, O., Lamb, A., Arjovsky, M., & Courville, A. (2017). Adversarially learned inference. *International Conference on Learning Representations*. 305, 351

Dumoulin, V., & Visin, F. (2016). A guide to convolution arithmetic for deep learning. *arXiv:1603.07285*. 180

Dupont, E., Doucet, A., & Teh, Y. W. (2019). Augmented neural ODEs. *Neural Information Processing Systems*, *32*, 3134–3144. 329

Durkan, C., Bekasov, A., Murray, I., & Papamakarios, G. (2019a). Cubic-spline flows. *ICML Invertible Neural Networks and Normalizing Flows*. 328

Durkan, C., Bekasov, A., Murray, I., & Papamakarios, G. (2019b). Neural spline flows. *Neural Information Processing Systems*, *32*, 7509–7520. 328

Duvenaud, D. K., Maclaurin, D., Iparraguirre, J., Bombarell, R., Hirzel, T., Aspuru-Guzik, A., & Adams, R. P. (2015). Convolutional networks on graphs for learning molecular fingerprints. *Neural Information Processing Systems*, *28*, 2224–2232. 266

D'Amour, A., Heller, K., Moldovan, D., Adlam, B., Alipanahi, B., Beutel, A., Chen, C., Deaton, J., Eisenstein, J., Hoffman, M. D., et al. (2020). Underspecification presents challenges for credibility in modern machine learning. *Journal of Machine Learning Research*, 1–61. 419

Ebrahimi, J., Rao, A., Lowd, D., & Dou, D. (2018). HotFlip: White-box adversarial examples for text classification. *Meeting of the Association for Computational Linguistics*, 31–36. 160

El Asri, L., & Prince, J. D., Simon (2020). Tutorial #6: Neural natural language generation – decoding algorithms. `https://www.borealisai.com/research-blogs/tutorial-6-neural-natural-language-generation-decoding-algorithms/`. 238

Eldan, R., & Shamir, O. (2016). The power of depth for feedforward neural networks. *PMLR Conference on Learning Theory*, 907–940. 53, 423

Elfwing, S., Uchibe, E., & Doya, K. (2018). Sigmoid-weighted linear units for neural network function approximation in reinforcement learning. *Neural Networks*, *107*, 3–11. 38

Eren, L., Ince, T., & Kiranyaz, S. (2019). A generic intelligent bearing fault diagnosis system using compact adaptive 1D CNN classifier. *Journal of Signal Processing Systems*, *91*(2), 179–189. 182

Erhan, D., Bengio, Y., Courville, A., & Vincent, P. (2009). Visualizing higher-layer features of a deep network. *Technical Report, University of Montreal*, *1341*(3). 184

Errica, F., Podda, M., Bacciu, D., & Micheli, A. (2019). A fair comparison of graph neural networks for graph classification. *International Conference on Learning Representations*. 266

Eslami, S., Heess, N., Weber, T., Tassa, Y., Szepesvari, D., Hinton, G. E., et al. (2016). Attend, infer, repeat: Fast scene understanding with generative models. *Neural Information Processing Systems*, *29*, 3225–3233. 350

Eslami, S. A., Jimenez Rezende, D., Besse, F., Viola, F., Morcos, A. S., Garnelo, M., Ruderman, A., Rusu, A. A., Danihelka, I., Gregor, K., et al. (2018). Neural scene representation and rendering. *Science*, *360*(6394), 1204–1210. 350

Esling, P., Masuda, N., Bardet, A., Despres, R., et al. (2019). Universal audio synthesizer control with normalizing flows. *International Conference on Digital Audio Effects*. 327

Esser, P., Rombach, R., & Ommer, B. (2021). Taming transformers for high-resolution image synthesis. *IEEE/CVF Computer Vision & Pattern Recognition*, 12873–12883. 305

Esteves, C., Allen-Blanchette, C., Zhou, X., & Daniilidis, K. (2018). Polar transformer networks. *International Conference on Learning Representations*. 183

Etmann, C., Ke, R., & Schönlieb, C.-B. (2020). iunets: Fully invertible U-Nets with learnable up-and downsampling. *IEEE International Workshop on Machine Learning for Signal Processing*. 327

FAIR (2022). Human-level play in the game of Diplomacy by combining language models with strategic reasoning. *Science*, *378*(6624), 1067–1074. 402

Falk, T., Mai, D., Bensch, R., Çiçek, Ö., Abdulkadir, A., Marrakchi, Y., Böhm, A., Deubner, J., Jäckel, Z., Seiwald, K., et al. (2019). U-Net: Deep learning for cell counting, detection, and morphometry. *Nature Methods*, *16*(1), 67–70. 200

Falkner, S., Klein, A., & Hutter, F. (2018). BOHB: Robust and efficient hyperparameter optimization at scale. *International Conference on Machine Learning*, 1437–1446. 136

Fallah, N., Gu, H., Mohammad, K., Seyyedsalehi, S. A., Nourijelyani, K., & Eshraghian, M. R. (2009). Nonlinear Poisson regression using neural networks: A simulation study. *Neural Computing and Applications*, *18*(8), 939–943. 74

Fan, A., Lewis, M., & Dauphin, Y. N. (2018). Hierarchical neural story generation. *Meeting of the Association for Computational Linguistics*, 889–898. 238

Fan, H., Xiong, B., Mangalam, K., Li, Y., Yan, Z., Malik, J., & Feichtenhofer, C. (2021). Multiscale vision transformers. *IEEE/CVF International Conference on Computer Vision*, 6824–6835. 241

Fan, K., Li, B., Wang, J., Zhang, S., Chen, B., Ge, N., & Yan, Z. (2020). Neural zero-inflated quality estimation model for automatic speech recognition system. *Interspeech*, 606–610. 73

Fang, F., Yamagishi, J., Echizen, I., & Lorenzo-Trueba, J. (2018). High-quality nonparallel voice conversion based on cycle-consistent adversarial network. *International Conference on Acoustics, Speech and Signal Processing*, 5279–5283. 303

Fang, Y., Liao, B., Wang, X., Fang, J., Qi, J., Wu, R., Niu, J., & Liu, W. (2021). You only look at one sequence: Rethinking transformer in vision through object detection. *Neural Information Processing Systems*, *34*, 26183–26197. 241

Fawzi, A., Balog, M., Huang, A., Hubert, T., Romera-Paredes, B., Barekatain, M., Novikov, A., R Ruiz, F. J., Schrittwieser, J., Swirszcz, G., et al. (2022). Discovering faster matrix multiplication algorithms with reinforcement learning. *Nature*, *610*(7930), 47–53. 402

Fedus, W., Goodfellow, I., & Dai, A. M. (2018). MaskGAN: Better text generation via filling in the_. *International Conference on Learning Representations*. 303

Feng, S. Y., Gangal, V., Kang, D., Mitamura, T., & Hovy, E. (2020). GenAug: Data augmentation for finetuning text generators. *ACL Deep Learning Inside Out*, 29–42. 160

Feng, Z., Zhang, Z., Yu, X., Fang, Y., Li, L., Chen, X., Lu, Y., Liu, J., Yin, W., Feng, S., et al. (2022). ERNIE-ViLG 2.0: Improving text-to-image diffusion model with knowledge-enhanced mixture-of-denoising-experts. *arXiv:2210.15257*. 377

Fernández-Madrigal, J.-A., & González, J. (2002). Multihierarchical graph search. *IEEE Transactions on Pattern Analysis and Machine Intelligence*, *24*(1), 103–113. 246

Finlay, C., Jacobsen, J., Nurbekyan, L., & Oberman, A. M. (2020). How to train your neural ODE: The world of Jacobian and kinetic regularization. *International Conference on Machine Learning*, 3154–3164. 329

Fort, S., Hu, H., & Lakshminarayanan, B. (2019). Deep ensembles: A loss landscape perspective. *arXiv:1912.02757*. 158

Fort, S., & Jastrzebski, S. (2019). Large scale structure of neural network loss landscapes. *Neural Information Processing Systems*, vol. 32, 6706–6714. 414

Fort, S., & Scherlis, A. (2019). The Goldilocks zone: Towards better understanding of neural network loss landscapes. *AAAI Conference on Artificial Intelligence*, 3574–3581. 415, 416, 418, 419

Fortunato, M., Azar, M. G., Piot, B., Menick, J., Osband, I., Graves, A., Mnih, V., Munos, R., Hassabis, D., Pietquin, O., et al. (2018). Noisy networks for exploration. *International Conference on Learning Representations*. 403

François-Lavet, V., Henderson, P., Islam, R., Bellemare, M. G., Pineau, J., et al. (2018). An introduction to deep reinforcement learning. *Foundations and Trends in Machine Learning*, *11*(3-4), 219–354. 402

Frankle, J., & Carbin, M. (2019). The lottery ticket hypothesis: Finding sparse, trainable neural networks. *International Conference on Learning Representations*. 412, 421

Frankle, J., Dziugaite, G. K., Roy, D. M., & Carbin, M. (2020). Linear mode connectivity and the lottery ticket hypothesis. *International Conference on Machine Learning*, 3259–3269. 158, 414

Frankle, J., Schwab, D. J., & Morcos, A. S. (2021). Training BatchNorm and only BatchNorm: On the expressive power of random features in CNNs. *International Conference on Learning Representations*. 424

Freund, Y., & Schapire, R. E. (1997). A decision-theoretic generalization of on-line learning and an application to boosting. *Journal of Computer and System Sciences*, *55*(1), 119–139. 74

Friedman, J. H. (1997). On bias, variance, 0/1—loss, and the curse-of-dimensionality. *Data Mining and Knowledge Discovery*, *1*(1), 55–77. 133

Fujimoto, S., Hoof, H., & Meger, D. (2018). Addressing function approximation error in actor-critic methods. *International Conference on Machine Learning*, 1587–1596. 403

Fujimoto, S., Meger, D., & Precup, D. (2019). Off-policy deep reinforcement learning without exploration. *International Conference on Machine Learning*, 2052–2062. 404

Fukushima, K. (1969). Visual feature extraction by a multilayered network of analog threshold elements. *IEEE Transactions on Systems Science and Cybernetics*, *5*(4), 322–333. 37

Fukushima, K., & Miyake, S. (1982). Neocognitron: A self-organizing neural network model for a mechanism of visual pattern recognition. *Competition and Cooperation in Neural Nets*, 267–285. 181

Gal, Y., & Ghahramani, Z. (2016). Dropout as a Bayesian approximation: Representing model uncertainty in deep learning. *International Conference on Machine Learning*, 1050—1059. 158

Gales, M. J. (1998). Maximum likelihood linear transformations for HMM-based speech recognition. *Computer Speech & Language*, *12*(2), 75–98. 160

Gales, M. J., Ragni, A., AlDamarki, H., & Gautier, C. (2009). Support vector machines for noise robust ASR. *2009 IEEE Workshop on Automatic Speech Recognition & Understanding*, 205–210. 160

Ganaie, M., Hu, M., Malik, A., Tanveer, M., & Suganthan, P. (2022). Ensemble deep learning: A review. *Engineering Applications of Artificial Intelligence*, *115*. 158

Gao, H., & Ji, S. (2019). Graph U-Nets. *International Conference on Machine Learning*, 2083–2092. 269

Gao, R., Song, Y., Poole, B., Wu, Y. N., & Kingma, D. P. (2021). Learning energy-based models by diffusion recovery likelihood. *International Conference on Learning Representations*. 376

Garg, R., Bg, V. K., Carneiro, G., & Reid, I. (2016). Unsupervised CNN for single view depth estimation: Geometry to the rescue. *European Conference on Computer Vision*, 740–756. 207

Garipov, T., Izmailov, P., Podoprikhin, D., Vetrov, D., & Wilson, A. G. (2018). Loss surfaces, mode connectivity, and fast ensembling of DNNs. *Neural Information Processing Systems*, vol. 31, 8803—8812. 158, 414

Gastaldi, X. (2017a). Shake-shake regularization. *arXiv:1705.07485*. 204

Gastaldi, X. (2017b). Shake-shake regularization of 3-branch residual networks. 204

Gemici, M. C., Rezende, D., & Mohamed, S. (2016). Normalizing flows on Riemannian manifolds. *NIPS Workshop on Bayesian Deep Learning*. 329

Germain, M., Gregor, K., Murray, I., & Larochelle, H. (2015). MADE: Masked autoencoder for distribution estimation. *International Conference on Machine Learning*, 881–889. 328

Ghosh, A., Kulharia, V., Namboodiri, V. P., Torr, P. H., & Dokania, P. K. (2018). Multi-agent diverse generative adversarial networks. *IEEE/CVF Computer Vision & Pattern Recognition*, 8513–8521. 304

Gidaris, S., Singh, P., & Komodakis, N. (2018). Unsupervised representation learning by predicting image rotations. *International Conference on Learning Representations*. 159

Gilmer, J., Schoenholz, S. S., Riley, P. F., Vinyals, O., & Dahl, G. E. (2017). Neural message passing for quantum chemistry. *International Conference on Machine Learning*, 1263–1272. 266

Girdhar, R., Carreira, J., Doersch, C., & Zisserman, A. (2019). Video action transformer network. *IEEE/CVF Computer Vision & Pattern Recognition*, 244–253. 241

Girshick, R. (2015). Fast R-CNN. *IEEE International Conference on Computer Vision*, 1440–1448. 184

Girshick, R., Donahue, J., Darrell, T., & Malik, J. (2014). Rich feature hierarchies for accurate object detection and semantic segmentation. *IEEE Computer Vision & Pattern Recognition*, 580–587. 183

Glorot, X., & Bengio, Y. (2010). Understanding the difficulty of training deep feedforward neural networks. *International Conference on Artificial Intelligence and Statistics*, *9*, 249–256. 113, 183

Glorot, X., Bordes, A., & Bengio, Y. (2011). Deep sparse rectifier neural networks. *International Conference on Artificial Intelligence and Statistics*, 315–323. 37, 38

Goh, G. (2017). Why momentum really works. Distill, `http://distill.pub/2017/momentum`. 92

Gomez, A. N., Ren, M., Urtasun, R., & Grosse, R. B. (2017). The reversible residual network: Backpropagation without storing activations. *Neural Information Processing Systems*, *30*, 2214–2224. 114, 327, 329

Gómez-Bombarelli, R., Wei, J. N., Duvenaud, D., Hernández-Lobato, J. M., Sánchez-Lengeling, B., Sheberla, D., Aguilera-Iparraguirre, J., Hirzel, T. D., Adams, R. P., & Aspuru-Guzik, A. (2018). Automatic chemical design using a data-driven continuous representation of molecules. *ACS Central Science*, *4*(2), 268–276. 350

Gong, S., Bahri, M., Bronstein, M. M., & Zafeiriou, S. (2020). Geometrically principled connections in graph neural networks. *IEEE/CVF Computer Vision & Pattern Recognition*, 11415–11424. 270

Goodfellow, I. (2016). Generative adversarial networks. *NIPS 2016 Tutorial*. 303

Goodfellow, I., Bengio, Y., & Courville, A. (2016). *Deep learning*. MIT Press. 15, 157

Goodfellow, I., Pouget-Abadie, J., Mirza, M., Xu, B., Warde-Farley, D., Ozair, S., Courville, A., & Bengio, Y. (2014). Generative adversarial networks. *Communications of the ACM*, *63*(11), 139–144. 278, 303, 304

Goodfellow, I. J., Shlens, J., & Szegedy, C. (2015a). Explaining and harnessing adversarial examples. *International Conference on Learning Representations*. 159, 419

Goodfellow, I. J., Vinyals, O., & Saxe, A. M. (2015b). Qualitatively characterizing neural network optimization problems. *International Conference on Learning Representations*. 413, 414

Gordon, G. J. (1995). Stable fitted reinforcement learning. *Neural Information Processing Systems*, *8*, 1052–1058. 402

Gori, M., Monfardini, G., & Scarselli, F. (2005). A new model for learning in graph domains.

IEEE International Joint Conference on Neural Networks, 2005, 729–734. 266

Gouk, H., Frank, E., Pfahringer, B., & Cree, M. J. (2021). Regularisation of neural networks by enforcing Lipschitz continuity. *Machine Learning*, *110*(2), 393—416. 156

Goyal, A., Bochkovskiy, A., Deng, J., & Koltun, V. (2021). Non-deep networks. *arXiv:2110.07641*. 423

Goyal, P., Dollár, P., Girshick, R., Noordhuis, P., Wesolowski, L., Kyrola, A., Tulloch, A., Jia, Y., & He, K. (2018). Accurate, large minibatch SGD: Training ImageNet in 1 hour. *arXiv:1706.02677*. 93, 240

Graesser, L., & Keng, W. L. (2019). *Foundations of deep reinforcement learning*. Addison-Wesley Professional. 402

Grathwohl, W., Chen, R. T., Bettencourt, J., Sutskever, I., & Duvenaud, D. (2019). Ffjord: Free-form continuous dynamics for scalable reversible generative models. *International Conference on Learning Representations*. 329

Grattarola, D., Zambon, D., Bianchi, F. M., & Alippi, C. (2022). Understanding pooling in graph neural networks. *IEEE Transactions on Neural Networks and Learning Systems*. 269

Greensmith, E., Bartlett, P. L., & Baxter, J. (2004). Variance reduction techniques for gradient estimates in reinforcement learning. *Journal of Machine Learning Research*, *5*(9), 1471–1530. 403

Gregor, K., Besse, F., Jimenez Rezende, D., Danihelka, I., & Wierstra, D. (2016). Towards conceptual compression. *Neural Information Processing Systems*, *29*, 3549–3557. 349, 350

Gregor, K., Papamakarios, G., Besse, F., Buesing, L., & Weber, T. (2019). Temporal difference variational auto-encoder. *International Conference on Learning Representations*. 350

Grennan, L., Kremer, A., Singla, A., & Zipparo, P. (2022). *Why businesses need explainable AI—and how to deliver it*. McKinsey, September 29, 2022. `https://www.mckinsey.com/capabilities/quantumblack/our-insights/why-businesses-need-explainable-ai-and-how-to-deliver-it/`. 14

Greydanus, S. (2020). Scaling down deep learning. *arXiv:2011.14439*. 119

Griewank, A., & Walther, A. (2008). *Evaluating derivatives: Principles and techniques of algorithmic differentiation*. SIAM. 113

Gu, J., Kwon, H., Wang, D., Ye, W., Li, M., Chen, Y.-H., Lai, L., Chandra, V., & Pan, D. Z. (2022). Multi-scale high-resolution vision transformer for semantic segmentation. *IEEE/CVF Computer Vision & Pattern Recognition*, 12094–12103. 241

Guan, S., Tai, Y., Ni, B., Zhu, F., Huang, F., & Yang, X. (2020). Collaborative learning for faster StyleGAN embedding. *arXiv:2007.01758*. 305

Gui, J., Sun, Z., Wen, Y., Tao, D., & Ye, J. (2021). A review on generative adversarial networks: Algorithms, theory, and applications. *IEEE Transactions on Knowledge and Data Engineering*. 303

Guimaraes, G. L., Sanchez-Lengeling, B., Outeiral, C., Farias, P. L. C., & Aspuru-Guzik, A. (2017). Objective-reinforced generative adversarial networks (ORGAN) for sequence generation models. *arXiv:1705.10843*. 303

Gulrajani, I., Kumar, K., Ahmed, F., Taiga, A. A., Visin, F., Vazquez, D., & Courville, A. (2016). PixelVAE: A latent variable model for natural images. *International Conference on Learning Representations*. 303, 349, 350, 351

Ha, D., Dai, A., & Le, Q. V. (2017). Hypernetworks. *International Conference on Learning Representations*. 238

Haarnoja, T., Hartikainen, K., Abbeel, P., & Levine, S. (2018a). Latent space policies for hierarchical reinforcement learning. *International Conference on Machine Learning*, 1851–1860. 327

Haarnoja, T., Zhou, A., Abbeel, P., & Levine, S. (2018b). Soft actor-critic: Off-policy maximum entropy deep reinforcement learning with a stochastic actor. *International Conference on Machine Learning*, 1861–1870. 404

Hamilton, W., Ying, Z., & Leskovec, J. (2017a). Inductive representation learning on large graphs. *Neural Information Processing Systems*, *30*, 1024–1034. 266, 267, 268, 269, 271

Hamilton, W. L. (2020). Graph representation learning. *Synthesis Lectures on Artifical Intelligence and Machine Learning*, *14*(3), 1–159. 16, 265

Hamilton, W. L., Ying, R., & Leskovec, J. (2017b). Representation learning on graphs: Methods and applications. *IEEE Data Engineering Bulletin*, *40*(3), 52–74. 267

Han, S., Mao, H., & Dally, W. J. (2016). Deep compression: Compressing deep neural networks with pruning, trained quantization and

Huffman coding. *International Conference on Learning Representations*. 420, 421

Han, S., Pool, J., Tran, J., & Dally, W. (2015). Learning both weights and connections for efficient neural network. *Neural Information Processing Systems*, vol. 28, 1135–1143. 420

Hannun, A. Y., Case, C., Casper, J., Catanzaro, B., Diamos, G., Elsen, E., Prenger, R., Satheesh, S., Sengupta, S., Coates, A., & Ng, A. Y. (2014). Deep speech: Scaling up end-to-end speech recognition. *arXiv:1412.5567*. 160

Hanson, S. J., & Pratt, L. Y. (1988). Comparing biases for minimal network construction with back-propagation. *Neural Information Processing Systems*, vol. 2, 177—185. 155

Härkönen, E., Hertzmann, A., Lehtinen, J., & Paris, S. (2020). GANSpace: Discovering interpretable GAN controls. *Neural Information Processing Systems*, *33*, 9841–9850. 305

Hartmann, K. G., Schirrmeister, R. T., & Ball, T. (2018). EEG-GAN: Generative adversarial networks for electroencephalograhic (EEG) brain signals. *arXiv:1806.01875*. 303

Harvey, W., Naderiparizi, S., Masrani, V., Weilbach, C., & Wood, F. (2022). Flexible diffusion modeling of long videos. *Neural Information Processing Systems*, *35*. 375

Hasanzadeh, A., Hajiramezanali, E., Boluki, S., Zhou, M., Duffield, N., Narayanan, K., & Qian, X. (2020). Bayesian graph neural networks with adaptive connection sampling. *International Conference on Machine Learning*, 4094–4104. 269

Hassibi, B., & Stork, D. G. (1993). Second order derivatives for network pruning: Optimal brain surgeon. *Neural Information Processing Systems*, vol. 6, 164–171. 420

Hausknecht, M., & Stone, P. (2015). Deep recurrent Q-learning for partially observable MDPs. *AAAI Fall Symposia*, 29–37. 403

Hayou, S., Clerico, E., He, B., Deligiannidis, G., Doucet, A., & Rousseau, J. (2021). Stable ResNet. *International Conference on Artificial Intelligence and Statistics*, 1324–1332. 206

He, F., Liu, T., & Tao, D. (2019). Control batch size and learning rate to generalize well: Theoretical and empirical evidence. *Neural Information Processing Systems*, *32*, 1143–1152. 92, 416, 417

He, J., Neubig, G., & Berg-Kirkpatrick, T. (2018). Unsupervised learning of syntactic structure with invertible neural projections. *ACL Empirical Methods in Natural Language Processing*, 1292–1302. 327

He, K., Zhang, X., Ren, S., & Sun, J. (2015). Delving deep into rectifiers: Surpassing human-level performance on ImageNet classification. *IEEE International Conference on Computer Vision*, 1026–1034. 38, 113, 183

He, K., Zhang, X., Ren, S., & Sun, J. (2016a). Deep residual learning for image recognition. *IEEE/CVF Computer Vision & Pattern Recognition*, 770–778. 189, 203, 329, 411

He, K., Zhang, X., Ren, S., & Sun, J. (2016b). Identity mappings in deep residual networks. *European Conference on Computer Vision*, 630–645. 203, 411

He, P., Liu, X., Gao, J., & Chen, W. (2021). DeBERTa: Decoding-enhanced BERT with disentangled attention. *International Conference on Learning Representations*. 239

He, X., Haffari, G., & Norouzi, M. (2020). Dynamic programming encoding for subword segmentation in neural machine translation. *Meeting of the Association for Computational Linguistics*, 3042–3051. 237

He, Y., Zhang, X., & Sun, J. (2017). Channel pruning for accelerating very deep neural networks. *IEEE/CVF International Conference on Computer Vision*, 1389–1397. 421

Heess, N., Wayne, G., Silver, D., Lillicrap, T., Erez, T., & Tassa, Y. (2015). Learning continuous control policies by stochastic value gradients. *Neural Information Processing Systems*, *28*, 2944–2952. 350

Heikkilä, M. (2022). *Why business is booming for military AI startups*. MIT Technology Review, July 7 2022. `https://www.technologyreview.com/2022/07/07/1055526/why-business-is-booming-for-military-ai-startups/`. 14

Henaff, M., Bruna, J., & LeCun, Y. (2015). Deep convolutional networks on graph-structured data. *arXiv:1506.05163*. 266

Hendrycks, D., & Gimpel, K. (2016). Gaussian error linear units (GELUs). *arXiv:1606.08415*. 38

Hermann, V. (2017). Wasserstein GAN and the Kantorovich-Rubinstein duality. `https://vincentherrmann.github.io/blog/wasserstein/`. 288, 303

Hernández, C. X., Wayment-Steele, H. K., Sultan, M. M., Husic, B. E., & Pande, V. S. (2018). Variational encoding of complex dynamics. *Physical Review E*, *97*(6), 062412. 350

Hertz, A., Mokady, R., Tenenbaum, J., Aberman, K., Pritch, Y., & Cohen-Or, D. (2022). Prompt-to-prompt image editing with cross attention control. *arXiv:2208.01626*. 375

Hessel, M., Modayil, J., van Hasselt, H., Schaul, T., Ostrovski, G., Dabney, W., Horgan, D., Piot, B., Azar, M., & Silver, D. (2018). Rainbow: Combining improvements in deep reinforcement learning. *AAAI Conference on Artificial Intelligence*, 3215–3222. 403

Heusel, M., Ramsauer, H., Unterthiner, T., Nessler, B., & Hochreiter, S. (2017). GANs trained by a two time-scale update rule converge to a local Nash equilibrium. *Neural Information Processing Systems*, *30*, 6626–6637. 278

Higgins, I., Matthey, L., Pal, A., Burgess, C., Glorot, X., Botvinick, M., Mohamed, S., & Lerchner, A. (2017). Beta-VAE: Learning basic visual concepts with a constrained variational framework. *International Conference on Learning Representations*. 352

Hindupur, A. (2022). The GAN zoo. GitHub Retrieved January 17, 2023. `https://github.com/hindupuravinash/the-gan-zoo`. 303

Hinton, G., Srivastava, N., & Swersky, K. (2012a). Neural networks for machine learning: Lecture 6a – Overview of mini-batch gradient descent. `https://www.cs.toronto.edu/~tijmen/csc321/slides/lecture_slides_lec6.pdf`. 93

Hinton, G., & van Camp, D. (1993). Keeping neural networks simple by minimising the description length of weights. *Computational learning theory*, 5–13. 159

Hinton, G., Vinyals, O., Dean, J., et al. (2015). Distilling the knowledge in a neural network. *arXiv:1503.02531*, *2*(7). 421

Hinton, G. E., & Salakhutdinov, R. R. (2006). Reducing the dimensionality of data with neural networks. *Science*, *313*(5786), 504–507. 350

Hinton, G. E., Srivastava, N., Krizhevsky, A., Sutskever, I., & Salakhutdinov, R. R. (2012b). Improving neural networks by preventing co-adaptation of feature detectors. *arXiv:1207.0580*. 158

Ho, J., Chen, X., Srinivas, A., Duan, Y., & Abbeel, P. (2019). Flow++: Improving flow-based generative models with variational dequantization and architecture design. *International Conference on Machine Learning*, 2722–2730. 327, 328

Ho, J., Jain, A., & Abbeel, P. (2020). Denoising diffusion probabilistic models. *Neural Information Processing Systems*, *33*, 6840–6851. 278, 375, 376

Ho, J., Saharia, C., Chan, W., Fleet, D. J., Norouzi, M., & Salimans, T. (2022a). Cascaded diffusion models for high fidelity image generation. *Journal of Machine Learning Research*, *23*, 47–1. 376, 377

Ho, J., & Salimans, T. (2022). Classifier-free diffusion guidance. *NeurIPS Workshop on Deep Generative Models and Downstream Applications*. 377

Ho, J., Salimans, T., Gritsenko, A., Chan, W., Norouzi, M., & Fleet, D. J. (2022b). Video diffusion models. *International Conference on Learning Representations*. 375

Hochreiter, S., & Schmidhuber, J. (1997a). Flat minima. *Neural Computation*, *9*(1), 1–42. 417

Hochreiter, S., & Schmidhuber, J. (1997b). Long short-term memory. *Neural computation*, *9*(8), 1735–1780. 236

Hoffer, E., Hubara, I., & Soudry, D. (2017). Train longer, generalize better: Closing the generalization gap in large batch training of neural networks. *Neural Information Processing Systems*, *30*, 1731–1741. 205

Hoffman, M. D., & Johnson, M. J. (2016). ELBO surgery: Yet another way to carve up the variational evidence lower bound. *NIPS Workshop in Advances in Approximate Bayesian Inference*, 2. 352

Hoffmann, J., Borgeaud, S., Mensch, A., Buchatskaya, E., Cai, T., Rutherford, E., Casas, D. d. L., Hendricks, L. A., Welbl, J., Clark, A., et al. (2023). Training compute-optimal large language models. *arXiv:2203.15556*. 237

Holland, C. A., Ebner, N. C., Lin, T., & Samanez-Larkin, G. R. (2019). Emotion identification across adulthood using the dynamic faces database of emotional expressions in younger, middle aged, and older adults. *Cognition and Emotion*, *33*(2), 245–257. 9

Holtzman, A., Buys, J., Du, L., Forbes, M., & Choi, Y. (2020). The curious case of neural text degeneration. *International Conference on Learning Representations*. 238

Hoogeboom, E., Nielsen, D., Jaini, P., Forré, P., & Welling, M. (2021). Argmax flows and multinomial diffusion: Learning categorical distributions. *Neural Information Processing Systems*, *34*, 12454–12465. 375

Hoogeboom, E., Peters, J., Van Den Berg, R., & Welling, M. (2019a). Integer discrete flows and lossless compression. *Neural Information Processing Systems*, *32*, 12134–12144. 329

Hoogeboom, E., Van Den Berg, R., & Welling, M. (2019b). Emerging convolutions for generative normalizing flows. *International Conference on Machine Learning*, 2771–2780. 327, 328

Höppe, T., Mehrjou, A., Bauer, S., Nielsen, D., & Dittadi, A. (2022). Diffusion models for video prediction and infilling. *ECCV Workshop on AI for Creative Video Editing and Understanding*. 375

Hornik, K. (1991). Approximation capabilities of multilayer feedforward networks. *Neural Networks*, *4*(2), 251–257. 38

Howard, A., Sandler, M., Chu, G., Chen, L.-C., Chen, B., Tan, M., Wang, W., Zhu, Y., Pang, R., Vasudevan, V., et al. (2019). Searching for MobileNetV3. *IEEE/CVF International Conference on Computer Vision*, 1314–1324. 38

Howard, A. G., Zhu, M., Chen, B., Kalenichenko, D., Wang, W., Weyand, T., Andreetto, M., & Adam, H. (2017). MobileN ets: Efficient convolutional neural networks for mobile vision applications. *arXiv:1704.04861*. 181

Howard, R. A. (1960). *Dynamic programming and Narkov processes*. Wiley. 402

Hsu, C.-C., Hwang, H.-T., Wu, Y.-C., Tsao, Y., & Wang, H.-M. (2017a). Voice conversion from unaligned corpora using variational autoencoding Wasserstein generative adversarial networks. *INTERSPEECH*, 3364–3368. 351

Hsu, W.-N., Zhang, Y., & Glass, J. (2017b). Learning latent representations for speech generation and transformation. *INTERSPEECH*, 1273–1277. 349

Hu, H., Gu, J., Zhang, Z., Dai, J., & Wei, Y. (2018a). Relation networks for object detection. *IEEE/CVF Computer Vision & Pattern Recognition*, 3588–3597. 241

Hu, H., Zhang, Z., Xie, Z., & Lin, S. (2019). Local relation networks for image recognition. *IEEE/CVF International Conference on Computer Vision*, 3464–3473. 241

Hu, J., Shen, L., & Sun, G. (2018b). Squeeze-and-excitation networks. *IEEE/CVF Computer Vision & Pattern Recognition*, 7132–7141. 181, 238

Hu, W., Pang, J., Liu, X., Tian, D., Lin, C.-W., & Vetro, A. (2022). Graph signal processing for geometric data and beyond: Theory and applications. *IEEE Transactions on Multimedia*, *24*, 3961–3977. 246

Hu, Z., Yang, Z., Liang, X., Salakhutdinov, R., & Xing, E. P. (2017). Toward controlled generation of text. *International Conference on Machine Learning*, 1587–1596. 350

Huang, C.-W., Krueger, D., Lacoste, A., & Courville, A. (2018a). Neural autoregressive flows. *International Conference on Machine Learning*, 2078–2087. 328, 329

Huang, G., Li, Y., Pleiss, G., Liu, Z., Hopcroft, J. E., & Weinberger, K. Q. (2017a). Snapshot ensembles: Train 1, get M for free. *International Conference on Learning Representations*. 158

Huang, G., Liu, Z., Van Der Maaten, L., & Weinberger, K. Q. (2017b). Densely connected convolutional networks. *IEEE/CVF Computer Vision & Pattern Recognition*, 4700–4708. 207, 411

Huang, G., Sun, Y., Liu, Z., Sedra, D., & Weinberger, K. Q. (2016). Deep networks with stochastic depth. *European Conference on Computer Vision*, 646–661. 204

Huang, W., Zhang, T., Rong, Y., & Huang, J. (2018b). Adaptive sampling towards fast graph representation learning. *Neural Information Processing Systems*, *31*, 4563–4572. 268, 269

Huang, X., Li, Y., Poursaeed, O., Hopcroft, J., & Belongie, S. (2017c). Stacked generative adversarial networks. *IEEE/CVF Computer Vision & Pattern Recognition*, 5077–5086. 304

Huang, X. S., Perez, F., Ba, J., & Volkovs, M. (2020a). Improving transformer optimization through better initialization. *International Conference on Machine Learning*, 4475–4483. 114, 240, 241

Huang, Y., Cheng, Y., Bapna, A., Firat, O., Chen, D., Chen, M., Lee, H., Ngiam, J., Le, Q. V., Wu, Y., et al. (2019). GPipe: Efficient training of giant neural networks using pipeline parallelism. *Neural Information Processing Systems*, *32*, 103–112. 114

Huang, Z., Liang, D., Xu, P., & Xiang, B. (2020b). Improve transformer models with better relative position embeddings. *Empirical Methods in Natural Language Processing*. 239

Huang, Z., & Wang, N. (2018). Data-driven sparse structure selection for deep neural networks. *European Conference on Computer Vision*, 304–320. 421

Hussein, A., Gaber, M. M., Elyan, E., & Jayne, C. (2017). Imitation learning: A survey of learning methods. *ACM Computing Surveys*, *50*(2), 1–35. 404

Huszár, F. (2019). Exponentially growing learning rate? Implications of scale invariance induced by batch normalization. https://www.inference.vc/exponentially-growing-learning-rate-implications-of-scale-invariance-induced-by-BatchNorm/. 205

Hutchinson, M. F. (1989). A stochastic estimator of the trace of the influence matrix for Laplacian smoothing splines. *Communications in Statistics-Simulation and Computation*, *18*(3), 1059–1076. 329

Hutter, F., Hoos, H. H., & Leyton-Brown, K. (2011). Sequential model-based optimization for general algorithm configuration. *International Conference on Learning and Intelligent Optimization*, 507–523. 136

Iglovikov, V., & Shvets, A. (2018). TernausNet: U-Net with VGG11 encoder pretrained on ImageNet for image segmentation. *arXiv:1801.05746*. 207

Ilyas, A., Santurkar, S., Tsipras, D., Engstrom, L., Tran, B., & Madry, A. (2019). Adversarial examples are not bugs, they are features. *Neural Information Processing Systems*, *32*, 125–136. 420

Inoue, H. (2018). Data augmentation by pairing samples for images classification. *arXiv:1801.02929*. 159

Inoue, T., Choudhury, S., De Magistris, G., & Dasgupta, S. (2018). Transfer learning from synthetic to real images using variational autoencoders for precise position detection. *IEEE International Conference on Image Processing*, 2725–2729. 350

Ioffe, S. (2017). Batch renormalization: Towards reducing minibatch dependence in batch-normalized models. *Neural Information Processing Systems*, *30*, 1945–1953. 205

Ioffe, S., & Szegedy, C. (2015). Batch normalization: Accelerating deep network training by reducing internal covariate shift. *International Conference on Machine Learning*, 448–456. 114, 204, 205

Ishida, T., Yamane, I., Sakai, T., Niu, G., & Sugiyama, M. (2020). Do we need zero training loss after achieving zero training error? *International Conference on Machine Learning*, 4604–4614. 134, 158

Isola, P., Zhu, J.-Y., Zhou, T., & Efros, A. A. (2017). Image-to-image translation with conditional adversarial networks. *IEEE/CVF Computer Vision & Pattern Recognition*, 1125–1134. 207, 297, 305

Izmailov, P., Podoprikhin, D., Garipov, T., Vetrov, D., & Wilson, A. G. (2018). Averaging weights leads to wider optima and better generalization. *Uncertainly in Artificial Intelligence*, 876–885. 158, 417

Jackson, P. T., Abarghouei, A. A., Bonner, S., Breckon, T. P., & Obara, B. (2019). Style augmentation: Data augmentation via style randomization. *IEEE Computer Vision and Pattern Recognition Workshops*, 10–11. 159

Jacobs, R. A., Jordan, M. I., Nowlan, S. J., & Hinton, G. E. (1991). Adaptive mixtures of local experts. *Neural Computation*, *3*(1), 79–87. 73

Jacobsen, J.-H., Smeulders, A., & Oyallon, E. (2018). i-RevNet: Deep invertible networks. *International Conference on Learning Representations*. 327, 329

Jaini, P., Kobyzev, I., Yu, Y., & Brubaker, M. A. (2020). Tails of Lipschitz triangular flows. *International Conference on Machine Learning*, 4673–4681. 329

Jaini, P., Selby, K. A., & Yu, Y. (2019). Sum-of-squares polynomial flow. *International Conference on Machine Learning*, 3009–3018. 328

Jaitly, N., & Hinton, G. E. (2013). Vocal tract length perturbation (VTLP) improves speech recognition. *ICML Workshop on Deep Learning for Audio, Speech and Language*. 160

Jarrett, K., Kavukcuoglu, K., Ranzato, M., & LeCun, Y. (2009). What is the best multi-stage architecture for object recognition? *IEEE International Conference on Computer Vision*, 2146–2153. 37

Jastrzębski, S., Kenton, Z., Arpit, D., Ballas, N., Fischer, A., Bengio, Y., & Storkey, A. (2018). Three factors influencing minima in SGD. *arXiv:1711.04623*. 92

Ji, S., Xu, W., Yang, M., & Yu, K. (2012). 3D convolutional neural networks for human action recognition. *IEEE Transactions on Pattern Analysis & Machine Intelligence*, *35*(1), 221–231. 182

Jia, X., De Brabandere, B., Tuytelaars, T., & Gool, L. V. (2016). Dynamic filter networks. *Neural Information Processing Systems*, *29*. 183

Jiang, Z., Zheng, Y., Tan, H., Tang, B., & Zhou, H. (2016). Variational deep embedding: An unsupervised and generative approach to clustering. *International Joint Conference on Artificial Intelligence*, 1965–1972. 350

Jin, L., Doshi-Velez, F., Miller, T., Schwartz, L., & Schuler, W. (2019). Unsupervised learning of PCFGs with normalizing flow. *Meeting of the Association for Computational Linguistics*, 2442–2452. 327

Jing, L., & Tian, Y. (2020). Self-supervised visual feature learning with deep neural networks: A survey. *IEEE Transactions on Pattern Analysis & Machine Intelligence*, *43*(11), 4037–4058. 159

Johnson, R., & Zhang, T. (2013). Accelerating stochastic gradient descent using predictive variance reduction. *Neural Information Processing Systems*, *26*, 315–323. 91

Jolicoeur-Martineau, A. (2019). The relativistic discriminator: A key element missing from standard GAN. *International Conference on Learning Representations*. 303

Jurafsky, D., & Martin, J. H. (2000). *Speech and Language Processing, 2nd Edition*. Pearson. 235

Kakade, S. M. (2001). A natural policy gradient. *Neural Information Processing Systems*, *14*, 1531–1538. 403

Kanazawa, A., Sharma, A., & Jacobs, D. (2014). Locally scale-invariant convolutional neural networks. *Neural Information Processing Systems Workshop*. 183

Kanda, N., Takeda, R., & Obuchi, Y. (2013). Elastic spectral distortion for low resource speech recognition with deep neural networks. *IEEE Workshop on Automatic Speech Recognition and Understanding*, 309–314. 160

Kaneko, T., & Kameoka, H. (2017). Parallel-data-free voice conversion using cycle-consistent adversarial networks. *arXiv:1711.11293*. 303

Kang, G., Dong, X., Zheng, L., & Yang, Y. (2017). PatchShuffle regularization. *arXiv:1707.07103*. 159

Kanwar, G., Albergo, M. S., Boyda, D., Cranmer, K., Hackett, D. C., Racaniere, S., Rezende, D. J., & Shanahan, P. E. (2020). Equivariant flow-based sampling for lattice gauge theory. *Physical Review Letters*, *125*(12), 121601. 327

Karras, T., Aila, T., Laine, S., & Lehtinen, J. (2018). Progressive growing of GANs for improved quality, stability, and variation. *International Conference on Learning Representations*. 290, 291, 303, 304, 324, 351

Karras, T., Aittala, M., Aila, T., & Laine, S. (2022). Elucidating the design space of diffusion-based generative models. *Neural Information Processing Systems*. 375, 376

Karras, T., Aittala, M., Hellsten, J., Laine, S., Lehtinen, J., & Aila, T. (2020a). Training generative adversarial networks with limited data. *Neural Information Processing Systems*, *33*, 12104–12114. 305

Karras, T., Aittala, M., Laine, S., Härkönen, E., Hellsten, J., Lehtinen, J., & Aila, T. (2021). Alias-free generative adversarial networks. *Neural Information Processing Systems*, *34*, 852–863. 305

Karras, T., Laine, S., & Aila, T. (2019). A style-based generator architecture for generative adversarial networks. *IEEE/CVF Computer Vision & Pattern Recognition*, 4401–4410. 303, 304

Karras, T., Laine, S., Aittala, M., Hellsten, J., Lehtinen, J., & Aila, T. (2020b). Analyzing and improving the image quality of StyleGAN. *IEEE/CVF Computer Vision & Pattern Recognition*, 8110–8119. 8, 304, 305

Katharopoulos, A., Vyas, A., Pappas, N., & Fleuret, F. (2020). Transformers are RNNs: Fast autoregressive transformers with linear attention. *International Conference on Machine Learning*, 5156–5165. 240

Kawaguchi, K., Huang, J., & Kaelbling, L. P. (2019). Effect of depth and width on local minima in deep learning. *Neural Computation*, *31*(7), 1462–1498. 411

Ke, G., He, D., & Liu, T.-Y. (2021). Rethinking positional encoding in language pre-training. *International Conference on Learning Representations*. 239

Kearnes, S., McCloskey, K., Berndl, M., Pande, V., & Riley, P. (2016). Molecular graph convolutions: Moving beyond fingerprints. *Journal of computer-aided molecular design*, *30*(8), 595–608. 268

Kendall, A., & Gal, Y. (2017). What uncertainties do we need in Bayesian deep learning for computer vision? *Neural Information Processing Systems*, *30*, 5574–5584. 158

Keskar, N. S., Mudigere, D., Nocedal, J., Smelyanskiy, M., & Tang, P. T. P. (2017). On large-batch training for deep learning: Generalization gap and sharp minima. *International Conference on Learning Representations*. 158, 409, 417

Keskar, N. S., & Socher, R. (2017). Improving generalization performance by switching from Adam to SGD. *arXiv:1712.07628*. 94, 416

Khan, S., Naseer, M., Hayat, M., Zamir, S. W., Khan, F. S., & Shah, M. (2022). Transformers in vision: A survey. *ACM Computing Surveys*, *54*(10), 200:1–200:41. 241

Killoran, N., Lee, L. J., Delong, A., Duvenaud, D., & Frey, B. J. (2017). Generating and designing DNA with deep generative models. *NIPS 2017 Workshop on Computational Biology*. 303

Kim, H., & Mnih, A. (2018). Disentangling by factorising. *International Conference on Machine Learning*, 2649–2658. 352

Kim, I., Han, S., Baek, J.-w., Park, S.-J., Han, J.-J., & Shin, J. (2021). Quality-agnostic image recognition via invertible decoder. *IEEE/CVF Computer Vision & Pattern Recognition*, 12257–12266. 327

Kim, S., Lee, S.-g., Song, J., Kim, J., & Yoon, S. (2018). FloWaveNet: A generative flow for raw audio. *International Conference on Machine Learning*, 3370–3378. 327, 328

Kingma, D., Salimans, T., Poole, B., & Ho, J. (2021). Variational diffusion models. *Neural Information Processing Systems*, *34*, 21696–21707. 376

Kingma, D. P., & Ba, J. (2015). Adam: A method for stochastic optimization. *International Conference on Learning Representations*. 93, 240

Kingma, D. P., & Dhariwal, P. (2018). Glow: Generative flow with invertible 1x1 convolutions. *Neural Information Processing Systems*, *31*, 10236–10245. 324, 327, 328

Kingma, D. P., Salimans, T., Jozefowicz, R., Chen, X., Sutskever, I., & Welling, M. (2016). Improved variational inference with inverse autoregressive flow. *Neural Information Processing Systems*, *29*, 4736–4744. 328, 350

Kingma, D. P., & Welling, M. (2014). Auto-encoding variational Bayes. *International Conference on Learning Representations*. 278, 349

Kingma, D. P., Welling, M., et al. (2019). An introduction to variational autoencoders. *Foundations and Trends in Machine Learning*, *12*(4), 307–392. 349

Kipf, T. N., & Welling, M. (2016). Variational graph auto-encoders. *NIPS Bayesian Deep Learning Workshop*. 159, 350

Kipf, T. N., & Welling, M. (2017). Semi-supervised classification with graph convolutional networks. *International Conference on Learning Representations*. 266, 267, 268, 269

Kiranyaz, S., Avci, O., Abdeljaber, O., Ince, T., Gabbouj, M., & Inman, D. J. (2021). 1D convolutional neural networks and applications: A survey. *Mechanical Systems and Signal Processing*, *151*, 107398. 182

Kiranyaz, S., Ince, T., Hamila, R., & Gabbouj, M. (2015). Convolutional neural networks for patient-specific ECG classification. *International Conference of the IEEE Engineering in Medicine and Biology Society*, vol. 37, 2608–2611. 182

Kitaev, N., Kaiser, Ł., & Levskaya, A. (2020). Reformer: The efficient transformer. *International Conference on Learning Representations*. 240

Klambauer, G., Unterthiner, T., Mayr, A., & Hochreiter, S. (2017). Self-normalizing neural networks. *Neural Information Processing Systems*, vol. 30, 972–981. 38, 113

Kleinberg, R., Li, Y., & Yuan, Y. (2018). An alternative view: When does SGD escape local minima? *International Conference on Machine Learning*, 2703–2712. 417

Kobyzev, I., Prince, S. J., & Brubaker, M. A. (2020). Normalizing flows: An introduction and review of current methods. *IEEE Transactions on Pattern Analysis & Machine Intelligence*, *43*(11), 3964–3979. i, 327, 329

Koenker, R., & Hallock, K. F. (2001). Quantile regression. *Journal of Economic Perspectives*, *15*(4), 143–156. 73

Köhler, J., Klein, L., & Noé, F. (2020). Equivariant flows: Exact likelihood generative learning for symmetric densities. *International Conference on Machine Learning*, 5361–5370. 327, 329

Koller, D., & Friedman, N. (2009). *Probabilistic graphical models: Principles and techniques.* MIT Press. 15

Kolomiyets, O., Bethard, S., & Moens, M.-F. (2011). Model-portability experiments for textual temporal analysis. *Meeting of the Association for Computational Linguistics*, 271–276. 160

Konda, V., & Tsitsiklis, J. (1999). Actor-critic algorithms. *Neural Information Processing Systems*, *12*, 1008–1014. 403, 404

Kong, Z., Ping, W., Huang, J., Zhao, K., & Catanzaro, B. (2021). DiffWave: A versatile diffusion model for audio synthesis. *International Conference on Learning Representations*. 375

Kool, W., van Hoof, H., & Welling, M. (2019). Attention, learn to solve routing problems! *International Conference on Learning Representations*. 402

Krizhevsky, A., & Hinton, G. (2009). Learning multiple layers of features from tiny images. *Technical Report, University of Toronto*. 189

Krizhevsky, A., Sutskever, I., & Hinton, G. E. (2012). ImageNet classification with deep convolutional neural networks. *Neural Information Processing Systems*, *25*, 1097–1105. 52, 113, 159, 176, 181

Kruse, J., Detommaso, G., Köthe, U., & Scheichl, R. (2021). HINT: Hierarchical invertible neural transport for density estimation and Bayesian inference. *AAAI Conference on Artificial Intelligence*, 8191–8199. 328

Kudo, T. (2018). Subword regularization: Improving neural network translation models with multiple subword candidates. *Meeting of the Association for Computational Linguistics*, 66–75. 237

Kudo, T., & Richardson, J. (2018). SentencePiece: A simple and language independent subword tokenizer and detokenizer for neural text processing. *Empirical Methods in Natural Language Processing*, 66–71. 237

Kukačka, J., Golkov, V., & Cremers, D. (2017). Regularization for deep learning: A taxonomy. *arXiv:1710.10686*. 155

Kulikov, I., Miller, A. H., Cho, K., & Weston, J. (2018). Importance of search and evaluation strategies in neural dialogue modeling. *ACL International Conference on Natural Language Generation*, 76–87. 238

Kumar, A., Fu, J., Soh, M., Tucker, G., & Levine, S. (2019a). Stabilizing off-policy Q-learning via bootstrapping error reduction. *Neural Information Processing Systems*, *32*, 11761–11771. 404

Kumar, A., Sattigeri, P., & Balakrishnan, A. (2018). Variational inference of disentangled latent concepts from unlabeled observations. *International Conference on Learning Representations*. 352

Kumar, A., Singh, S. S., Singh, K., & Biswas, B. (2020a). Link prediction techniques, applications, and performance: A survey. *Physica A: Statistical Mechanics and its Applications*, *553*, 124289. 266

Kumar, A., Zhou, A., Tucker, G., & Levine, S. (2020b). Conservative Q-learning for offline reinforcement learning. *Neural Information Processing Systems*, *33*, 1179–1191. 404

Kumar, M., Babaeizadeh, M., Erhan, D., Finn, C., Levine, S., Dinh, L., & Kingma, D. (2019b). VideoFlow: A flow-based generative model for video. *ICML Workshop on Invertible Neural Networks and Normalizing Flows*. 327

Kumar, M., Weissenborn, D., & Kalchbrenner, N. (2021). Colorization transformer. *International Conference on Learning Representations*. 241

Kurach, K., Lučić, M., Zhai, X., Michalski, M., & Gelly, S. (2019). A large-scale study on regularization and normalization in GANs. *International Conference on Machine Learning*, 3581–3590. 304

Kurenkov, A. (2020). *A Brief History of Neural Nets and Deep Learning*. `https://www.skynettoday.com/overviews/neural-net-history`. 37

Kynkäänniemi, T., Karras, T., Laine, S., Lehtinen, J., & Aila, T. (2019). Improved precision and recall metric for assessing generative models. *Neural Information Processing Systems*, *32*, 3929–3938. 278

Lakshminarayanan, B., Pritzel, A., & Blundell, C. (2017). Simple and scalable predictive uncertainty estimation using deep ensembles. *Neural Information Processing Systems*, *30*, 6402–6413. 157, 158

Lamb, A., Dumoulin, V., & Courville, A. (2016). Discriminative regularization for generative models. *arXiv:1602.03220*. 350

Lample, G., & Charton, F. (2020). Deep learning for symbolic mathematics. *International Conference on Learning Representations*. 236

Larsen, A. B. L., Sønderby, S. K., Larochelle, H., & Winther, O. (2016). Autoencoding beyond pixels using a learned similarity metric. *International Conference on Machine Learning*, 1558–1566. 350, 351

Lasseck, M. (2018). Acoustic bird detection with deep convolutional neural networks. *Detection and Classification of Acoustic Scenes and Events*, 143–147. 160

Lattimore, T., & Szepesvári, C. (2020). *Bandit algorithms*. Cambridge University Press. 136

Lawrence, S., Giles, C. L., Tsoi, A. C., & Back, A. D. (1997). Face recognition: A convolutional neural-network approach. *IEEE Transactions on Neural Networks*, *8*(1), 98–113. 181

LeCun, Y. (1985). Une procedure d'apprentissage pour reseau a seuil asymmetrique. *Proceedings of Cognitiva*, 599–604. 113

LeCun, Y., Bengio, Y., & Hinton, G. (2015). Deep learning. *Nature*, *521*(7553), 436–444. 52

LeCun, Y., Boser, B., Denker, J., Henderson, D., Howard, R., Hubbard, W., & Jackel, L. (1989a). Handwritten digit recognition with a back-propagation network. *Neural Information Processing Systems*, *2*, 396–404. 181

LeCun, Y., Boser, B., Denker, J. S., Henderson, D., Howard, R. E., Hubbard, W., & Jackel, L. D. (1989b). Backpropagation applied to handwritten zip code recognition. *Neural Computation*, *1*(4), 541–551. 181

LeCun, Y., Bottou, L., Bengio, Y., & Haffner, P. (1998). Gradient-based learning applied to document recognition. *Proceedings of the IEEE*, *86*(11), 2278–2324. 159, 181

LeCun, Y., Chopra, S., Hadsell, R., Ranzato, M., & Huang, F. (2006). A tutorial on energy-based learning. *Predicting structured data*, *1*(0). 278

LeCun, Y., Denker, J. S., & Solla, S. A. (1990). Optimal brain damage. *Neural Information Processing Systems*, vol. 3, 598–605. 420

LeCun, Y. A., Bottou, L., Orr, G. B., & Müller, K.-R. (2012). Efficient backprop. *Neural Networks: Tricks of the trade*, 9–48. Springer. 113, 416

Ledig, C., Theis, L., Huszár, F., Caballero, J., Cunningham, A., Acosta, A., Aitken, A., Tejani, A., Totz, J., Wang, Z., et al. (2017). Photo-realistic single image super-resolution using a generative adversarial network. *IEEE/CVF Computer Vision & Pattern Recognition*, 4681–4690. 298, 305

Lee, J., Lee, I., & Kang, J. (2019). Self-attention graph pooling. *International Conference on Machine Learning*, 3734–3743. 269

Lee, J. B., Rossi, R. A., Kong, X., Kim, S., Koh, E., & Rao, A. (2018). Higher-order graph convolutional networks. *arXiv:1809.07697*. 267

Li, C., Chen, C., Carlson, D., & Carin, L. (2016a). Preconditioned stochastic gradient Langevin dynamics for deep neural networks. *AAAI Conference on Artificial Intelligence*, 1788–1794. 159

Li, C., Farkhoor, H., Liu, R., & Yosinski, J. (2018a). Measuring the intrinsic dimension of objective landscapes. *International Conference on Learning Representations*. 413, 414

Li, G., Müller, M., Ghanem, B., & Koltun, V. (2021a). Training graph neural networks with 1000 layers. *International Conference on Machine Learning*, 6437–6449. 270, 327

Li, G., Müller, M., Qian, G., Perez, I. C. D., Abualshour, A., Thabet, A. K., & Ghanem, B. (2021b). DeepGCNs: Making GCNs go as deep as CNNs. *IEEE Transactions on Pattern Analysis and Machine Intelligence*. 270

Li, G., Xiong, C., Thabet, A., & Ghanem, B. (2020a). DeeperGCN: All you need to train deeper GCNs. *arXiv:2006.07739*. 270

Li, H., Kadav, A., Durdanovic, I., Samet, H., & Graf, H. P. (2017a). Pruning filters for efficient ConvNets. *International Conference on Learning Representations*. 421

Li, H., Xu, Z., Taylor, G., Studer, C., & Goldstein, T. (2018b). Visualizing the loss landscape of neural nets. *Neural Information Processing Systems*, *31*, 6391–6401. 202, 203, 413

Li, L., Jamieson, K., DeSalvo, G., Rostamizadeh, A., & Talwalkar, A. (2017b). Hyperband: A novel bandit-based approach to hyperparameter optimization. *Journal of Machine Learning Research*, *18*(1), 6765–6816. 136

Li, L. H., Yatskar, M., Yin, D., Hsieh, C.-J., & Chang, K.-W. (2019). VisualBERT: A simple and performant baseline for vision and language. *arXiv:1908.03557*. 241

Li, Q., Han, Z., & Wu, X.-M. (2018c). Deeper insights into graph convolutional networks for semi-supervised learning. *AAAI Conference on Artificial Intelligence*, 3438–3545. 269

Li, S., Zhao, Y., Varma, R., Salpekar, O., Noordhuis, P., Li, T., Paszke, A., Smith, J., Vaughan, B., Damania, P., & Chintala, S. (2020b). Pytorch distributed: Experiences on accelerating data parallel training. *International Conference on Very Large Databases*. 114

Li, W., Lin, Z., Zhou, K., Qi, L., Wang, Y., & Jia, J. (2022). MAT: Mask-aware transformer for large hole image inpainting. *IEEE/CVF Computer Vision & Pattern Recognition*, 10758–10768. 241

Li, Y. (2017). Deep reinforcement learning: An overview. *arXiv:1701.07274*. 402

Li, Y., Cohn, T., & Baldwin, T. (2017c). Robust training under linguistic adversity. *Meeting of the Association for Computational Linguistics*, 21–27. 160

Li, Y., & Liang, Y. (2018). Learning overparameterized neural networks via stochastic gradient descent on structured data. *Neural Information Processing Systems*, *31*, 8168–8177. 413

Li, Y., Tarlow, D., Brockschmidt, M., & Zemel, R. (2016b). Gated graph sequence neural networks. *International Conference on Learning Representations*. 266

Li, Y., & Turner, R. E. (2016). Rényi divergence variational inference. *Neural Information Processing Systems*, *29*, 1073–1081. 352

Li, Z., & Arora, S. (2019). An exponential learning rate schedule for deep learning. *International Conference on Learning Representations*. 205

Liang, D., Krishnan, R. G., Hoffman, M. D., & Jebara, T. (2018). Variational autoencoders for collaborative filtering. *World Wide Web Conference*, 689–698. 350

Liang, J., Zhang, K., Gu, S., Van Gool, L., & Timofte, R. (2021). Flow-based kernel prior with application to blind super-resolution. *IEEE/CVF Computer Vision & Pattern Recognition*, 10601–10610. 327

Liang, S., & Srikant, R. (2016). Why deep neural networks for function approximation? *International Conference on Learning Representations*. 53, 423

Lillicrap, T. P., Hunt, J. J., Pritzel, A., Heess, N., Erez, T., Tassa, Y., Silver, D., & Wierstra, D. (2016). Continuous control with deep reinforcement learning. *International Conference on Learning Representations*. 403

Lin, K., Li, D., He, X., Zhang, Z., & Sun, M.-T. (2017a). Adversarial ranking for language generation. *Neural Information Processing Systems*, *30*, 3155–3165. 303

Lin, M., Chen, Q., & Yan, S. (2014). Network in network. *International Conference on Learning Representations*. 181

Lin, T., Wang, Y., Liu, X., & Qiu, X. (2022). A survey of transformers. *AI Open*, *3*, 111–132. 236

Lin, T.-Y., Dollár, P., Girshick, R., He, K., Hariharan, B., & Belongie, S. (2017b). Feature pyramid networks for object detection. *IEEE Computer Vision & Pattern Recognition*, 2117–2125. 184

Lin, T.-Y., Goyal, P., Girshick, R., He, K., & Dollár, P. (2017c). Focal loss for dense object detection. *IEEE/CVF International Conference on Computer Vision*, 2980–2988. 73

Lin, Z., Khetan, A., Fanti, G., & Oh, S. (2018). PacGAN: The power of two samples in generative adversarial networks. *Neural Information Processing Systems*, *31*, 1505–1514. 304

Ling, H., Kreis, K., Li, D., Kim, S. W., Torralba, A., & Fidler, S. (2021). EditGAN: High-precision semantic image editing. *Neural Information Processing Systems*, *34*, 16331–16345. 306

Lipton, Z. C., & Tripathi, S. (2017). Precise recovery of latent vectors from generative adversarial networks. *International Conference on Learning Representations*. 305

Liu, G., Reda, F. A., Shih, K. J., Wang, T.-C., Tao, A., & Catanzaro, B. (2018a). Image inpainting for irregular holes using partial convolutions. *European Conference on Computer Vision*, 85–100. 181

Liu, H., Simonyan, K., & Yang, Y. (2019a). DARTS: Differentiable architecture search. *International Conference on Learning Representations*. 421

Liu, L., Jiang, H., He, P., Chen, W., Liu, X., Gao, J., & Han, J. (2021a). On the variance of the adaptive learning rate and beyond. *International Conference on Learning Representations*. 93

Liu, L., Liu, X., Gao, J., Chen, W., & Han, J. (2020). Understanding the difficulty of training transformers. *Empirical Methods in Natural Language Processing*, 5747–5763. 240, 241

Liu, L., Luo, Y., Shen, X., Sun, M., & Li, B. (2019b). Beta-dropout: A unified dropout. *IEEE Access*, *7*, 36140–36153. 158

Liu, P. J., Saleh, M., Pot, E., Goodrich, B., Sepassi, R., Kaiser, L., & Shazeer, N. (2018b). Generating Wikipedia by summarizing long sequences. *International Conference on Learning Representations*. 240

Liu, X., Zhang, F., Hou, Z., Mian, L., Wang, Z., Zhang, J., & Tang, J. (2023a). Self-supervised learning: Generative or contrastive. *IEEE Transactions on Knowledge and Data Engineering*, *35*(1), 857–876. 159

Liu, Y., Qin, Z., Anwar, S., Ji, P., Kim, D., Caldwell, S., & Gedeon, T. (2021b). Invertible denoising network: A light solution for real noise removal. *IEEE/CVF Computer Vision & Pattern Recognition*, 13365–13374. 327

Liu, Y., Zhang, Y., Wang, Y., Hou, F., Yuan, J., Tian, J., Zhang, Y., Shi, Z., Fan, J., & He, Z. (2023b). A survey of visual transformers. *IEEE Transactions on Neural Networks and Learning Systems*. 241

Liu, Z., Hu, H., Lin, Y., Yao, Z., Xie, Z., Wei, Y., Ning, J., Cao, Y., Zhang, Z., Dong, L., Wei, F., & Guo, B. (2022). Swin transformer V2: Scaling up capacity and resolution. *IEEE/CVF Computer Vision & Pattern Recognition*, 12009–12019. 241

Liu, Z., Lin, Y., Cao, Y., Hu, H., Wei, Y., Zhang, Z., Lin, S., & Guo, B. (2021c). Swin transformer: Hierarchical vision transformer using shifted windows. *IEEE/CVF International Conference on Computer Vision*, 10012–10022. 235, 241

Liu, Z., Luo, P., Wang, X., & Tang, X. (2015). Deep learning face attributes in the wild. *IEEE International Conference on Computer Vision*, 3730–3738. 351

Liu, Z., Michaud, E. J., & Tegmark, M. (2023c). Omnigrok: Grokking beyond algorithmic data. *International Conference on Learning Representations*. 412, 418, 419

Liu, Z., Sun, M., Zhou, T., Huang, G., & Darrell, T. (2019c). Rethinking the value of network pruning. *International Conference on Learning Representations*. 238

Livni, R., Shalev-Shwartz, S., & Shamir, O. (2014). On the computational efficiency of training neural networks. *Neural Information Processing Systems*, *27*, 855–863. 411

Locatello, F., Weissenborn, D., Unterthiner, T., Mahendran, A., Heigold, G., Uszkoreit, J., Dosovitskiy, A., & Kipf, T. (2020). Object-centric learning with slot attention. *Neural Information Processing Systems*, *33*, 11525–11538. 241

Long, J., Shelhamer, E., & Darrell, T. (2015). Fully convolutional networks for semantic segmentation. *IEEE/CVF Computer Vision & Pattern Recognition*, 3431–3440. 181

Loshchilov, I., & Hutter, F. (2019). Decoupled weight decay regularization. *International Conference on Learning Representations*. 94, 156

Louizos, C., Welling, M., & Kingma, D. P. (2018). Learning sparse neural networks through l_0 regularization. *International Conference on Learning Representations*. 156

Lu, J., Batra, D., Parikh, D., & Lee, S. (2019). VilBERT: Pretraining task-agnostic visiolinguistic representations for vision-and-language tasks. *Neural Information Processing Systems*, *32*, 13–23. 241

Lu, S.-P., Wang, R., Zhong, T., & Rosin, P. L. (2021). Large-capacity image steganography based on invertible neural networks. *IEEE/CVF Computer Vision & Pattern Recognition*, 10816–10825. 327

Lu, Z., Pu, H., Wang, F., Hu, Z., & Wang, L. (2017). The expressive power of neural networks: A view from the width. *Neural Information Processing Systems*, *30*, 6231–6239. 53

Lubana, E. S., Dick, R., & Tanaka, H. (2021). Beyond BatchNorm: Towards a unified understanding of normalization in deep learning. *Neural Information Processing Systems*, *34*, 4778–4791. 205

Lucas, J., Tucker, G., Grosse, R., & Norouzi, M. (2019a). Understanding posterior collapse in generative latent variable models. *ICLR Workshop on Deep Generative Models for Highly Structured Data*. 351

Lucas, J., Tucker, G., Grosse, R. B., & Norouzi, M. (2019b). Don't blame the ELBO! A linear VAE perspective on posterior collapse. *Neural Information Processing Systems*, *32*, 9403–9413. 351

Lucic, M., Kurach, K., Michalski, M., Gelly, S., & Bousquet, O. (2018). Are GANs created equal? A large-scale study. *Neural Information Processing Systems*, *31*, 698–707. 303

Lücke, J., Forster, D., & Dai, Z. (2020). The evidence lower bound of variational autoencoders converges to a sum of three entropies. *arXiv:2010.14860*. 352

Luo, C. (2022). Understanding diffusion models: A unified perspective. *arXiv:2208.11970*. 375

Luo, G., Heide, M., & Uecker, M. (2022). MRI reconstruction via data driven Markov chain with joint uncertainty estimation. *arXiv:2202.01479*. 375

Luo, J., Xu, Y., Tang, C., & Lv, J. (2017a). Learning inverse mapping by autoencoder based generative adversarial nets. *Neural Information Processing Systems*, vol. 30, 207–216. 305

Luo, J.-H., Wu, J., & Lin, W. (2017b). ThiNet: A filter level pruning method for deep neural network compression. *IEEE/CVF International Conference on Computer Vision*, 5058–5066. 421

Luo, P., Wang, X., Shao, W., & Peng, Z. (2018). Towards understanding regularization in batch normalization. *International Conference on Learning Representations*. 206

Luo, S., & Hu, W. (2021). Diffusion probabilistic models for 3D point cloud generation. *IEEE/CVF Computer Vision & Pattern Recognition*, 2837–2845. 375

Luong, M.-T., Pham, H., & Manning, C. D. (2015). Effective approaches to attention-based neural machine translation. *Empirical Methods in Natural Language Processing*, 1412–1421. 238

Luther, K. (2020). Why BatchNorm causes exploding gradients. `https://kyleluther.github.io/2020/02/18/BatchNorm-exploding-gradients.html`. 204

Ma, Y., & Tang, J. (2021). *Deep learning on graphs*. Cambridge University Press. 266

Ma, Y.-A., Chen, T., & Fox, E. (2015). A complete recipe for stochastic gradient MCMC. *Neural Information Processing Systems*, *28*, 2917–2925. 159

Maaløe, L., Sønderby, C. K., Sønderby, S. K., & Winther, O. (2016). Auxiliary deep generative models. *International Conference on Machine Learning*, 1445–1453. 350, 351

Maas, A. L., Hannun, A. Y., & Ng, A. Y. (2013). Rectifier nonlinearities improve neural network acoustic models. *ICML Workshop on Deep Learning for Audio, Speech, and Language Processing*. 38

MacKay, D. J. (1995). Ensemble learning and evidence maximization. *Neural Information Processing Systems*, vol. 8, 4083–4090. 159

MacKay, M., Vicol, P., Ba, J., & Grosse, R. B. (2018). Reversible recurrent neural networks. *Neural Information Processing Systems*, *31*, 9043–9054. 327

Mackowiak, R., Ardizzone, L., Kothe, U., & Rother, C. (2021). Generative classifiers as a basis for trustworthy image classification. *IEEE/CVF Computer Vision & Pattern Recognition*, 2971–2981. 327

Madhawa, K., Ishiguro, K., Nakago, K., & Abe, M. (2019). GraphNVP: An invertible flow model for generating molecular graphs. *arXiv:1905.11600*. 327

Mahendran, A., & Vedaldi, A. (2015). Understanding deep image representations by inverting them. *IEEE/CVF Computer Vision & Pattern Recognition*, 5188–5196. 184

Makhzani, A., Shlens, J., Jaitly, N., Goodfellow, I., & Frey, B. (2015). Adversarial autoencoders. *arXiv:1511.05644*. 351

Mangalam, K., Fan, H., Li, Y., Wu, C.-Y., Xiong, B., Feichtenhofer, C., & Malik, J. (2022). Reversible vision transformers. *IEEE/CVF Computer Vision & Pattern Recognition*, 10830–10840. 327

Manning, C., & Schutze, H. (1999). *Foundations of statistical natural language processing*. MIT Press. 235

Mao, Q., Lee, H.-Y., Tseng, H.-Y., Ma, S., & Yang, M.-H. (2019). Mode seeking generative adversarial networks for diverse image synthesis. *IEEE/CVF Computer Vision & Pattern Recognition*, 1429–1437. 304

Mao, X., Li, Q., Xie, H., Lau, R. Y., Wang, Z., & Paul Smolley, S. (2017). Least squares generative adversarial networks. *IEEE/CVF International Conference on Computer Vision*, 2794–2802. 303

Marchesi, M. (2017). Megapixel size image creation using generative adversarial networks. *arXiv:1706.00082*. 303

Martin, G. L. (1993). Centered-object integrated segmentation and recognition of overlapping handprinted characters. *Neural Computation*, *5*(3), 419–429. 181

Masci, J., Boscaini, D., Bronstein, M., & Vandergheynst, P. (2015). Geodesic convolutional neural networks on Riemannian manifolds. *IEEE International Conference on Computer Vision Workshop*, 832–840. 269

Masrani, V., Le, T. A., & Wood, F. (2019). The thermodynamic variational objective. *Neural Information Processing Systems*, *32*, 11521–11530. 352

Maturana, D., & Scherer, S. (2015). VoxNet: A 3D convolutional neural network for real-time object recognition. *IEEE/RSJ International Conference on Intelligent Robots and Systems*, 922–928. 182

Mazoure, B., Doan, T., Durand, A., Pineau, J., & Hjelm, R. D. (2020). Leveraging exploration in off-policy algorithms via normalizing flows. *Conference on Robot Learning*, 430–444. 327

Mazyavkina, N., Sviridov, S., Ivanov, S., & Burnaev, E. (2021). Reinforcement learning for combinatorial optimization: A survey. *Computers & Operations Research*, *134*, 105400. 402

McCoy, R. T., Pavlick, E., & Linzen, T. (2019). Right for the wrong reasons: Diagnosing syntactic heuristics in natural language inference. *Meeting of the Association for Computational Linguistics*, 2428–3448. 237

McCulloch, W. S., & Pitts, W. (1943). A logical calculus of the ideas immanent in nervous activity. *The Bulletin of Mathematical Biophysics*, *5*(4), 115–133. 36

Meng, C., Song, Y., Song, J., Wu, J., Zhu, J.-Y., & Ermon, S. (2021). SDEdit: Image synthesis and editing with stochastic differential equations. *International Conference on Learning Representations*. 375

Metz, L., Poole, B., Pfau, D., & Sohl-Dickstein, J. (2017). Unrolled generative adversarial networks. *International Conference on Learning Representations.* 303

Mézard, M., & Mora, T. (2009). Constraint satisfaction problems and neural networks: A statistical physics perspective. *Journal of Physiology-Paris*, *103*(1-2), 107–113. 94

Milletari, F., Navab, N., & Ahmadi, S.-A. (2016). V-Net: Fully convolutional neural networks for volumetric medical image segmentation. *International Conference on 3D Vision*, 565–571. 207

Min, J., McCoy, R. T., Das, D., Pitler, E., & Linzen, T. (2020). Syntactic data augmentation increases robustness to inference heuristics. *Meeting of the Association for Computational Linguistics*, 2339–2352. 160

Minaee, S., Boykov, Y. Y., Porikli, F., Plaza, A. J., Kehtarnavaz, N., & Terzopoulos, D. (2021). Image segmentation using deep learning: A survey. *IEEE Transactions on Pattern Analysis & Machine Intelligence*, *44*(7), 3523–3542. 184

Minsky, M., & Papert, S. A. (1969). *Perceptrons: An introduction to computational geometry.* MIT Press. 37, 236

Mirza, M., & Osindero, S. (2014). Conditional generative adversarial nets. *arXiv:1411.1784*. 305

Mishkin, D., & Matas, J. (2016). All you need is a good init. *International Conference on Learning Representations.* 113

Miyato, T., Kataoka, T., Koyama, M., & Yoshida, Y. (2018). Spectral normalization for generative adversarial networks. *International Conference on Learning Representations.* 303

Miyato, T., & Koyama, M. (2018). cGANs with projection discriminator. *International Conference on Learning Representations.* 305

Mnih, V., Badia, A. P., Mirza, M., Graves, A., Lillicrap, T., Harley, T., Silver, D., & Kavukcuoglu, K. (2016). Asynchronous methods for deep reinforcement learning. *International Conference on Machine Learning*, 1928–1937. 404

Mnih, V., Kavukcuoglu, K., Silver, D., Rusu, A. A., Veness, J., Bellemare, M. G., Graves, A., Riedmiller, M., Fidjeland, A. K., Ostrovski, G., et al. (2015). Human-level control through deep reinforcement learning. *Nature*, *518*(7540), 529–533. 402

Moerland, T. M., Broekens, J., Plaat, A., Jonker, C. M., et al. (2023). Model-based reinforcement learning: A survey. *Foundations and Trends in Machine Learning*, *16*(1), 1–118. 404

Mogren, O. (2016). C-RNN-GAN: Continuous recurrent neural networks with adversarial training. *NIPS 2016 Constructive Machine Learning Workshop.* 303

Monti, F., Boscaini, D., Masci, J., Rodola, E., Svoboda, J., & Bronstein, M. M. (2017). Geometric deep learning on graphs and manifolds using mixture model CNNs. *IEEE/CVF Computer Vision & Pattern Recognition*, 5115–5124. 267, 269

Monti, F., Shchur, O., Bojchevski, A., Litany, O., Günnemann, S., & Bronstein, M. M. (2018). Dual-primal graph convolutional networks. *arXiv:1806.00770*. 268

Montúfar, G. (2017). Notes on the number of linear regions of deep neural networks. 52, 53

Montufar, G. F., Pascanu, R., Cho, K., & Bengio, Y. (2014). On the number of linear regions of deep neural networks. *Neural Information Processing Systems*, *27*, 2924–2932. 52, 53

Moreno-Torres, J. G., Raeder, T., Alaiz-Rodríguez, R., Chawla, N. V., & Herrera, F. (2012). A unifying view on dataset shift in classification. *Pattern Recognition*, *45*(1), 521–530. 135

Morimura, T., Sugiyama, M., Kashima, H., Hachiya, H., & Tanaka, T. (2010). Nonparametric return distribution approximation for reinforcement learning. *International Conference on Machine Learning*, 799–806. 403

Müller, R., Kornblith, S., & Hinton, G. E. (2019a). When does label smoothing help? *Neural Information Processing Systems*, *32*, 4696–4705. 159

Müller, T., McWilliams, B., Rousselle, F., Gross, M., & Novák, J. (2019b). Neural importance sampling. *ACM Transactions on Graphics (TOG)*, *38*(5), 1–19. 327, 328

Mun, S., Shon, S., Kim, W., Han, D. K., & Ko, H. (2017). Deep neural network based learning and transferring mid-level audio features for acoustic scene classification. *IEEE International Conference on Acoustics, Speech and Signal Processing*, 796–800. 160

Murphy, K. P. (2022). *Probabilistic machine learning: An introduction.* MIT Press. 15

Murphy, K. P. (2023). *Probabilistic machine learning: Advanced topics.* MIT Press. 15

Murphy, R. L., Srinivasan, B., Rao, V., & Ribeiro, B. (2018). Janossy pooling: Learning deep permutation-invariant functions for variable-size inputs. *International Conference on Learning Representations*. 267

Murty, K. G., & Kabadi, S. N. (1987). Some NP-complete problems in quadratic and nonlinear programming. *Mathematical Programming*, *39*(2), 117–129. 407

Mutlu, E. C., Oghaz, T., Rajabi, A., & Garibay, I. (2020). Review on learning and extracting graph features for link prediction. *Machine Learning and Knowledge Extraction*, *2*(4), 672–704. 266

Nair, V., & Hinton, G. E. (2010). Rectified linear units improve restricted Boltzmann machines. *International Conference on Machine Learning*, 807–814. 37

Nakkiran, P., Kaplun, G., Bansal, Y., Yang, T., Barak, B., & Sutskever, I. (2021). Deep double descent: Where bigger models and more data hurt. *Journal of Statistical Mechanics: Theory and Experiment*, *2021*(12), 124003. 130, 134

Narang, S., Chung, H. W., Tay, Y., Fedus, W., Fevry, T., Matena, M., Malkan, K., Fiedel, N., Shazeer, N., Lan, Z., et al. (2021). Do transformer modifications transfer across implementations and applications? *Empirical Methods in Natural Language Processing*, 5758–5773. 236

Narayanan, D., Phanishayee, A., Shi, K., Chen, X., & Zaharia, M. (2021a). Memory-efficient pipeline-parallel DNN training. *International Conference on Machine Learning*, 7937–7947. 114

Narayanan, D., Shoeybi, M., Casper, J., LeGresley, P., Patwary, M., Korthikanti, V., Vainbrand, D., Kashinkunti, P., Bernauer, J., Catanzaro, B., et al. (2021b). Efficient large-scale language model training on GPU clusters using Megatron-LM. *International Conference for High Performance Computing, Networking, Storage and Analysis*, 1–15. 114

Nash, C., Menick, J., Dieleman, S., & Battaglia, P. W. (2021). Generating images with sparse representations. *International Conference on Machine Learning*, 7958–7968. 241, 278

Neal, R. M. (1995). *Bayesian learning for neural networks*. Springer. 159

Neimark, D., Bar, O., Zohar, M., & Asselmann, D. (2021). Video transformer network. *IEEE/CVF International Conference on Computer Vision*, 3163–3172. 241

Nesterov, Y. E. (1983). A method for solving the convex programming problem with convergence rate. *Doklady Akademii Nauk SSSR*, vol. 269, 543–547. 92

Newell, A., Yang, K., & Deng, J. (2016). Stacked hourglass networks for human pose estimation. *European Conference on Computer Vision*, 483–499. 201, 207

Neyshabur, B., Bhojanapalli, S., McAllester, D., & Srebro, N. (2017). Exploring generalization in deep learning. *Neural Information Processing Systems*, *30*, 5947–5956. 134, 418

Neyshabur, B., Bhojanapalli, S., & Srebro, N. (2018). A PAC-Bayesian approach to spectrally-normalized margin bounds for neural networks. *International Conference on Learning Representations*. 156

Ng, N. H., Gabriel, R. A., McAuley, J., Elkan, C., & Lipton, Z. C. (2017). Predicting surgery duration with neural heteroscedastic regression. *PMLR Machine Learning for Healthcare Conference*, 100–111. 74

Nguyen, Q., & Hein, M. (2017). The loss surface of deep and wide neural networks. *International Conference on Machine Learning*, 2603–2612. 411

Nguyen, Q., & Hein, M. (2018). Optimization landscape and expressivity of deep CNNs. *International Conference on Machine Learning*, 3730–3739. 411

Nichol, A. Q., & Dhariwal, P. (2021). Improved denoising diffusion probabilistic models. *International Conference on Machine Learning*, 8162–8171. 376

Nichol, A. Q., Dhariwal, P., Ramesh, A., Shyam, P., Mishkin, P., McGrew, B., Sutskever, I., & Chen, M. (2022). GLIDE: towards photorealistic image generation and editing with text-guided diffusion models. *International Conference on Machine Learning*, 16784–16804. 375, 377

Nie, W., Guo, B., Huang, Y., Xiao, C., Vahdat, A., & Anandkumar, A. (2022). Diffusion models for adversarial purification. *International Conference on Machine Learning*, 16805–16827. 375

Nix, D. A., & Weigend, A. S. (1994). Estimating the mean and variance of the target probability distribution. *IEEE International Conference on Neural Networks*, 55–60. 73

Noci, L., Roth, K., Bachmann, G., Nowozin, S., & Hofmann, T. (2021). Disentangling the roles of curation, data-augmentation and the prior in the cold posterior effect. *Neural Information Processing Systems*, *34*, 12738–12748. 159

Noé, F., Olsson, S., Köhler, J., & Wu, H. (2019). Boltzmann generators: Sampling equilibrium states of many-body systems with deep learning. *Science*, *365*(6457). 327

Noh, H., Hong, S., & Han, B. (2015). Learning deconvolution network for semantic segmentation. *IEEE International Conference on Computer Vision*, 1520–1528. 6, 179, 180, 184

Noroozi, M., & Favaro, P. (2016). Unsupervised learning of visual representations by solving jigsaw puzzles. *European Conference on Computer Vision*, 69–84. 159

Nowozin, S., Cseke, B., & Tomioka, R. (2016). f-GAN: Training generative neural samplers using variational divergence minimization. *Neural Information Processing Systems*, *29*, 271–279. 303

Nye, M., & Saxe, A. (2018). Are efficient deep representations learnable? *International Conference on Learning Representations (Workshop)*. 423

Odena, A. (2019). Open questions about generative adversarial networks. Distill, `https://distill.pub/2019/gan-open-problems`. 303

Odena, A., Dumoulin, V., & Olah, C. (2016). Deconvolution and checkerboard artifacts. Distill, `https://distill.pub/2016/deconv-checkerboard/`. 181

Odena, A., Olah, C., & Shlens, J. (2017). Conditional image synthesis with auxiliary classifier GANs. *International Conference on Machine Learning*, 2642–2651. 294, 305

Oono, K., & Suzuki, T. (2019). Graph neural networks exponentially lose expressive power for node classification. *International Conference on Learning Representations*. 269

Orhan, A. E., & Pitkow, X. (2017). Skip connections eliminate singularities. *International Conference on Learning Representations*. 203

Pablok, J. (2017). *Chess pieces and board improved*. Wikimedia Commons. Retrieved January 17, 2023. `https://commons.wikimedia.org/wiki/File:Chess_pieces_and_board_improved.svg`. 13

Papamakarios, G., Nalisnick, E. T., Rezende, D. J., Mohamed, S., & Lakshminarayanan, B. (2021). Normalizing flows for probabilistic modeling and inference. *Journal of Machine Learning Research*, *22*(57), 1–64. 327

Papamakarios, G., Pavlakou, T., & Murray, I. (2017). Masked autoregressive flow for density estimation. *Neural Information Processing Systems*, *30*, 2338–2347. 328

Park, D., Hoshi, Y., & Kemp, C. C. (2018). A multimodal anomaly detector for robot-assisted feeding using an LSTM-based variational autoencoder. *IEEE Robotics and Automation Letters*, *3*(3), 1544–1551. 350

Park, D. S., Chan, W., Zhang, Y., Chiu, C.-C., Zoph, B., Cubuk, E. D., & Le, Q. V. (2019). SpecAugment: A simple data augmentation method for automatic speech recognition. *INTERSPEECH*. 160

Park, S., & Kwak, N. (2016). Analysis on the dropout effect in convolutional neural networks. *Asian Conference on Computer Vision*, 189–204. 183

Park, S.-W., Ko, J.-S., Huh, J.-H., & Kim, J.-C. (2021). Review on generative adversarial networks: Focusing on computer vision and its applications. *Electronics*, *10*(10), 1216. 303

Parker, D. B. (1985). *Learning-logic: Casting the cortex of the human brain in silicon*. Alfred P. Sloan School of Management, MIT. 113

Parmar, N., Ramachandran, P., Vaswani, A., Bello, I., Levskaya, A., & Shlens, J. (2019). Stand-alone self-attention in vision models. *Neural Information Processing Systems*, *32*, 68–80. 241

Parmar, N., Vaswani, A., Uszkoreit, J., Kaiser, L., Shazeer, N., Ku, A., & Tran, D. (2018). Image transformer. *International Conference on Machine Learning*, 4055–4064. 241

Pascanu, R., Dauphin, Y. N., Ganguli, S., & Bengio, Y. (2014). On the saddle point problem for non-convex optimization. *arXiv:1405.4604*. 411

Pascanu, R., Montufar, G., & Bengio, Y. (2013). On the number of response regions of deep feed forward networks with piece-wise linear activations. *arXiv:1312.6098*. 53

Paschalidou, D., Katharopoulos, A., Geiger, A., & Fidler, S. (2021). Neural parts: Learning expressive 3D shape abstractions with invertible neural networks. *IEEE/CVF Computer Vision & Pattern Recognition*, 3204–3215. 327

Patashnik, O., Wu, Z., Shechtman, E., Cohen-Or, D., & Lischinski, D. (2021). StyleCLIP: Text-driven manipulation of StyleGAN imagery. *IEEE/CVF International Conference on Computer Vision*, 2085–2094. 305

Pateria, S., Subagdja, B., Tan, A.-h., & Quek, C. (2021). Hierarchical reinforcement learning: A comprehensive survey. *ACM Computing Surveys*, *54*(5), 1–35. 404

Pathak, D., Krahenbuhl, P., Donahue, J., Darrell, T., & Efros, A. A. (2016). Context encoders: Feature learning by inpainting. *IEEE/CVF Computer Vision & Pattern Recognition*, 2536–2544. 159

Patrick, M., Campbell, D., Asano, Y., Misra, I., Metze, F., Feichtenhofer, C., Vedaldi, A., & Henriques, J. F. (2021). Keeping your eye on the ball: Trajectory attention in video transformers. *Neural Information Processing Systems*, *34*, 12493–12506. 241

Peluchetti, S., & Favaro, S. (2020). Infinitely deep neural networks as diffusion processes. *International Conference on Artificial Intelligence and Statistics*, 1126–1136. 329

Peng, C., Guo, P., Zhou, S. K., Patel, V., & Chellappa, R. (2022). Towards performant and reliable undersampled MR reconstruction via diffusion model sampling. *Medical Image Computing and Computer Assisted Intervention*, *13436*, 623–633. 375

Pennington, J., & Bahri, Y. (2017). Geometry of neural network loss surfaces via random matrix theory. *International Conference on Machine Learning*, 2798–2806. 411

Perarnau, G., Van De Weijer, J., Raducanu, B., & Álvarez, J. M. (2016). Invertible conditional GANs for image editing. *NIPS 2016 Workshop on Adversarial Training*. 305

Pereyra, G., Tucker, G., Chorowski, J., Kaiser, ., & Hinton, G. (2017). Regularizing neural networks by penalizing confident output distributions. *International Conference on Learning Representations Workshop*. 158

Peters, J., & Schaal, S. (2008). Reinforcement learning of motor skills with policy gradients. *Neural Networks*, *21*(4), 682–697. 403

Peyré, G., Cuturi, M., et al. (2019). Computational optimal transport with applications to data science. *Foundations and Trends in Machine Learning*, *11*(5-6), 355–607. 303

Pezeshki, M., Mitra, A., Bengio, Y., & Lajoie, G. (2022). Multi-scale feature learning dynamics: Insights for double descent. *International Conference on Machine Learning*, 17669–17690. 134

Pham, T., Tran, T., Phung, D., & Venkatesh, S. (2017). Column networks for collective classification. *AAAI Conference on Artificial Intelligence*, 2485–2491. 267

Phuong, M., & Hutter, M. (2022). Formal algorithms for transformers. *Technical Report, DeepMind*. 236

Pieters, M., & Wiering, M. (2018). Comparing generative adversarial network techniques for image creation and modification. *arXiv:1803.09093*. 303

Pintea, S. L., Tömen, N., Goes, S. F., Loog, M., & van Gemert, J. C. (2021). Resolution learning in deep convolutional networks using scale-space theory. *IEEE Transactions on Image Processing*, *30*, 8342–8353. 183

Poggio, T., Mhaskar, H., Rosasco, L., Miranda, B., & Liao, Q. (2017). Why and when can deep-but not shallow-networks avoid the curse of dimensionality: A review. *International Journal of Automation and Computing*, *14*(5), 503–519. 53

Polyak, B. T. (1964). Some methods of speeding up the convergence of iteration methods. *USSR Computational Mathematics and Mathematical Physics*, *4*(5), 1–17. 92

Poole, B., Jain, A., Barron, J. T., & Mildenhall, B. (2023). DreamFusion: Text-to-3D using 2D diffusion. *International Conference on Learning Representations*. 375

Power, A., Burda, Y., Edwards, H., Babuschkin, I., & Misra, V. (2022). Grokking: Generalization beyond overfitting on small algorithmic datasets. *arXiv:2201.02177*. 418

Prenger, R., Valle, R., & Catanzaro, B. (2019). Waveglow: A flow-based generative network for speech synthesis. *IEEE International Conference on Acoustics, Speech and Signal Processing*, 3617–3621. 327, 328

Prince, S. J. D. (2012). *Computer vision: Models, learning, and inference*. Cambridge University Press. 15, 159

Prince, S. J. D. (2021a). Transformers II: Extensions. `https://www.borealisai.com/en/blog/tutorial-16-transformers-ii-extensions/`. 239, 240

Prince, S. J. D. (2021b). Transformers III: Training. `https://www.borealisai.com/en/blog/tutorial-17-transformers-iii-training/`. 241

Prokudin, S., Gehler, P., & Nowozin, S. (2018). Deep directional statistics: Pose estimation with uncertainty quantification. *European Conference on Computer Vision*, 534–551. 74

Provilkov, I., Emelianenko, D., & Voita, E. (2020). BPE-Dropout: Simple and effective subword regularization. *Meeting of the Association for Computational Linguistics*, 1882–1892. 237

Qi, G.-J. (2020). Loss-sensitive generative adversarial networks on Lipschitz densities. *International Journal of Computer Vision*, *128*(5), 1118–1140. 303

Qi, J., Du, J., Siniscalchi, S. M., Ma, X., & Lee, C.-H. (2020). On mean absolute error for deep neural network based vector-to-vector regression. *IEEE Signal Processing Letters*, *27*, 1485—1489. 73

Qin, Z., Yu, F., Liu, C., & Chen, X. (2018). How convolutional neural network see the world — A survey of convolutional neural network visualization methods. *arXiv:1804.11191*. 184

Qiu, S., Xu, B., Zhang, J., Wang, Y., Shen, X., De Melo, G., Long, C., & Li, X. (2020). EasyAug: An automatic textual data augmentation platform for classification tasks. *Companion Proceedings of the Web Conference 2020*, 249–252. 160

Radford, A., Kim, J. W., Hallacy, C., Ramesh, A., Goh, G., Agarwal, S., Sastry, G., Askell, A., Mishkin, P., Clark, J., et al. (2021). Learning transferable visual models from natural language supervision. *International Conference on Machine Learning*, 8748–8763. 241, 377

Radford, A., Metz, L., & Chintala, S. (2015). Unsupervised representation learning with deep convolutional generative adversarial networks. *International Conference on Learning Representations*. 284, 303

Radford, A., Wu, J., Child, R., Luan, D., Amodei, D., Sutskever, I., et al. (2019). Language models are unsupervised multitask learners. *OpenAI Blog*, *1*(8), 9. 159, 237

Rae, J. W., Borgeaud, S., Cai, T., Millican, K., Hoffmann, J., Song, F., Aslanides, J., Henderson, S., Ring, R., Young, S., et al. (2021). Scaling language models: Methods, analysis & insights from training Gopher. *arXiv:2112.11446*. 237

Raffel, C., Shazeer, N., Roberts, A., Lee, K., Narang, S., Matena, M., Zhou, Y., Li, W., Liu, P. J., et al. (2020). Exploring the limits of transfer learning with a unified text-to-text transformer. *Journal of Machine Learning Research*, *21*(140), 1–67. 239

Rajpurkar, P., Zhang, J., Lopyrev, K., & Liang, P. (2016). SQuAD: 100,000+ questions for machine comprehension of text. *Empirical Methods in Natural Language Processing*, 2383–2392. 237

Ramachandran, P., Zoph, B., & Le, Q. V. (2017). Searching for activation functions. *arXiv:1710.05941*. 38

Ramesh, A., Dhariwal, P., Nichol, A., Chu, C., & Chen, M. (2022). Hierarchical text-conditional image generation with CLIP latents. *arXiv:2204.06125*. 10, 11, 242, 375, 377

Ramesh, A., Pavlov, M., Goh, G., Gray, S., Voss, C., Radford, A., Chen, M., & Sutskever, I. (2021). Zero-shot text-to-image generation. *International Conference on Machine Learning*, 8821–8831. 242, 377

Ramsauer, H., Schäfl, B., Lehner, J., Seidl, P., Widrich, M., Adler, T., Gruber, L., Holzleitner, M., Pavlović, M., Sandve, G. K., et al. (2021). Hopfield networks is all you need. *International Conference on Learning Representations*. 239

Ranganath, R., Tran, D., & Blei, D. (2016). Hierarchical variational models. *International Conference on Machine Learning*, 324–333. 351

Ravanbakhsh, S., Lanusse, F., Mandelbaum, R., Schneider, J., & Poczos, B. (2017). Enabling dark energy science with deep generative models of galaxy images. *AAAI Conference on Artificial Intelligence*, 1488–1494. 350

Rawat, W., & Wang, Z. (2017). Deep convolutional neural networks for image classification: A comprehensive review. *Neural Computation*, *29*(9), 2352–2449. 181

Razavi, A., Oord, A. v. d., Poole, B., & Vinyals, O. (2019a). Preventing posterior collapse with delta-VAEs. *International Conference on Learning Representations*. 351

Razavi, A., Van den Oord, A., & Vinyals, O. (2019b). Generating diverse high-fidelity images with VQ-VAE-2. *Neural Information Processing Systems*, *32*, 14837–14847. 350, 351

Recht, B., Re, C., Wright, S., & Niu, F. (2011). Hogwild!: A lock-free approach to parallelizing stochastic gradient descent. *Neural Information Processing Systems*, *24*, 693–701. 114

Reddi, S. J., Kale, S., & Kumar, S. (2018). On the convergence of Adam and beyond. *International Conference on Learning Representations*. 93

Redmon, J., Divvala, S., Girshick, R., & Farhadi, A. (2016). You only look once: Unified, real-time object detection. *IEEE/CVF Computer Vision & Pattern Recognition*, 779–788. 178, 184

Reed, S., Akata, Z., Yan, X., Logeswaran, L., Schiele, B., & Lee, H. (2016a). Generative adversarial text to image synthesis. *International Conference on Machine Learning*, 1060–1069. 305

Reed, S. E., Akata, Z., Mohan, S., Tenka, S., Schiele, B., & Lee, H. (2016b). Learning what and where to draw. *Neural Information Processing Systems*, *29*, 217–225. 305

Ren, S., He, K., Girshick, R., & Sun, J. (2015). Faster R-CNN: Towards real-time object detection with region proposal networks. *Neural Information Processing Systems*, *28*. 184

Rezende, D. J., & Mohamed, S. (2015). Variational inference with normalizing flows. *International Conference on Machine Learning*, 1530–1538. 278, 327, 350

Rezende, D. J., Racanière, S., Higgins, I., & Toth, P. (2019). Equivariant Hamiltonian flows. *arXiv:1909.13739*. 329

Rezende Jimenez, D., Eslami, S., Mohamed, S., Battaglia, P., Jaderberg, M., & Heess, N. (2016). Unsupervised learning of 3D structure from images. *Neural Information Processing Systems*, *29*, 4997–5005. 350

Riad, R., Teboul, O., Grangier, D., & Zeghidour, N. (2022). Learning strides in convolutional neural networks. *International Conference on Learning Representations*. 183

Ribeiro, M. T., Wu, T., Guestrin, C., & Singh, S. (2021). Beyond accuracy: Behavioral testing of NLP models with CheckList. 4824–4828. 237

Richardson, E., Alaluf, Y., Patashnik, O., Nitzan, Y., Azar, Y., Shapiro, S., & Cohen-Or, D. (2021). Encoding in style: A StyleGAN encoder for image-to-image translation. *IEEE/CVF Computer Vision & Pattern Recognition*, 2287–2296. 305

Riedmiller, M. (2005). Neural fitted Q iteration — first experiences with a data efficient neural reinforcement learning method. *European Conference on Machine Learning*, 317–328. 402

Rippel, O., & Adams, R. P. (2013). High-dimensional probability estimation with deep density models. *arXiv:1302.5125*. 327

Rissanen, J. (1983). A universal prior for integers and estimation by minimum description length. *The Annals of Statistics*, *11*(2), 416–431. 417

Rissanen, S., Heinonen, M., & Solin, A. (2022). Generative modelling with inverse heat dissipation. *arXiv:2206.13397*. 375

Rives, A., Meier, J., Sercu, T., Goyal, S., Lin, Z., Liu, J., Guo, D., Ott, M., Zitnick, C. L., Ma, J., et al. (2021). Biological structure and function emerge from scaling unsupervised learning to 250 million protein sequences. *Proceedings of the National Academy of Sciences*, *118*(15). 236

Robbins, H., & Monro, S. (1951). A stochastic approximation method. *The Annals of Mathematical Statistics*, *22*(3), 400–407. 91

Rodrigues, F., & Pereira, F. C. (2020). Beyond expectation: Deep joint mean and quantile regression for spatiotemporal problems. *IEEE Transactions on Neural Networks and Learning Systems*, *31*(12), 5377–5389. 73

Roich, D., Mokady, R., Bermano, A. H., & Cohen-Or, D. (2022). Pivotal tuning for latent-based editing of real images. *ACM Transactions on Graphics (TOG)*, *42*(1), 1–13. 305

Rolfe, J. T. (2017). Discrete variational autoencoders. *International Conference on Learning Representations*. 350

Rombach, R., Blattmann, A., Lorenz, D., Esser, P., & Ommer, B. (2022). High-resolution image synthesis with latent diffusion models. *IEEE/CVF Computer Vision & Pattern Recognition*, 10684–10695. 376

Romero, D. W., Bruintjes, R.-J., Tomczak, J. M., Bekkers, E. J., Hoogendoorn, M., & van Gemert, J. C. (2021). FlexConv: Continuous kernel convolutions with differentiable kernel sizes. *International Conference on Learning Representations*. 183

Rong, Y., Huang, W., Xu, T., & Huang, J. (2020). DropEdge: Towards deep graph convolutional networks on node classification. *International Conference on Learning Representations*. 268

Ronneberger, O., Fischer, P., & Brox, T. (2015). U-Net: Convolutional networks for biomedical image segmentation. *International Conference on Medical Image Computing and Computer-Assisted Intervention*, 234–241. 184, 200, 207

Rosenblatt, F. (1958). The perceptron: A probabilistic model for information storage and organization in the brain. *Psychological review*, *65*(6), 386. 37

Rossi, E., Frasca, F., Chamberlain, B., Eynard, D., Bronstein, M., & Monti, F. (2020). SIGN: Scalable inception graph neural networks. *ICML Graph Representation Learning and Beyond Workshop*, *7*, 15. 267

Roy, A., Saffar, M., Vaswani, A., & Grangier, D. (2021). Efficient content-based sparse attention with routing transformers. *Transactions* *of the Association for Computational Linguistics*, *9*, 53–68. 240

Rozemberczki, B., Kiss, O., & Sarkar, R. (2020). Little ball of fur: A Python library for graph sampling. *ACM International Conference on Information & Knowledge Management*, 3133–3140. 268

Rubin, D. B., & Thayer, D. T. (1982). EM algorithms for ML factor analysis. *Psychometrika*, *47*(1), 69–76. 350

Ruder, S. (2016). An overview of gradient descent optimization algorithms. *arXiv:1609.04747*. 91

Rumelhart, D. E., Hinton, G. E., & Williams, R. J. (1985). Learning internal representations by error propagation. *Techical Report, La Jolla Institute for Cognitive Science, UCSD*. 113, 235, 350

Rumelhart, D. E., Hinton, G. E., & Williams, R. J. (1986). Learning representations by back-propagating errors. *Nature*, *323*(6088), 533–536. 113

Rummery, G. A., & Niranjan, M. (1994). *On-line Q-learning using connectionist systems*. Technical Report, University of Cambridge. 402

Russakovsky, O., Deng, J., Su, H., Krause, J., Satheesh, S., Ma, S., Huang, Z., Karpathy, A., Khosla, A., Bernstein, M., et al. (2015). ImageNet large scale visual recognition challenge. *International Journal of Computer Vision*, *115*(3), 211–252. 175, 181

Sabour, S., Frosst, N., & Hinton, G. E. (2017). Dynamic routing between capsules. *Neural Information Processing Systems*, *30*, 3856–3866. 238

Safran, I., & Shamir, O. (2017). Depth-width tradeoffs in approximating natural functions with neural networks. *International Conference on Machine Learning*, 2979–2987. 53

Saha, S., Singh, G., Sapienza, M., Torr, P. H., & Cuzzolin, F. (2016). Deep learning for detecting multiple space-time action tubes in videos. *British Machine Vision Conference*. 182

Saharia, C., Chan, W., Chang, H., Lee, C., Ho, J., Salimans, T., Fleet, D., & Norouzi, M. (2022a). Palette: Image-to-image diffusion models. *ACM SIGGRAPH*. 8, 375

Saharia, C., Chan, W., Saxena, S., Li, L., Whang, J., Denton, E., Ghasemipour, S. K. S., Ayan, B. K., Mahdavi, S. S., Lopes, R. G., et al. (2022b). Photorealistic text-to-image diffusion models with deep language understanding. *arXiv:2205.11487*. 373, 374, 375, 377

Saharia, C., Ho, J., Chan, W., Salimans, T., Fleet, D. J., & Norouzi, M. (2022c). Image super-resolution via iterative refinement. *IEEE Transactions on Pattern Analysis & Machine Intelligence*, 1–14. 375

Sainath, T. N., Kingsbury, B., Mohamed, A.-r., Dahl, G. E., Saon, G., Soltau, H., Beran, T., Aravkin, A. Y., & Ramabhadran, B. (2013). Improvements to deep convolutional neural networks for LVCSR. *IEEE Workshop on Automatic Speech Recognition and Understanding*, 315–320. 182

Saito, Y., Takamichi, S., & Saruwatari, H. (2017). Statistical parametric speech synthesis incorporating generative adversarial networks. *IEEE/ACM Transactions on Audio, Speech, and Language Processing*, *26*(1), 84–96. 303, 305

Salamon, J., & Bello, J. P. (2017). Deep convolutional neural networks and data augmentation for environmental sound classification. *IEEE Signal Processing Letters*, *24*(3), 279–283. 159

Salimans, T., Goodfellow, I., Zaremba, W., Cheung, V., Radford, A., & Chen, X. (2016). Improved techniques for training GANs. *Neural Information Processing Systems*, *29*, 2226–2234. 278, 303, 304

Salimans, T., & Ho, J. (2022). Progressive distillation for fast sampling of diffusion models. *International Conference on Learning Representations*. 377

Salimans, T., Kingma, D., & Welling, M. (2015). Markov chain Monte Carlo and variational inference: Bridging the gap. *International Conference on Machine Learning*, 1218–1226. 351

Salimans, T., & Kingma, D. P. (2016). Weight normalization: A simple reparameterization to accelerate training of deep neural networks. *Neural Information Processing Systems*, *29*, 901–909. 205

Sanchez-Lengeling, B., Reif, E., Pearce, A., & Wiltschko, A. B. (2021). A gentle introduction to graph neural networks. Distill, `https://distill.pub/2021/gnn-intro/`. 265

Sankararaman, K. A., De, S., Xu, Z., Huang, W. R., & Goldstein, T. (2020). The impact of neural network overparameterization on gradient confusion and stochastic gradient descent. *International Conference on Machine Learning*, 8469–8479. 203

Santurkar, S., Tsipras, D., Ilyas, A., & Madry, A. (2018). How does batch normalization help optimization? *Neural Information Processing Systems*, *31*, 2488–2498. 205

Sauer, A., Schwarz, K., & Geiger, A. (2022). StyleGAN-XL: Scaling StyleGAN to large diverse datasets. *ACM SIGGRAPH*. 10

Scarselli, F., Gori, M., Tsoi, A. C., Hagenbuchner, M., & Monfardini, G. (2008). The graph neural network model. *IEEE Transactions on Neural Networks*, *20*(1), 61–80. 266

Schaul, T., Quan, J., Antonoglou, I., & Silver, D. (2016). Prioritized experience replay. *International Conference on Learning Representations*. 402

Scherer, D., Müller, A., & Behnke, S. (2010). Evaluation of pooling operations in convolutional architectures for object recognition. *International Conference on Artificial Neural Networks*, 92–101. 181

Schlag, I., Irie, K., & Schmidhuber, J. (2021). Linear transformers are secretly fast weight programmers. *International Conference on Machine Learning*, 9355–9366. 238

Schlichtkrull, M., Kipf, T. N., Bloem, P., Berg, R. v. d., Titov, I., & Welling, M. (2018). Modeling relational data with graph convolutional networks. *European Semantic Web Conference*, 593–607. 269

Schmidhuber, J. (2022). Annotated history of modern AI and deep learning. *arXiv:2212.11279*. 37

Schneider, S., Baevski, A., Collobert, R., & Auli, M. (2019). wav2vec: Unsupervised pre-training for speech recognition. *INTERSPEECH*, 3465–3469. 159

Schrittwieser, J., Antonoglou, I., Hubert, T., Simonyan, K., Sifre, L., Schmitt, S., Guez, A., Lockhart, E., Hassabis, D., Graepel, T., et al. (2020). Mastering Atari, Go, chess and shogi by planning with a learned model. *Nature*, *588*(7839), 604–609. 404

Schroecker, Y., Vecerik, M., & Scholz, J. (2019). Generative predecessor models for sample-efficient imitation learning. *International Conference on Learning Representations*. 327

Schuhmann, C., Vencu, R., Beaumont, R., Kaczmarczyk, R., Mullis, C., Katta, A., Coombes, T., Jitsev, J., & Komatsuzaki, A. (2021). Laion-400m: Open dataset of clip-filtered 400 million image-text pairs. *NeurIPS Workshop on Data-centric AI*. 241

Schulman, J., Levine, S., Abbeel, P., Jordan, M., & Moritz, P. (2015). Trust region policy optimization. *International Conference on Machine Learning*, 1889–1897. 403

Schulman, J., Moritz, P., Levine, S., Jordan, M., & Abbeel, P. (2016). High-dimensional continuous control using generalized advantage estimation. *International Conference on Learning Representations*. 404

Schulman, J., Wolski, F., Dhariwal, P., Radford, A., & Klimov, O. (2017). Proximal policy optimization algorithms. *arXiv:1707.06347*. 403

Schuster, M., & Nakajima, K. (2012). Japanese and Korean voice search. *IEEE International Conference on Acoustics, Speech and Signal Processing*, 5149–5152. 237

Schwarz, J., Jayakumar, S., Pascanu, R., Latham, P., & Teh, Y. (2021). Powerpropagation: A sparsity inducing weight reparameterisation. *Neural Information Processing Systems*, *34*, 28889–28903. 156

Sejnowski, T. J. (2018). *The deep learning revolution*. MIT press. 37

Sejnowski, T. J. (2020). The unreasonable effectiveness of deep learning in artificial intelligence. *Proceedings of the National Academy of Sciences*, *117*(48), 30033–30038. 410

Selsam, D., Lamm, M., Bünz, B., Liang, P., de Moura, L., & Dill, D. L. (2019). Learning a SAT solver from single-bit supervision. *International Conference on Learning Representations*. 266

Selva, J., Johansen, A. S., Escalera, S., Nasrollahi, K., Moeslund, T. B., & Clapés, A. (2022). Video transformers: A survey. *arXiv:2201.05991*. 241

Sennrich, R., Haddow, B., & Birch, A. (2015). Neural machine translation of rare words with subword units. *Meeting of the Association for Computational Linguistics*. 237

Serra, T., Tjandraatmadja, C., & Ramalingam, S. (2018). Bounding and counting linear regions of deep neural networks. *International Conference on Machine Learning*, 4558–4566. 52

Shang, W., Sohn, K., Almeida, D., & Lee, H. (2016). Understanding and improving convolutional neural networks via concatenated rectified linear units. *International Conference on Machine Learning*, 2217–2225. 38

Sharif Razavian, A., Azizpour, H., Sullivan, J., & Carlsson, S. (2014). CNN features off-the-shelf: An astounding baseline for recognition. *IEEE Conference on Computer Vision and Pattern Recognition Workshop*, 806–813. 159

Shaw, P., Uszkoreit, J., & Vaswani, A. (2018). Self-attention with relative position representations. *ACL Human Language Technologies*, 464–468. 239

Shen, S., Yao, Z., Gholami, A., Mahoney, M., & Keutzer, K. (2020a). PowerNorm: Rethinking batch normalization in transformers. *International Conference on Machine Learning*, 8741–8751. 240

Shen, X., Tian, X., Liu, T., Xu, F., & Tao, D. (2017). Continuous dropout. *IEEE Transactions on Neural Networks and Learning Systems*, *29*(9), 3926–3937. 158

Shen, Y., Gu, J., Tang, X., & Zhou, B. (2020b). Interpreting the latent space of GANs for semantic face editing. *IEEE/CVF Computer Vision & Pattern Recognition*, 9243–9252. 305

Shi, W., Caballero, J., Huszár, F., Totz, J., Aitken, A. P., Bishop, R., Rueckert, D., & Wang, Z. (2016). Real-time single image and video super-resolution using an efficient sub-pixel convolutional neural network. *IEEE/CVF Computer Vision & Pattern Recognition*, 1874–1883. 182

Shoeybi, M., Patwary, M., Puri, R., LeGresley, P., Casper, J., & Catanzaro, B. (2019). Megatron-LM: Training multi-billion parameter language models using model parallelism. *arXiv:1909.08053*. 114

Shorten, C., & Khoshgoftaar, T. M. (2019). A survey on image data augmentation for deep learning. *Journal of Big Data*, *6*(1), 1–48. 159

Siddique, N., Paheding, S., Elkin, C. P., & Devabhaktuni, V. (2021). U-Net and its variants for medical image segmentation: A review of theory and applications. *IEEE Access*, 82031–82057. 207

Sifre, L., & Mallat, S. (2013). Rotation, scaling and deformation invariant scattering for texture discrimination. *IEEE/CVF Computer Vision & Pattern Recognition*, 1233–1240. 183

Silver, D., Huang, A., Maddison, C. J., Guez, A., Sifre, L., Van Den Driessche, G., Schrittwieser, J., Antonoglou, I., Panneershelvam, V., Lanctot, M., et al. (2016). Mastering the game of Go with deep neural networks and tree search. *Nature*, *529*(7587), 484–489. 402, 404

Silver, D., Lever, G., Heess, N., Degris, T., Wierstra, D., & Riedmiller, M. (2014). Deterministic policy gradient algorithms. *International Conference on Machine Learning*, 387–395. 403

Simonovsky, M., & Komodakis, N. (2018). GraphVAE: Towards generation of small graphs using variational autoencoders. *International Conference on Artificial Neural Networks*, 412–422. 350

Simonyan, K., & Zisserman, A. (2014). Very deep convolutional networks for large-scale image recognition. *International Conference on Learning Representations*. 177, 181

Singh, S. P., & Sutton, R. S. (1996). Reinforcement learning with replacing eligibility traces. *Machine learning*, *22*(1), 123–158. 402

Sinha, S., Zhao, Z., Goyal, A., Raffel, C., & Odena, A. (2020). Top-k training of GANs: Improving GAN performance by throwing away bad samples. *Neural Information Processing Systems*, *33*, 14638–14649. 303

Sjöberg, J., & Ljung, L. (1995). Overtraining, regularization and searching for a minimum, with application to neural networks. *International Journal of Control*, *62*(6), 1391–1407. 157

Smith, S., Elsen, E., & De, S. (2020). On the generalization benefit of noise in stochastic gradient descent. *International Conference on Machine Learning*, 9058–9067. 157

Smith, S., Patwary, M., Norick, B., LeGresley, P., Rajbhandari, S., Casper, J., Liu, Z., Prabhumoye, S., Zerveas, G., Korthikanti, V., et al. (2022). Using DeepSpeed and Megatron to train Megatron-Turing NLG 530B, a large-scale generative language model. *arXiv:2201.11990*. 237

Smith, S. L., Dherin, B., Barrett, D. G. T., & De, S. (2021). On the origin of implicit regularization in stochastic gradient descent. *International Conference on Learning Representations*. 157

Snoek, J., Larochelle, H., & Adams, R. P. (2012). Practical Bayesian optimization of machine learning algorithms. *Neural Information Processing Systems*, vol. 25, 2951–2959. 136

Sohl-Dickstein, J., Weiss, E., Maheswaranathan, N., & Ganguli, S. (2015). Deep unsupervised learning using nonequilibrium thermodynamics. *International Conference on Machine Learning*, 2256–2265. 278, 375

Sohn, K., Lee, H., & Yan, X. (2015). Learning structured output representation using deep conditional generative models. *Neural Information Processing Systems*, *28*, 3483–3491. 350

Sohoni, N. S., Aberger, C. R., Leszczynski, M., Zhang, J., & Ré, C. (2019). Low-memory neural network training: A technical report. *arXiv:1904.10631*. 114

Sønderby, C. K., Raiko, T., Maaløe, L., Sønderby, S. K., & Winther, O. (2016a). How to train deep variational autoencoders and probabilistic ladder networks. *arXiv:1602.02282*. 350

Sønderby, C. K., Raiko, T., Maaløe, L., Sønderby, S. K., & Winther, O. (2016b). Ladder variational autoencoders. *Neural Information Processing Systems*, *29*, 738–3746. 376

Song, J., Meng, C., & Ermon, S. (2021a). Denoising diffusion implicit models. *International Conference on Learning Representations*. 376

Song, Y., & Ermon, S. (2019). Generative modeling by estimating gradients of the data distribution. *Neural Information Processing Systems*, *32*, 11895–11907. 375, 377

Song, Y., & Ermon, S. (2020). Improved techniques for training score-based generative models. *Neural Information Processing Systems*, *33*, 12438–12448. 377

Song, Y., Meng, C., & Ermon, S. (2019). MintNet: Building invertible neural networks with masked convolutions. *Neural Information Processing Systems*, *32*, 11002–11012. 327

Song, Y., Shen, L., Xing, L., & Ermon, S. (2021b). Solving inverse problems in medical imaging with score-based generative models. *International Conference on Learning Representations*. 375

Song, Y., Sohl-Dickstein, J., Kingma, D. P., Kumar, A., Ermon, S., & Poole, B. (2021c). Score-based generative modeling through stochastic differential equations. *International Conference on Learning Representations*. 376, 377

Springenberg, J. T., Dosovitskiy, A., Brox, T., & Riedmiller, M. (2015). Striving for simplicity: The all convolutional net. *International Conference on Learning Representations*. 182

Srivastava, A., Rastogi, A., Rao, A., Shoeb, A. A. M., Abid, A., Fisch, A., Brown, A. R., Santoro, A., Gupta, A., Garriga-Alonso, A., et al. (2022). Beyond the imitation game: Quantifying and extrapolating the capabilities of language models. *arXiv:2206.04615*. 237

Srivastava, A., Valkov, L., Russell, C., Gutmann, M. U., & Sutton, C. (2017). VEEGAN: Reducing mode collapse in GANs using implicit variational learning. *Neural Information Processing Systems*, *30*, 3308–3318. 304

Srivastava, N., Hinton, G., Krizhevsky, A., Sutskever, I., & Salakhutdinov, R. (2014). Dropout: A simple way to prevent neural networks from overfitting. *Journal of Machine Learning Research*, *15*(1), 1929–1958. 158

Srivastava, R. K., Greff, K., & Schmidhuber, J. (2015). Highway networks. *arXiv:1505.00387*. 203

Su, H., Jampani, V., Sun, D., Gallo, O., Learned-Miller, E., & Kautz, J. (2019a). Pixel-adaptive convolutional neural networks. *IEEE/CVF Computer Vision & Pattern Recognition*, 11166–11175. 183

Su, J., Lu, Y., Pan, S., Wen, B., & Liu, Y. (2021). Roformer: Enhanced transformer with rotary position embedding. *arXiv:2104.09864*. 239

Su, W., Zhu, X., Cao, Y., Li, B., Lu, L., Wei, F., & Dai, J. (2019b). VL-BERT: Pre-training of generic visual-linguistic representations. *International Conference on Learning Representations*. 241

Sultan, M. M., Wayment-Steele, H. K., & Pande, V. S. (2018). Transferable neural networks for enhanced sampling of protein dynamics. *Journal of Chemical Theory and Computation*, *14*(4), 1887–1894. 350

Summers, C., & Dinneen, M. J. (2019). Improved mixed-example data augmentation. *Winter Conference on Applications of Computer Vision*, 1262–1270. 159

Sun, C., Myers, A., Vondrick, C., Murphy, K., & Schmid, C. (2019). VideoBERT: A joint model for video and language representation learning. *IEEE/CVF International Conference on Computer Vision*, 7464–7473. 241

Sun, C., Shrivastava, A., Singh, S., & Gupta, A. (2017). Revisiting unreasonable effectiveness of data in deep learning era. *IEEE/CVF International Conference on Computer Vision*, 843–852. 241

Sun, R.-Y. (2020). Optimization for deep learning: An overview. *Journal of the Operations Research Society of China*, *8*(2), 249–294. 91

Susmelj, I., Agustsson, E., & Timofte, R. (2017). ABC-GAN: Adaptive blur and control for improved training stability of generative adversarial networks. *ICML Workshop on Implicit Models*. 303

Sutskever, I., Martens, J., Dahl, G., & Hinton, G. (2013). On the importance of initialization and momentum in deep learning. *International Conference on Machine Learning*, 1139–1147. 92

Sutton, R. S. (1984). *Temporal credit assignment in reinforcement learning.* Ph.D., University of Massachusetts Amherst. 402

Sutton, R. S. (1988). Learning to predict by the methods of temporal differences. *Machine learning*, *3*(1), 9–44. 402

Sutton, R. S., & Barto, A. G. (1999). *Reinforcement learning: An introduction*. MIT press. 402

Sutton, R. S., & Barto, A. G. (2018). *Reinforcement learning: An introduction, 2nd Edition*. MIT Press. 16, 402

Sutton, R. S., McAllester, D., Singh, S., & Mansour, Y. (1999). Policy gradient methods for reinforcement learning with function approximation. *Neural Information Processing Systems*, *12*, 1057–1063. 403

Szegedy, C., Ioffe, S., Vanhoucke, V., & Alemi, A. A. (2017). Inception-v4, Inception-Resnet and the impact of residual connections on learning. *AAAI Conference on Artificial Intelligence*, 4278–4284. 181, 183, 411

Szegedy, C., Vanhoucke, V., Ioffe, S., Shlens, J., & Wojna, Z. (2016). Rethinking the Inception architecture for computer vision. *IEEE/CVF Computer Vision & Pattern Recognition*, 2818–2826. 155, 158, 278

Szegedy, C., Zaremba, W., Sutskever, I., Bruna, J., Erhan, D., Goodfellow, I., & Fergus, R. (2014). Intriguing properties of neural networks. *International Conference on Learning Representations*. 420

Szeliski, R. (2022). *Computer vision: Algorithms and applications, 2nd Edition*. Springer. 15

Tabak, E. G., & Turner, C. V. (2013). A family of nonparametric density estimation algorithms. *Communications on Pure and Applied Mathematics*, *66*(2), 145–164. 327

Tabak, E. G., & Vanden-Eijnden, E. (2010). Density estimation by dual ascent of the log-likelihood. *Communications in Mathematical Sciences*, *8*(1), 217–233. 327

Tan, H., & Bansal, M. (2019). LXMERT: Learning cross-modality encoder representations from transformers. *Empirical Methods in Natural Language Processing*, 5099–5110. 241

Tan, M., & Le, Q. (2019). EfficientNet: Rethinking model scaling for convolutional neural networks. *International Conference on Machine Learning*, 6105–6114. 411

Tay, Y., Bahri, D., Metzler, D., Juan, D.-C., Zhao, Z., & Zheng, C. (2021). Synthesizer: Rethinking self-attention for transformer models. *International Conference on Machine Learning*, 10183–10192. 238

Tay, Y., Bahri, D., Yang, L., Metzler, D., & Juan, D.-C. (2020). Sparse Sinkhorn attention. *International Conference on Machine Learning*, 9438–9447. 240

Tay, Y., Dehghani, M., Bahri, D., & Metzler, D. (2023). Efficient transformers: A survey. *ACM Computing Surveys*, *55*(6), 109:1–109:28. 240

Tegmark, M. (2018). *Life 3.0: Being human in the age of artificial intelligence*. Vintage. 14

Telgarsky, M. (2016). Benefits of depth in neural networks. *PMLR Conference on Learning Theory*, 1517–1539. 53, 423

Teru, K., Denis, E., & Hamilton, W. (2020). Inductive relation prediction by subgraph reasoning. *International Conference on Machine Learning*, 9448–9457. 269

Tewari, A., Elgharib, M., Bharaj, G., Bernard, F., Seidel, H.-P., Pérez, P., Zollhofer, M., & Theobalt, C. (2020). StyleRig: Rigging StyleGAN for 3D control over portrait images. *IEEE/CVF Computer Vision & Pattern Recognition*, 6142–6151. 305

Teye, M., Azizpour, H., & Smith, K. (2018). Bayesian uncertainty estimation for batch normalized deep networks. *International Conference on Machine Learning*, 4907–4916. 205

Theis, L., Oord, A. v. d., & Bethge, M. (2016). A note on the evaluation of generative models. *International Conference on Learning Representations*. 327

Thomas, P. (2014). Bias in natural actor-critic algorithms. *International Conference on Machine Learning*, 441–448. 403

Thompson, W. R. (1933). On the likelihood that one unknown probability exceeds another in view of the evidence of two samples. *Biometrika*, *25*(3-4), 285–294. 402

Thompson, W. R. (1935). On the theory of apportionment. *American Journal of Mathematics*, *57*(2), 450–456. 402

Thoppilan, R., De Freitas, D., Hall, J., Shazeer, N., Kulshreshtha, A., Cheng, H.-T., Jin, A., Bos, T., Baker, L., Du, Y., et al. (2022). LaMDA: Language models for dialog applications. *arXiv:2201.08239*. 237

Tipping, M. E., & Bishop, C. M. (1999). Probabilistic principal component analysis. *Journal of the Royal Statistical Society: Series B*, *61*(3), 611–622. 350

Tolstikhin, I., Bousquet, O., Gelly, S., & Schoelkopf, B. (2018). Wasserstein autoencoders. *International Conference on Learning Representations*. 351

Tomczak, J. M., & Welling, M. (2016). Improving variational auto-encoders using Householder flow. *NIPS Workshop on Bayesian Deep Learning*. 327

Tompson, J., Goroshin, R., Jain, A., LeCun, Y., & Bregler, C. (2015). Efficient object localization using convolutional networks. *IEEE/CVF Computer Vision & Pattern Recognition*, 648–656. 183

Torralba, A., Freeman, W., & Isola, P. (forthcoming). *Computer vision: A deep learning approach.* MIT Press. 15

Touati, A., Satija, H., Romoff, J., Pineau, J., & Vincent, P. (2020). Randomized value functions via multiplicative normalizing flows. *Uncertainty in Artificial Intelligence*, 422–432. 327

Touvron, H., Cord, M., Douze, M., Massa, F., Sablayrolles, A., & Jégou, H. (2021). Training data-efficient image transformers & distillation through attention. *International Conference on Machine Learning*, 10347–10357. 241

Tran, D., Bourdev, L., Fergus, R., Torresani, L., & Paluri, M. (2015). Learning spatiotemporal features with 3D convolutional networks. *IEEE International Conference on Computer Vision*, 4489–4497. 182

Tran, D., Vafa, K., Agrawal, K., Dinh, L., & Poole, B. (2019). Discrete flows: Invertible generative models of discrete data. *Neural Information Processing Systems*, *32*, 14692–14701. 327, 329

Tran, D., Wang, H., Torresani, L., Ray, J., LeCun, Y., & Paluri, M. (2018). A closer look at spatiotemporal convolutions for action recognition. *IEEE/CVF Computer Vision & Pattern Recognition*, 6450–6459. 181

Tsitsulin, A., Palowitch, J., Perozzi, B., & Müller, E. (2020). Graph clustering with graph neural networks. *arXiv:2006.16904*. 266

Tzen, B., & Raginsky, M. (2019). Neural stochastic differential equations: Deep latent Gaussian models in the diffusion limit. *arXiv:1905.09883*. 329

Ulku, I., & Akagündüz, E. (2022). A survey on deep learning-based architectures for semantic segmentation on 2D images. *Applied Artificial Intelligence*, *36*(1). 184

Ulyanov, D., Vedaldi, A., & Lempitsky, V. (2016). Instance normalization: The missing ingredient for fast stylization. *arXiv:1607.08022*. 205

Ulyanov, D., Vedaldi, A., & Lempitsky, V. (2018). Deep image prior. *IEEE/CVF Computer Vision & Pattern Recognition*, 9446–9454. 424

Urban, G., Geras, K. J., Kahou, S. E., Aslan, O., Wang, S., Caruana, R., Mohamed, A., Philipose, M., & Richardson, M. (2017). Do deep convolutional nets really need to be deep and convolutional? *International Conference on Learning Representations*. 424

Vahdat, A., Andriyash, E., & Macready, W. (2018a). DVAE#: Discrete variational autoencoders with relaxed Boltzmann priors. *Neural Information Processing Systems*, *31*, 1869–1878. 350

Vahdat, A., Andriyash, E., & Macready, W. (2020). Undirected graphical models as approximate posteriors. *International Conference on Machine Learning*, 9680–9689. 350

Vahdat, A., & Kautz, J. (2020). NVAE: A deep hierarchical variational autoencoder. *Neural Information Processing Systems*, *33*, 19667–19679. 346, 351, 376

Vahdat, A., Kreis, K., & Kautz, J. (2021). Score-based generative modeling in latent space. *Neural Information Processing Systems*, *34*, 11287–11302. 376

Vahdat, A., Macready, W., Bian, Z., Khoshaman, A., & Andriyash, E. (2018b). DVAE++: Discrete variational autoencoders with overlapping transformations. *International Conference on Machine Learning*, 5035–5044. 350

Van den Oord, A., Dieleman, S., Zen, H., Simonyan, K., Vinyals, O., Graves, A., Kalchbrenner, N., Senior, A., & Kavukcuoglu, K. (2016a). WaveNet: A generative model for raw audio. *ISCA Speech Synthesis Workshop*. 328

Van den Oord, A., Kalchbrenner, N., Espeholt, L., Vinyals, O., Graves, A., et al. (2016b). Conditional image generation with PixelCNN decoders. *Neural Information Processing Systems*, *29*, 4790–4798. 278

Van den Oord, A., Kalchbrenner, N., & Kavukcuoglu, K. (2016c). Pixel recurrent neural networks. *International Conference on Machine Learning*, 1747–1756. 236, 351

Van den Oord, A., Li, Y., Babuschkin, I., Simonyan, K., Vinyals, O., Kavukcuoglu, K., Driessche, G., Lockhart, E., Cobo, L., Stimberg, F., et al. (2018). Parallel WaveNet: Fast high-fidelity speech synthesis. *International Conference on Machine Learning*, 3918–3926. 328

Van Den Oord, A., Vinyals, O., et al. (2017). Neural discrete representation learning. *Neural Information Processing Systems*, *30*, 6306–6315. 350, 351

Van Hasselt, H. (2010). Double Q-learning. *Neural Information Processing Systems*, *23*, 2613–2621. 403

Van Hasselt, H., Guez, A., & Silver, D. (2016). Deep reinforcement learning with double Q-learning. *AAAI Conference on Artificial Intelligence*, 2094–2100. 403

Van Hoof, H., Chen, N., Karl, M., van der Smagt, P., & Peters, J. (2016). Stable reinforcement learning with autoencoders for tactile and visual data. *IEEE/RSJ International Conference on Intelligent Robots and Systems*, 3928–3934. IEEE. 350

Vapnik, V. (1995). *The nature of statistical learning theory*. New York: Springer Verlag. 74

Vapnik, V. N., & Chervonenkis, A. Y. (1971). On the uniform convergence of relative frequencies of events to their probabilities. *Measures of Complexity*, 11–30. 134

Vardi, G., Yehudai, G., & Shamir, O. (2022). Width is less important than depth in ReLU neural networks. *PMRL Conference on Learning Theory*, 1–33. 53

Vaswani, A., Shazeer, N., Parmar, N., Uszkoreit, J., Jones, L., Gomez, A. N., Kaiser, Ł., & Polosukhin, I. (2017). Attention is all you need. *Neural Information Processing Systems*, *30*, 5998–6008. 158, 236, 237, 238, 239, 240

Veit, A., Wilber, M. J., & Belongie, S. (2016). Residual networks behave like ensembles of relatively shallow networks. *Neural Information Processing Systems*, *29*, 550–558. 203, 423

Veličković, P., Cucurull, G., Casanova, A., Romero, A., Lio, P., & Bengio, Y. (2019). Graph attention networks. *International Conference on Learning Representations*. 236, 267, 269

Vijayakumar, A. K., Cogswell, M., Selvaraju, R. R., Sun, Q., Lee, S., Crandall, D., & Batra, D. (2016). Diverse beam search: Decoding diverse solutions from neural sequence models. *arXiv:1610.02424*. 238

Vincent, P., Larochelle, H., Bengio, Y., & Manzagol, P.-A. (2008). Extracting and composing robust features with denoising autoencoders. *International Conference on Machine Learning*, 1096–1103. 350

Voita, E., Talbot, D., Moiseev, F., Sennrich, R., & Titov, I. (2019). Analyzing multi-head self-attention: Specialized heads do the heavy lifting, the rest can be pruned. *Meeting of the Association for Computational Linguistics*, 5797–5808. 238

Voleti, V., Jolicoeur-Martineau, A., & Pal, C. (2022). MCVD: Masked conditional video diffusion for prediction, generation, and interpolation. *Neural Information Processing Systems*, *35*. 375

Vondrick, C., Pirsiavash, H., & Torralba, A. (2016). Generating videos with scene dynamics. *Neural Information Processing Systems*, *29*, 613–621. 303

Waibel, A., Hanazawa, T., Hinton, G., Shikano, K., & Lang, K. J. (1989). Phoneme recognition using time-delay neural networks. *IEEE Transactions on Acoustics, Speech, and Signal Processing*, *37*(3), 328–339. 181

Wan, L., Zeiler, M., Zhang, S., Le Cun, Y., & Fergus, R. (2013). Regularization of neural networks using DropConnect. *International Conference on Machine Learning*, 1058–1066. 158

Wan, Z., Zhang, J., Chen, D., & Liao, J. (2021). High-fidelity pluralistic image completion with transformers. *IEEE/CVF International Conference on Computer Vision*, 4692–4701. 241

Wang, A., Pruksachatkun, Y., Nangia, N., Singh, A., Michael, J., Hill, F., Levy, O., & Bowman, S. (2019a). SuperGLUE: A stickier benchmark for general-purpose language understanding systems. *Neural Information Processing Systems*, *32*, 3261–3275. 237

Wang, A., Singh, A., Michael, J., Hill, F., Levy, O., & Bowman, S. R. (2019b). GLUE: A multi-task benchmark and analysis platform for natural language understanding. *International Conference on Learning Representations*. 237

Wang, B., Shang, L., Lioma, C., Jiang, X., Yang, H., Liu, Q., & Simonsen, J. G. (2020a). On position embeddings in BERT. *International Conference on Learning Representations*. 239

Wang, C.-Y., Bochkovskiy, A., & Liao, H.-Y. M. (2022a). Yolov7: Trainable bag-of-freebies sets new state-of-the-art for real-time object detectors. *arXiv:2207.02696*. 184

Wang, P. Z., & Wang, W. Y. (2019). Riemannian normalizing flow on variational Wasserstein autoencoder for text modeling. *ACL Human Language Technologies*, 284–294. 329

Wang, S., Li, B. Z., Khabsa, M., Fang, H., & Ma, H. (2020b). Linformer: Self-attention with linear complexity. *arXiv:2006.04768*. 240

Wang, T., Liu, M., Zhu, J., Yakovenko, N., Tao, A., Kautz, J., & Catanzaro, B. (2018a). Video-to-video synthesis. *Neural Information Processing Systems*, vol. 31, 1152–1164. 303

Wang, T.-C., Liu, M.-Y., Zhu, J.-Y., Tao, A., Kautz, J., & Catanzaro, B. (2018b). High-resolution image synthesis and semantic manipulation with conditional GANs.

IEEE/CVF Computer Vision & Pattern Recognition, 8798–8807. 304, 305

Wang, W., Xie, E., Li, X., Fan, D.-P., Song, K., Liang, D., Lu, T., Luo, P., & Shao, L. (2021). Pyramid vision transformer: A versatile backbone for dense prediction without convolutions. *IEEE/CVF International Conference on Computer Vision*, 568–578. 241

Wang, W., Yao, L., Chen, L., Lin, B., Cai, D., He, X., & Liu, W. (2022b). Crossformer: A versatile vision transformer hinging on cross-scale attention. *International Conference on Learning Representations*. 241

Wang, X., Girshick, R., Gupta, A., & He, K. (2018c). Non-local neural networks. *IEEE/CVF Computer Vision & Pattern Recognition*, 7794–7803. 241

Wang, X., Wang, S., Liang, X., Zhao, D., Huang, J., Xu, X., Dai, B., & Miao, Q. (2022c). Deep reinforcement learning: A survey. *IEEE Transactions on Neural Networks and Learning Systems*. 402

Wang, Y., Mohamed, A., Le, D., Liu, C., Xiao, A., Mahadeokar, J., Huang, H., Tjandra, A., Zhang, X., Zhang, F., et al. (2020c). Transformer-based acoustic modeling for hybrid speech recognition. *IEEE International Conference on Acoustics, Speech and Signal Processing*, 6874–6878. 236

Wang, Z., Bapst, V., Heess, N., Mnih, V., Munos, R., Kavukcuoglu, K., & de Freitas, N. (2017). Sample efficient actor-critic with experience replay. *International Conference on Learning Representations*. 404

Wang, Z., Schaul, T., Hessel, M., van Hasselt, H., Lanctot, M., & Freitas, N. (2016). Dueling network architectures for deep reinforcement learning. *International Conference on Machine Learning*, 1995–2003. 403

Ward, P. N., Smofsky, A., & Bose, A. J. (2019). Improving exploration in soft-actor-critic with normalizing flows policies. *ICML Workshop on Invertible Neural Networks and Normalizing Flows*. 327

Watkins, C. J., & Dayan, P. (1992). Q-learning. *Machine learning*, *8*(3-4), 279–292. 402

Watkins, C. J. C. H. (1989). *Learning from delayed rewards*. Ph.D., University of Cambridge. 402

Wehenkel, A., & Louppe, G. (2019). Unconstrained monotonic neural networks. *Neural Information Processing Systems*, *32*, 1543–1553. 328

Wei, J., Ren, X., Li, X., Huang, W., Liao, Y., Wang, Y., Lin, J., Jiang, X., Chen, X., & Liu, Q. (2019). NEZHA: Neural contextualized representation for Chinese language understanding. *arXiv:1909.00204*. 239

Wei, J., & Zou, K. (2019). EDA: Easy data augmentation techniques for boosting performance on text classification tasks. *ACL Empirical Methods in Natural Language Processing*, 6382–6388. 160

Weisfeiler, B., & Leman, A. (1968). The reduction of a graph to canonical form and the algebra which appears therein. *NTI, Series*, *2*(9), 12–16. 268

Welling, M., & Teh, Y. W. (2011). Bayesian learning via stochastic gradient Langevin dynamics. *International Conference on Machine Learning*, 681–688. 159

Wen, Y.-H., Yang, Z., Fu, H., Gao, L., Sun, Y., & Liu, Y.-J. (2021). Autoregressive stylized motion synthesis with generative flow. *IEEE/CVF Computer Vision & Pattern Recognition*, 13612–13621. 327

Wenzel, F., Roth, K., Veeling, B. S., Świątkowski, J., Tran, L., Mandt, S., Snoek, J., Salimans, T., Jenatton, R., & Nowozin, S. (2020a). How good is the Bayes posterior in deep neural networks really? *International Conference on Machine Learning*, 10248–10259. 159

Wenzel, F., Snoek, J., Tran, D., & Jenatton, R. (2020b). Hyperparameter ensembles for robustness and uncertainty quantification. *Neural Information Processing Systems*, *33*, 6514–6527. 157

Werbos, P. (1974). Beyond regression: New tools for prediction and analysis in the behavioral sciences. *Ph.D. dissertation, Harvard University*. 113

White, T. (2016). Sampling generative networks. *arXiv:1609.04468*. 348, 350

Whitney, H. (1932). Congruent graphs and the connectivity of graphs. *Hassler Whitney Collected Papers*, 61–79. 268

Wightman, R., Touvron, H., & Jégou, H. (2021). ResNet strikes back: An improved training procedure in timm. *Neural Information Processing Systems Workshop*. 203

Williams, C. K., & Rasmussen, C. E. (2006). *Gaussian processes for machine learning*. MIT Press. 15

Williams, P. M. (1996). Using neural networks to model conditional multivariate densities. *Neural Computation*, *8*(4), 843–854. 73

Williams, R. J. (1992). Simple statistical gradient-following algorithms for connectionist reinforcement learning. *Machine learning*, *8*(3), 229–256. 403

Wilson, A. C., Roelofs, R., Stern, M., Srebro, N., & Recht, B. (2017). The marginal value of adaptive gradient methods in machine learning. *Neural Information Processing Systems*, *30*, 4148–4158. 94, 416

Wirnsberger, P., Ballard, A. J., Papamakarios, G., Abercrombie, S., Racanière, S., Pritzel, A., Jimenez Rezende, D., & Blundell, C. (2020). Targeted free energy estimation via learned mappings. *The Journal of Chemical Physics*, *153*(14), 144112. 327

Wolf, S. (2021). ProGAN: How NVIDIA generated images of unprecedented quality. `https://towardsdatascience.com/progan-how-nvidia-generated-images-of-unprecedented-quality-51c98ec2cbd2`. 290

Wolf, V., Lugmayr, A., Danelljan, M., Van Gool, L., & Timofte, R. (2021). DeFlow: Learning complex image degradations from unpaired data with conditional flows. *IEEE/CVF Computer Vision & Pattern Recognition*, 94–103. 327

Wolfe, C. R., Yang, J., Chowdhury, A., Dun, C., Bayer, A., Segarra, S., & Kyrillidis, A. (2021). GIST: Distributed training for large-scale graph convolutional networks. *NeurIPS Workshop on New Frontiers in Graph Learning*. 268

Wolpert, D. H. (1992). Stacked generalization. *Neural Networks*, *5*(2), 241–259. 157

Wong, K. W., Contardo, G., & Ho, S. (2020). Gravitational-wave population inference with deep flow-based generative network. *Physical Review D*, *101*(12), 123005. 327

Worrall, D. E., Garbin, S. J., Turmukhambetov, D., & Brostow, G. J. (2017). Harmonic networks: Deep translation and rotation equivariance. *IEEE/CVF Computer Vision & Pattern Recognition*, 5028–5037. 183

Wu, B., Xu, C., Dai, X., Wan, A., Zhang, P., Yan, Z., Tomizuka, M., Gonzalez, J., Keutzer, K., & Vajda, P. (2020a). Visual transformers: Token-based image representation and processing for computer vision. *arXiv:2006.03677*. 241

Wu, F., Fan, A., Baevski, A., Dauphin, Y. N., & Auli, M. (2019). Pay less attention with lightweight and dynamic convolutions. *International Conference on Learning Representations*. 238

Wu, H., & Gu, X. (2015). Max-pooling dropout for regularization of convolutional neural networks. *Neural Information Processing Systems*, vol. 18, 46–54. 183

Wu, J., Huang, Z., Thoma, J., Acharya, D., & Van Gool, L. (2018a). Wasserstein divergence for GANs. *European Conference on Computer Vision*, 653–668. 303

Wu, J., Zhang, C., Xue, T., Freeman, B., & Tenenbaum, J. (2016). Learning a probabilistic latent space of object shapes via 3D generative-adversarial modeling. *Neural Information Processing Systems*, *29*, 82–90. 303

Wu, N., Green, B., Ben, X., & O'Banion, S. (2020b). Deep transformer models for time series forecasting: The influenza prevalence case. *arXiv:2001.08317*. 236

Wu, R., Yan, S., Shan, Y., Dang, Q., & Sun, G. (2015a). Deep image: Scaling up image recognition. *arXiv:1501.02876*, *7*(8). 154

Wu, S., Sun, F., Zhang, W., Xie, X., & Cui, B. (2023). Graph neural networks in recommender systems: A survey. *ACM Computing Surveys*, *55*(5), 97:1–97:37. 266

Wu, Y., Burda, Y., Salakhutdinov, R., & Grosse, R. (2017). On the quantitative analysis of decoder-based generative models. *International Conference on Learning Representations*. 304

Wu, Y., & He, K. (2018). Group normalization. *European Conference on Computer Vision*, 3–19. 205, 206

Wu, Z., Lischinski, D., & Shechtman, E. (2021). Stylespace analysis: Disentangled controls for StyleGAN image generation. *IEEE/CVF Computer Vision & Pattern Recognition*, 12863–12872. 305

Wu, Z., Nagarajan, T., Kumar, A., Rennie, S., Davis, L. S., Grauman, K., & Feris, R. (2018b). BlockDrop: Dynamic inference paths in residual networks. *IEEE/CVF Computer Vision & Pattern Recognition*, 8817–8826. 204

Wu, Z., Pan, S., Chen, F., Long, G., Zhang, C., & Philip, S. Y. (2020c). A comprehensive survey on graph neural networks. *IEEE Transactions on Neural Networks and Learning Systems*, *32*(1), 4–24. 265

Wu, Z., Song, S., Khosla, A., Yu, F., Zhang, L., Tang, X., & Xiao, J. (2015b). 3D ShapeNets: A deep representation for volumetric shapes. *IEEE/CVF Computer Vision & Pattern Recognition*, 1912–1920. 182

Xia, F., Liu, T.-Y., Wang, J., Zhang, W., & Li, H. (2008). Listwise approach to learning to rank: theory and algorithm. *International Conference on Machine Learning*, 1192–1199. 73

Xia, W., Zhang, Y., Yang, Y., Xue, J.-H., Zhou, B., & Yang, M.-H. (2022). GAN inversion: A survey. *IEEE Transactions on Pattern Analysis and Machine Intelligence*, 1–17. 306

Xiao, L., Bahri, Y., Sohl-Dickstein, J., Schoenholz, S., & Pennington, J. (2018a). Dynamical isometry and a mean field theory of CNNs: How to train 10,000-layer vanilla convolutional neural networks. *International Conference on Machine Learning*, 5393–5402. 114, 183

Xiao, S., Wang, S., Dai, Y., & Guo, W. (2022a). Graph neural networks in node classification: Survey and evaluation. *Machine Vision and Applications*, *33*(1), 1–19. 266

Xiao, T., Hong, J., & Ma, J. (2018b). DNA-GAN: Learning disentangled representations from multi-attribute images. *International Conference on Learning Representations*. 305

Xiao, Z., Kreis, K., & Vahdat, A. (2022b). Tackling the generative learning trilemma with denoising diffusion GANs. *International Conference on Learning Representations*. 376

Xie, E., Wang, W., Yu, Z., Anandkumar, A., Alvarez, J. M., & Luo, P. (2021). SegFormer: Simple and efficient design for semantic segmentation with transformers. *Neural Information Processing Systems*, *34*, 12077–12090. 241

Xie, L., Wang, J., Wei, Z., Wang, M., & Tian, Q. (2016). DisturbLabel: Regularizing CNN on the loss layer. *IEEE/CVF Computer Vision & Pattern Recognition*, 4753–4762. 159

Xie, S., Girshick, R., Dollár, P., Tu, Z., & He, K. (2017). Aggregated residual transformations for deep neural networks. *IEEE/CVF Computer Vision & Pattern Recognition*, 1492–1500. 181, 203, 411

Xie, Y., & Li, Q. (2022). Measurement-conditioned denoising diffusion probabilistic model for under-sampled medical image reconstruction. *Medical Image Computing and Computer Assisted Intervention*, vol. 13436, 655–664. 375

Xing, E. P., Ho, Q., Dai, W., Kim, J. K., Wei, J., Lee, S., Zheng, X., Xie, P., Kumar, A., & Yu, Y. (2015). Petuum: A new platform for distributed machine learning on big data. *IEEE Transactions on Big Data*, *1*(2), 49–67. 114

Xing, Y., Qian, Z., & Chen, Q. (2021). Invertible image signal processing. *IEEE/CVF Computer Vision & Pattern Recognition*, 6287–6296. 327

Xiong, R., Yang, Y., He, D., Zheng, K., Zheng, S., Xing, C., Zhang, H., Lan, Y., Wang, L., & Liu, T. (2020a). On layer normalization in the transformer architecture. *International Conference on Machine Learning*, 10524–10533. 240

Xiong, Z., Yuan, Y., Guo, N., & Wang, Q. (2020b). Variational context-deformable convnets for indoor scene parsing. *IEEE/CVF Computer Vision & Pattern Recognition*, 3992–4002. 183

Xu, B., Wang, N., Chen, T., & Li, M. (2015). Empirical evaluation of rectified activations in convolutional network. *arXiv:1505.00853*. 158, 159

Xu, K., Hu, W., Leskovec, J., & Jegelka, S. (2019). How powerful are graph neural networks? *International Conference on Learning Representations*. 268

Xu, K., Li, C., Tian, Y., Sonobe, T., Kawarabayashi, K.-i., & Jegelka, S. (2018). Representation learning on graphs with jumping knowledge networks. *International Conference on Machine Learning*, 5453–5462. 267, 269, 270

Xu, K., Zhang, M., Jegelka, S., & Kawaguchi, K. (2021a). Optimization of graph neural networks: Implicit acceleration by skip connections and more depth. *International Conference on Machine Learning*, 11592–11602. 270

Xu, P., Cheung, J. C. K., & Cao, Y. (2020). On variational learning of controllable representations for text without supervision. *International Conference on Machine Learning*, 10534–10543. 350, 351

Xu, P., Kumar, D., Yang, W., Zi, W., Tang, K., Huang, C., Cheung, J. C. K., Prince, S. J. D., & Cao, Y. (2021b). Optimizing deeper transformers on small datasets. *Meeting of the Association for Computational Linguistics*. 114, 236, 241

Yamada, Y., Iwamura, M., Akiba, T., & Kise, K. (2019). Shakedrop regularization for deep residual learning. *IEEE Access*, *7*, 186126–186136. 204

Yamada, Y., Iwamura, M., & Kise, K. (2016). Deep pyramidal residual networks with separated stochastic depth. *arXiv:1612.01230*. 204

Yan, X., Yang, J., Sohn, K., & Lee, H. (2016). Attribute2Image: Conditional image generation from visual attributes. *European Conference on Computer Vision*, 776–791. 305

Yang, F., Yang, H., Fu, J., Lu, H., & Guo, B. (2020a). Learning texture transformer network for image super-resolution. *IEEE/CVF Computer Vision & Pattern Recognition*, 5791–5800. 241

Yang, G., Pennington, J., Rao, V., Sohl-Dickstein, J., & Schoenholz, S. S. (2019). A mean field theory of batch normalization. *International Conference on Learning Representations*. 204

Yang, K., Goldman, S., Jin, W., Lu, A. X., Barzilay, R., Jaakkola, T., & Uhler, C. (2021). Mol2Image: Improved conditional flow models for molecule to image synthesis. *IEEE/CVF Computer Vision & Pattern Recognition*, 6688–6698. 327

Yang, Q., Zhang, Y., Dai, W., & Pan, S. J. (2020b). *Transfer learning*. Cambridge University Press. 159

Yang, R., Srivastava, P., & Mandt, S. (2022). Diffusion probabilistic modeling for video generation. *arXiv:2203.09481*. 375, 377

Yao, W., Zeng, Z., Lian, C., & Tang, H. (2018). Pixel-wise regression using U-Net and its application on pansharpening. *Neurocomputing*, *312*, 364–371. 207

Ye, H., & Young, S. (2004). High quality voice morphing. *IEEE International Conference on Acoustics, Speech, and Signal Processing*, 1–9. 160

Ye, L., Rochan, M., Liu, Z., & Wang, Y. (2019). Cross-modal self-attention network for referring image segmentation. *IEEE/CVF Computer Vision & Pattern Recognition*, 10502–10511. 241

Ye, W., Liu, S., Kurutach, T., Abbeel, P., & Gao, Y. (2021). Mastering Atari games with limited data. *Neural Information Processing Systems*, *34*, 25476–25488. 402

Ying, R., He, R., Chen, K., Eksombatchai, P., Hamilton, W. L., & Leskovec, J. (2018a). Graph convolutional neural networks for web-scale recommender systems. *ACM SIGKDD International Conference on Knowledge Discovery & Data Mining*, 974–983. 268, 269

Ying, Z., You, J., Morris, C., Ren, X., Hamilton, W., & Leskovec, J. (2018b). Hierarchical graph representation learning with differentiable pooling. *Neural Information Processing Systems*, *31*, 4805–4815. 269

Yoshida, Y., & Miyato, T. (2017). Spectral norm regularization for improving the generalizability of deep learning. *arXiv:1705.10941*. 156

You, Y., Chen, T., Wang, Z., & Shen, Y. (2020). When does self-supervision help graph convolutional networks? *International Conference on Machine Learning*, 10871–10880. 159

Yu, F., & Koltun, V. (2015). Multi-scale context aggregation by dilated convolutions. *International Conference on Learning Representations*. 181

Yu, J., Lin, Z., Yang, J., Shen, X., Lu, X., & Huang, T. S. (2019). Free-form image inpainting with gated convolution. *IEEE/CVF International Conference on Computer Vision*, 4471–4480. 181

Yu, J., Zheng, Y., Wang, X., Li, W., Wu, Y., Zhao, R., & Wu, L. (2021). FastFlow: Unsupervised anomaly detection and localization via 2D normalizing flows. *arXiv:2111.07677*. 327

Yu, J. J., Derpanis, K. G., & Brubaker, M. A. (2020). Wavelet flow: Fast training of high resolution normalizing flows. *Neural Information Processing Systems*, *33*, 6184–6196. 327

Yu, L., Zhang, W., Wang, J., & Yu, Y. (2017). SeqGAN: Sequence generative adversarial nets with policy gradient. *AAAI Conference on Artificial Intelligence*, 2852–2858. 303

Yun, S., Han, D., Oh, S. J., Chun, S., Choe, J., & Yoo, Y. (2019). CutMix: Regularization strategy to train strong classifiers with localizable features. *IEEE/CVF International Conference on Computer Vision*, 6023–6032. 160

Zagoruyko, S., & Komodakis, N. (2016). Wide residual networks. *British Machine Vision Conference*. 203, 423

Zagoruyko, S., & Komodakis, N. (2017). Paying more attention to attention: Improving the performance of convolutional neural networks via attention transfer. *International Conference on Learning Representations*. 422

Zaheer, M., Kottur, S., Ravanbakhsh, S., Poczos, B., Salakhutdinov, R. R., & Smola, A. J. (2017). Deep sets. *Neural Information Processing Systems*, *30*, 3391–3401. 267

Zaheer, M., Reddi, S., Sachan, D., Kale, S., & Kumar, S. (2018). Adaptive methods for nonconvex optimization. *Neural Information Processing Systems*, *31*, 9815–9825. 93

Zaslavsky, T. (1975). *Facing up to arrangements: Face-count formulas for partitions of space by hyperplanes: Face-count formulas for partitions of space by hyperplanes*. Memoirs of the American Mathematical Society. 38, 40

Zeiler, M. D. (2012). ADADELTA: An adaptive learning rate method. *arXiv:1212.5701*. 93

Zeiler, M. D., & Fergus, R. (2014). Visualizing and understanding convolutional networks. *European Conference on Computer Vision*, 818–833. 181, 182, 184

Zeiler, M. D., Taylor, G. W., & Fergus, R. (2011). Adaptive deconvolutional networks for mid and high level feature learning. *IEEE International Conference on Computer Vision*, 2018–2025. 182

Zeng, H., Zhou, H., Srivastava, A., Kannan, R., & Prasanna, V. (2020). GraphSAINT: Graph sampling based inductive learning method. *International Conference on Learning Representations*. 268

Zeng, Y., Fu, J., Chao, H., & Guo, B. (2019). Learning pyramid-context encoder network for high-quality image inpainting. *IEEE/CVF Computer Vision & Pattern Recognition*, 1486–1494. 207

Zhai, S., Talbott, W., Srivastava, N., Huang, C., Goh, H., Zhang, R., & Susskind, J. (2021). An attention free transformer. 238

Zhang, A., Lipton, Z. C., Li, M., & Smola, A. J. (2023). *Dive into deep learning*. Cambridge University Press. 15

Zhang, C., Bengio, S., Hardt, M., Recht, B., & Vinyals, O. (2017a). Understanding deep learning requires rethinking generalization. *International Conference on Learning Representations*. 156, 409, 424

Zhang, C., Ouyang, X., & Patras, P. (2017b). ZipNet-GAN: Inferring fine-grained mobile traffic patterns via a generative adversarial neural network. *International Conference on emerging Networking EXperiments and Technologies*, 363–375. 303

Zhang, H., Cisse, M., Dauphin, Y. N., & Lopez-Paz, D. (2017c). mixup: Beyond empirical risk minimization. *International Conference on Learning Representations*. 160

Zhang, H., Dauphin, Y. N., & Ma, T. (2019a). Fixup initialization: Residual learning without normalization. *International Conference on Learning Representations*. 114, 206

Zhang, H., Goodfellow, I., Metaxas, D., & Odena, A. (2019b). Self-attention generative adversarial networks. *International Conference on Machine Learning*, 7354–7363. 303

Zhang, H., Hsieh, C.-J., & Akella, V. (2016a). Hogwild++: A new mechanism for decentralized asynchronous stochastic gradient descent. *IEEE International Conference on Data Mining*, 629–638. 114

Zhang, H., Xu, T., Li, H., Zhang, S., Wang, X., Huang, X., & Metaxas, D. N. (2017d). StackGAN: Text to photo-realistic image synthesis with stacked generative adversarial networks. *IEEE/CVF International Conference on Computer Vision*, 5907–5915. 304, 305

Zhang, J., & Meng, L. (2019). GResNet: Graph residual network for reviving deep gnns from suspended animation. *arXiv:1909.05729*. 267

Zhang, J., Shi, X., Xie, J., Ma, H., King, I., & Yeung, D.-Y. (2018a). GaAN: Gated attention networks for learning on large and spatiotemporal graphs. *Uncertainty in Artificial Intelligence*, 339–349. 267

Zhang, J., Zhang, H., Xia, C., & Sun, L. (2020). Graph-Bert: Only attention is needed for learning graph representations. *arXiv:2001.05140*. 267

Zhang, K., Yang, Z., & Başar, T. (2021a). Multi-agent reinforcement learning: A selective overview of theories and algorithms. *Handbook of Reinforcement Learning and Control*, 321–384. 404

Zhang, M., & Chen, Y. (2018). Link prediction based on graph neural networks. *Neural Information Processing Systems*, *31*, 5171–5181. 266

Zhang, M., Cui, Z., Neumann, M., & Chen, Y. (2018b). An end-to-end deep learning architecture for graph classification. *AAAI Conference on Artificial Intelligence*, 4438–4445. 266, 269

Zhang, Q., & Chen, Y. (2021). Diffusion normalizing flow. *Neural Information Processing Systems*, *34*, 16280–16291. 377

Zhang, R. (2019). Making convolutional networks shift-invariant again. *International Conference on Machine Learning*, 7324–7334. 182, 183

Zhang, R., Isola, P., & Efros, A. A. (2016b). Colorful image colorization. *European Conference on Computer Vision*, 649–666. 159

Zhang, S., Tong, H., Xu, J., & Maciejewski, R. (2019c). Graph convolutional networks: A comprehensive review. *Computational Social Networks*, *6*(1), 1–23. 266

Zhang, S., Zhang, C., Kang, N., & Li, Z. (2021b). iVPF: Numerical invertible volume preserving flow for efficient lossless compression. *IEEE/CVF Computer Vision & Pattern Recognition*, 620–629. 327

Zhang, X., Zhao, J., & LeCun, Y. (2015). Character-level convolutional networks for text classification. *Neural Information Processing Systems*, *28*, 649–657. 182

Zhao, H., Jia, J., & Koltun, V. (2020a). Exploring self-attention for image recognition. *IEEE/CVF Computer Vision & Pattern Recognition*, 10076–10085. 241

Zhao, J., Mathieu, M., & LeCun, Y. (2017a). Energy-based generative adversarial network. *International Conference on Learning Representations*. 303

Zhao, L., & Akoglu, L. (2020). PairNorm: Tackling oversmoothing in GNNs. *International Conference on Learning Representations*. 269

Zhao, L., Mo, Q., Lin, S., Wang, Z., Zuo, Z., Chen, H., Xing, W., & Lu, D. (2020b). UCTGAN: Diverse image inpainting based on unsupervised cross-space translation. *IEEE/CVF Computer Vision & Pattern Recognition*, 5741–5750. 241

Zhao, S., Song, J., & Ermon, S. (2017b). InfoVAE: Balancing learning and inference in variational autoencoders. *AAAI Conference on Artificial Intelligence*, 5885–5892. 351

Zhao, S., Song, J., & Ermon, S. (2017c). Towards deeper understanding of variational autoencoding models. *arXiv:1702.08658*. 351

Zheng, C., Cham, T.-J., & Cai, J. (2021). TFill: Image completion via a transformer-based architecture. *arXiv:2104.00845*. 241

Zheng, G., Yang, Y., & Carbonell, J. (2017). Convolutional normalizing flows. *arXiv:1711.02255*. 328

Zheng, Q., Zhang, A., & Grover, A. (2022). Online decision transformer. *International Conference on Machine Learning*, *162*, 27042–27059. 404

Zhong, Z., Zheng, L., Kang, G., Li, S., & Yang, Y. (2020). Random erasing data augmentation. *AAAI Conference on Artificial Intelligence*, 13001–13008. 159

Zhou, C., Ma, X., Wang, D., & Neubig, G. (2019). Density matching for bilingual word embedding. *ACL Human Language Technologies*, 1588–1598. 327

Zhou, H., Alvarez, J. M., & Porikli, F. (2016a). Less is more: Towards compact CNNs. *European Conference on Computer Vision*, 662–677. 421

Zhou, J., Cui, G., Hu, S., Zhang, Z., Yang, C., Liu, Z., Wang, L., Li, C., & Sun, M. (2020a). Graph neural networks: A review of methods and applications. *AI Open*, *1*, 57–81. 265

Zhou, K., Huang, X., Li, Y., Zha, D., Chen, R., & Hu, X. (2020b). Towards deeper graph neural networks with differentiable group normalization. *Neural Information Processing Systems*, *33*, 4917–4928. 269

Zhou, L., Du, Y., & Wu, J. (2021). 3D shape generation and completion through point-voxel diffusion. *IEEE/CVF International Conference on Computer Vision*, 5826–5835. 375

Zhou, T., Krahenbuhl, P., Aubry, M., Huang, Q., & Efros, A. A. (2016b). Learning dense correspondence via 3D-guided cycle consistency. *IEEE/CVF Computer Vision & Pattern Recognition*, 117–126. 305

Zhou, Y.-T., & Chellappa, R. (1988). Computation of optical flow using a neural network. *IEEE International Conference on Neural Networks*, 71–78. 181

Zhou, Z., & Li, X. (2017). Graph convolution: A high-order and adaptive approach. *arXiv:1706.09916*. 267

Zhou, Z., Rahman Siddiquee, M. M., Tajbakhsh, N., & Liang, J. (2018). UNet++: A nested U-Net architecture for medical image segmentation. *Deep Learning in Medical Image Analysis Workshop*, 3–11. 207

Zhu, C., Ni, R., Xu, Z., Kong, K., Huang, W. R., & Goldstein, T. (2021). GradInit: Learning to initialize neural networks for stable and efficient training. *Neural Information Processing Systems*, *34*, 16410–16422. 113

Zhu, J., Krähenbühl, P., Shechtman, E., & Efros, A. A. (2016). Generative visual manipulation on the natural image manifold. *European Conference on Computer Vision*, 597–613. 306

Zhu, J., Shen, Y., Zhao, D., & Zhou, B. (2020a). In-domain GAN inversion for real image editing. *European Conference on Computer Vision*, 592–608. 305

Zhu, J.-Y., Park, T., Isola, P., & Efros, A. A. (2017). Unpaired image-to-image translation using cycle-consistent adversarial networks. *IEEE/CVF International Conference on Computer Vision*, 2223–2232. 300, 305

Zhu, X., Su, W., Lu, L., Li, B., Wang, X., & Dai, J. (2020b). Deformable DETR: Deformable transformers for end-to-end object detection. *International Conference on Learning Representations*. 241

Zhuang, F., Qi, Z., Duan, K., Xi, D., Zhu, Y., Zhu, H., Xiong, H., & He, Q. (2020). A comprehensive survey on transfer learning. *Proceedings of the IEEE*, *109*(1), 43–76. 159

Ziegler, Z., & Rush, A. (2019). Latent normalizing flows for discrete sequences. *International*

Conference on Machine Learning, 7673–7682. 327, 328

Zong, B., Song, Q., Min, M. R., Cheng, W., Lumezanu, C., Cho, D., & Chen, H. (2018). Deep autoencoding Gaussian mixture model for unsupervised anomaly detection. *International Conference on Learning Representations*. 350

Zou, D., Cao, Y., Zhou, D., & Gu, Q. (2020). Gradient descent optimizes over-parameterized deep ReLU networks. *Machine Learning*, *109*, 467–492. 410

Zou, D., Hu, Z., Wang, Y., Jiang, S., Sun, Y., & Gu, Q. (2019). Layer-dependent importance sampling for training deep and large graph convolutional networks. *Neural Information Processing Systems*, *32*, 11247–11256. 268

Zou, H., & Hastie, T. (2005). Regularization and variable selection via the elastic net. *Journal of the Royal Statistical Society: Series B*, *67*(2), 301–320. 156

Zou, Z., Chen, K., Shi, Z., Guo, Y., & Ye, J. (2023). Object detection in 20 years: A survey. *Proceedings of the IEEE*. 184

Index